

Université de Strasbourg
Ecole Doctorale Sciences de la Terre et de l'Univers

THÈSE DE DOCTORAT

Pour obtenir le grade de
DOCTEUR EN SCIENCES
Spécialité Sciences de la Terre et de l'Univers
de l'Université de Strasbourg

Par
Elise Kali

**De la déformation long-terme à court-terme sur les failles normales du
Sud - Tibet : approche géochronologique multi-méthodes**
(^{10}Be , ^{26}Al , ($\text{U-Th}/\text{He}$, $^{40}\text{Ar}/^{39}\text{Ar}$, U/Pb).

Soutenue le 22 novembre 2010
devant le jury composé de :

Luis Rivera	Université de Strasbourg	Directeur de Thèse
Jérôme van der Woerd	Université de Strasbourg	Co-Encadrant
Philippe-Hervé Leloup	Université de Lyon I	Co-Encadrant
Daniel Stockli	University of Kansas	Rapporteur
Jean-François Ritz	Université de Montpellier II	Rapporteur
Gianreto Manatschal	Université de Strasbourg	Rapporteur
Nicolas Arnaud	Université de Montpellier II	Co-Encadrant
Gweltaz Mahéo	Université de Lyon I	Co-Encadrant
Robin Lacassin	Institut de Physique du Globe de Paris	Examinateur

Image de couverture:

Vue des faces nord de deux des plus hauts massifs du globe: à gauche, le Lhotse (8516 m), à droite, l'Everest, ou Chomolangma en tibétain (8848 m), depuis le côté ouest du Massif de l'Ama Drime, un des deux sites d'étude de cette thèse. Au premier plan s'étend la plaine de la rivière transhimalayenne de l'Arun, à travers laquelle subsistent les reliques d'un paléo-lac vieux de plus de 200000 ans.

Université de Strasbourg
Ecole Doctorale Sciences de la Terre et de l'Univers

THÈSE DE DOCTORAT

Pour obtenir le grade de
DOCTEUR EN SCIENCES
Spécialité Sciences de la Terre et de l'Univers
de l'Université de Strasbourg

Par
Elise Kali

**De la déformation long-terme à court-terme sur les failles normales du
Sud - Tibet : approche géochronologique multi-méthode
(^{10}Be , ^{26}Al , ($\text{U-Th}/\text{He}$, $^{40}\text{Ar}/^{39}\text{Ar}$; U/Pb).**

Soutenue le 22 novembre 2010
devant le jury composé de :

Luis Rivera	Université de Strasbourg	Directeur de Thèse
Jérôme van der Woerd	Université de Strasbourg	Co-Encadrant
Philippe-Hervé Leloup	Université de Lyon I	Co-Encadrant
Daniel Stockli	University of Kansas	Rapporteur
Jean-François Ritz	Université de Montpellier II	Rapporteur
Gianreto Manatschal	Université de Strasbourg	Rapporteur
Nicolas Arnaud	Université de Montpellier II	Co-Encadrant
Gweltaz Mahéo	Université de Lyon I	Co-Encadrant
Robin Lacassin	Institut de Physique du Globe de Paris	Examinateur

Remerciements

Je tiens d'abord à remercier mes encadrants, Jérôme, Hervé, Gweltaz et Nicolas, qui par leur collaboration, m'ont permis de travailler sur un sujet passionnant dans la continuité de mon travail de master. Merci à Jérôme d'avoir accepté de prendre la suite du master encadré par Nicolas, Hervé et Gweltaz, en ajoutant le volet de la tectonique active au sujet de thèse. Merci pour sa disponibilité, sa gentillesse et sa bonne humeur qui m'ont permis de mener à bien cette thèse en trois ans dans de bonnes conditions. Merci à Nicolas de m'avoir introduit dans les dédales de l'argon, à Hervé de m'avoir fait escalader des montagnes et à Gweltaz pour m'avoir appris à lire dans les apatites. Merci également à Luis Rivera mon cinquième chef !

Je tiens également à remercier les rapporteurs, Jean-François Ritz, Daniel Stockli et Gianreto Manatschal, pour avoir accepté de faire partie du jury de thèse.

Un grand merci à Robert Thuizat qui m'a transmis tout son savoir pour traquer le beryllium dans les cailloux les plus réticents et qui m'a beaucoup aidé à la préparation des échantillons datés au ^{10}Be . Merci à Liu-Zheng Jing pour sa collaboration et la mission de terrain de 2007 à l'Ama Drime. Merci à Mima pour sa conduite de pilote lors de cette mission.

Merci à tout ceux qui sont intervenus dans l'analyse des échantillons, René Boutin pour l'ICP-MS à l'EOST, l'équipe du CEREGE à Aix-en-Provence, Paul Clapier pour les analyses de roches totales et pour son aide à Lyon. Merci à Patrick Monié et Michaël Bonno qui ont analysé les apatites, permis les datations (U-Th)/He et qui ont résisté à la pression des appels hebdomadaires dans les derniers mois de rédaction.

Merci aux stagiaires et étudiants en master, Julie Baron, Sofiane Gharbi, Jean-Rémi Dujardin et Lilas Collet.

Merci à Philippe Goncalves qui m'a présenté à PerpleX.

Passons maintenant aux amis et à la famille... 50 thésards à l'EOST... sacrée ambiance !!! Merci aux doctorants et ex-doctorants de l'EOST pour les fous rires lors de nos discussions perchées, allant de Pouilly à super-chinchilla et son concombre de mer, et aboutissant toujours à la question wikipédia du midi complètement farfelue ! Je me risque à des remerciements nominatifs et j'espère n'oublier personne car la liste est longue...

Merci à mes co-bureaux Zac, l'imperturbable, qui m'a sauvé la vie plusieurs fois avec ses petits programmes, Aude avec qui on a partagé les joies du beryllium et de l'aluminium et Indrah qui est la plus forte, même en sismologie ! Merci à Aurore et Julia pour avoir formé le trio de choc ! Merci à Etienne pour la relecture rapide des parties en français ! Merci à Jérémy pour la formation ArcGis qui m'a permis de faire des belles figures ! Merci à tous ceux qui m'ont aidée pendant ces trois ans et particulièrement dans l'urgence de la fin de rédaction ! Petit clin d'œil à Magali qui m'a tenu compagnie virtuellement depuis Montpellier pendant nos derniers jours de rédaction. Merci à Marie-Laure, Mélanie, Estelle, Marco, Vincent, Antony, Pierre, Julien, Max, Florence, Francis, Geoffroy, Florian, Manu, Angèle, Flavia, Thomas, Moussa, Chloé, Benoît, Joachim, Edouard, Emilie, Paul, Alexandra, ..., et les autres thésards pour tous les bons moments passés ensemble.

Merci Violette, Côme, François, et la famille d'avoir pris le temps et fait tant de chemin pour venir à la soutenance un lundi, merci aux amis et proches qui sont venus, merci à ceux qui y ont pensé, faute de venir !! Merci au soutien des amis de la famille. Merci à ma mère de m'avoir soutenu et pour sa soupe de courge qui m'a permis de ne plus décoller de mon bureau pourachever cette thèse. Merci à mon frère Vincent, de m'avoir donné le goût des sciences en essayant de m'inculquer les bases de la physique nucléaire en classe de 6^{ème}. Mais préférant ramasser sable et cailloux sur les plages de Guadeloupe (merci à mon père), j'ai choisi la voie de la géologie. Un grand merci à Sophie qui m'a appris les rudiments d'Indesign, ce qui m'a sauvé pour les derniers mois et m'a permis de faire une mise en page sans trop d'embûches. Merci aussi pour son accueil à Lyon !

Et le MERCI final pour Damien, ma moitié, qui a aussi été mis à contribution pour le broyage des échantillons, qui a permis que cette thèse se passe sereinement et qui m'a soutenue et supportée tout ce temps.

SOMMAIRE

1. INTRODUCTION	15
1.1. Les modèles tectoniques du Tibet	17
1.2. L'extension au Tibet	22
<i>1.2.1. Les marqueurs de l'extension au Sud-Tibet</i>	22
<i>1.2.2. Le rôle de l'extension dans l'évolution du plateau tibétain</i>	27
1.3. La démarche de ce travail : l'approche géochronologique multi-méthode	28
2. LA DEFORMATION LONG-TERME SUR LES FAILLES NORMALES DU SUD TIBET	33
2.1. L'utilisation de la thermochronologie et de la pétrologie dans la quantification des vitesses de déformation.	33
<i>2.1.1. L'utilisation des âges</i>	34
2.1.1.1. La construction de trajets Pression – Température	34
2.1.1.2. La notion de température de fermeture	34
2.1.1.3. La relation âge-altitude	36
<i>2.1.2. Les méthodes de datation</i>	36
2.1.2.1. L'équation d'âge générale	36
2.1.2.2. La méthode U/Pb sur zircon et monazite	37
2.1.2.3. La méthode (U-Th)/He sur apatite	37
<i>2.1.3. La méthode $^{40}\text{Ar}/^{39}\text{Ar}$</i>	39
2.1.3.1. La séparation des minéraux, l'analyse et la présentation des résultats d' $^{40}\text{Ar}/^{39}\text{Ar}$	39
2.1.3.2. Le protocole de chauffage spécifique pour les feldspaths	39
2.1.3.3. Les rapports K/Ca et Cl/K	40
2.1.3.4. La modélisation des résultats d'analyses $^{40}\text{Ar}/^{39}\text{Ar}$ sur feldspaths potassiques	41
2.2. Evaluation des vitesses d'exhumation au niveau du massif de l'Ama Drime, Trajet Pression-température-temps-déformation	49
<i>2.2.1. Exhumation history of the deepest central Himalayan rocks (Ama Drime range): key P-T-D-t constraints on orogenic models. (Published in Tectonics review)</i>	49
<i>2.2.2. Les résultats d'$^{40}\text{Ar}/^{39}\text{Ar}$ sur feldspaths issus de la zone de cisaillement de Kharta</i>	83
2.2.2.1. Introduction	83
2.2.2.2. Les échantillons	84
2.2.2.3. Les résultats $^{40}\text{Ar}/^{39}\text{Ar}$ et les interprétations	88
2.2.2.4. Discussion	94
<i>2.2.3. Conclusion sur la déformation long terme du massif de l'Ama Drime</i>	99

2.3. Evaluation des vitesses d'exhumation et d'extension au niveau du détachement de la chaîne du Nyainqntenglha : thermochronologie moyenne à basse température.	111
2.3.1. Contexte géologique	111
2.3.1.1. Le Massif du Nyainqntanglha dans le contexte du Bloc de Lhasa	111
2.3.1.2. Géologie du Massif du Nyainqntanglha	115
2.3.1.3. La faille de détachement du Nyainqntanglha	119
2.3.1.4. Initiation de l'extension et vitesses d'exhumation le long du détachement.	122
2.3.2. Les Ages $^{40}\text{Ar}/^{39}\text{Ar}$, résultats et interprétations	124
2.3.2.1. Le site de Chepa-Ouest	124
2.3.2.2. Le site de Kumulalungpa	132
2.3.2.3. Le site de Gulu	133
2.3.3. Les Ages (U-Th)/He	139
2.3.4. Discussion - Conclusion	141
 3. LA DÉFORMATION COURT-TERME SUR LES FAILLES NORMALES ACTIVES DU SUD TIBET	153
3.1. La détermination de vitesses de glissement quaternaires à l'aide des datations aux isotopes cosmogéniques (^{10}Be et ^{26}Al in situ)	153
3.1.1. La datation ^{10}Be - ^{26}Al	153
3.1.1.1. Origine des isotopes cosmogéniques	154
3.1.1.2. Le calcul des âges	156
3.1.1.3. L'utilisation de deux isotopes cosmogéniques : ^{26}Al et ^{10}Be	157
3.1.1.4. L'âge d'exposition	158
3.1.2. Les incertitudes	160
3.1.2.1. Les erreurs aléatoires	160
3.1.2.2. Les erreurs systématiques	161
3.1.2.3. L'échantillonnage	161
3.1.2.4. Les erreurs sur l'âge des surfaces	162
3.1.2.5. La quantification des décalages	163
3.2. Late Pleistocene-Holocene slip-rates on the normal faults of the Ama Drime horst (South Tibet) from in situ ^{10}Be and ^{26}Al cosmogenic isotopes dating	165
3.2.1. Introduction	166
3.2.2. Geological and geomorphological context	168
3.2.3. Description of faulted structures	173
3.2.3.1. The Kharta Fault	173

3.2.3.2. The Mabja Fault	192
3.2.3.3. The Dinggye Fault	197
3.2.4. Surface dating and vertical throw rates	205
3.2.4.1. Dating Method	205
3.2.4.2. Results	206
3.2.4.3. Vertical throw rates in the Ama Drime – Mabja area	212
3.2.5. Discussion and conclusion	213
3.2.5.1. Terrace age and formation modulated by climate	213
3.2.5.2. Consistent slip rates on the normal faults of south Tibet	214
3.2.5.3. Implication for the geodynamic of Tibet	215
3.3. Late Pleistocene kinematic constraints on the active faults of the Gulu-Yangbajain rift from cosmogenic nuclide dating	231
3.3.1. Introduction	232
3.3.2. The study area	232
3.3.3. The Damxung site	240
3.3.4. Yangbajain basin	246
3.3.4.1. The West-Chepa moraine site	246
3.3.4.2. The Gyekar terraces site	251
3.3.5. The Gulu half-graben	256
3.3.5.1. North Gulu moraine site	256
3.3.5.2. The south Gulu terrace site	261
3.3.6. Discussion and conclusion	267
4. DISCUSSION – CONCLUSION	279
5. RÉFÉRENCES BIBLIOGRAPHIQUES	291
6. ANNEXE	315
ANNEXE A : Leloup et al., 2010, EPSL	
ANNEXE B : Appendix & Data Repository of the Kali et al., 2010, Tectonics	
ANNEXE C : Example of photos of dated apatites (T5G2 & T5G3)	
ANNEXE D : Examples of 40Ar/39Ar data	
ANNEXE E : Analysis of the Helium Standard, Durango Fluoroapatite	
ANNEXE F : Protocole d'extraction des isotopes cosmogéniques	

Partie 1

INTRODUCTION

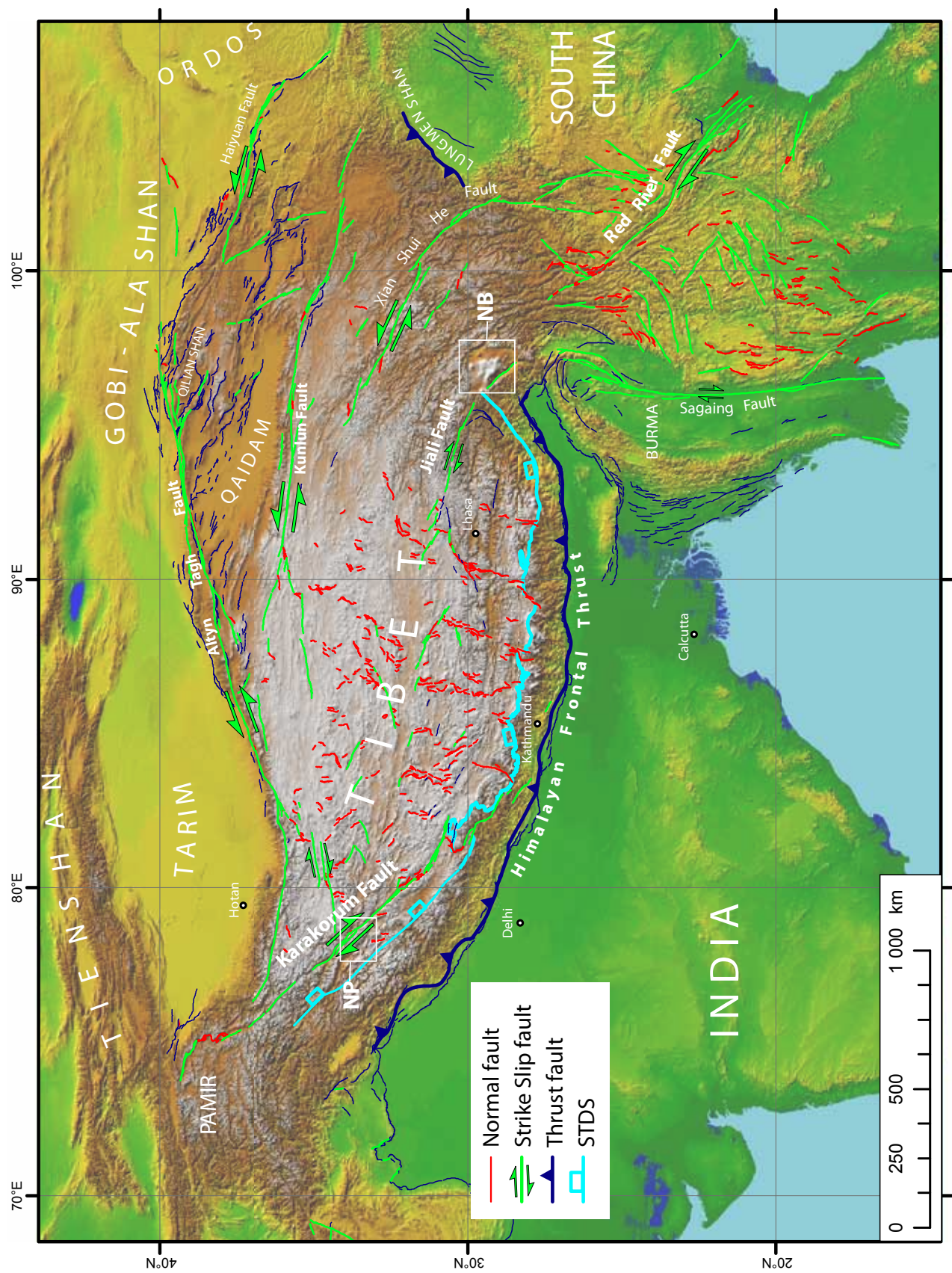


Figure I.1: Map of the active faults of Tibet. Faults traces are from Armijo et al. (1986), and a compilation of IPG Paris (pers. comm. R. Lacassin) derived from satellite image interpretations (Landsat, SPOT, ASTER, Quickbird and Ikonos), air photos, and field work. (GTOPO30). NP = Namche Barwa, NB = Nanga Parbat, STDS = South Tibetan Detachment System.

1. INTRODUCTION

La chaîne de l'Himalaya et le plateau tibétain constituent les reliefs les plus imposants de la surface terrestre issus d'une collision continentale. A l'origine de cette collision, il y a la convergence entre la plaque indienne et la plaque asiatique à une vitesse entre 8 et 3 cm/an depuis 50 millions d'années. C'est la seule zone de collision qui comporte des sommets à plus de 8000 m d'altitude, un plateau aussi vaste et un épaississement de la croûte continentale jusqu'à 80 km d'épaisseur.

La convergence Inde-Asie est accommodée par différents types de déformations au niveau du plateau Tibétain. Les chevauchements accommodent du raccourcissement essentiellement au front Himalayen, au nord-est du Tibet et dans le Tien Shan, les décrochements permettent le coulissement horizontal de blocs (faille du Fleuve rouge, de l'Altyn Tagh) et les failles normales accommodent de l'extension syn-convergence (Figure I.1). C'est à ces failles normales que nous allons nous intéresser dans cette thèse.

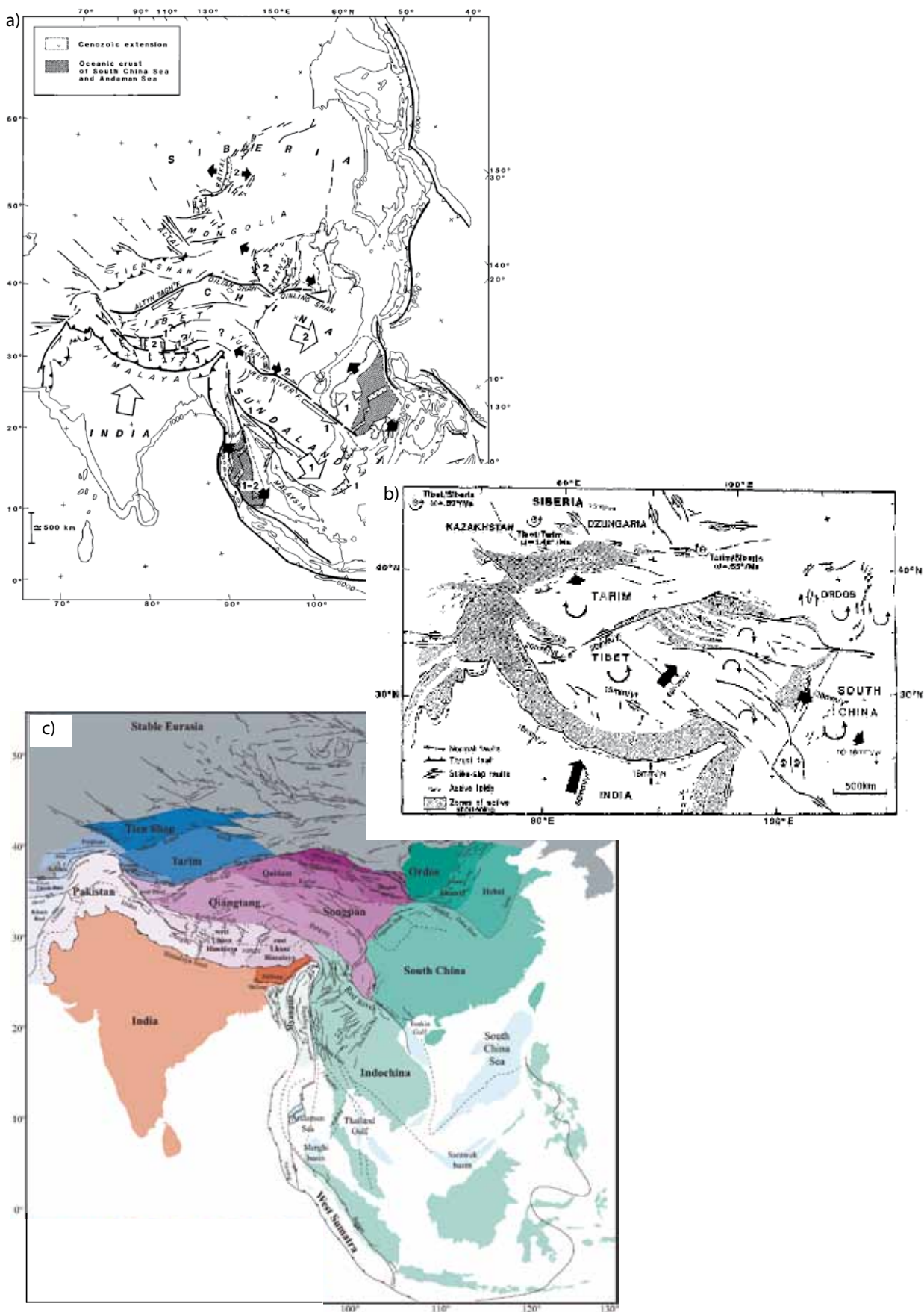


Figure I.2: a) Model of large scale Cenozoic extrusion in eastern Asia, insight from plasticine analogical model, Peltzer and Tapponnier 1988. b) Simplified kinematic model of extrusion transfer from Tibet to South-China, across Qinghai and Sichuan, by rotation and escape, Avouac and Tapponnier 1993. c) Block contours defined from active fault map of Asia, from Replumaz et al., 2003.

1.1. Les modèles tectoniques du Tibet

De nombreux modèles tectoniques (cinématique, géophysique, géodynamique) ont été proposés pour expliquer la manière dont s'est formé le plateau tibétain au cours de la collision. Depuis trente années, deux écoles s'opposent.

D'une part, des modèles de déformation localisée souvent appelés « modèles de blocs » proposent une évolution de la collision Inde-Asie à travers le mouvement de blocs non ou peu déformables à l'aide de contacts majeurs sur lesquels s'effectuent l'essentiel des déplacements (Peltzer et Tapponnier, 1988 ; Tapponnier et al., 2001 ; Replumaz et Tapponnier, 2003). Les contacts majeurs limitant les blocs non déformés correspondent aux grands décrochements et aux chevauchements principaux (Figure I.2). Dans ce type de modèle, la déformation interne des blocs joue un rôle beaucoup moins important et n'est pas prise en compte. Ainsi, ces modèles de blocs rigides expliquent bien les mouvements horizontaux par contre, l'épaisseur crustale est moins bien pris intégré. Il est envisagé à la fois comme résultant de l'activation de chevauchements qui se branchent sur les décrochements et à la fois de la capture de sédiments dans des bassins rendus endoréiques par la croissance du relief. Ces chevauchements s'enracinent au niveau de subductions continentales réactivant les anciennes sutures (Mattauer et al., 1986 ; Tapponnier et al., 2001 ; Métivier et al., 1998 ; Meyer et al., 1996). Ce type de modèle implique donc une certaine « hiérarchie » de déformation et une évolution par étape : les décrochements et le chevauchement frontal himalayen montrent des déplacements importants et les structures accommodant la déformation interne montrent des déplacements moindres, et la déformation progresse par étape, une phase d'extrusion Oligo-Miocène de l'Indochine suivie de l'extrusion Tibet-Chine du sud Plio-Quaternaire, et de l'épaisseur progressif du sud du Tibet vers le Nord-Est.

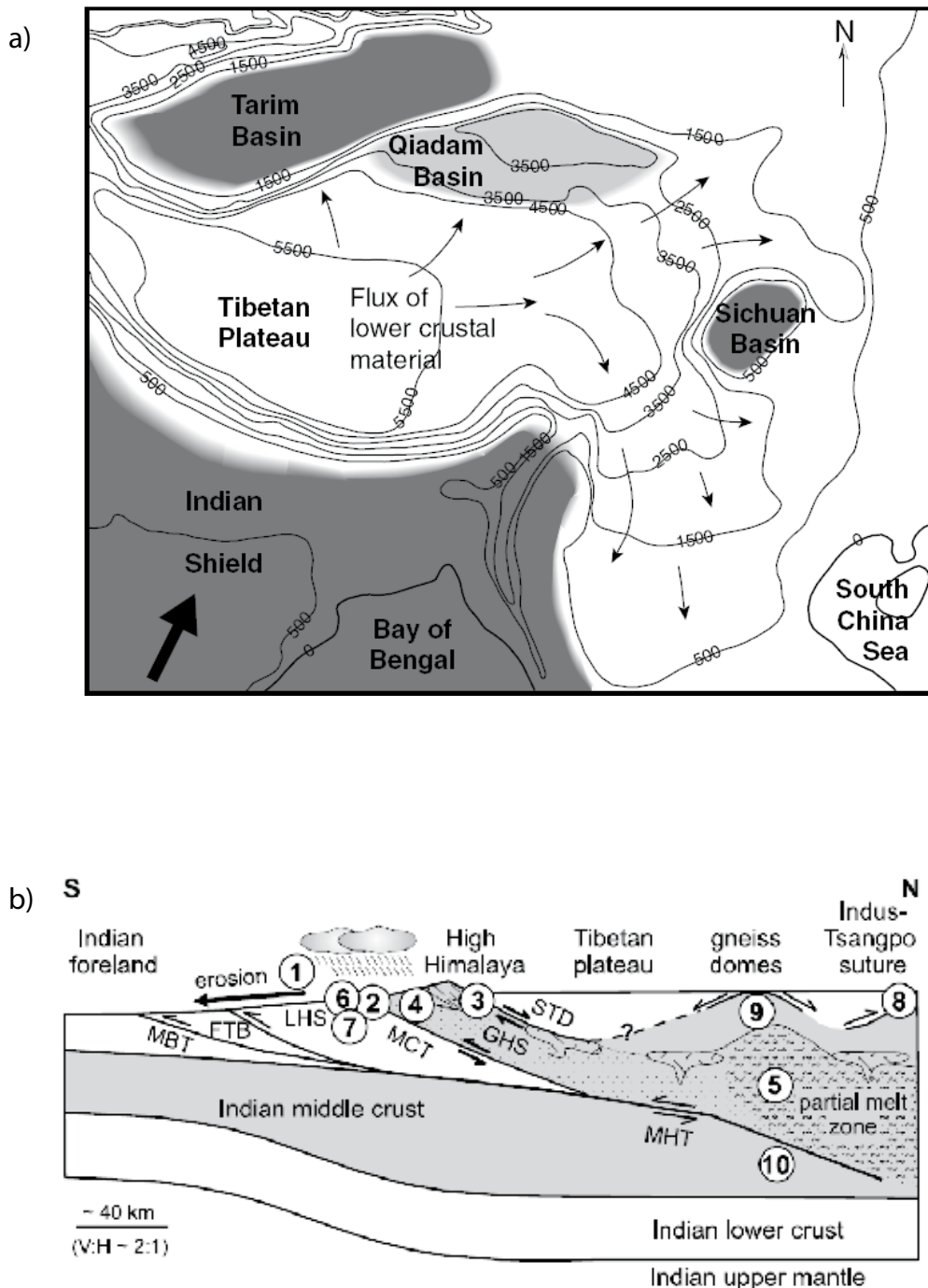


Figure I.3: a) Representation of lower crust escapes. *Contour plot of smoothed elevations of Tibetan Plateau and surrounding regions. Contour interval is 1000 m. Areas shaded in dark gray represent regions of cold, strong, continental material; light gray area represents intermediate strength; and white areas represent weak crustal regions. Thus, lower crust escapes from beneath thickened, elevated central plateau through regions where crust is weak.* From Clark and Royden 2000. b) *Application of the crustal channel flow to Himalaya-South-Tibet zone. Illustration of a representative north-south tectonic cross section of the Himalaya and southern Tibet showing the processes that act together to provide an internally consistent explanation for the dynamical behavior of this system.* From Beaumont et al., 2004.

D'autre part, les modèles de déformation diffuse suggèrent que le mécanisme principal de la convergence Inde-Asie se fait par épaississement continu et homogène de la croûte et du manteau lithosphérique, suivi de la délamination de la partie mantellique qui serait à l'origine de la fabrication d'un relief de plateau (Figure I.3). Ces modèles laissent peu de place aux mouvements horizontaux de blocs cohérents et minimisent le rôle des grands décrochements (England et Houseman, 1989 ; England et Molnar, 2005). Ce type de modèle implique un style de déformation plus homogène à travers le plateau et associe généralement l'extension ou la présence de failles normales au sein du plateau à de l'effondrement gravitaire post-délamination. Plus récemment, il a été proposé qu'un flux canalisé de croûte inférieure, (« lower crustal channel flow ») expulsé gravitairement ou aspiré dynamiquement du haut plateau vers ses bordures soit responsable de la formation des bordures nord-est et sud-est du Tibet (e.g., Bird, 1991; Royden et al., 1997; Clark and Royden, 2000) et ait permis le maintien dynamique de la chaîne Himalayenne lors du fonctionnement concomitant du MCT (Main Central Thrust) et du STDS (South Tibetan Detachment System) (e.g., Beaumont et al., 2001 ; Burchfiel et al., 1992 ; Searle, 1999).

Pour chacun de ces modèles, les données géologiques ou géophysiques s'ajustent partiellement. Par exemple, les décrochements actuels actifs de 1500 à 2000 km de long aux vitesses centimétriques (Altyn Tagh, Kunlun, Karakorum) ou ayant fonctionné dans le passé à une vitesse de plusieurs centimètres par an (Fleuve Rouge) impliquent la présence de discontinuités lithosphériques majeures. Les bassins du Tarim et du Sichuan, peu déformés intérieurement, illustrent également la discontinuité de la déformation et l'existence de blocs non déformables. L'importance de l'évidence géologique de ces discontinuités est discutée du point de vue cinématique. Par exemple, la discussion s'est portée sur l'importance relative de la déformation absorbée par les décrochements bordiers du Tibet par rapport à la déformation interne du plateau au vue des champs de déplacements géodésiques issus de mesures GPS. Ainsi, la déformation interne du plateau pourrait égaler la déformation accommodée par les grandes failles.

D'autre part, la déformation à l'intérieur des blocs a été bien observée : les failles normales, associées ou non avec des décrochements, qui jalonnent le plateau Tibétain montrent que l'extension est le régime de déformation dominant actuellement au centre et au sud du Tibet (Drury et Rothery, 1984 ; Armijo et al., 1986 ; Tapponnier and Molnar, 1977 ; Taylor et al., 2003). On notera cependant

que la région du haut plateau du Tibet (2 millions de km²) affectée par l'extension est loin de l'homogénéité de l'extension de la province du Basin and Range, certes moins étendue (500 000 km²). Il faut souligner d'une part que les régions les plus hautes du plateau ne sont pas en extension (région ou bloc de Tianshuihai au nord-ouest du plateau, 60000 km², ou région de Kokoxili, 100 000 km²) et d'autre part, que la géométrie et l'ampleur de l'extension change entre le nord et le sud de la zone de Karakorum-Jiali ou suture de Bangong (Armijo et al., 1986 ; Blisniuk et al., 2003). Pour prendre en compte les particularités des différents modèles, certains proposent des modèles intermédiaires.

A travers les études géodésiques (Figure I.4), les mesures de champs GPS sont interprétées avec des modèles de petits blocs à l'intérieur des grands blocs principaux pour prendre en compte la déformation interne (Figure I.5) (Shen et al., 2005 ; Thatcher, 2007 ; Meade, 2007 ; Holt et al., 2000). Ces modèles de « sous-blocs » à l'intérieur des grands blocs n'enlèvent rien à la hiérarchisation des déformations qu'implique ce type de modèle. Taylor et al. (2003) proposent que les petits systèmes de décrochements conjugués à l'intérieur du bloc du Qiantang aient encaissé des déplacements non négligeables ce qui diminuerait d'autant les déplacements accumulés sur les grands décrochements aux « limites de bloc ».

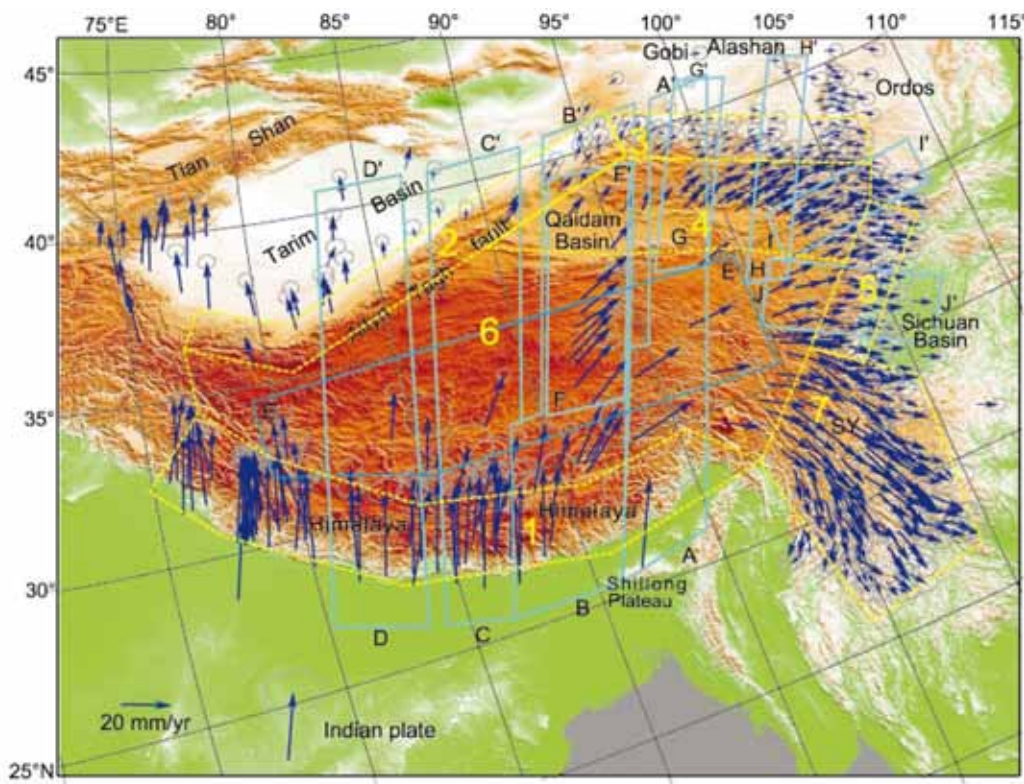


Figure I.4: Global positioning system (GPS) velocities (mm/yr) in and around Tibetan Plateau with respect to stable Eurasia, plotted on shaded relief map using oblique Mercator projection. Ellipses denote 1σ errors. From Zhang et al., 2004.

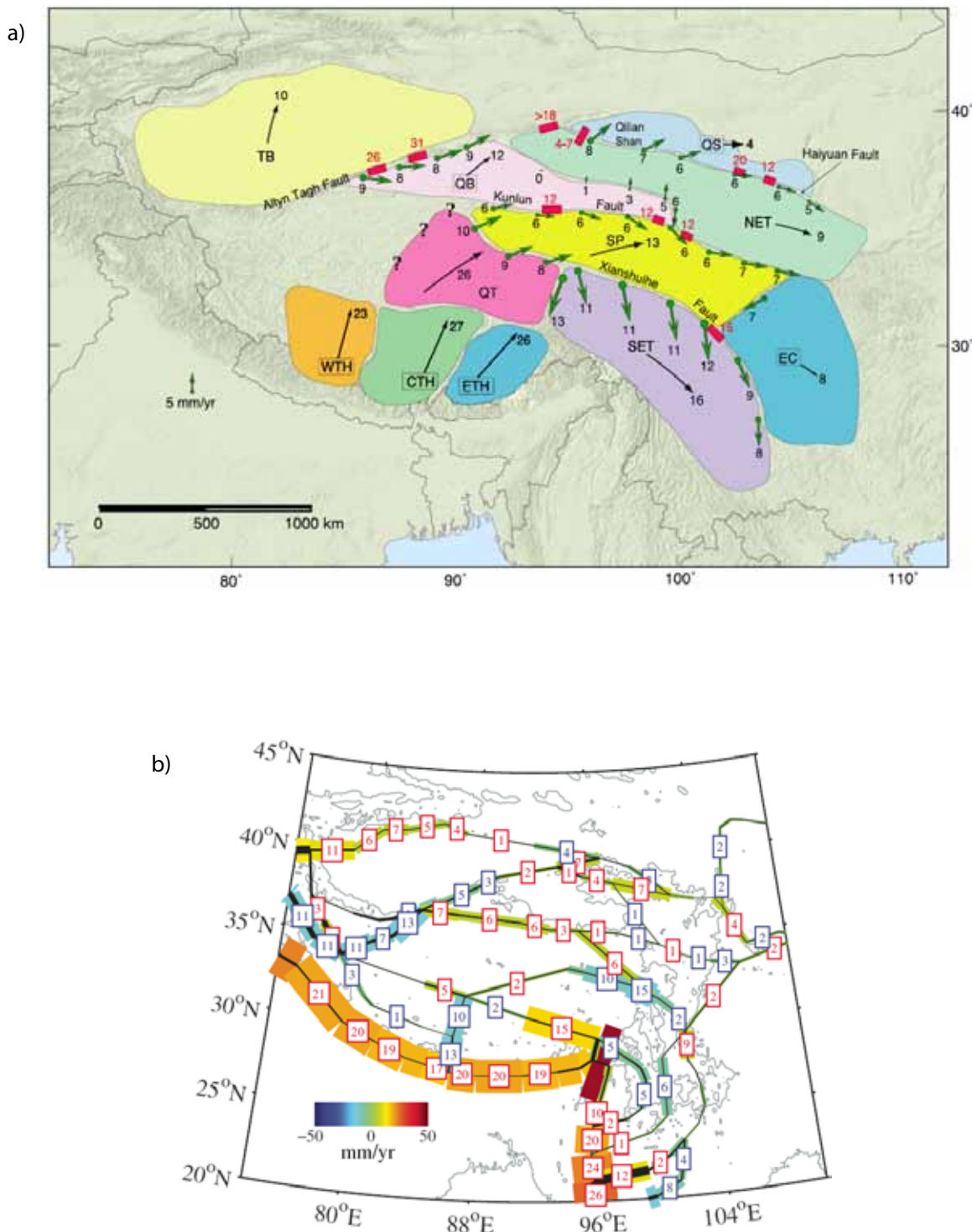


Figure I.5: a) Predicted interblock velocities (thicker green arrows with numbers), with average block velocities relative to Eurasia (thinner black arrows) and geologically estimated slip rates (red numerals). All rates are in mm/yr. From Thatcher et al., 2007. b) Model tensile and dip-slip rates (rounded to nearest whole number). Reddish and bluish colors indicate convergence and extension, respectively. With the exception of faults along Himalayan range front, all faults are vertical and slip rates are tensile. Highest dip-slip rates are located along Himalayan arc. North-south-trending faults near central Tibetan Plateau show east-west extension. From Meade et al., 2007.

1.2. L'extension au Tibet

1.2.1. Les marqueurs de l'extension au Sud-Tibet

C'est dans les années 1970 que la sismologie a mis en évidence que la tectonique active à l'intérieur du plateau du Tibet est dominée par de l'extension E-W et du décrochement (Figure I.6) (Fitch, 1970 ; Molnar et al., 1973 ; Ni et York, 1978 ; Molnar et Tapponnier, 1978). Dans le même temps, les études des images satellites Landsat ont permis d'identifier les structures nord-sud correspondant aux mécanismes au foyer en faille normale Nord-Sud (Molnar et Tapponnier 1978). Les premières cartes des failles actives du Tibet ont alors été publiées (Ni et York, 1978 ; Tapponnier et Molnar, 1977 ; Molnar et Tapponnier, 1975, 1978). Aujourd'hui, le développement du réseau sismologique au Tibet permet de mieux en mieux documenter les études de sismotectoniques (Figure II.7).

Ensuite à partir de 1980, les expéditions Sino-Françaises ont commencé et ont permis l'étude de terrain des failles normales nord-sud ainsi que des décrochements (Tapponnier et al 1981a,b ; Armijo et al. 1986, 1989). Armijo et al. (1986) ont proposé les premières quantifications du déplacement engendré par ces failles normales nord-sud.

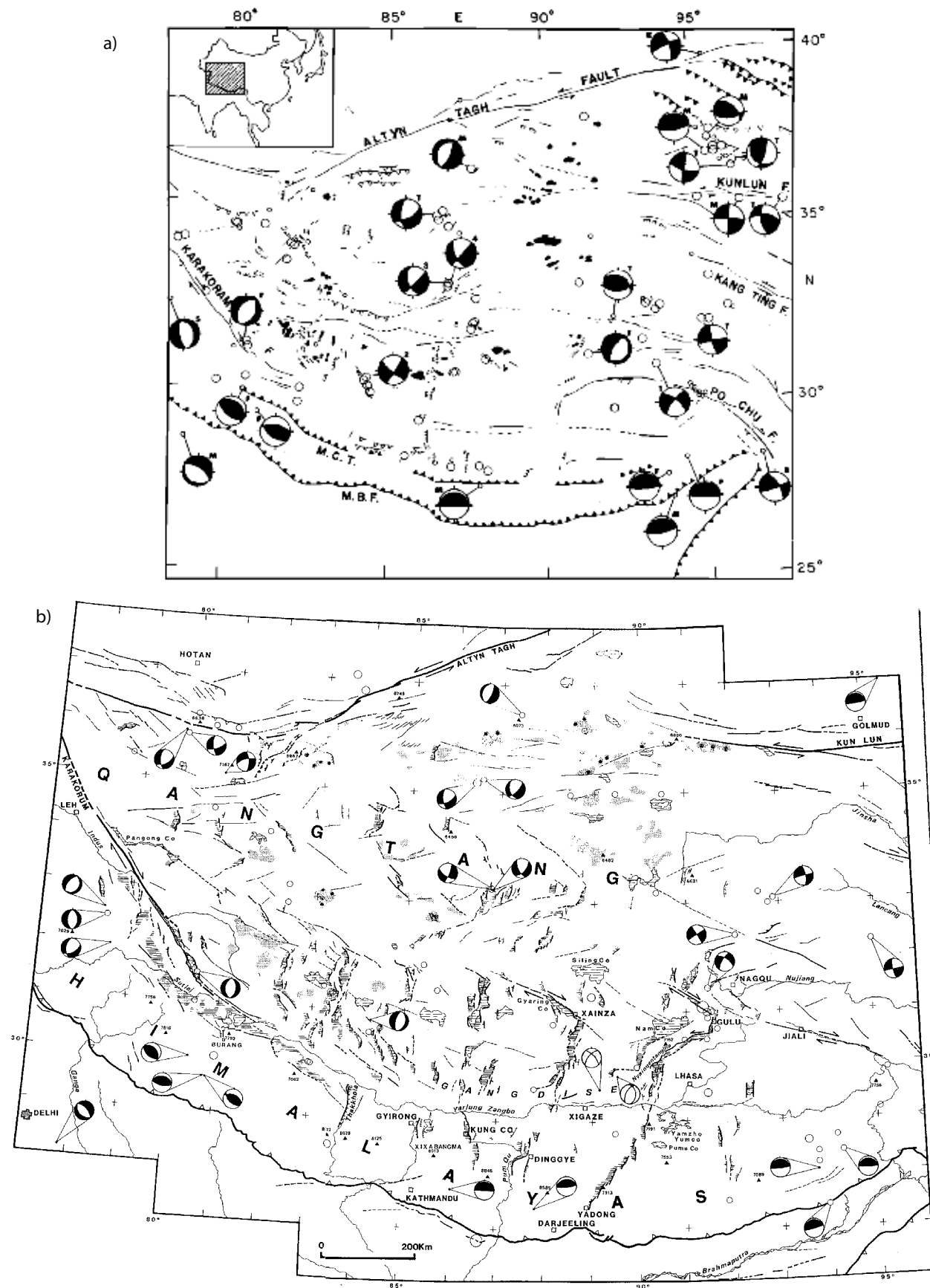


Figure I.6: a) Seismotectonic map of the Tibetan Plateau, with faults and type of faulting interpreted from Landsat imagery. From Ni and York 1978. b) Seismotectonic map of Tibet. From Armijo et al., 1986.

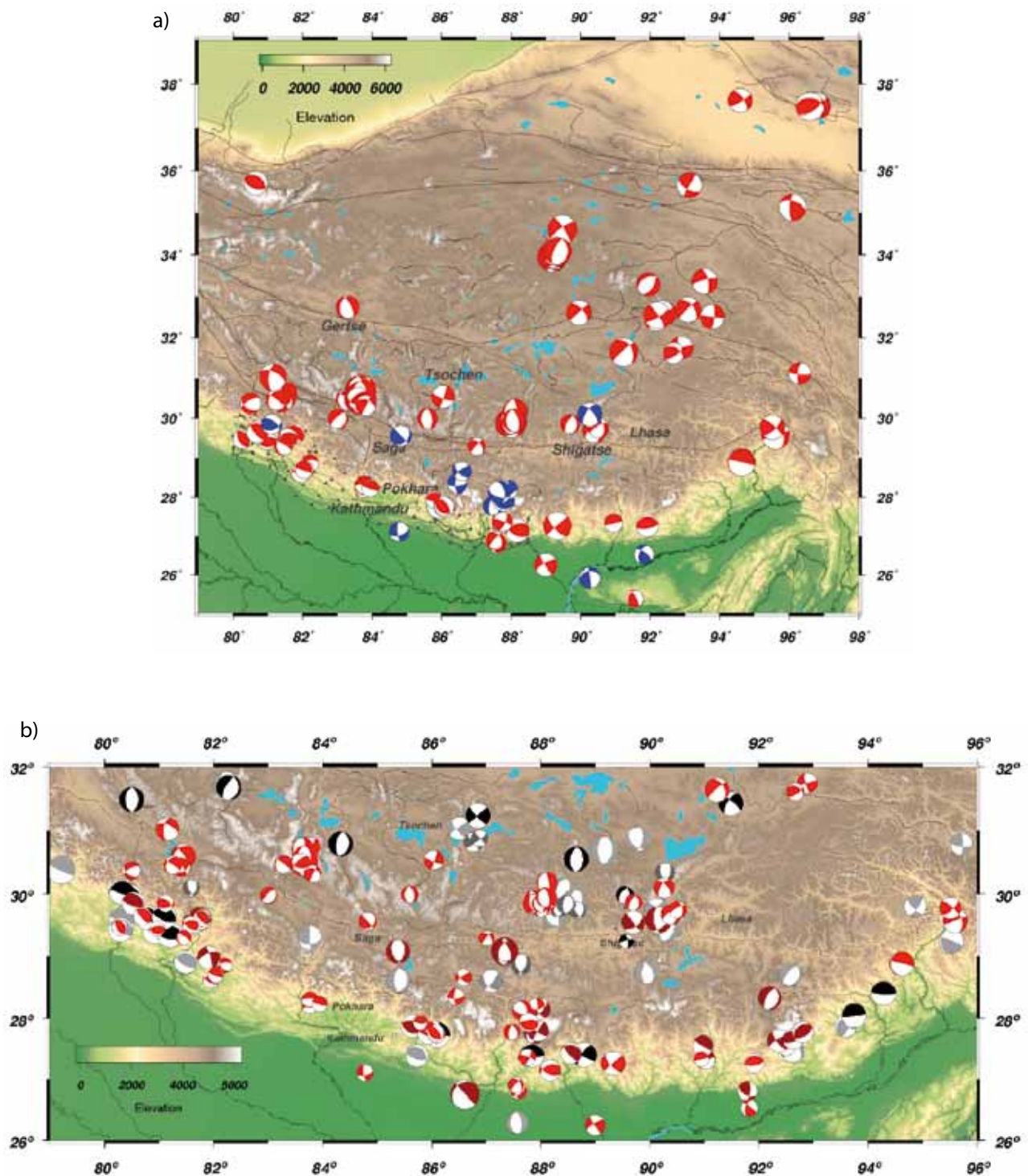


Figure I.7: Seismologic data from HiCLIMB project. From Baur 2007. a) *Overview map of focal mechanisms of Central Tibet. Events with centroid depth < 50 km are shown in red, events with centroid depth ≥ 50 km are shown in blue.* b) Compilation of focal mechanisms from Baur 2007 and previous studies in South-Tibet.

Les failles normales sont présentes à travers tout le plateau tibétain (Figure I.8). Elles sont réparties différemment de part et d'autre des sutures du Yarlung-Zangpo et de Bangong-Nujiang au niveau de la Karakorum-Jiali Fault Zone (Armijo et al. 1986). Au nord de la Karakorum-Jiali Fault Zone (KJFZ), les failles normales sont moins marquées, de longueurs réduites et associées à des décrochements dextres ou senestres (Armijo et al., 1989 ; Taylor et al., 2003). La distance entre les rifts est plus petite (50-800 km) et les failles sont moins continues avec moins de relief (Armijo et al., 1986 ; Yin, 2000). L'extension au nord de la KJFZ semble être donc moins intense. Mais Yin et al. (1999, 2000) et Taylor et al (2003) proposent néanmoins que la quantité d'extension sur les failles normales est semblable au nord et au sud de la KJFZ et que celle-ci est une zone de transfert liant les structures d'extensions de part et d'autre de cette limite. La comparaison des vitesses de glissement sur ces différentes failles peut permettre de quantifier la part d'extension accommodée par ces différentes failles.

Dans cette thèse, nous nous focalisons sur l'extension au sud Tibet. Au sud de la KJFZ, l'extension est répartie principalement le long sept systèmes de rifts (Figure I.8). Trois de ces rifts (Thakkola, Xainza-Dinggye et Yadong-Gulu) recoupent le South Tibetan Detachment System (STDS) et pénètrent dans la chaîne de l'Himalaya. Les zones étudiées ici sont l'extrémité sud du rift de Xainza-Dinggye, au niveau du massif de l'Ama Drime et le nord du rift de Yadong-Gulu au niveau du massif du Nyainqntanglha.

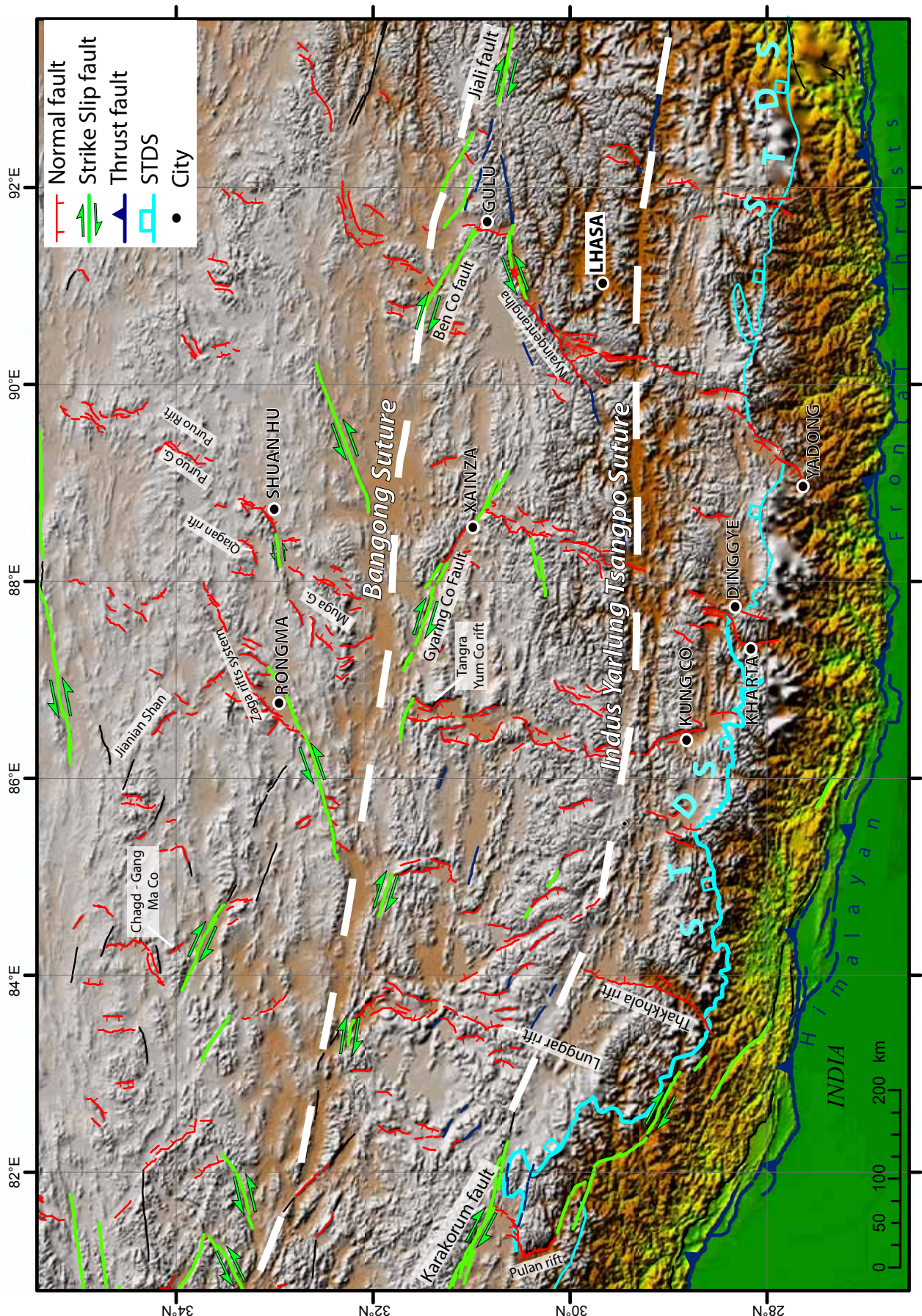


Figure I.8: Map of the active faults of central and south Tibet. Named areas refer to normal faults systems and basins that were targeted in recent studies. STDS (South Tibetan Detachment System) is from Leloup et al., 2010 (see Annexe A), Puruo G = Puruo Gangri, Muga G = Muga Gangri.

1.2.2. Le rôle de l'extension dans l'évolution du plateau tibétain

La manière dont est absorbée la convergence entre Inde et l'Asie dans la zone de collision est complexe car elle s'exprime à travers différents processus comme le raccourcissement, le chevauchement, l'extension, l'extrusion latérale dont la géométrie et le rôle change au cours du temps. Entre l'Inde et l'Asie (c'est-à-dire l'Eurasie ou la Sibérie fixe), la convergence est estimée à environ 50 mm/an par Demets et al., 1990, 1994 avec le modèle NUVEL-1et -1A. Plus récemment avec les réseaux GPS, des vitesses comprises entre 36 et 40 mm/an ont été proposées (Paul et al., 2001; Shen et al., 2000; Wang et al., 2001).

Au niveau de l'Himalaya et du Main Frontal Thrust, la vitesse de convergence est comprise entre 10 et 25 mm/an soit 20 à 70 % de la convergence totale (Armijo et al., 1986, Bilham et al., 1997; Larson et al., 1999; Paul et al., 2001; Banerjee et Bürgmann, 2002, Lavé et Avouac 2000, Cattin et Avouac 2000, Molnar et Lyon-Caen, 1989, Bettinelli et al., 2006). La détermination des budgets de déformation a permis de déterminer que l'extrusion vers l'est a accommodé 30 % de la convergence (Replumaz et Tapponnier 2003).

Il est plus difficile de déterminer la part de l'extension dans l'accommodation de la convergence. D'après Tapponnier et al., 2001, la quantité totale d'extension liées aux failles normales actives est petite, au mieux de 40 km (déterminée par des estimations du relief structural par Armijo et al., 1986), sur les ~1200 km de longueur du plateau. Ainsi, la quantité correspondante d'amincissement crustal serait inférieure à 2 km pour une croûte de 70 à 80 km d'épaisseur (Armijo et al., 1986, 1989) et serait négligeable à l'échelle de la zone de collision (Tapponnier et al., 2001). Ces estimations de quantité d'extension sont basées sur des mesures de rejets cumulés associés à des datations relatives peu précises.

Avec les méthodes actuelles de datations absolues, il est sans doute possible de vérifier ou d'améliorer la précision de ces estimations de quantité et de vitesse d'extension. Dans cette thèse nous espérons apporter des précisions sur ces vitesses grâce à des méthodes de datation absolue et des mesures de déplacements verticaux mieux contraints.

Afin de mieux comprendre le rôle et les causes de l'extension interne au Tibet il est d'abord nécessaire de quantifier cette déformation en termes de vitesse d'extension, quantité totale d'extension et initiation de l'extension. En particulier, répondre aux questions suivantes permettrait de mieux discuter du rôle de l'extension et de la manière dont il faut intégrer cette extension dans les modèles d'évolution tectonique :

- L'extension est-elle homogène sur tout le plateau ?

- A-t-elle été constante au cours du temps ?

- Quand a-t-elle commencé et où?

1.3. La démarche de ce travail : l'approche géochronologique multi-méthode

Afin d'apporter des éléments de réponses à ces questions, il est nécessaire de quantifier des déformations actuelles ou sub-actuelles et des déformations passées. Pour cela, il faut choisir une zone d'étude présentant les deux types de déformation. Les massifs de l'Ama Drime et du Nyainqntanglha présentent tous deux des zones de cisaillement ductile en faille normale, témoignant d'une déformation en extension ancienne, associées à des failles normales actives, montrant l'extension récente (Figure I.9).

Deux types de méthode de datation ont été appliqués pour quantifier les vitesses de déformation sub-actuelles et plus anciennes au niveau de ces deux massifs. Dans la deuxième partie de cette thèse, la quantification des déformations long-terme (de l'ordre du Ma) sera abordée. Des méthodes telles que l'analyse structurale et pétrologique des zones de déformation ductile associée aux datations à $^{39}\text{Ar}/^{40}\text{Ar}$, l'(U-Th)/He et l'U/Pb ont permis d'estimer des taux d'exhumation des formations anciennes. Dans la troisième partie, nous abordons la quantification des déformations court terme (de l'ordre du ka) grâce à une étude géomorphologique des structures quaternaires déformées (terrasses alluviales et moraines). Couplée aux datations au ^{10}Be et à ^{26}Al , l'analyse géomorphologique a permis de déterminer des vitesses de glissement des failles actives. Les vitesses long-terme et court-

terme obtenues ainsi sont comparées et contribuent à la caractérisation tectonique de l'extension à l'échelle du Tibet.

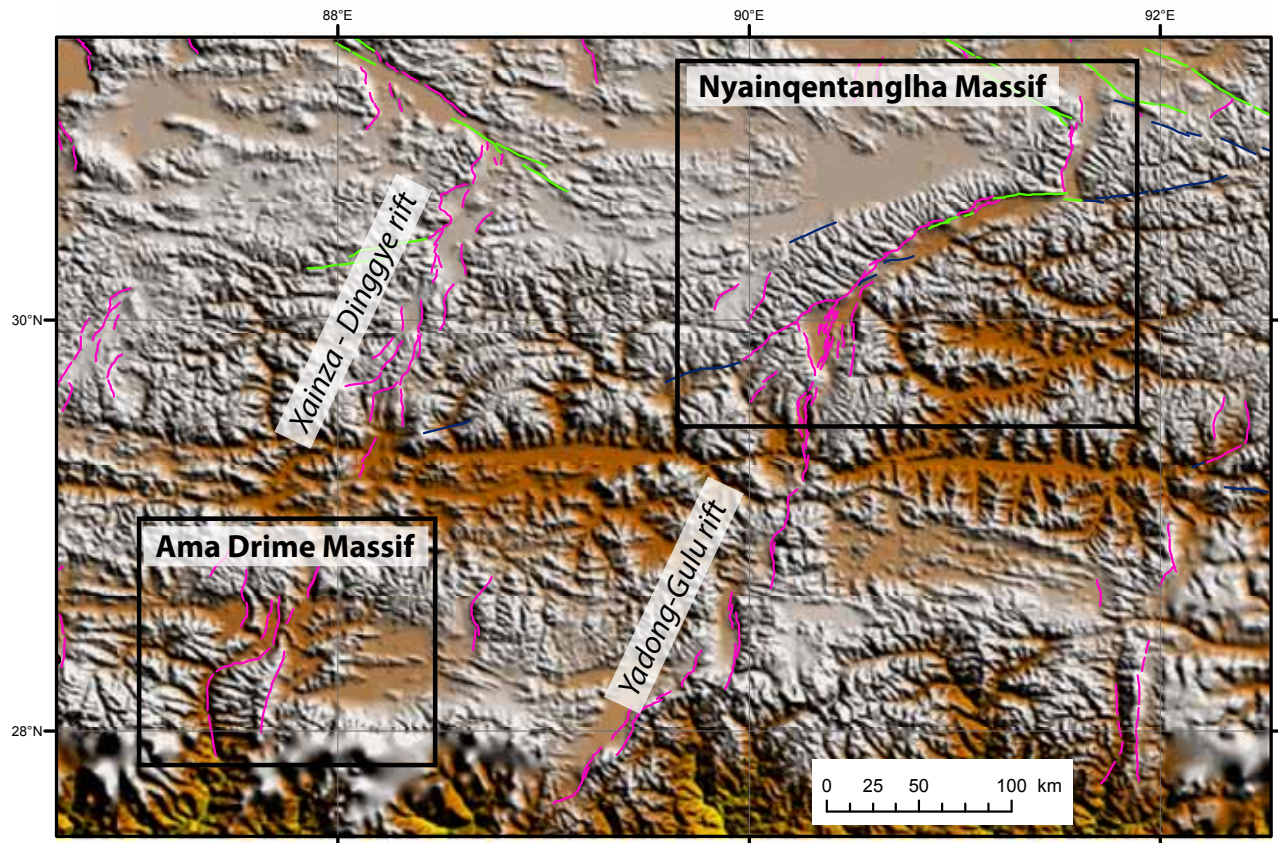


Figure I.9: Location of the two study areas.

Partie 2



LA DEFORMATION
LONG-TERME
SUR LES FAILLES
NORMALES DU SUD TIBET

Photographie du Titre 2 :

Panorama en direction de la première gorge de l'Arun, depuis une terrasse (T4, Figure III.12) suspendue au mur de la faille de Kharta (Massif de l'Ama Drime). Le sommet en premier plan est le sommet de Yo Ri sous lequel apparaît la zone de cisaillement ductile en faille normale. Elle comporte des granites déformés et non déformés (voir la carte et la coupe correspondantes Figure 2 p.59, et des vues rapprochées Figure II.11). Elle a joué un rôle majeur dans l'exhumation des roches du cœur de l'Ama Drime, depuis 50 à 60 km de profondeur.

2. LA DEFORMATION LONG-TERME SUR LES FAILLES NORMALES DU SUD TIBET

L'enjeu de cette partie est de déterminer des distances de mouvements verticaux dans la croûte associées à une durée déterminée afin d'en déduire une vitesse d'exhumation verticale.

D'une part, dans cette thèse, la quantification des mouvements verticaux est abordée de deux façons :
 1/ à l'échelle de la croûte, grâce à des études pétrologiques qui permettent la détermination des conditions pression-température d'équilibration des assemblages minéraux.
 2/ à l'échelle du relief de surface, grâce à des études géomorphologiques par des mesures sur le terrain et/ou grâce à un modèle numérique de terrain.

D'autre part, plusieurs méthodes de datation (U/Pb sur zircon et monazite, $^{40}\text{Ar}/^{39}\text{Ar}$ sur mica et feldspath et (U-Th)/He sur apatite) ont été appliquées pour déterminer les durées et les âges associés à ces mouvements verticaux.

L'association de la quantité de déplacement vertical avec les âges et les durées déterminées peut être faite à travers différentes approches :

- 1/ Les trajets Pression – Température – temps (trajets P-T-t)
- 2/ Les relations Age-Altitude
- 3/ Les trajets Température – temps (trajets T-t)

La partie 2.1 est une partie méthodologique permettant de rappeler succinctement le principe des méthodes de datation utilisées pour la quantification de la déformation long-terme. Dans la partie 2.2, concernant le Massif de l'Ama Drime, les deux premières approches sont utilisées. Cette partie est séparée en deux sous-parties. La partie 2.2.1 correspond à l'article publié dans *Tectonics* dans lequel nous présentons la reconstitution des trajets P-T-t-d du massif, la partie 2.2.2 est un complément de l'article montrant les données de datation $^{40}\text{Ar}/^{39}\text{Ar}$ sur feldspaths non publiées. Dans la partie 2.3, traitant le Massif du Nyainqntanglha, la deuxième approche est appliquée.

2.1. L'utilisation de la thermochronologie et de la pétrologie dans la quantification des vitesses de déformation.

La partie méthodologique présentée ci-dessous consiste à expliquer la construction de ces différentes relations que sont les trajets P-T- t, T-t et Age-Altitude.

2.1.1. L'utilisation des âges

2.1.1.1. La construction de trajets Pression – Température

La méthode est décrite dans l'Annexe B (correspondant à l'Appendix I de l'article publié dans Tectonics).

2.1.1.2. La notion de température de fermeture

Cette notion permet d'associer un âge (t) à une température (T) et donc d'obtenir un trajet $T-t$ ou de compléter un trajet pression (P) - température (T) avec des âges pour obtenir un trajet $P-T-t$.

La température de fermeture correspond à la température à partir de laquelle un minéral retient ou libère les éléments chimiques qu'il contient (Figure II.1), (Dodson 1973). C'est-à-dire que les éléments fils produits par les désintégrations radioactives seront retenus dans le réseau cristallin en dessous d'une température donnée lors d'un refroidissement et libérés au dessus d'une température donnée lors d'un réchauffement. L'âge obtenu à partir de l'analyse de minéraux permet donc de dater le passage en dessous de la température de fermeture. Cette température varie en fonction de l'espèce minérale (Figure II.2). Lorsque pour un même échantillon on a : une étude pétrologique permettant d'obtenir un trajet $P-T$, et l'âge t de plusieurs espèces minérales correspondant à différentes températures de fermeture, il est donc possible de reconstituer un trajet $P-T-t$, à partir duquel des vitesses d'exhumation verticales peuvent être déduites (voir partie 2.2.1). En ajoutant les observations structurales à différentes échelles (du microscope au terrain), les conditions $P-T$ datées sont associées à des phases de déformation D , ce qui permet d'obtenir un trajet $P-T-t-D$.

Quand il s'agit d'une approche thermochronologique, le volet pétrographie est absent, et un trajet $T-t$ est obtenu. Un certain nombre d'informations peut être extrait d'une relation $T-t$. Certains auteurs utilisent des modèles thermo-mécaniques pour déterminer quel mécanisme tectonique pourrait produire un type de trajet $T-t$ donné, des vitesses de glissement sur des failles peuvent être ainsi obtenues (e.g. Harrison et al., 1995, Kapp et al., 2005). Dans cette thèse, ce type de modèle n'est pas utilisé, mais les vitesses déduite par ce type d'approche seront comparées avec nos résultats (partie 2.3).

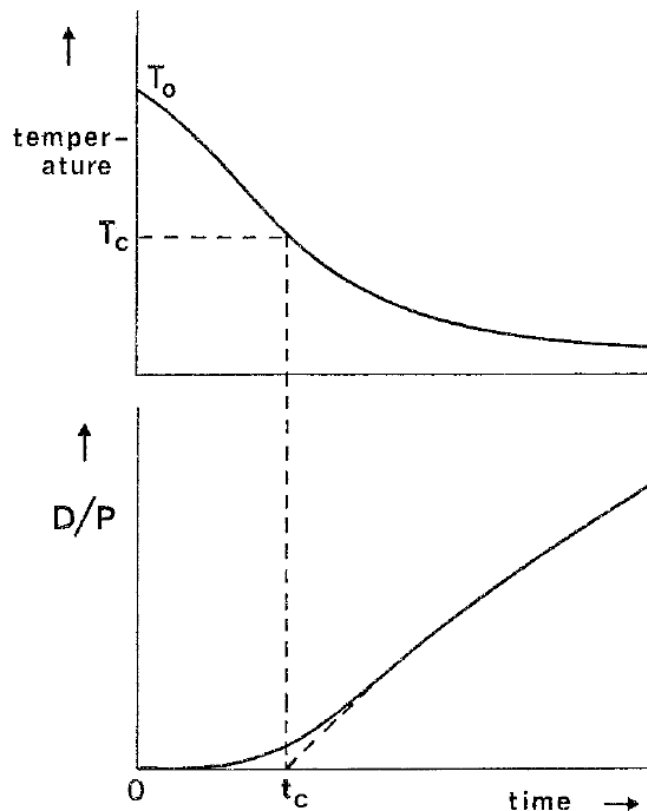


Figure II.1: Graphic definition of the closure temperature (T_c) corresponding to an apparent age (t_c). During the slow cooling from high temperature, the daughter-to-parent ratio (D/P) passes from completely open state (i.e., $D/P = 0$) through a zone of partial accumulation, shown by the curved portion of the curve in the lower diagram, until the temperature is sufficiently low that diffusion loss ceases and the D/P ratio grows at constant rate with time. (From Dodson et al., 1973)

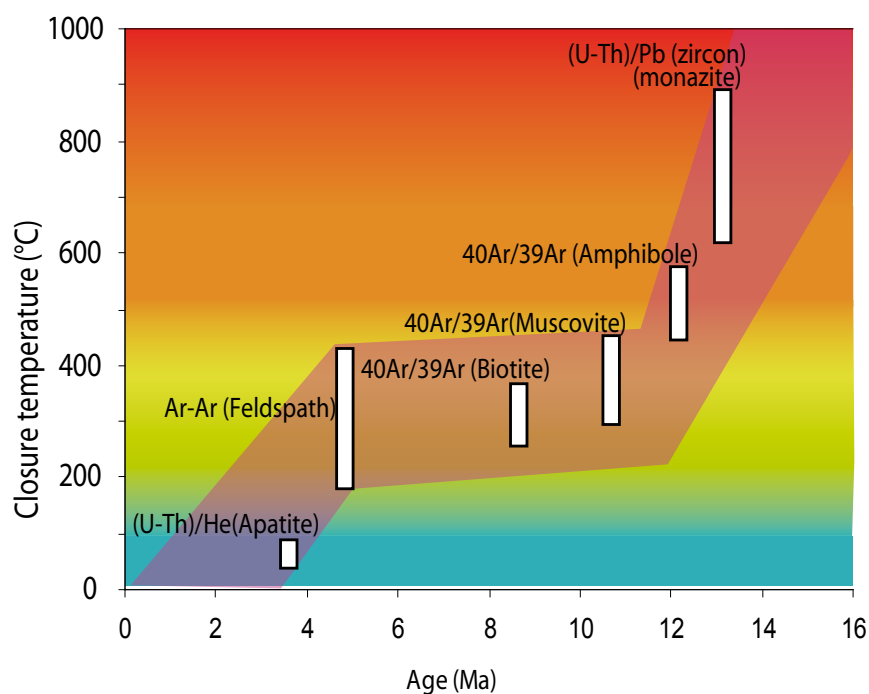


Figure II.2: Simplified representation of thermochronometers and T-t path.

2.1.1.3. La relation âge-altitude

Cette approche consiste à mettre en relation les âges obtenus sur une même espèce de minéraux pour différents échantillons prélevés à différentes altitudes. La différence d'âge reliée à la différence d'altitude permet donc d'obtenir une vitesse de mouvement vertical (Figure II.3).

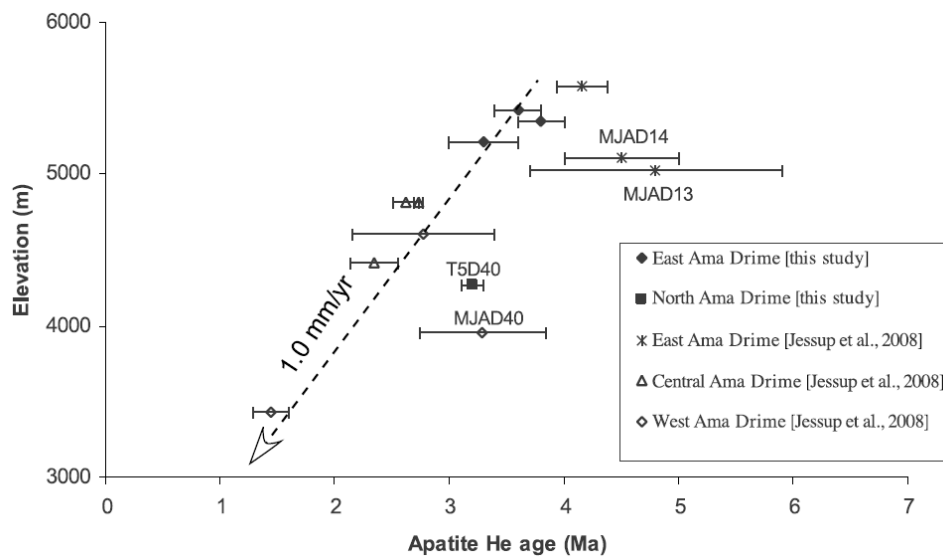


Figure II.3: (U-Th)/He apatite ages versus elevation plot, from the Ama Drime massif. (see Tectonics paper, § 2.2.1)

2.1.2. Les méthodes de datation

2.1.2.1. L'équation d'âge générale

L'équation appliquée dans les méthodes de datation utilisées dans cette thèse découle de la loi de désintégration par radioactivité et se présente ainsi :

$$t = \frac{1}{\lambda} \ln \left(\frac{N_f}{N_p} + 1 \right)$$

où t est l'âge

λ est la constante de désintégration radioactive

N_f correspond au nombre d'isotopes fils produits

N_p correspond au nombre d'atomes pères restants

Cette équation est déclinée de différentes façons en fonctions des systèmes isotopiques radioactifs utilisés.

2.1.2.2. La méthode U/Pb sur zircon et monazite

La méthode est décrite dans l'Annexe B (correspondant à l' Appendix II-1 de l'article publié dans Tectonics).

2.1.2.3. La méthode (U-Th)/He sur apatite

Les aspects techniques

Les apatites issues des échantillons du massif de l'Ama Drime ont été analysées au *Caltech Noble Gas Laboratory*. Des détails sur l'analyse de ces échantillons sont fournis dans la partie 2.2.1 (paragraphe 4.2.3 de l'article).

Les apatites des échantillons du massif du Nyainqntanglha, ont été analysées au laboratoire de Géosciences Montpellier, avec la ligne d'extraction de l'hélium connectée à un spectromètre de type MASS (Figure II.4), selon la procédure de House et al., 2000. Quatre répliques par échantillon ont été analysées. Chacune de ces répliques contenait 1 à 5 grains d'apatites, répartis en fonction de leur taille (annexe C).

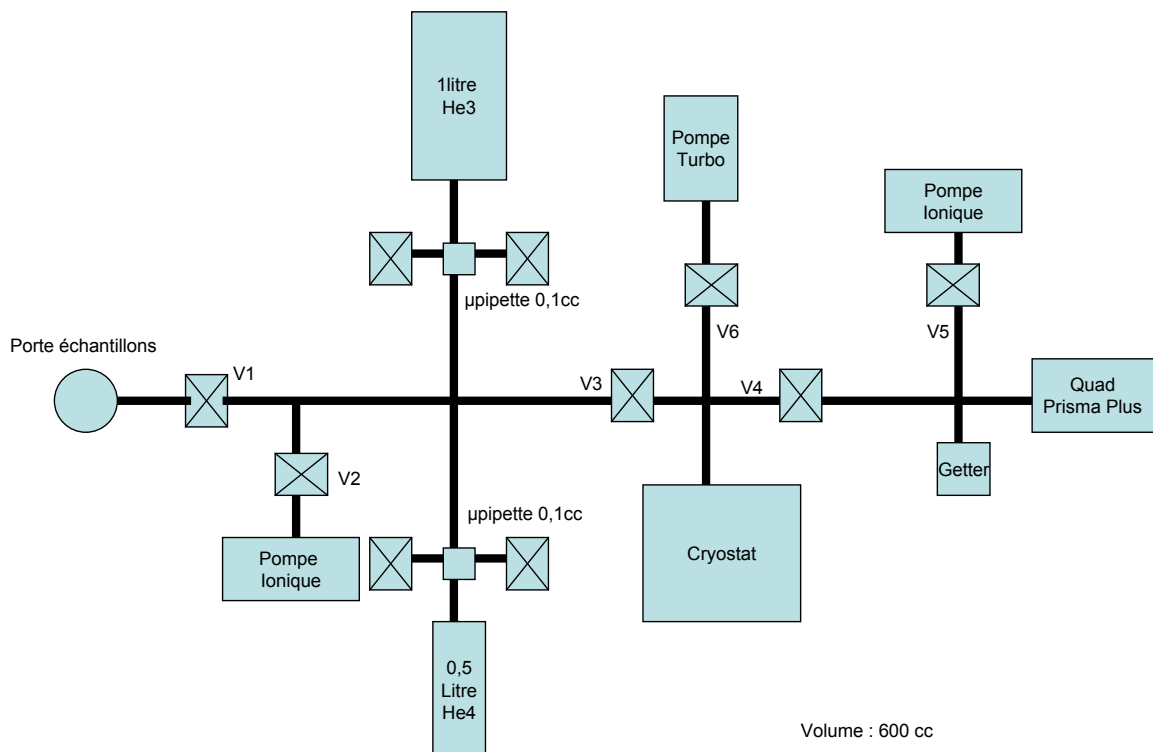


Figure II.4: Schematic representation of the helium extraction line of the Geoscience Montpellier laboratory

Le principe de la datation

La datation (U-Th)/He sur apatite est basée sur les chaînes de désintégration radioactive de ^{235}U , ^{238}U et du ^{232}Th par émission de particules alpha (noyau d' ^4He).

La production de particules alpha suit la loi suivante :

$${}^4\text{He}_0 = 8 {}^{238}\text{U}_0(\exp(\lambda_{238}t)-1) + 7({}^{238}\text{U}_0/137.88)(\exp(\lambda_{235}t)-1) + 6 {}^{232}\text{Th}_0(\exp(\lambda_{232}t)-1) \quad (1)$$

où He_0 , U_0 et Th_0 sont les quantités actuelles,

t le temps d'accumulation ou âge He

λ les constantes de désintégration radioactive.

Les coefficients précédents les quantités d'U et de Th correspondent aux nombres de particules alpha émises dans chaque chaîne de désintégration.

$1/137.88$ correspond au rapport ${}^{235}\text{U}_0/{}^{238}\text{U}_0$

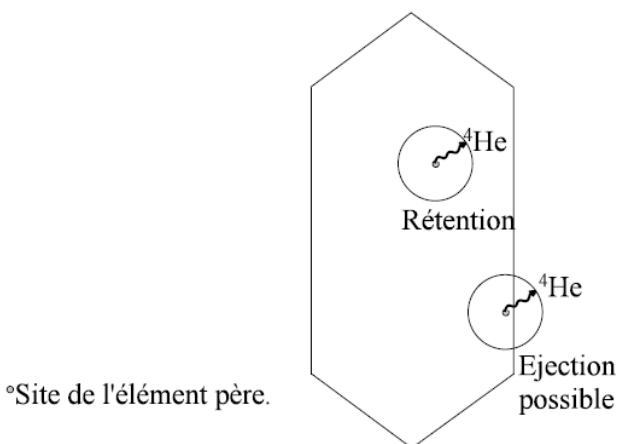


Figure II.5: Effect of the localisation of the parent elements of ${}^4\text{He}$ on the retention with ejection distance of ${}^4\text{He}$.

Cette quantité d'hélium est ensuite injectée dans l'équation d'âge.

La quantité d'hélium à l'intérieur d'un minéral dépend aussi du phénomène d'éjection (dû à l'énergie cinétique issue de la réaction de désintégration) qui a pour conséquence l'expulsion des noyaux d'hélium hors du minéral (Figure II.5) (Farley, 2002). Ce phénomène est pris en compte dans le calcul d'âge grâce à la détermination d'un facteur de forme F_t , qui permet de prendre en compte la forme de l'apatite ou du groupe d'apatites

de chaque réplique. La valeur du F_t est donnée par l'équation suivante :

$$F_t \text{ moyen} = a_{238} {}^{238}\text{UF}_t + (1 - a_{238}) {}^{232}\text{Th}_t$$

dans laquelle : a_{238} est la proportion de particules alpha produites par la chaîne de ${}^{238}\text{U}$. Cette proportion peut être obtenue à partir de l'équation (1), ou approximée à partir de la mesure du rapport U_0/Th_0 suite à une période de désintégration d'environ 200 000 ans, ce qui donne :

$$a_{238} = (1,04 + 0,245(\text{U}_0/\text{Th}_0)) - 1$$

L'âge de l'échantillon est donc déterminé ainsi :

$$\text{Age corrigé} = \frac{\text{Age He}}{F_t}$$

2.1.3. La méthode $^{40}\text{Ar}/^{39}\text{Ar}$

2.1.3.1. La séparation des minéraux, l'analyse et la présentation des résultats d' $^{40}\text{Ar}/^{39}\text{Ar}$

La méthode est décrite dans l'Annexe B (correspondant à l'Appendix II-2 de l'article à Tectonics).

2.1.3.2. Le protocole de chauffage spécifique pour les feldspaths

Le protocole de chauffage correspond à la procédure employée pour dégazer l'échantillon par palier de température d'une durée donnée. Généralement, l'échantillon est chauffé séquentiellement avec un protocole adapté à une résolution optimum recherchée sur le spectre d'âge. En fonction des étapes de déstructuration attendue des micas, le protocole est en général défini par 13 paliers de température de 30 minutes tous les 50 ou 100°C, à partir de 700° C (voir le protocole de chauffage des échantillons T5D6 et T5G2, Table II.1 à la page suivante, et Annexe D) et jusqu'à la fusion de l'échantillon, autour de 1400°C. Dans le cas des feldspaths, il est courant d'utiliser un autre protocole de chauffage pour essayer de minimiser les effets de l'excès d'argon (Harrison et al., 1994) et augmenter la résolution du dégazage en ^{39}Ar qui est utilisé pour calculer les paramètres de diffusion. Pour cela, le dégazage commence à plus basse température (400°C) et les paliers de température sont doublés entre 400 et 850 °C (exemple de l'échantillon T5Y10 Table II.1, Annexe D). Si des excès d'argon importants sont détectés au cours de l'analyse d'une série d'échantillons à feldspaths, il arrive de changer le protocole en programmant des paliers de température tous les 25°C entre 500 et 800°C. Afin d'avoir une meilleure résolution dans les basses températures, certains échantillons ont été analysés avec 42 paliers de température (voir page suivante l'exemple de l'échantillon T7A10 -Table II.1-, et l'Annexe D). Dans cette thèse, tous les micas et les feldspaths de l'Ama Drime côté Est (exemple, échantillon T5D6, région de Dinggye) ont subi un protocole à 13 paliers de température, les feldspaths du massif du Nyainqntanglha un protocole à 28 paliers et les feldspaths du massif de l'Ama Drime côté ouest (région de Kharta), un protocole à 42 paliers (sauf pour le premier échantillon analysé, le T7A33 qui a subi 28 paliers). La partie 2.2.2 sur les feldspaths de l'Ama Drime montre l'intérêt de l'utilisation de ce protocole spécial pour les feldspaths présentant des excès d'argon.

Table II.1: Heating Schedule for different type of minerals, $^{40}\text{Ar}/^{39}\text{Ar}$ dating

Step N°	T7A10_Kf Temp (°C)	Time (min)	T5Y10_Kf Temp (°C)	Time (min)	T5D6_Kf Temp (°C)	Time (min)	T5G2_Bio Temp (°C)	Time (min)
1	400	30	400	30	700	30	700	30
2	400	35	400	35	800	30	750	30
3	450	30	450	30	850	30	800	30
4	450	35	450	35	900	30	833	30
5	500	30	500	30	950	30	866	30
6	500	35	500	35	1000	30	900	30
7	525	30	550	30	1000	30	950	30
8	525	35	550	35	1050	30	1000	30
9	550	30	600	30	1050	30	1033	30
10	550	35	600	35	1100	30	1066	30
11	575	30	650	30	1100	30	1100	30
12	575	35	650	35	1200	10	1200	30
13	600	30	700	30	1400	30	1400	30
14	600	35	700	35				
15	625	30	750	30				
16	625	35	750	35				
17	650	30	800	30				
18	650	35	800	40				
19	675	30	800	60				
20	675	35	750	60				
21	700	30	950	30				
22	700	35	1000	30				
23	725	30	1050	30				
24	725	35	1050	40				
25	750	30	1100	30				
26	750	35	1150	30				
27	775	30	1200	30				
28	775	30	1400	30				
29	800	30						
30	800	40						
31	800	60						
32	700	60						
33	750	40						
34	800	40						
35	850	30						
36	900	30						
37	950	30						
38	1000	30						
39	1050	30						
40	1100	30						
41	1200	30						
42	1400	30						

2.1.3.3. Les rapports K/Ca et Cl/K

Les résultats d'analyses $^{40}\text{Ar}/^{39}\text{Ar}$ permettent de fournir les rapports K/Ca et Cl/K à chaque palier de température en utilisant les radio-éléments (^{37}Ar , ^{38}Ar , et ^{39}Ar) produits par ces éléments lors de l'irradiation. Les variations de ces rapports reflètent l'hétérogénéité du matériel analysé notamment l'existence de différentes phases à chimie différente dans l'échantillon analysé (Mc Dougall et Harrison 1999), par exemple des recristallisations ou des perthites. Quand les variations de ces rapports sont corrélées avec les variations d'âges du spectre, des phases différentes analysées pourront donc expliquer des différences d'âges pour un même échantillon analysé (Annexe D).

2.1.3.4. La modélisation des résultats d'analyse $^{40}\text{Ar}/^{39}\text{Ar}$ sur feldspaths potassiques

Contrairement aux micas ou aux amphiboles, les feldspaths potassiques ont la caractéristique d'être suffisamment stables pendant le chauffage sous vide pour que la diffusion observée puisse être interprétée comme reflétant celle ayant lieu dans le milieu naturel, sans déstabilisation majeure du minéral avant le début de la fusion incongruente. De plus leurs propriétés de rétention complexe permettent d'enregistrer l'histoire thermique subie par l'échantillon avec une résolution supérieure à celle des autres minéraux. Le chauffage par palier de température est donc considéré comme une expérience de diffusion de l'argon de plusieurs heures à quelques jours, à travers les feldspaths. Cette expérience, représentée par le spectre d'âge, peut être comparée à la diffusion de l'argon sur des périodes de temps de l'ordre du million d'années. Dans cette partie est présentée la méthode de reconstitution de l'histoire thermique subie par l'échantillon à partir des données d'analyse $^{40}\text{Ar}/^{39}\text{Ar}$. Quand le spectre d'âges des feldspaths est correct (c'est-à-dire qu'il ne présente pas trop d'excès d'argon), il peut être exploité pour retrouver l'histoire de refroidissement qui a permis d'obtenir ce spectre. Cela nécessite deux étapes. La première consiste à déterminer les paramètres de diffusion des feldspaths analysés, en supposant qu'ils reflètent les paramètres ayant présidés à la perte d'argon dans le milieu naturel. Ensuite ces paramètres de diffusion seront utilisés pour reconstituer l'histoire thermique.

La détermination des paramètres de diffusion

Elle est basée sur la construction du graphique d'Arrhénius et du graphique $\log(r/r_0)$. Le graphique d'Arrhénius est construit grâce à la relation entre la quantité d'argon dégazée à chaque palier de température (f) et la diffusion (Dt/r^2) en faisant l'hypothèse que la diffusion est contrôlée par une loi qui peut être représentée par une relation d'Arrhénius. Cette relation est représentée par l'équation ci-dessous et le graphique de la Figure II.6:

$$f = \frac{M_0 - M_t}{M_0} = 1 - \frac{6}{\pi^2} \sum_{n=1}^{\infty} \frac{1}{n^2} \exp\left(\frac{-Dn^2\pi^2 t}{r^2}\right)$$

où M_0 est la masse d' ^{40}Ar initialement présente dans un domaine de diffusion du feldspath, M est la masse d' ^{40}Ar restante dans le minéral après le temp t , r est le facteur géométrique et D est le coefficient de diffusion (Fechting and Kalbitzer, 1966).

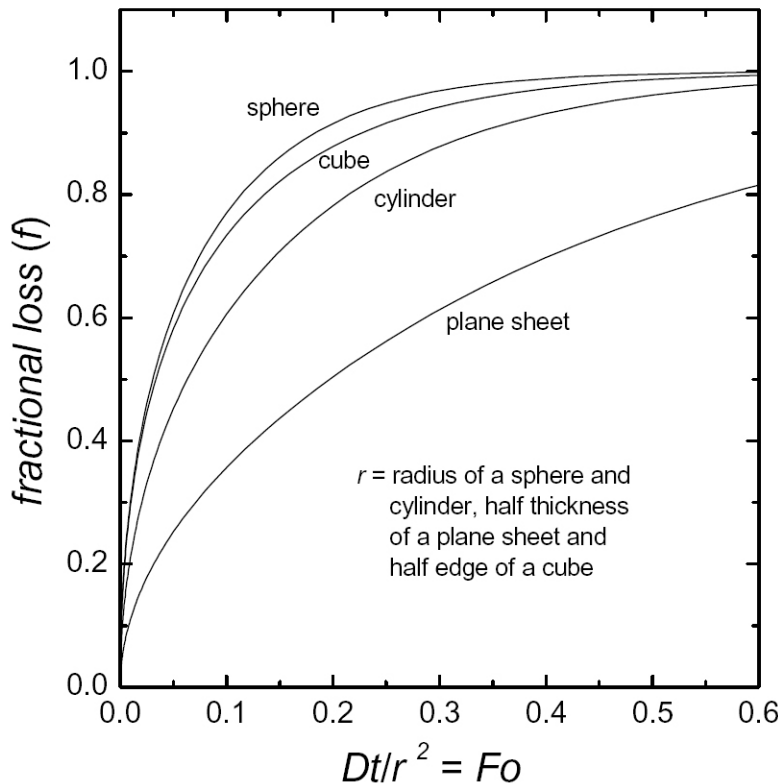


Figure II.6: Relationship between fractional loss and the Fourier number (Dt/r^2) for spherical, cylindrical, plane sheet, and cubic geometries. (From Mc Dougall 1999 and Harrison, 1999)

L'expérience de chauffage nous fournissant la quantité d'argon dégazée f et la durée t correspondante, on peut donc retrouver le coefficient F_o ($= Dt/r^2$) qui permettra à son tour de déduire le graphique d'Arrhenius. Le graphique d'Arrhenius représenté par l'équation ci-dessous et le graphique de la Figure II.7, permettent de représenter les coefficients de diffusion en fonction de l'inverse de la température de chauffage lors du dégazage de l'échantillon. En d'autres termes, on obtient pour chaque palier de température les paramètres de diffusions de l'échantillon, qui pourront être ensuite calculés à partir du graphique obtenu grâce à l'expérience de chauffage.

$$D/r_0^2 = D_0/r_0^2 \exp(E/RT)$$

(from Mc Dougall and Harrison, 1999)

Pour un graphique d'Arrhénius montrant une droite (lors de l'analyse d'une biotite par exemple, Figure II.7), les paramètres de diffusion sont facilement déduits : la pente de la droite permet de définir l'énergie d'activation E et l'ordonnée à l'origine définit le coefficient de diffusion donnée par $\log(D/r^2)$.

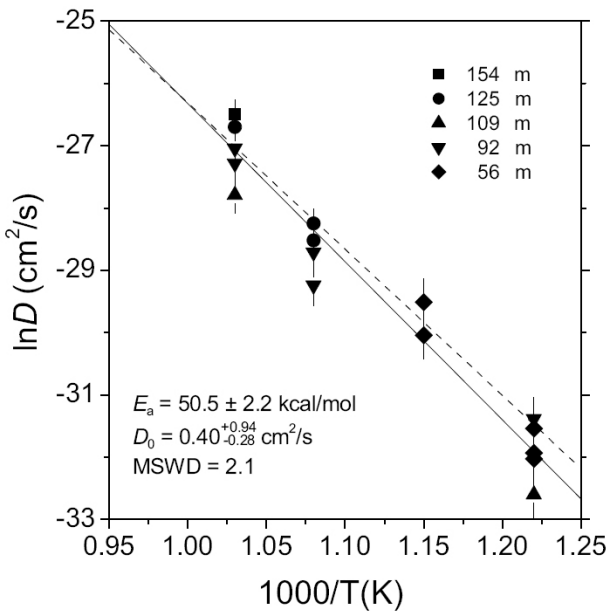


Figure II.7: Arrhenius plot showing argon diffusion results for iron-rich Fe-mica. (From Grove and Harrison 1996)

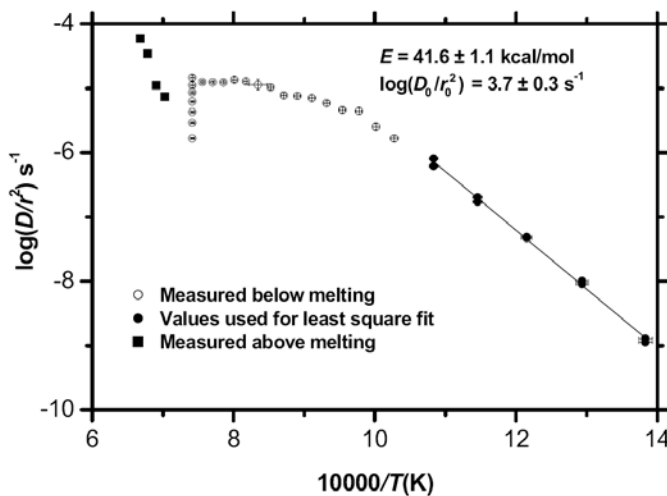


Figure II.8: Arrhenius plot showing argon diffusion results for iron-rich Fe-mica. (From Lovera et al., 1997)

Les graphiques d'Arrhénius obtenus lors de l'analyse de feldspaths sont généralement plus complexes (Figure II.8), et ces données de diffusions ne peuvent pas être expliquées par une diffusion à travers un seul domaine. Cette complexité est expliquée par le « *Multiple Diffusion Domain model* » (*MDD model*) proposé par Lovera et al. (1989), qui implique la présence de plusieurs domaines de diffusion de tailles et rétentivités différentes dans un minéral de feldspath potassique. Les paramètres de ces différents domaines de diffusion sont aussi mieux déterminés à partir du graphique d'Arrhénius, grâce à un protocole de chauffage adapté. Dans le cas des feldspaths potassiques, les paramètres de ces différents domaines de diffusion ne sont pas déterminés directement avec le graphique d'Arrhénius.

Effectivement, il présente l'inconvénient d'être projeté en fonction de l'inverse de la température ce qui rend la représentation dépendante du protocole de chauffage, et rend difficile la comparaison avec le spectre d'âge projeté par rapport à la quantité d' ^{39}Ar dégazée. Pour palier à ce problème et pour pouvoir estimer les paramètres de diffusion des différents domaines, Richter et al. (1991) et Lovera et al. (1991) ont proposé de représenter les paramètres de diffusion avec une fonction $\log(r/r_0)$ (Figure II.9). Le dégazage à basse température (entre 400 et 600°C) des échantillons à « multi-domaines » comme les feldspaths, montre un comportement s'apparentant à un grain uniforme auquel on associe une taille effective r_0 . Ceci est représenté par la ligne droite qui relie les cinq premiers points du graphique d'Arrhénius de la Figure II-8. On soustrait les données réelles ($\log D/r^2$) à l'ordonnée à l'origine de cette ligne droite ($\log D/r_0^2$) puis on divise par deux :

$$0.5 (\log D/r_0^2 - \log D/r^2)$$

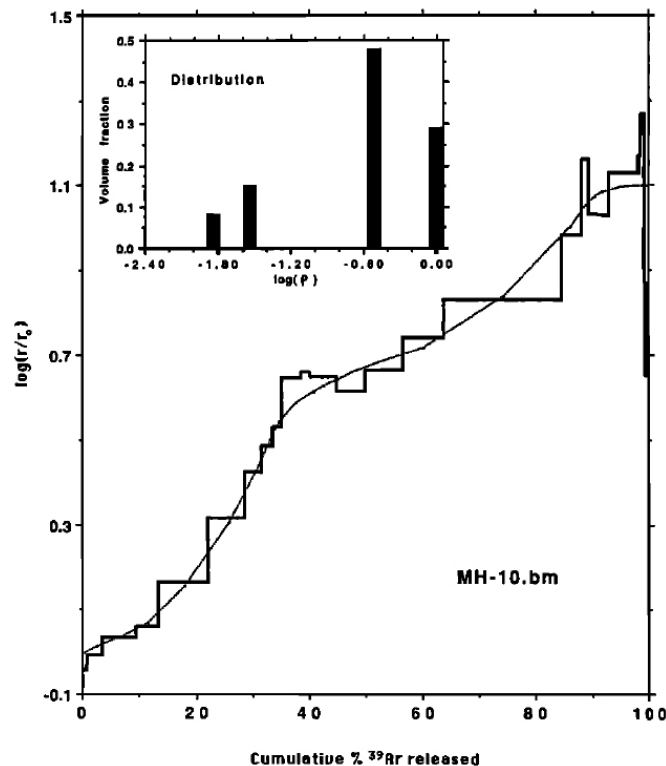


Figure II.9: $\log(r/r_0)$ plot from sample MH-10.bm (solid curve) compared to the theoretical plot (dotted curve) obtained using the distribution parameters shown in the inset. (From Lovera et al., 1991)

On obtient le graphique $\log(r/r_0)$ (Figure II.9). Ainsi en plus de l'énergie d'activation E et du coefficient de diffusion D_0 calculés avec cette droite (E et D_0 considérés communs à tous les domaines de diffusion), le graphique $\log(r/r_0)$ permet de déterminer la fraction volumique ϕ et la taille ρ (encart dans le graphique de la Figure II.9). Sur ce graphique on observe quatre changements

de pente qui correspondent à quatre domaines de distribution dont la fraction volumique ϕ et la taille ρ sont représentées dans l'encart du graphique. Les expressions reliant les valeurs de $\log(r/r_0)$ avec les paramètres ϕ et ρ sont présentées dans Lovera et al. (1991). Une fois les paramètres E , D_0 , ϕ et ρ déterminés, des graphiques synthétiques d'Arrhénius et $\log(r/r_0)$ sont recalculés avec ces paramètres afin d'être comparés avec les données réelles et ainsi confirmer que ces paramètres de diffusion correspondent bien à l'échantillon analysé (voir les deux courbes sur le graphique de la Figure II.7). Des programmes de calcul basé sur Lovera et al., 1992, 1997, ont été mis en place pour déterminer les paramètres de diffusion à partir des données de l'expérience de chauffage. Ils sont en ligne sur les sites suivants : n°1/ <http://oro.ess.ucla.edu/labdata/> ; n°2/ <http://sims.ess.ucla.edu/argonlab/argon.htm>. Le programme « autoarr » du site n°1 a été utilisé dans cette thèse pour déterminer les paramètres de diffusions de nos échantillons.

La reconstitution de l'histoire thermique

L'étape suivante est de définir quelles histoires de refroidissement permettent d'obtenir nos spectres d'âge avec les paramètres de diffusion précédemment déterminés par le *MMD model*. Pour cela une autre modélisation est utilisée. Les résultats d' $^{40}\text{Ar}/^{39}\text{Ar}$ vont être inversés pour retrouver l'histoire thermique correspondante. En d'autres termes, des spectres synthétiques vont être calculés à partir d'histoires thermiques variées, non par une véritable inversion mais par simulations multiples de type Monte Carlo. Les histoires thermiques correspondant aux spectres synthétiques qui s'ajustent le mieux au spectre de l'échantillon seront retenues pour interpréter les données (Figure II.10). Différents programmes existent pour faire ces inversions, basés sur différentes méthodes statistiques, Zeitler et al., 2004 utilisent l'approche du « *Controlled Random Search method* » alors que Lovera et al., 1997, utilisent le polynome de Chebyshev (pour plus de détails voir Harrison et al., 2005). Ici les programmes « autoage-mon » du site n°1 et « agesme » du site n°2 ont été utilisés pour retrouver des histoires thermiques s'ajustant à nos données. Le programme « autoage-mon » permet de générer et tester automatiquement des histoires thermiques correspondant à un refroidissement (*monotonic cooling*). En entrée, il est possible de choisir le nombre de tests et l'âge de début de l'histoire thermique. Dans un premier temps, quelques tests sont effectués afin de déceler si nos données permettent de reconstituer une histoire thermique. Dans le cas favorable, des tests de 50 à 150 essais peuvent être opérés pour mieux contraindre le modèle. Dans cette étude, cette méthode a été utilisée pour un seul feldspath (échantillon T5Y10, chapitre 2.3). Dans ce cas, seuls quelques tests

ont été effectués. Dans certains cas, le refroidissement simple testé par le programme « autoage-mon » ne permet pas d'expliquer les données (exemple des feldspaths de l'Ama Drime, partie 2.2.2). Le programme « agesme » permet d'imposer une histoire thermique plus complexe (avec, par exemple, un réchauffement) et de tester différents scénarii un à un. Cette approche a été appliquée aux feldspaths de l'Ama Drime (partie 2.2.2).

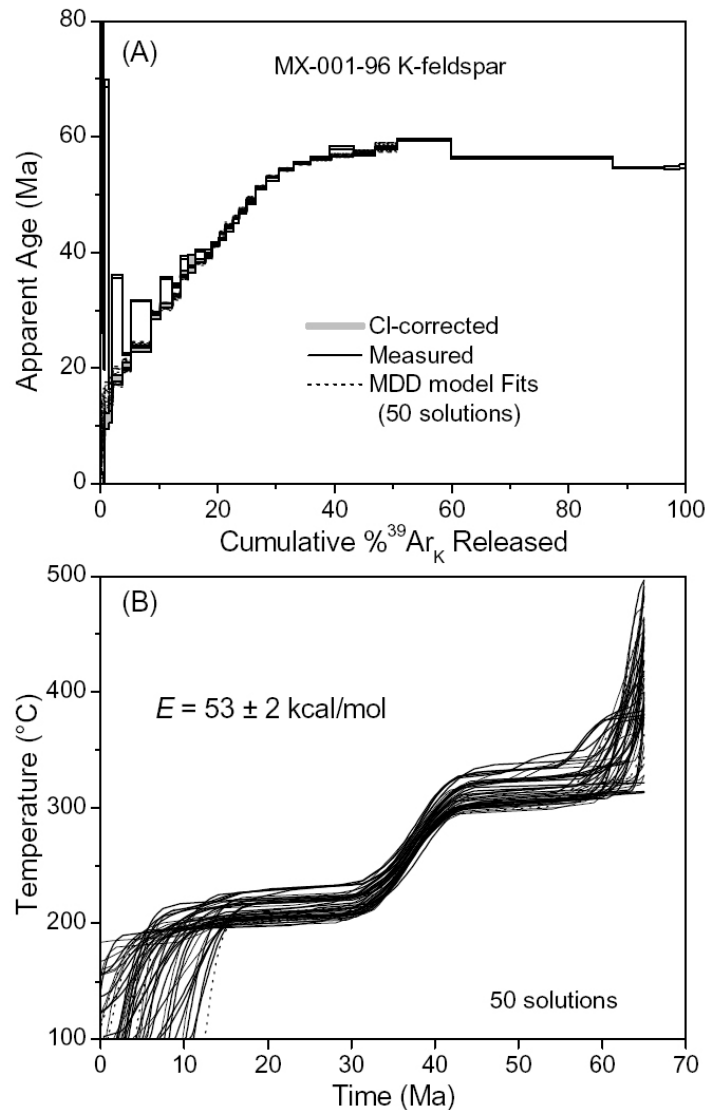


Figure II.10: (A) *Measured age spectrum and 50 best-fit MDD age spectra calculated from ten equivalent MDD domain distributions with activation energy (E) values defining a normal distribution about the measured activation energy for the sample ($53 \pm 2 \text{ kcal/mol}$). (B) Set of 50 thermal histories corresponding to best-fit age spectra. Note that $\pm 17^\circ\text{C}$ variation in temperature-time histories results from propagation of $\pm 2 \text{ kcal/mol}$ error in E .* (From Lovera et al., 2002 and Harrison et al., 2007).

Les limites du MDD model

Les résultats obtenus avec le *MDD model* sont à interpréter avec précaution. En effet, il présente certaines limites. Par exemple, l'hypothèse de base du *MDD model* est que les gaz sont transportés dans les minéraux par des mécanismes de diffusion, et que les paramètres calculés par expérience en laboratoire sont exploitables à l'échelle géologique. Certains auteurs proposent par exemple que le transport dans les minéraux soit accompli par une variété de mécanismes de transport et que le MDD model n'est pas la meilleure solution pour expliquer les spectres d'âges issus des analyses $d^{40}\text{Ar}/^{39}\text{Ar}$ (Villa et al., 1994a, 1994b, 1996, Arnaud and Kelley 1995). La modélisation suppose aussi que la structure du grain n'ait pas été modifiée pendant ou après la partie de l'histoire thermique que l'on cherche à modéliser. Afin d'évaluer la signification des résultats du *MDD model* appliqués aux feldspaths, il est donc important de les comparer avec les autres résultats $d^{40}\text{Ar}/^{39}\text{Ar}$ sur les autres minéraux, et les résultats de thermo-barométrie qui peuvent être faits dans les mêmes échantillons ou à proximité.

2.2. Evaluation des vitesses d'exhumation au niveau du massif de l'Ama Drime, Trajet Pression-température-temps-déformation

**2.2.1. Exhumation history of the deepest central Himalayan rocks (Ama Drime range): key
*P-T-D-t constraints on orogenic models. (Published in Tectonics review)***

Complete citation :

E. Kali, P. H. Leloup, N. Arnaud, G. Maheo, D. Y. Liu, E. Boutonnet, J. Van der Woerd, X. H. Liu, L. Z. Jing, and H. B. Li (2010), Exhumation history of the deepest central Himalayan rocks, Ama Drime range: Key pressure-temperature-deformation-time constraints on orogenic models, *Tectonics*, 29.



Exhumation history of the deepest central Himalayan rocks, Ama Drime range: Key pressure-temperature-deformation-time constraints on orogenic models

E. Kali,¹ P. H. Leloup,² N. Arnaud,³ G. Mahéo,² Dunyi Liu,⁴ E. Boutonnet,²
J. Van der Woerd,¹ Xiaohan Liu,⁵ Jing Liu-Zeng,⁵ and Haibing Li⁴

Received 8 June 2009; revised 26 September 2009; accepted 21 October 2009; published 14 April 2010.

[1] The Ama Drime range located at the transition between the high Himalayan range and south Tibet is a N–S active horst that offsets the South Tibetan Detachment System (STDS). Within the horst, a paragneissic unit, possibly attributed to the upper Himalayan crystalline series, overlies the lower Himalayan crystalline series Ama Drime orthogneissic unit containing large metabasite layers and pods that have experienced pressure ≥ 1.4 GPa. Combining structural analysis with new and published pressure-temperature (P-T) estimates as well as U-Th/Pb, $^{39}\text{Ar}/^{40}\text{Ar}$ and (U-Th)/He ages, the P-T-deformation-time (P-T-D-t) paths of the main units within and on both sides of the horst are reconstructed. They imply that N–S normal faults initiated prior to 11 Ma and have accounted for a total exhumation ≤ 0.6 GPa (22 km) that probably occurred in two phases: the first one until ~ 9 Ma and the second one since 6 to 4 Ma at a rate of ~ 1 mm/yr. In the Ama Drime unit, 1 to 1.3 GPa (37 to 48 km) of exhumation occurred after partial melting since ~ 30 Ma until ~ 13 Ma, above the Main Central Thrust (MCT) and below the STDS when these two fault systems were active together. The switch from E–W (STDS) to N–S (Ama Drime horst) normal faulting between 13 and 12 Ma occurs at the time of propagation of thrusting from the MCT to the Main Boundary Thrust. These data are in favor of a wedge extrusion or thrust system rather than a crustal flow model for the building of the Himalaya. We propose that the kinematics of south Tibet Cenozoic extension phases is fundamentally driven by the direction and rate of India underthrusting.

Citation: Kali, E., P. H. Leloup, N. Arnaud, G. Mahéo, D. Liu, E. Boutonnet, J. Van der Woerd, X. Liu, J. Liu-Zeng, and H. Li

(2010), Exhumation history of the deepest central Himalayan rocks, Ama Drime range: Key pressure-temperature-deformation-time constraints on orogenic models, *Tectonics*, 29, TC2014, doi:10.1029/2009TC002551.

1. Introduction

[2] Synconvergence arc-parallel and arc-perpendicular extension phases have taken place in mountain ranges such as the Himalaya-Tibet and the Alps, focusing the attention of many scientists that discuss their rheological and/or kinematics significance. In the Himalaya-Tibet orogen, arc-perpendicular extension is mostly related to Miocene top-to-the-north normal faulting along the South Tibetan Detachment System (STDS) [Burg *et al.*, 1984; Burchfiel *et al.*, 1992]. This structure has been linked either to gravitational collapse of the range [Dewey, 1988], or thrusting of Himalayan crystalline slab (HCS) above the Main Central Thrust (MCT). Some authors consider that the HCS was extruded in a thrust wedge [i.e., Burchfiel and Royden, 1985; Grujic *et al.*, 1996; Guillot and Allemand, 2002, Webb *et al.*, 2007], while others make it a result of ductile channel flow [Nelson *et al.*, 1996; Beaumont *et al.*, 2001; Jamieson *et al.*, 2004]. Arc parallel extension is accommodated by numerous N–S trending normal faults that affect south Tibet with few of them extending across the high Himalayan chain [Molnar and Tapponnier, 1978; Tapponnier *et al.*, 1981; Armijo *et al.*, 1986]. Such extension has been attributed either to dissipation of excess potential energy accumulated, either during the thickening of the Asian margin [Molnar and Tapponnier, 1978] or during uplift of the plateau following detachment of the upper mantle part of the Asian lithosphere [e.g., England and Houseman, 1989], or to accommodation of boundary forces and displacements [e.g., Armijo *et al.*, 1986; Yin, 2000; Tapponnier *et al.*, 2001].

[3] In a few localities, such as the Nyainqntanglha graben [Pan and Kidd, 1992], the Gurla-Mandata dome [Murphy *et al.*, 2002], the Lunggar rift [Kapp *et al.*, 2008], and Dinggye rift [e.g., Burchfiel *et al.*, 1992] ductile deformation related to N–S active normal faults has been observed. Most authors consider that ductile and brittle structures are related to the same, continuous extension phase [Harrison *et al.*, 1995; Kapp *et al.*, 2008; Cottle *et al.*, 2009]. However, initiation of normal faulting in the KungCo graben has been dated at ≤ 4 Ma, implying that two successive arc-perpendicular extension episodes may have taken place in south Tibet, one around 10–12 Ma and another since ~ 4 –6 Ma [Mahéo *et al.*, 2007].

¹Institut de Physique du Globe de Strasbourg, UMR 7516, UDS, EOST, CNRS, Strasbourg, France.

²LST, UMR 5570, Université de Lyon, ENS Lyon, UCB Lyon1, CNRS, Villeurbanne, France.

³Géosciences Montpellier, Université de Montpellier 2, Montpellier, France.

⁴Laboratory of Continental Dynamics, Institute of Geology, CAGS, Beijing, China.

⁵Institute of Tibetan Plateau Research, Chinese Academy of Sciences, Beijing, China.

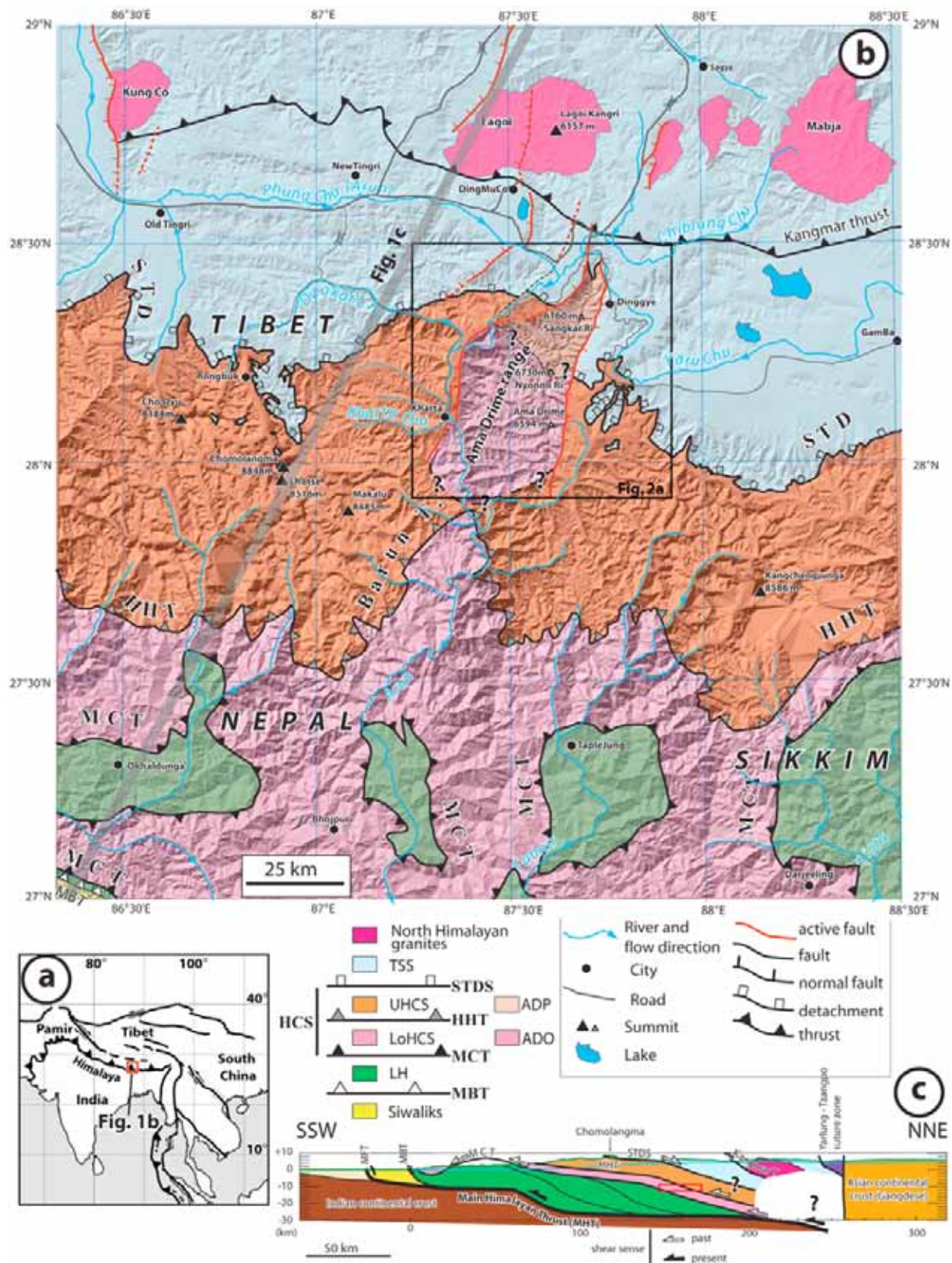


Figure 1

2 of 31

[4] In order to quantify the amount and clarify the mechanisms of rock exhumation in the HCS and to constrain the timing of arc-perpendicular and arc-parallel extensions in south Tibet, we performed a detailed structural, petrologic and thermochronologic study of the Ama Drime range located at the southern end of the Xainza-Dinggye rift. The targeted area is located northeast of the Chomolangma-Makalu massif of the Himalayan range (Figure 1). The Ama Drime range is a key area for at least four reasons. (1) The Ama Drime is located at the transition between the high chain and the Tibetan Plateau, where the STDS is crosscut by N-S active normal faults (Figure 1b), allowing assessment of the relative and absolute timing of these structures. (2) Arc-parallel extension is in brittle and ductile domains so that the continuity of the deformation can be addressed. (3) The Ama Drime range contains the only eclogite found so far in the central Himalayas [Lombardo and Rolfo, 2000; Groppo et al., 2007] implying exhumation of deep-seated rocks that can be used to quantify the magnitudes of vertical and horizontal movements between the MCT and the STDS. (4) The Arun-Phung Chu river that flows along the Ama Drime, is one of the few rivers that leaves the Tibetan Plateau by crossing the central Himalayan chain in between the syntaxes, bringing up the issue of the relation between erosion and exhumation.

[5] Our integrated approach combining structural geology, geomorphology, petrography and multimethod geochronology aims at deciphering and quantifying the structural history of the Ama Drime area and the pressure-temperature-time (P-T-t) evolution of the continental crust, to bring important constraints on orogenic lithospheric deformation models.

2. Geological Setting

[6] Near the Tibet-Nepal-Sikkim borders a ~150 km stretch of the Himalayan range encompass 4 of the 5 highest summits on Earth, including the Chomolangma (Everest) (8848 m above sea level (asl), Figure 1b). The Arun-Phung Chu river, flowing toward the south from Tibet, has cut down to ~2200 m asl across the range, less than 30 km away from the Makalu summit (8485 m asl) (Figure 1b). Headward,

the Arun River is flowing along the western flank of the Ama Drime range, the only significant topographic range protruding from the Himalaya to the north (Figure 1b).

[7] The north-south Arun valley provides a complete geological cross section across the central Himalayas. The main lithotectonic units define stripes, more or less parallel to the range, dipping to the north and separated by major tectonic contacts (Figure 1b). The central unit, the Himalayan crystalline series (HCS) is a sliver of gneiss and granites, sandwiched between less metamorphosed rocks (Figures 1b and 1c). To the bottom (south) the HCS rests on the phyllites and quartzites of the Lesser Himalaya (LH, Tumlingtar unit of Lombardo et al. [1993]). To the top (north) the HCS is separated from the weakly metamorphosed Tethyan sedimentary series (TSS) by the South Tibetan Detachment (STD).

[8] There has been debate on the internal lithotectonic subdivision of the HCS. Within the Arun area two main lithotectonic units have been distinguished within the HCS [e.g., Bordet, 1961; Brunel, 1983; Groppo et al. 2007]: the Lesser and Greater Himalayan crystalline sequences (LHCS and GHCS, respectively). The base of the GHCS corresponds to a thrust zone, locally termed "Barun thrust" whose hanging wall is marked by discontinuous exposure of the Barun orthogneiss [Brunel, 1983]. That thrust zone has been considered by some as the main central thrust (MCT of Brunel [1983] and Goscombe and Hand [2000]). Goscombe et al. [2006] also consider it as the main structure of the belt and termed it "High Himal Thrust" (HHT) (Figure 1b). Most of the GHCS consists of paragneiss and amphibolites, often migmatitic [Brunel, 1983; Lombardo et al., 1993], intruded by Miocene leucogranites including huge laccolithes such as the Makalu-Cho Oyu leucogranite [e.g., Borghi et al., 2003]. Toward the top of the GHCS all rocks, except very few late dikes, are affected by top-to-the-northeast, ductile shearing in the STD shear zone [Burg et al., 1984; Burchfiel et al., 1992; Carosi et al., 1998; Cottle et al., 2007].

[9] Below the GHCS, the LHCS is mostly composed of metapelites overlying the Num/Ulleri orthogneiss [Bordet, 1961; Brunel, 1983; Goscombe et al., 2006]. The LHCS series belong in fact to two distinct basinal sequences deposited on the Indian passive margin, the Mesoproterozoic

Figure 1. Structure of the central high Himalayas. (a) Simplified geological frame of the India–Asia continental collision. (b) Simplified structural map of the Himalayas between the Cho Oyu and the Kangchengjunga. Shaded SRTM DEM is shown in background by transparency. The South Tibet Detachment (STD) and the north Himalayan domes have been mapped from the interpretation of Landsat 7 satellite data checked against personal field observations and published maps [e.g., Burchfiel et al., 1992; Carosi et al., 1998; Searle, 2007]. The HHT (Barun thrust) and MCT are from Goscombe et al. [2006] and Harris et al. [2004]. Active faults appear in red and are from Armijo et al. [1986], Landsat 7 satellite data interpretation, and field observations. Projection is UTM 45. The gray thick line corresponds to the trace of Figure 1c cross section. (c) Simplified generalized cross section of the Himalayas. NNE–SSW interpretative cross section at ~87°E, few kilometers west of the Ama Drime range. Main geological units are as in Figure 1b, and main structures geometry is from Bollinger et al. [2004]. The green line corresponds to the upper relief (i.e., Chomolangma), and the blue line corresponds to the lower relief (i.e., Arun valley); no vertical exaggeration. The box indicates the approximate location of the Ama Drime rock before their exhumation in the horst (see Figure 12b). TSS, Tethyan sedimentary series; HCS, Himalayan crystalline series, UHCS, upper Himalayan crystalline series; LoHCS, lower Himalayan crystalline series; LH Lesser Himalaya series; ADP, Ama Drime paragneisses; ADO, Ama Drime orthogneisses; STDS, South Tibet Detachment System; HHT, High Himal Thrust; MCT, Main Central Thrust; MBT, Main Boundary Thrust; see section 2 for definitions.

Lesser Himalayan Sequence and the Neoproterozoic-Cambrian Greater Himalayan Sequence, separated by the Himalayan unconformity (HU) [Goscombe *et al.*, 2006]. The LHCS is strongly deformed, is bounded at its base by mylonites and thrust sheets [Bordet, 1961; Meier and Hiltner, 1993], and has often been referred as the MCT zone. The basal contact of the LHCS will be referred here as the Main Central Thrust or MCT (MCT2 of Arita [1983], MCT of Heim and Gansser [1939], Le Fort [1975], DeCelles *et al.* [2001], and Goscombe *et al.* [2006]).

[10] In order to avoid the ambiguities resulting from various definitions of the MCT and of the GHCS and LHCS series we use in the following a structural terminology: the upper Himalayan crystalline series (UHCS) corresponds to the series bounded at their top by the STDS and at their bottom by the HHT as mapped by Goscombe *et al.* [2006] (Figure 1b). The lower Himalayan crystalline series (LoHCS) are bounded at their top by the HHT and are their bottom by the MCT as mapped by Goscombe *et al.* [2006] (Figure 1b).

[11] In map view, the range-parallel orientation of the MCT and parallel thrusts are locally sinuous, particularly around the main rivers flowing down from the Himalayas (Figure 1b). Along the Arun River, such map pattern is attributed to the Arun anticline with a ~N-S axis [Bordet, 1961], and some [e.g., Borghi *et al.*, 2003; Liu *et al.*, 2007] have interpreted the Ama Drime range as the northern prong of the Arun anticline. There is still considerable debate whether the main structures can be traced at the scale of the whole orogen but one possible interpretation is that two main thrusts can be traced for several hundreds of kilometers: the upper MCT (MCT_U, joining the Vaikrita, Mahbharat, Chomrong, Barun, HHT and Kakhtang thrusts) and the lower MCT (MCT_L joining the Ramgarh and Muniari thrusts).

3. Geology and Structure of the Ama Drime Range and the Dinggye–Kharta Area

3.1. Topography, Morphology, and Active Tectonics

[12] The Ama Drime range exhibits a double-crested horst morphology that is mostly controlled by active normal faults [Armijo *et al.*, 1986]. The range displays several peaks over 6000 m asl, the highest being the Nyonno Ri (6730 m asl) (Figures 2a and S1 in the auxiliary material).¹ To the east, the range shows for more than 50 km a very steep linear

NNE–SSW crest at 5000 to 6700 m asl. This 500 to 1000 m high wall is bounded by a ~50° east dipping active normal fault, the Dinggye fault, whose recent activity is attested by spectacular triangular facets and offset moraine ridges [Armijo *et al.*, 1986; Zhang and Guo, 2007] (Figure 3a). To the west, the Arun River flows parallel to the west dipping Kharta active normal fault (Figure 2a). The active fault length is shorter (~30 km) than the Dinggye fault and the elevation of the western Ama Drime crest is slightly lower than to the east, but the flank is steeper and the activity of the fault attested by ~1500 m high triangular facets, fluvial terraces and moraines offsets (Figures 3b and 3c).

[13] On both sides of the range, quartz cataclasite outcrops on the topographic scarps (Figures 3a and 3c). Brittle faults strike almost N–S and generally dip steeply (~45 to 55° on average) to the west on the western side of the range and to the east on the eastern one, in good accordance with the geometry of the active faults deduced from the morphology (Figures 2a, 4e, 4f, 4g, 4h, 4k, and 4m). Slickensides when present indicate almost pure dip slip motions (Figure 4). On the eastern side of the range, normal faults parallel to the Dinggye fault slice the foothills to at least 5 km away from the topographic front and have tilted to the west the metamorphic series of the STD shear zone (Figure 2b, top).

[14] At the northern end of the range, the Sangkar fault exhibits clear evidences for recent activity with triangular facets and fault scarps (Figure 3d). It is probable that the Sangkar and Kharta active faults are linked by an ~E–W active fault [Armijo *et al.*, 1986]. At the northern end of the Kharta fault, the Arun–Phung Chu river has a very peculiar course: it enters within the footwall of the active fault, where it carves deep gorges and turns around the Yo Ri promontory before exiting in the Kharta basin (Figure 2a). This fact was already noticed by Wager [1937], who interpreted the river to be antecedent to the building of the high relief of the Ama Drime, while Armijo *et al.* [1986] interpreted that pattern as resulting from the capture of the Phung Chu by the Arun River.

[15] While the eastern and western crest of the Ama Drime have almost the same altitude, the water divide is located along the eastern one (Figure 2a), highlighting a profound asymmetry in recent tectonics and/or erosion that may be in part induced by the Arun River down cutting.

[16] The Ama Drime area shows a relatively high microseismic level documented both by the seismic network of Nepal [Pandey *et al.*, 1995; Cattin and Avouac, 2000] and by temporary seismic networks in Nepal and southern Tibet [Monsalve *et al.*, 2006]. In the south of the Ama Drime area, all instrumental $M \geq 5$ and part of the $2 \leq M \leq 4$ earthquakes occur at depths ≥ 50 km, and are thought to take place in the lower Indian crust and upper mantle as a result of continuous

¹Auxiliary materials are available in the HTML. doi:10.1029/2009TC002551.

Figure 2. Structure of the Ama Drime Range. (a) Structural map of the Dinggye–Kharta area corresponding to the frame on Figure 1b. Drawn from satellite image interpretation and fieldwork. Projection is UTM45. The Kartha–Saer unit is attributed to the upper Himalayan crystalline series while the Ama Drime orthogneisses are attributed to the lower Himalayan crystalline series (see text). Structural observations are reported as well as samples discussed in this study. For other sample locations, see Figure S1. Each lettered black box corresponds to a stereonet (Figure 4). Sections A–B and C–D (Figure 2b) are located. (b) Geological schematic cross sections of both flanks of the Ama Drime range. Cross sections located on Figure 2a. Drawn from field observations (see text and Figure 3). No vertical exaggeration.

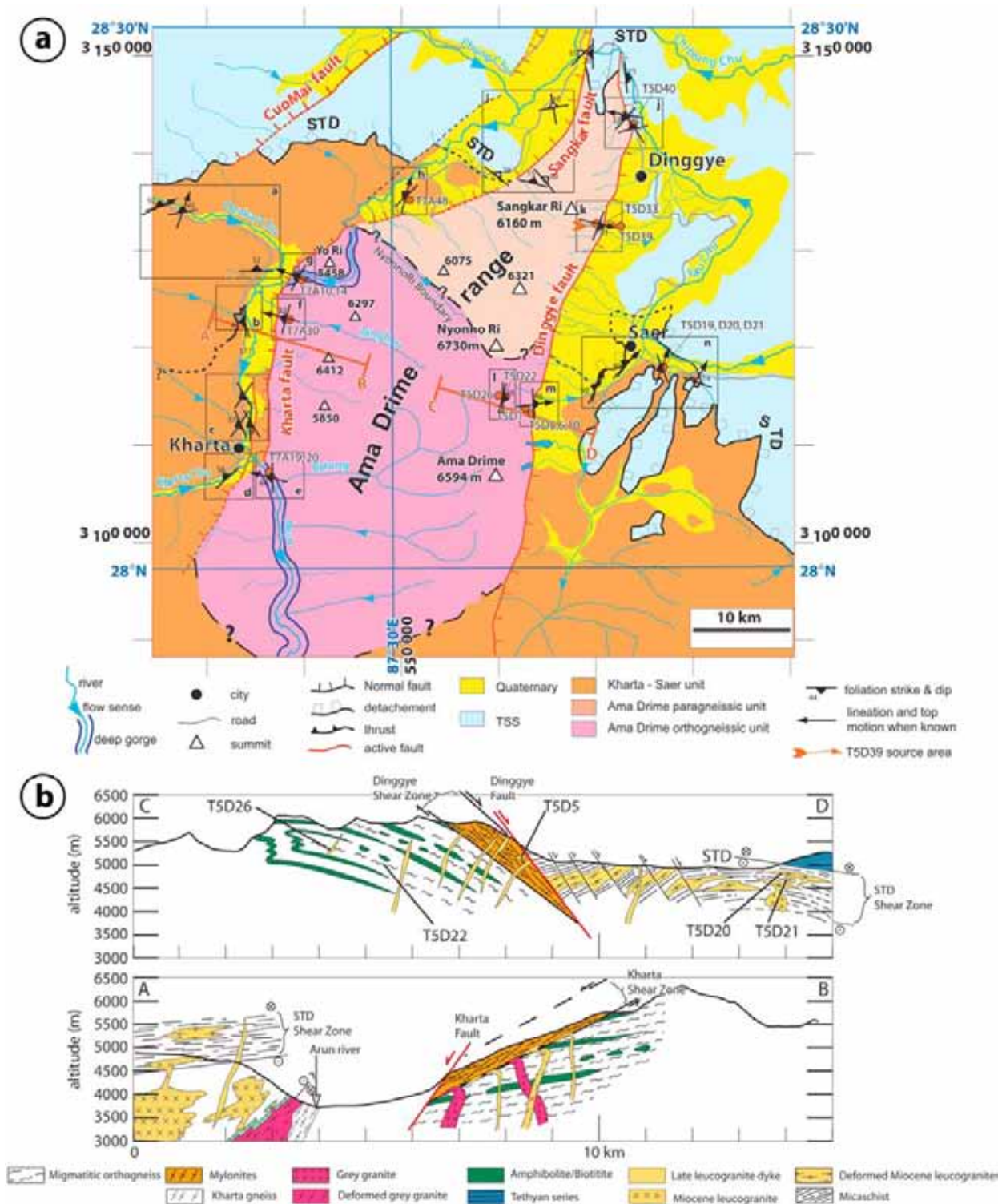


Figure 2

subduction and eclogitization [Monsalve *et al.*, 2006; Schulte-Pelkum *et al.*, 2005; Baur, 2007]. In the north, earthquakes are much shallower (depth ≤ 25 km) and have focal mechanisms compatible with north-south trending normal faulting. This seismic activity occurs on active normal faults that connect the Ama Drime horst to the Xainza rift located north of the Yarlung-Tsanpo suture zone [Pandey *et al.*, 1999; Monsalve *et al.*, 2006].

[17] The Ama Drime range is thus an active horst bounded by two conjugate active normal fault systems, at the southern end of the Xainza-Dinggye fault system [e.g., Armijo *et al.*, 1986].

3.2. Rock Lithology, Structures, and Microstructures

[18] Three main lithologic units can be distinguished in the study area. (1) The Kharta-Saer unit, mostly composed of metasedimentary rocks and rare amphibolites intruded by numerous leucogranites. This unit includes the STD shear zone and the Kharta gneiss. (2) The Ama Drime orthogneissic unit, which mainly consists in granitic gneisses and migmatites embedding numerous metabasic layers and pods. (3) The Ama Drime paragneissic unit localized above the Ama Drime orthogneissic unit, which is mostly represented by paragneisses and pelitic schists. Leucogranite dikes crosscut all units (Figures 2a and 2b).

3.2.1. South Tibetan Detachment and Shear Zone

[19] Near the Ama Drime range, the STD has been described across the Dzakar river [Burg *et al.*, 1984; Cottle *et al.*, 2007], and south of Dinggye [Burchfiel *et al.*, 1992; Leloup *et al.*, 2009, 2010]. The STD separates deformed

garnet-micaschists and leucogranites of the UHCS characterized in the STD shear zone (STDSZ) by ~E-W foliations gently dipping to the north, NE trending lineation and normal (top-to-the-north) sense of shear, from weakly metamorphosed Tethyan sedimentary series above. In the STDSZ, few undeformed leucogranites postdating deformation have also been observed [Leloup *et al.*, 2009, 2010]. As the foliation dips gently, there is no access to a complete section of the STDSZ near Saer and its total thickness cannot be assessed. However, along other sections, as near Rongbuk or at the top of the Kula Kangri leucogranite, the STDSZ is typically 200 to 300 m thick [Murphy and Harrison, 1999; Edwards *et al.*, 1996]. 100 m below the STD, garnet-micaschists of the STDSZ are characterized by the transition from a staurolite-garnet paragenesis (prekyematic?) to sillimanite-garnet (synkinematic) assemblage [Leloup *et al.*, 2009, 2010]. The corresponding P-T evolution constrained by pseudosections and garnet isopleths, is characterized by a peak pressure of ~0.6 GPa (~22 km) and 550°C followed by a slight heating and decompression until ~0.45 GPa (~27 km) and ~625°C, preceding a phase of decompression and cooling (Figure 5c) [Leloup *et al.*, 2009, 2010].

[20] Combining published observations, fieldwork, and Landsat satellite image interpretation, Leloup *et al.* [2010] propose a map of the STD (Figure 2a). This mapping confirms that the STD dipping $\sim 10 \pm 5^\circ$ to the NNE, is deflected to the north around the Ama Drime range, and is cut and offset by the N-S active normal faults. The apparent horizontal offsets of the STD are of 35 ± 5 km along the

Figure 3. Figures 3a–3d are field pictures of active faults bounding the Ama Drime Range. (a) Triangular facets along the Dinggye active normal fault. View toward west. The closest facet is ~500 m high. The two converging black arrows indicate the fault trace. White arrow points to quartz cataclasites whose fault surface strikes N06 49E. Nyonno Ri summit (6730 m) in the background. (b) Triangular facets along the Kharta active normal fault. View toward east. In the background, black arrows indicate the trace of the east branch of the Kharta active fault. Facets are ~1300 m high above the arrows. In the foreground, white arrows indicate the trace of the west branch of the Kharta fault offsetting alluvial terraces of the Kharta Chu. (c) Along-strike view of the north Kharta active normal fault. View toward the SSW from north of the outlet of the upper Arun gorges. White arrows point to a 100 m high offset of an alluvial terrace. Outcrop in the foreground is a fault surface striking N15 55W at the top of quartz cataclasites. (d) Sangkar active normal fault. View toward the SE. Trace of the STD on the northern Ama Drime crest is drawn. The two converging black arrows indicate the fault trace. The Sangkar Ri summit (6160 m) sticks out in the background. An enlargement of this summit from a different point of view shows UHCS series gently dipping to the north. Figures 3e–3h are field pictures orthogneiss of the Ama Drime south of the Nyonno Ri. (e) Folded basic layers within migmatites south of the Nyonno Ri. The cliff is ~400 m high. The fold axes trend ~N-S. (f) Cliff north of the Ama Drime summit showing leucocratic dikes cutting across previous foliation including boudinaged basic layers (inset with dikes highlighted in white). The visible part of the cliff is ~500 m high. View toward the south. (g) Basic enclave within migmatite. Hammer for scale. Note centimeter-scale garnets in basic level (inset). Migmatitic sample T5D22 comes from this outcrop. (h) Basic layer within migmatites crosscut by a leucocratic pegmatitic dike (LD, sample T5D26). Figures 3e, 3g, and 3h are from a glacial valley south of the Nyonno Ri (zone 1, Figure 2a). Figures 3i–3m are field pictures normal shear zones on both side of the Ama Drime range. (i) Chlorite-grade C/S deformation in orthogneiss showing top-to-the-east normal motion. Footwall of Dinggye normal fault. Glacial valley south of the Nyonno Ri summit (zone m, Figure 2a). See Figure 4m for foliation and lineation attitude. (j) Late leucocratic dike (LD, sample T5D5) crosscutting mylonitic orthogneiss (sample T5D6). Footwall of Dinggye normal fault. Hammer gives scale. Glacial valley south of the Nyonno Ri summit (zone m, Figure 2a). (k) Close-up of Figure 3j mylonitic orthogneiss, showing top-to-the-east (normal) shear sense. Hammer gives scale. See Figure 4m for foliation and lineation attitude. (l) Mylonitic orthogneiss and biotite-rich enclave. Knife gives scale. Footwall of Kharta normal fault in Arun-Phung Chu gorges (zone g, Figure 2a). Shear planes indicate top-to-the-west (normal) shear sense. See Figure 4g for foliation and lineation attitude. (m) Stretched remnants of tourmaline bearing leucocratic dikes. Hammer gives scale. Footwall of Kharta normal fault in Arun-Phung Chu gorges (zone g, Figure 2a).

Dinggye active normal fault, and of ~15 km across the Sangkar fault (Figure 2a), which correspond to vertical offsets of 4.4 to 9.4 and 1.3 to 4 km, respectively [Leloup *et al.*, 2009, 2010].

[21] At the scale of the orogen the STD is broadly located at the transition between the Tibetan Plateau and the high Himalayan chain. However, it has no clear morphological expression, it is crosscut by active N-S normal faults and no crustal earthquake indicative of ~E-W normal faulting has been reported. The STD is thus a fossil structure.

3.2.2. Kharta Area

[22] Along the Dzakar-Phung Chu valley, ~12 km south of the STD (~8 km below), foliations dip to the west (Figures 2a, 4b, 4c, and 4d). In this area the main lithologies are garnet bearing metapelites, often migmatitic, associated with minor orthogneiss, metabasite and calc-silicate rocks.

These lithologies are named the Kartha gneiss and attributed to the GHCS (our UHCS) by Borghi *et al.* [2003] that document an adiabatic decompression from ~0.8 GPa and ~700°C, prior to a roughly isobaric cooling at ~0.2 GPa (Figure 5a). Several generations of leucosomes are conspicuous, ranging from concordant leucogranitic Gt-Sill orthogneiss to discordant cordierite bearing leucogranite veins and pods [Borghi *et al.*, 2003]. All these rocks are crosscut by Miocene tourmaline leucogranitic dikes [Visonà and Lombardo, 2002]. North of Kharta a large granite body that crosscuts the gneiss is overlaid by a west dipping shear zone with N-S lineations (Figure 4b). The Kharta gneiss exhibits either no lineation or N-S to NE-SW trending lineations (Figures 2a, 4c, and 4d). In the absence of clear shear criteria it is difficult to relate this deformation to a precise tectonic episode.

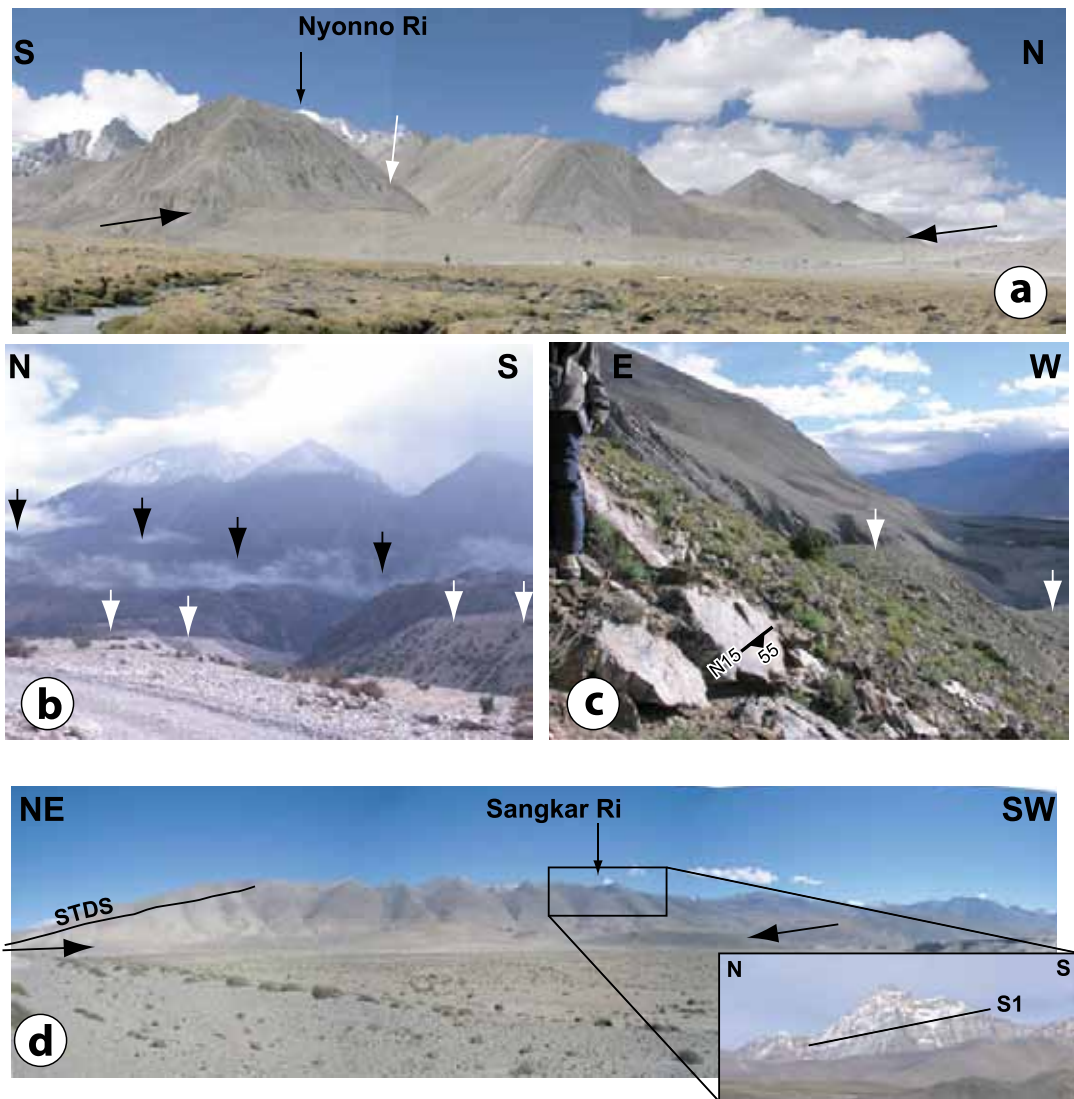


Figure 3

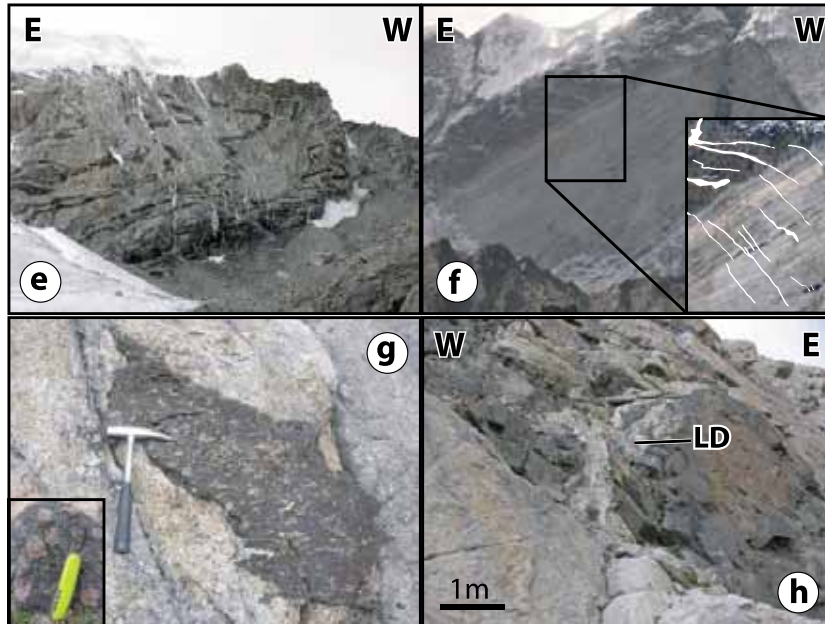


Figure 3. (continued)

3.2.3. Ama Drime Range

[23] Except at the very northern tip of the range, above the STD, all rocks comprised between the Kharta–Sangkar and Dinggye active faults are crystalline rocks belonging to the HCS. Along the Belung and Tanghyu valleys most rocks are migmatitic orthogneiss containing large layers and boudins of metabasites that have recorded eclogite facies metamorphism, and that have been attributed to the LHCS (our LoHCS) because of similar rock types [Groppi *et al.*, 2007]. Inherited U-Pb zircon and monazite ages from these orthogneisses provide similar 1.7–1.8 Ga age than in the Uleri orthogneisses of the LoHCS [Robinson *et al.*, 2001; Liu *et al.*, 2007; Cottle *et al.*, 2009] confirming the possible correlation. Similar rocks outcrop in the core of the range and south of the Nyonna Ri on the eastern side of the Ama Drime (Figures 2a and 3b). These lithologies constitute the Ama Drime orthogneissic unit (ADO).

[24] Deformed rocks outcropping east of Kharta in the footwall of the Kharta fault have been interpreted by Groppo *et al.* [2007] as corresponding to the main thrust between the LHCS (LoHCS) and the GHCS (UHCS) (MCTu). In that area, rocks indeed show a strong deformation, with foliations dipping N179 44W on average and lineations striking ESE-WNW to NW-SE (Figures 2a and 4e). However, analysis of the deformation in rocks that show a clear downdip lineation reveals top-to-the-west shear senses and thus a normal ductile shear zone. That ductile shear zone is in the direct prolongation of the eastern branch of the Kharta active fault (Figure 2a). The relative dispersion of the lineations (Figure 4e) suggests that a pre-

vious deformation lineation has been affected by the ductile normal fault. Ductile mylonites with ~N-S foliation and top-to-the-west motion (Figure 3) are observed everywhere in the footwall of the Kharta fault and constitute the Kharta shear zone (Figure 2a). The mylonites trend N15 32W with lineations striking N284 on average in Tanghyu valley (Figure 4f). In the upper Arun gorges the foliations strike N29 27W and the lineations N290 (Figures 2a and 4g).

[25] Similarly, east dipping mylonites have been described on the eastern side of the range in the footwall of the Dinggye fault defining the Dinggye shear zone (Figures 2b, 3i, 3j, and 3k) [Zhang and Guo, 2007]. The mylonites trend N178 46E SE of the Nyonna Ri and N21 33E east of the Sangkar Ri, with lineations trending N82 and N103, respectively (Figures 2a, 4k, and 4m).

[26] On both sides of the Ama Drime, normal deformation is observed to occur at various temperatures from ductile mylonites to cataclasites with the temperature of deformation decreasing toward the active fault. This pattern is classically interpreted as the progressive uplift of the deep part of the fault in its footwall [e.g., Leloup *et al.*, 1993]. All leucocratic dikes appear to be affected by the normal ductile deformation along the western flank (Figures 2b and 3m) while several dikes crosscut the mylonitic foliation along the eastern flank (Figures 2b and 3j). This could indicate that the western shear zone was active until more recent times than its eastern counterpart.

[27] In the northern part of the Ama Drime range, north of the Nyonna Ri, lithology change to paragneisses and pelitic schists crosscut by leucogranites here defined as the Ama

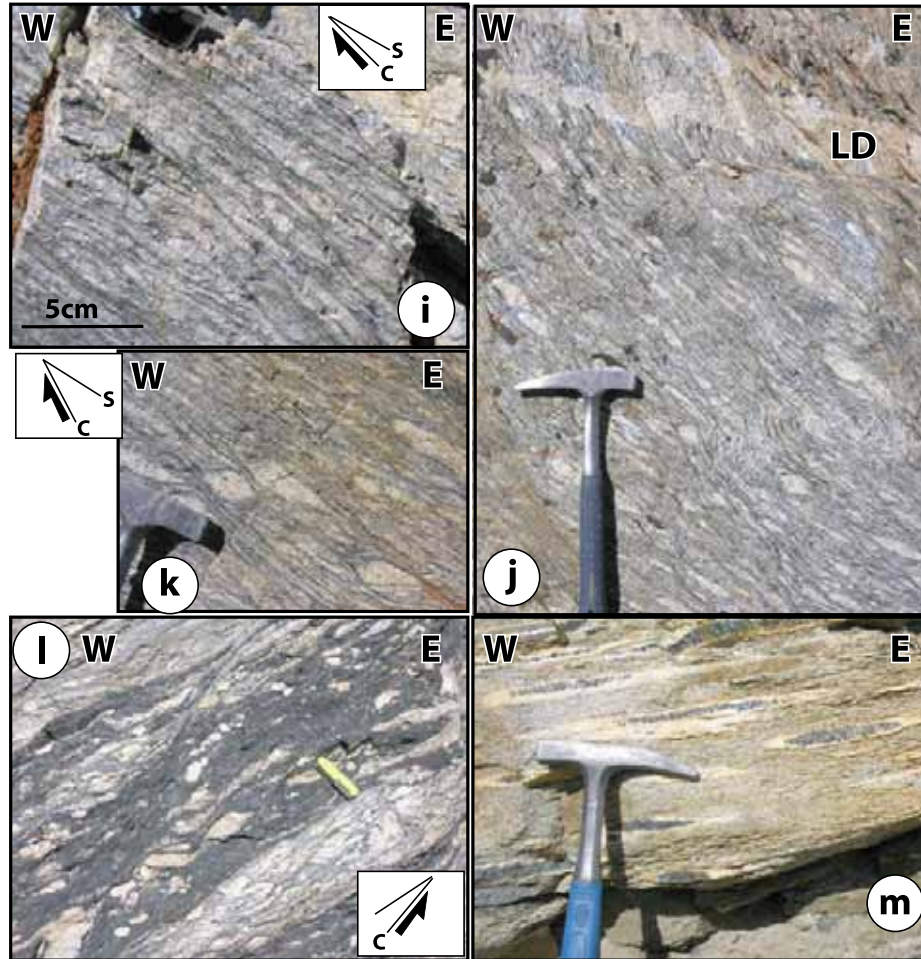


Figure 3. (continued)

Drime paragneissic unit (ADP). The top of this lithologic unit, just bellow the STD is mostly composed of highly sheared pelitic schists and leucogranites similar to those found in the Kharta-Saer unit within the STD SZ. Such rocks are visible dipping to the north below the Sangkar Ri summit (Figure 3d). Paragneiss also outcrop farther south on the eastern flank of the range where they are affected by the Dinggye shear zone (zone k, Figure 2a). Given their structural position, above the ADO attributed to the LoHCS and just below the STD shear zone within the UHCS, such gneisses could be the equivalent of the Kharta gneiss. However, the lack of observation and detailed fieldwork between the Sangkar Ri and the Nyonno Ri leave open other interpretations, as for example a correlation with the LoHCS paragneisses overlying the Uleri Gneiss [Goscombe *et al.*, 2006]. We propose a possible map for the boundary between the Ama Drime paragneissic and orthogneissic units (Figure 2a), although precise mapping and characterization would require further fieldwork. We named this boundary the Nyonno Ri boundary.

[28] There are no precise descriptions of the deformation of the orthogneiss in the core of the Ama Drime. Away from the bounding normal faults, however, the metabasic rocks, when they have not been disrupted in the surrounding migmatites (Figure 3g), define kilometer long layers that are affected by folds with approximately horizontal axial planes and ~N-S trending axis (Figure 3e). South of the Nyonno Ri, deformation at the contact between a ~3 m thick metabasic layer (Figure 3h) and the migmatites is characterized by foliation gently dipping to the east and N-S lineations (Figure 4l).

[29] North of the Ama Drime range, quartzites very similar to those outcropping on the active normal fault scarps farther south outcrop ~1 km north of the Kharta-Sangkar fault (Figure 2a). Foliation in the quartzites trends N24 38W (Figure 4h) parallel to normal faults that affect and tilt the surrounding micaschists and gneiss. When back-tilted the gneiss show a ~N15 striking lineation parallel to STD shear zone lineations in the area (Figure 4h).

[30] Some authors [e.g., Borghi *et al.*, 2003; Liu *et al.*, 2007] have proposed that the Ama Drime is the northern

continuation of the Arun anticline described by *Bordet* [1961]. The Ama Drime is bounded on both sides not only by active normal faults, but also by ductile ones. In that context it appears more as a horst than a fold. Because low-angle ductile normal faults outcrop in the footwall of the steeper active normal faults it is very tempting to interpret these structures as resulting from a single continuous metamorphic core complex type of deformation [e.g., *Zhang and Guo*, 2007; *Jessup et al.*, 2008; *Cottle et al.*, 2009].

4. P-T-D-t Path of the Crystalline Rocks of the Ama Drime

4.1. P-T Paths

[31] The petrologic and thermobarometric studies of *Lombardo and Rolfo* [2000], *Liu et al.* [2005], *Groppi et al.* [2007], and *Liu et al.* [2007] have established that the Ama Drime orthogneissic unit contains the only eclogite found so far in the central Himalayas. These rocks have recorded pressure of at least 1.4 GPa (~52 km depth) and have been granulitized at high temperature (~800°C) during their exhumation (Figure 5b).

[32] In the following, we present the first petrologic data of the Ama Drime paragneissic unit within the Ama Drime range. Until now such data were restricted to Kharta-Saer unit in the hanging wall of the Kharta fault [*Borghi et al.*, 2003] (Figure 5a) or the Dinggye fault [*Leloup et al.*, 2009, 2010] (Figure 5c). This study is based on the combination of thin section analyses, measurement of mineral chemical composition (punctual and mapping) on a SX100 Cameca CAMEBAX Microprobe at the University of Montpellier operating at 15 kV and 15 nA with a counting time of 10 s per element, and pseudosection and isopleth calculation using Perple_X software [*Connolly*, 1990] (detailed procedure available in Text S1, Appendix I) at fixed bulk-rock composition (see Text S1, Appendix I).

4.1.1. P-T Path of the Ama Drime Paragneissic Unit in the Footwall of the Dinggye Active Fault

[33] West of Dinggye, in the footwall of the Dinggye active fault, paragneiss and intruding leucogranites are both affected by top-to-the-east (N103) normal ductile shear (k , Figures 2a and 4). Sample T5D33 from such paragneisses was collected at an elevation of 5125 m east of the Sangkar Ri, while T5D39b is a boulder collected from the downstream river fan (Table 1 and Figure 2a). Despite not having sampled in situ, T5D39b was selected because it comes unambiguously from the Sangkar Ri eastern flank and is much fresher than T5D33.

[34] The paragneiss contains biotite, sillimanite, garnet (with biotite, plagioclase, quartz, oxyde and muscovite inclusions), quartz, plagioclase, muscovite, and accessory zircon, apatite and oxides. This paragneiss is locally migmatitic and contains K-feldspar within millimeter-scale unconnected pods. The foliation is defined by biotite, and rare late muscovite while the lineation is outlined by sillimanite. Sample T5D33 is strongly retrogressed and garnet is mostly replaced by chlorite. T5D39b does not show any evidence of such late retrogression and few kyanite relicts have been preserved in the foliation.

[35] Synkinematic biotite, sillimanite and muscovite as well as prekinematic to synkinematic garnets indicate top-to-the-east high-temperature ductile normal shearing (Figure 6a).

[36] Four successive paragenesis are recognized in the paragneiss: (P1) biotite + plagioclase + quartz + muscovite as inclusions in large garnets + garnet core; (P2) kyanite or sillimanite + biotite + plagioclase + quartz (including myrmekites) + garnet rim (inclusion-poor zone) + K-feldspar + melt with kyanite predating sillimanite. Note that locally kyanite is included in the garnet rim. This paragenesis is found in the main foliation and in the shear planes (Figure 6a). This implies that a top-to-the-east normal ductile shearing occurred under granulite facies conditions, contemporaneously with partial melting; (P3) biotite + plagioclase + quartz; (P4) The medium- to low-temperature evolution is characterized by replacement of aluminosilicates by muscovite, growth of andalusite replacing kyanite and destabilization of garnet replaced by chlorite, muscovite and chlorobiotite. Continuation of top-to-the-east normal motion during medium temperature evolution is evidenced by the truncation of sillimanite with fractures filled by muscovite and the rare occurrence of synkinematic muscovite in the foliation (Figure 6a). The low-temperature evolution is associated with the garnet fracturation and chloritization.

[37] Biotites (P1 and P3) show high X_{Fe} [(Fe/(Fe + Mg)] of 0.57 to 0.62 in both samples (Table S2, section 1). In sample T5D39b, the Si(IV) amount in muscovite is significantly higher in garnet inclusions (6.4–6.6 atoms per formula unit (apfu) on the basis of 22 oxygens) than in the matrix (6.1–6.3 apfu) (Table S2, section 2). This suggests that the muscovite in inclusions (P1) crystallized at higher pressure than muscovite in the matrix (P4) [*Powell and Evans*, 1983].

[38] X-ray map and microprobe traverse of T5D39b garnet show complex zoning, with a high-calcium and inclusion-

Figure 4. Structure geometry in the Ama Drime area. Lower hemisphere, equal-area stereonet diagrams. Corresponding areas are located on Figure 2a. All data are listed in Table S1. Foliations and lineations and brittle faults (in gray) are plotted. (a) South Tibetan shear zone of the Dzakar Chu valley. (b) Arun valley below the STDSZ (Kharta-Saer unit). (c) Kharta gneiss immediately north of Kharta. (d) Kharta gneiss SE of Kharta. (e) Arun gorges south of Kharta (Kharta SZ) (here gray corresponds to low-grade deformations). (f) Western part of the Tanghyu valley (Ama Drime orthogneisses, Kharta SZ). (g) SW part of the upper Arun-Phung Chu gorge (Ama Drime orthogneisses, Kharta SZ). (h) Kharta-Saer unit north of the Ama Drime. (i) Foliations in the Ama Drime paragneisses and schistosity (dashed) in the Tethyan Sedimentary Sequence (TSS) NW of the Sangkar Ri. (j) North of Dinggye (Ama Drime paragneisses). (k) SE of the Sangkar Ri (Ama Drime paragneisses, Dinggye SZ). (l) South of the Nyonno Ri (Ama Drime orthogneisses). (m) SE of the Nyonno Ri (Ama Drime orthogneisses, Dinggye SZ). (n) STDSZ south of Dinggye (east of Saer) and S0/S1 and lineation in TSS.

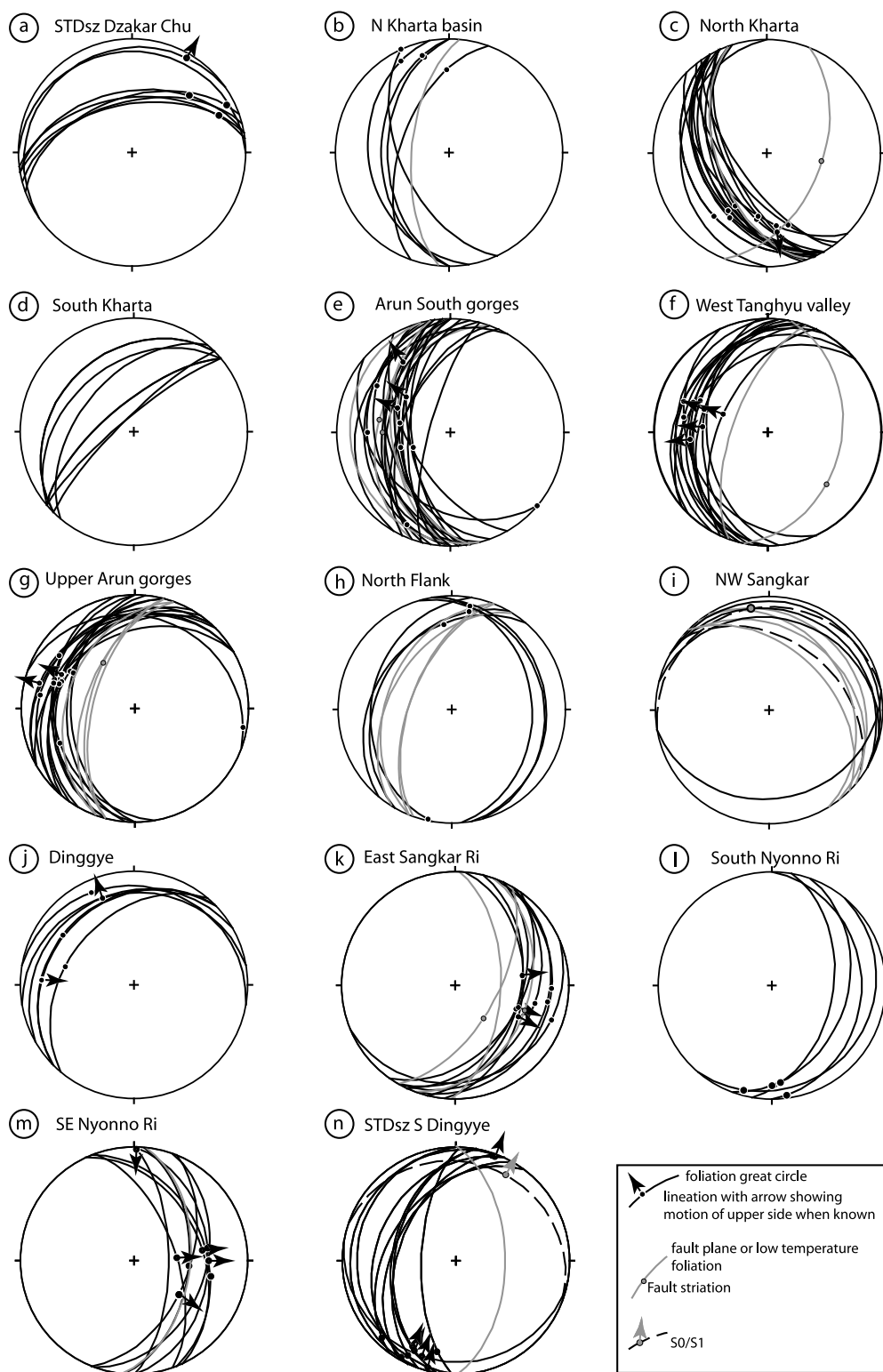


Figure 4

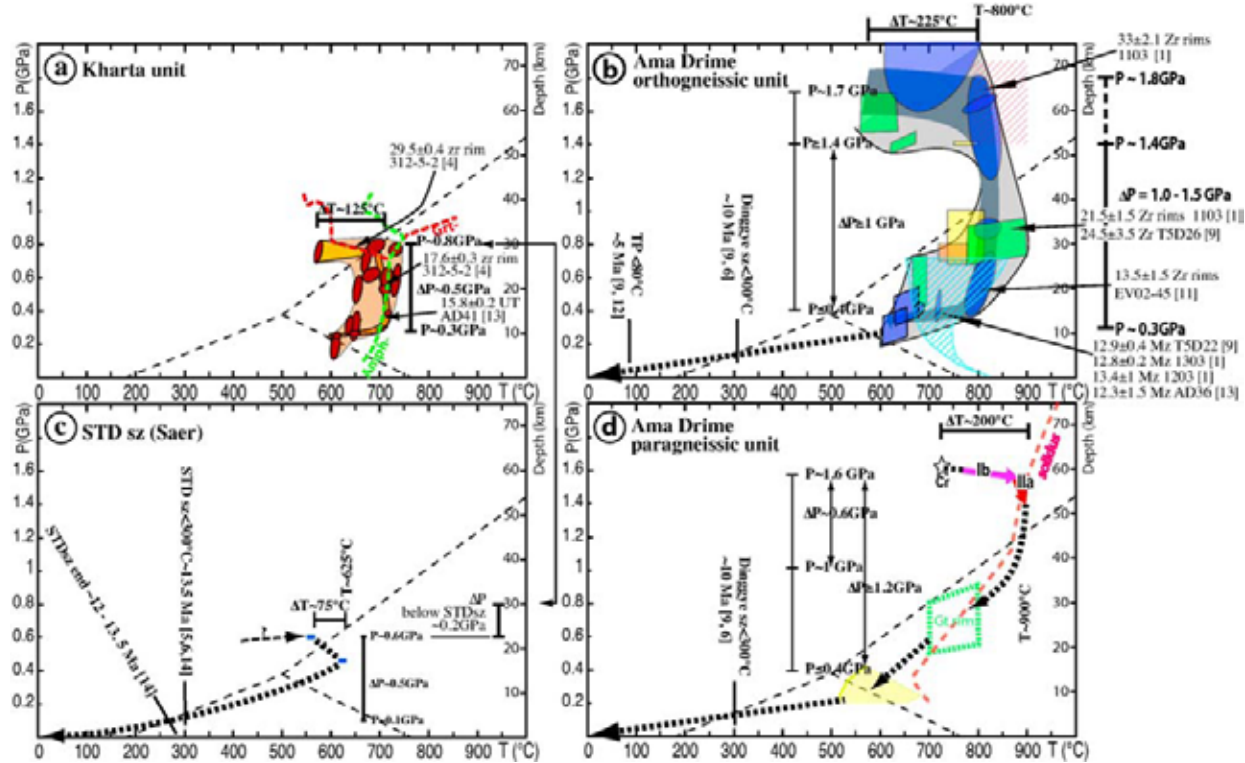


Figure 5. P-T paths and corresponding timing constraints. Aluminosilicates fields are plotted for reference. Samples are located on Figures 2b and S1. Numbers without units are ages in Ma. See text for details. (a) Kharta gneiss (Khart-Saer unit west of the Kharta fault). P-T constraints from *Borghi et al.* [2003] for samples Ev8, Ev13, Ev16, Ev21, Ev45, Ev70, Ev80, and TB25. Ellipses correspond to individual sample and paragenesis P-T determinations. The narrow dark path corresponds to P-T conditions constrained from isopleths. The lighter path connects the largest documented pressure (M2, sample Ev45) with the earliest paragenesis (M1, sample Ev45). The stability fields of amphibole and garnet are drawn for metabasite chemistry [*Groppi et al.*, 2007] in order to discuss the ages of zircons overgrowths within sample 312-5-2. Age constraints from *Li et al.* [2003] [4] (sample 312-5-2) and *Cottle et al.* [2009] [13] (sample AD41). (b) Ama Drime orthogneisses. P-T data from *Liu et al.* [2005] (green, samples T01–T386 and T01–T389); *Liu et al.* [2007] [1] (yellow, samples 1103 and 1303); *Groppi et al.* [2007] (blue, samples Ev02–Ev42 and Ev45, Ev97–Ev60), and *Cottle et al.* [2009] [13] (orange, sample AD43). All samples are amphibolite boudins unless the ones dark framed that correspond to embedding gneiss. Range of initial vapor-absent melting by mica breakdown between 1.4 and 1.8 GPa (red hatching) compiled from *Vielzeuf and Holloway* [1988], *Vielzeuf and Clemens* [1992], *Vielzeuf and Montel* [1994], *Patiño-Douce and Beard* [1996], *Castro et al.* [2000], *Harris et al.* [2004], *Auzanneau et al.* [2006], and *Indares et al.* [2008]. Range of monazite crystallization below 0.7 GPa (blue hatching) from *Kelsey et al.* [2008]. Timing constraints from *Liu et al.* [2007] [1] (samples 1103 and 1303), *Rolfö et al.* [2005] [11] (Ev02–45), *Cottle et al.* [2009] [13] and this study [9] (sample T5D22). (c) STD shear zone near Saer. P-T constraints from *Leloup et al.* [2010] [14]. The ~300°C timing constraint comes from micas argon dating [*Leloup et al.*, 2009, 2010] [14]; *Hodges et al.* [1994] [5]; *Zhang and Guo* [2007] [6]). (d) Ama Drime paragneisses. P-T constraints from this study [9] (T5D33 and T5D39b, see Figure 6). The ~300°C timing constraint comes from micas argon dating (this study [9] and *Zhang and Guo* [2007] [6]).

rich core (garnet I, P1) and a late, low-calcium, inclusion-poor rim (garnet II, P2) (Table S2, section 3, and Figures 6b and 6c).

[39] In more detail, garnet I (P1) can be separated into two zones. The innermost zone (Ia, Figure 6c) is rich in muscovite and plagioclase inclusions, and does not present clear

composition zoning (Alm 0.662–0.685, Pyr 0.180–0.192, Gros 0.104–0.124, Spes 0.031–0.034) (Table S2, section 3, and Figure 6c). Detailed analysis of zone Ia X-ray map shows that grossular and pyrope contents decrease and almandine content increases concentrically around the inclusions (Figure 6b). Such pattern suggests that chemical

Table 1. Sample Locations and Facies^a

Samples	General Location	Zone in Figure 2a ^b	GPS Outcrop	UTM Coordinates (Zone 45R)			Rock Type	Geochronology and Petrology	Reference
				Easting	Northing	Altitude (m)			
T5D1	SE Nyondo Ri	m	179	562748	3113774	5217	orthogneiss	U/He (ap)	this study
T5D5	SE Nyondo Ri	m	178	563487	3113287	5069	late leucoocratic dike	U/Pb (mz SHRIMP Beijing)	this study
T5D6	SE Nyondo Ri	m	178	563487	3113287	5069	orthogneiss	Ar/Ar (bio)	this study
T5D10	SE Nyondo Ri	m	184	563427	3114679	5237	garnet migmatitic gneiss	Ar/Ar (bio)	this study
T5D19b	STDSDZ S Dinggye	o	222	576656	3117898	4263	garnet-sillimanite micaschist	Ar/Ar (bio); Petrology	Leloup et al. [2010]
T5D20	STDSDZ S Dinggye	o	222	576656	3117898	4263	deformed leucogranite	U/Pb (zr IMS1270 Nancy, mz SHRIMP Beijing); Ar/Ar (bio, mu)	Leloup et al. [2010]
T5D21	STDSDZ S Dinggye	o	222	576656	3117898	4263	undeformed leucogranite	U/Pb (zr IMS1270 Nancy, mz SHRIMP Beijing); Ar/Ar (mu)	Leloup et al. [2010]
T5D22	south Nyondo Ri	1	224	560531	3114923	5346	migmatitic orthogneiss	U/Pb (mz SHRIMP Beijing); Ar/Ar (mu)	this study
T5D26	south Nyondo Ri	1	225	559995	3115086	5419	undeformed late pegmatite	U/He (ap)	this study
T5D33	east Sangkar Ri	k	230	570192	3132561	5124	garnet-sillimanite paragneiss	U/He (ap)	this study
T5D39b	east Sangkar Ri	k	226	572515	3132527	4613	boulder of garnet-sillimanite paragneiss	Ar/Ar (bio); Petrology	this study
T5D40	north Dinggye	j	237	573786	3142785	4266	not in place	U/He (ap)	this study
T7A10	upper Arun gorges	g	7-33	539159	3127192	3938	undeformed granite	Ar/Ar (bio)	this study
T7A14	upper Arun gorges	g	7-37	538926	3127119	3944	orthogneiss	Ar/Ar (bio)	this study
T7A19	Arun South gorges	e	7-61	536095	3107586	3670	deformed microgranite mylonite	Ar/Ar (bio)	this study
T7A20	Arun South gorges	e	7-62	535994	3107747	3628	cataclastic orthogneiss	Ar/Ar (mu)	this study
T7A33	west Tanghyu valley	f	7-66	537600	3123282	4119	gneiss	Ar/Ar (mu)	this study
T7A48b	north Flank	h	7-88	550322	3135144	4408	quartz cataclasite with chlorite and muscovite recrystallization	Ar/Ar (bio, mu)	this study

^aAll samples used in this study are listed. For map location see Figure 2.^bAlso in Table S1.

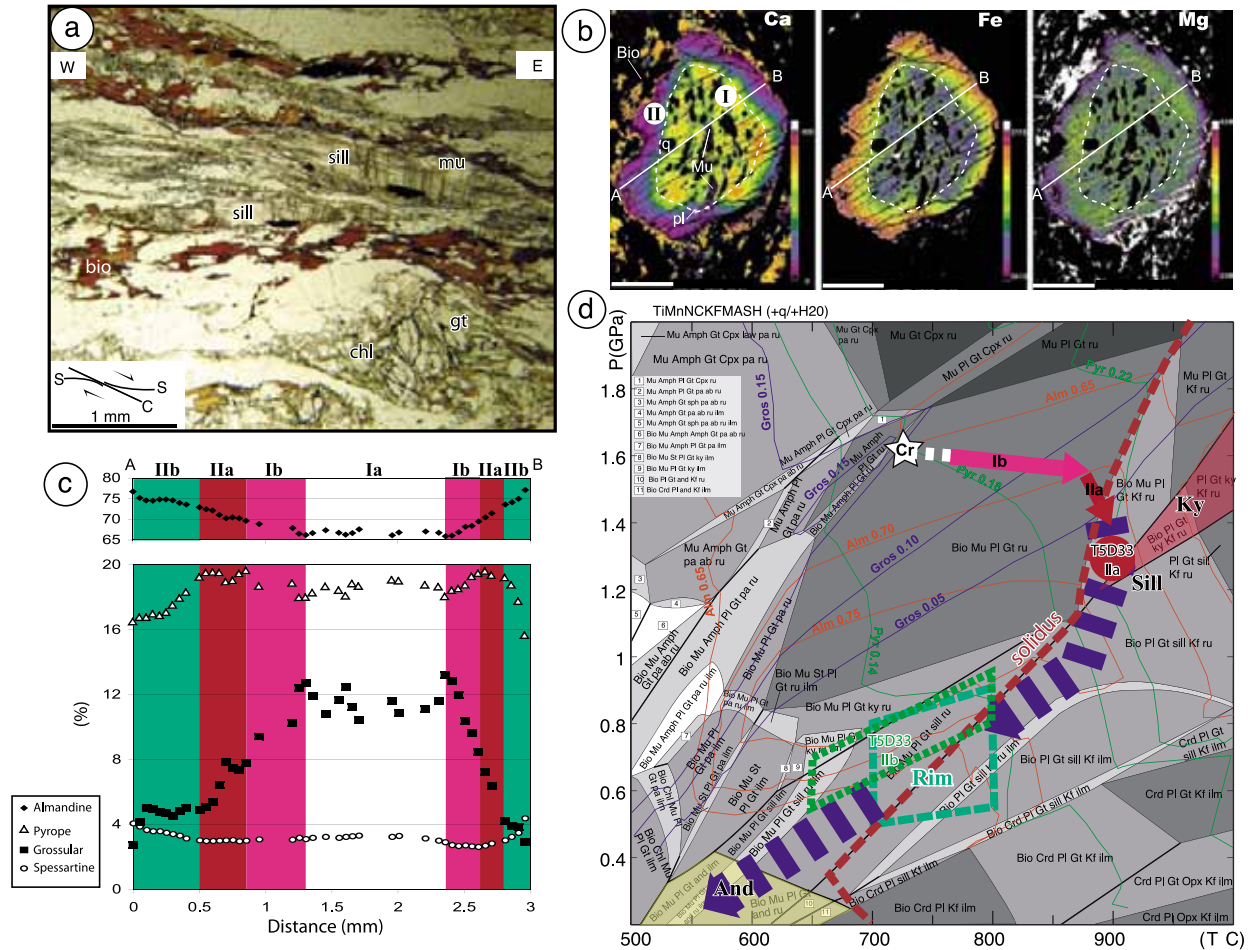


Figure 6. P-T path of the Ama Drime paragneisses in the footwall of the Dinggye normal fault. (a) T5D33 thin section picture microphoto showing syn-sillimanite-bearing top-to-the-east shear planes. Optical microscope, section parallel to lineation and perpendicular to foliation. (b) X-ray maps showing Ca, Fe, and Mg compositional zoning of garnets in sample T5D39b. (c) Garnet composition along the profile (white line) shown in Figure 6b. (d) H₂O saturated NCKFMAS-Mn-Ti pseudosection for garnet-biotite-sillimanite micaschist T5D39b (Perple_X2007) for the corresponding whole-rock composition. White, light gray, medium gray, and dark gray fields are divariant, trivariant, quadravariant, and quintavariant fields, respectively. Mineral abbreviations follow Holland and Powell [1998]. Red, green, and blue lines are almandine, pyrope, and grossular isopleths, respectively. T5D39b P-T path is constrained by the white star (Cr, garnet core), pink and red arrows and the green long-dashed box (garnet outer rim). Constraints on T5D33 P-T path are plotted for comparison. In Figures 6b, 6c, and 6d, I and II indicate garnet core (paragenesis 1) and rim (paragenesis 2), respectively.

diffusion occurred around the inclusions after their incorporation, modifying garnet composition. Garnet initial chemistry is only preserved away from the inclusions, and is not present along the Figure 6c transect. It is characterized by relatively high grossular content (0.124), low almandine and pyrope contents (0.662 and 0.180, respectively) and intermediate spessartine content (0.032) (Table S2, section 3). Zone Ib is characterized by pyrope and almandine increase from 0.66 and 0.18 to 0.70 and 0.20, respectively, by grossular content decrease from 0.13 to 0.08 (Table S2,

section 3, and Figure 2c) and almost constant spessartine content (~0.03).

[40] Within garnet rims (zone II, P2), which contain few biotite, quartz, kyanite, and plagioclase inclusions, two zones can be distinguished (Figure 6c). Zone IIa shows continuous grossular decrease from 0.08 to 0.05 and almandine increase from 0.70 to 0.73 but constant pyrope and spessartine (~0.19 and ~0.03, respectively) (Table S2, section 3, and Figure 6c). In zone IIb, grossular is constant (0.05) as almandine and spessartine slightly increase (0.73

to 0.75 and 0.04 to 0.03, respectively) and pyrope decrease from 0.19 to 0.17. Outermost rim is characterized by high almandine (up to 0.79) and spessartine (>0.05) and relatively low grossular and pyrope content (0.03 and 0.13, respectively) (Table S2, section 3, and Figure 6c).

[41] In sample T5D33 no garnet with muscovite and plagioclase inclusions (P1, garnet zone I) were observed. Only small porphyroclasts are still visible with zone II compositions (P2).

[42] In sample T5D39b, plagioclases have higher Ca content when included within or in contact with garnet (An 0.25–0.46) than in the matrix (An 0.29–0.24) (Table S2, section 4). In sample T5D33 the Ca content of the matrix plagioclase are even higher (An 0.40–0.43) probably because T5D33 is highly retrogressed as evidenced by the replacement of garnet by chlorite. K-feldspar (P2) are similar in both samples (Or 0.88–0.89).

[43] T5D39b P-T path was obtained using pseudosections, calculations of garnet isopleths and classical thermobarometry (Figure 6d). Despite some evidences for partial melting, constant chemistry is assumed as melts are only restricted to small unconnected pods at the microscopic scale, and because there are no evidences for local melt escape nor intrusion on macroscopic samples or outcrops.

[44] The garnet chemical zoning presented above yields to the interpretation that high temperatures following paragenesis 1 have induced chemical reequilibration of plagioclase and biotite inclusions with the surrounding garnet in garnet cores. Garnet composition corresponding to initial garnet growth has thus to be found in garnet cores but away from inclusions, while early plagioclase composition would be preserved in the matrix away from garnets. These compositions correspond to high-pressure (~1.6 GPa) and temperature around 775°C (star Cr on Figure 6d). Garnet compositions and evolution in zone Ib (pyrope and almandine increase and grossular decrease) reflect P-T conditions during the garnet core growth. They correspond to heating up to ~850°C, at almost constant pressure (~1.6 GPa) (Ib arrow on Figure 6d). Inner part of zone II (IIa, P2) is compatible with late high-temperature growth or reequilibration at ~875°C during decompression from 1.6 to 1.4 GPa (IIc arrow on Figure 6d). This high-temperature event induced the reequilibration in garnet cores around biotite and plagioclase inclusions. Based on Figure 6d pseudosection, presence of kyanite during the P2 implies that T was still at least at 875°C when decompression reached 1.2 GPa (Ky zone on Figure 6d). The outer part of zone II most likely corresponds with late diffusion at garnet rim. This late re-equilibration was constrained coupling garnet-biotite thermometry and garnet-sillimanite-plagioclase barometry from the GTP compilation [Reche and Martinez, 1996] for mineral in close contact (plagioclase, biotite, and garnet rim). Only calibration based on Fe, Mg, Ca, Mn, and Ti exchange were used. Results indicate that this late diffusion occurred at 700–800°C and 0.9–0.5 GPa (green dashed box on Figure 6d).

[45] These latter P-T estimates, compared with the ones obtained for garnet zone IIa, imply that an important decompression event took place from ~1.6 GPa to ~0.7 ± 0.2 GPa and during a small decrease of temperature from ~875 to 750 ± 50°C. This episode was associated with

partial melting by muscovite breakdown and successive growth of kyanite and sillimanite (P2, Figure 6d). The late retrograde evolution is only constrained by the presence of andalusite and the absence of cordierite suggesting pressures comprised between 0.4 and 0.2 GPa and temperature lower than 675°C (yellow area on Figure 6d).

[46] T5D33 provides similar P-T evolution, but starting at 1.3 GPa and 900°C (Figure 6d) based on pseudosection since only P2 garnets have been preserved. Late diffusion at T5D33 garnet rim is constrained to occur at 0.75 ± 0.2 GPa and 725 ± 75 °C (Figure 6d) based on garnet-biotite thermometry and garnet-sillimanite-plagioclase barometry. The retrograde evolution yielded to the crystallization of Ca-rich plagioclases in T5D33.

4.1.2. P-T Path of the Ama Drime Orthogneissic Unit: Comparison With the Paragneissic Unit

[47] Lombardo and Rolfo [2000] were the first to suggest that the rocks now outcropping in the heart of the Ama Drime, here referred as the Ama Drime orthogneissic unit, were among the deepest in the Himalayan belt. Since then, the P-T path of the Ama Drime unit, has been documented by the studies of Liu *et al.* [2005], Groppo *et al.* [2007], Liu *et al.* [2007], and Cottle *et al.* [2009]. These studies appear to document a common P-T path (Figure 5b). The path starts with an isobaric heating ($\Delta T \sim 225$ °C) at pressures above 1.4 GPa, most probably between 1.6 and 1.8 GPa, prior to reach conditions compatible with partial melting at ~800°C of metapelitic and metagranitic rocks. This is followed by a large nearly adiabatic decompression ($\Delta P = 1.0$ to 1.5 GPa corresponding to 37 to 56 km) at ~800°C, ending around 0.3 GPa (~11 km depth). From this point, cooling starts and the path entered the field where vapor-absent melting for metapelite and metagranite may initiate (Figure 5b). The end of the P-T path is still poorly constrained.

[48] Such P-T path is broadly similar to the one obtained in the overlying Ama Drime paragneissic unit (see section 4.1.1), but with a peak temperature ~100°C cooler (Figure 5d). From these data the Ama Drime paragneissic unit could simply correspond to the metamorphosed sedimentary cover of the Ama Drime orthogneissic unit, the two units being exhumed together. However, the two units can also be separated by a tectonic contact along the postulated Nyonno Ri boundary, which finite offset would be small.

4.2. Geochronology

4.2.1. U-Th/Pb

[49] T5D22 is a sample from the migmatitic gneisses, which constitute most of the Ama Drime orthogneissic unit, sampled south of the Nyonno Ri in the footwall of the Dinggye normal fault (Figure 2b).

[50] Monazites selected for SHRIMP dating are fairly big (100 µm in average) and well crystallized. In thin section, they are observed as inclusion within micas and quartz. No significant relationship appears between the age and the spot locations (Table S4, section 2). T5D22 monazite ages show scatter, with $^{208}\text{Pb}/^{232}\text{Th}$ ages ranging from 11.6 to 14.4 Ma, for an average at 12.85 ± 0.39 Ma ($n = 15$, MSWD = 3.3) (Figure 7a). On a Tera-Wasserburg isochron most data concentrate just above the Concordia (Figure 7b). If one excludes the youngest and the three oldest data points,

regression forced through present-day common lead and the 11 remaining data, gives an age of 13.54 ± 0.14 Ma (MSWD 1.9) (Figure 7b). Keeping all points would not change the age (13.59 ± 0.27 Ma) but would significantly alter the MSWD (10.8). The TW regression age is 1 Ma older than the $^{208}\text{Pb}/^{232}\text{Th}$ average one. In the absence of any clue for lead overcorrection, the average age is preferred.

[51] As monazite is easily dissolved into the melt during partial melting and appears during final melt crystallization [Kelsey *et al.*, 2008], the 12.9 Ma age most likely represent final melt crystallization.

[52] This age of ~ 12.9 Ma is close to other monazite ages found in the Ama Drime orthogneisses west of the range: 12.8 ± 0.2 (sample 1303 [Liu *et al.*, 2007]), 13.4 ± 1 Ma (sample 1203 [Liu *et al.*, 2007]), and 12.3 ± 1.5 Ma (sample AD36 [Cottle *et al.*, 2009]), confirming crystallization of the Ama Drime migmatites at that time (Figure 9). In such rocks, however, zircon rims yield older Cenozoic ages of 33 ± 2.1 and 22.9 ± 2.1 Ma in sample 1103, and between 30 and 23 Ma in sample 1303 [Liu *et al.*, 2007] that could correspond to previous magmatic evolution (Figure 9).

[53] T5D5 is a small (~ 10 cm wide) leucocratic dike crosscutting the ductile foliation in the footwall of the Dinggye fault in the Ama Drime orthogneissic unit (Figures 3j and 2b). Monazites are well crystallized and fairly big ($100 \mu\text{m}$ in average). In thin section, they are observed as inclusion within micas and quartz. Some grains were systematically avoided for dating because CL images revealed they were patchy, or had zircon inclusions. Corrected $^{208}\text{Pb}/^{232}\text{Th}$ ages range from 10.4 to 13.9 Ma (Table S4, section 1, and Figure 7a). The average of the whole population is 12.52 ± 0.54 Ma with a fairly large MSWD at 6. A cumulative probability plot exhibits two maxima at ~ 11 and ~ 13 Ma suggesting two age populations (Figure 7c). Average $^{208}\text{Pb}/^{232}\text{Th}$ ages of the two subpopulations are 13.09 ± 0.32 Ma (MSWD = 1.5) and 10.98 ± 0.39 Ma (MSWD = 1.13), respectively (Figure 7a and Table S4, section 1). When plotted in a Tera-Wasserburg diagram, the data display again two statistically different populations, whose ages do not overlap within uncertainties. Regressions forced though present-day common lead give intercepts at 13.96 ± 0.27 Ma (13 points, MSWD = 1.9) and 12.54 ± 0.47 Ma (5 points, MSWD = 1.5) for these two populations (Figure 7d and Table S4, section 1).

[54] We interpret these results as indicating a long period of monazite crystallization with final dike emplacement at the time of the youngest monazite crystallization: 10.98 ± 0.39 Ma. This suggests that down to the east ductile normal faulting was over, at least locally, at ~ 11 Ma. Note that the oldest monazite population in T5D5 is very similar to the monazites from T5D22 (Figure 9) and thus probably corresponds to inheritance from this main crystallization event.

[55] T5D26 is a pegmatite dike that cuts across an amphibolite-rich layer (Figure 3h) of the Ama Drime orthogneissic unit ~ 4 km west of the Dinggye active fault (Figure 2). The dike is restricted to the basic layer and does not appear to cut the migmatites. However, observation of similar dikes in the high cliff north of the Ama Drime summit reveals that the dikes cut across all facies of the Ama Drime orthogneissic unit even if they are locally

restricted to the basic layers probably because of rheology contrasts (Figure 3f).

[56] The sample yielded clear elongated zircons with well developed facets and no zoning. In thin section, they are observed as inclusion within micas and quartz. All the analyzed points are concordant but show a wide range in age from 7 to 27 Ma (Figure 7e and Table S3), thus yielding the youngest concordant ages from this study. The distribution of $^{206}\text{Pb}/^{238}\text{U}$ ages, which suffer the least from ^{204}Pb correction shows 9 ages out of 12 ages younger than 12 Ma. The average of these ages (9.8 ± 1.2 Ma, MSWD = 126) is interpreted as the best estimate for the pegmatite crystallization. The few older ages, between 21 and 27 Ma, suggest zircons inherited from the surrounding Ama Drime orthogneissic unit (Figure 9). One cannot exclude, however, that the data correspond to a discordia chord between ~ 7 and ~ 27 Ma. In that case the crystallization age of T5D26 would be 7.3 ± 0.2 Ma.

[57] The 9.8 ± 1.2 Ma age is close to the crystallization age of T5D5 (10.98 ± 0.39 Ma, see above) that seems to belong to the same dike generation from field observation (Figure 2b). On the western side of the range, six monazites of a leucocratic dike crosscutting a large amphibolite boudin (A.D. 35, Figure S1) yield an age of 11.6 ± 0.4 Ma [Cottle *et al.*, 2009] very close to the final crystallization age we propose for T5D26 and T5D5.

4.2.2. Argon Results

[58] Argon results are summarized in Table 3, and all data are listed in Table S5.

4.2.2.1. Dinggye Shear Zone

[59] New argon ages from the Ama Drime paragneissic unit in the footwall of the Dinggye normal fault were obtained from T5D33 and T5D39. Biotites from paragneiss T5D33 show a saddle shaped age spectra with minimum ages at circa 11.8 Ma (Figure 8a), suggesting excess, which is correctly resolved by the inverse isochron approach yielding an age of 10.8 ± 0.4 Ma (MSWD = 7.1) (Figure 8b). Biotites from sample T5D39 also display a rugged age spectra, with a minimum age close to 11.5 Ma (Figure S2g). Excess argon is not completely resolved on the inverse isochron, which age of 13.1 ± 0.8 Ma is probably a maximum (Figure S2h). That range of biotite ages in the paragneisses compares well with that obtained by Zhang and Guo [2007] on similar facies, ranging from 10.2 to 13.2 Ma.

[60] Within the Ama Drime orthogneissic unit, sample T5D6 corresponds to an orthogneiss showing down to the east ductile normal faulting and crosscut by T5D5 leucogranite (Figure 3j). Biotites yield a saddle age spectra with a pseudoplateau at 10.8 ± 0.1 Ma and an inverse isochron age of 10.7 ± 0.3 Ma (Figures 8a and 8b). Cooling of T5D6 below $\sim 300^\circ\text{C}$ thus happened immediately after the emplacement of T5D5. In the same unit, T5D10 biotites show a strong excess argon effect (Figure S2g). The inverse isochron is tied up close to the $^{36}\text{Ar}/^{40}\text{Ar}$ axis and points to an old age of 18.6 ± 1.2 Ma, which must be regarded with great care (Figure S2h).

[61] Six muscovite and biotite $^{39}\text{Ar}/^{40}\text{Ar}$ ages from the footwall of the Dinggye fault were published by Zhang and Guo [2007] (samples T01-17, T01-24, T01-25, T01-26,

TC2014

KALI ET AL.: AMA DRIME EXHUMATION HISTORY

TC2014

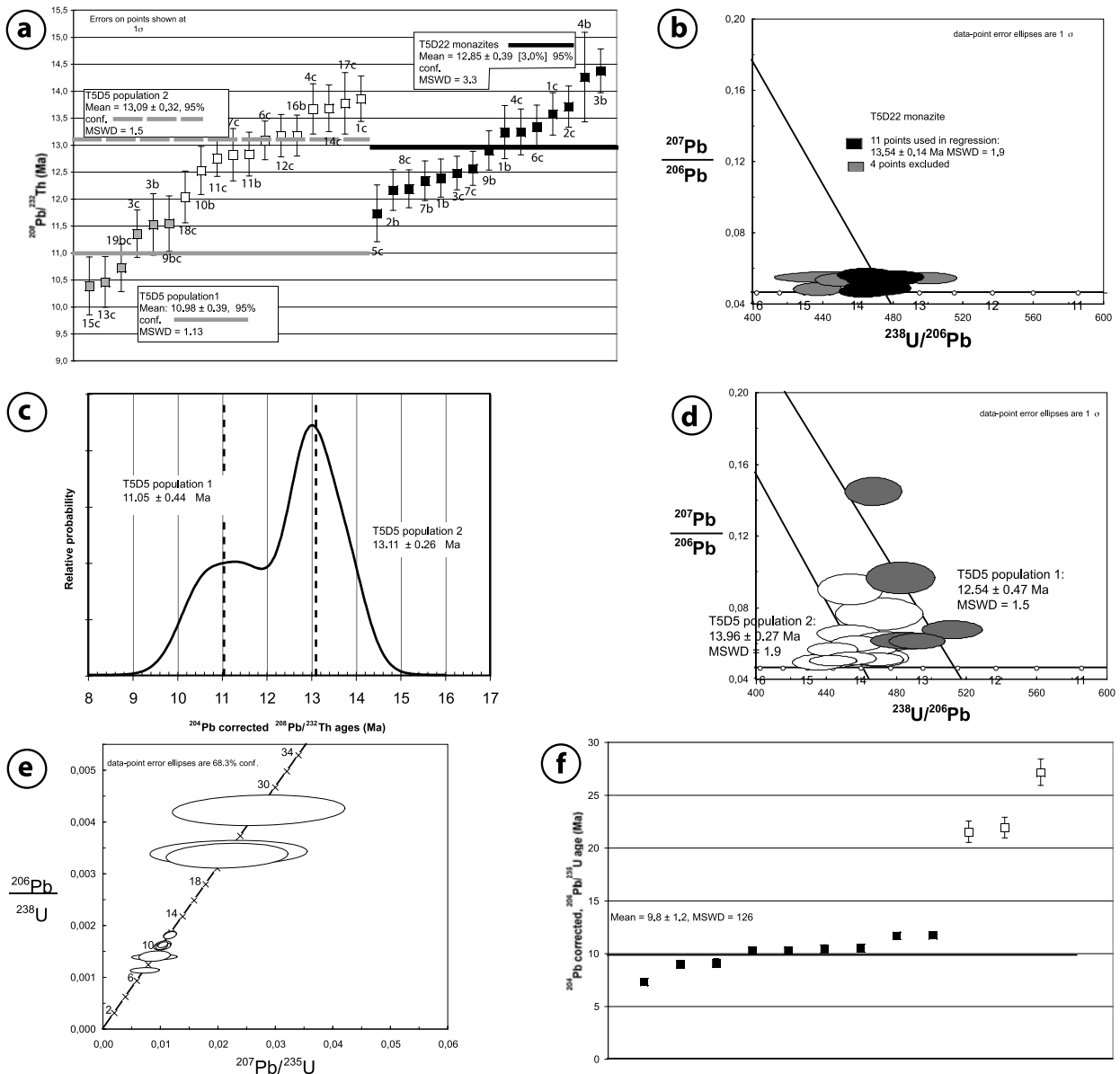


Figure 7. U-Th/Pb data. Corresponding data are listed in Tables S3 and S4. (a) Averages of $^{208}\text{Pb}/^{232}\text{Th}$ monazite ages corrected for common lead via ^{204}Pb for T5D5 (2 populations) and T5D22. Spot numbers are indicated. (b) T5D22 monazite Tera-Wasserburg diagram, with regression forced through present-day common lead. (c) Cumulative probability plot of T5D5 monazite $^{208}\text{Pb}/^{232}\text{Th}$ ages from which isoplot software [Ludwig, 2003] extracts two subpopulations. (d) T5D5 monazites Tera-Wasserburg diagram, with regressions forced through present-day common lead (two populations are distinguished). (e) Concordia diagram for zircons from pegmatite dike (T5D26). All points are concordant but show a wide age range. (f) T5D26 zircon $^{206}\text{Pb}/^{238}\text{U}$ corrected for common lead via ^{204}Pb ages. A crude average (with a high MSWD) is calculated excluding the three oldest points.

T01-29, T01-33, Figure S1). All these ages are comprised between 13.34 and 10.2 Ma, which together with our data yield an overall age range between 18.5 and 10.2 Ma (Figure 9). Excluding only one outlier (T5D10 biotite that happens to be the less reliable) out of the eleven available

data restrains the age range to 13.7–10.2 Ma and yield average ages of 10.72 ± 0.73 Ma for the biotites and 12.1 ± 2.4 Ma for the muscovites (Figure 9). Muscovites and biotites have nearly the same age suggesting a very rapid cooling at medium temperatures. This event is ~ 2 Myr younger than the

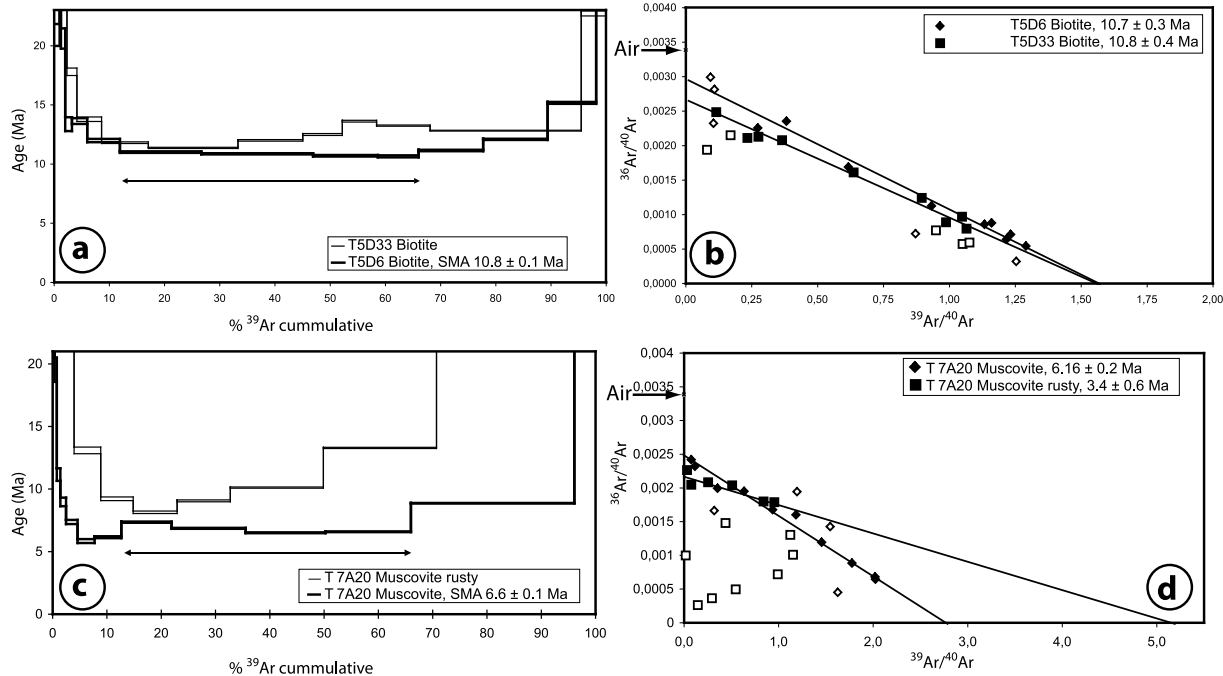


Figure 8. Examples of argon data from the Ama Drime range. Other data are plotted in Figure S2. All data are summarized in Table 3 and listed in Table S5. For inverse isochron plots, empty symbols where not used in the regression calculation. (a) T5D33 and T5D6 biotites age spectra. (b) T5D33 and T5D6 biotites inverse isochron plot. (c) T7A20 muscovites age spectra. Note that two populations (normal and rusty) have been distinguished. (d) T7A20 muscovites inverse isochron plot.

rapid cooling event observed in the STDSZ [Leloup *et al.*, 2009, 2010] and corresponds to the final age of crystallization of T5D5 (crosscutting dike).

4.2.2.2. Kharta Shear Zone

[62] On the western side of the Ama Drime range micas $^{39}\text{Ar}/^{40}\text{Ar}$ ages in the Kharta shear zone appear even younger than on the eastern flank.

[63] T7A19 biotites yield the oldest ages with a saddle age spectra, a pseudo plateau at 24.1 ± 0.3 Ma and an isochron age of 23.5 ± 0.5 (Figures S2a and S2b). T7A33 biotites show the same kind of age spectra with a 10.9 ± 0.2 Ma plateau and a isochron age of 10.1 ± 0.9 Ma (Figures S2a and S2b). The pseudo plateau age of T7A10 biotites is 8.5 ± 0.2 Ma and the isochron age is 8.5 ± 0.3 Ma (Figures S2c and S2d). T7A14 biotites show minimum ages around 10 Ma and an ill-defined isochrone age of 6.2 ± 0.8 Ma (Figures S2c and S2d). All these biotites come from the ductile part of the Kharta normal fault, which deformation temperature encompasses the biotite closure temperature ($300 \pm 40^\circ\text{C}$). This suggests that the Kharta SZ was active in the time interval 10–6 Ma, while T7A19 was probably not reset from a previous thermal event (Figure 9). Indeed, T7A19 is a meta-arenite in which biotite, plagioclase, garnet and quartz detrital grains have only been partly recrystallized during shearing and chlorite-grade metasomatism within the Kharta SZ. We thus suggest that T7A19

biotites cooled below $\sim 300^\circ\text{C}$ at ~ 25 Ma were eroded and deposited in a small basin later affected by the Kharta SZ.

[64] T7A20 sampled within the Kharta SZ less than 200 m away from T7A19 (Figure 2a) contains two generations of muscovite: big (~ 0.2 mm) porphyroclasts and smaller minerals aligned within the foliation and shear zones. Two populations of muscovite have also been distinguished during the separation process on their clear or rusty appearance. The two populations have been dated separately. The clear one shows a pseudoplateau at 6.6 ± 0.1 Ma and an inverse isochron at 6.2 ± 0.2 Ma (Figures 8c and 8d), while the rusty one is associated with a saddle age spectrum and an ill-defined isochron age of 3.4 ± 0.6 Ma (Figures 8c and 8d).

[65] T7A48 comes from the north part of the Ama Drime range in the hanging wall of the fault linking the Kharta and Sangkar active faults (Figure 2a). There, cataclastic quartzites outline NNW trending normal faults (see section 3.2.3). The sample yielded two generations of muscovite: clear porphyroclasts within the foliation of the cataclasite, and rusty muscovites that, together with chlorobiotite, fill vertical late fractures. The porphyroclasts yield ages close to those of most muscovites from the Dinggye SZ [Zhang and Guo, 2007] (Figure 9), with a saddle pseudoplateau at 11.7 ± 0.2 Ma and an inverse isochrone at 12.2 ± 0.2 Ma (Figures S2e and S2f). The second muscovite generation gives a saddle age spectrum without any plateau and an ill-defined isochron age of 3.3 ± 0.8 Ma (Figures S2e and S2f).

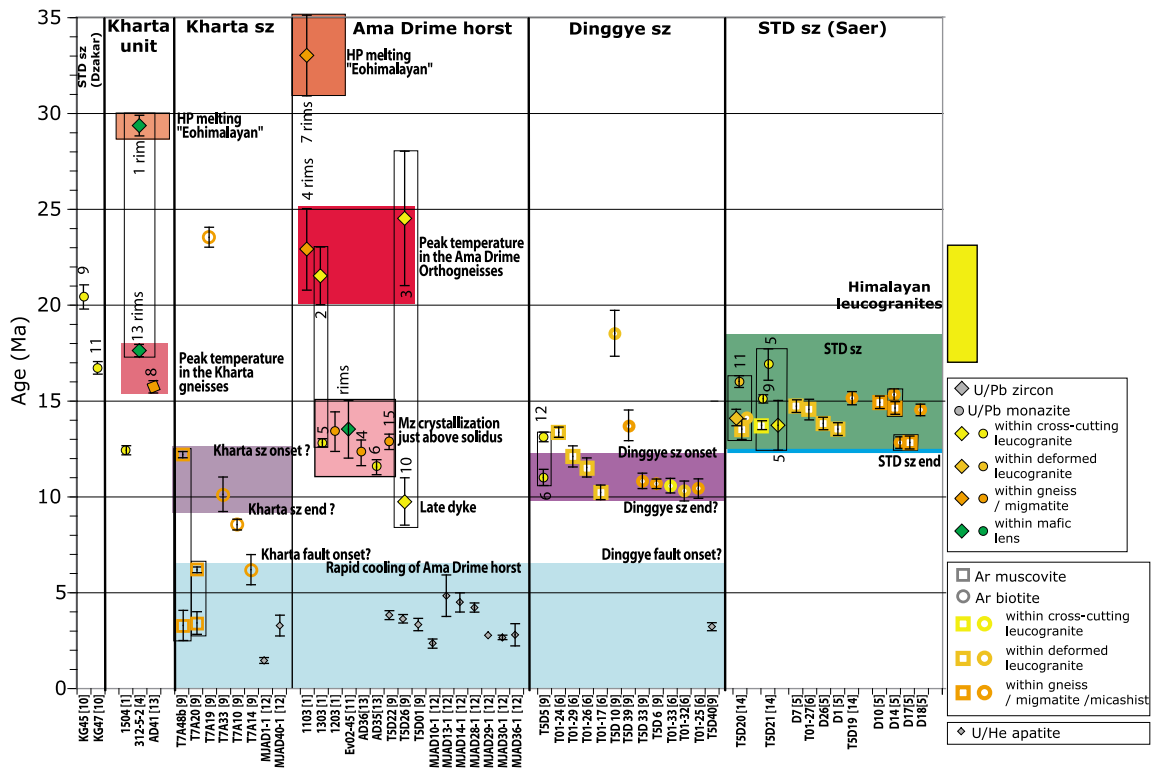


Figure 9. Geochronologic ages synthesis. Geochronologic ages of Ama Drime area from bibliography and this study. Samples are labeled at the bottom of the graph and organized by tectonometamorphic units presented from west to east. Symbols correspond to mineral and techniques, and colors relate to rock types. References are [1] Liu et al. [2007]; [4] Li et al. [2003]; [5] Hedges et al. [1994]; [6] Zhang and Guo [2007]; [9] this study; [10] Cottle et al. [2007]; [11] Rolfo et al. [2005]; [12] Jessup et al. [2008]; [13] Cottle et al. [2009]; and [14] Leloup et al. [2009, 2010]. The age range of Higher Himalayan leucogranites is plotted for comparison [Harrison et al., 1998]. Main tectonometamorphic events are outlined by color boxes.

4.2.3. Apatite U-Th/He Results

[66] In order to constrain the timing of the latest stages of exhumation of the Ama Drime massif in the footwall of the Dinggye normal fault, apatite (U-Th)/He dating was performed on three samples from the valley south of the Nyondon Ri (T5D01, 22 and 26) spanning in elevation between 5217 and 5419 m, and one sample collected east of the Sangkar Ri at 4270 m (T5D40) (Figure 2a). Samples are orthogneiss (T5D01), migmatite (T5D22) and granites (T5D26 and T5D40). Apatites have been analyzed at the Caltech Noble Gas Laboratory following the procedure of House et al. [2000]. As the samples were relatively poor in good quality apatite (i.e., inclusion free) we ran single grains and 1 (T5D01), 2 (T5D40) or 4 replicates (T5D22 and T5D26). The 1σ error on age is taken as the standard deviation of the replicate analyses divided by $(n - 1)^{1/2}$, where n is the number of replicate analyses performed. Samples with multiple replicates gave good reproducibility, with a 1σ error lower than 10% of the mean age. For the sample with only one replicate (T5D01) we use a conservative 1σ error corresponding to 10% of the age.

[67] All ages range between 3.2 and 3.8 Ma (average 3.4 ± 0.4 Ma) (Table S6 and Figure 9). Altogether ages appear to

correlate with elevation giving an apparent exhumation rate of ~ 2.9 km/Myr (Figure 10). However, this correlation rests on only four points, and the single point at an altitude significantly lower than the 3 others is located ~ 35 km farther to the north (T5D40, Figure 2a). Other apatite (U-Th)/He ages have been obtained by Jessup et al. [2008] for samples (1) close to samples T5D01, 22, and 26, (2) from the western side of the Ama Drime massif next to the Kharta normal fault, and (3) in the core of the massif. All these samples are located between $28^{\circ}4'N$ and $28^{\circ}15'N$ (Figure S1). Altogether most of Jessup et al. [2008] apatite (U-Th)/He ages and our data for samples T5D01, 22 and 26 correlate with elevation (Figure 10) defining an apparent elevation rate of ~ 1 mm/yr for ages comprised between 1.4 and 4.2 Ma. The two samples (MJAD13 and MJAD14) from Jessup et al. [2008] with errors superior to 10% of the mean age, have been excluded from the age-elevation relationship as for these samples age replicates correlate negatively with grain size, which suggest He implantation, but that can also be related with zoning or presence of U-rich inclusions. Another sample (MJAD40) is significantly older than expected from the age-elevation relationship (Figure 10). This sample is located in the Kharta shear zone and was

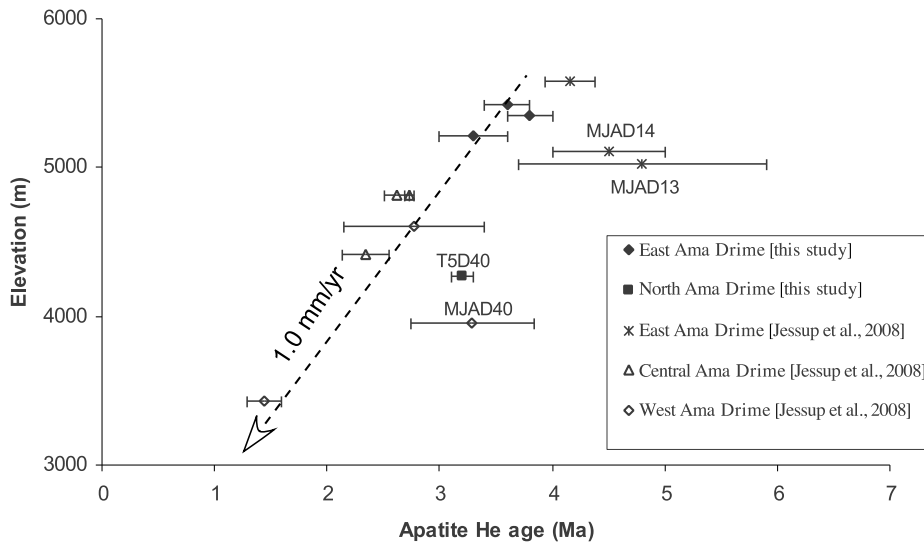


Figure 10. Plot of Ama Drime (U-Th)/He apatite ages versus elevation. Data from this study (Table S6) and Jessup *et al.* [2008]. This plot suggests that the Ama Drime range was vertically exhumed as a single block since at least 4 Ma with a rate of about 1 mm/yr. See text for details.

then most probably less exhumed than the sample located in the range outside of the deformation zones explaining the relatively old measured age.

[68] The age-elevation relationship obtained (Figure 10) suggests that the part of the Ama Drime massif covered by Jessup *et al.* [2008] and our sampling (i.e., the central part between the Nyondon Ri and the Ama Drime peaks) was exhumed as a single block with no tilting between the Dinggye and the Kharta normal faults since at least 4.2 Ma. This implies that in this area, and since 4.2 Ma, the slip rate is the same on both normal faults. The relatively old age obtained for sample T5D40, located about 35 km north of the other samples could indicate a lower amount of exhumation toward the northern Ama Drime, where the normal faults terminate. This is coherent with the decrease of the crest elevation (~6000 m in the central part and ~5500 in the northernmost part), together with the decrease of the height of the triangular facets (700–800 m in the central part and 400–500 in the northernmost part), both suggesting a decrease of the throw and/or rate of the active faults toward the north.

5. Discussion: Structural Evolution of the Ama Drime Area

[69] In the central and eastern Himalayan range, amphibolitic and granulitic rocks recording peak pressure between 1.2 and 1.0 GPa have been observed close to the MCTI [Guillot, 1999; Kohn *et al.*, 2001; Harris *et al.*, 2004]. Farther north, in the HCS, between the MCTI and the STD shear zone peak pressure is usually comprised between 0.7 and 1.0 GPa [Vance and Mahar, 1998; Searle *et al.*, 1999; Vannay *et al.*, 1999; Goscombe and Hand, 2000; Borgi *et al.*, 2003; Dasgupta *et al.*, 2004; Kohn *et al.*, 2004]. So far

pressures higher than 1.4 GPa are only found in the Ama Drime range.

[70] P-T-t path reconstructions of the amphibolitic and granulitic events of the HCS evidence that two main tectonometamorphic events occurred all across the Himalaya. One Eo-himalayan event, between 50 and 30 Ma, probably associated to burial and subsequent thermal reequilibration (see Hodges [2000] and Kohn *et al.* [2005] for reviews) and one HT event at 25–20 Ma related to leucogranite formation [Simpson *et al.*, 2000]. P-T path reconstruction, away from the STD shear zone, indicates that this HT event is generally coeval to a slight T increase (50–100°C) and a strong decompression [Guillot, 1999; Searle *et al.*, 1999; Goscombe and Hand, 2000; Harris *et al.*, 2004]. This HT event is generally considered as contemporaneous with thrusting along the MCTI [Hodges *et al.*, 1996; Catlos *et al.*, 2004].

[71] We discuss below if, and how, the Ama Drime area rocks conform with, or depart from this general pattern, and what constraints their P-T-D-t path brings on orogenic models.

5.1. P-T-t Path of Ama Drime Rocks During the Himalayan Orogeny

[72] Comparison of the P-T paths of the various units and compilation of more than 60 radiochronologic data (Figure 9 and Tables 2 and 3), allow us to propose a coherent scenario for the timing and duration of the metamorphism and exhumation phases of the Ama Drime rocks during the Himalayan orogeny.

[73] U-Th/Pb zircon and monazite dating of the Ama Drime orthogneissic unit, in orthogneisses, paragneisses, metabasites as well as undeformed leucocratic dikes and granites, yield Cambrian to Precambrian inherited ages as well as numerous Cenozoic ages between 33 and 10 Ma

Table 2. U-Th/Pb Data Summary for Dinggye Normal Fault^a

Number	Rock Type	Altitude (m)	Mineral Type	Population	Average $^{206}\text{Pb}/^{238}\text{U}$ Age for Zircon and $^{208}\text{Pb}/^{232}\text{U}$ Age for Monazite				Inverse Isochron (Tera-Wasserburg) $^{207}\text{Pb}/^{206}\text{Pb}$ Versus $^{238}\text{U}/^{206}\text{Pb}$				
					Age (Ma)	MSWD	Number of Spots	Spots ^b	Age (Ma)	Upper Intercept	MSWD of Spots	Number of Spots	
T5D5	late leucocratic dike	5065	monazite	1	11.1 ± 0.4	1.1	6	15c, 13c, 19bc, 3c, 3b, 9bc	12.5 ± 0.5	common lead	1.5	5	15c, 13c, 19bc, 3c, 3b
				2	13.1 ± 0.3	1.5	12	18c, 10b, 11c, 7c, 11b, 6c, 12c, 16b, 4c, 14c, 17c, 1c all spots	14.0 ± 0.3	common lead	1.9	13	9bc, 18c, 10b, 11c, 7c, 11b, 6c, 12c, 16b, 4c, 17c, 1c
T5D22	migmatitic orthogneiss	5346	monazite	whole sample	12.5 ± 0.5	6.1	18		13.5 ± 0.1	common lead	1.9	11	2.2, 8, 17, 2, 1, 3, 3, 1, 7, 19.1, 1.2, 4, 1, 6, 1, 1
T5D26	undeformed late pegmatite	5419	zircon		9.8 ± 1.2	126	9	6b2, 4b, 1c, 7c, 5b2, 6b1, 8c, 3b, 3c					

^aSee Figure 7. For sample locations see Table 1 and Figure 2a. Detailed data are given in Tables S3 and S4. Most reliable results are in bold.
^bCrystal number and b, border, or c, core.

(Figure 9). The Cambrian ages are characteristic of Himalayan Crystalline Series [Richards et al., 2005, and reference therein].

[74] The Cenozoic ages indicate that the high-temperature and high-pressure, metamorphic event is Oligo-Miocene and relates to the Himalaya building, not to a previous metamorphic episode. However, the detailed interpretation of these ages is not always straightforward. The spread in age results from the variety of minerals and facies dated as well as from mechanisms inducing several age populations of a given mineral in a given sample.

[75] Published U/Pb ages of the Ama Drime migmatitic paragneisses in the Ama Drime orthogneissic unit reveal two populations of metamorphic zircon at 33 ± 2 Ma and 23 ± 2 Ma (sample 1103 [Liu et al., 2007]) (Figure 9). In such amphibolitic to granulitic facies rocks metamorphic zircon are only formed during anatexis [Schiotte et al., 1989; Vavra et al., 1999]. In this environment overgrowth mostly occurs during two phases (1) subsolidus growth at the onset of partial melting and (2) at peak temperature and during subsequent cooling [Roberts and Finger, 1997; Schaltegger et al., 1999; Vavra et al., 1999; Rubatto et al., 2001; Kelsey et al., 2008]. In metapelitic system partial melting temperature is dependant of the bulk composition. Based on granite chemistry and our pseudosection, partial melting is related with vapor-absent melting by mica breakdown [Visonà and Lombardo, 2002]. Combining data from experimental petrology at $\sim 1.4\text{--}1.8$ GPa [Vielzeuf and Holloway, 1988; Vielzeuf and Clemens, 1992; Vielzeuf and Montel, 1994; Patiño-Douce and Beard, 1996; Castro et al., 2000; Auzanneau et al., 2006] as well as pseudosection calculation [Harris et al., 2004; Indares et al., 2008], pelites, granites and graywackes partial melting initiate between 800°C and 900°C . We propose that the 33 ± 2 Ma age corresponds to the onset of partial melting most probably occurring during the isobaric temperature increase, and the 23 ± 2 Ma age to the peak T and start of the subsequent cooling ($1.0\text{--}0.5$ GPa and $\sim 800\text{--}850^\circ\text{C}$ (Figure 5b). We note that zircons of similar ages have been found in undeformed granites and leucogranitic dikes of the Ama Drime (samples 1033 of Liu et al. [2007] and T5D26 of this study; Figure 9) where they are probably inherited from this high-temperature event.

[76] Monazites ages obtained from similar migmatitic gneisses are all comprised between 13 and 12 Ma [Liu et al., 2007; Cottle et al., 2009; this study] (Figure 9). As monazite is easily dissolved during partial melting, inherited or prograde grains are usually not preserved, and U-Th/Pb ages most likely correspond to cooling close to the solidus [Kelsey et al., 2008]. Based on a detailed study on various bulk rock compositions in the NCKFMASH system, monazite crystallization occurs between 650 and 850°C for pressure below 0.7 GPa [Kelsey et al., 2008].

[77] We propose that the 12–13 Ma monazite ages correspond to P-T conditions of 0.3–0.4 GPa and $650\text{--}750^\circ\text{C}$ occurring during the cooling event following the adiabatic decompression (Figure 5b).

[78] Within metabasic rocks of the same Ama Drime orthogneissic unit, Rolfo et al. [2005] obtained 12–15 Ma U/Pb ages on metamorphic zircons. In such rocks zircon

Table 3. Ar/Ar Data Summary^a

Number	Rock Type	Sample	Altitude (m)	Mineral Type	Mean Age ^b (Ma)	Plateau Age			Inverse Isochron Age			Total Fusion Age (Ma)	
						Steps	Dinggye Shear Zone	$^{40}\text{Ar}/^{36}\text{Ar}_\text{i}$	MSWD	Steps	$^{40}\text{Ar}/^{36}\text{Ar}_\text{i}$		
T5D6	orthogneiss	5069	biotite	SMA	10.8 ± 0.1	4 steps/14 (7–10)	56% of gas	10.7 ± 0.3	354 ± 12	6.3	9 steps/14 (4–12)	90% of gas	12.1 ± 0.1
T5D10	garnet migmatitic gneiss	5237	biotite					18.6 ± 1.2	343 ± 2.5	2	11 steps/11	100% of gas	49.6 ± 0.6
T5D33	garnet-sillimanite paragneiss	5124	biotite					10.8 ± 0.4	382 ± 9	8	9 steps/14 (5–13)	90% of gas	13.7 ± 0.1
T5D39	garnet-sillimanite paragneiss	not in place	biotite				<13.1 ± 0.8	319 ± 13	15.4	8 steps/14 (5–9, 11–13)	90% of gas	16.5 ± 0.3	
T7A19	mylonite	3670	biotite	WMP	24.1 ± 0.3	6 steps/14 (7–12)	8% of gas	23.5 ± 0.5	318 ± 5	5.3	10 steps/14 (4–13)	56% of gas	25.5 ± 0.3
T7A33	gneiss	3638	biotite	WMP	10.9 ± 0.2	5 steps/14 (7–11)	68% of gas	10.1 ± 0.9	345 ± 33	14.4	5 steps/14 (7–11)	68% of gas	21.6 ± 0.2
T7A10	orthogneiss deformed	4446	biotite	SMA	8.5 ± 0.2	2 steps/14 (7–8)	52% of gas	8.5 ± 0.3	339 ± 11	6.4	6 steps/14 (7–12)	79% of gas	10.9 ± 0.1
T7A14	microgranite	4445	biotite					6.2 ± 0.8	688 ± 114	4.4	6 steps/14 (6–11)	54% of gas	12.2 ± 0.1
T7A20	cataclastic orthogneiss	3670	muscovite fresh	SMA	6.6 ± 0.1	5 steps/14 (8–12)	59% of gas	6.2 ± 0.2	402 ± 8	3.7	10 steps/14 (2–5, 8–13)	97% of gas	8.4 ± 0.1
T7A48	quartz cataclasite with chlorite and muscovite recrystallization	3677	muscovite rusty	WMP	11.7 ± 0.2	5 steps/10 (2–7)	70% of gas	12.2 ± 0.2	455 ± 11	5.9	6 steps/14 (5–10)	61% of gas	34.9 ± 0.3
			muscovite rusty					293 ± 3	0.1	5 steps/10 (2–7)	70% of gas	17.6 ± 0.2	
								3.3 ± 0.8	875 ± 37	3.8	8 steps/14 (6–13)	85% of gas	44.7 ± 0.5

^aSee Figures 8 and S2. For sample locations, see Table 1 and Figure 2a. Detailed data are given in Table S5. Most reliable results are in bold.^bSMA, standard mean age; WMP, weighted mean plateau age.

growth is rather related with garnet and/or hornblende breakdown than anatexis [Fraser *et al.*, 1997]. Thus, coupling these ages with their petrogenetic grid, Groppe *et al.* [2007] proposed that 12–15 Ma zircon growth most probably occurred at 0.7–0.4 GPa and 750–840°C near the end of the nearly adiabatic decompression event. Such timing matches well our interpretation of the monazites and zircons ages in the migmatitic orthogneiss (Figure 5b).

5.2. P-T-t Paths of the Kharta-Saer Unit

[79] East of the Ama Drime, the 15.09 ± 0.11 Ma U-Th/Pb age of a crosscutting granite (T5D21) suggest that deformation stopped in the STDSZ at ~ 15 Ma east of Saer [Leloup *et al.*, 2009, 2010] (Figure 9). Muscovite and biotite argon ages further suggest rapid cooling between 15 and 13.5 Ma and that temperature dropped below $\sim 300^\circ\text{C}$ at ~ 13.5 Ma (Figures 5 and 9). Brittle motion could have carried on along the STD after that date. However, the STD is offset by the Dinggye shear zone, which was active before ~ 11 Ma, because T5D5 dike dated at 11 ± 0.4 Ma (Figures 7a and 7c and Table 2) crosscuts the foliation. Motion on the STDS thus stopped between ~ 13.5 and 11 Ma [Leloup *et al.*, 2009, 2010]. Together with the P-T path, this indicates that rocks now outcropping in the STDSZ near Saer were at less than 0.1 GPa pressure (~ 4 km depth) at the end of motion along the STDS (Figure 5c).

[80] West of the Ama Drime within the Kharta gneiss, U/Pb zircon ages from a granulitic metabasite are mostly around 17.6 ± 0.3 Ma with two outliers at 29.5 ± 0.4 Ma and 1991 ± 26 Ma (sample 312-5-2 [Li *et al.*, 2003]). If the last age is clearly inherited from the protolith, the Cenozoic ages provide constraints on the timing of Himalayan metamorphism. As previously discussed, in metabasic rocks, zircon most likely forms following garnet and/or amphibole breakdown [Fraser *et al.*, 1997]. Breakdown of garnet into orthopyroxene + plagioclase has been clearly identified in the sample dated by Li *et al.* [2003], but in the absence of chemical data the position of the garnet and amphibole reactions in the P-T space cannot be precisely reconstructed. Bearing in mind that the rock bulk composition strongly influences the position of these reactions, first-order estimates can be obtained by combining the petrogenetic grid of Groppe *et al.* [2007] with the P-T path of the Kharta-Saer unit proposed by Borghi *et al.* [2003]. Zircon formation may have occurred (1) by amphibole breakdown during either isobaric heating or adiabatic decompression, and/or (2) by garnet breakdown during early decompression (Figure 5a). We thus suggest that the 29.5 ± 0.4 Ma zircon rim developed during the isobaric heating (Figure 5a), while the 17.6 ± 0.3 Ma zircon formed during the adiabatic decompression (Figure 5a). Uranothorites within the melanosome of a migmatitic orthogneiss attributed to the Kartha gneisses and affected by deformation in the Kharta SZ (AD41, Figure S1), yield a concordant U-Pb age of 15.8 ± 0.2 Ma (Figure 9) [Cottle *et al.*, 2009]. Cottle *et al.* [2009] interpret this age as the timing of partial melting. Based on partial melting curve for $P < 1$ GPa for metapelitic, metagranite and meta-greywacke (see Patiño-Douce and Harris [1998] for a review), such event may occur above 700°C . Altogether,

these data are compatible with high-temperature conditions around 17–15 Ma. It is, however, not possible to determine precisely to which pressure the obtained ages are associated.

5.3. From P-T-t to P-T-D-t: Structures Accommodating the Exhumation

[81] Structural studies have identified several structures that could have accommodated the exhumation of the Ama Drime rocks and surrounding units since ~ 30 Ma. The first main structures are the MCTs (HHT/MCTu and MCT/MCTi) that do not outcrop in the Ama Drime area (Figure 1b), but that most probably prolongate below (Figure 1c). The STDS that lies immediately north of the investigated area may also have absorbed a significant part of the Ama Drime exhumation. Finally, N–S normal faults and shear zones on both sides of the Ama Drime horst have absorbed the final exhumation of the Ama Drime rocks. A detailed analysis of the P-T paths and available geochronologic data allows deciphering of the timing and amount of exhumation linked with each structure.

5.3.1. Differential Exhumations

[82] All P-T paths of the Kharta area share a nearly isobaric heating prior to decompression. When timing constraints are available, this isobaric heating appears to start at ~ 30 Ma, corresponding to the Eo-Himalayan stage of metamorphism described elsewhere in the Himalayas. This event can be used as a reference for the relative exhumation amounts between the structural units of the Ama Drime area. For example the ~ 0.2 GPa pressure difference (~ 7.5 km) observed between Saer and Kharta gives a first-order estimate of the differential exhumation absorbed within the Kharta-Saer unit below the STDSZ. Tibetan sedimentary series are epimetamorphic and have probably been exhumed by a very small amount since 12 Ma. Vertical exhumation linked with the STDSZ can thus be estimated from the STDSZ P-T path to be ≤ 0.6 GPa (22 km) at Saer (Figure 5c).

[83] The differential exhumation between the Ama Drime orthogneissic and paragneissic units appears very small, less than the uncertainty on the peak pressure of the ADO (Figures 5b and 5d). There is thus no apparent motion on the Nyonna Ri boundary since more than ~ 30 Ma.

5.3.2. Exhumation Amounts at the Time of STDS Activity

[84] As discussed previously (see section 5.2) motion along the STDS ended between 13.5 and ~ 12 Ma near Saer [Leloup *et al.*, 2009, 2010]. Such timing when compared with the P-T-t path of the Ama Drime orthogneissic unit implies that the adiabatic decompression, larger than 1.0 GPa (37 km) and most probably ~ 1.3 GPa (48 km), occurred during normal motion on the STDS (Figure 5b). This interpretation differs significantly from that of Cottle *et al.* [2009], which relates the adiabatic decompression since 0.7–0.8 GPa to normal motion on the Dinggye and Kharta shear zones. In our interpretation, the total exhumation linked to the Ama Drime horst is less than 0.4 GPa (15 km) (Figure 5b).

[85] The amount of exhumation linked with the STDS measured on the Ama Drime rocks P-T path is 0.2 to 0.7 GPa higher than the ≤ 0.8 GPa value obtained by summing

the relative pressure differences from deformation below the STDSZ (0.2 GPa) and the STDSZ itself (≤ 0.6 GPa, see section 5.3.1). This discrepancy may have several causes:

[86] 1. Vertical motion could have occurred at the base of the Kharta unit and above the Ama Drime orthogneissic unit for example on the Nyonna Ri Boundary. However, as discussed above, such motion, if any, is probably small.

[87] 2. Increase of the dip of the STDS (and MCT) toward the south could induce rotation of the HCS pile and larger uplift in the south than in the north. However, this last hypothesis is unlikely, as the STDS dips shallowly from the top of the Chomolangma to Rongbuk and appears to steepen, not flatten, farther north (Dzakar Chu section) (Figure 2a).

[88] 3. The differential estimates are only first order as they are based on global P-T path from whole units.

[89] 4. A combination of these causes.

[90] The amount of adiabatic decompression appears to increase away from the STD: ~ 1.3 GPa in the Ama Drime orthogneissic unit, 0.6 in the Ama Drime paragneisses, 0.5 GPa in the Kharta gneiss and no adiabatic decompression in the STDSZ (Figure 5). This could be interpreted as a progressive decrease of the exhumation linked with the STDS together with the structural height, implying a distribution of down to the north deformation within the whole UHCS metamorphic pile. However, the end of the adiabatic decompression was reached at ~ 16 Ma in the Kharta unit (Figure 5a), at least 2 Ma earlier than in the Ama Drime orthogneissic unit (Figure 5b). This is probably due to the fact that close to the surface (≤ 0.4 GPa or depths ≤ 15 km) the thermal gradient is so steep, because temperature at the surface is low, that even fast exhumation cannot stay adiabatic but is necessarily accompanied by cooling. As a matter of fact, gneiss in the STDSZ never experienced adiabatic exhumation (Figure 5c) because they are located at the top of the metamorphic pile. It follows that most, of the exhumation (and cooling) of the Kharta unit occurred coevally with the STDS (Figure 5a), and that in the Ama Drime paragneissic unit, the amount of exhumation syn- and post-STDS are probably on the same order of the Ama Drime orthogneissic unit (Figure 5d).

[91] We estimate that, between ~ 30 and 12 Ma, ≤ 0.6 GPa (≤ 22 km) of vertical exhumation occurred linked to brittle motion on the STD and ductile deformation in the STDSZ. This corresponds to exhumation rates on the order of ≤ 1.2 mm/yr immediately below the STDS. This would correspond to ≤ 125 km of displacement and a shear rate of ≤ 7 mm/yr on the STDS, assuming a regular dip of 10° and simple shear in the STDSZ. During the same time span, units within the Ama Drime horst experienced the largest exhumation (1.0 to 1.5 GPa, 37 to 56 km) corresponding to vertical rates of 2 to 3 mm/yr. Such exhumation occurred while HCS rocks, at the exclusion of amphibolite levels, were partially molten following a phase of isobaric heating.

5.3.3. Exhumation Mechanisms at the Time of STDS Activity

[92] Thrust imbrications, wedge extrusion and post-thickening thermal reequilibration have been proposed as the main mechanisms for burial, heating and exhumation of HCS rocks. For some, internal deformations within the Himalayan thrust system could explain the STDS geometry

[Webb et al., 2007]. Other consider a larger thrust wedge system whose shape may vary significantly from one author to the other, being a few tenth of kilometers [Burchfiel and Royden, 1985; Gruijic et al., 1996] to more than 120 km long [Guillot and Allemand, 2002]. Alternatively other authors consider that HCS rocks have been expulsed from farther north, below the Tibetan Plateau, through ductile channel flow following crustal melting [Beaumont et al., 2001; Gruijic et al., 2002; Jamieson et al., 2004].

[93] In all these models, exhumation of the HCS occurs coevally with normal motion along the STDS, but amount of motion on the STDS vary widely. In the thrust system hypothesis, motion on the STDS can be very small (≤ 30 km) and is localized in a narrow shear zone [Webb et al., 2007]. At the opposite, STDS amount of motion is much larger in the channel flow hypothesis, on the same order of magnitude as motion on the MCT (some hundreds of km), but deformation could be distributed in all the upper half of the channel. Timing and throw estimates of the MCTs and STDS are thus crucial to decipher between the models.

[94] Given its dip to the north, the MCT is probably located only ~ 20 km below Kharta (Figure 1c). Age of motion along the MCT (MCT1) and HHT (MCTu) has been constrained through dating of the metamorphic evolution of the HCS gneisses and migmatites affected by top-to-the-south high-temperature thrusting [Hodges et al., 1996; Vance and Harris, 1999; Walker et al., 1999; Foster et al., 2000; Simpson et al., 2000; Johnson et al., 2001; Viskupic and Hodges, 2001; Catlos et al., 2001, 2002a, 2002b, 2004; Kohn et al., 2005; Martin et al., 2007]. Ages were obtained by U-(Th)-Pb method on zircon in leucosome and on monazite in leucosome, matrix or as inclusion within garnet (see Kohn et al. [2005] for a review). Ages interpretation has been widely discussed, especially for monazite (see Catlos et al. [2004] and Kohn et al. [2005] for a review). Based on their Y and Th content and textural relationships, monazite age has been either associated with leucosome crystallization or crystal formation during garnet growth, this latter mostly occurring during temperature increase (prograde evolution). Considering the various published ages it appears that temperature increase of the HCS gneisses occurred between ~ 40 and 16 Ma and that crystallization of melt produced during this temperature increase occurred between 18 and 10 Ma [Hodges et al., 1996; Walker et al., 1999; Foster et al., 2000; Simpson et al., 2000; Johnson et al., 2001; Viskupic and Hodges, 2001; Catlos et al., 2001, 2002a, 2002b, 2004; Kohn et al., 2005; Martin et al., 2007]. Coupling these dating with the P-T evolution of the HCS gneisses and migmatites places some constraints on the age of their exhumation and thus on the extrusion between the MCT1 and/or MCTu and the STDS. The P-T evolution is characterized by a strong decompression starting at ~ 1 GPa [Vance and Mahar, 1998; Guillot, 1999; Searle et al., 1999; Vannay et al., 1999; Goscombe and Hand, 2000; Kohn et al., 2001; Borghi et al., 2003; Dasgupta et al., 2004; Harris et al., 2004]. During this event the rocks keep heating as the thickened Indian continental crust has not yet reached thermal equilibrium and exhumation rate are slow enough [Thompson and Connolly, 1995]. Consequently, monazite crystallization might still occur during exhumation, especially if the mus-

covite dehydration melting reaction is reached which is the case during decompression and heating for the migmatitic samples [Guillot, 1999; Searle et al., 1999; Goscombe and Hand, 2000; Borghi et al., 2003; Dasgupta et al., 2004; Harris et al., 2004]. Actually, petrogenetic modeling by Harris et al. [2004] evidences that significant garnet crystallization occurred when this reaction was reached. Thus, the ages of the prograde monazites are an upper bound for the exhumation of the HCS, i.e., between 40 and 16 Ma. Coupling the age of the prograde evolution and of the melt crystallization gives an interval for the age of melting. Detailed study by Kohn et al. [2005] in central Nepal (Langtang area) suggests that this event took place at 20 ± 2 Ma for the northern part of the HCS, between the STDS and the Langtang thrust, the possible westward prolongation of the Barun thrust (HHT or MCTu), and at 15 ± 2 Ma for the southern part, between the MCTu and the MCTl. Similar age pattern was also evidenced by Catlos et al. [2004] in NE India (Sikkim). Altogether this suggests that the MCTu was active at and before 20 ± 2 Ma and the MCTl at and before 15 ± 2 Ma. Consequently, MCTl and MCTu are most probably active during the adiabatic decompression event recorded by the Ama Drime rocks (see section 5.2) as well as during STDS activity.

[95] Cessation of top-to-the-south thrusting within the HCS gneisses and migmatites and of significant motion along MCTl and MCTu is indirectly constrained by the age of the top-to-the-south thrusting in the Lesser Himalaya unit, below the MCTl, associated with Main Boundary Thrust (MBT) activation. This shift is supposed to occur around 8–12 Ma [Harrison et al., 1997; Catlos et al., 2001, 2002a, 2002b; Daniel et al., 2003; DeCelles et al., 2001; Kohn et al., 2004] coevally with MBT activation at ~ 11 Ma [Meigs et al., 1995]. This southward migration of deformation localization is also supported by the detrital record in the Nepalese Siwalik, suggesting a change of sediment provenance indicating erosion of the Lesser Himalayan at ~ 10 –12 Ma [Szulc et al., 2006]. Thus, the cessation of thrusting along MCTl seems to be coeval with the end of most of the STDS deformation. Note that possible Pliocene reactivation of the MCTl in central Nepal was proposed by Macfarlane [1993] and Catlos et al. [2001].

[96] Throw on the MCTl in Nepal has been estimated to be between 140 and 210 km [Schelling and Arita, 1991; Schelling, 1992] or 200 km [Hauck et al., 1998]. More recently, DeCelles et al. [2001] have raised this estimate to ~ 500 km. Our estimate of the offset on the STDS of only ≤ 125 km appears significantly lower than thrusting on the MCTl, even when neglecting possible thrusting on the MCTu. This implies that either the whole HCS does not exhumed as a single coherent bloc or as proposed by Webb et al. [2007] that both the HCS and the Tethyan Series are transported southward over the MCT.

[97] Numerical models of channel flow in the Himalayan orogeny show that rocks initially buried at depth less than 1.35 GPa can be brought to the surface above the MCTl [Jamieson et al., 2004]. This depth, which corresponds to the base of the horizontal ductile channel below Tibet, is broadly compatible with the metamorphic grade of the HCS near the MCTl, and thus appear to confirm the model

[Jamieson et al., 2004]. However, because the channel flattens to the north and is horizontal below Tibet, there is no reason to expect exhumation of deeper rock anywhere within the channel. Late exhumation in the Ama Drime horst has brought to the surface rocks that were at 15 km depth at the end of motion on the STDS (see section 5.3.3). This gives us access to the deep part of wedge/channel ~ 140 km north of the emergence of the MCTl (Figure 1c). The Ama Drime orthogneissic unit has been buried to depth ≥ 52 km (≥ 1.4 GPa) and exhumed more than 1 GPa (37 km) below the STDS, while the overlying Ama Drime paragneissic unit has been buried to 1.6 GPa (60 km). Such depths would thus correspond to rocks from below the channel (i.e., below the MCTl). This would imply that most of the HCS rocks do not correspond to the channel and that the MCTl and the whole channel would now be exposed above T5D33 locality, thus north of the Sangkar Ri. This corresponds to a maximum thickness of the channel of only 1.3 to 4 km (15 km distance for $10^\circ \pm 5^\circ$ dip) (Figure 2a). Furthermore, most of the exhumation (37 to 48 km) took place between the MCTl and STDS, that thus did not bound a horizontal channel at that time. It also appears that, even it has been largely migmatized, the Ama Drime orthogneissic unit represents a coherent unit as metabasite layers can be followed without interruption for distances of few kilometers (Figure 3e). The large-scale folds affecting these layers are more compatible with vertical thinning and/or N–S simple shear rather than with a partially molten medium that would have flowed for some hundreds of kilometers.

[98] It is logical that rocks sampled deeper in a given thrust slice have experienced higher-pressure conditions. In that case the maximum possible pressure corresponds to the minimum rooting depth of the thrust system, or thrust wedge, and the horizontal pressure gradient in a given thrust sheet may be used to evaluate the dipping angle of the underlying thrust system. In the case of the Ama Drime, this would imply that the MCT–MHT system roots at more than 52–63 km depth and dips 6 – 9° to the north, which is in good accordance with the value proposed from geophysical evidences [e.g., Makovsky et al., 1996].

5.3.4. Final Exhumation of the Ama Drime Horst

[99] As previously discussed, deformation started prior to ~ 11 Ma in the Dinggye shear zone (age of T5D5 crosscutting dike, see sections 4.2.1 and 5.2). The ~ 0.4 GPa of exhumation (15 km) of the Ama Drime unit orthogneissic unit that occurred during the last ~ 12 Ma are thus related to ductile and brittle motion along the N–S Kharta and Dinggye shear zones and the formation of the Ama Drime horst (Figure 5b). This estimate suggests an average exhumation rate of ~ 1.2 mm/yr. The vertical offset of the STD is of 4.4 to 9.4 km at the northern tip of the Ama Drime (see section 3.2.1) (Figure 2a). This is coherent with a progressive decrease of the finite motion toward the northern tip of the Dinggye fault. Fifteen km of exhumation could have been sufficient to bring the MCTu at the surface, confirming that the Nyonno Ri Boundary could be an equivalent of the Barun thrust that separates the LHCS and the GHCS.

[100] (U-Th)/He apatite ages collected at various locations within the horst [Jessup et al., 2008; this study] appear to give a coherent picture corresponding to vertical exhu-

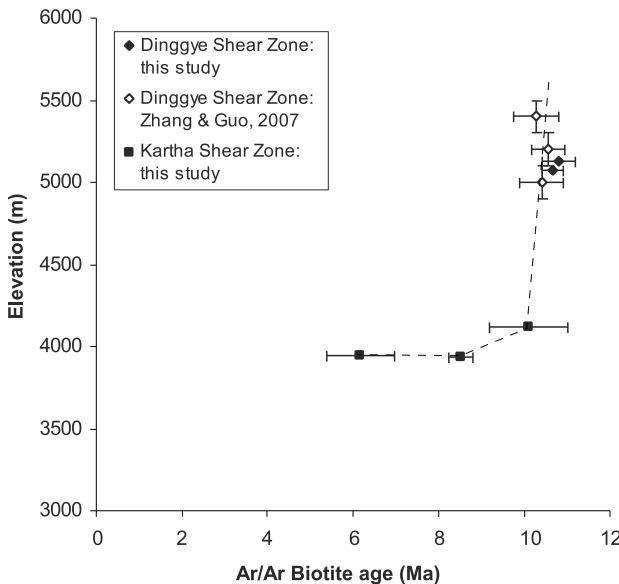


Figure 11. Plot of Ama Drime Ar/Ar biotite age versus elevation. Data from this study (Table 3), and Zhang and Guo [2007]. Elevation of Zhang and Guo [2007] samples has been inferred from SRTM digital elevation model and was attributed a conservative 1σ uncertainty of 100 m. This plot suggests that exhumation rate was very fast at ~ 10 Ma and then significantly slowed down at least until 6 Ma. See text for details.

tion at about 1 mm/yr since at least 4.2 Ma (see section 4.2.4, Figure 10). This corresponds to ~ 4 km of vertical exhumation. All (U-Th)/He data fit in the same trend suggesting that there is no differential exhumation across the horst. The straightforward interpretation is that the two active faults bounding the horst are active since at least 4.2 Ma with vertical slip rates of ~ 1 mm/yr.

[101] Both active faults exhibit ductile shear zones in their footwall. The fact that the motion direction on the ductile mylonites and brittle faults are the same (Figure 4) favors the interpretation of one continuous phase of deformation, as it is classically interpreted in metamorphic core complexes. In that case, initial exhumation related to ductile

deformation would have started at a fast rate of at least 1.4 mm/yr and would have slowed down to ~ 1 mm/yr in the last 4 Ma in order to reach an average rate of ~ 1.2 mm/yr.

[102] Total exhumation of ~ 15 km would correspond to ~ 21 km displacement on the Dinggye shear zone (dip $\sim 45^\circ$), and ~ 30 km on the Kharta one (dip $\sim 30^\circ$). This implies that 41 km (measured horizontally, parallel to the motion direction) of the hanging plates would have been eroded. Following the interpretation that part of the Ama Drime orthogneissic unit adiabatic decompression is contemporaneous with E–W extension, and not with the STDS, would increase the vertical exhumation to 24 ± 2 km [Cottle et al., 2009]. The amount of removed upper plate would thus rise to 60 to 71 km. Such estimates are problematic as the two faults are only 28 km away from each other, leaving place for a maximum 28 km of removed upper plate. In order to stay compatible with 15 km of exhumation both faults should dip by 47° to 52° , and join at the surface at the onset of deformation. Conversely, maximum possible exhumations for faults dipping 30° and 45° are 14 km and 8 km, respectively. It thus appears that the structural history of the Ama Drime horst is more complicated, either that the fault have not been synchronous and/or that their dip was significantly larger than the present dip of the mylonites.

[103] Ductile deformation in the Dinggye shear zone started prior to ~ 11 Ma and stopped at ~ 10 Ma, as temperature had dropped below $\sim 300^\circ\text{C}$ according to the biotite and muscovite argon ages (Figure 9). The age of the Kharta shear zone is much less well constrained. The fact that all leucocratic dikes are deformed in the Kharta SZ while many of them crosscut the Dinggye SZ (Figure 2b) could suggest that ductile deformation initiate later, or lasted longer, on the western side than on the eastern one. Such dikes are dated between 12.8 ± 0.2 and 9.8 ± 1.2 Ma (Figure 9), suggesting that the main ductile deformation event could have occurred prior to ~ 10 Ma in the Dinggye SZ and after that date in the Kartha SZ. On the other hand, ~ 12 Ma muscovite and ~ 10 Ma biotite $^{39}\text{Ar}/^{40}\text{Ar}$ ages could suggest that ductile deformation was active in the Kharta shear zone in the 12–10 Ma interval coevally with the Dinggye SZ. However, $^{39}\text{Ar}/^{40}\text{Ar}$ ages in the Kharta SZ span between 24 and 3 Ma (Table 3 and Figure 9) and another interpretation can be proposed. T7A19 meta-arenite biotite $^{39}\text{Ar}/^{40}\text{Ar}$ age (23.5 ± 0.5 Ma) is interpreted as inherited from the peak temperature

Figure 12. Speculative sketches of exhumation phases of the Ama Drime rocks. Schematic drawings depicting the main exhumation phases of the Ama Drime rocks. The burial stage (prograde metamorphism) is not depicted. Drawings have been oversimplified in order to highlight structures related to the exhumation of the Ama Drime. The topographic profiles are arbitrary for Figures 12a and 12b and based on SRTM data for Figure 12c. Shaded color above topography. ADO, Ama Drime orthogneissic unit; ADP, Ama Drime paragneissic unit. Figures 12a–12c show the main exhumation stages, with cross section(s) (left) and corresponding P-T path for the Ama Drime pragneisses (top right) and orthogneisses (bottom right). For Figures 12b and 12c, two cross sections are presented: NNE–SSW parallel to Figure 2b but going through Ama Drime range (left) and east–west across the south Ama Drime (middle). In each case the arrow corresponds to the path during the whole time interval. (a) Exhumation in the hanging wall of the lower MCT–MHT and in the footwall of the STDS, between ~ 33 and 12 Ma. This is the main exhumation phase during which both units are partially melted. Timing of exhumation initiation is not precisely constrained. The upper MCT–HHT is probably active only during a limited time. KT, Kangmar thrust; CT, counterthrust. (b) Exhumation in the footwall of the Kharta and Dinggye shear zones. The Dinggye shear zone was probably the master fault and is figured in bold. (c) Exhumation in the footwall of the Kharta and Dinggye faults.

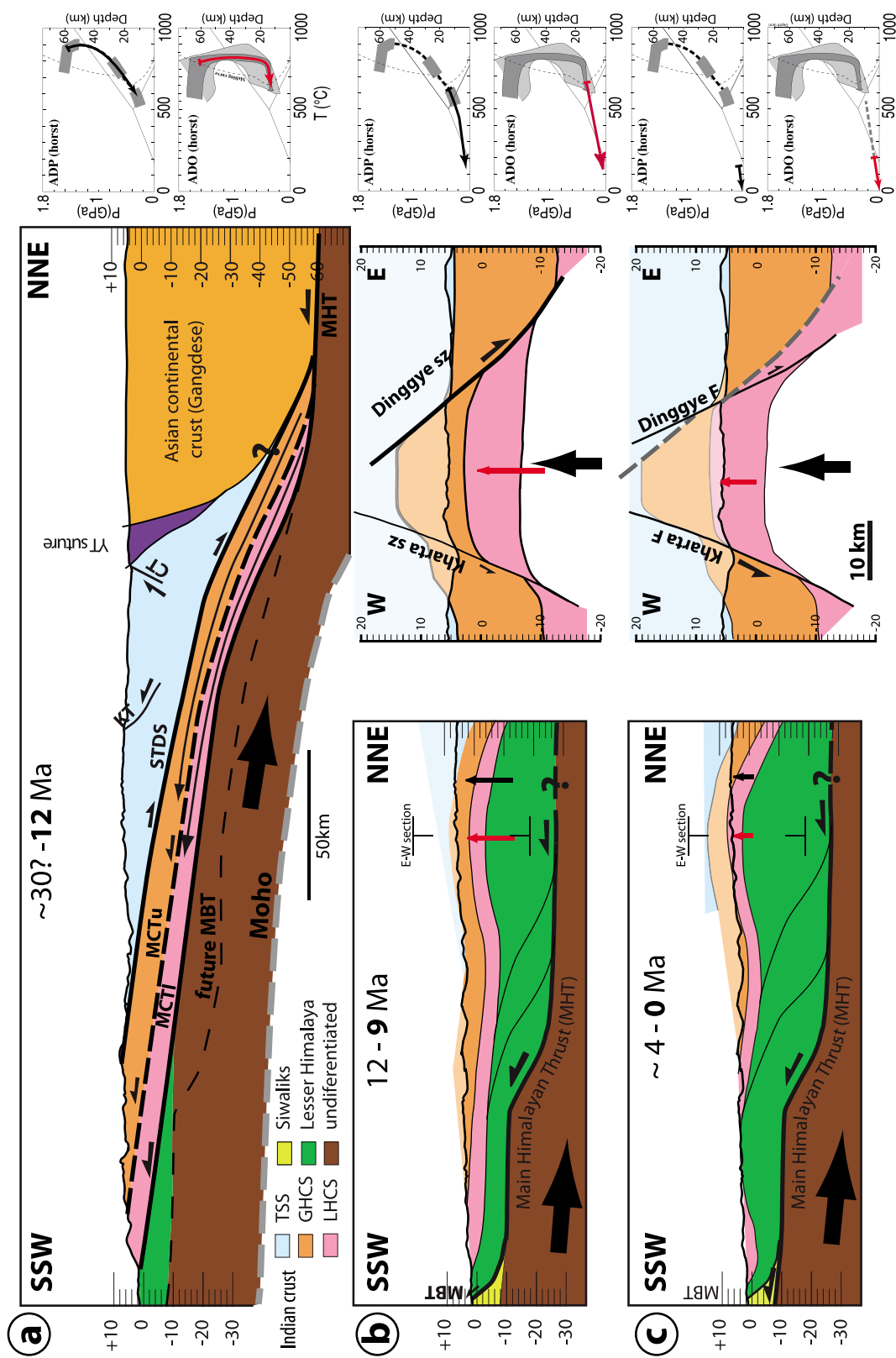


Figure 12

metamorphism in the Ama Drime series (see section 4.2.2). When plotted against elevation, the other $^{39}\text{Ar}/^{40}\text{Ar}$ biotite argon ages suggest a slow exhumation rate in the Kharta shear zone from ~ 10 to ~ 6 Ma (Figure 11). The same plot for the Dinggye shear zone confirms fast exhumation at ~ 10.5 Ma. (Figure 11). Together with the (U-Th)/He data, this could imply two pulses of rapid cooling and exhumation for the Ama Drime horst: one at ~ 10 Ma and another since ~ 4 Ma. In that case the biotite ages of the western flank would be interpreted as cooling ages and the muscovite ages as reflecting deformation phases at ~ 12 Ma and since ~ 6 Ma (Figure 9). In the Dinggye SZ the $^{39}\text{Ar}/^{40}\text{Ar}$ biotite and muscovite ages are the same (Figure 9) suggesting a major cooling and deformation phase between 13.7 and 10.2 Ma.

[104] We propose that two successive normal faulting events took place in the Ama Drime massif. At ~ 12 Ma, E–W extension immediately following the end of motion on the STDS induced the formation of the Dinggye shear zone and induced rapid cooling and exhumation (~ 4 mm/yr) on the eastern side of the range (Figure 12b). Exhumation (and cooling) was probably slower on the western side resulting in a more complex thermochronologic signal. This could indicate that the master fault was on the eastern side, a fact that could explain the bulge of the STD observed to the NW of the Ama Drime. By ~ 10 Ma temperature was below 300°C in the Dinggye shear zone. That deformation phase ended ~ 9 Ma ago, and induced 11 to 13 km of exhumation. Prior to 4 Ma ago, probably at ~ 6 Ma, two conjugate N–S normal faults affected the Ama Drime range, inducing exhumation at a rate of ~ 1 mm/yr, for a total of at least 4 km (Figure 12c). Hydrothermal circulation along brittle faults induced the crystallization of a second generation of muscovites near the Kharta fault (Figure 9). The late normal faults belong to the Xainza-Dinggye fault system and are contemporaneous with the major east-west extensional episode recognized in numerous localities in southern Tibet (e.g., Mahéo *et al.* [2007] for a review). This structural history, compatible with presently available data would need to be tested at the light of new data.

[105] In any case the onset of E–W extension appears to closely follow or to be contemporaneous with the time of the end of motion along the STDS and MCTI between 12 and 10 Ma. This brutal transition from N–S to E–W extension in south Tibet while $\sim \text{N–S}$ convergence still takes place between India and Eurasia has to be explained.

[106] In a context of $\sim \text{N–S}$ shortening, north south trending normal faults can be related (1) with east-west extension during orogen parallel midcrustal flow [Cottle *et al.*, 2009], (2) stress reorganization(s) related with kinematics and/or geometry change(s) of the underlying thrust system and (3) focused erosion of the Arun River [Jessup *et al.*, 2008].

[107] Focused erosion of the Arun River can be ruled out as the river is not centered on the massif, where the deepest rocks outcrop, but flows in the half graben located along the western flank of the massif. Possible recent migration of the river from the core of the horst to its present-day location, is unlikely as (1) focused erosion implies deep incision incompatible with significant river migration, and (2) (U-Th)/

He data indicates constant exhumation with no significant tilting since at least 4 Ma.

[108] The exact distribution of the early (12–10 Ma) phases of E–W extension is not yet well recognized. It starts to be documented in few localities through Tibet: in the Thakkola graben [Garzzone *et al.*, 2003], in Tangra Yum Co [Dewane *et al.*, 2006], Lopu fault [Arnaud *et al.*, 2008] as well as in the Xainza Rift [Hager *et al.*, 2006] in the northern prolongation of the Dinggye fault. In all these localities the exhumation seems to last less than 2 Myr [Hager *et al.*, 2006]. Some have proposed that, at the scale of Tibet, crustal flow toward the south (Himalaya) was followed by crustal flow toward the east (LongmenShan and Yunnan) that would still be active today [e.g., Royden *et al.*, 1997]. In that context, the switch from N–S to E–W extension in the Ama Drime would correspond to the change in direction of the channel flow [Cottle *et al.*, 2009]. However, the reason(s) for such radical change, and for the occurrence of two distinct phases of extension rather than a continuous one, would stay mysterious as the main boundary conditions driving channel flow (thermal state of the crust beneath Tibet and topography) do not appear to have radically changed at that time. Furthermore, the direction of extension in the Ama Drime area is neither perpendicular to the regional high topography nor directed toward the region where crustal flow is expected to leave Tibet north of the eastern syntaxis.

[109] On the other hand the timing of the end of motion along the MCTI appears closely related to the activation of the Main Boundary Thrust (Figures 12a and 12b). This corresponds to the propagation of surface expression of the deep main Himalayan thrust (MHT) toward the external part or the accretionary prism, as it is classically observed in many mountain belts. From plate kinematics reconstruction based on magnetic anomalies, Lee and Lawver [1995] infer a change in India-Eurasia convergence direction from $\sim \text{N}30$ to $\sim \text{N}13$ at 10–12 Ma together with a slight increase in rate. Using a different plate circuit, Molnar and Stock [2009] infer a $\geq 40\%$ rate decrease together with a direction change between 20 and ~ 10 Ma. From their data, the change may have occurred gradually or abruptly near 11 Ma. The timing coincidence suggest that changes in the locus, direction and rate of thrusting at ~ 11 Ma may have annihilate the conditions favorable for slip of a passive roof fault (The STDS) along the top of the prism, and locally promoted $\sim \text{E–W}$ extension. We also note that the Molnar and Stock [2009] plate reconstruction shows a constant convergence rate since ~ 10 Ma but a marked change in direction between ~ 5 and ~ 6 Ma ago, at the time that we infer for the initiation of the still active E–W extension phase that has been interpreted as directly related to India punch [Armijo *et al.*, 1986; McCaffrey and Nabelek, 1998; Kapp and Guynn, 2004]. We thus propose that south Tibet Cenozoic extension phases kinematics are fundamentally driven by the direction and rate of India underthrusting.

5.4. Conclusion and Summary

[110] From the observations and interpretations presented above the structural and metamorphic evolution of the Ama

Drime range can be summarized as follows. In the Ama Drime range, both the Ama Drime orthogneissic and paragneissic unit were buried to depth of 52 to 63 km. Most of the exhumation corresponds to an adiabatic decompression of 37 to 48 km, initiated after 33 Ma, between the MCTs and the STDS until ~13.5 Ma (Figure 12a). That phase ended when motion along the STDS switched to local E–W extension between 13.5 and 12 Ma. This timing is compatible with a contemporaneous end of the STDS and the MCTI motion at ~12 Ma. Vertical exhumation in the STDSZ and below the STD is smaller than 0.6 GPa (22 km), corresponding to ~125 km of displacement and a rate of ~7 mm/yr on the STDS between ~30 and ~12 Ma. During the same time span, further 0.3 to 0.7 GPa (11 to 26 km) of exhumation occurred below the STDSZ probably above the MCTI. The coeval end of motion on the STDS and MCTI, and the fact that the HCS rocks were partially molten at the time of their exhumation appear compatible with the lower crustal flow hypothesis. However, the fact that motion on the STDS is much smaller than on the MCTI and that rocks have been exhumed from greater depths than those envisaged for the channel model are more compatible with a wedge extrusion or thrust system model. In that case, the

change of direction of extension at the top of the belt was triggered by propagation of thrusting from the MCTI to the lower and more external MBT. While exhumation may have been continuous since ~12 Ma, some clues suggest that it took place in two distinct phases: (1) The Dinggye normal shear zone was active until ~9 Ma, accounting for 9 to 12 km of exhumation (Figure 12b), and (2) final exhumation of the Ama Drime horst along the Dinggye and Kharta normal faults from ~6 to 4 Ma to present at a vertical rate of ~1 mm/yr (Figure 12c). The fact that the Arun River flows outside of the Ama Drime horst excludes that it may have played a major role in the exhumation of the range.

[111] **Acknowledgments.** We thank E. Deloule and the ion probe team of the CRPG, CNRS UPR 2300, Nancy, France, for their help in dating the zircons. Claude Merlet and the electronic microprobe team of Géosciences Montpellier, Université de Montpellier 2, France. We thank Paul Capiez for the whole rock X-fluorescence analysis at UMR 5570, Lyon, France. This paper benefited for constructive review by C. Groppo and one anonymous reviewer. The first field trip was financed by INSU DyETI grant to R. Lacassin and P.H.L. This project has benefited from the Sino-French PRA program to D.L. and J.V.W.

References

- Arita, K. (1983), Origin of the inverted metamorphism of the Lower Himalayas, central Nepal, *Tectonophysics*, **95**, 43–60, doi:10.1016/0040-1951(83)90258-5.
- Armijo, R., P. Tapponnier, J. L. Mercier, and T. L. Han (1986), Quaternary extension in southern Tibet: Field observations and tectonic implications, *J. Geophys. Res.*, **91**, 13,803–13,872, doi:10.1029/JB091iB14p13803.
- Arnaud, N., J. C. Aitchison, P. H. Leloup, F. Valli, and S. Wilde (2008), Constraints on the initiation of normal faulting across the Yarlung Tsangpo suture zone, from the Lopu Gangri range, southern Tibet, *Geophys. Res. Abstr.*, **10**, EGU2008-A-00000.
- Auzanneau, E., D. Vielzeuf, and M. W. Schmidt (2006), Experimental evidence of decompression melting during exhumation of subducted continental crust, *Contrib. Mineral. Petrol.*, **152**, 125–148, doi:10.1007/s00410-006-0104-5.
- Baur, J. R. (2007), Seismotectonics of the Himalayas and the Tibetan Plateau: Moment tensor analysis of regional seismograms, Ph.D. thesis, 298 pp., Oreg. State Univ., Corvallis.
- Beaumont, C., R. A. Jamieson, M. H. Nguyen, and B. Lee (2001), Himalayan tectonics explained by extrusion of a low-viscosity crustal channel coupled to focused surface denudation, *Nature*, **414**, 738–742, doi:10.1038/414738a.
- Bollinger, L., J. P. Avouac, O. Beyssac, E. J. Catlos, T. M. Harrison, M. Grove, B. Goffe, and S. Sapkota (2004), Thermal structure and exhumation history of the Lesser Himalaya in central Nepal, *Tectonics*, **23**, TC5015, doi:10.1029/2003TC001564.
- Bordet, P. (1961), *Recherches Géologiques dans l'Himalaya du Népal, Région du Makalu*, 275 pp., Cent. Natl. de la Rech. Sci., Paris.
- Borghesi, A., D. Castelli, B. Lombardo, and D. Visona (2003), Thermal and baric evolution of garnet granulites from the Kharta region of S Tibet, E Himalaya, *Eur. J. Mineral.*, **15**, 401–418, doi:10.1127/0935-1221/2003/0015-0401.
- Brunel, M. (1983), *Etude Pétro-Structurale des Chevauchements Ductiles en Himalaya (Népal Oriental et Himalaya du Nord-Ouest)*, 395 pp., Univ. of Paris VII, Paris.
- Burchfiel, B. C., and L. H. Royden (1985), North-south extension within the convergent Himalayan region, *Geology*, **13**, 679–682, doi:10.1130/0091-7613(1985)13<679:NEWTC>2.0.CO;2.
- Burchfiel, B. C., Z. Chen, K. V. Hodges, Y. Liu, L. H. Royden, C. Deng, and J. Xu (1992), The South Tibetan Detachment System, Himalayan Orogen: Extension contemporaneous with and parallel to shortening in a collisional mountain belt, *Spec. Pap. Geol. Soc. Am.*, **269**, 41 pp.
- Burg, J. P., M. Brunel, D. Gapais, G. M. Chen, and G. H. Liu (1984), Deformation of leucogranites of the crystalline main central sheet in southern Tibet (China), *J. Struct. Geol.*, **6**, 535–542, doi:10.1016/0191-8141(84)90063-4.
- Carosi, R., B. Lombardo, G. Molli, G. Musumeci, and P. C. Pertusati (1998), The South Tibetan Detachment System in the Rongbuk valley, Everest region. Deformation features and geological implications, *J. Asian Earth Sci.*, **16**, 299–311, doi:10.1016/S0743-9547(98)00014-2.
- Castro, A., L. G. Corretge, M. El-Biad, H. El-Hmidi, C. Fernandez, and A. E. P. Douce (2000), Experimental constraints on Hercynian anatexis in the Iberian Massif, Spain, *J. Petrol.*, **41**, 1471–1488.
- Catlos, E. J., T. M. Harrison, M. J. Kohn, M. Grove, F. J. Ryerson, C. E. Manning, and B. N. Upadhyay (2001), Geochronologic and thermobarometric constraints on the evolution of the Main Central Thrust, central Nepal Himalaya, *J. Geophys. Res.*, **106**, 16,177–16,204, doi:10.1029/2000JB900375.
- Catlos, E. J., L. D. Gilley, and T. M. Harrison (2002a), Interpretation of monazite ages obtained via in situ analysis, *Chem. Geol.*, **188**, 193–215, doi:10.1016/S0009-2541(02)00099-2.
- Catlos, E. J., T. M. Harrison, C. E. Manning, M. Grove, S. M. Rai, M. S. Hubbard, and B. N. Upadhyay (2002b), Records of the evolution of the Himalayan orogen from in situ Th-Pb ion microprobe dating of monazite: Eastern Nepal and western Garhwal, *J. Asian Earth Sci.*, **20**, 459–479, doi:10.1016/S1367-9120(01)00039-6.
- Catlos, E. J., C. S. Dubey, T. M. Harrison, and M. A. Edwards (2004), Late Miocene movement within the Himalayan Main Central Thrust shear zone, Sikkim, north-east India, *J. Metamorph. Geol.*, **22**, 207–226, doi:10.1111/j.1525-1314.2004.00509.x.
- Cattin, R., and J. P. Avouac (2000), Modeling mountain building and the seismic cycle in the Himalaya of Nepal, *J. Geophys. Res.*, **105**, 13,389–13,407, doi:10.1029/2000JB900032.
- Connolly, J. A. D. (1990), Multivariable phase-diagrams —An algorithm based on generalized thermodynamics, *Am. J. Sci.*, **290**, 666–718.
- Cottle, J. M., M. J. Jessup, D. L. Newell, M. P. Searle, R. D. Law, and M. S. A. Horstwood (2007), Structural insights into the early stages of exhumation along an orogen-scale detachment: The South Tibetan Detachment System, Dzakaa Chu section, eastern Himalaya, *J. Struct. Geol.*, **29**, 1781–1797, doi:10.1016/j.jsg.2007.08.007.
- Cottle, J. M., M. J. Jessup, D. L. Newell, M. S. A. Horstwood, S. R. Noble, R. R. Parrish, D. J. Waters, and M. P. Searle (2009), Geochronology of granularized eclogite from the Ama Drime Massif: Implications for the tectonic evolution of the south Tibetan Himalaya, *Tectonics*, **28**, TC1002, doi:10.1029/2008TC002256.
- Daniel, C. G., L. S. Hollister, R. R. Parrish, and D. Gruijic (2003), Exhumation of the Main Central Thrust from lower crustal depths, eastern Bhutan Himalaya, *J. Metamorph. Geol.*, **21**, 317–334.
- Dasgupta, S., J. Ganguly, and S. Neogi (2004), Inverted metamorphic sequence in the Sikkim Himalayas: Crystallization history, P-T gradient and implications, *J. Metamorph. Geol.*, **22**, 395–412, doi:10.1111/j.1525-1314.2004.00522.x.
- DeCelles, P. G., D. M. Robinson, J. Quade, T. P. Ojha, C. N. Garzione, P. Copeland, and B. N. Upadhyay (2001), Stratigraphy, structure, and tectonic evolution of the Himalayan fold-thrust belt in western Nepal, *Tectonics*, **20**, 487–509, doi:10.1029/2000TC001226.
- Dewane, T. J., D. F. Stockli, C. Hager, M. Taylor, L. Ding, J. Lee, and S. Wallis (2006), Timing of Cenozoic E–W Extension in the Tangra-Yum Co-Kung Co Rift, south-central Tibet, *Eos Trans. AGU*, **87**(52), Fall Meet. Suppl., Abstract T34C-04.
- Dewey, J. F. (1988), Extensional collapse of orogens, *Tectonics*, **7**, 1123–1139, doi:10.1029/TC007i006p01123.
- Edwards, M. A., W. S. F. Kidd, J. X. Li, Y. J. Yu, and M. Clark (1996), Multi-stage development of the southern Tibet detachment system near Khula Kangri. New data from Gonto La, *Tectonophysics*, **260**, 1–19, doi:10.1016/0040-1951(96)00073-X.

- England, P., and G. Houseman (1989), Extension during continental convergence, with application to the Tibetan Plateau, *J. Geophys. Res.*, **94**, 17,561–17,579, doi:10.1029/JB094iB12p17561.
- Foster, G., P. Kinny, D. Vance, C. Prince, and N. Harris (2000), The significance of monazite U-Th-Pb age data in metamorphic assemblages: A combined study of monazite and garnet chronometry, *Earth Planet. Sci. Lett.*, **181**, 327–340, doi:10.1016/S0012-821X(00)00212-0.
- Fraser, G., D. Ellis, and S. Eggins (1997), Zirconium abundance in granulite-facies minerals, with implications for zircon geochronology in high-grade rocks, *Geology*, **25**, 607–610, doi:10.1130/0091-7613(1997)025<0607:ZAIGFM>2.3.CO;2.
- Garzione, C. N., P. G. DeCelles, D. G. Hodkinson, T. P. Ojha, and B. N. Upreti (2003), East-west extension and Miocene environmental change in the southern Tibetan Plateau: Thakkholi graben, central Nepal, *Geol. Soc. Am. Bull.*, **115**, 3–20, doi:10.1130/0016-7606(2003)115<0003:EWEAME>2.0.CO;2.
- Goscombe, B., and M. Hand (2000), Contrasting P-T paths in the Eastern Himalaya, Nepal: Inverted isograds in a paired metamorphic mountain belt, *J. Petrol.*, **41**, 1673–1719, doi:10.1093/petrology/41.12.1673.
- Goscombe, B., D. Gray, and M. Hand (2006), Crustal architecture of the Himalayan metamorphic front in eastern Nepal, *Gondwana Res.*, **10**, 232–255, doi:10.1016/j.gr.2006.05.003.
- Groppi, C., B. Lombardo, F. Rolfo, and P. Pertusati (2007), Clockwise exhumation path of granulitized eclogites from the Ama Drime range (Eastern Himalayas), *J. Metamorph. Geol.*, **25**, 51–75, doi:10.1111/j.1525-1314.2006.00678.x.
- Grujic, D., M. Casey, C. Davidson, L. S. Hollister, R. Kundig, T. Pavlis, and S. Schmid (1996), Ductile extrusion of the higher Himalayan crystalline in Bhutan: Evidence from quartz microfabrics, *Tectonophysics*, **260**, 21–43, doi:10.1016/0040-1951(96)00074-1.
- Grujic, D., L. S. Hollister, and R. R. Parrish (2002), Himalayan metamorphic sequence as an orogenic channel: Insight from Bhutan, *Earth Planet. Sci. Lett.*, **198**, 177–191, doi:10.1016/S0012-821X(02)00482-X.
- Guillot, S. (1999), An overview of the metamorphic evolution in central Nepal, *J. Asian Earth Sci.*, **17**, 713–725, doi:10.1016/S1367-9120(99)00045-0.
- Guillot, S., and P. Allemand (2002), Two-dimensional thermal modelling of the early tectonometamorphic evolution in central Himalaya, *J. Geodyn.*, **34**, 77–98, doi:10.1016/S0264-3707(02)00016-9.
- Hager, C., D. Stockli, T. Dewane, and L. Ding (2006), Episodic Mio-Pliocene rifting in south-central Tibet. Thermochronometric constraints from the Xainza rift, *Eos Trans. AGU*, **87**(52), Fall Meet. Suppl., Abstract T34C-02.
- Harris, N. B. W., M. Caddick, J. Kosler, S. Goswami, D. Vance, and A. G. Tindle (2004), The pressure-temperature-time path of migmatites from the Sikkim Himalaya, *J. Metamorph. Geol.*, **22**, 249–264, doi:10.1111/j.1525-1314.2004.00511.x.
- Harrison, T. M., P. Copeland, W. S. F. Kidd, and O. M. Lovera (1995), Activation of the Nyainqntanglha Shear Zone: Implications for uplift of the southern Tibetan Plateau, *Tectonics*, **14**, 658–676, doi:10.1029/95TC00608.
- Harrison, T. M., F. J. Ryerson, P. LeFort, A. Yin, O. M. Lovera, and E. J. Catlos (1997), A late Miocene-Pliocene origin for the central Himalayan inverted metamorphism, *Earth Planet. Sci. Lett.*, **146**, E1–E7, doi:10.1016/S0012-821X(96)00215-4.
- Harrison, T. M., M. Grove, O. M. Lovera, and E. J. Catlos (1998), A model for the origin of Himalayan anatexis and inverted metamorphism, *J. Geophys. Res.*, **103**, 27,017–27,032, doi:10.1029/98JB02468.
- Hauck, M. L., K. D. Nelson, L. D. Brown, W. J. Zhao, and A. R. Ross (1998), Crustal structure of the Himalayan orogen at ~90° east longitude from Project INDEPTH deep reflection profiles, *Tectonics*, **17**, 481–500, doi:10.1029/98TC01314.
- Heim, A., and A. Gansser (1939), Central Himalaya: Geological 999 observations of the Swiss expedition 1936, *Mem. Soc. Helv. Sci. Nat.*, **1**, 245.
- Hodges, K. V. (2000), Tectonics of the Himalaya and southern Tibet from two perspectives, *Geol. Soc. Am. Bull.*, **112**, 324–350, doi:10.1130/0016-7606(2000)112<0324:TOTHAS>2.3.CO;2.
- Hodges, K. V., W. E. Hames, W. Olszewski, B. C. Burchfiel, L. H. Royden, and Z. Chen (1994), Thermobarometric and $^{40}\text{Ar}/^{39}\text{Ar}$ geochronologic constraints on Eohimalayan metamorphism in the Dinggyê area, southern Tibet, *Contrib. Mineral. Petro.*, **117**, 151–163, doi:10.1007/BF00286839.
- Hodges, K. V., R. R. Parrish, and M. P. Searle (1996), Tectonic evolution of the central Annapurna Range, Nepalese Himalayas, *Tectonics*, **15**, 1264–1291, doi:10.1029/96TC01791.
- Holland, T. J. B., and R. Powell (1998), An internally consistent thermodynamic data set for phases of petrological interest, *J. Metamorph. Geol.*, **16**, 309–343, doi:10.1111/j.1525-1314.1998.00140.x.
- House, M. A., K. A. Farley, and D. Stockli (2000), Helium chronometry of apatite and titanite using Nd-YAG laser heating, *Earth Planet. Sci. Lett.*, **183**, 365–368, doi:10.1016/S0012-821X(00)00286-7.
- Indares, A., R. W. White, and R. Powell (2008), Phase equilibria modelling of kyanite-bearing anatetic paragneisses from the central Grenville Province, *J. Metamorph. Geol.*, **26**, 815–836, doi:10.1111/j.1525-1314.2008.00788.x.
- Jamieson, R. A., C. Beaumont, S. Medvedev, and M. H. Nguyen (2004), Crustal channel flows: 2. Numerical models with implications for metamorphism in the Himalayan-Tibetan orogen, *J. Geophys. Res.*, **109**, B06407, doi:10.1029/2003JB002811.
- Jessup, M. J., D. L. Newell, J. M. Cottle, A. L. Berger, and J. A. Spotila (2008), Orogen-parallel extension and exhumation enhanced by denudation in the trans-Himalayan Arun River gorge, Ama Drime Massif, Tibet-Nepal, *Geology*, **36**, 587–590, doi:10.1130/G24722A.1.
- Johnson, M. R. W., G. J. H. Oliver, R. R. Parrish, and S. P. Johnson (2001), Synthrusting metamorphism, cooling, and erosion of the Himalayan Kathmandu Complex, Nepal, *Tectonics*, **20**, 394–415, doi:10.1029/2001TC900005.
- Kapp, P., and J. H. Guynn (2004), Indian punch rifts Tibet, *Geology*, **32**, 993–996, doi:10.1130/G20689.1.
- Kapp, P., M. Taylor, D. Stockli, and L. Ding (2008), Development of active low-angle normal fault systems during orogenic collapse: Insight from Tibet, *Geology*, **36**, 7–10, doi:10.1130/G24054A.1.
- Kelsey, D. E., C. Clark, and M. Hand (2008), Thermobarometric modelling of zircon and monazite growth in melt-bearing systems: Examples using model metapelite and metapsammitic granulites, *J. Metamorph. Geol.*, **26**, 199–212, doi:10.1111/j.1525-1314.2007.00757.x.
- Kohn, M. J., E. J. Catlos, F. J. Ryerson, and T. M. Harrison (2001), Pressure-temperature-time path discontinuity in the Main Central Thrust zone, central Nepal, *Geology*, **29**, 571–574, doi:10.1130/0091-7613(2001)029<0571:PTTPDI>2.0.CO;2.
- Kohn, M. J., M. S. Wieland, C. D. Parkinson, and B. N. Upreti (2004), Miocene faulting at plate tectonic velocity in the Himalaya of central Nepal, *Earth Planet. Sci. Lett.*, **228**, 299–310, doi:10.1016/j.epsl.2004.10.007.
- Kohn, M. J., M. S. Wieland, C. D. Parkinson, and B. N. Upreti (2005), Five generations of monazite in Langtang gneisses: Implications for chronology of the Himalayan metamorphic core, *J. Metamorph. Geol.*, **23**, 399–406, doi:10.1111/j.1525-1314.2005.00584.x.
- Lee, T. Y., and L. A. Lawver (1995), Cenozoic plate reconstruction of Southeast Asia, *Tectonophysics*, **251**, 85–138, doi:10.1016/0040-1951(95)00023-2.
- Le Fort, P. (1975), Himalayas-collided range—Present knowledge of continental arc, *Am. J. Sci.*, **A275**, 1–44.
- Leloup, P. H., T. M. Harrison, F. J. Ryerson, W. J. Chen, Q. Li, P. Tappognier, and R. Lacassin (1993), Structural, petrological and thermal evolution of a Tertiary ductile strike-slip shear zone, I ncang Shan, Yunnan, *J. Geophys. Res.*, **98**, 67 6743, doi:10.1029/92JB02791.
- Leloup, P. H., E. Kali, N. Arnaud, G. Mahéo, E. Boutor Liu X., D. Liu, H. Li, and J. Liu-Zeng (2001), Miocene (~12 Ma) transition from E-W to N syn-convergence normal faulting in the central Himalayas (Ama Drime range), *Geophys. Abstr.*, **11**, EGU2009-9690-2001.
- Leloup, P. H., G. Maheo, N. Arnaud, E. Kali, E. Boutonnet, D. Liu, Liu X., and Li H. (2010), The South Tibet detachment shear zone in the Dinggye area: Time constraints on extrusion models of the Himalayas, *Earth Planet. Sci. Lett.*, **292**, 1–doi:10.1016/j.epsl.2009.12.035.
- Li, D., Q. Liao, Y. Yuan, Y. Wan, D. Liu, X. Zhang, S. Yi, S. Cao, and D. Xie (2003), SHRIMP U zircon geochronology of granulites at Rimana (southern Tibet) in the central segment of Himalayan Orogen, *Chin. Sci. Bull.*, **48**, 2647–2650, doi:10.1360/03wd0080.
- Liu, S. W., J. J. Zhang, G. M. Shu, and Q. G. Li (2005), Mineral chemistry, P-T-t paths and exhumation processes of mafic granulites in Dinggye, southern Tibet, *Sci. Ch. Ser. Earth Sci.*, **48**, 1870–1881.
- Liu, Y., W. Siebel, H. J. Massonne, and X. C. Xiao (2007), Geochronological and petrological constraints for tectonic evolution of the central Greater Himalayan Sequence in the Kharta area, southern Tibet, *J. Geol.*, **115**, 215–230, doi:10.1086/510108.
- Lombardo, B., and F. Rolfo (2000), Two contrasting eclogite types in the Himalayas: Implications for the Himalayan orogeny, *J. Geodyn.*, **30**, 37–doi:10.1016/S0264-3707(99)00026-5.
- Lombardo, B., P. Pertusati, and A. Borghi (1993), Geology and tectono-magmatic evolution of the eastern Himalaya along the Chomolungma-Mal transect, in *Himalayan Tectonics*, edited by P. J. Treloar and M. P. Searle, *Geol. Soc. Spec. Publ.*, **74**, 341–355.
- Ludwig, K. R. (2003), Isoplot 3.00 a geochronological toolkit for Microsoft Excel, *Spec. Publ.*, **4**, Berkeley Geochronol. Cent., Berkeley, Calif.
- Macfarlane, A. M. (1993), Chronology of tectonic events in the crystalline core of the Himalaya, Langtang National Park, central Nepal, *Tectonics*, **1004–1025**, doi:10.1029/93TC00916.
- Mahéo, G., P. H. Leloup, F. Valli, R. Lacassin, N. Arnaud, J. L. Paquette, A. Fernandez, L. Haibing, K. A. Farley, and P. Tappognier (2007), Post 4 Ma initiation of normal faulting in southern Tibet: Constraints from the Kung Co half graben, *Earth Pla. Sci. Lett.*, **256**, 233–243, doi:10.1016/j.epsl.2007.01.029.
- Makovska, Y., S. L. Klemperer, L. Y. Huang, and D. Y. Lu (1996), Structural elements of the southern Tethyan Himalaya crust from wide-angle seismic data, *Tectonics*, **15**, 997–1005, doi:10.1029/96TC003.
- Martin, A. J., G. E. Gehrels, and P. G. DeCelles (2007), The tectonic significance of (U, Th)/Pb ages of monazite inclusions in garnet from the Himalaya of central Nepal, *Chem. Geol.*, **244**, 1–24, doi:10.1010/chemgeo.2007.005.003.
- McCaffrey, R., and J. Nabelek (1998), Role of oblique convergence in the active deformation of the Himalayas and southern Tibet Plateau, *Geology*, **26**, 694, doi:10.1130/0091-7613(1998)026<0694:ROOCIT>2.3.CO;2.
- Meier, K., and E. Hiltner (1993), Deformation and metamorphism within the Main Central Thrust zone, Arun tectonic Window, eastern Nepal, in *Himalayan Tectonics*, edited by P. J. Treloar and M. P. Searle, *Geol. Soc. Spec. Publ.*, **74**, 511–522.
- Meigs, A. J., D. W. Burbank, and R. A. Beck (1995), Middle-late Miocene (>10 Ma) Formation of the Main Boundary Thrust in the western Himalaya, *Geology*, **23**, 423–426, doi:10.1130/0091-7613(1995)023<0423:MLMMFO>2.3.CO;2.

- Molnar, P., and J. Stock (2009), Slowing of India's convergence with Eurasia since 20 Ma and its implications for Tibetan mantle dynamics, *Tectonics*, 28, TC3001, doi:10.1029/2008TC002271.
- Molnar, P., and P. Tapponier (1978), Active tectonics of Tibet, *J. Geophys. Res.*, 83, 5361–5373, doi:10.1029/JB083iB11p05361.
- Monsalve, G., A. Sheehan, V. Schulte-Pelkum, S. Rajauria, M. R. Pandey, and F. Wu (2006), Seismicity and one-dimensional velocity structure of the Himalayan collision zone: Earthquakes in the crust and upper mantle, *J. Geophys. Res.*, 111, B10301, doi:10.1029/2005JB004062.
- Murphy, M. A., and T. M. Harrison (1999), Relationship between leucogranites and the Qomolangma detachment in the Rongbuk Valley, south Tibet, *Geology*, 27, 831–834, doi:10.1130/0091-7613(1999)027<0831:RBLATQ>2.3.CO;2.
- Murphy, M. A., A. Yin, P. Kapp, T. M. Harrison, C. E. Manning, F. J. Ryerson, L. Ding, and J. H. Guo (2002), Structural evolution of the Gurka Mandhata detachment system, southwest Tibet: Implications for the eastward extent of the Karakoram fault system, *Geol. Soc. Am. Bull.*, 114, 428–447, doi:10.1130/0016-7606(2002)114<0428:SEOTGM>2.0.CO;2.
- Nelson, K. D., et al. (1996), Partially molten middle crust beneath southern Tibet: Synthesis of project INDEPTH results, *Science*, 274, 1684–1688, doi:10.1126/science.274.5293.1684.
- Pan, Y., and W. S. F. Kidd (1992), Nyainqntangla Shear Zone—A late Miocene extensional detachment in the southern Tibetan Plateau, *Geology*, 20, 775–778, doi:10.1130/0091-7613(1992)020<0775:NSZALM>2.3.CO;2.
- Pandey, M. R., R. P. Tandukar, J. P. Avouac, J. Lave, and J. P. Massot (1995), Interseismic Strain Accumulation on the Himalayan Crustal Ramp (Nepal), *Geophys. Res. Lett.*, 22, 751–754, doi:10.1029/94GL02971.
- Pandey, M. R., R. P. Tandukar, J. P. Avouac, J. Vergne, and T. Heritier (1999), Seismotectonics of the Nepal Himalaya from a local seismic network, *J. Asian Earth Sci.*, 17, 703–712, doi:10.1016/S1367-9120(99)00034-6.
- Patino-Douce, A. E., and J. S. Beard (1996), Effects of $P_f(O_2)$ and Mg/Fe ratio on dehydration melting of model metagreywackes, *J. Petrol.*, 37, 999–1024, doi:10.1093/petrology/37.5.999.
- Patino-Douce, A. E., and N. Harris (1998), Experimental constraints on Himalayan anatexis, *J. Petrol.*, 39, 689–710, doi:10.1093/petrology/39.4.689.
- Powell, R., and J. A. Evans (1983), A new geobarometer for the assemblage biotite-muscovite-chlorite-quartz, *J. Metamorph. Geol.*, 1, 331–336, doi:10.1111/j.1525-1314.1983.tb00278.x.
- Reche, J., and F. J. Martinez (1996), GPT: An Excel spreadsheet for thermobarometric calculations in metapelitic rocks, *Comput. Geosci.*, 22, 775–784, doi:10.1016/0098-3004(96)00007-6.
- Richards, A., T. Argles, N. Harris, R. Parrish, T. Ahmad, F. Darbyshire, and E. Draganits (2005), Himalayan architecture constrained by isotopic tracers from clastic sediments, *Earth Planet. Sci. Lett.*, 236, 773–796, doi:10.1016/j.epsl.2005.05.034.
- Roberts, M. P., and F. Finger (1997), Do U-Pb zircon ages from granulites reflect peak metamorphic conditions?, *Geology*, 25, 319–322, doi:10.1130/0091-7613(1997)025<0319:DUPZAF>2.3.CO;2.
- Robinson, D. M., P. G. DeCelles, P. J. Patchett, and C. N. Garzione (2001), The kinematic evolution of the Nepalese Himalaya interpreted from Nd isotopes, *Earth Planet. Sci. Lett.*, 192, 507–521, doi:10.1016/S0012-821X(01)00451-4.
- Rolfo, F., W. McClelland, and B. Lombardo (2005), Geochronological constraints on the age of the eclogite-facies metamorphism in the eastern Himalaya, in *Geology*, 33, 105–108, doi:10.1130/G26444A.1.
- Royden, L. H., B. C. Burchfiel, R. W. King, E. Wang, Z. L. Chen, F. Shen, and Y. P. Liu (1997), Surface deformation and lower crustal flow in eastern Tibet, *Science*, 276, 788–790, doi:10.1126/science.276.5313.788.
- Rubatto, D., I. S. Williams, and I. S. Buick (2001), Zircon and monazite response to prograde metamorphism in the Reynolds Range, central Australia, *Contrib. Mineral. Petrol.*, 140, 458–468, doi:10.1007/PL00007673.
- Schaltegger, U., C. M. Fanning, D. Gunther, J. C. Maurin, K. Schulmann, and D. Gebauer (1999), Growth, annealing and recrystallization of zircon and preservation of monazite in high-grade metamorphism: Conventional and in-situ U-Pb isotope, cathodoluminescence and microchemical evidence, *Contrib. Mineral. Petrol.*, 134, 186–201, doi:10.1007/s004100050478.
- Schelling, D. (1992), The tectonostratigraphy and structure of the eastern Nepal Himalaya, *Tectonics*, 11, 925–943, doi:10.1029/92TC00213.
- Schelling, D., and K. Arita (1991), Thrust tectonics, crustal shortening, and the structure of the far-eastern Nepal Himalaya, *Tectonics*, 10, 851–862, doi:10.1029/91TC01011.
- Schiotte, L., W. Compston, and D. Bridgwater (1989), Ion probe U-Th-Pb zircon dating of polymetamorphic orthogneisses from northern Labrador, Canada, *Can. J. Earth Sci.*, 26(8), 1533–1556, doi:10.1139/e89-131.
- Schulte-Pelkum, V., G. Monsalve, A. Sheehan, M. R. Pandey, S. Sapkota, R. Bilham, and F. Wu (2005), Imaging the Indian subcontinent beneath the Himalaya, *Nature*, 435, 1222–1225, doi:10.1038/nature03678.
- Searle, M. P. (2007), Geological map of the Mount Everest-Makalu region Nepal-South Tibet Himalaya, scale 1:100 000, Dep. of Earth Sci., Oxford Univ., Oxford, U. K.
- Searle, M. P., S. R. Noble, A. J. Hurford, and D. C. Rex (1999), Age of crustal melting, emplacement and exhumation history of the Shivaling leucogranite, Garhwal Himalaya, *Geol. Mag.*, 136, 513–525, doi:10.1017/S0016756899002885.
- Simpson, R. L., R. R. Parrish, M. P. Searle, and D. J. Waters (2000), Two episodes of monazite crystallization during metamorphism and crustal melting in the Everest region of the Nepalese Himalaya, *Geology*, 28, 403–406, doi:10.1130/0091-7613(2000)28<403:TEOMCD>2.0.CO;2.
- Szulc, A. G., et al. (2006), Tectonic evolution of the Himalaya constrained by detrital ^{40}Ar - ^{39}Ar , Sm-Nd and petrographic data from the Siwalik foreland basin succession, SW Nepal, *Basin Res.*, 18, 375–391, doi:10.1111/j.1365-2117.2006.00307.x.
- Tapponier, P., J. L. Mercier, R. Armijo, T. L. Han, and J. Zhou (1981), Field evidence for active normal faulting in Tibet, *Nature*, 294, 410–414, doi:10.1038/294410a0.
- Tapponier, P., Z. Q. Xu, F. Roger, B. Meyer, N. Arnaud, G. Wittlinger, and J. S. Yang (2001), Geology—Oblique stepwise rise and growth of the Tibet Plateau, *Science*, 294, 1671–1677, doi:10.1126/science.105978.
- Thompson, A. B., and J. A. D. Connolly (1995), Melting of the continental crust: Some thermal and petrological constraints on anatexis in continental collision zones and other tectonic settings, *J. Geophys. Res.*, 100, 15,565–15,579, doi:10.1029/95JB00191.
- Vance, D., and N. Harris (1999), Timing of prograde metamorphism in the Zanskar Himalaya, *Geology*, 27, 395–398, doi:10.1130/0091-7613(1999)027<0395:TOPMIT>2.3.CO;2.
- Vance, D., and E. Mahar (1998), Pressure-temperature paths from P-T pseudosections and zoned garnets: Potential, limitations and examples from the Zanskar Himalaya, NW India, *Contrib. Mineral. Pet.*, 132, 225–245, doi:10.1007/s004100050419.
- Vannay, J. C., Z. D. Sharp, and B. Grasemann (1999), Himalayan inverted metamorphism constrained by oxygen isotope thermometry, *Contrib. Mine Petro.*, 137, 90–101, doi:10.1007/s004100050505.
- Vavra, G., R. Schmid, and D. Gebauer (1999), Internal morphology, habit and U-Th-Pb microanalysis amphibolite-to-granulite facies zircons: Geochronology of the Ivrea Zone (Southern Alps), *Contrib. Mineral. Petro.*, 134, 380–404, doi:10.1017/S004100050492.
- Vielzeuf, D., and J. D. Clemens (1992), The fluid absent melting of phlogopite + quartz: Experiments and models, *Am. Mineral.*, 77, 1206–1222.
- Vielzeuf, D., and J. R. Holloway (1988), Experimental determination of the fluid-absent melting relation in the pelitic system, *Contrib. Mineral. Petro.*, 98, 257–276, doi:10.1007/BF00375178.
- Vielzeuf, D., and J. M. Montel (1994), Partial melting of metagreywackes. Part I. Fluid-absent experiments and phase relationships, *Contrib. Mine Petro.*, 117, 375–393, doi:10.1007/BF0030727.
- Viskupic, K., and K. V. Hodges (2001), Monazite xenotime thermochronometry: Methodology and an example from the Nepalese Himalaya, *Contrib. Mineral. Petro.*, 141, 233–247.
- Visonà, D., and B. Lombardo (2002), Two-mica tourmaline leucogranites from the Everest-Makalu region (Nepal-Tibet). Himalayan leucogranite genesis by isobaric heating?, *Lithos*, 62, 125–131, doi:10.1016/S0024-4937(02)00112-3.
- Wager, L. R. (1937), The Arun River drainage pattern and the rise of the Himalaya, *Geol. J.*, 89, 239–242.
- Walker, J. D., M. W. Martin, S. A. Bowring, M. P. Searle, D. J. Waters, and K. V. Hodges (1999), Metamorphism, melting, and extension: Age constraints from the High Himalayan Slab of southeast Zanskar and northwest Lahaul, *J. Geol.*, 107, 449–495, doi:10.1086/314360.
- Webb, A. A. G., A. Yin, T. M. Harrison, J. Celerier, and W. P. Burgess (2007), The leading edge of the Greater Himalayan Crystalline complex revealed in the NW Indian Himalaya: Implications for the evolution of the Himalayan orogen, *Geology*, 955–958, doi:10.1130/G23931A.1.
- Yin, A. (2000), Mode of Cenozoic east-west extension in Tibet suggesting a common origin of rifts in Asia during the Indo-Asian collision, *J. Geophys. R*, 105, 21,745–21,759, doi:10.1029/2000JB90016.
- Zhang, J. J., and L. Guo (2007), Structure and geochemistry of the southern Xainza-Dinggye rift and relationship to the South Tibetan Detachment System, *J. Asian Earth Sci.*, 29, 722–727, doi:10.1016/j.jseas.2006.05.003.
- N. Arnaud, Géosciences Montpellier, Université de Montpellier 2, Cc.060, Pl. E. Bataillon, F-34092 Montpellier CEDEX 05, France.
- E. Boutonnet, P. H. Leloup, and G. Mahéo, LST, UMR 5570, Université de Lyon, ENS Lyon, UCB Lyon1, CNRS, bat Géode, 43 Bd du 11 Novembre 1918, F-69622 Villeurbanne CEDEX, France. (herve.leloup@univ-lyon1.fr)
- E. Kali and J. Van der Woerd, Institut de Physique du Globe de Strasbourg, UMR 7516, CNRS, UDS/EOST, 5 rue René Descartes, F-67084 Strasbourg, France.
- J. Liu-Zeng and X. Liu, Institute of Tibetan Plateau Research, Chinese Academy of Sciences, 18 Shuang Qing Rd, Beijing 100085, China.
- H. Li and D. Liu, Laboratory of Continental Dynamics, Institute of Geology, CAGS, 26 Baiwanzhuang Rd, Beijing 100037, China.

2.2.2. Les résultats d' $^{40}\text{Ar}/^{39}\text{Ar}$ sur feldspaths issus de la zone de cisaillement de Kharta

2.2.2.1. Introduction

Dans cette partie, un complément aux datations $^{40}\text{Ar}/^{39}\text{Ar}$ sur micas au niveau des deux zones de cisaillement de Kharta et de Dinggye est apporté (suite de la partie 4.2.2.2 de l'article à Tectonics) et la discussion sur l'exhumation finale du horst de l'Ama Drime abordé dans le paragraphe 5.3.4-Tectonics est poursuivie.

Nous commençons ici par un rappel de la discussion sur l'exhumation postérieure à 12 Ma afin de mettre en valeur l'enjeu de la datation $^{40}\text{Ar}/^{39}\text{Ar}$ des feldspaths à l'Ama Drime. Puis après avoir exposé brièvement le contexte géologique des échantillons (en complément de la partie 3.2.3. de l'article à Tectonics), les résultats de datation $^{40}\text{Ar}/^{39}\text{Ar}$ sur feldspath combinés aux résultats sur mica et interprétations seront présentés.

La quantification des conditions pression-température combinée avec les datations a permis de déterminer deux scénari possibles pour expliquer l'exhumation du horst de l'Ama Drime après l'arrêt du mouvement sur le STDS, c'est-à-dire après ~12 Ma (Partie 5.3.4.-Tectonics, Article EPSL Annexe A) :

1/ Depuis ~12 Ma (âge U/Pb de granites non déformés), une unique phase de déformation en extension a permis une exhumation de 15 km au niveau des deux zones de cisaillement et des deux failles normales conjuguées. Ceci indique une vitesse d'exhumation verticale apparente de 1.2 mm/an depuis ~12 Ma. D'autre part, les âges (U-Th)/He indiquent que 4 km ont été exhumés depuis 4 Ma. Les vitesses sont donc ici de ~1 mm/an, suggérant ainsi une vitesse de ~1.4 mm/an entre 12 et 4 Ma.

2/ Deux phases de déformation ont eu lieu depuis ~12 Ma. D'après les datations $^{40}\text{Ar}/^{39}\text{Ar}$ des biotites sur chaque faille, un mouvement différent est distingué (Figure 11-Tectonics). Pour la zone de cisaillement de Kharta, une vitesse d'exhumation lente prédomine entre ~10 et ~6 Ma, alors que pour la zone de cisaillement de Dinggye, une exhumation plus rapide entre 12 et 9 Ma avec une vitesse verticale de ~4 mm/an est mise en valeur (pour 11 à 13 km exhumés). Les données (U-Th)/He

réparties sur l'ensemble du massif peuvent être considérées dans ce cas comme une deuxième phase de déformation à partir de ~4Ma, après le mouvement plus lent entre 10-9 et 6 Ma.

La datation $^{40}\text{Ar}/^{39}\text{Ar}$ sur feldspath est un moyen pertinent pour tenter de faire le lien entre la datation des températures vers 300°C ($^{40}\text{Ar}/^{39}\text{Ar}$ sur mica) et la datation des basses températures vers 75°C ((U-Th)/He sur apatite). Ainsi un « signal thermochronologique » permettant de distinguer ou non ces deux phases d'exhumation pourrait être obtenu.

2.2.2.2. Les échantillons

Cinq échantillons du flanc Ouest du massif ont été datés grâce aux micas et aux feldspaths : T7A10, T7A14, T7A33 et T7A20 au niveau de la faille de Kharta et T7A48 au nord, au niveau de la faille de Sangkar (Figure II.20).

T7A10 et T7A14 viennent tous deux de la gorge creusée par l'Arun autour du sommet de Yo Ri (Figure II.11a). Ce sont des orthogneiss à gros feldspaths oeillés, présentant de remarquables structures C-S (Figure II.11b, c, d). T7A33, issu de la vallée de Tanghyu, est un orthogneiss fin à petits feldspaths et muscovites (Figure II.12b). T7A19 et T7A20, les plus au Sud au début des gorges de l'Arun, sont des orthogneiss mylonitiques et orthogneiss respectivement (Figure II.12a, c). T7A20 contient deux générations de muscovites, d'importants porphyroclastes et de plus petits minéraux alignés dans la foliation et le cisaillement (Figure II.12d). Enfin T7A48, au nord, est issu de quartzites cataclastiques à muscovites. Ces muscovites montrent clairement deux générations : des porphyroclastes parallèles à la foliation et des petites muscovites altérées (Figure II.13) qui, avec la biotite chloritisée, remplissent des fractures verticales tardives (voir partie sur T7A48 paragraphe 4.2.2.2-Tectonics).

Concernant la zone de cisaillement de Dinggye (Figure II.20), les feldspaths des échantillons T5D33, T5D39 et T5D6 ont aussi été mesurés. En raison du résultat complexe obtenu (et d'un problème analytique sur T5D33), nous allons ici présenter uniquement le spectre d'âge de T5D6 et seulement mentionner les résultats des deux autres échantillons.

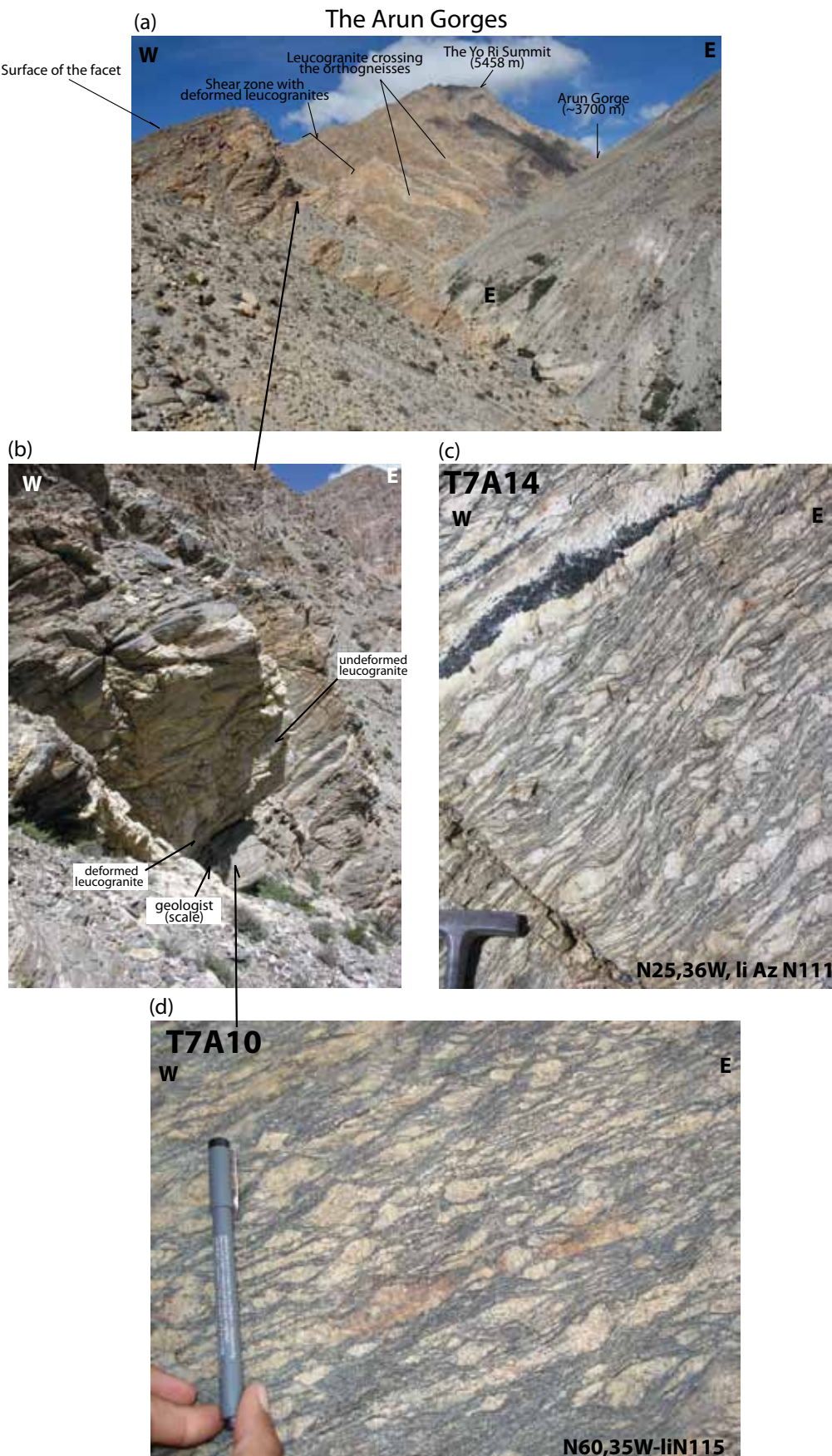


Figure II.11: (a) View of the footwall of the Kharta fault exposing the ductile shear zone, crossed by deformed and undeformed leucogranites and incised by the Arun gorges (see also the title picture, p. 35-36). (b) Close up view of the sampled shear zone. (c) & (d) Ama Drime orthogneiss of the Kharta shear zone showing top-to-the-west (normal) shear sense (T7A14 and T7A10 samples, respectively).



Figure II.12: (a) Mylonitic orthogneiss (T7A19 sample), (b) Fine grained orthogneiss (T7A33 sample), (c) Rough orthogneiss (T7A20 sample), (d) T7A20 thin section picture microphoto showing two generations of muscovites.

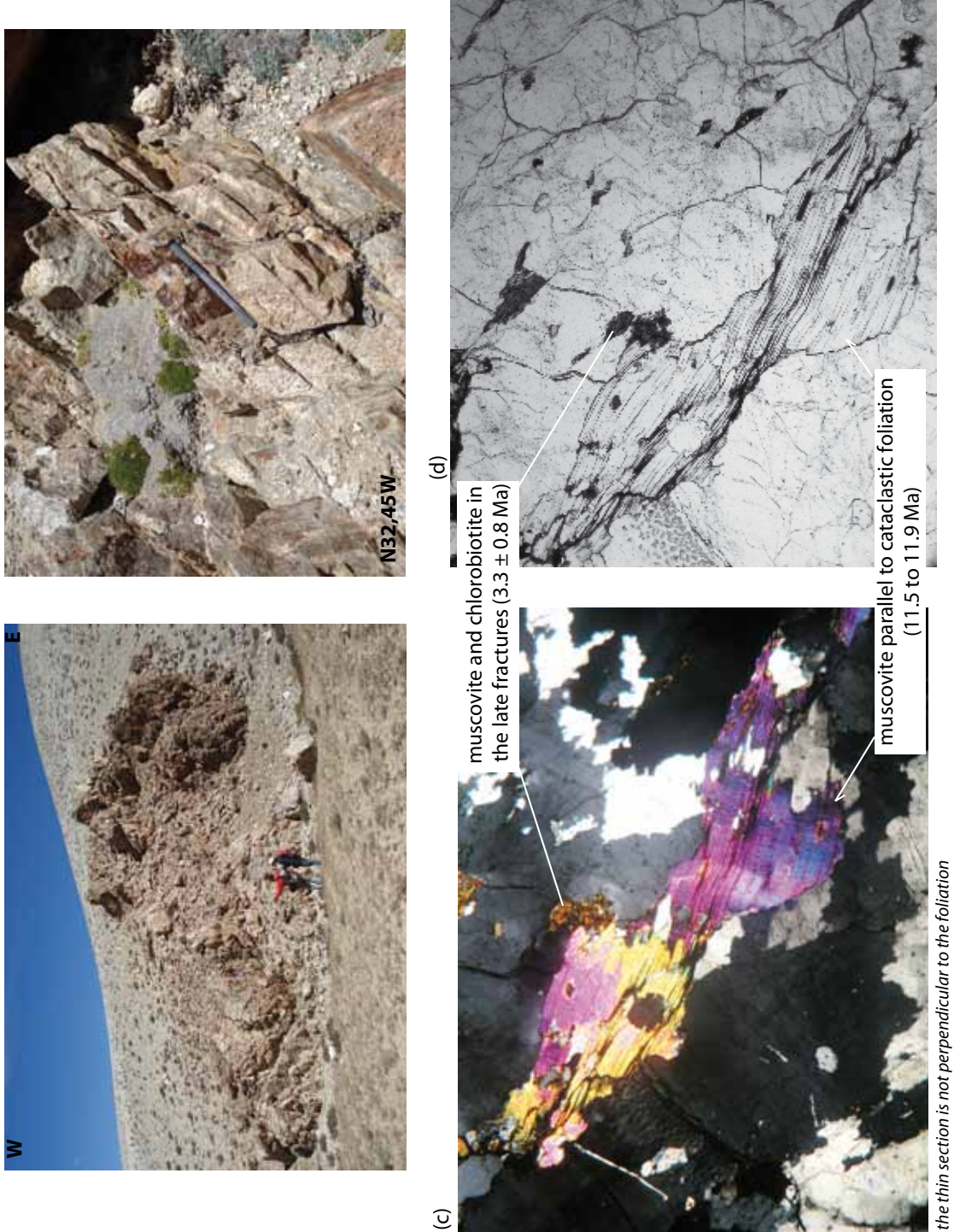


Figure II.13: Pictures of the T7A48 sample. (a) Cataclasites of the Sankar Ri fault that emerge from quaternary sediments, (b) close up of the sampled zone, (c) T7A487 thin section picture microphoto showing two generations of muscovites (crossed polars), (d) idem (plane-polarized)

2.2.2.3. Les résultats $^{40}\text{Ar}/^{39}\text{Ar}$ et les interprétations

Les spectres d'âges

Les spectres d'âges des micas présentés Figure 8-Tectonics et Annexe B (Figure S2-DR9-et Tables DR5-2 et DR5-3-Tectonics) sont superposés dans cette partie aux spectres d'âges des feldspaths (Figures II.9 à II.14). Toutes les données $d^{40}\text{Ar}/^{39}\text{Ar}$ sur les feldspaths sont listées dans la Table II.2.

Les spectres de tous les échantillons de la zone de cisaillement de Kharta et celui de l'échantillon T5D6 issu de la zone de cisaillement de Dinggye montrent la même tendance : les âges entre 40 et 100 % $d^{39}\text{Ar}$ cumulatif sont très vieux, entre 200 et 60 Ma (Figure II.14, Table II.2), comparés aux âges correspondant à 20-40 % $d^{39}\text{Ar}$, allant jusque 5 Ma. Les âges vieux sont également nettement supérieurs aux âges associés aux trajets P-T-t-d déterminés pour l'Ama Drime, le pic de pression étant associé à l'âge de 33 Ma (Figure 5b et d-Tectonics). Malheureusement, le début des spectres est affecté par d'importants excès d'argon. On distingue deux types d'excès : un excès important entre 0 et 20 % $d^{39}\text{Ar}$ cumulatif et entre 20 et 30 % $d^{39}\text{Ar}$ où le spectre est plutôt aplati. Cet excès est davantage mis en évidence pour les spectres des échantillons de la faille Kharta que pour l'échantillon T5D6 de Dinggye en raison du protocole de chauffage différent. Il est courant pour les feldspaths de doubler les paliers de chauffage de basses températures (entre 450 et 800°C), il en résulte un spectre d'âge en dents de scie où le second des deux paliers est systématiquement plus jeune que le premier (voir table II.1). Ce palier plus jeune, étant moins affecté par l'excès d'argon, sera donc pris en compte pour déterminer l'âge du feldspath (Harrison et al., 1994). Avant 20 % $d^{39}\text{Ar}$ cumulatif, l'excès est tel que cette partie du spectre n'est pas du tout prise en compte pour la détermination des âges de basses températures de chauffage du four. Pour les interprétations, nous allons donc utiliser les âges les plus jeunes des spectres qui seront considérés comme des âges maximaux, pouvant toujours contenir de l'excès d'argon.

Après ce « nettoyage de spectre », une deuxième tendance ressort : pour les échantillons de Kharta, les âges les plus jeunes des spectres de feldspaths correspondent aux âges des biotites et des muscovites, ils sont généralement légèrement plus jeunes (Figures II.14 à II.19). Pour l'échantillon T5D6 la biotite est nettement plus jeune (~10 Ma, Figure 8-Tectonics) que le palier le plus bas du spectre des feldspaths (situé vers 20 Ma, Figure II.14), cela suggère que l'excès dans les feldspaths est plus important ici et que le protocole de chauffage de T5D6 n'est pas constitué par suffisamment de paliers pour quantifier cet excès (Table II.1).

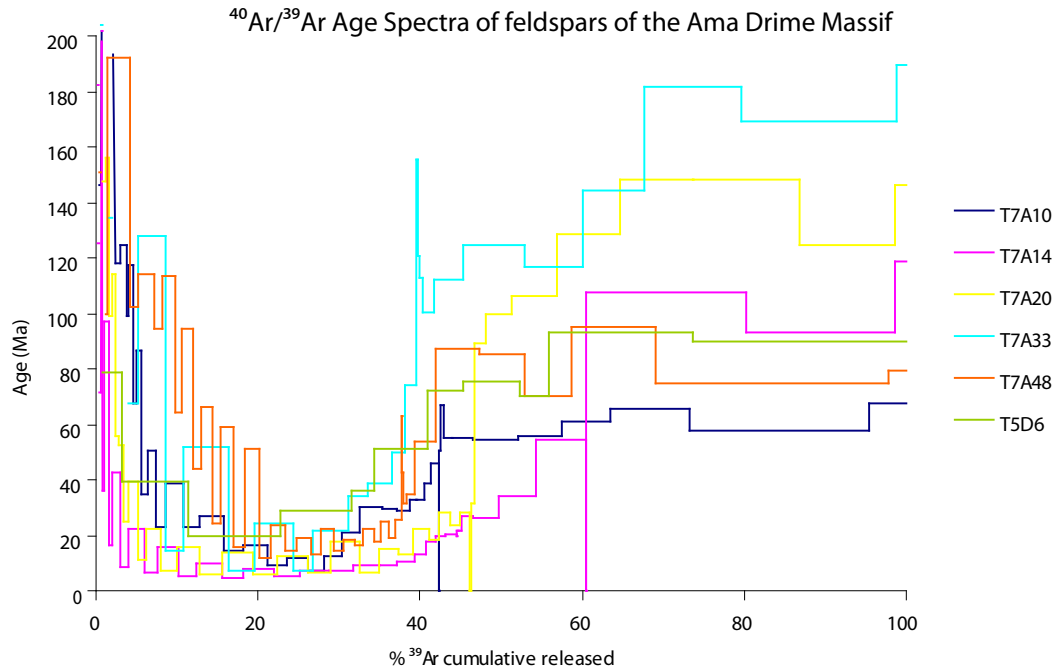


Figure II.14: K-feldspar $^{40}\text{Ar}/^{39}\text{Ar}$ age spectra samples from the Kharta and Dinggye shear zones

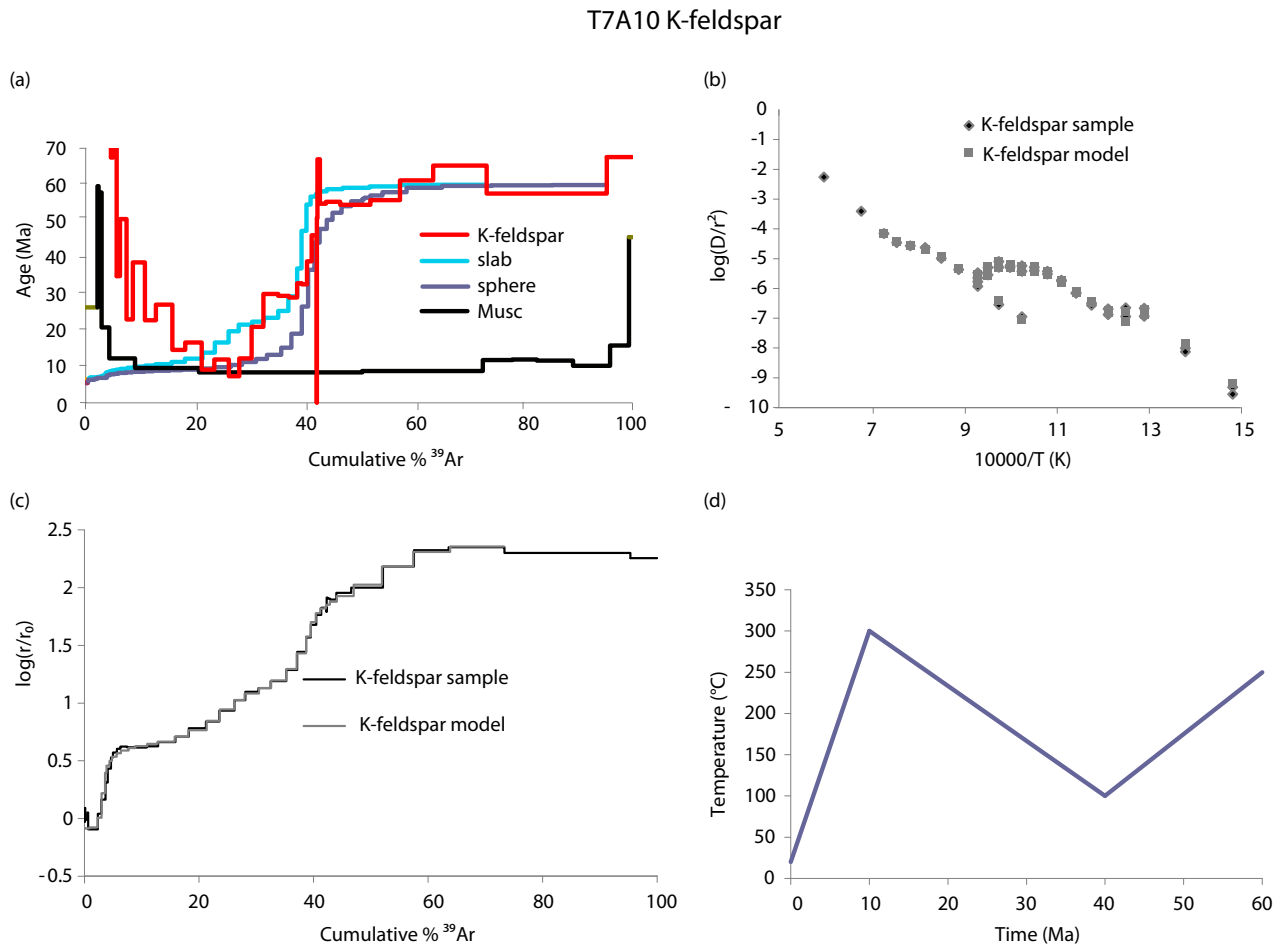


Figure II.15: $^{40}\text{Ar}/^{39}\text{Ar}$ results for K-feldspars of T7A10. (a) Red and black curves correspond to the measured age spectra of K-feldspars and muscovites, respectively. Blue and purple curves represent synthetic age spectra calculated with the thermal history represented in (d) for a slab or sphere diffusion geometry of K-feldspars, respectively. (b) Modeled and measured Arrhenius plot. (c) Modeled and measured $\log(r/r_0)$ plot, (d) Thermal history. All data are listed in table II.2.

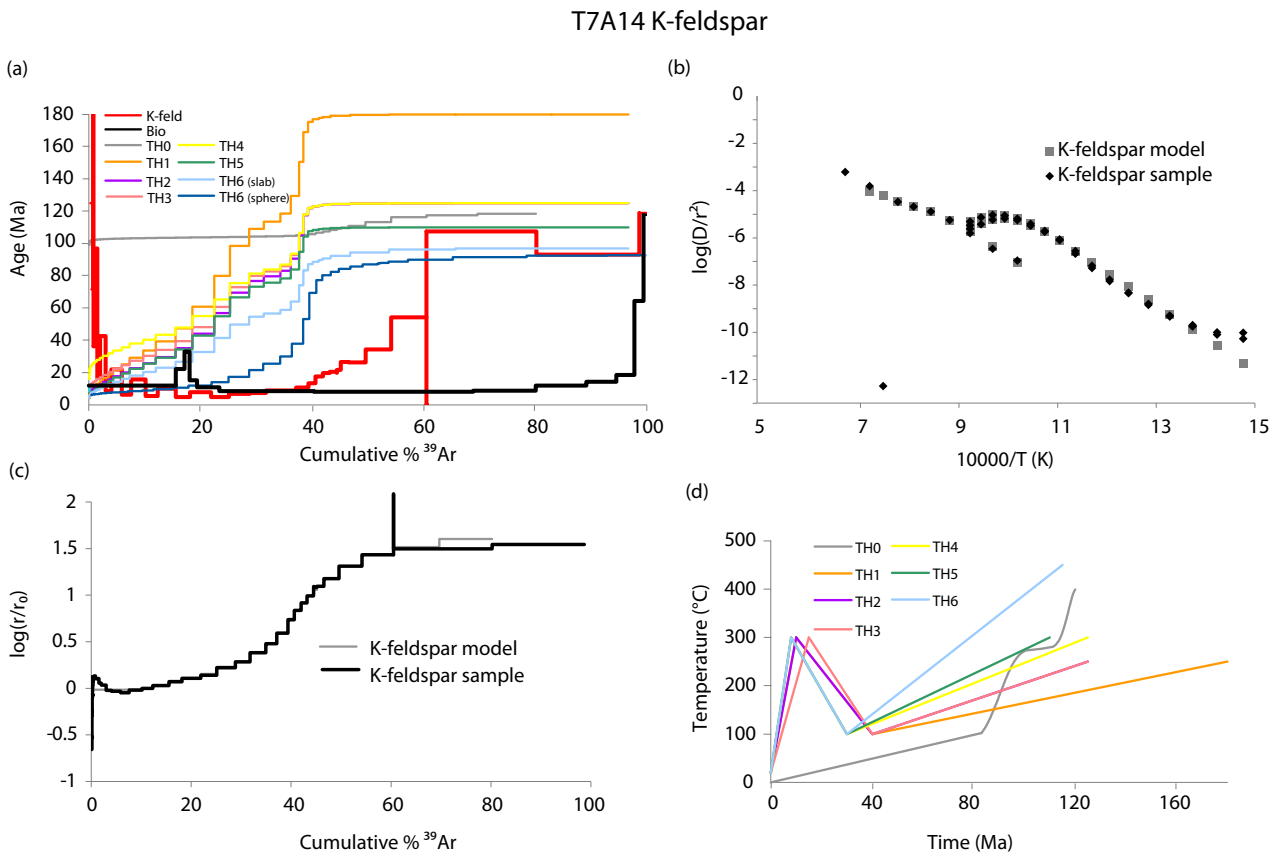


Figure II.16: $^{40}\text{Ar}/^{39}\text{Ar}$ results for K-feldspars of T7A14, (a) Red and black curves correspond to the measured age spectra of K-feldspars and biotites, respectively. Other colored curves represent synthetic age spectra calculated with the thermal histories represented in (d) for a slab diffusion geometry of K-feldspars. (b) Modeled and measured Arrhenius plot. (c) Modeled and measured $\log(r/r_0)$ plot, (d) Thermal histories (TH). All data are listed in table II.2.

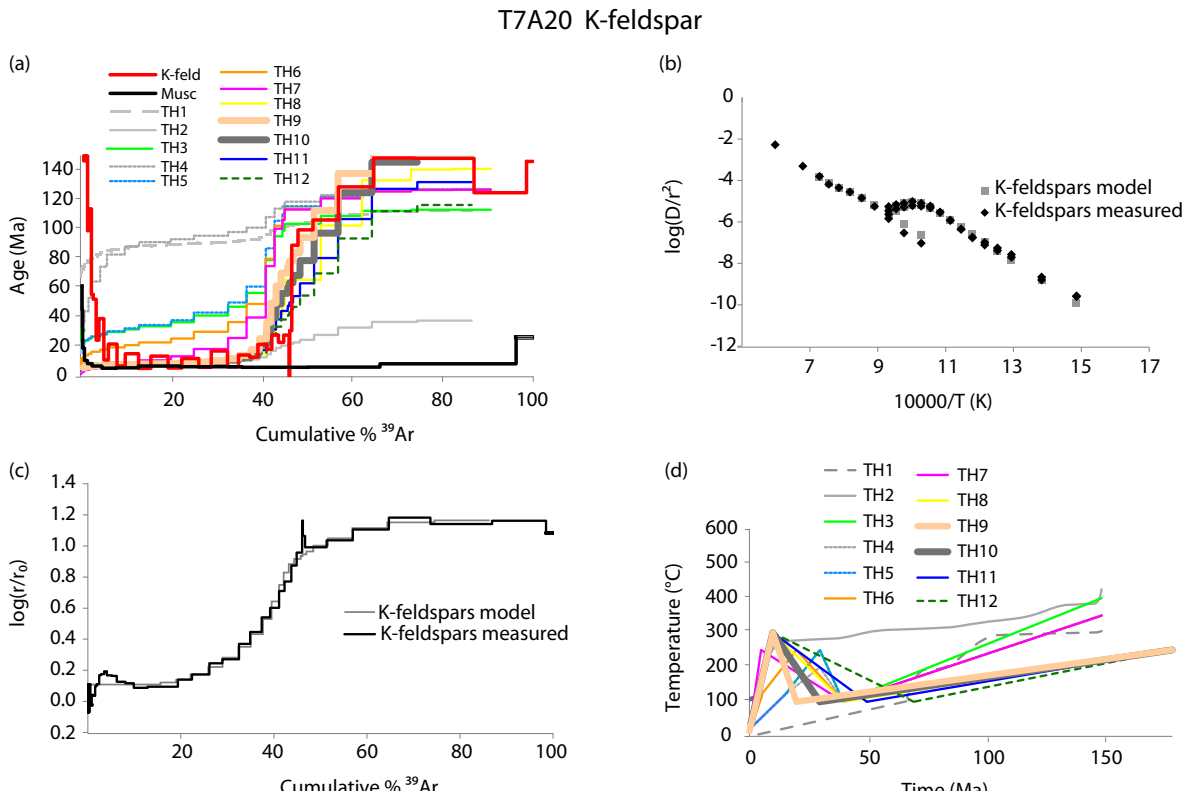


Figure II.17: $^{40}\text{Ar}/^{39}\text{Ar}$ results for K-feldspars of T7A20. (a) Red and black curves correspond to the measured age spectra of K-feldspars and muscovites respectively. Other colored curves represent synthetic age spectra calculated with the thermal histories represented in (d), for a slab diffusion geometry of K-feldspars. (b) Modeled and measured Arrhenius plot, (c) Modeled and measured $\log(r/r_0)$ plot, (d) Thermal histories (TH). All data are listed in table II.2.

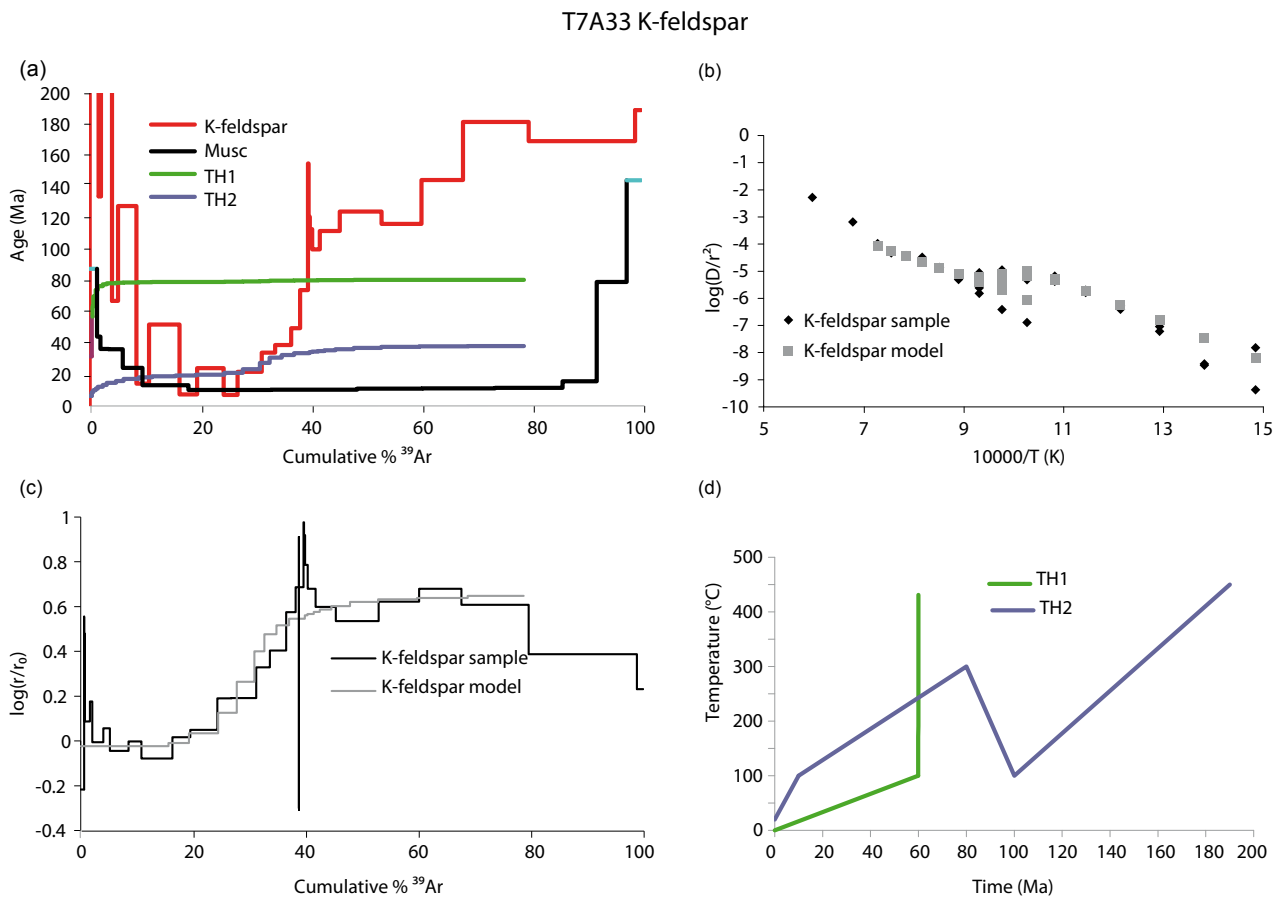


Figure II.18: $^{40}\text{Ar}/^{39}\text{Ar}$ results for K-feldspars of T7A33, (a) Red and black curves correspond to the measured age spectra of K-feldspars and muscovites respectively. Other colored curves represent synthetic age spectra calculated for the thermal histories (TH) represented in (d). (b) Modeled and measured Arrhenius plot. (c) Modeled and measured $\log(r/r_0)$ plot, (d) Thermal histories (TH). All data are listed in table II.2.

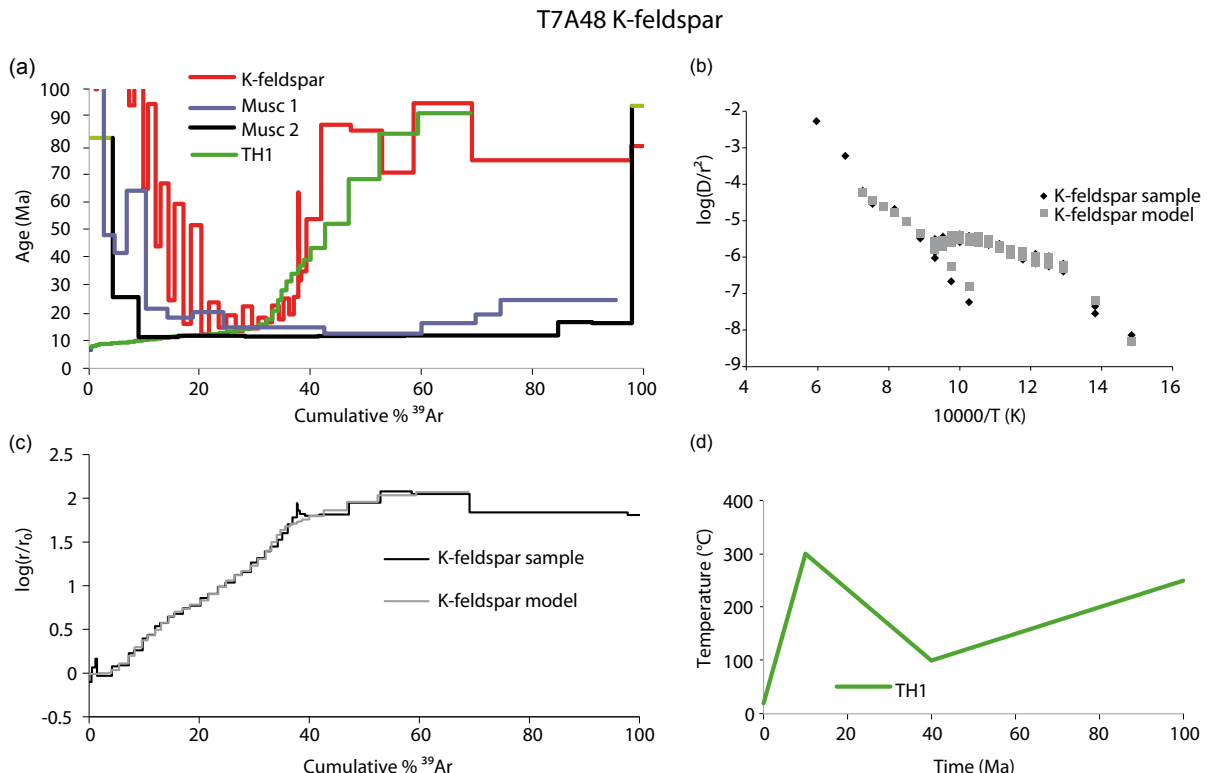


Figure II.19: $^{40}\text{Ar}/^{39}\text{Ar}$ results for K-feldspars of T7A48, (a) Red, black and blue curves correspond to the measured age spectra of K-feldspars and two generation of muscovites respectively. The green curve is the synthetic age spectra calculated for the thermal history (TH) represented in (d). (b) Modeled and measured Arrhenius plot. (c) Modeled and measured $\log(r/r_0)$ plot, (d) Thermal histories (TH). All data are listed in table II.2.

Pour T7A10, le palier le plus jeune du spectre d'âge des feldspaths est à 7.34 ± 0.23 Ma, l'âge plateau de la biotite correspondante est à 8.5 ± 0.2 Ma (Figure II.15, Table II.2). De même, pour T7A14, les feldspaths donnent 4.84 ± 0.08 Ma et les biotites 6.2 ± 0.8 (Figure II.16). Pour T7A20, les feldspaths sont à 5.65 ± 0.06 Ma et les deux générations de muscovites entre 6 et 6.7 Ma et à 3.4 ± 0.6 Ma (Figure II.17). Pour T7A33, les feldspaths sont à 7.07 ± 0.21 Ma et les muscovites correspondantes entre 9.2 et 11.1 et 6.7 Ma (Figure II.18) et pour T7A48 l'âge plus jeune des feldspaths est à 12.10 ± 0.37 et les deux générations de muscovites sont entre 11.5 et 12.4 et à 3.3 ± 0.8 Ma (Figure II.19).

Généralement la température de fermeture des feldspaths qui correspond aux paliers de basse température de chauffage du four, est une température de fermeture entre 150 et 200°C. Or ici, les âges de feldspaths sont très proches des âges de micas. Cela signifierait peut-être que ces âges correspondent à des températures de fermeture plutôt peu élevées pour des paliers de basse température de four ou que le refroidissement a été très rapide entre la fermeture des micas et celle des domaines de basse température des feldspaths.

La partie des spectres située après 40 % d' ^{39}Ar cumulatif montre une progression vers des âges du Mésozoïque. Ceci est une tendance remarquable des deux côtés du massif, car T5D6, situé côté Est du massif, montre également cet écart d'âge (Figure II.14). Les analyses des feldspaths sur T5D33 et T5D39 (côté Est) montrent aussi cette caractéristique avec des âges entre 30 et 180 Ma. Ces feldspaths ont donc conservé un héritage significatif. Cela signifierait que ces échantillons n'ont pas subit des températures supérieures à la température de fermeture des feldspaths (soit 450°C maximum). Les rapports K/Ca semblent être corrélés avec les variations d'âges (Annexe D) et pourraient montrer que ces deux groupes d'âges correspondraient à des phases différentes.

Utilisation du MDD model

Au vu de ces observations, ces feldspaths semblent signaler des propriétés de rétention forte. Afin de mieux connaître les propriétés de diffusion de ces feldspaths la routine « autoarr » du *MDD model* a été utilisée pour déterminer les paramètres d'Arrhenius et les routines « autoage-mon » et « agesme » ont été utilisées pour tester les histoires thermiques pouvant correspondre à ces spectres.

Les valeurs des graphiques d'Arrhénius et $\log(r/r_0)$ construits à partir des données d'échantillons s'ajustent bien avec les valeurs obtenues avec le *MDD model*. Ceci est le cas pour tous les échantillons, sauf pour le T7A33 pour lequel l'ajustement est mauvais (Figure II.18c). Les énergies d'activations calculées à partir de ces valeurs sont en moyenne de 51.1 kcal/mol, et si la valeur pour T7A33, qui semble moins bien définie, est exclue, l'énergie d'activation moyenne est de 55.7 kcal/mol (Table II.2). Cette valeur est bien plus élevée que la valeur moyenne de 46 ± 6 kcal/mol fournie par Lovera al., 1997 pour une population de 115 feldspaths issus de différents contextes géologiques. Cette énergie d'activation élevée semble confirmer les observations précédentes suggérant que ces feldspaths sont particulièrement rétentifs.

L'inversion des données d'âges en considérant un refroidissement constant a d'abord été testée avec la routine « autoage-mon » (« mon » pour *monotonic cooling*). Comme le montrent les courbes TH1 et TH2, Figure II.17a et d, pour l'échantillon T7A20, ce test ne fut pas concluant : avec un refroidissement simple, les deux écarts d'âges du spectre ne sont pas résolus. On remarque qu'il est très difficile de concilier les spectres d'âges avec une très large variation d'âges et une rétention de l'argon supérieure à la moyenne des feldspaths de socle comme le montre la forte énergie d'activation. Pour contraindre un rajeunissement fort du début du spectre, même un refroidissement presque stoppé à moyenne/haute température n'est pas suffisant.

Ensuite, la routine « agesme » a été utilisée en entrant une à une des histoires thermiques impliquant un réchauffement, qui pourrait permettre une diffusion accélérée de l'argon dans un période tertiaire. Différents âges pour le début et la fin du réchauffement ont été testés, ainsi que différentes températures pour la fin du réchauffement (Figure II.17d). Dans un premier temps, différentes histoires thermiques ont été testées sur les échantillons T7A20 et T7A14. Ensuite l'histoire thermique correspondant le mieux à ces deux échantillons a été appliquée aux autres échantillons. Pour l'échantillon T7A20, les histoires thermiques qui correspondent le mieux au spectre sont TH9 et TH10, pour lesquelles le réchauffement commence à 20 ou 30 Ma et à 100°C et atteint 300°C à 10 Ma (Figure II.17a et d). Pour T7A14, l'ajustement entre le modèle et le spectre est plus difficile à obtenir (Figure II.16a). L'histoire thermique qui fournit les spectres synthétiques qui correspondent le mieux à tous nos échantillons montre un réchauffement commençant à 100°C et à 40 Ma et finissant à 10 Ma (Figures II.15d à II.19d). Pour T7A10 et T7A48, cette histoire thermique correspond assez bien aux données (Figures II.15 et II.19). Pour T7A33 (Figure II.18), aucune histoire thermique n'a pu être déterminée pour

expliquer le spectre d'âge. La valeur de l'énergie d'activation de 33.1 déterminée par le *MDD model* (Table II.2) suggère qu'aucune des histoires thermiques testées ne s'ajuste à ce spectre.

Pour quatre échantillons sur les cinq traités ici, une histoire thermique avec un réchauffement débutant entre 20 et 40 Ma à 100°C et se terminant à 10 Ma et à 300°C (et pouvant aller jusqu'à 450°C) à 10 Ma semble expliquer les spectres d'âges des feldspaths de l'Ama Drime.

2.2.2.4. Discussion

Bien qu'une histoire thermique montrant un réchauffement permette une modélisation satisfaisante des spectres, il convient de savoir maintenant si cette histoire thermique a une réelle signification géologique. Plusieurs tests permettent de vérifier cette histoire thermique:

- L'existence d'un évènement thermique avec un pic de température à 10 Ma : les âges U/Pb sur zircon et monazite de leucogranites déformés et non déformés dans les zones de cisaillement de Kharta et Dinggye montrent qu'un évènement magmatique important a lieu entre 9 et 14 Ma (Figure 9-Tectonics) (Liu et al., 2007, Rolfo et al., 2005, Cottle et al., 2009, cette étude). Cette observation est donc en accord avec les histoires thermiques deduites par le *MDD model*.
- La datation d'autres minéraux dans les mêmes échantillons: nous avons vu précédemment que les âges de muscovites et biotites sont semblables voire même légèrement inférieurs aux âges des paliers de basses températures des feldspaths (entre 20 et 30 % d' ^{39}Ar). Cet écart d'âge réduit entre les feldspaths et les micas peut être expliqué soit par des excès d'argon non quantifiés qui augmentent les âges des feldspaths, ou soit un refroidissement très rapide après 12 Ma, qui aurait pour conséquence la fermeture quasi-simultanée des différents systèmes thermochronologiques. Ces données montrent que les âges de basses-températures des feldspaths sont cohérents avec les âges des micas, et l'hypothèse du refroidissement rapide est en accord avec la fin de l'histoire thermique déduite du *MDD model*.

- La comparaison avec les chemins pression-température-temps reconstitués pour des paragneiss et des métabasites du massif de l'Ama Drime, présentés dans l'article publié dans Tectonics (Figures 5 et 6d), montre qu'entre 20 et 40 Ma, les températures étaient largement supérieures à 700°C au niveau de ces roches. Les histoires thermiques (ou trajet T-t) du *MDD model*, reconstituées pour des orthogneiss à proximité des échantillons pour lesquels des trajets P-T-t ont été reconstitués (Figure II.20), montrent des températures inférieures à 450°C depuis des âges Mésozoïque. L'histoire thermique déterminée à partir des feldspaths avec le *MDD model* n'est donc pas en accord avec les chemins P-T-t de l'Ama Drime. Plusieurs hypothèses peuvent être fournies pour expliquer cette incohérence:

- 1/ Les différences de composition des roches comparées
- 2/ Les différentes positions structurales des roches comparées;

En effet, les trajets P-T-t montrant les conditions de métamorphisme de plus haut grade (1.4 à 2 GPa et 700 à 800°C, Figure 5b-Tectonics), sont issus d'échantillons prélevés plus au cœur du massif que les échantillons utilisés pour les analyses argon (Figure II.20). Les roches situées près ou dans la zone de cisaillement correspondent à des positions structurales moins profondes et donc présentent des conditions de métamorphisme moins élevées que les roches du cœur du massif. Ceci pourrait expliquer que des températures inférieures soient enregistrées par les feldspaths des orthogneiss échantillonnés tandis que des températures plus élevées sont enregistrées par les assemblages minéralogiques des échantillons au cœur du massif.

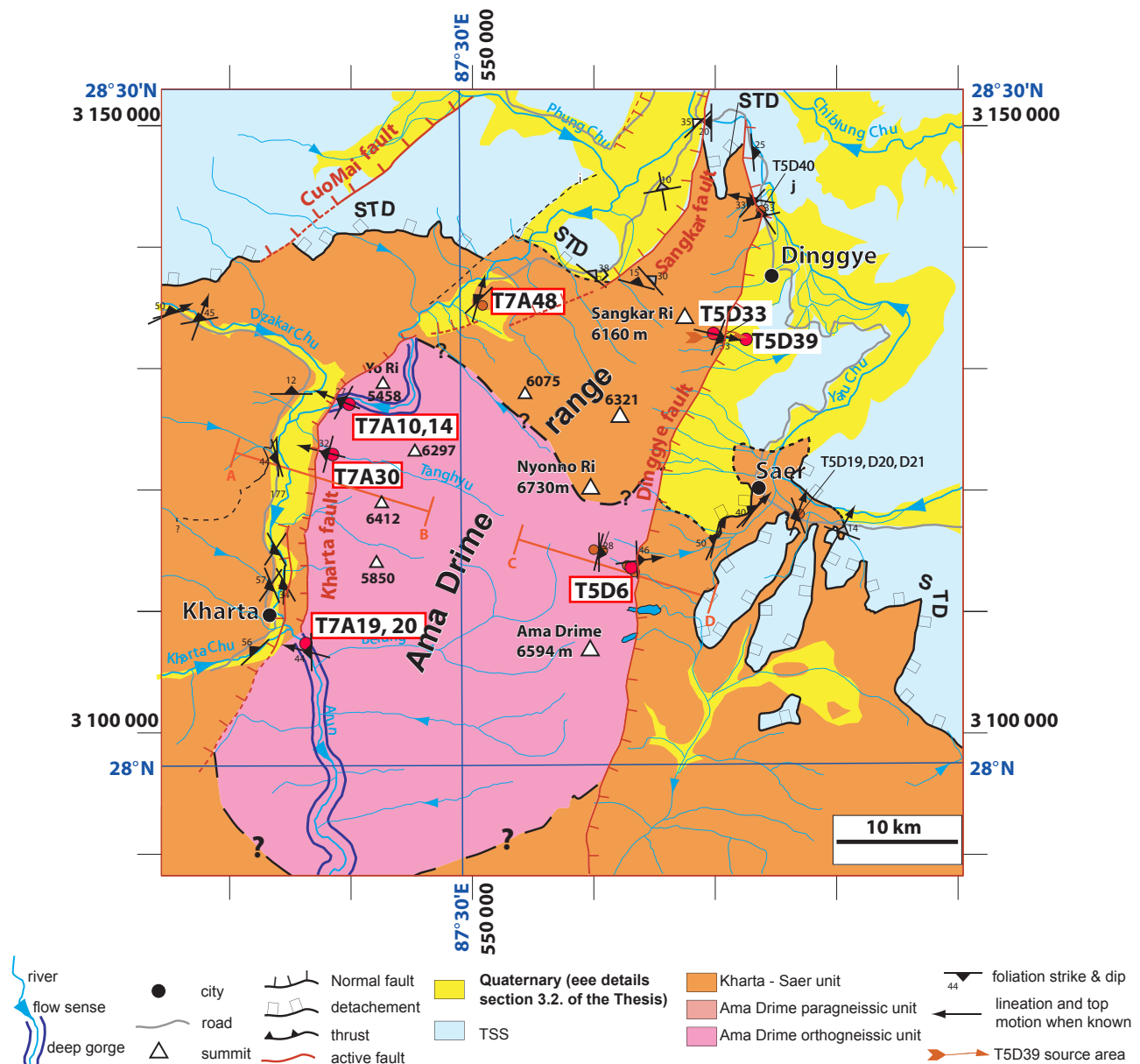


Figure II.20: Structural map of the Dinggye-Kharta area. Samples used in this part are shown in white boxes. Traces of sections A-B and C-D of Figure 2b of the Tectonics paper (2.2.1 part of the thesis) are located.

- 3/ La structure des feldspaths

Ce réchauffement mis en évidence par le *MDD model* peut être un artefact dû uniquement à la structure des feldspaths. L'application du *MDD model* implique l'hypothèse que le spectre d'âge est l'image d'un profil de diffusion complexe dans un grain considéré comme formé de sous-domaines mais homogène du point de vue cristallographique. Si une recristallisation partielle des feldspaths a lieu à un temps donné en raison d'un événement magmatique ou métamorphique, nous nous trouvons en présence de deux cristaux différents lors de l'analyse. La distribution apparente des

âges peut alors être le simple produit d'une différence d'âges entre les deux cristaux, ou le résultat de processus plus complexes devant tenir compte de caractéristiques potentiellement différentes de chaque partie du grain mixte en terme de rétention de l'argon. Ainsi il est possible d'avoir dans un même échantillon des feldspaths qui préserveraient des âges anciens en conservant partiellement la mémoire du protolith (la forte rétention apparente du feldspath expliquerait la rémanence des âges mésozoïque au minimum) même à des températures élevées et des feldspaths d'âge plus jeune qui auraient recristallisé au moment de l'événement magmatique ou métamorphique. Dans ce cas, les âges jeunes des feldspaths seraient des âges de recristallisation. La préservation d'une mémoire héritée au sein des feldspaths n'est pas qu'une question de température, mais également une question de solubilité de l'argon dans le milieu intergranulaire. Ainsi certains exemples montrent que les minéraux peuvent conserver leur mémoire même après des phases métamorphiques intenses, car le milieu intergranulaire, saturé d'argon pendant le métamorphisme, n'a pas permis la diffusion de l'argon hors des grains. C'est le cas par exemple des minéraux de haute pression dans les Alpes (Arnaud et Kelley, 1995). Un modèle de diffusion simple dans un grain homogène, comme le *MDD model*, n'explique donc pas la distribution des âges observés dans les feldspaths.

Cependant, nos observations en lame mince ne semblent pas montrer une structure complexe des feldspaths potassiques. D'autre part, Langille et al., 2010, ont mené une étude pétrologique et structurale sur des échantillons d'orthogneiss prélevés à proximité de nos échantillons pour en déduire des températures de déformation (voir leur localisation à la Figure III.12). L'angle d'ouverture de l'axe [c] du quartz d'échantillons au bord de la faille de Kharta permet de déterminer des température de déformation dans les quartz et par déduction dans les feldspaths à 50°C près. Ils ont montré que des températures entre 400 et 650°C ont été subies dans la zone de cisaillement de Kharta (qu'ils appellent l'*Ama Drime Detachment*). Leurs analyses pétrographiques et chimiques montrent que les feldspaths présentent une structure complexe avec des porphyroclastes de feldspath potassique en partie remplacés par des myrmékites (pauvres en potassium et riches en sodium). Ils indiquent aussi qu'ils se déforment essentiellement par *brittle fracturing* et en moindre importance par *bulging recrystallization at grain boundaries*, cela indiquant des températures de déformation dans les feldspaths entre 400 et 650°C (d'après Tullins et Yund 1991). La thermométrie avec basée sur la myrmékitisation du feldspath potassique fournit également des températures de 400-650°C également (Simpson et Wintsch, 1989).

Cette étude de Langille et al., 2010 montre que les températures de déformation enregistrées par les quartz et feldspaths sont supérieures aux températures de fermeture du « système thermochronologique feldspath potassique » (entre 150 et 450°C). Les mécanismes de déformation impliquant une recristallisation partielle du feldspath (e.g. *bulging recrystallization at grain boundaries*) pourraient être responsables de la remise à zéro partielle du système thermochronologique et pourraient expliquer la rémanence d'âges anciens et l'allure des spectres en marche des feldspaths observés (Figure II.14).

Afin de vérifier et de comprendre le lien entre mécanisme de déformation et diffusion de l'Ar dans le minéral, une étude pétro-structurale détaillée combinée à des analyses $^{40}\text{Ar}/^{39}\text{Ar}$ sur feldspaths dans le même échantillon permettrait peut-être de répondre à cette problématique. Toutefois, la connaissance de la correspondance entre les domaines de diffusion et des entités physiques du réseau cristallin correspondant dans les feldspaths est limitée et fait l'objet de nombreuses recherches actuelles. D'autre part, des analyses supplémentaires de feldspaths dans d'autres types de roches et plus au cœur du massif, ou dans le toit des zones de cisaillement, permettraient de vérifier l'existence de cet héritage ancien à travers toute la région.

2.2.3. Conclusion sur la déformation long terme du massif de l'Ama Drime

La quantification des conditions pression-température combinée avec les données de datations ont permis de déterminer deux scénarios possibles pour expliquer l'exhumation du horst de l'Ama Drime à partir de 12 Ma :

1/ Depuis ~12 Ma, une unique phase de déformation en extension a permis une exhumation de 15 km au niveau des deux zones de cisaillement et des deux failles normales conjuguées. Avec une vitesse d'exhumation verticale apparente de 1.2 mm/an depuis ~12 Ma.

2/ Deux phases de déformation ont eu lieu depuis ~12 Ma: une exhumation plus rapide entre 12 et 9 Ma avec une vitesse verticale de ~4 mm/an pour la zone de cisaillement de Dinggye, puis une exhumation plus lente à ~1 mm/an à partir de 4 Ma pour l'ensemble du massif.

Les datations $^{40}\text{Ar}/^{39}\text{Ar}$ sur feldspath ne nous permettent pas de faire le lien entre les datations $^{40}\text{Ar}/^{39}\text{Ar}$ sur biotite et (U-Th)/He sur apatite et de faire la différence entre les deux scénari. Au contraire, ils révèlent une histoire bien plus ancienne et suggèrent une rétention des âges hérités dans ces minéraux, en liaison sans doute avec une forte rétentivité intrinsèque des feldspaths et un épisode métamorphique dans des conditions amplifiant cette rétention. Néanmoins, les âges jeunes de basses températures (de chauffage, correspondant à 20 -30% d' ^{39}Ar) confirment le refroidissement rapide à partir de 12 Ma.

Les données de pétrologie posent la question du modèle de système d'extension qui correspond le mieux au massif de l'Ama Drime. Si l'on considère que l'exhumation de 15 km s'est produite sur les zones de cisaillement de Dinggye et de Kharta avec leurs pendages actuels (i.e., 45°W pour Dinggye, 30°E pour Kharta) alors on obtient des déplacements sur les zones cisaillantes (21 km et 30 km, respectivement) dont la somme dépasse la largeur actuelle du massif (~41 km). Ceci est encore aggravé si l'on considère les données de Cottle et al. (2009) qui conduisent à 60-71 km de cisaillement total. Cela implique que les zones cisaillantes ductiles ont fonctionné avec des pendages plus fort avant d'être recoupées par les failles normales actives. Ceci correspond donc à une structure de dôme métamorphique bordé par des structures de type détachement à vergence opposée, et avec des variations de pendage au cours du temps. La question maintenant est de savoir quel modèle explique cette configuration. Pour cela il faut d'abord comparer ces observations avec les modèles classiques

de système d'extension, détachement, *metamorphic core complex*, ou dôme évoluant en horst. Des analyses complémentaires sont envisageables pour densifier le « signal thermochronologique » afin de mieux contraindre l'évolution tardive du massif ainsi que des modélisations thermomécaniques.

Table II-2

Table : Results $^{40}\text{Ar}/^{39}\text{Ar}$ Dating by Step Heating Analysis - K-feldspar of the Ama Drime Massif, Kharta fault

Temperature °C	40/39	38/39	37/39	36/39 (E-3)	39Ar (E-14 moles`) released	F39Ar	%40* 40*/39K	Age Ma	$\pm 1\sigma$ Ma
T7A10_Kf	K-feldspar	J=	0.01094						
400	155.578	0.235	11.501	186131	6.10E+12	0.106	65.08	102	1352.25
400	61.807	0.150	14.638	162089	1.80E+12	0.137	23.91	14.92	272.74
450	40.451	0.067	12.357	39670	2.08E+13	0.497	72.82	29.7	507.52
450	17.755	0.054	13.498	36854	9.90E+12	0.668	43.15	7.73	146.45
500	20.054	0.041	13.028	29268	9.61E+13	2.333	60.71	12.28	227.38
500	13.616	0.036	13.384	28024	3.41E+13	2.923	44.99	6.18	118.01
525	13.461	0.035	12.053	26029	4.48E+13	3.699	48.14	6.53	124.51
525	10.606	0.030	9.826	20502	2.25E+13	4.088	48.3	5.16	99.00
550	10.971	0.028	6.246	17658	3.12E+13	4.629	55.71	6.14	117.22
550	6.393	0.022	5.992	11052	2.12E+13	4.996	54.28	3.48	67.48
575	6.691	0.020	3.310	8052	3.95E+13	5.680	67.14	4.5	86.73
575	3.063	0.017	2.295	4739	3.54E+13	6.293	58.16	1.78	34.87
600	3.939	0.018	2.373	4969	6.71E+13	7.455	65.86	2.6	50.56
600	2.390	0.017	1.806	4443	6.83E+13	8.637	48.81	1.17	22.90
625	3.541	0.018	2.544	5750	1.28E+14	10.852	55.81	1.98	38.65
625	2.276	0.016	1.860	4108	1.17E+14	12.869	50.73	1.16	22.67
650	2.403	0.016	1.596	3725	1.73E+14	15.867	57.37	1.38	27.03
650	1.322	0.015	0.970	2103	1.37E+14	18.234	55.92	0.74	14.54
675	1.372	0.015	0.739	1874	1.72E+14	21.209	61.42	0.84	16.56
675	0.758	0.014	0.531	1040	1.36E+14	23.555	61.08	0.46	9.12
700	1.053	0.015	0.395	1526	1.53E+14	26.210	57.57	0.61	11.93
700	0.540	0.014	0.266	555	1.08E+14	28.080	68.96	0.37	7.34
725	0.852	0.013	0.039	718	1.33E+14	30.376	73.01	0.62	12.24
725	1.191	0.014	0.063	375	1.24E+14	32.524	89.35	1.06	20.88
750	1.777	0.015	0.069	786	1.57E+14	35.246	86.03	1.53	29.92
750	1.970	0.015	0.090	1527	1.10E+14	37.157	76.35	1.5	29.44
775	2.267	0.014	0.084	2612	8.82E+13	38.685	65.29	1.48	28.98
775	2.345	0.015	0.155	2213	4.83E+13	39.521	71.67	1.68	32.88
800	2.601	0.015	0.000	3097	5.56E+13	40.484	64.05	1.67	32.58
800	2.673	0.015	0.000	2227	4.86E+13	41.325	74.63	2	38.96
800	2.948	0.015	0.000	1905	5.37E+13	42.255	80.23	2.37	46.09
700	12.390	0.013	0.004	4	3.50E+12	42.316	99.83	0	0.00
750	2.454	0.014	2.823	2	6.00E+12	42.420	99.19	2.61	50.77
800	3.869	0.015	0.001	1330	2.44E+13	42.842	89.32	3.46	66.95
850	3.773	0.015	0.000	3164	6.51E+13	43.970	74.69	2.82	54.78
900	3.512	0.015	0.000	2198	1.50E+14	46.567	80.94	2.84	55.26
950	3.309	0.014	0.000	1652	3.20E+14	52.105	84.64	2.8	54.45
1000	3.360	0.015	0.000	1598	3.12E+14	57.514	85.35	2.87	55.73
1050	3.531	0.015	0.000	1217	3.50E+14	63.572	89.25	3.15	61.15
1100	3.627	0.015	0.000	812	5.65E+14	73.347	92.83	3.37	65.25
1200	3.202	0.000	0.000	747	1.27E+15	95.319	92.48	2.96	57.52
1400	3.794	0.014	0.000	964	2.70E+14	100	91.96	3.49	67.59
10000/T (1/K)	-log(D/r ²)	C-%39Ar	log(r/r _o)						
14.859	9.313	0.106	-0.027	E=		10.0761 kcal/mol			
14.859	9.549	0.137	0.091	log(Do/ro)=	59.8662				
13.831	8.002	0.497	-0.010	Domains=	6				
13.831	8.127	0.668	0.052						
12.937	6.662	2.333	-0.095						
12.937	6.935	2.923	0.042						
12.531	6.649	3.699	0.164						
12.531	6.945	4.088	0.312						
12.151	6.687	4.629	0.432						

12.151	6.879	4.996	0.528							
11.792	6.497	5.680	0.571							
11.792	6.561	6.293	0.604							
11.455	6.157	7.455	0.622							
11.455	6.148	8.637	0.618							
11.136	5.725	10.852	0.615							
11.136	5.747	12.869	0.626							
10.834	5.425	15.867	0.662							
10.834	5.520	18.234	0.710							
10.549	5.291	21.209	0.782							
10.549	5.406	23.555	0.840							
10.277	5.239	26.210	0.934							
10.277	5.421	28.080	1.024							
10.020	5.232	30.376	1.099							
10.020	5.297	32.524	1.131							
9.775	5.094	35.246	1.190							
9.775	5.286	37.157	1.286							
9.542	5.296	38.685	1.443							
9.542	5.545	39.521	1.568							
9.320	5.474	40.484	1.678							
9.320	5.647	41.325	1.764							
9.320	5.771	42.255	1.826							
10.277	6.951	42.316	1.790							
9.775	6.540	42.420	1.913							
9.320	5.929	42.842	1.905							
8.905	5.370	43.970	1.897							
8.525	4.989	46.567	1.955							
8.177	4.623	52.105	2.000							
7.855	4.569	57.514	2.183							
7.559	4.461	63.572	2.323							
7.283	4.153	73.347	2.349							
6.789	3.407	95.319	2.300							
5.977	2.257	100.000	2.256							
Temperature °C	40/39	38/39	37/39	36/39 (E-3)	39Ar (E-14 moles)	F39Ar released	%40*	40*/39K	Age Ma	± 1σ Ma
T7A14Kf	K-feldspar	J=	0.01094							
400	142.244	0.124	0.002	233737	6.30E+26	0.047	51.43	73.16	1060.73	18.10
400	111.625	0.110	0.007	328718	1.80E+26	0.060	12.96	14.47	265.10	58.19
425	104.664	0.088	0.006	153568	2.20E+26	0.077	56.62	59.27	901.64	24.82
425	58.833	0.078	0.007	153705	1.70E+26	0.090	22.77	13.39	246.68	30.16
450	96.775	0.069	3.573	75094	3.10E+26	0.113	77.27	74.96	1080.36	10.62
450	29.792	0.055	5.899	55548	2.60E+26	0.132	46.04	13.77	253.11	12.74
475	81.020	0.053	4.369	30878	5.20E+26	0.171	89.04	72.35	1051.83	13.87
475	17.655	0.034	3.789	27693	4.50E+26	0.204	54.84	9.71	182.05	7.02
500	58.583	0.040	3.022	19472	1.02E+27	0.280	90.46	53.1	826.23	10.38
500	10.507	0.020	1.003	13524	8.30E+26	0.342	62.35	6.56	124.96	3.47
525	29.565	0.026	1.439	10124	1.73E+27	0.471	90.11	26.67	461.80	5.98
525	5.215	0.017	0.001	5057	1.61E+27	0.591	70.97	3.7	71.61	1.83
550	13.559	0.019	0.546	4518	3.19E+27	0.829	90.25	12.24	226.74	1.05
550	2.354	0.015	0.302	1677	3.20E+27	1.067	78.87	1.86	36.28	0.84
575	5.589	0.015	0.251	1821	6.21E+27	1.531	90.28	5.05	96.95	0.68
575	1.153	0.014	0.000	956	6.61E+27	2.024	73.75	0.85	16.70	0.37
600	2.418	0.014	0.000	722	1.31E+28	2.999	90.35	2.18	42.60	0.36
600	0.572	0.014	0.025	406	1.40E+28	4.045	75.79	0.43	8.53	0.18

625	1.254	0.014	0.000	376	2.47E+28	5.888	89.54	1.12	22.02	0.15
625	0.395	0.014	0.000	182	2.29E+28	7.599	81.37	0.32	6.34	0.09
650	0.905	0.014	0.000	265	3.43E+28	10.157	89.13	0.81	15.84	0.09
650	0.338	0.014	0.000	130	2.92E+28	12.336	82.72	0.28	5.51	0.07
675	0.621	0.015	0.000	295	4.34E+28	15.575	82.72	0.51	10.11	0.07
675	0.330	0.014	0.048	226	3.47E+28	18.159	74.53	0.25	4.84	0.08
700	0.526	0.014	0.029	364	5.02E+28	21.904	76.1	0.4	7.89	0.06
700	0.295	0.014	0.000	85	4.30E+28	25.109	84.69	0.25	4.92	0.05
725	0.403	0.014	0.009	114	5.00E+28	28.838	86.78	0.35	6.89	0.05
725	0.429	0.013	0.000	123	3.92E+28	31.763	86.85	0.37	7.34	0.07
750	0.520	0.013	0.000	159	4.26E+28	34.942	87.11	0.45	8.91	0.06
750	0.521	0.013	0.000	152	2.95E+28	37.140	87.58	0.46	8.99	0.09
775	0.695	0.014	0.000	432	2.97E+28	39.352	78.77	0.55	10.78	0.10
775	0.805	0.013	0.102	373	1.70E+28	40.621	84.59	0.68	13.39	0.15
800	1.076	0.013	0.000	539	1.82E+28	41.977	83.32	0.9	17.61	0.16
800	1.149	0.013	0.000	424	1.62E+28	43.185	87.36	1	19.70	0.15
800	1.233	0.013	0.018	567	1.68E+28	44.436	84.87	1.05	20.53	0.14
700	1.669	0.016	0.002	2153	7.50E+26	44.492	60.68	1.01	19.87	1.43
750	1.165	0.013	0.001	130	1.60E+27	44.611	95	1.11	21.72	0.22
800	1.326	0.014	0.063	687	7.15E+27	45.145	83.48	1.11	21.71	0.33
850	1.618	0.014	0.000	808	1.87E+28	46.543	84	1.36	26.62	0.17
900	1.513	0.014	0.034	516	4.10E+28	49.604	88.74	1.34	26.30	0.11
950	1.909	0.014	0.000	448	6.16E+28	54.197	92.01	1.76	34.34	0.12
1000	2.976	0.013	0.030	572	8.47E+28	60.518	93.71	2.79	54.22	0.15
1050	541142607	1484741	149678	7.69E+10	0.00E+00	60.518	95.8	0	0.00	0.00
1100	5.789	0.014	0.012	536	2.64E+29	80.208	96.93	5.61	107.48	0.31
1200	4.988	0.013	0.011	433	2.48E+29	98.678	97.04	4.84	93.09	0.17
1400	6.609	0.014	0.000	1217	1.77E+28	100.000	94.25	6.23	118.93	0.18

10000/T -log(D/r²) C-%39Ar log(r/r₀)
(1/K)

14.858841	-10.01727	0.04693	-0.6532	E=	63.4727 kcal/mol
14.858841	-10.27412	0.06021	-0.5248	log(Do/ro)=	9.2902
14.326648	-10.0023	0.07684	-0.2915	Domains=	8
14.326648	-10.0926	0.08981	-0.2464		
13.831259	-9.692926	0.11275	-0.1026		
13.831259	-9.754166	0.13199	-0.072		
13.368984	-9.290451	0.17077	0.01684		
13.368984	-9.329772	0.20415	0.0365		
12.936611	-8.792469	0.28042	0.06776		
12.936611	-8.843094	0.34207	0.09308		
12.531328	-8.339118	0.47115	0.12221		
12.531328	-8.321801	0.59112	0.11356		
12.150668	-7.831746	0.82889	0.13258		
12.150668	-7.771971	1.06727	0.10269		
11.792453	-7.279424	1.53083	0.10489		
11.792453	-7.183237	2.02408	0.0568		
11.454754	-6.670363	2.99877	0.03461		
11.454754	-6.559531	4.04535	-0.0208		
11.135857	-6.097505	5.8885	-0.0306		
11.135857	-6.064091	7.59894	-0.0473		
10.834236	-5.70284	10.1575	-0.0187		
10.834236	-5.736831	12.3363	-0.0017		
10.548523	-5.404096	15.5746	0.03009		
10.548523	-5.4867	18.159	0.07139		
10.277492	-5.183965	21.9042	0.10802		

10.277492 -5.249064 25.1093 0.14057
 10.02004 -5.05671 28.8376 0.22298
 10.02004 -5.178428 31.7632 0.28384
 9.7751711 -5.033785 34.9419 0.38137
 9.7751711 -5.227225 37.1401 0.47809
 9.5419847 -5.131759 39.3522 0.59211
 9.5419847 -5.420922 40.6206 0.73669
 9.3196645 -5.310715 41.9774 0.8358
 9.3196645 -5.472907 43.1851 0.9169
 9.3196645 -5.62149 44.4357 0.99119
 10.277492 -6.964612 44.4916 0.99835
 9.7751711 -6.457257 44.6113 1.09311
 9.3196645 -5.804917 45.1448 1.0829
 8.9047195 -5.252296 46.543 1.09442
 8.5251492 -4.891363 49.6041 1.17725
 8.1766149 -4.674567 54.1966 1.31061
 7.8554595 -4.475773 60.5176 1.43399
 7.558579 -12.27429 60.5176 5.53918
 7.2833212 -3.808296 80.2081 1.49711
 6.7888663 -3.215152 98.6781 1.54352

Temperature °C	40/39	38/39	37/39	36/39 (E-3)	39Ar (E-14 moles`) released	F39Ar	%40*	40*/39K	Age Ma	± 1σ Ma
T7A20_Kf	K-feldspar	J=	0.01094							
400	227.804	0.079	4.841	98.871	0.067	0.075	87.29	199.49	2088.47	31.73
400	71.446	0.049	4.931	118.109	0.034	0.113	51.54	36.94	612.36	18.33
450	101.304	0.041	6.900	45.376	0.122	0.250	87.16	88.69	1223.48	13.16
450	26.337	0.031	4.849	40.588	0.066	0.323	55.50	14.66	268.40	5.00
500	39.691	0.033	9.614	24.402	0.463	0.840	83.25	33.25	559.70	10.59
500	13.372	0.030	8.767	20.722	0.240	1.108	58.03	7.80	147.81	3.71
525	13.444	0.028	8.442	19.376	0.422	1.579	61.07	8.26	155.99	4.28
525	9.122	0.024	6.263	14.670	0.284	1.896	56.42	5.17	99.21	2.61
550	9.469	0.023	5.479	12.998	0.477	2.429	62.73	5.96	113.99	2.36
550	4.931	0.018	2.756	7.451	0.351	2.821	58.33	2.88	55.99	1.21
575	4.168	0.015	0.929	5.073	0.592	3.483	64.91	2.71	52.66	2.15
575	1.921	0.014	0.945	2.338	0.530	4.074	65.98	1.27	24.86	0.62
600	2.526	0.014	0.643	1.770	0.969	5.156	80.05	2.02	39.50	0.54
600	0.812	0.013	0.272	0.770	0.936	6.201	71.55	0.58	11.44	0.30
625	1.302	0.013	0.120	0.525	1.678	8.075	87.11	1.13	22.24	0.30
625	0.408	0.013	0.118	0.076	1.627	9.892	91.37	0.37	7.34	0.13
650	0.889	0.012	0.000	0.236	2.660	12.863	89.90	0.80	15.70	0.15
650	0.324	0.012	0.000	0.058	2.405	15.549	88.50	0.29	5.65	0.06
675	0.767	0.013	0.022	0.112	3.417	19.366	93.26	0.71	14.05	0.07
675	0.334	0.012	0.000	0.039	2.703	22.385	90.60	0.30	5.97	0.04
700	0.711	0.013	0.040	0.203	3.350	26.126	89.10	0.63	12.47	0.07
700	0.426	0.013	0.000	0.262	2.485	28.902	77.15	0.33	6.47	0.07
725	1.084	0.013	0.000	0.584	3.202	32.478	82.25	0.89	17.51	0.09
725	0.360	0.013	0.000	0.000	2.161	34.891	94.44	0.34	6.69	0.03
750	0.771	0.013	0.000	0.000	2.239	37.391	97.40	0.75	14.76	0.04
750	0.708	0.013	0.000	0.041	1.595	39.173	95.47	0.68	13.30	0.04
775	1.148	0.013	0.000	0.022	1.751	41.128	97.69	1.12	22.00	0.05
775	0.971	0.013	0.000	0.000	1.025	42.272	97.94	0.95	18.67	0.04
800	1.469	0.013	0.000	0.000	1.304	43.729	98.64	1.45	28.38	0.07
800	1.209	0.013	0.000	0.000	1.053	44.905	98.34	1.19	23.32	0.09
800	1.463	0.013	0.000	0.000	1.045	46.072	98.63	1.44	28.25	0.10
700	7.762	0.009	0.003	0.003	0.042	46.118	99.73	0.00	0.00	0.00
750	2.637	0.011	0.001	0.001	0.086	46.214	99.23	0.00	0.00	0.00

800	1.620	0.012	0.000	0.000	0.417	46.680	98.76	1.60	31.30	0.08
850	4.713	0.013	0.136	0.227	1.202	48.022	98.33	4.63	89.22	0.18
900	5.296	0.013	0.000	0.276	2.969	51.338	98.08	5.19	99.72	0.26
950	5.654	0.013	0.000	0.265	5.049	56.977	98.26	5.56	106.46	0.26
1000	6.885	0.013	0.015	0.337	6.937	64.724	98.28	6.77	128.84	0.31
1050	7.983	0.013	0.000	0.416	7.998	73.657	98.21	7.84	148.47	0.29
1100	7.972	0.013	0.000	0.417	11.860	86.902	98.20	7.83	148.25	0.30
1200	6.709	0.013	0.000	0.458	10.391	98.507	97.68	6.55	124.91	0.33
1400	8.408	0.014	0.000	2.274	1.337	100.000	91.77	7.72	146.20	0.24
10000/T (1/K)	-log(D/r ²)	C-%39Ar	log(r/r ₀)							
14.858841	9.606	0.07532	-0.0471	E=		49.3988 kcal/mol				
14.858841	9.570	0.11344	-0.0652	log(Do/ro)=	6.3426					
13.831259	8.667	0.24952	0.03775	Domains=	4					
13.831259	8.804	0.32281	0.10674							
12.936611	7.581	0.84038	-0.0223							
12.936611	7.710	1.10795	0.04249							
12.531328	7.258	1.57887	0.03526							
12.531328	7.384	1.89649	0.09837							
12.150668	6.998	2.42923	0.11057							
12.150668	7.114	2.8211	0.16866							
11.792453	6.740	3.48258	0.17518							
11.792453	6.777	4.07411	0.19356							
11.454754	6.361	5.15625	0.16779							
11.454754	6.353	6.2014	0.16378							
11.135857	5.933	8.07495	0.12606							
11.135857	5.913	9.89213	0.11623							
10.834236	5.530	12.8634	0.08752							
10.834236	5.545	15.5492	0.09471							
10.548523	5.235	19.366	0.09442							
10.548523	5.327	22.3845	0.14002							
10.277492	5.101	26.1264	0.17362							
10.277492	5.243	28.902	0.24459							
10.02004	5.019	32.478	0.27136							
10.02004	5.216	34.8911	0.37003							
9.7751711	5.103	37.3912	0.44577							
9.7751711	5.292	39.1727	0.54033							
9.5419847	5.164	41.1279	0.6022							
9.5419847	5.380	42.2721	0.7103							
9.3196645	5.262	43.7288	0.77125							
9.3196645	5.467	44.9047	0.87366							
9.3196645	5.635	46.0717	0.95769							
10.277492	7.028	46.1183	1.13706							
9.7751711	6.538	46.2142	1.16297							
9.3196645	5.849	46.6796	1.06474							
8.9047195	5.256	48.0221	0.99205							
8.5251492	4.846	51.3379	0.99188							
8.1766149	4.557	56.9765	1.03569							
7.8554595	4.350	64.724	1.10536							
7.558579	4.182	73.6567	1.18188							
7.2833212	3.803	86.9021	1.14099							
6.7888663	3.311	98.5072	1.16168							

	5.9772863	2.278	100	1.08336						
Temperature °C	40/39	38/39	37/39	36/39	39Ar (E-3)	F39Ar (E-14 moles released)	%40*	40*/39K	Age Ma	± 1σ Ma
T7A33Kf	K-feldspar	J=	0.01094							
400	1085176	1.021	759.877	160675	0.00E+00	1.22E-07	95.63	0.00	0.00	0.00
400	22.019	0.023	6.288	24.156	0.600	0.588	69.22	15.30	279.28	3.15
400	64.717	0.000	0.010	82.894	0.010	0.598	62.12	40.20	657.62	115.76
450	26.577	0.006	0.001	41.640	0.072	0.668	53.63	14.25	261.41	10.55
450	28.687	0.041	5.821	61.286	0.066	0.733	38.03	10.95	204.14	9.27
500	47.780	0.035	15.530	40.008	0.911	1.624	77.18	37.25	616.75	30.84
500	16.196	0.037	12.149	33.550	0.451	2.066	43.21	7.05	134.10	8.27
550	22.845	0.040	9.276	19.400	2.007	4.031	77.28	17.76	320.35	24.41
550	9.247	0.029	8.056	21.179	1.162	5.169	37.38	3.47	67.30	8.24
600	10.029	0.023	4.617	12.153	3.405	8.503	66.78	6.72	127.95	7.64
600	1.438	0.014	0.737	2.488	2.320	10.774	50.56	0.73	14.30	0.69
650	3.082	0.014	0.218	1.358	5.656	16.312	86.76	2.67	52.02	0.35
650	0.504	0.013	0.072	0.387	3.224	19.469	74.19	0.37	7.37	0.19
700	1.511	0.013	0.100	0.874	4.923	24.289	81.98	1.24	24.28	0.28
700	0.540	0.013	0.167	0.579	2.575	26.810	66.48	0.36	7.07	0.21
750	1.317	0.013	0.054	0.633	4.481	31.198	84.53	1.11	21.84	0.32
750	2.022	0.013	0.011	0.858	2.476	33.622	86.50	1.75	34.19	0.44
800	2.518	0.013	0.000	1.692	2.972	36.532	79.35	2.00	39.01	0.32
800	3.397	0.013	0.000	2.783	1.688	38.185	75.20	2.55	49.73	0.31
800	5.325	0.014	0.009	4.973	1.454	39.608	72.04	3.84	74.17	0.38
700	12.027	0.019	0.209	12.909	0.076	39.682	68.22	8.21	155.10	1.95
750	8.132	0.013	0.000	6.003	0.228	39.906	77.94	6.34	120.95	0.72
800	7.917	0.015	0.000	6.708	0.446	40.343	74.71	5.91	113.11	0.64
850	7.058	0.014	0.000	6.163	1.423	41.736	73.91	5.22	100.14	0.44
900	6.917	0.014	0.000	3.541	3.682	45.341	84.58	5.85	111.92	0.37
950	7.096	0.014	0.000	1.864	7.768	52.947	91.96	6.53	124.40	0.37
1000	6.681	0.014	0.000	1.923	7.369	60.162	91.20	6.09	116.42	0.29
1050	8.182	0.014	0.009	1.828	7.689	67.690	93.16	7.62	144.50	0.28
1100	10.081	0.014	0.009	1.270	12.185	79.620	96.08	9.69	181.70	0.36
1200	9.262	0.014	0.000	0.830	19.679	98.888	97.14	9.00	169.36	0.31
1400	11.025	0.014	0.000	3.023	1.135	100.000	91.72	10.11	189.29	0.73
10000/T (1/K)	-log(D/r²)	C-%39Ar	log(r/r₀)							
14.858841	21.185	1.2E-07	6.46446	E=	33.1469	kcal/mol				
14.858841	7.822	0.58783	-0.217	log(Do/ro)= 2.509						
14.858841	9.367	0.59752	0.55571	Domains= 3						
13.831259	8.412	0.6676	0.45058							
13.831259	8.469	0.73253	0.47861							
12.936611	7.038	1.62415	0.08728							
12.936611	7.215	2.06577	0.17596							
12.150668	6.282	4.03116	-0.0061							
12.150668	6.407	5.16909	0.05674							
11.454754	5.701	8.50267	-0.0441							
11.454754	5.786	10.7742	-0.0019							
10.834236	5.184	16.312	-0.078							
10.834236	5.374	19.4689	0.01711							
10.277492	5.036	24.2889	0.04971							
10.277492	5.317	26.81	0.19024							
9.7751711	4.954	31.1976	0.19087							
9.7751711	5.231	33.6221	0.32904							
9.3196645	5.050	36.5316	0.4038							
9.3196645	5.393	38.1845	0.57536							

9.3196645	5.617	39.6077	0.68715							
10.277492	6.889	39.6823	0.97617							
9.7751711	6.411	39.9059	0.91914							
9.3196645	5.815	40.3428	0.7863							
8.9047195	5.302	41.7358	0.67996							
8.5251492	4.863	45.3412	0.59811							
8.1766149	4.485	52.9473	0.53505							
7.8554595	4.426	60.1622	0.62215							
7.558579	4.326	67.6903	0.6798							
7.2833212	3.984	79.6203	0.60828							
6.7888663	3.184	98.8884	0.38731							
5.9772863	2.283	100	0.23105							
Temperature °C	40/39	38/39	37/39	36/39 (E-3)	39Ar (E-14 moles)	F39Ar released	%40*	40*/39K	Age Ma	± 1σ Ma
T7A48_Kf	K-feldspar	J=	0.01094							
400	39.498	0.064	5.274	43.145	0.287	0.407	68.48	27.14	469.06	5.81
400	20.015	0.038	6.181	42.076	0.091	0.537	39.65	7.97	150.78	5.95
450	26.028	0.033	6.342	22.743	0.431	1.148	75.58	19.75	352.96	5.31
450	10.726	0.030	5.214	19.736	0.208	1.442	48.38	5.21	99.95	2.71
500	15.703	0.030	8.460	20.262	1.904	4.141	65.01	10.26	191.99	10.93
500	10.258	0.026	7.968	18.291	0.804	5.280	51.82	5.34	102.49	3.16
525	11.279	0.028	8.279	19.658	1.363	7.213	52.77	5.98	114.39	6.26
525	9.609	0.026	7.300	17.455	0.681	8.178	50.71	4.90	94.13	4.15
550	10.569	0.025	6.634	17.095	1.109	9.749	55.82	5.92	113.30	2.76
550	6.854	0.022	4.570	12.878	0.618	10.626	48.23	3.32	64.27	3.36
575	8.187	0.021	4.767	12.002	0.966	11.995	59.97	4.92	94.67	4.42
575	4.303	0.017	2.627	7.474	0.646	12.911	51.91	2.24	43.63	1.66
600	5.285	0.017	2.071	6.693	1.005	14.335	64.57	3.42	66.21	1.44
600	2.137	0.014	0.880	3.148	0.768	15.424	58.03	1.24	24.32	0.64
625	2.970	0.014	13.317	2.531	1.143	17.045	99.33	3.04	58.93	0.77
625	1.113	0.013	0.326	1.027	0.914	18.340	72.70	0.81	15.90	0.53
650	3.231	0.013	0.130	1.982	1.336	20.235	81.50	2.63	51.24	0.84
650	0.826	0.012	0.044	0.655	0.971	21.611	74.47	0.62	12.10	0.37
675	1.408	0.013	0.000	0.627	1.268	23.409	85.42	1.20	23.59	0.38
675	0.890	0.013	0.000	0.430	0.950	24.755	83.49	0.74	14.61	0.25
700	1.344	0.013	0.030	1.206	1.205	26.463	72.13	0.97	19.03	0.32
700	0.948	0.013	0.000	0.839	0.892	27.728	71.74	0.68	13.37	0.27
725	1.435	0.013	0.068	0.966	1.190	29.415	78.99	1.13	22.23	0.22
725	0.798	0.012	0.000	0.172	0.806	30.558	91.12	0.73	14.30	0.14
750	0.977	0.013	0.039	0.122	0.965	31.926	94.52	0.92	18.14	0.12
750	0.922	0.012	0.069	0.233	0.761	33.005	90.83	0.84	16.45	0.16
775	1.175	0.012	0.000	0.034	0.878	34.250	97.45	1.15	22.46	0.07
775	1.090	0.012	0.000	0.613	0.594	35.092	81.55	0.89	17.45	0.27
800	1.447	0.012	0.000	0.512	0.716	36.106	88.18	1.28	25.01	0.25
800	1.166	0.013	0.000	0.550	0.583	36.933	84.34	0.98	19.30	0.22
800	1.473	0.013	0.000	0.496	0.595	37.776	88.70	1.31	25.61	0.18
700	3.270	0.000	0.005	0.005	0.025	37.811	99.35	3.25	63.00	0.66
750	2.213	0.008	0.002	0.002	0.062	37.899	99.07	2.19	42.76	0.29
800	1.835	0.012	0.000	0.686	0.269	38.280	87.87	1.61	31.54	0.36
850	2.008	0.012	0.000	0.721	0.681	39.245	88.39	1.77	34.69	0.28
900	2.990	0.013	0.000	0.747	1.851	41.869	91.95	2.75	53.47	0.18
950	4.766	0.013	0.000	0.736	3.782	47.230	95.02	4.53	87.24	0.20
1000	4.595	0.013	0.054	0.547	4.008	52.912	96.12	4.42	85.12	0.21
1050	3.851	0.013	0.000	0.708	4.010	58.596	94.05	3.62	70.09	0.12
1100	5.238	0.013	0.010	0.946	7.431	69.131	94.30	4.94	94.95	0.24
1200	4.163	0.013	0.000	0.984	20.276	97.875	92.53	3.85	74.47	0.17
1400	4.712	0.013	0.000	1.926	1.499	100.000	87.50	4.12	79.59	0.19

10000/T (1/K)	-log(D/r ²)	C-%39Ar	log(r/r _o)	
14.858841	8.140	0.40738	-0.0998	E= 49.8894 kcal/mol
14.858841	8.341	0.53666	0.00044	log(Do/ro)= 8
13.831259	7.348	1.14758	0.06428	Domains= 7.8627
13.831259	7.545	1.44202	0.16283	
12.936611	6.182	4.14057	-0.0307	
12.936611	6.396	5.28009	0.07632	
12.531328	5.977	7.21291	0.08778	
12.531328	6.255	8.17778	0.22682	
12.150668	5.910	9.74932	0.26183	
12.150668	6.175	10.6256	0.39436	
11.792453	5.869	11.9954	0.43647	
11.792453	6.069	12.9106	0.53661	
11.454754	5.771	14.3347	0.57176	
11.454754	5.916	15.4238	0.64429	
11.135857	5.639	17.0447	0.67943	
11.135857	5.766	18.3403	0.74287	
10.834236	5.496	20.2347	0.7726	
10.834236	5.667	21.6111	0.85775	
10.548523	5.452	23.4086	0.90622	
10.548523	5.615	24.7552	0.98776	
10.277492	5.418	26.463	1.03709	
10.277492	5.591	27.728	1.1235	
10.02004	5.376	29.4153	1.15632	
10.02004	5.591	30.5578	1.26395	
9.7751711	5.428	31.9258	1.31597	
9.7751711	5.582	33.0051	1.39259	
9.5419847	5.437	34.2497	1.44767	
9.5419847	5.594	35.092	1.52578	
9.3196645	5.501	36.1065	1.60089	
9.3196645	5.705	36.9326	1.70242	
9.3196645	5.862	37.7757	1.78114	
10.277492	7.234	37.8111	1.94479	
9.7751711	6.662	37.8989	1.93291	
9.3196645	6.022	38.2802	1.86118	
8.9047195	5.486	39.245	1.81956	
8.5251492	5.032	41.8687	1.79942	
8.1766149	4.681	47.2304	1.81387	
7.8554595	4.603	52.9119	1.94986	
7.558579	4.538	58.5965	2.07936	
7.2833212	4.180	69.1305	2.05027	
6.7888663	3.220	97.8749	1.83999	
5.9772863	2.271	100	1.80811	

2.3. Evaluation des vitesses d'exhumation et d'extension au niveau du détachement de la chaîne du Nyainqntenglha : thermochronologie moyenne à basse température.

Dans cette partie, nous allons aborder la quantification des mouvements verticaux au Miocène-supérieur - Pliocène au niveau du Massif du Nyainqntanglha et du rift de Yadong-Gulu associé. Ce massif est bordé sur son flanc Sud-Est par un détachement ancien recoupé par endroit par le rift de Yadong-Gulu. Le lien entre les failles normales actives de ce rift et le détachement est mal compris. Une question importante est de savoir si les failles normales actives correspondent à la continuité de la phase d'extension liée au détachement ou si l'on est en présence de deux phases bien distinctes. Nous allons quantifier la déformation au niveau de la zone de cisaillement et au niveau des failles actives, à différentes périodes de temps afin de constater ou non des différences de vitesse d'exhumation au cours de temps. Ceci nous permettra de répondre à la question de la continuité de l'extension

2.3.1. Contexte géologique

2.3.1.1. Le Massif du Nyainqntanglha dans le contexte du Bloc de Lhasa

Le massif du Nyainqntanglha s'est formé au niveau du bloc de Lhasa (Figure II.21). L'héritage structural et géologique mésozoïque et paléogène de ce bloc, marque très fortement le style de déformation et la chimie des roches du Néogène à l'actuel, période correspondant à l'activité de l'extension au Sud-Tibet. Pour prendre en compte cet héritage dans l'interprétation de nos résultats, les formations lithologiques constituant le bloc de Lhasa sont présentées ici à travers la succession des événements géodynamiques qu'il a subie. Nous verrons ensuite quelles sont les spécificités de la région du Nyainqntanglha à l'intérieur de ce bloc.

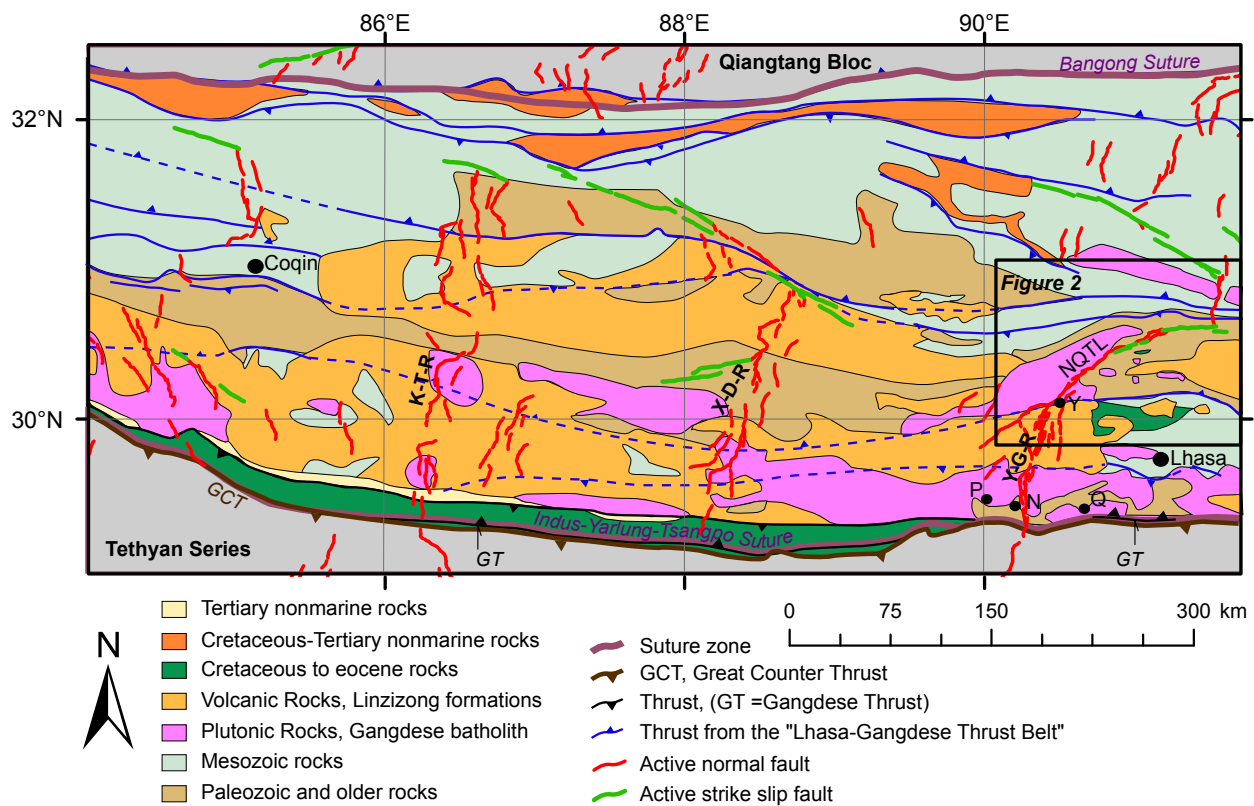


Figure II.21: Geological map of the Lhasa block. Lithologies and inactive faults are from Kapp et al., 2005, 2007 and Pullen et al., 2008. Active faults are from Armijo et al., 1986. Squares indicate towns and villages, Y = Yangbajain, P = Pachu, N = Nyemo, Q = Quxu. K-T-R = Kung Co - Tangra Yum Co Rift, X-D-R = Xainza-Dinggye Rift, Y-G-R= Yadong-Gulu Rift, NQTL = Nyainqntanglha massif, GCT = Great Counter Thrust, GT = Gangdese Thrust.

Avant la subduction de la Néotéthys (évolution pré-Crétacé)

Le bloc de Lhasa (Figure II.21) est un bloc continental appartenant au Gondwana, entré en collision avec le bloc du Qiangtang (Laurasia) entre le Jurassique supérieur et le Crétacé moyen en fonction de la région, suite à la fermeture de la Paléotéthys (Dewey et al., 1988, Matte et al., 1996). Ces deux blocs sont séparés par la suture de Bangong. La couverture sédimentaire du bloc de Lhasa comprend des dépôts océaniques anté-collision du Paléozoïque au Jurassique. Les sédiments marins marginaux et fluviatiles du Jurassique supérieur à Crétacé inférieur (Figure II.21) sont considérés comme étant des dépôts de bassin d'avant pays périphérique lié à la collision des blocs de Lhasa et du Qiangtang (Leeder et al., 1988 ; Yin et al., 1994 ; Kapp et al., 2003, 2005b ; Zhang et al., 2004 ; Leier et al., 2005)

Pendant la subduction de la Néotéthys (Crétacé - Paléocène)

Au Sud du bloc de Lhasa la suture de l'Indus-Yarlung-Tsangpo témoigne de la subduction de la Néotéthys, pendant le Crétacé moyen (Durr et al., 1996). Au niveau du continent, donc du bloc de Lhasa accréte au Qiangtang, une sédimentation importante a lieu pendant le Crétacé moyen. Les séries marines carbonatées d'âge Crétacé moyen Aptien-Albien (114-96 Ma) (unité inférieure des *Takena formations*) s'étendent sur tout le bloc de Lhasa. Elles ont été interprétées comme s'étant déposées dans un bassin marin d'avant pays périphérique (Kapp et al., 2003, 2005b ; Leier et al., 2007) ou d'un bassin d'extension arrière arc (Zhang et al., 2004). Cette série marine est surmontée par la série fluviatile des *redbeds* de plus de 2 km d'épaisseur, d'âge supérieur à 90 Ma (unité supérieure des *Takena formations*), interprétée comment étant des dépôts de retro-arc foreland basin, dérivés de l'arc du Gangdese (Yin et al., 1988 ; Leier et al., 2007). Pendant et essentiellement après cette sédimentation et pendant la subduction de la Néotéthys sous le bloc de Lhasa, un magmatisme d'arc de type Andin génère le batholithe du Gangdese et les formations volcaniques associées, les *Linzizong formations* (Tapponnier et al., 1981, Burg et al., 1983, Harris et al., 1988). Des âges entre 205 et 13 Ma caractérisent le batholithe du Gangdese. Ils peuvent être séparés en quatre étapes d'activité magmatique (Ji et al., 2009), l'étape la plus importante étant située entre 65 et 41 Ma (Schärer et al., 1984; Xu et al., 1985; Coulon et al., 1986; Debon et al., 1986; Harris et al., 1988a; Copeland et al., 1995; Quidelleur et al., 1997; Harrison et al., 2000; Kapp et al., 2005a, Ji et al., 2009). Les formations volcaniques des *Linzizong Formations* montrent également une gamme d'âge importante entre ~120 et ~40 Ma, avec, comme pour le batholithe du Gangdese, un épisode intense vers 50 Ma

(Lee et al., 2009). Ces *Linzizong Formations* du Paleocène, très peu déformées, recouvrent donc les séries sédimentaires qui sont, elles, affectées par de grands plis d'axe Est-Ouest et par une série de chevauchements (Figures II.21 et II.22) (Burg et al., 1983; Allègre et al., 1984; Burg and Chen, 1984; Pan, 1993 Liu, 1988; Murphy et al., 1997).

Ces chevauchements, qui mettent en contact les sédiments crétacés avec les sédiments paléozoïques (Figures II.21 et II.22) peuvent être attribués au développement d'une ceinture de chevauchement arrière arc appelée *Gangdese Retroarc Thrust Belt*. Elle se serait propagée vers le Nord entre 105 et 53 Ma (Kapp et al., 2007 ; Pullent et al., 2008). Cette ceinture de chevauchement implique que l'épaississement de la croûte tibétaine ait commencé avant la collision.

La collision (évolution Néogène)

Au niveau du bloc de Lhasa, la collision s'exprime essentiellement par le *Gangdese Thrust*, situé au sud du bloc (Figure II.21). Il a été actif entre 30 et 24 Ma (Yin et al., 1994, 1999a, Harrison et al., 1999b). L'activité de ce chevauchement aurait joué un rôle important dans le soulèvement du bloc de Lhasa. En effet, les données $^{40}\text{Ar}/^{39}\text{Ar}$ de Copeland et al., 1995 sur des plutons du batholithe du Gangdese (i.e. Quxu, Pachu) dans la région de Lhasa montrent des vitesses de refroidissement rapides entre 26 et 15 Ma correspondant à des taux de dénudation entre 0.18 et 0.30 mm/an. Deux autres plutons (les plutons de Yangbajain et de Nyemo bordés par des failles du rift de Yadong-Gulu) montrent une histoire différente avec des périodes de refroidissement rapide vers 29 et vers 9 Ma, cette dernière étant certainement influencée par une combinaison de l'érosion et de l'ouverture du graben de Yadong-Gulu.

Le soulèvement dû à l'érosion au niveau de Pachu est estimé à 2 mm/an. A Yangbajain (Figure II.22), les données $^{40}\text{Ar}/^{39}\text{Ar}$ montrent un refroidissement lent entre 29 et 20 Ma suivi par un refroidissement rapide. Le modèle de diffusion implique une vitesse de dénudation moyenne de 0.33 mm/an depuis 20 Ma avec la possibilité de pics de dénudation à 2 mm/an entre 20 et 5 Ma (Copeland et al., 1995). Donc au Néogène, l'intérieur du bloc de Lhasa (comme le reste du Tibet) est davantage marqué par la déformation en régime extensif que par la compression (qui s'exprime davantage au front de la chaîne himalayenne et au nord du Tibet). Cette extension est marquée par les rifts Nord-Sud qui traversent le Tibet (Figure II.21). Le rift de Yadong-Gulu est le plus important. Il présente des zones de cisaillement ductile en faille normale dans les murs de certaines failles actives, principalement au niveau du massif du Nyainqntanglha mais aussi plus au Sud dans la vallée de

Nieru et la vallée de Duoqen vers le village de Nyemo (Figure II.21) (Armijo et al., 1986 ; Burchfiel et al., 1991) .

Plusieurs hypothèses dont le soulèvement du plateau (et donc du bloc de Lhasa) permettent d'expliquer l'existence de ce régime extensif. L'âge d'initiation de ces rifts, ainsi que la vitesse d'exhumation des failles qui les constituent sont souvent considérées comme étant une preuve pour déterminer l'âge et les mécanismes du soulèvement du plateau tibétain. Le massif du Nyainqntanglha est un excellent candidat pour fournir ces preuves.

Avant de présenter nos résultats, la géologie du massif du Nyainqntanglha sera rapidement présentée puis un état des lieux des connaissances sur l'âge d'initiation et la vitesse du détachement sera exposé.

2.3.1.2. Géologie du Massif du Nyainqntanglha

Le cœur du Massif du Nyainqntanglha, situé sous la faille de détachement, entre les villes de Chepa et Damxung, est majoritairement constitué de granites s'apparentant au batholithe du Gangdese. Kapp et al., 2005 ont montré qu'il existe une gamme très large d'âges pour ces granites, entre ~140 et 8 Ma avec un âge Triasique à ~211 Ma (Figure II.22, et II.24). Les granites miocènes (coupe de Goring La et Balum Chum La Figure II.24a, b) indiquent que la structure thermique du massif a pu être perturbée à partir de 15 Ma et devront être pris en compte dans les interprétations des données thermochronologiques.

C'est dans la partie Nord-Est métasédimentaire du massif, ainsi qu'au niveau de la fenêtre tectonique au Sud de Damxung, qu'ont été identifiés les chevauchements (*Lhasa-Damxung Thrust*, *Lagen La Thrust*, *Nam Co Thrust*, Figure II.22 et Figure II.24c, d, e) attribués à la *Gangdese Thrust Belt* (Kapp et al., 2007, Pullen et al., 2008). Cette zone fortement parcourue de structures de déformation anciennes, peut être considérée comme étant une zone de faiblesse crustale ayant joué un rôle significatif dans la localisation de la *Damxung-Jiali Shear Zone* (DJSZ) (Edwards et Ratschbacher 2005, Figure II.24f, g). Cette zone relaie le détachement entre la vallée de Lagen La et la gorge de Jangra (juste au Nord de Damxung), (Figure II.22). Elle montre une déformation ductile en transtension (décrochement ductile senestre) qui affecte les roches métaclastiques de la bordure Sud du massif au niveau de Damxung et qui se prolonge vers l'Est. La zone de failles active en décrochement senestre recouvrant la DJSZ ductile est interprétée comme étant une zone de transfert liant les failles normales de la région de Yangbajain-Nyinzhong à celle de la région de Gulu (Armijo et al., 1986). Le lien entre la DJSZ et le détachement n'est pas bien établi. Nous allons dans la suite aborder uniquement la déformation au niveau du détachement du Nyainqntanglha.

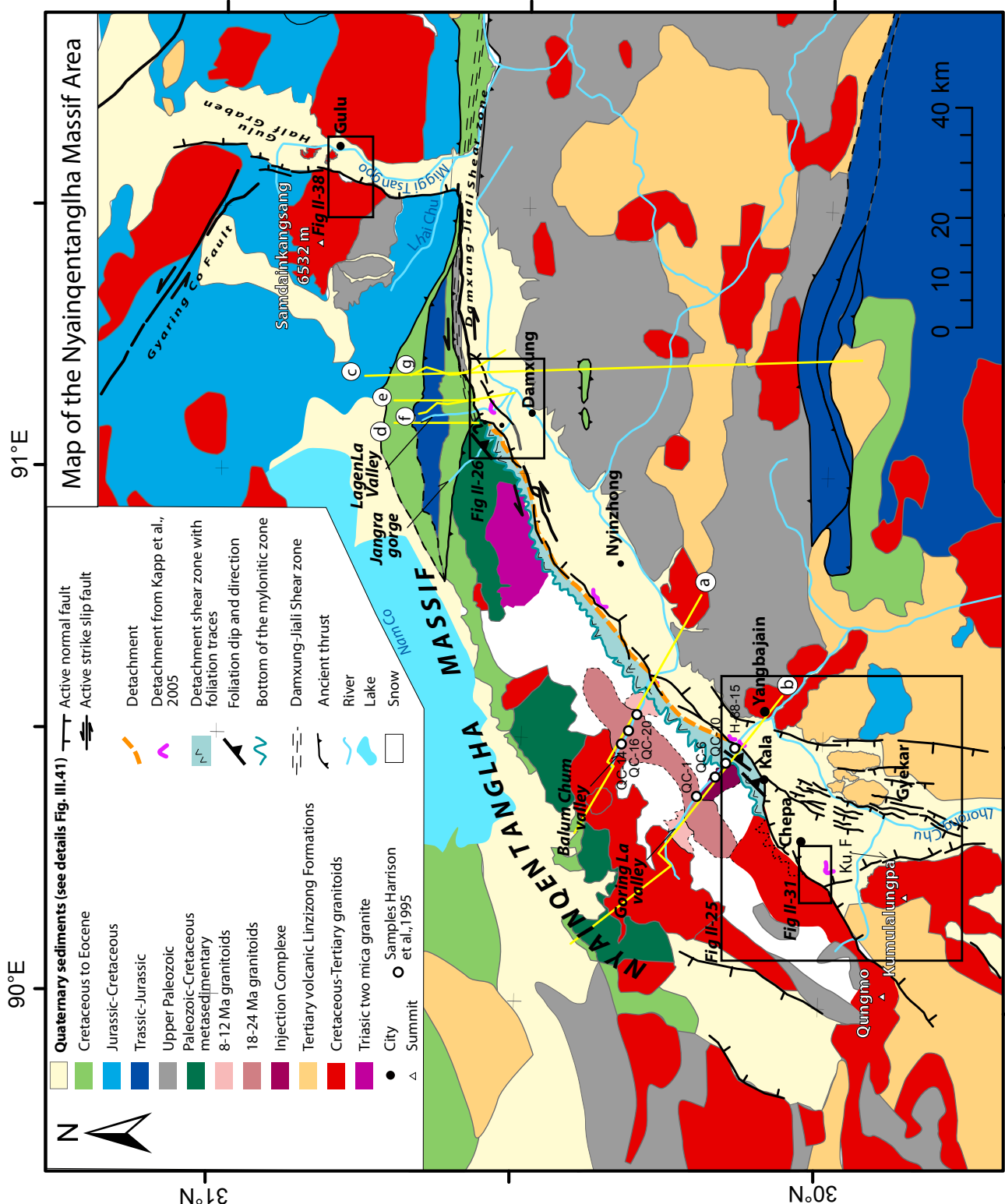


Figure II.22: Geological map of the Nyainqntanglha Massif. Projection is WGS84-UTM. Geological contours are drawn from Kapp et al., 2005 for the southwestern part of the massif. The geology of the Northeastern part (Damxung area) is from Pullen et al., 2008. The rest of the map is from the Chinese geological map of Tibet combined with interpretation of Landsat image. Trace of the detachment is from Kapp et al., 2005. Quaternary faults are from Armijo et al., 1986. Other samples are from Harrison et al., 1995. Trace of cross sections of the Figure II.24 are located.

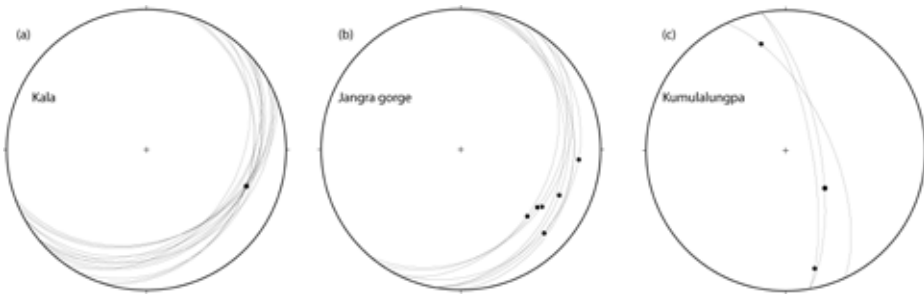


Figure II.23: Structure geometry in the Nyainqntanglha area. Lower hemisphere, equal-area stereonet diagrams. Corresponding areas are shown on the Figure II.22. (a) Orientations of foliations and stretching lineations of the Nyainqntanglha detachment in the Kala zone, and (b) in the Jangra gorge, (c) fault planes and striation lineations in the zone of the Kumulalungpa fault.

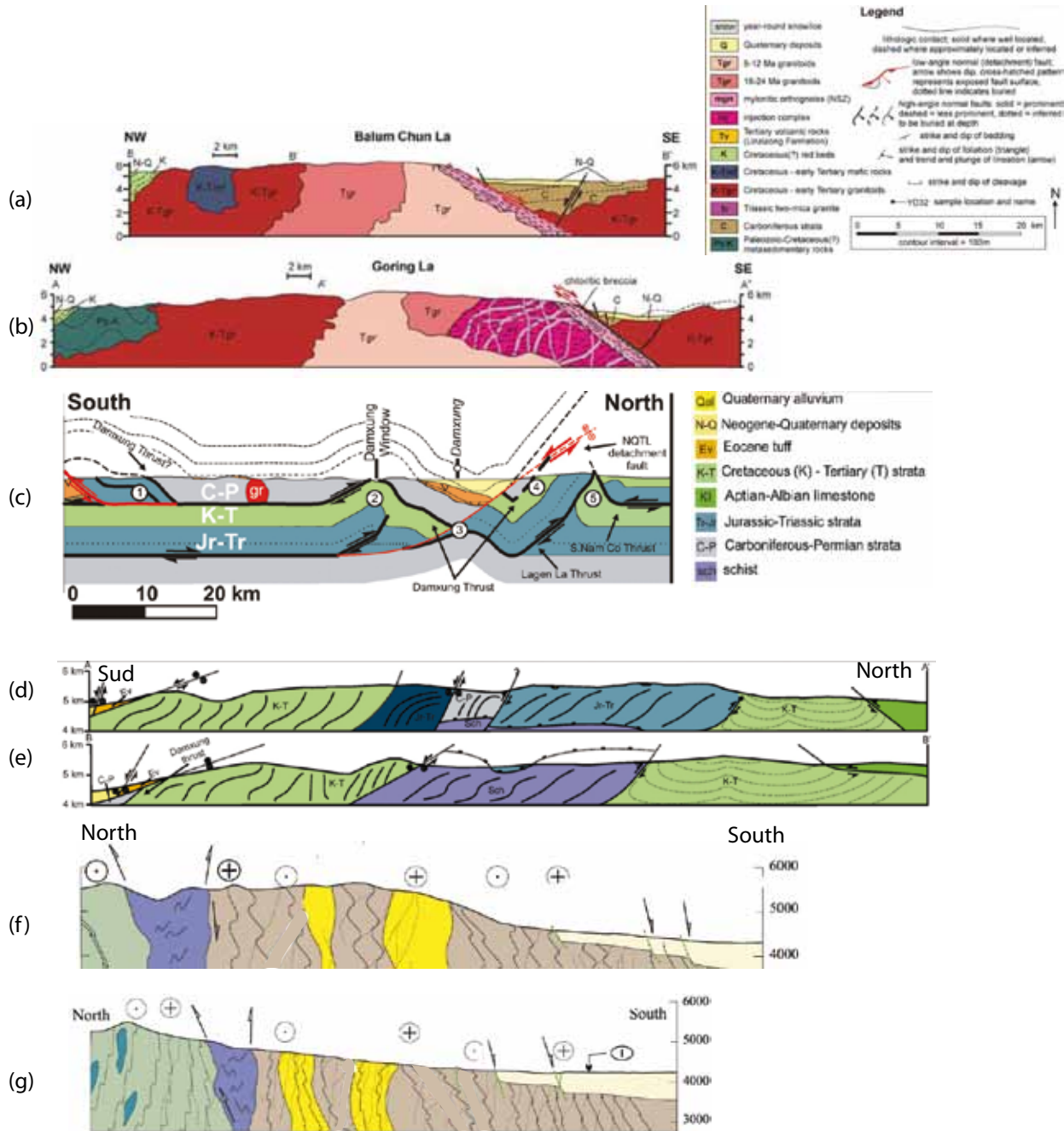


Figure II.24: Geological interpretative cross sections of the Nyainqntanglha area, localized on map Figure II.22. (a) Section from the Balum Chun La valley. (from Kapp et al., 2005). (b) Section from the Balum Chun La valley (from Kapp et al., 2005). (c) Schematic S-N cross section (from Kapp et al., 2007 and Pullen et al., 2008). (d) Section in the the Langen La Valley (from Pullen et al., 2008); (e) and (f) Sections located to the east of the Langen La valley (from Edwards and Ratschbacher 2005): colours are (left to right): pale green, general Cretaceous(?) country rock; deep blue, staurolite schist; brown, undifferentiated DJSZ rocks; rich yellow, stretched pebble conglomerate; pale yellow, unconsolidated fill of Damxung pull-apart graben. Fabric is schematically illustrated: dashed or solid black line represents weak or strong foliation, respectively. Buckling (schematically shown) of main foliations and minor crenulation is related to general vertical shortening. Open half-arrows show the relative displacement across faults and shear zones.

2.3.1.3. La faille de détachement du Nyainqntanglha

Le détachement du Nyainqntanglha (description)

La faille ductile à pendage faible (22 à 37°) vers le Sud-Est est exposée au niveau de plusieurs localités le long du flanc Sud-Est du massif, entre le site d'échantillonnage juste à l'Ouest de Chepa et la gorge de Jangra (Figure II.26 et II.28). Le détachement est souligné par une zone mylonitique d'environ 300 m d'épaisseur (Coward et al., 1988 ; Pan et Kidd, 1992 ; Kapp et al., 2005) (Figure II.22). Les linéations d'étirement à la surface des plans de foliation sont généralement inclinées vers le Sud-Est (Pan et Kidd, 1992; Kapp et al., 2005). Les profils sismiques du projet INDEPTH (des années 1990) le long du rift de Yadong-Gulu montrent que le détachement garde un pendage faible en profondeur, sous le graben (Cogan et al., 1998). Ils ont aussi permis d'estimer l'épaisseur des sédiments remplissant le rift de Yadong-Gulu, comprise entre 100 et 1500 m. Par endroit, la zone de cisaillement du détachement est recoupé par les failles normales actives du rift (Figure II.25 et II.27). La seule cartographie précise des mylonites et du détachement a été publiée par Kapp et al. 2005. Nous avons géoréférencé cette carte pour la confronter avec nos propres observations de terrain et aux images Landsat. Si dans l'ensemble notre cartographie (Figure II.22) concorde avec celle de Kapp et al. 2005, des points de divergence apparaissent. 1) Le tracé du détachement de Kapp est souvent localisé dans le bassin quaternaire, dans le hanging wall des failles normales actives ce qui est très peu probable. 2) Nous n'avons trouvé aucune trace de mylonites ni du détachement à l'Ouest de Chepa. Dans la nouvelle cartographie que nous proposons, les mylonites sont clairement recoupées par les failles normales actives au point que les mylonites et le détachement n'affleurent plus à l'Ouest de Chepa car elles ont probablement été abaissées par la faille normale active (Figure II.25 et II.27). D'autre part les mylonites en failles normales semblent être recoupées, ou se brancher, sur la zone décrochante ductile senestre de Damxung (DJSZ) au Nord-Est (Figure II.26).

Une question importante est de savoir si les failles normales actives correspondent à la continuité de la phase d'extension liée au détachement ou si l'on est en présence de deux phases bien distinctes. La quantification des vitesses de déformation au niveau de la zone de cisaillement et au niveau des failles actives nous permettra de répondre à cette question.

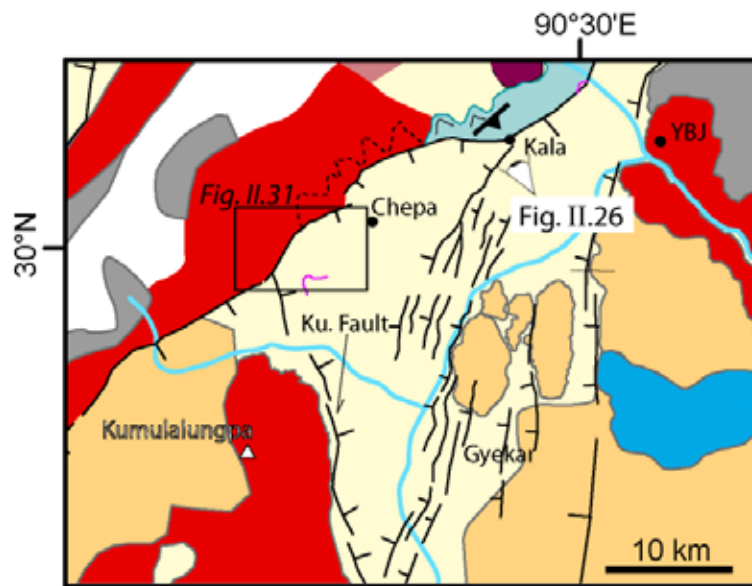


Figure II.25: Zoom of figure II.22 on the Yangbajain basin. Dashed line is the base of mylonitic zone of the Nyainqntanglha detachment by Kapp et al., 2005. After them, detachment (represented by the purple line) merges just to the north-east of Kala, cartography of the detachment is less clear to the south-west of Chepa. We propose that the shear zone stop to the north-east of Chepa.

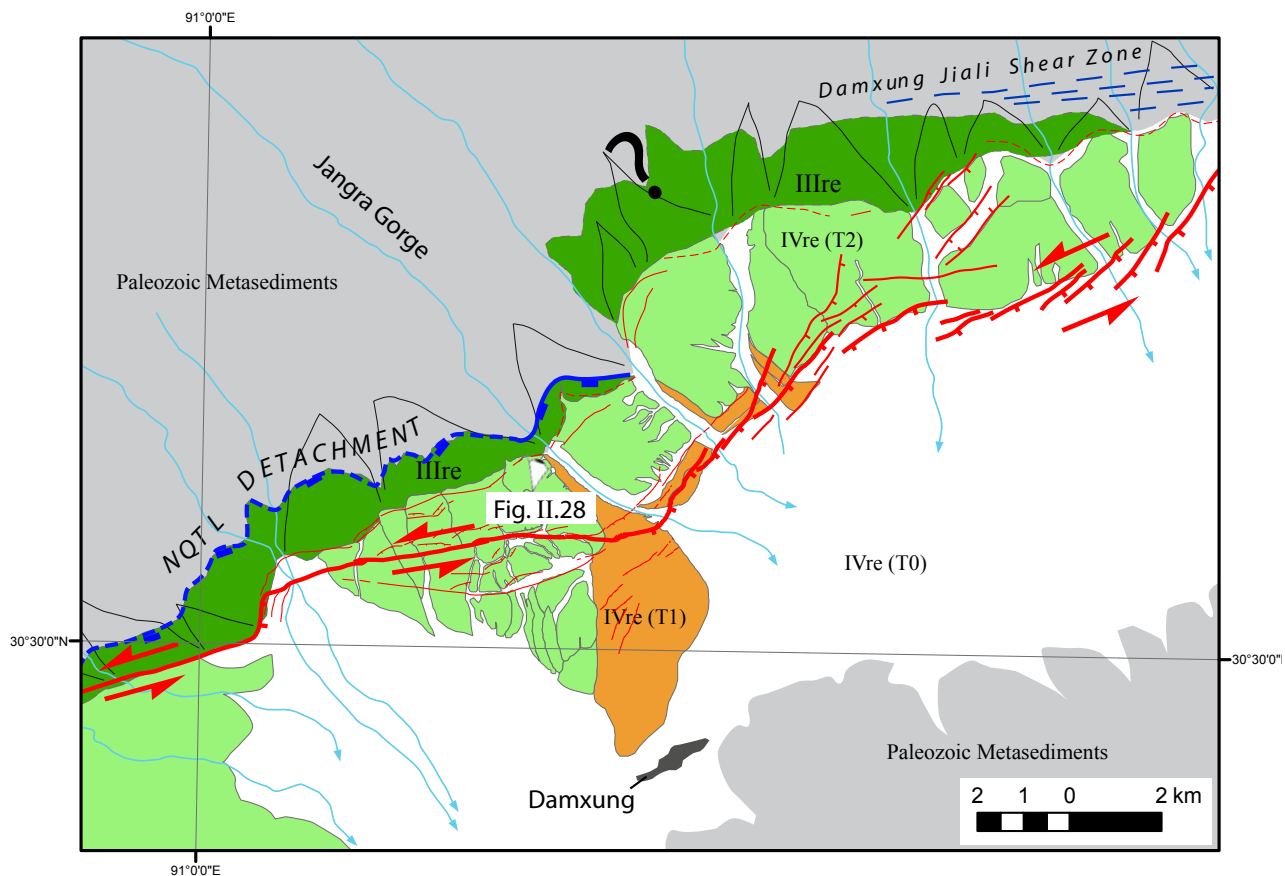


Figure II.26: Zoom on the Damxung Area (see location on figure II.22). Blue line indicated the Nyainqntanglha (NQTL) Detachment, (dashed line is inferred detachment). Sinistral ductile strike-slip of Damxung-Jiali Shear Zone is indicated. Junction between the detachment and the ancient strike slip is not known. See details on quaternary faulting and deposits in section 3.3.3 of the thesis.



Figure II.27: (a) Picture of the Nyainqntanglha detachment shear zone cut by the normal fault near the Kala Monastery. Structural measurements are shown Figure II.23a. Point of view is located by the small white eye on Figure II.25.

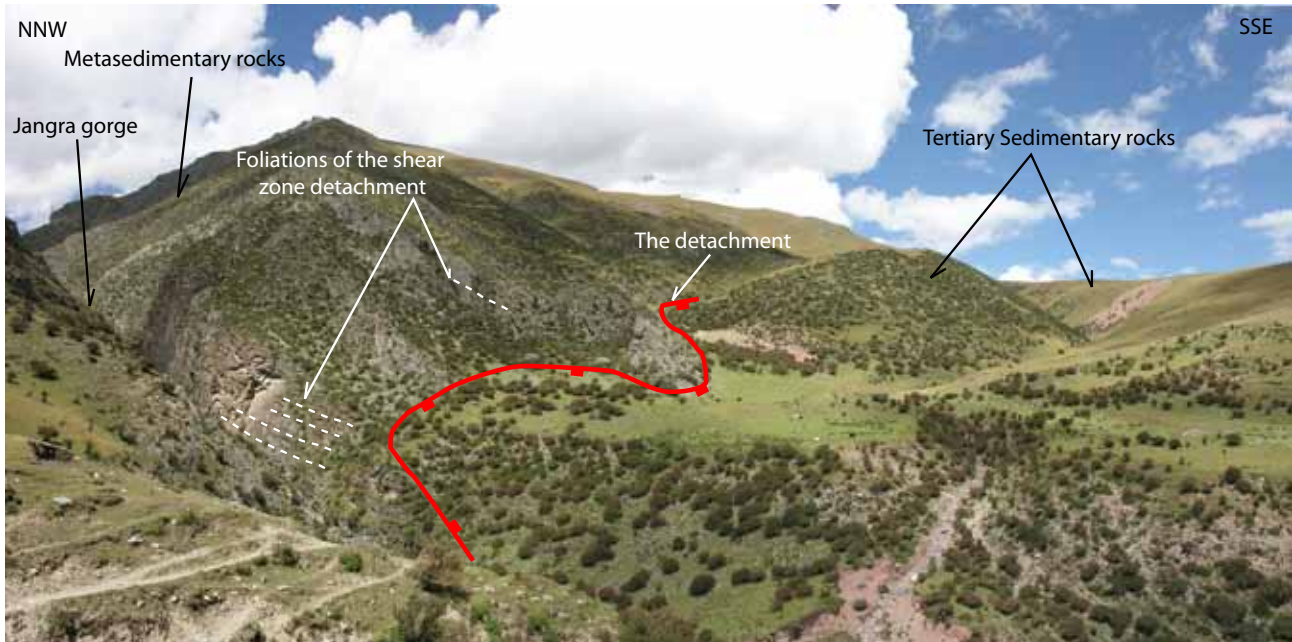


Figure II.28: Picture of the Nyainqntanglha detachment in the Jangra gorge area. Structural measurements are shown Figure II.23b. Point of view is located by the small white eye on Figure II.26.

2.3.1.4. Initiation de l'extension et vitesses d'exhumation le long du détachement.

Dans les vallées du Goring La et du Balum Chum La, les résultats des analyses $^{40}\text{Ar}/^{39}\text{Ar}$ sur biotite et feldspath et leur modélisation avec le *MDD model* par Harrison et al., 1995, suggèrent un refroidissement rapide du massif entre ~8 et 3 Ma au niveau de la zone mylonitique. Ce refroidissement semble commencer plus tôt à mesure que l'on s'éloigne du détachement en s'enfonçant dans le massif (Figure II.29). Ils ont ensuite utilisé un modèle thermomécanique qui permet de produire des histoires thermiques synthétiques comparables à celles obtenues avec le *MDD model*. Ainsi il est déduit que la vitesse de glissement le long de la faille est d'environ 3 mm/an pour un pendage de 63° , un angle largement supérieur à celui observé aujourd'hui. Harrison et al., 1995 expliquent une diminution du pendage depuis 8 Ma par la rotation du bloc en mur de faille exposé en surface. Kapp et al., 2005 ont proposé que le bloc en mur de faille n'a pas subi de rotation en se basant sur l'orientation de dykes granitiques datés à 8.7 Ma. Ces dykes sont interprétés comme étant injectés le long de directions potentielles de failles normales conjuguées et n'ayant pas subi de rotation depuis leur mise en place. Dans la suite du travail d'Harrison et al., 1995, en utilisant la même vitesse de 3 mm/an, Kapp et al., 2005 ont proposé un modèle plus complexe avec une rampe qui permet d'expliquer un pendage plus faible d'environ 30° pour la zone mylonitique (Figure II-30). Avec un tel pendage, la vitesse d'exhumation verticale serait de 1,5 mm/an et la vitesse d'extension est 2.6 mm/an.

La cartographie des failles actives et du détachement (Fig. II.22) suggère que l'on pourrait être en présence de deux générations de failles: dans un premier temps un décollement de direction NE-SW le long du Nyainqntanglha, puis dans un deuxième temps des failles N-S au niveau de Gulu et de Chepa connectées par un système de failles actives normales-décrochantes senestres (Armijo et al., 1986, 1989, Figure II.22) recoupant le détachement. Pour tester cette hypothèse nous avons prélevé des échantillons à l'Ouest de Chepa au mur du détachement et de la faille normale du Nyainqntanglha (Figures II.22, II.25 et II.31), pour comparer les histoires thermiques, les âges et vitesses d'exhumation avec ceux obtenus par Harrison et al., 1995 au niveau de Goring La et Balum La. D'autre part, des profils verticaux ont été échantillonnés au mur des failles de Gulu et Kumulalungpa pour tester si elles correspondent à un épisode d'extension plus récent. Stockli et al. 2002 indiquent que les données (U-Th)/He sur apatites permettent de déduire que l'extension et l'exhumation dans la zone de Gulu aurait commencé à ~7-5 Ma.

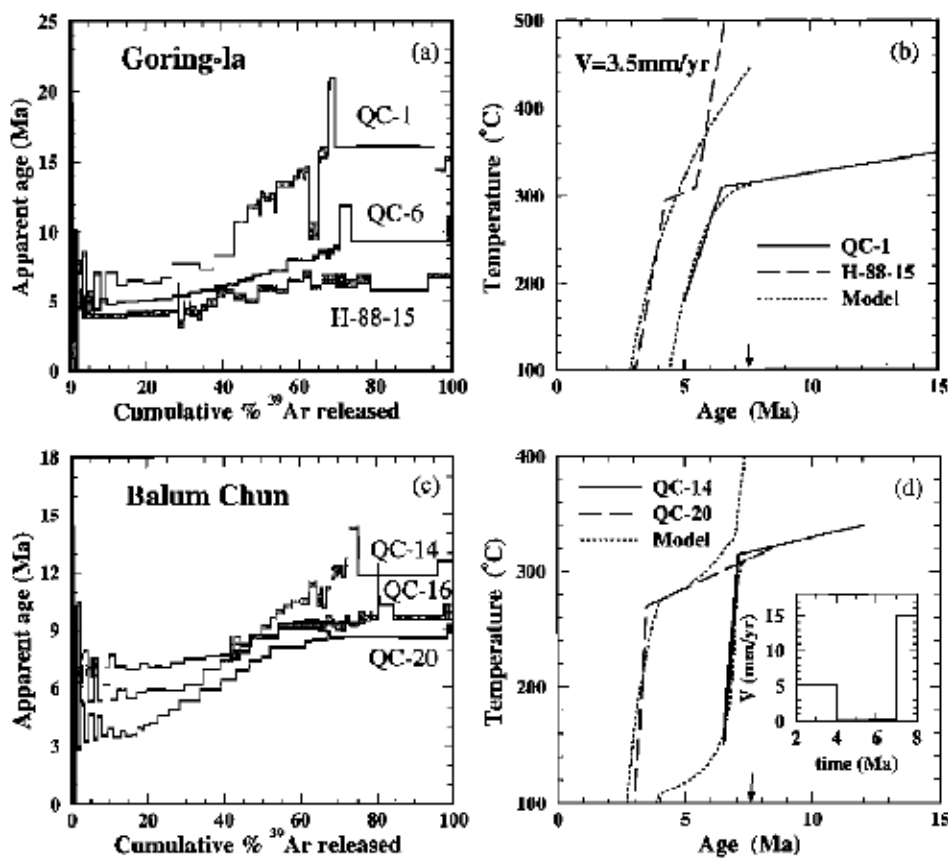


Figure II.29: (a) Goring-la age spectra and (b) isotopically derived thermal histories shown together with results from forward modeling to the thermal histories from the locations at the top and bottom of the valley. The model fit (dashed lines) assumes faulting began at 7.6 Ma (shown by the arrow) at a rate of 3.5 mm/yr. (c) Balm Chun age spectra and (d) isotopically derived thermal histories together with forward modeling results (dashed lines) for the top and bottom of the valley. The model fit is based on fault initiation at 7.6 Ma (shown by the arrow) with the slip history shown in the inset in Figure 16d. (From Harrison et al., 1995).

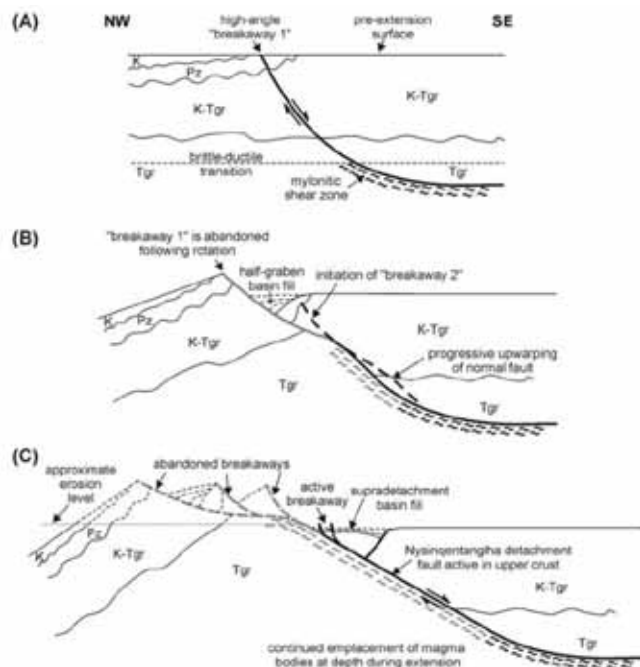


Figure II.30: Schematic cross-sectional model for the late Cenozoic extensional evolution of the NQTL massif and rift system, proposed by Kapp et al., 2005.

2.3.2. Les Ages $^{40}\text{Ar}/^{39}\text{Ar}$, résultats et interprétations

2.3.2.1. Le site de Chepa-Ouest

La zone d'échantillonnage

Le site de Chepa-Ouest correspond au site n°12 d'Armijo et al., 1986. D'après la carte de Kapp et al., 2005, il est situé dans la zone de cisaillement à proximité d'un granite du Miocene supérieur. Nous n'avons cependant observé aucune roche déformée et d'après notre cartographie le site se situe sous la zone de mylonites et au mur de la faille normale active (Figure II.25).

Quatre échantillons (T5Y9 à T5Y12) ont été collectés le long d'une coupe verticale entre 5300 et 4925 m d'altitude (Figure II.31 à II.34). La différence verticale maximale entre les échantillons est de 380 m et la distance horizontale maximale de 580 m. Tous les échantillons ont fait l'objet de datations $^{40}\text{Ar}/^{39}\text{Ar}$ sur biotite, et sur feldspath pour les échantillons T5Y10 et T5Y12. L'échantillon T5Y9 (4920 m) est un granite à biotites et feldspaths en dent de cheval (Figure II.34). Les échantillons T5Y10 (5020 m), T5Y11 (5140 m), et T5Y12 (5304) font partie d'un même granite à biotite à texture équante.

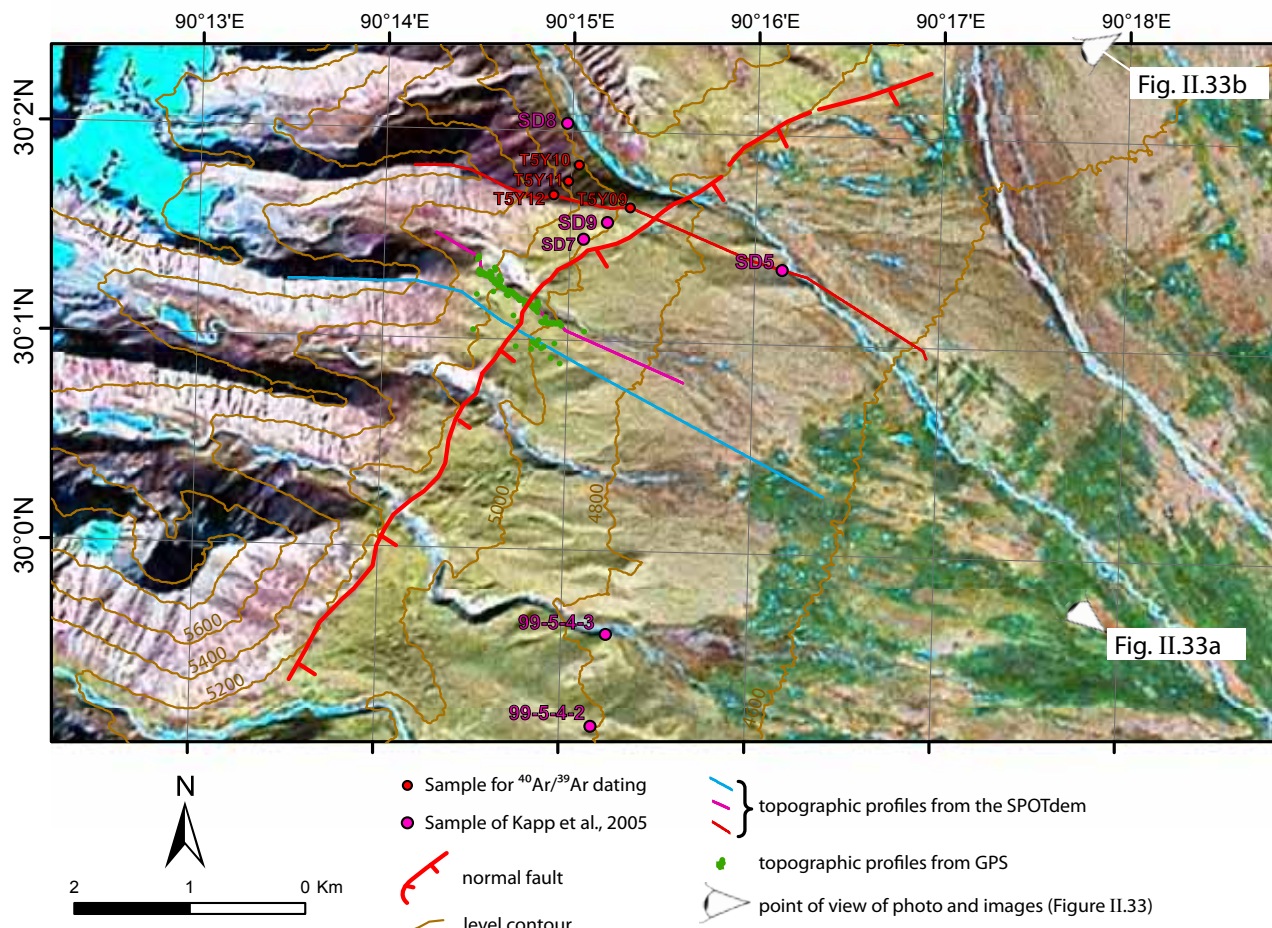


Figure II.31: Map of the West-Chepa sampling site. Samples for $^{40}\text{Ar}/^{39}\text{Ar}$ dating and samples from Kapp et al., 2005 are localized on the Landsat satellite image. Traces of the topographic profiles (Figure II.32) are represented. Contour levels are drawn from the SPOTdem. See also Figure 48a for comparison with the short-term study.

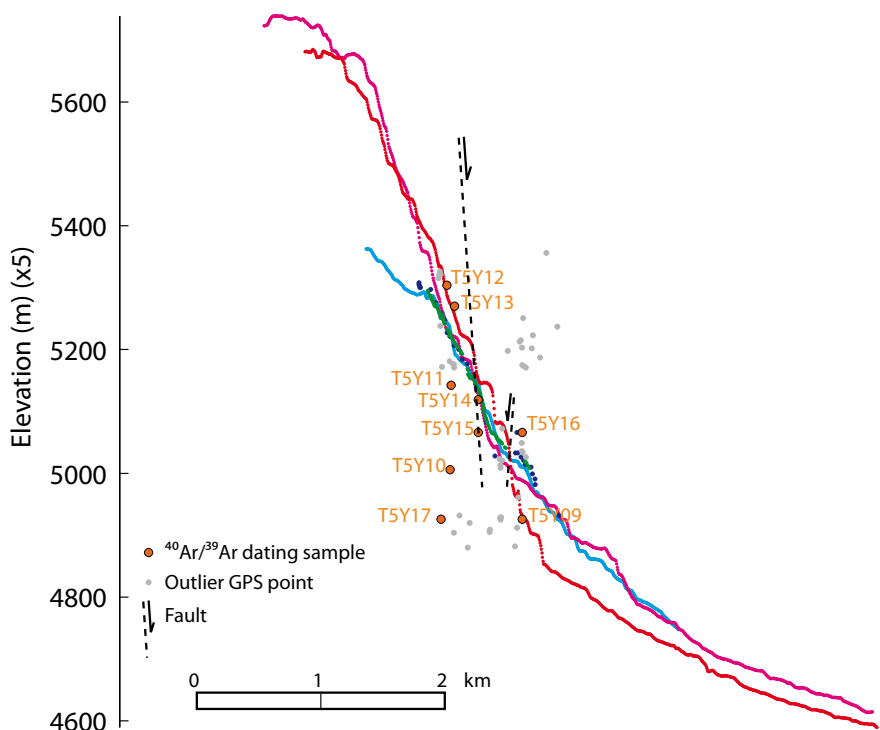


Figure II.32: Topographic profiles, in the West-Chepa area, across the fault trace and passing through the samples (trace of the profiles are represented on the Figure II.31). Outliers from the GPS points are corrected with the SPOTdem. See also Figure 49a for comparison with the short-term study.

The Chepa Site - Sampling for Ar/Ar and Be-Al dating

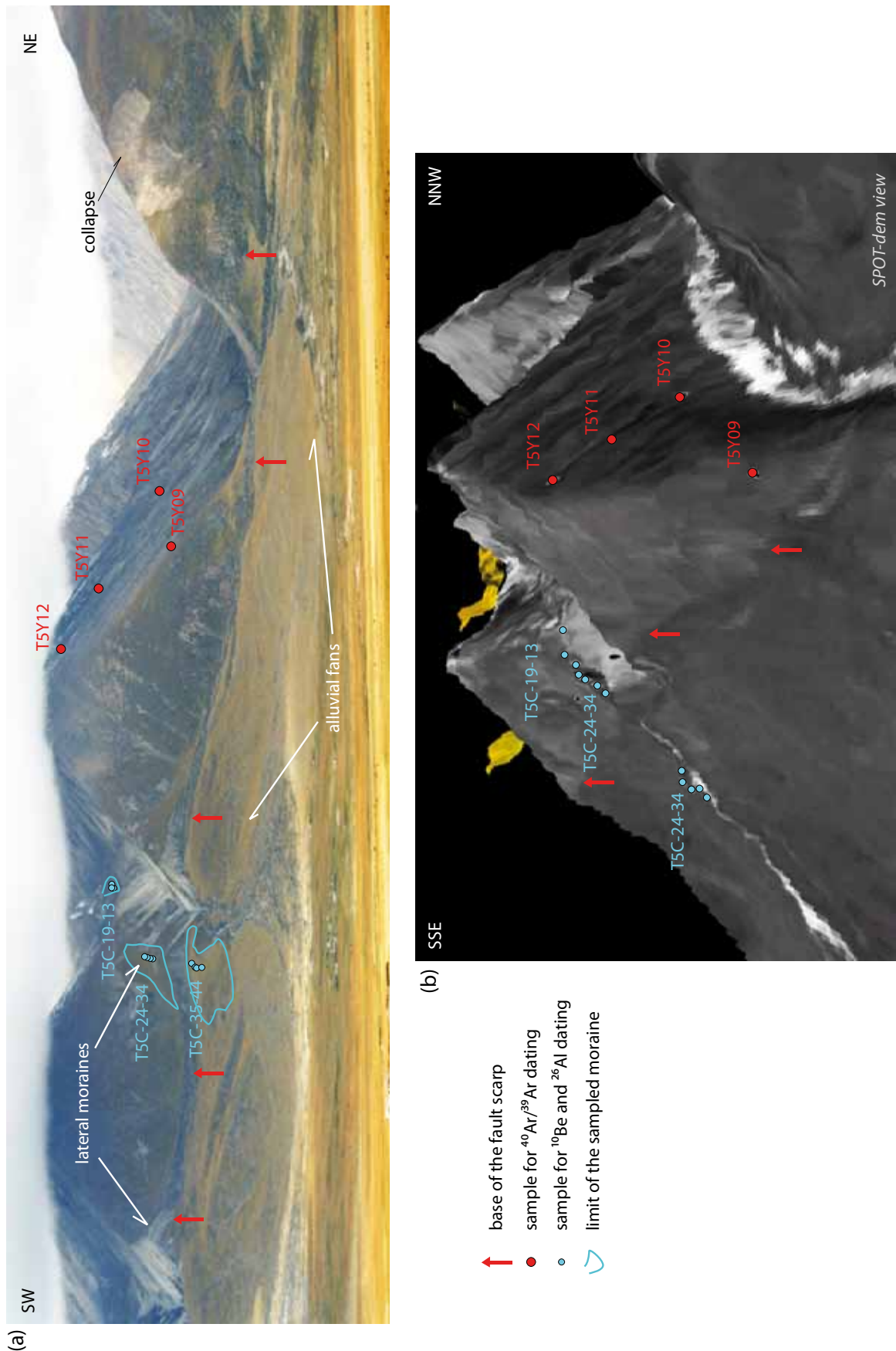


Figure II.33: (a) Field view and (b) 3D picture (from SPOTdem) of the West-Chepa sampling site. See also Figures 48a and 49b for comparison with the short-term study.

Samples of the Chepa site

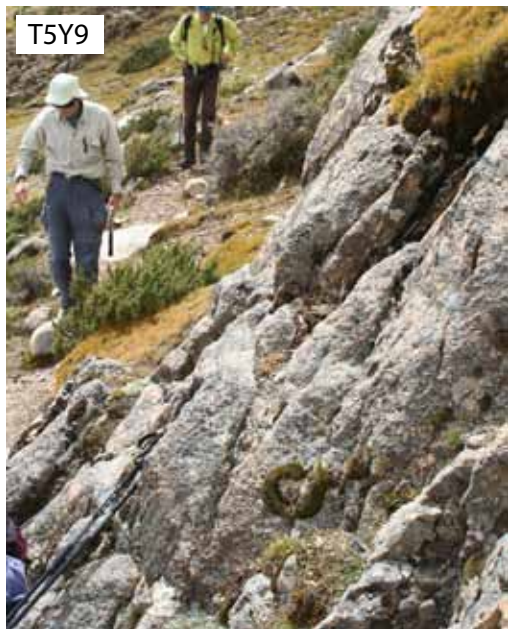


Figure II.34: Pictures of the dated granite in the West-Chepa area.

Les âges

Les spectres d'âges de biotite ne permettent pas de déterminer un âge plateau. Néanmoins les âges déterminés avec les isochrones inverses sont assez bien définis et sont utilisées pour déterminer les âges des échantillons (Table II.3, Figure II.35 et II.36).

L'analyse des feldspaths de l'échantillon le plus élevé en altitude (T5Y12, 5304 m) montre un spectre d'âge perturbé mais relativement plat, avec de nombreux âges compris entre 10 et 16 Ma entre 10 et 90% du gaz libéré (Figure II.36e, f). L'âge de fusion totale est 13.43 ± 0.37 Ma, presque identique à l'âge isochrone inverse : 13.12 ± 0.99 Ma. Cet âge de 13.4 Ma sera considéré comme l'âge moyen. La biotite correspondante a un âge de 10.11 ± 0.59 Ma. Pour l'échantillon suivant (T5Y11, Figure II.15c), l'âge biotite déterminé par l'isochrone inverse est de 10.10 ± 0.17 Ma. Les biotites des échantillons T5Y10 et T5Y9 (Figure II.35a et b) indiquent des âges d'isochrone inverse quasi identiques, respectivement 8.18 ± 0.40 Ma et 8.37 ± 0.22 Ma. Ils sont séparés par une altitude de 80 m, la plus petite distance par rapport aux autres échantillons, eux séparés de 150 m.

Les feldspaths de l'échantillon T5Y10 fournissent des résultats préliminaires. Ici sont présentés avec les résultats d'analyses et les tests effectués avec le *MDD model* (Figure II.36a-d et Table II.3). Les feldspaths de l'échantillon T5Y10 montrent des âges globalement plus vieux que les biotites correspondantes, entre 10 et 30 Ma (Figure II.36d). Cependant certaines parties du spectre n'ayant pas de signification géologique peuvent être ignorées. Premièrement, le début du spectre (entre 0 et ~5 % d' ^{39}Ar cumulé) indique des excès d'argon importants et ne seront pas pris en compte. Ensuite, la diminution des valeurs de $\log(r/r_0)$ Figure II.16c, indique que la diffusion dans les feldspaths ne correspond plus aux paramètres de diffusion obtenus avec le *MDD model*, donc cette partie du spectre, après 50% voire même 40% d' ^{39}Ar cumulé, ne sera pas prise en compte non plus pour la reconstitution de l'histoire thermique. Il nous reste donc les âges entre 10 et 15 Ma, toujours incohérents par rapport aux âges de biotites. Ces âges plus anciens ne sont pas non plus expliqués par des propriétés de forte rétention des feldspaths car la valeur de l'énergie d'activation indiquée par le *MDD model* est seulement de 37.3 kcal/mol.

La routine « autoage-mon » de Lovera a été utilisée pour reconstituer l'histoire thermique afin de vérifier si une histoire cohérente est obtenue. Un refroidissement de ~250 à ~170°C a lieu entre 20 et 15 Ma, suivit d'une stabilisation de la température jusqu'à 10 Ma (Figure II.36d). Comparons ce chemin température-temps (T-t) avec l'âge de biotite du même échantillon. Si une température de

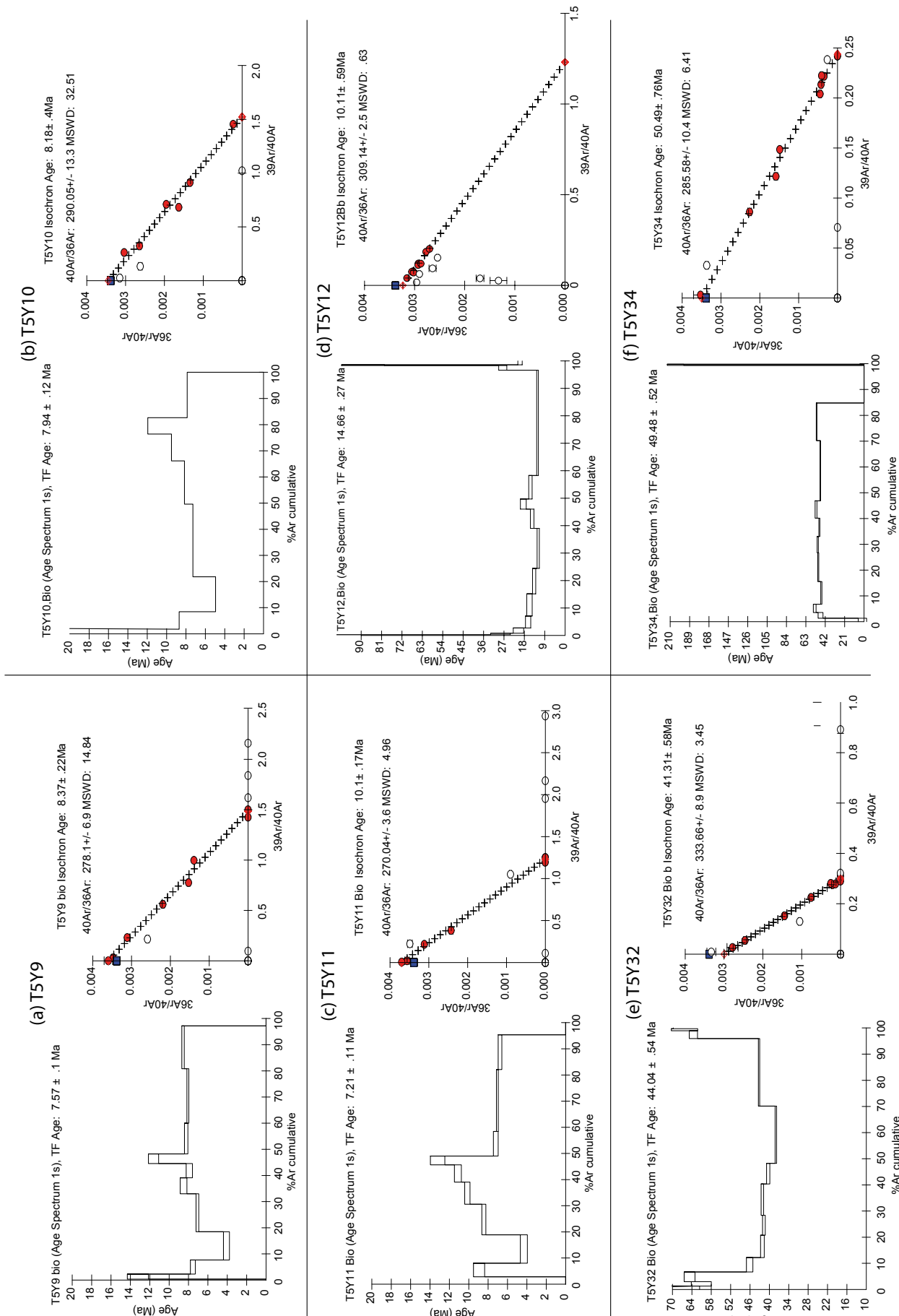


Figure II.35: Biotite $^{40}\text{Ar}/^{39}\text{Ar}$ data from the West-Chepa and the Kumulalungma sites. All data are listed in table II.3. Steps used for plateau age calculation are shown by the arrow. For inverse isochrone plots, empty symbols were not used in the regression calculation.

fermeture de 320 ± 40 °C est considérée (Dodson 1973, Harrison et al., 1979), le point représenté par la biotite n'appartient pas à ce chemin T-t (Figure II.16d). Ce chemin température-temps n'est pas non plus en accord avec ceux d'Harrison et al., 1995, situés plus au nord-ouest (Figure II.36d). Il semble donc avoir une signification géologique limitée. Le *MDD model* ne semble pas bien s'appliquer ici.

Nous nous tiendrons donc ici aux données d' $^{40}\text{Ar}/^{39}\text{Ar}$ sur biotites pour fournir une interprétation cohérente. Contrairement aux feldsaphs, les biotites des échantillons T5Y9, T5Y10 et T5Y11 sont compatibles avec les histoires thermiques proposées par Harrsion et al., 1995 (Figure II.29 et II.36d). D'autre part, la relation âge-altitude (Figure II.37) montre une vitesse d'exhumation verticale apparente de ~0.13 mm/an entre ~10 et 8 Ma. Harrison et al., 1995 ont montré que l'activité du détachement a été initiée à 8 Ma, et une vitesse d'exhumation verticale de 1.5 mm/an entre 8 et 3 Ma est deduite de ses données. Ces âges $^{40}\text{Ar}/^{39}\text{Ar}$ sur biotite, sont plus anciens que l'âge d'initiation déterminé par Harrison et al., 19995 et la vitesse déduite à partir de nos données, est largement inférieure à 1.5 mm/an. Ces données indiquent donc qu'entre 8 et 10 Ma le détachement du Nyainqntanglha n'affectait pas la région à l'Ouest de Chepa.

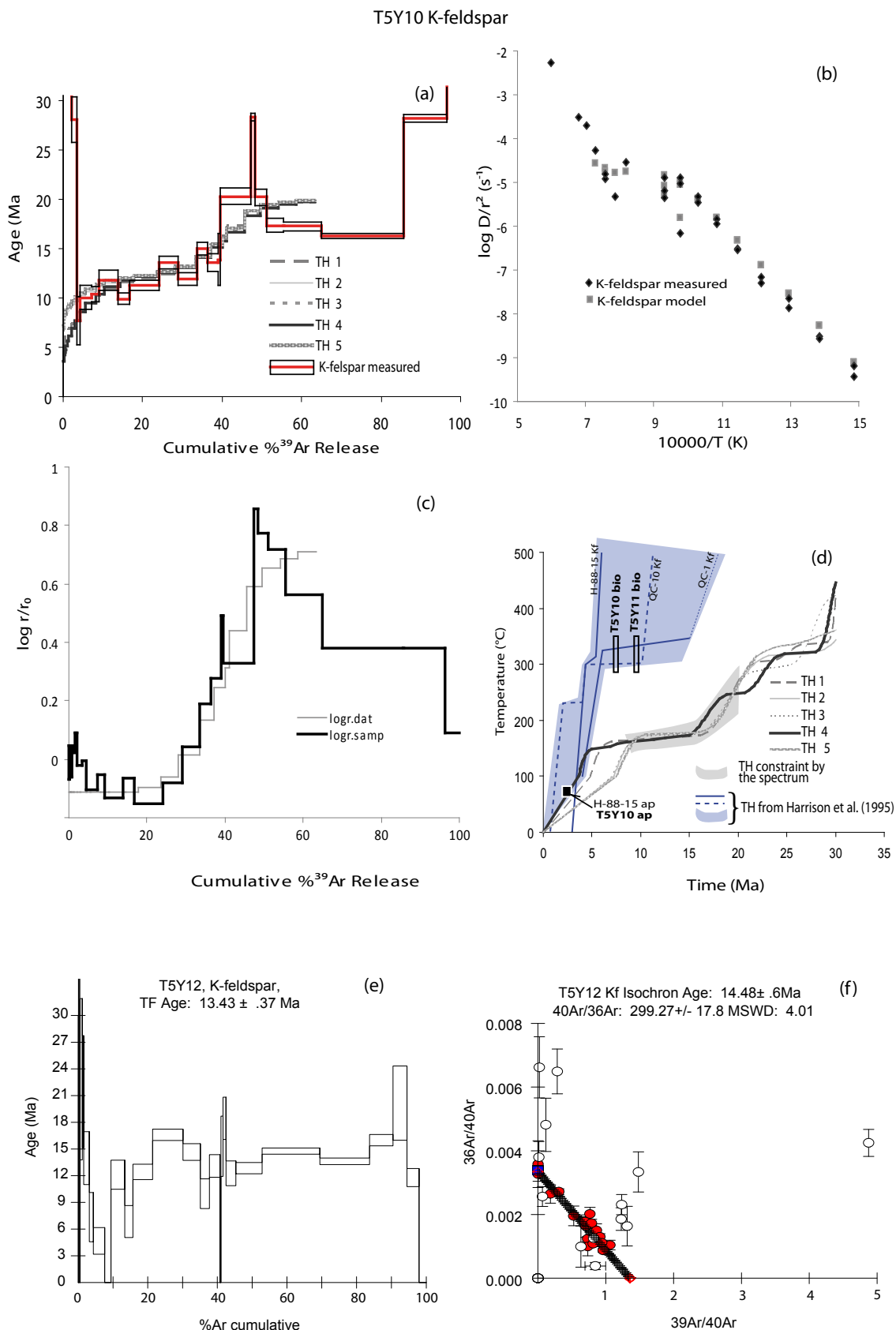


Figure II.36: ⁴⁰Ar/³⁹Ar results for K-feldspars of T5Y10 and T5Y12, West-Chepa sampling site: (a) Measured age spectra and synthetic age spectra calculated with the MDD model for T5Y10, (b) Arrhenius plot for T5Y10, (c) $\log(r/r_0)$ plot for T5Y10, (d) cooling history for T5Y10, biotite T-t datum of T5Y10 is plotted, also showing thermal history from samples of Harrison et al., 1995 (QC-1, QC-10 and QC-20), (e) age spectrum of T5Y12, and (f) inverse isochrone plots for T5Y12, empty symbols were not used in the regression calculation. All data are listed in table II.3.

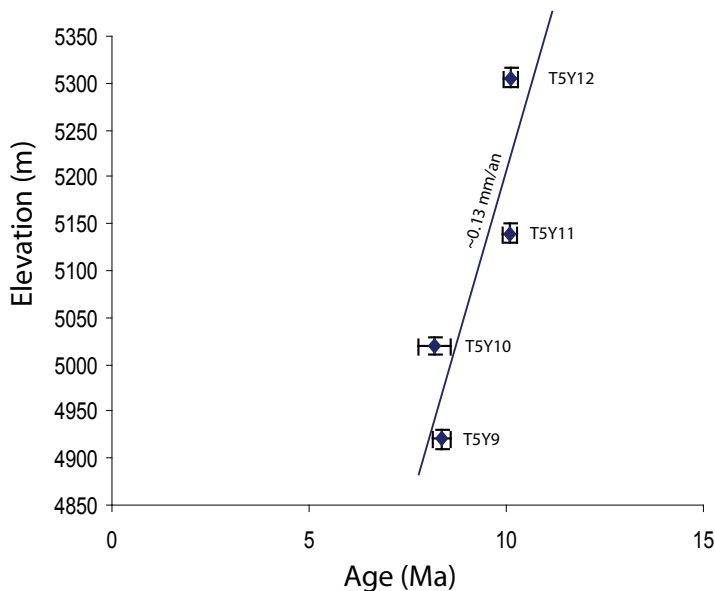


Figure II.37: Plot of biotite $^{40}\text{Ar}/^{39}\text{Ar}$ age versus elevation in the West-Chepa sampling site

2.3.2.2. Le site de Kumulalungpa

Ce site d'échantillonnage au Sud de Chepa, est situé au mur de la faille normale active Ouest du graben N-S de Yangbajain, Figure II.25 (un séisme de magnitude 6.6 a eu lieu le 06/10/2008 sur cette faille). Le but ici est de voir si cette faille normale est très récente ou si elle a une origine miocène comme au front du massif du Nyainqntanglha. Les biotites de deux échantillons de leucogranite ont été datées. Les échantillons T5Y32 et T5Y34 indiquent des âges eocènes (Figure II.35d et e, Table II.3). T5Y32 montre un âge isochrone inverse de 41.71 ± 0.61 Ma en accord avec l'âge donné par un « sub-plateau » du spectre de 41.74 ± 0.85 Ma. L'autre échantillon T5Y34 donne un âge plateau à 48.73 ± 0.70 Ma dans les mêmes marges d'incertitude que l'âge isochrone inverse de 50.49 ± 0.76 Ma. Ces âges « anciens » correspondent certainement au refroidissement après la mise en place des granites du batholithe du Gangdese et montrent l'absence d'un épisode magmatique Miocène. Ils montrent aussi l'absence d'un événement thermique supérieur à 300°C (correspondant à la température de fermeture des biotites) après l'événement magmatique du Gangdese. Ceci implique que l'exhumation le long de cette faille n'est pas suffisante pour mettre l'isotherme 300°C à l'affleurement. En prenant un gradient géothermique de $30^\circ\text{C}/\text{km}$, l'isotherme 300°C est située vers 10 km de profondeur, le site a donc subi moins de 10 km d'exhumation depuis ~ 50 Ma, ce qui est beaucoup moins important que l'exhumation au mur du détachement (~ 15 km d'exhumation). Ceci est aussi montré par la présence des formations volcaniques des Linzizong qui auraient été érodées si l'exhumation avait été plus importante. En suposant que l'âge d'initiation de l'exhumation

au niveau du massif du Nyainqntanglha de 8 Ma pourrait être un âge maximal pour l'initiation de l'exhumation au niveau de la faille de Kumulalungpa, avec 10 km d'exhumation maximale, une vitesse d'exhumation verticale minimale de ~1.2 mm/an peut être une indication significative de la vitesse de cette faille.

2.3.2.3. Le site de Gulu

Description succincte de la zone d'échantillonnage

Quatre échantillons d'une coupe verticale ont été datés ici (Figure II.39 à II.41). Les trois plus élevés en altitude (T5G2, T5G3 et T5G5) à $\text{l}^{40}\text{Ar}/\text{l}^{39}\text{Ar}$ sur biotites, et le moins élevé, ne contenant pas de biotite (T5G8) à $\text{l}^{40}\text{Ar}/\text{l}^{39}\text{Ar}$ sur muscovite. Les échantillons sont situés entre 5340 et 4820 m d'altitude (Figure II.19). T5G2 et T5G5 sont séparés par une distance verticale de ~450 m et une distance horizontale de ~400 m. Avec l'échantillon le plus bas, T5G8, la différence verticale maximum est de 520 m et la différence horizontale de ~1300 m.

Les trois échantillons les plus élevés appartiennent à la même granodiorite (Figure II.42). Les échantillons T5G3 et T5G5 sont situés à proximité de notable filons hypermagnésiens (riches en biotites) de diamètre inférieur à 1 m, dont l'influence thermique semble être limitée. L'échantillon T5G8 est un microgranite à muscovite.

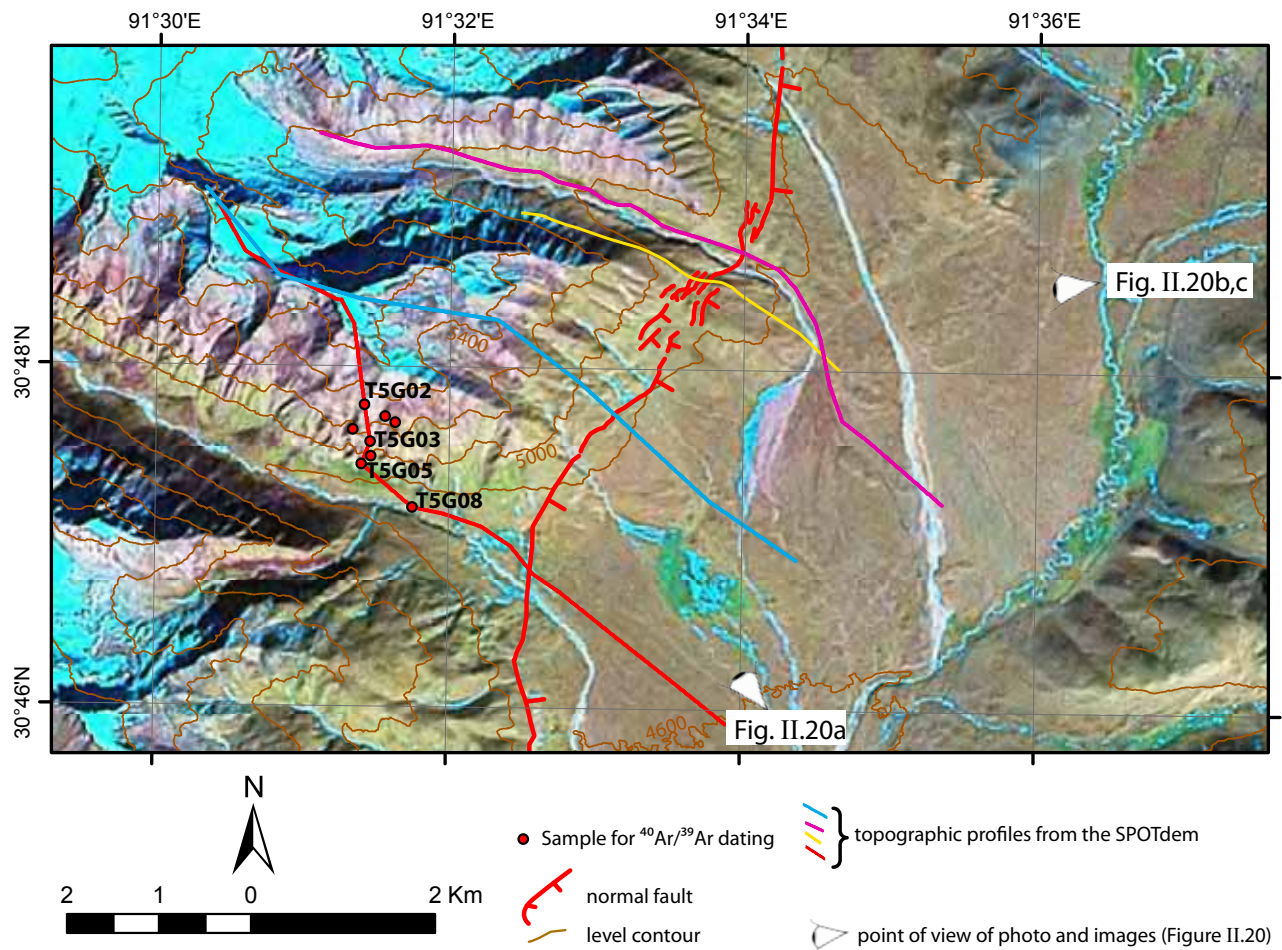


Figure II.38: Map of the Gulu sampling site. Samples for $^{40}\text{Ar}/^{39}\text{Ar}$ dating are localized on the Landsat satellite image. Traces of the topographic profiles are represented (Figure II.20). Contour levels are drawn from the SPOTdem. See also Figure 56b for comparison with the short-term study.

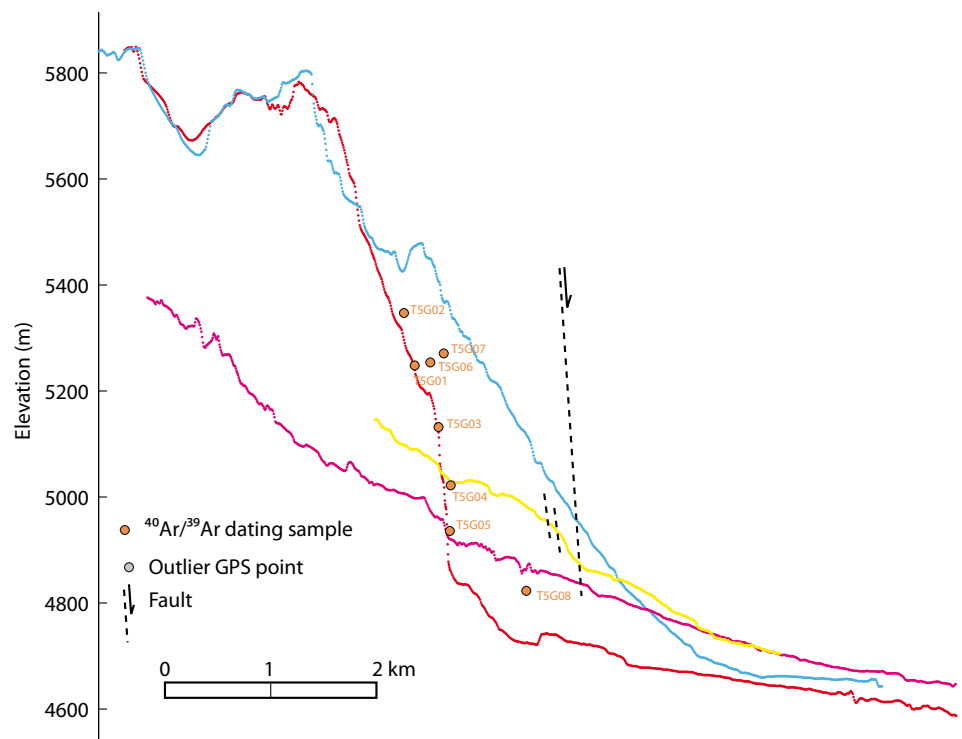
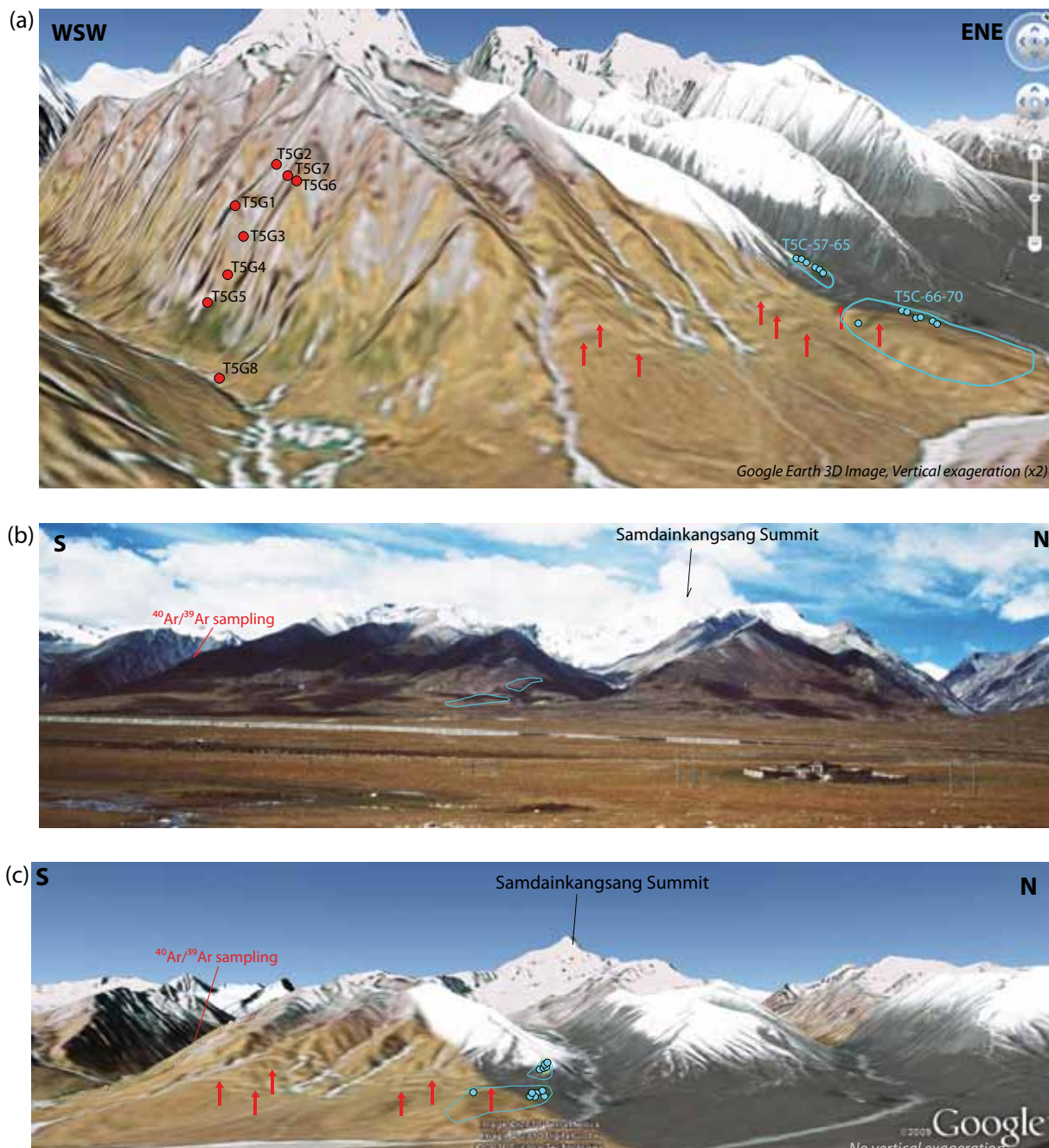


Figure II.39: Topographic profiles in the Gulu region across the fault trace and passing through the samples (trace of the profiles are represented on the Figure II.19). See also Figure 57a for comparison with the short-term study.

Gulu site - sampling for $^{40}\text{Ar}/^{39}\text{Ar}$ and $^{10}\text{Be}-^{26}\text{Al}$ dating



- ↑ base of the fault scarp
- sample for $^{40}\text{Ar}/^{39}\text{Ar}$ dating
- sample for ^{10}Be and ^{26}Al dating
- ↙ limit of the sampled moraine

Figure II.40: 3D picture (from Google Earth) (a, c) field view (b) of the Gulu sampling site. See also Figures 56b and 57a for comparison with the short-term study.

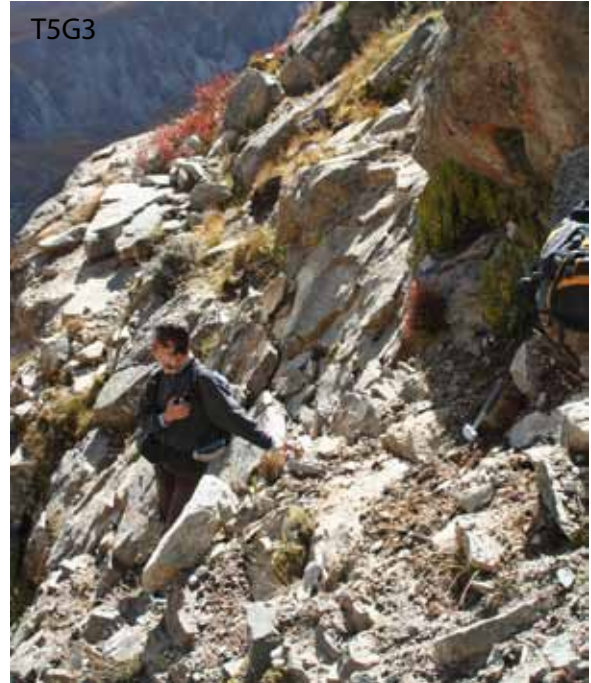
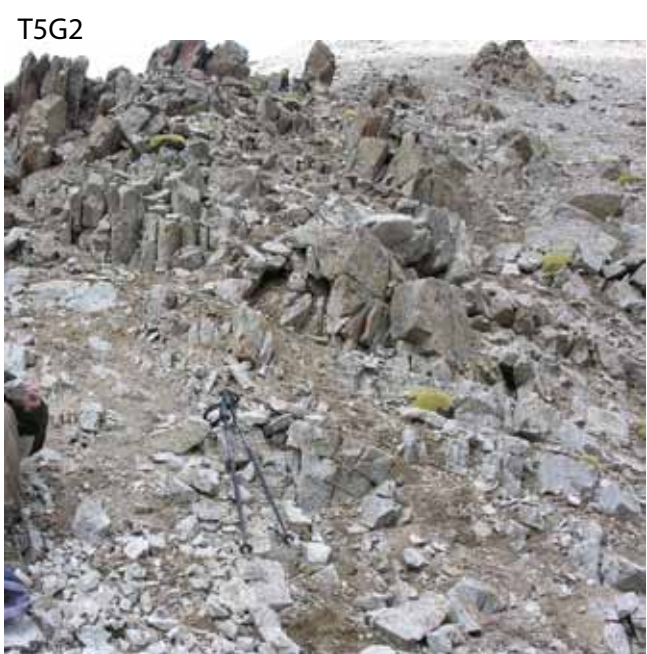


Figure II.41: Pictures of the dated granite in the Gulu area.

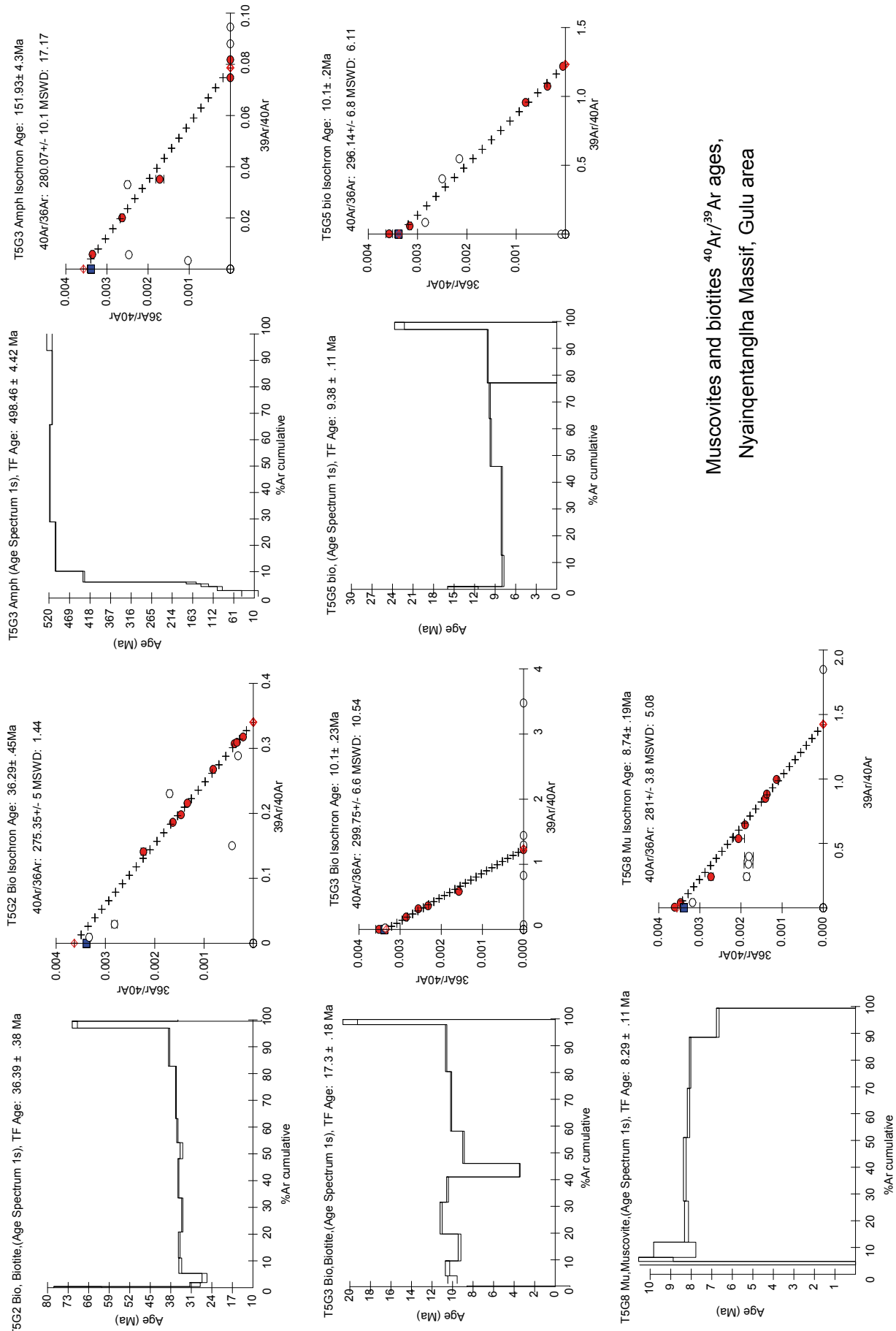


Figure II.42: Mica $^{40}\text{Ar}/^{39}\text{Ar}$ data from the Gulu site. All data are listed in table II.3. For inverse isochrone plots, empty symbols where not used in the regression calculation.

Les âges

L'échantillon le plus élevé en altitude (T5G2, 5335 m) montre un âge $^{40}\text{Ar}/^{39}\text{Ar}$ sur biotites (âge plateau) de 35.68 ± 0.41 Ma en accord avec l'âge isochrone inverse 36.39 ± 0.38 Ma (Figure II.42, Table II.3). L'âge $^{40}\text{Ar}/^{39}\text{Ar}$ sur biotites de l'échantillon suivant (T5G3, 5100 m), déterminé grâce à l'isochrone inverse, est beaucoup plus jeune, 10.10 ± 0.23 Ma. Environ 210 m plus bas, l'échantillon T5G5 (4885 m) a le même âge (sur biotites), 10.10 ± 0.20 Ma (isochrone inverse).

Enfin, l'échantillon le plus bas (T5G08, 4823 m) a un âge $^{40}\text{Ar}/^{39}\text{Ar}$ sur muscovite de 8.14 ± 0.10 Ma (âge plateau) qui correspond avec l'âge isochrone inverse, 8.74 ± 0.19 Ma.

La différence d'âge de mica entre l'échantillon le plus haut T5G2 et les trois autres échantillons plus de 230 m plus bas, est importante : elle varie d'environ 36 Ma pour T5G2 à des âges entre 7 et 10 Ma pour les autres échantillons (Fig. II-33). Ce saut en âge signifie qu'à ~ 36 Ma, l'échantillon T5G2 a franchi l'isotherme correspondant à la température de fermeture de la biotite, soit $\sim 300^\circ\text{C}$, alors que les autres échantillons subissaient encore des températures supérieures. Ensuite, avant, 7-10 Ma, ces échantillons ont franchi l'isotherme 300°C . Ce passage au dessus de cette isotherme peut être expliqué de trois manières : 1/ un événement tectonique local tel que l'activation d'une faille normale qui aurait provoqué un soulèvement avant 7-10 Ma, 2/ la surrection régionale du bloc de Lhasa qui a eu lieu vers 20 Ma, 3/ des intrusions magmatiques. La dernière solution n'est pas à exclure dans la mesure où des intrusions hypermagnésiennes sont observées à proximité des échantillons T5G3 et T5G5. Cependant, aucune intrusion n'est observée vers l'échantillon le plus bas (T5G8) qui présente aussi un âge jeune. Si on exclut l'influence des intrusions magmatiques dans la zone d'échantillonnage, ces données permettent donc d'envisager qu'une accélération de l'exhumation aurait commencé avant 10 Ma.

Cette exhumation est bien illustrée par la Figure II.43, montrant la relation âge-altitude entre les échantillons. T5G3 et T5G5 peuvent être utilisés pour fournir une vitesse d'exhumation apparente verticale minimale, en prenant les bornes minimale (9.87 Ma) et maximale (10.3 Ma) des âges sur T5G3 et T5G5 respectivement. Les deux échantillons étant séparés de 215 m, une vitesse d'exhumation verticale apparente minimale de 0.5 mm/an est déduite. Ainsi, la vitesse d'exhumation verticale apparente est multipliée par 50, on passe d'une vitesse de ~ 0.01 mm/an avant 10 Ma, à une vitesse d' ~ 0.5 mm/an après 10 Ma. Cette donnée devra être confirmée par l'analyse d'échantillons supplémentaires sur le profil vertical. Il semble quand même clair qu'il y ait une accélération notable à partir de 10 Ma. Une telle augmentation de la vitesse peut être expliquée par l'activité d'une faille

qui se serait initiée vers 10 Ma. Comparé aux âges (U-Th)/He de Stockli et al., 2002 qui montrent une initiation de l'exhumation entre 5 et 7 Ma, ces nouvelles données repoussent encore un peu plus l'âge d'initiation de la faille normale du demi-graben de Gulu.

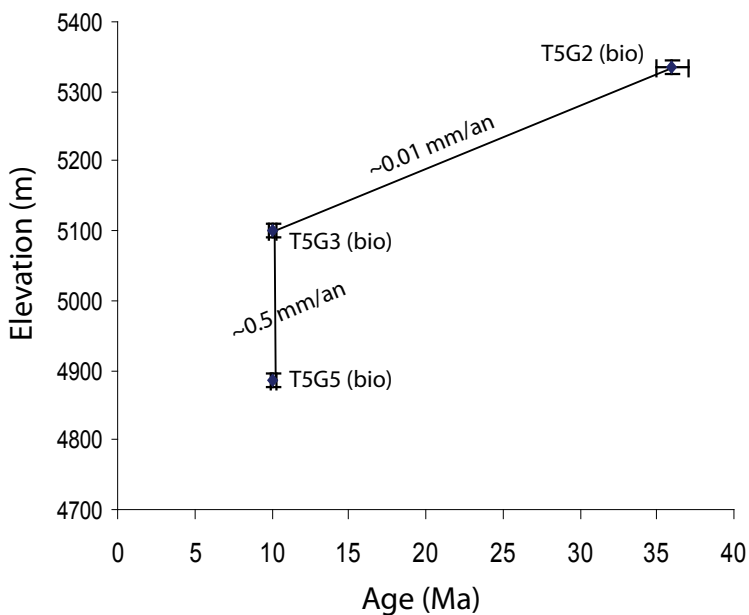


Figure II.43: Plot of biotite $^{40}\text{Ar}/^{39}\text{Ar}$ age versus elevation in the Gulu sampling site.

2.3.3. Les Ages (U-Th)/He

Nous présentons ici des données préliminaires de datation d'apatites à l'(U-Th)/He.

Pour le site de Gulu, les âges de T5G2, T5G3 et T5G5 sont compris entre ~1.5 et ~2.2 Ma (du plus haut au plus bas) et montrent une bonne reproductibilité (Table II.4 et Figure II.44). Au contraire l'échantillon T5G8 montre des répliques d'âges très différents compris entre 14.4 et 4.4 Ma. Ces âges jeunes sont en accord avec les âges de Stockli et al., 2002 montrant des âges aussi jeunes que 1.7 Ma dans la région de Gulu. Sans prendre en compte l'échantillon T5G8 qui montre des problèmes de reproductibilité, une vitesse d'exhumation préliminaire de ~0.6 mm/an peut être proposée sur les trois échantillons les plus élevés (Figure II.44).

Pour le site de Chepa-Ouest, T5Y9, T5Y10 et T5Y11 ont été daté à l'(U-Th)/He. La reproductibilité est moins bonne sur ce groupe d'échantillons et les répliques les plus jeunes sont utilisées pour déterminer l'âge moyen de chaque échantillon (Table II.4). En relation avec l'altitude, ces trois âges donnent une indication de la vitesse d'exhumation verticale apparente à ~0.2 mm/an entre 2.6 et 4.5 Ma (Figure II.45).

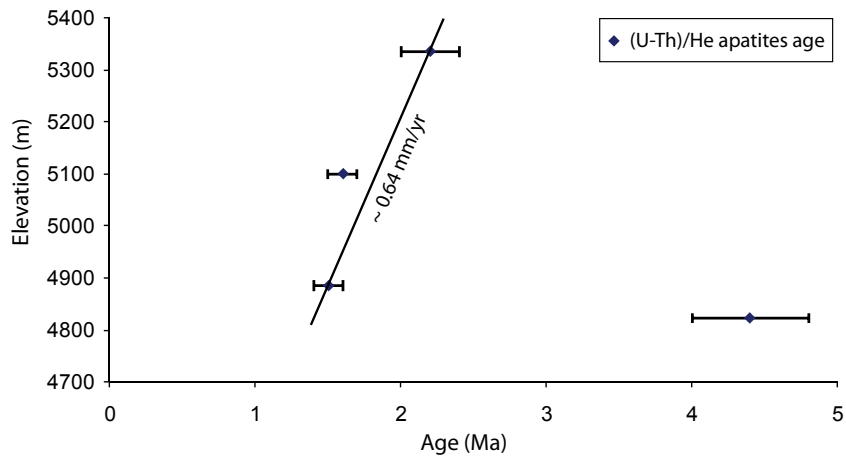


Figure II.44: Plot of (U-Th)/He apatite ages versus elevation in the Gulu sampling site.

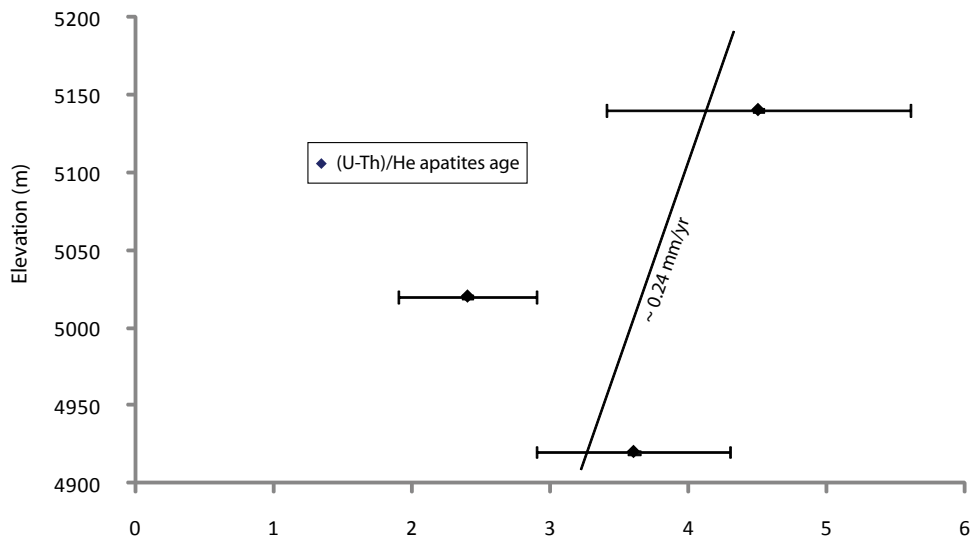


Figure II.45: Plot of (U-Th)/He apatite ages versus elevation in the West-Chepa sampling site.

2.3.4. Discussion - Conclusion

Au mur de la faille de Kumulalungpa, aucun évènement thermique supérieur à 300°C depuis l'évènement magmatique du batholithe du Gangdese n'a été observé indiquant une exhumation inférieure de 10 km depuis le refroidissement du granite échantillonné. Si l'on suppose une initiation de la faille de Kumulalungpa à 8 Ma maximum, la vitesse minimum d'exhumation verticale apparente est de 1.2 mm/an.

A Chepa-Ouest, les deux spectres d'âges de feldspaths (échantillons T5Y10 et T5Y12) fournissent des âges avec d'importants excès d'argon, qui sont difficilement comparables avec les analyses des autres minéraux dans les mêmes échantillons et avec les histoires thermiques présentées dans la littérature. Dans ce cas, le *MDD model* ne semble pas applicable. Les âges $^{40}\text{Ar}/^{39}\text{Ar}$ sur biotites sont plus cohérents et sont utilisés pour extraire des informations sur les vitesses d'exhumation. Ils permettent donc de déterminer une vitesse d'~0.13 mm/an entre ~10 et 8 Ma (Figure II.46). D'autre part, les résultats préliminaires des datations (U-Th)/He sur apatite obtenus sur les mêmes échantillons fournissent une vitesse de ~0.2 mm/an entre ~4.5 et 2.5 Ma. En supposant qu'entre aujourd'hui et 8 Ma, cette vitesse de 0.2 mm/an soit restée constante, ~5 km de roche aurait été exhumés. Avec un gradient géothermique de 30°C/km, ces 5 km correspondent à une isotherme de 150°C, qui est en dessous de la température de l'isotherme 300°C qui correspondant à la température de fermeture des biotites. Or nos analyses $^{40}\text{Ar}/^{39}\text{Ar}$ sur biotite montrent que cette isotherme est exhumée à l'heure actuelle ce qui correspond à ~10 km d'exhumation depuis 10-8 Ma. Ceci implique une vitesse de ~1.2 mm/an au niveau de ce site entre 8 Ma et l'actuel. Or nous avons vu que les données d'(U-Th)/He montrent une vitesse largement inférieure entre ~4.5 et 2.5 Ma. Ceci peut s'expliquer ainsi:

- les données d'(U-Th)/He ne sont pas suffisantes pour déterminer une vitesse cohérente et des analyses complémentaires sont nécessaires,
- si ces données préliminaires sont représentatives de l'ensemble de la zone et la vitesse d'exhumation a varié entre 8 et 4.5 Ma et/ou entre 2.5 et 0 Ma, ceci implique donc plusieurs phases d'exhumation au niveau du site de Oues-Chepa.

Au niveau de la faille du graben de Gulu, l'échantillon T5G8, situé à 1.3 km des autres échantillons en distance horizontale, semble montrer un comportement thermique différent. Cet échantillon n'est donc pas pris en compte dans la détermination des vitesses d'exhumation. A partir des âges $^{40}\text{Ar}/^{39}\text{Ar}$ sur biotite des trois autres échantillons, une initiation de l'exhumation à 10 Ma a été déterminée.

Cet âge est plus ancien que l'âge proposé par Stockli et al., 2002 (5-7 Ma, (U-Th)/He sur apatites). De plus, la vitesse d'exhumation est passé de ~0.01 mm/an à 0.5 mm/an à partir de 10 Ma. D'autre part, les âges (U-Th)/He sur T5G2, T5G3, et T5G5 montrent que la vitesse d'exhumation verticale apparente entre ~2 et ~1.5 Ma est probablement de ~0.6 mm/an. Si cette vitesse est restée constante depuis l'initiation de l'exhumation jusqu'à aujourd'hui, ~6 km aurait été exhumés en 10 Ma, or, de même que pour le site de Chepa-Ouest, cette zone à 10 km correspond à l'exhumation de l'isotherme 300°C (pour un gradient géothermique de 30°/km) qui est effectivement observée avec les analyses $^{40}\text{Ar}/^{39}\text{Ar}$ sur biotites. Ceci implique que plus de 6 km auraient été exhumés depuis 10 Ma, et donc des phases d'exhumations plus rapides sont nécessaires pour expliquer les 10 km d'exhumation.

Ces vitesses montrent qu'une seule phase d'exhumation constante n'explique pas les données de thermochronologie. Harrison et al., 1995 utilisent aussi des variations de vitesse importantes (qu'ils ne prennent pas en compte dans leur interprétation finale) pour expliquer leur données dans la vallée de Balum Chum La (inset de la Figure II.29d). Des ralentissements et des accélérations des mouvements verticaux pouvant correspondre à différentes phases d'exhumation et donc d'extension sont nécessaires pour expliquer le fonctionnement du détachement du Nyainqntanglha et celui des failles normales du rifts bordant le massif. Un modèle correspondant à un système de fonctionnement continu entre un détachement ductile et les failles normales actives cassantes comme celui proposé par Kapp et al., 2005 (Figure II.30), ne permet pas d'expliquer ces changements de vitesse au niveau du détachement du Nyainqntanglha.

Table II-3

Table: Results $^{40}\text{Ar}/^{39}\text{Ar}$ Dating by Step Heating, Nyainqntanglha Massif

Temp °C	40/39	38/39	37/39	36/39 (E-3)	39Ar (E-14 moles)	F39Ar released	%40*	40*/39K	Age Ma	$\pm 1\sigma$ Ma
T5G2	Biotite	J=	0.006911							
700	32.877	0.55	51.856	103.181	0.048	0.405	16.76	5.7	69.71	8.16
750	7.065	0.061	6.245	17.018	0.18	1.917	33.89	2.4	29.72	1.76
800	4.321	0.053	6.234	8.615	0.407	5.343	49.36	2.14	26.50	0.87
833	3.728	0.054	2.753	3.598	0.682	11.082	75.42	2.82	34.78	0.49
866	5.049	0.055	0.692	7.542	1.156	20.809	56.3	2.84	35.11	0.28
900	5.366	0.055	0.620	8.88	1.51	33.513	51.42	2.76	34.09	0.22
950	3.254	0.054	0.781	1.405	1.741	48.164	88.08	2.87	35.40	0.17
1000	4.632	0.054	0.930	6.386	0.714	54.174	60.05	2.78	34.37	0.44
1033	3.229	0.054	1.606	1.401	1.07	63.178	89.58	2.9	35.75	0.23
1066	3.147	0.054	0.527	0.757	2.321	82.712	93.27	2.94	36.24	0.13
1100	3.458	0.054	2.425	1.57	1.691	96.946	90.26	3.13	38.56	0.21
1200	6.606	0.054	10.723	5.044	0.31	99.554	86.97	5.79	70.73	0.88
1400	103.275	0.122	37.530	351.442	0.053	100.000	1.62	1.72	21.31	14.26
Temp	40/39	38/39	37/39	36/39	39Ar	F39Ar	%40*	40*/39K	Age	$\pm 1\sigma$
T5G3	Amphibole	J=	0.006911							
800	275.794	2.979	124.168	309.616	0.021	0.609	69.55	208.64	1610.66	18.50
900	168.221	0.243	45.290	572.996	0.075	2.829	0.97	1.67	20.75	20.62
933	29.495	0.088	39.749	81.874	0.052	4.368	26.07	7.89	95.81	6.20
966	48.096	0.107	53.270	137.439	0.034	5.371	22.23	11.07	133.04	9.48
1000	25.764	0.107	146.701	74.28	0.022	6.027	49.22	14.02	166.82	12.46
1033	10.066	0.404	380.180	11.803	0.14	10.158	99.8	39.3	433.49	2.05
1066	8.126	0.546	437.786	4.363	0.633	28.825	99.75	46.6	503.64	0.89
1100	7.495	0.582	447.504	1.614	1.251	65.687	99.73	48.1	517.73	0.83
1200	8.703	0.59	442.946	5.781	0.953	93.778	99.77	47.48	511.92	0.58
1400	116.132	0.639	534.877	396.133	0.211	100.000	27.09	48.22	518.90	6.77
Temp	40/39	38/39	37/39	36/39	39Ar	F39Ar	%40*	40*/39K	Age	$\pm 1\sigma$
T5G3	Biotite	J=	0.006911							
700	45.931	0.734	20.546	158.62	0.06	0.291	0.62	0.29	3.58	5.02
750	7.963	0.094	641.497	25.105	0.183	1.178	99.75	67.55	691.18	1.71
800	5.232	0.05	2.897	15.513	0.59	4.042	15.35	0.8	10.00	0.46
833	2.747	0.046	1.311	6.643	1.15	9.624	30.7	0.84	10.49	0.21
866	3.151	0.046	0.000	8.061	2.071	19.670	23.77	0.75	9.31	0.13
900	1.706	0.045	0.383	2.76	2.454	31.576	52.38	0.89	11.11	0.10
950	0.816	0.043	0.782	0	1.936	40.969	97.55	0.84	10.48	0.08
1000	0.287	0.043	0.157	0	1.047	46.051	93.04	0.28	3.45	0.03
1033	0.692	0.044	0.742	0	2.475	58.060	97.11	0.72	8.93	0.08
1066	0.791	0.044	0.725	0	4.595	80.353	97.47	0.82	10.14	0.05
1100	0.77	0.043	1.701	0	3.622	97.925	97.4	0.85	10.62	0.06
1200	1.193	0.041	17.667	2.205	0.392	99.825	98.32	1.61	19.96	0.71
1400	350.188	0.293	120.752	1254.63	0.036	100.000	-3.79	0	0	7.1E-07
Temp	40/39	38/39	37/39	36/39 (E-3)	39Ar (E-14 moles)	F39Ar released				
T5G5	Biotite	J=	0.007							
800	16.613	0.225	15.093	55.549	0.226	1.048	6.58	1.1	13.71	2.23
900	2.488	0.067	0.828	6.386	2.503	12.673	25.34	0.63	7.85	0.15
950	1.826	0.067	0.567	4.046	7.155	45.909	35.33	0.65	8.03	0.09
1000	1.045	0.066	1.043	1.058	3.853	63.808	74.21	0.78	9.64	0.09
1033	0.82	0.066	0.888	0.225	2.854	77.063	96.01	0.79	9.79	0.09
1066	5.5E+07	#####	5.0E+07	1.5E+07	0	77.063	97.49	0	0.00	0.00
1100	0.929	0.066	2.236	0.797	4.31	97.086	87.09	0.81	10.08	0.07
1200	11.52	0.072	31.012	39.124	0.568	99.724	15.78	1.85	22.98	0.71
1400	394.336	0.334	77.224	1425.394	0.059	100.000	-5.63	0	0	7.1E-07

Temp °C	40/39	38/39	37/39	36/39 (E-3)	39Ar (E-14 moles)	F39Ar released	%40*	40*/39K	Age Ma	± 1σ Ma
T5G8	Muscovite	J=	0.006911							
700	23.761	0.45	17.526	79.05	0.085	0.520	6.08	1.46	18.12	3.94
750	4.091	0.034	14.568	10.593	0.184	1.642	44.57	1.84	22.81	1.40
800	2.941	0.015	0.088	5.365	0.148	2.541	45.6	1.34	16.65	1.17
833	2.5	0.015	3.149	5.161	0.163	3.534	45.83	1.15	14.26	1.12
866	24.436	0.032	3.690	85.5	0.211	4.817	-2.56	0	0.00	0.00
900	4.136	0.014	0.117	11.307	0.247	6.322	18.9	0.78	9.72	0.84
950	1.86	0.013	0.001	3.833	0.936	12.019	38.04	0.71	8.80	1.03
1000	1.552	0.014	0.094	2.965	2.521	27.369	42.63	0.66	8.23	0.10
1033	1.177	0.013	0.000	1.652	3.887	51.032	56.8	0.67	8.31	0.06
1066	1.132	0.013	0.000	1.551	3.03	69.481	57.74	0.65	8.13	0.06
1100	1.003	0.013	0.000	1.137	3.13	88.534	64.52	0.65	8.05	0.04
1200	0.541	0.013	0.301	0	1.778	99.360	96.3	0.54	6.71	0.06
1400	174.001	0.143	8.175	630.353	0.105	100.000	-6.78	0	0	6.4E-08
Temp °C	40/39	38/39	37/39	36/39 (E-3)	39Ar (E-14 moles)	F39Ar released	%40*	40*/39K	Age Ma	± 1σ Ma
T5Y9	Biotite	J=	0.006911							
700	32.829	0.161	11.153	116.282	0.052	0.365	-2.67	0	0	0
750	4.593	0.035	8.922	13.724	0.275	2.295	23.04	1.06	13.22	1.09
800	1.78	0.033	0.001	3.902	0.764	7.666	34.11	0.61	7.55	0.26
833	4.312	0.035	1.214	13.665	1.538	18.473	7.61	0.33	4.09	0.31
866	1.002	0.033	0.302	1.458	2.066	32.991	56.83	0.57	7.08	0.14
900	1.286	0.033	1.161	2.209	0.873	39.125	53.17	0.68	8.51	0.35
950	0.617	0.032	1.462	0.169	0.775	44.571	96.76	0.64	7.92	0.33
1000	0.699	0.032	4.170	0	0.525	48.258	97.14	0.93	11.61	0.53
1033	0.543	0.032	2.285	0	1.667	59.975	96.31	0.66	8.24	0.18
1066	0.665	0.032	1.159	0.229	2.964	80.808	96.99	0.65	8.07	0.10
1100	0.461	0.032	4.047	0	2.334	97.213	95.67	0.69	8.56	0.12
1200	9.881	0.032	51.991	0	0.346	99.644	99.8	0	1E-10	1E-10
1400	668.063	0.501	222.066	2448.441	0.051	100.000	-6.29	0	0	1.0E-16
Temp °C	40/39	38/39	37/39	36/39 (E-3)	39Ar (E-14 moles)	F39Ar released	%40*	40*/39K	Age Ma	± 1σ Ma
T5Y10	Biotite	J=	0.006911							
700	39.006	0.188	34.237	129.84	0.048	0.485	6.9	2.75	34.01	6.61
750	7.479	0.051	3.052	20.233	0.127	1.780	22.26	1.67	20.68	1.91
800	3.081	0.046	1.234	8.387	0.657	8.466	21.33	0.66	8.18	0.52
833	3.805	0.047	0.970	11.751	1.314	21.829	9.77	0.37	4.63	0.32
866	1.407	0.045	0.445	2.838	2.73	49.595	40.88	0.58	7.16	0.12
900	1.094	0.045	0.841	1.639	1.63	66.167	58.57	0.64	7.98	0.18
950	1.462	0.045	1.861	2.765	1.008	76.420	50.46	0.74	9.19	0.31
1000	0.978	0.044	0.001	0	0.613	82.651	97.95	0.96	11.90	0.04
1033	0.687	0.045	1.040	0.371	1.706	99.998	90.31	0.62	7.72	0.16
1066	10749670	1.021	6942.250	1021.422	0	99.998	100	0	1E-10	1E-10
1100	14960339	1.021	6942.250	1021.422	0	99.998	100	0	1E-10	1E-10
1200	27344659	1.021	6942.250	1021.422	0	99.998	100	0	1E-10	1E-10
1400	35092.223	0.001	330.638	0.688	0	100.000	100	0	1E-10	1E-10
Temp °C	40/39	38/39	37/39	36/39 (E-3)	39Ar (E-14 moles)	F39Ar released	%40*	40*/39K	Age Ma	± 1σ Ma
T5Y10	K-feldspar	J=	0.01094							
400	590.667	0.792	2.4775	1896.164	0.008	0.121	5.16	30.53	519.90	939.63
400	310.232	1.066	0.0629	903.445	0.002	0.158	13.94	43.25	698.91	590.74
450	73.450	0.549	0.0153	220.498	0.009	0.306	11.27	8.27	156.33	71.06
450	34.322	0.241	3.8698	87.945	0.006	0.405	24.91	8.57	161.68	44.80
500	16.310	0.082	0.9947	36.565	0.026	0.832	34.00	5.55	106.33	12.94
500	13.879	0.031	8.0913	30.488	0.012	1.031	38.48	5.37	102.96	16.51

2. La Déformation Long-Terme

2.3. Les Vitesses d'Exhumation du Massif du Nyainqntanglha

550	8.010	0.019	1.1128	18.835	0.037	1.626	31.10	2.49	48.55	7.17
550	3.953	0.016	2.1544	1.943	0.023	1.999	88.27	3.49	67.69	2.95
600	2.445	0.014	0.0017	3.362	0.082	3.325	58.55	1.43	28.03	2.33
600	1.261	0.009	0.0023	2.885	0.062	4.328	30.80	0.39	7.65	2.45
650	1.127	0.014	0.0500	2.030	0.181	7.243	45.30	0.51	10.05	1.20
650	0.754	0.011	0.0012	0.699	0.116	9.111	69.97	0.53	10.38	0.80
700	2.419	0.016	0.0005	6.079	0.292	13.810	24.91	0.60	11.85	1.02
700	0.692	0.013	0.0008	0.570	0.188	16.836	72.78	0.50	9.91	0.61
750	0.786	0.013	0.0003	0.651	0.457	24.197	72.97	0.57	11.28	0.47
750	0.935	0.014	0.0005	0.762	0.296	28.963	73.80	0.69	13.57	0.62
800	0.828	0.013	0.0005	0.679	0.290	33.637	73.35	0.61	11.95	0.62
800	0.955	0.013	0.1345	0.608	0.176	36.472	79.94	0.76	15.00	0.64
800	1.132	0.013	0.0009	1.417	0.164	39.120	61.23	0.69	13.62	0.89
750	1.696	0.012	0.0057	3.278	0.025	39.518	41.72	0.71	13.91	2.63
950	6.015	0.017	0.0003	16.784	0.480	47.255	17.21	1.04	20.32	0.80
1000	1.476	0.013	0.0020	0.024	0.070	48.388	98.17	1.45	28.37	0.36
1050	1.326	0.014	0.0008	0.935	0.173	51.176	77.67	1.03	20.21	0.84
1050	1.438	0.014	0.0005	1.809	0.268	55.489	61.44	0.88	17.36	0.74
1100	1.297	0.014	0.0002	1.351	0.584	64.900	67.69	0.88	17.25	0.40
1150	1.322	0.014	0.0310	1.610	1.283	85.582	62.62	0.83	16.26	0.23
1200	2.143	0.013	0.0714	2.317	0.673	96.425	67.31	1.44	28.24	0.38
1400	5.389	0.014	0.0006	4.540	0.222	100.000	74.73	4.03	77.78	0.84

Temp °C	10000/T (1/K)	-log(D/r ²)	C-% ³⁹ Ar	log(r/r ₀)	E=	37.3307kcal/mol
400	14.86	9.19	0.12	-0.07		
400	14.86	9.42	0.16	0.05	log(Do/ro)=	2.7945
450	13.83	8.52	0.31	0.02	Domains=	7
450	13.83	8.58	0.41	0.04		
500	12.94	7.64	0.83	-0.06		
500	12.94	7.86	1.03	0.05		
550	12.15	7.16	1.63	0.02		
550	12.15	7.30	2.00	0.09		
600	11.45	6.51	3.33	-0.02		
600	11.45	6.54	4.33	0.00		
650	10.83	5.83	7.24	-0.11		
650	10.83	5.94	9.11	-0.05		
700	10.28	5.33	13.81	-0.13		
700	10.28	5.46	16.84	-0.07		
750	9.78	4.88	24.20	-0.15		
750	9.78	5.02	28.96	-0.08		
800	9.32	4.89	33.64	0.04		
800	9.32	5.19	36.47	0.19		
800	9.32	5.36	39.12	0.28		
750	9.78	6.17	39.52	0.49		
950	8.18	4.53	47.25	0.33		
1000	7.86	5.33	48.39	0.86		
1050	7.56	4.92	51.18	0.77		
1050	7.56	4.81	55.49	0.72		
1100	7.28	4.27	64.90	0.56		
1150	7.03	3.70	85.58	0.38		
1200	6.79	3.50	96.43	0.38		
1400	5.98	2.26	100.00	0.09		

Temp °C	40/39	38/39	37/39	36/39 (E-3)	39Ar (E-14 moles)	F39Ar released	%40*	40*/39K	Age Ma	± 1σ Ma
T5Y11	Biotite	J=	0.007							
700	46.452	0.317	0.019	165.306	0.046	0.405	-5.2	0	0	0
750	4.457	0.062	1.998	15.954	0.274	2.825	-3.5	0	0	0

2. La Déformation Long-Terme

2.3. Les Vitesses d'Exhumation du Massif du Nyainqntanglha

800	2.605	0.061	1.290	6.584	0.59	8.041	27.55	0.72	8.93	0.57
833	4.588	0.064	0.807	14.452	1.226	18.874	7.54	0.35	4.31	0.36
866	0.95	0.061	0.703	0.996	1.321	30.550	71.39	0.68	8.44	0.21
900	0.836	0.06	1.181	0.244	0.958	39.018	97.52	0.82	10.14	0.27
950	0.797	0.059	2.582	0.137	0.75	45.644	97.49	0.89	11.12	0.36
1000	0.797	0.058	4.683	0	0.38	49.001	97.49	1.06	13.21	0.74
1033	0.461	0.061	2.272	0	1.064	58.405	95.66	0.58	7.21	0.25
1066	0.511	0.061	1.232	0	2.681	82.098	96.09	0.57	7.05	0.10
1100	0.34	0.058	3.686	0	1.501	95.366	94.11	0.54	6.77	0.19
1200	8.981	0.043	9.107	0	0.381	98.729	99.78	0	1E-10	1E-10
1400	151.791	0.137	26.815	566.733	0.144	100.000	-9.27	0	0	1.0E-16
Temp	40/39	38/39	37/39	36/39	39Ar (E-3)	F39Ar (E-14 moles) released	%40*	40*/39K	Age Ma	± 1σ Ma
T5Y12	K-feldspar	J=	0.01094							
400	238.972	1.177	15.82699	784.001	0.003	0.071	3.45	8.32	157.23	288.23
400	288.351	1.749	5.8965	1034.007	0.001	0.087	-5.85	0.00	0.00	0.00
450	67.601	1.184	0.05419	256.846	0.003	0.143	-12.30	0.00	0.00	0.00
450	47.484	0.667	0.09233	314.26	0.002	0.176	-95.60	0.00	0.00	0.00
500	14.904	0.136	0.01223	38.234	0.012	0.426	24.07	3.59	69.44	26.55
500	8.534	0.02	0.02216	41.097	0.007	0.563	-42.53	0.00	0.00	0.00
550	5.425	0.03	0.00488	14.351	0.03	1.188	21.46	1.16	22.83	9.06
550	1.574	0.008	0.77281	1.724	0.02	1.603	69.35	1.09	21.43	6.30
600	1.413	0.016	0.00187	2.308	0.078	3.232	50.32	0.71	13.98	2.97
600	0.76	0.013	0.00266	1.243	0.055	4.380	49.04	0.37	7.34	2.77
650	0.81	0.015	0.00094	1.87	0.156	7.623	29.27	0.24	4.67	1.49
650	0.675	0.012	0.80789	2.415	0.087	9.428	-1.51	0.00	0.00	0.00
700	3.235	0.019	0.00077	8.797	0.191	13.389	19.03	0.62	12.11	1.63
700	0.814	0.015	1.36989	1.792	0.113	15.734	42.65	0.35	6.84	1.79
750	0.941	0.017	0.80027	1.144	0.273	21.398	67.09	0.63	12.42	0.86
750	1.362	0.022	0.26278	1.738	0.42	30.134	62.01	0.84	16.60	0.64
800	1.217	0.021	0.00061	1.528	0.24	35.117	61.27	0.75	14.66	0.94
800	1.302	0.018	0.90374	2.81	0.126	37.742	38.91	0.51	9.98	1.67
800	1.444	0.02	0.00102	2.565	0.144	40.744	46.12	0.67	13.09	1.27
700	3.492	0.025	0.01121	22.671	0.013	41.016	-92.38	0.00	0.00	0.00
750	1.893	0.023	0.00499	3.703	0.029	41.627	41.14	0.78	15.30	3.39
800	1.36	0.02	0.00357	1.357	0.041	42.481	69.07	0.94	18.45	2.38
850	1.158	0.017	0.00108	1.741	0.136	45.302	53.85	0.62	12.27	1.39
900	1.093	0.016	0.0004	1.421	0.363	52.851	59.76	0.65	12.85	0.63
950	1.039	0.016	0.00018	0.906	0.798	69.443	72.31	0.75	14.77	0.35
1000	1.063	0.016	0.00021	1.184	0.688	83.733	65.18	0.69	13.62	0.37
1050	1.226	0.017	0.00045	1.328	0.325	90.488	66.37	0.81	15.99	0.63
1100	1.181	0.019	0.00076	0.453	0.192	94.482	86.97	1.03	20.16	4.17
1200	1.263	0.016	1.37641	2.463	0.166	97.936	47.40	0.60	11.79	1.01
1400	0.205	0.009	1.86259	1.252	0.099	100.000	-35.33	0.00	0.00	0.00
Temp	10000/T	-log(D/r²)	C-%39Ar	log(r/r₀)						
°C	(1/K)									
400	14.85884	9.656	0.071	-0.320	E=	51.2554 kcal/mol				
400	14.85884	10.025	0.087	-0.135	log(Do/ro)=	6.3511				
450	13.83126	9.248	0.143	0.052	Domains=	5				
450	13.83126	9.404	0.176	0.130						
500	12.93661	8.184	0.426	0.021						
500	12.93661	8.294	0.563	0.076						
550	12.15067	7.322	1.188	0.030						
550	12.15067	7.363	1.603	0.051						
600	11.45475	6.464	3.232	-0.009						

2. La Déformation Long-Terme

2.3. Les Vitesses d'Exhumation du Massif du Nyainqntanglha

600	11.45475	6.486	4.380	0.002
650	10.83424	5.770	7.623	-0.008
650	10.83424	5.939	9.428	0.076
700	10.27749	5.404	13.389	0.121
700	10.27749	5.593	15.734	0.215
750	9.775171	5.037	21.398	0.219
750	9.775171	4.774	30.134	0.087
800	9.319664	4.848	35.117	0.379
800	9.319664	5.203	37.742	0.557
800	9.319664	5.289	40.744	0.600
700	10.27749	6.314	41.016	0.576
750	9.775171	5.958	41.627	0.679
800	9.319664	5.504	42.481	0.707
850	8.90472	4.966	45.302	0.671
900	8.525149	4.489	52.851	0.645
950	8.176615	4.010	69.443	0.601
1000	7.85546	3.848	83.733	0.699
1050	7.558579	3.918	90.488	0.901
1100	7.283321	3.911	94.482	1.052
1200	6.788866	3.655	97.936	1.200
1400	5.977286	2.272	100.000	0.963

Temp °C	40/39	38/39	37/39	36/39	39Ar (E-3)	F39Ar (E-14 moles)	%40*	40*/39K	Age Ma	± 1σ Ma
------------	-------	-------	-------	-------	---------------	-----------------------	------	---------	-----------	------------

T5Y32	Biotite	J=	0.007							
700	37.084	0.572	0.011	103.103	0.077	1.300	17.79	6.6	80.44	18.83
750	18.274	0.24	4.451	45.871	0.101	2.990	27.19	4.98	61.08	3.10
800	7.673	0.231	4.250	8.937	0.222	6.710	68.68	5.28	64.71	1.66
833	6.563	0.231	0.331	9.537	0.327	12.200	57.06	3.75	46.11	1.01
866	4.426	0.235	2.662	3.898	0.511	20.780	77.17	3.42	42.16	0.59
900	3.619	0.237	1.072	0.959	0.455	28.410	93.41	3.38	41.69	0.43
950	3.573	0.236	3.716	1.232	0.713	40.360	95.56	3.42	42.18	0.39
1000	3.55	0.232	2.416	1.381	0.472	48.290	92.06	3.27	40.36	0.50
1033	3.098	0.235	2.318	0.487	1.304	70.180	99.24	3.08	37.99	0.22
1066	3.444	0.239	1.316	0	1.54	96.040	99.42	3.51	43.20	0.20
1100	3.158	0.228	32.036	0.001	0.178	98.980	99.37	5.19	63.53	1.27
1200	1.071	0.21	68.081	0.003	0.048	99.740	98.13	5.41	66.28	4.08
1400	110.813	0.265	0.056	368.602	0.016	100.000	1.69	1.87	23.22	46.52

Temp °C	40/39	38/39	37/39	36/39	39Ar (E-3)	F39Ar (E-14 moles)	%40*	40*/39K	Age Ma	± 1σ Ma
------------	-------	-------	-------	-------	---------------	-----------------------	------	---------	-----------	------------

T5Y34	Biotite	J=	0.007							
700	30.63	0.467	0.015	103.118	0.058	1.334	0.45	0.14	1.74	4.56
750	11.542	0.187	9.933	28.16	0.097	3.555	32.94	3.83	47.10	2.65
800	8.215	0.202	1.386	13.303	0.14	6.765	52.93	4.35	53.46	1.44
833	6.725	0.204	1.250	10.253	0.38	15.509	55.78	3.75	46.21	0.65
866	4.505	0.207	1.966	1.963	0.486	26.681	89.32	4.03	49.54	0.55
900	4.684	0.206	0.003	1.982	0.275	33.007	87.07	4.08	50.15	0.64
950	4.496	0.206	0.003	1.839	0.309	40.111	87.47	3.93	48.37	0.56
1000	4.881	0.207	5.543	3.327	0.294	46.863	86.33	4.23	51.98	1.03
1033	4.189	0.209	2.048	1.524	1.014	70.183	91.74	3.85	47.36	0.35
1066	4.126	0.21	2.646	0.326	0.635	84.785	99.52	4.18	51.34	0.39
1066	4.126	0.21	2.646	0.326	0.635	99.386	99.52	4.18	0.00	0.00
1200	13.666	0.202	53.952	0.593	0.019	99.828	99.85	17.35	204.28	8.93
1400	308.626	0.415	97.398	1108.09	0.007	100.000	-4.19	0	0	8.9E-06

Table II.4: Results of apatite (U-Th)/He dating, Nyainqntanglha massif

échantillon	altitude (m)	^{238}U (E-3 nmol/g)	^{232}Th (E-3 nmol/g)	^4He (mol)	Age He brut (Ma)	Ft	Age corrigé	Répliques non utilisées	Age moyen - écart type
T5G2	5335	1.238	2.616	8.754E-15	1.47	0.77	1.91	T5G2 Age moyen écart type	2.15 0.19
	réplique 1	3.110	6.426	2.971E-14	1.97	0.83	2.37		
	réplique 2	1.040	2.140	8.046E-15	1.6	0.76	2.11		
	réplique 3	0.590	1.372	4.523E-15	1.52	0.69	2.20		
T5G3	5100	6.980	6.646	3.891E-14	1.39	0.88	1.58	T5G3 Age moyen écart type	1.63 0.11
	réplique 1	2.840	2.826	1.581E-14	1.37	0.80	1.71		
	réplique 2	3.308	2.672	1.597E-14	1.24	0.83	1.49		
	réplique 3	0.765	0.876	4.116E-15	1.3	0.75	1.73		
T5G5	4885	3.172	3.586	1.833E-14	1.25	0.87	1.44	T5G5 Age moyen écart type	1.53 0.07
	réplique 1	1.619	2.014	8.484E-15	1.24	0.78	1.59		
	réplique 2	2.485	4.582	1.507E-14	1.29	0.84	1.54		
	réplique 3	2.275	3.326	1.266E-14	1.26	0.80	1.58		
T5G8	4823	0.035	0.083	7.140E-16	4.02	0.73	5.51	T5G8 Age moyen écart type	4.42 0.44*
	réplique 1	0.153	0.119	3.735E-15	6.29	0.73	8.62		
	réplique 2	0.055	0.099	2.441E-15	9.5	0.66	14.39		
	réplique 3	0.031	0.061	4.351E-16	2.92	0.66	4.42		
T5Y9	4920	0.263	1.371	3.941E-15	2.07	0.74	2.80	T5Y9 Age moyen écart type	3.62 0.72
	réplique 1	0.336	1.351	4.940E-15	2.31	0.71	3.25		
	réplique 2			5.409E-15	2.92	0.72	4.06		
	réplique 3			3.650E-15	2.79	0.64	4.36		
T5Y10	5020	0.358	1.359	2.013E-14	9.08	0.76	11.95	T5Y10 Age moyen écart type	2.56 0.47
	réplique 1	0.286	1.359	4.126E-15	2.08	0.72	2.89		
	réplique 2			1.835E-14	6.36	0.75	8.48		
	réplique 3			3.188E-15	1.56	0.70	2.23		
T5Y11	5140	1.651	5.426	2.750E-14	2.87	0.83	3.46	T5Y11 Age moyen écart type	4.53 1.13
	réplique 1	0.765	1.582	1.127E-14	3.03	0.82	3.70		
	réplique 2			1.383E-14	4.20	0.81	5.19		
	réplique 3			7.747E-15	4.56	0.79	5.77		
	réplique 4			1.958E-14	7.88	0.88	8.95		
T5Y12	5140	1.651	5.426	2.750E-14	2.87	0.83	3.46	T5Y12 Age moyen écart type	4.53 1.13
	réplique 1	0.765	1.582	1.127E-14	3.03	0.82	3.70		
	réplique 2			1.383E-14	4.20	0.81	5.19		
	réplique 3			7.747E-15	4.56	0.79	5.77		
	réplique 4			1.958E-14	7.88	0.88	8.95		

Partie 3



LA DÉFORMATION COURT-TERME SUR LES FAILLES NORMALES ACTIVES DU SUD TIBET

Photographie du titre 3 :

Vue de la confluence entre les rivières de l'Arun et de Kharta, juste en amont la deuxième gorge de l'Arun, traversant l'Himalaya (voir la vue en carte correspondante, Figure III.16). Une ancienne terrasse (T4', Figure III.16) surplombe la rivière de Kharta. L'Arun traverse plusieurs fois la faille de Kharta qui façonne le paysage actuel de la partie Ouest du Massif de l'Ama Drime.

3. LA DÉFORMATION COURT-TERME SUR LES FAILLES NORMALES ACTIVES DU SUD TIBET

3.1. La détermination de vitesses de glissement quaternaires à l'aide des datations aux isotopes cosmogéniques (^{10}Be et ^{26}Al in situ)

Dans cette partie, l'objectif est de déterminer des vitesses de glissement verticaux sur les failles normales actives des deux systèmes étudiés. Pour ce faire, il s'agit d'une part, de définir des décalages verticaux dans les formations quaternaires qui constituent les bassins associés aux failles normales et, d'autre part, de dater ces formations quaternaires.

Les décalages verticaux et la cartographie des formations quaternaires sont déterminés par des mesures des escarpements de faille sur le terrain et grâce à des données satellitaires, imagerie haute-résolution et modèle numérique de terrain. Les formations quaternaires sont ensuite datées avec les isotopes cosmogéniques qui permettent de fournir un âge d'exposition des surfaces échantillonnées.

La combinaison de l'analyse morphotectonique avec la datation aux isotopes cosmogéniques permet ainsi de déterminer des vitesses de glissement quaternaires.

3.1.1. La datation ^{10}Be - ^{26}Al

Les principales applications de la datation par isotopes cosmogéniques sont la quantification de taux d'incision grâce à la datation de terrasses étagées, la détermination de la chronologie de glissements de terrain par la datation de la surface d'arrachement, les études de paléoclimat avec la datation des dépôts glaciaires et enfin, la quantification des déplacements tectoniques qui est utilisé dans cette thèse.

Ici les isotopes du béryllium et de l'aluminium ont été utilisés pour la datation. Nous allons voir dans la suite le principe et l'intérêt de cette double datation.

3.1.1.1. Origine des isotopes cosmogéniques

La datation par les isotopes cosmogéniques est basée sur l'accumulation de certains nucléides dans des matériaux exposés aux rayons cosmiques.

Il existe deux sources de rayonnement cosmique qui atteignent la surface terrestre, le rayonnement solaire (avec une énergie entre 10 et 100 MeV) et le rayonnement galactique (énergie entre 1 GeV et 1010 GeV).

Les particules de ce rayonnement (des protons et des noyaux d'hélium) interagissent d'abord avec les particules de l'atmosphère. Il s'ensuit une cascade de réactions nucléaires par laquelle est produite un rayonnement cosmique secondaire moins énergétique (Figure III.1). Ce sont les particules de ce rayonnement secondaire (neutrons et muons) qui vont interagir avec les atomes de la surface terrestre pour produire *in-situ* les nucléides cosmogéniques. Plusieurs types d'interactions peuvent produire les nucléides cosmogéniques (Table III.1). Les nucléides utilisés dans cette thèse sont le ^{10}Be et ^{26}Al , produits par spallation et par capture de muon. La production des isotopes cosmogéniques a lieu au niveau des premiers mètres de la surface, avec une diminution exponentielle de la production en fonction de la densité de matière traversée.

Le flux de rayonnement cosmique qui arrive à la surface terrestre varie avec le temps (modulation cyclique dû à l'activité solaire et variation du champ magnétique terrestre), et est fonction de la latitude et de l'altitude (épaisseur d'atmosphère), la production des nucléides cosmogénique varie donc en fonction de ces paramètres (Lal et al., 1991).

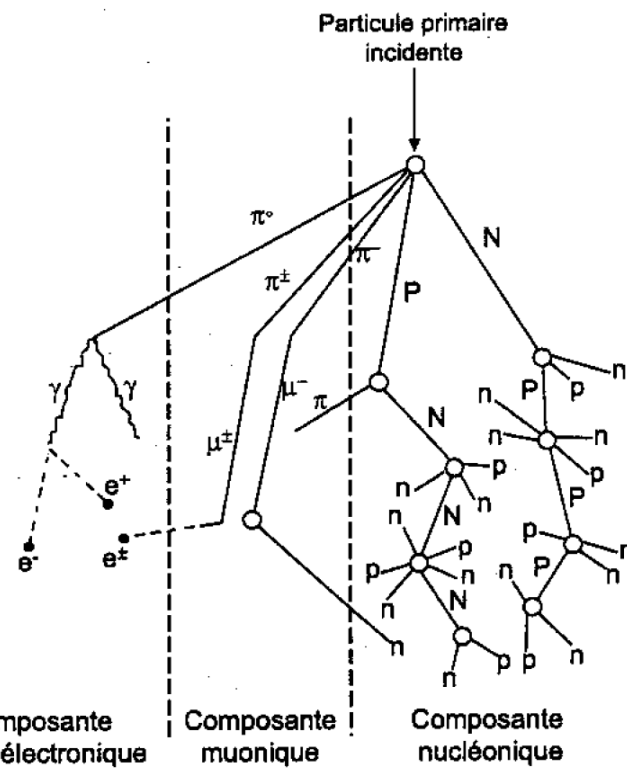


Figure III.1: Schematic representation of the development of particle production in the atmosphere. Secondary particles: N, P : high-energy neutrons and protons; n, p: thermal neutrons and protons; π , μ : muonic component; γ , e^+ , e^- : electron-proton component. From Siame et al., 2001

Cosmonucléide	Lieu de production	Période	Principales Cibles	Réactions	Mode de désintégration
^3He	Atm <i>in-situ</i>	Stable	N, O O, Mg, Si, Fe	Spallation Spallation	-
^{21}Ne	Atm <i>in-situ</i>	Stable	Ar Mg, Al, Si, Fe	Spallation Spallation	-
^{10}Be	Atm <i>in-situ</i>	$1,5 \cdot 10^6$ ans	N, O O, Si, Mg, Fe	Spallation Spallation	β^- ; 550 keV
^{26}Al	Atm <i>in-situ</i>	$7,3 \cdot 10^5$ ans	Ar Si, Al, Fe	Spallation Spallation	β^+ ; 1,2 MeV
^{36}Cl	Atm <i>in-situ</i>	$3,0 \cdot 10^5$ ans	Ar Fe, K, Ca, Cl	Spallation (atm., <i>in-situ</i>) Capture neutronique	β^- ; 714 keV
^{14}C	Atm <i>in-situ</i>	5730 ans	N O, Mg, Si, Fe	Capture neutronique Spallation	β^- ; 156 keV

Table III.1 : Selected atmospheric (Atm) and in situ-produced cosmonuclides (*in situ*). From Siame et al., 2001

3.1.1.2. Le calcul des âges

L'accumulation des isotopes cosmogéniques est représentée par cette équation :

$$N(z, t) = N(z, 0)e^{-\lambda t} - \lambda t + \frac{P_0}{\epsilon\mu + \lambda} e^{-\mu z} (1 - e^{-(\lambda + \mu\epsilon)t}) \quad (1)$$

où

$N(z, t)$ est la concentration en isotopes cosmogéniques à la profondeur z (cm) et au temps t (an)

P est le taux de production en surface (en atomes/g/an)

λ est la constante de décroissance radioactive (an-1)

ϵ est le taux d'érosion en surface (cm/an)

μ est le coefficient d'absorption des rayons cosmiques (cm-1), avec $\mu = \rho/\Lambda$, où ρ est la densité de la matière traversée et Λ est la longueur d'atténuation (g/cm^2).

Le représentation graphique de cette équation est montrée Figure III.2a.

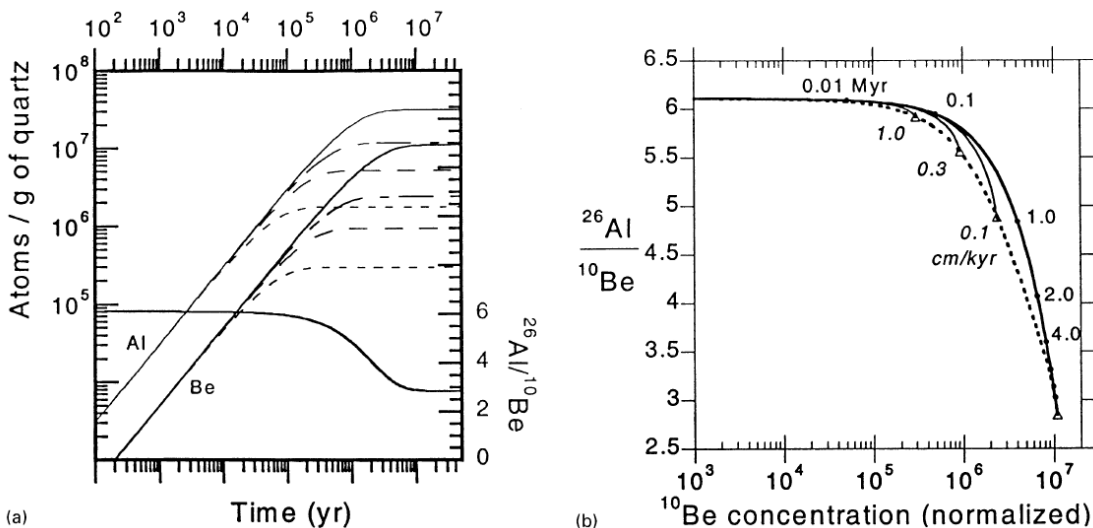


Figure III.2: Terrestrial Cosmogenic Nuclide ratio diagram for ²⁶Al and ¹⁰Be. (a) Production curves for ²⁶Al ($P_{26Al(20)} = 33.6 \text{ atoms/g/yr}$) and ¹⁰Be ($P_{10Be(20)} = 5.5 \text{ atoms/g/yr}$), with production ratio of 6.1 (these production rates will vary with sites above sea level or $\lambda_m < 60^\circ$). Additional curves for erosion rates of $\epsilon = 1, 3,$ and 10 mm/ka . The change in ²⁶Al/¹⁰Be also shown for $\epsilon = 0, 1, 3$ and 10 mm/ka . (b) As in (a), ²⁶Al/¹⁰Be shown for $\epsilon = 0, 1, 3$, and 10 mm/ka , but plotted (traditionally) against $\log^{10} \text{Be}$ concentration (normalized for production at sea level and high latitude). Samples with ratios plotting on the upper curve can be interpreted as having no erosion, and total exposure duration corresponds to distance along the $\epsilon = 0$ ratio curve. Samples plotting on or between erosion curves have experienced the modeled erosion rate (assumed continuous, constant, and gradual), and the total exposure time corresponds to the distance along the erosion trajectory. From Gosse and Phillips 2001.

La première partie de l'équation, $N(z, 0) e^{-\lambda t}$, représente la concentration en isotope cosmogénique présente dans l'échantillon avant l'exposition aux rayons cosmiques dans la surface considérée, cela représente donc, l'héritage en cosmonucléides de l'échantillon. Dans nos calculs d'âge, nous faisons

l'hypothèse de l'héritage nul dans un premier temps et discutons sa validité au vu de la distribution d'âges obtenue. La partie centrale de l'équation, $P_0 \cdot e^{-\mu z}$, représente la décroissance théorique du taux de production en fonction de la profondeur (Lal et al., 1991). Les échantillons traités dans cette thèse étant uniquement des échantillons de surface, la valeur de z correspond à l'épaisseur de l'échantillon effectivement analysé. Enfin, on fait l'hypothèse d'un taux d'érosion négligeable (donc dans l'équation $\epsilon=0$) et discutons la validité de cette hypothèse en fonction des sites et terrasses analysées.

Toutes ces hypothèses permettent de simplifier l'équation (1) ainsi :

$$N(t) = \frac{P_0}{\lambda} (1 - e^{-\lambda t}) \quad (2)$$

3.1.1.3. L'utilisation de deux isotopes cosmogéniques : ^{26}Al et ^{10}Be

Ces deux isotopes peuvent être extraits lors du même traitement chimique de chaque échantillon. L'utilisation de ces deux isotopes permet d'une part de comparer les âges obtenus, d'autre part, le rapport de concentration des deux isotopes permet en théorie de préciser l'histoire d'exposition des échantillons.

Le rapport des concentrations est constant au cours du temps pour une histoire d'exposition simple:

$$\frac{N_{26}}{N_{10}} = \frac{P_{26}\lambda_{10}}{P_{10}\lambda_{26}} \frac{(1 - e^{-\lambda_{10}t})}{(1 - e^{-\lambda_{26}t})} = 6.75$$

Ce rapport peut varier en cas d'exposition plus complexe. Par exemple, si un échantillon ancialement exposé est enfoui à l'abri des rayonnements cosmiques, la production de cosmonucléide cesse et la décroissance radioactive implique la diminution des concentrations, plus rapidement pour l' ^{26}Al (demi-vie de ~700 ka pour l' ^{26}Al et ~1500 ka pour le ^{10}Be), le rapport $N_{26\text{Al}}/N_{10\text{Be}}$ diminue donc également (Figure III.2).

3.1.1.4. L'âge d'exposition

L'équation (2) permet de déterminer l'âge ainsi :

$$t = \frac{1}{\lambda} \ln \frac{1 - N\lambda}{P}$$

La concentration N sera déterminée grâce à l'analyse au spectromètre de masse par accélération (AMS) du Be et de l'Al extraits des échantillons (l'ensemble des échantillons présenté a été analysé sur le spectromètre ASTER du CEREGE (Accélérateur pour les Sciences de la Terre, Environnement, Risques du Laboratoire National des Nucléides Cosmogéniques). Le taux de production P, le calcul d'âge, ainsi que le taux d'écrantage sont déterminés grâce au programme en ligne « ^{10}Be - ^{26}Al exposure age calculator » (<http://hess.ess.washington.edu/math/>; CRONUS-Earth online calculator Version 2.2 - 19 March 2009; Balco et al., 2008) du programme CRONUS-Earth Project de la NSF (USA) (Cosmic-Ray Produced Nuclide Systematics on Earth Project ; <http://www.physics.psu.edu/primelab/CronusProject/cronus/>).

Détermination de la concentration de ^{10}Be et l' ^{26}Al

La préparation chimique

Les mesures ICP-MS et la préparation chimique ont été effectuées au Laboratoire d'Hydrologie et de Géochimie de Strasbourg et les rapports isotopiques ont été mesurés à l'ASTER du CEREGE à Aix en Provence. Le protocole de laboratoire détaillé est fourni dans l'Annexe F.

Calcul de la concentration en nucléide cosmogénique

La concentration N en nucléide cosmogénique (^{10}Be) est donnée par cette équation :

$$N_{10} = \frac{(R_{10/9} n_9 - n_{10b})}{M_q}$$

où

$R_{10/9}$ est le rapport entre les concentrations d'isotope radioactif (^{10}Be) et d'isotope stable (^9Be) du beryllium contenu dans l'échantillon

n_9 est la quantité de ^9Be totale dans l'échantillon qui comprend le ^9Be du porteur et le ^9Be naturel présent dans l'échantillon (en nombre d'atome).

n_{10b} est la quantité de ^{10}Be contenue dans le blanc de laboratoire (provenant du porteur et du laboratoire) (en nombre d'atomes)

M_q est la masse de quartz dissoute à partir de laquelle ont été extraits les cosmonucléides (en g)

Pour l'aluminium, la même équation est appliquée, l'isotope stable étant ^{27}Al .

Les détails du calcul de la concentration en nucléides cosmogéniques sont disponibles dans Balco et al., 2006.

Le ^9Be et l' ^{27}Al naturel, mesure à l'ICP-MS

La quantité d'isotope stable (n_9 et n_{27}), est déterminée grâce à la mesure à l'ICP-MS. Pour que la quantité de Be soit mesurable à l'ASTER, un porteur contenant une quantité connue de ^9Be est ajouté à l'échantillon. L' ^{27}Al est déjà naturellement présent dans l'échantillon, il n'est donc pas toujours nécessaire d'y ajouter un porteur. Pour le savoir, une mesure à l'ICP-MS est effectuée. Quand l'échantillon contient moins de 2 mg d'Al, le porteur est ajouté. Il est courant de considérer que le quartz ne contient pas de ^9Be naturel. Or des mesures ICP-MS ont montré que certains échantillons peuvent contenir jusqu'à dix fois plus de ^9Be naturel par rapport à la quantité de porteur ajouté à l'échantillon (voir Table III.3). Si l'on ne s'assure pas que l'échantillon ne contient pas de ^9Be naturel, cela risque d'impliquer des erreurs sur les âges d'exposition. Compte tenu de l'évolution du protocole de laboratoire au cours de cette thèse, l'Al n'a pas été séparé et le Be naturel n'a pas été mesuré à l'ICP-MS systématiquement dans les premières séries d'échantillons (Table III.3 et III.5).

Calcul du taux de production et calcul de l'âge avec CRONUS

Le programme résout cette équation :

$$N = S_{thick} S_G P_{ref,sp,Xx} \int_0^T S_{Xx}(t) \exp(-\lambda t) \exp\left(\frac{-\varepsilon t}{\Lambda_{sp}}\right) dt + P_\mu \int_0^T \exp(-\lambda t) \exp\left(\frac{-\varepsilon t - z/2}{\Lambda_\mu}\right) dt$$

(Balco et al., 2008)

Les paramètres pris en compte dans le calcul sont :

- l'épaisseur de l'échantillon (S_{thick})
- la correction de l'écrantage (S_G , pour *Geometric Shielding*)
- le taux de production $P_{\text{ref,sp,Xx}}$, déterminé à partir d'un taux de production de référence et du facteur de calibration S_{Xx} , correspondant à la calibration Xx choisi pour le site daté. Cette calibration permet d'utiliser le taux de production de référence déterminé à un endroit donné situé à une distance éloignée du site daté.
- la calibration utilisé pour déduire le taux de production de la région étudiée
- λ , la constante de désintégration
- Λ_{sp} et Λ_{μ} , les longueurs d'atténuation effectives pour la production spallogénique et la production muonique (en g/cm²).

Le programme propose quatre calibrations différentes pour l'estimation de la production spallogénique qui tienne compte de la dépendance en altitude de P et des variations du champ magnétique (Dunai, 2001 ; Desilets, 2006 ; Lifton et al., 2005 ; Lal (1991) / Stone (2000)). En revanche, il n'y en a qu'une seule pour la production muonique car elle ne présente qu'un faible pourcentage de la production totale de ¹⁰Be (Balco, 2008). Ces quatre dernières calibrations, basées sur les variations du champ magnétique, définissent les variations du taux de production spallogénique comme une fonction de la rigidité géomagnétique R . R est l'énergie minimum qu'une particule primaire de l'environnement doit avoir pour générer une cascade de réactions nucléaires en un lieu donné de l'atmosphère. Elle a une valeur spécifique à chaque calibration selon le modèle de champ géomagnétique adopté, c'est aussi pourquoi on trouve des âges différents entre les calibrations. Ici, on a choisi de travailler avec la calibration de Lal (1991) / Stone (2000).

3.1.2. Les incertitudes

3.1.2.1. Les erreurs aléatoires

Elles varient selon les échantillons. Elles comprennent les erreurs sur :

- les caractérisques de l'échantillon (8%)
- la préparation des échantillons (3%)
- l'analyse au spectromètre de masse (4%)

(Voir la Table III.2)

Le calcul utilisé pour déterminer l'incertitude sur le nombre d'atome de ^{10}Be ou d' ^{26}Al est disponible dans Balco 2006.

3.1.2.2. Les erreurs systématiques

Elles sont les mêmes pour tous les échantillons. Elles comprennent principalement les erreurs sur :

- la constante radioactive (3%)
- le taux de production (9%)
- les variations temporelles du flux de rayon cosmique (3%)

(voie la Table III.2 ci-dessous)

1. Random Errors (8%)	2. Systematic Errors (10%)
1.1 <i>Sample characteristics</i> (5%)	2.1 <i>Radionuclide half life</i> (3%)
1.1.1 Surface geometry correction (1%)	2.2 <i>Production rate</i> (9%)
1.1.2 Shielding correction (1%)	2.2.1 Basic calibration (5%)
1.1.3 Thickness (2%)	2.2.2 Whole rock theoretical estimates (na)
1.1.4 Meteoric contamination (0%)	2.2.3 Nuclear cross sections (na)
1.1.5 Erosion rate and style (4%)	2.2.4 Attenuation lengths (rock and atmos.) (3%)
1.1.6 Burial (0%)	2.2.5 Altitude scaling, Standard Atmosphere (5%)
1.1.7 Prior irradiation (inheritance) (0%)	2.2.6 Latitude and longitude scaling (5%)
1.2 <i>Sample preparation and analyses</i> (3%)	2.3 <i>Temporal variations</i> (3%)
1.2.1 Sample interchange (0%)	2.3.1 Cosmic ray flux (0%)
1.2.2 Contamination from physical processing (0%)	2.3.2 Solar modulation (0%)
1.2.3 Weighing of sample (2%)	2.3.3 Geomagnetic polar wander (0%)
1.2.4 Addition of carrier (2%)	2.3.4 Geomagnetic paleointensity (3%)
1.2.5 Contamination with non-target minerals (na)	2.3.5 Non-dipole uncertainties (0%)
1.2.6 Analysis of stable isotope (1%)	2.3.6 Atmospheric thickness variations (0%)
1.2.7 Other major & trace elemental analyses (na)	2.4 <i>Stable element measurements</i> (2%)
1.3 <i>Mass spectrometric measurement</i> (4%)	2.5 <i>Carrier and standards</i> (2%)
1.3.1 Poisson (3%)	2.6 <i>Fractionation, spectrometry</i> (0%)
1.3.2 Background subtraction (0%)	2.7 <i>Other assigned constants</i> (0%)
1.3.3 Blank correction (0%)	2.8 <i>Calculation errors</i> (0%)
1.3.4 Sample reproducibility and normalization (3%)	
1.3.5 Precision of standard (1%)	
1.3.6 Correction for non-cosmogenic gases (na)	

Table III.2 : Sources of error for the Cosmogenic Nuclides methods. From Gosse and Phillips 2001.

3.1.2.3. L'échantillonnage

Deux facteurs limitent l'usage de la concentration en nucléides cosmogéniques pour la détermination des âges d'exposition. D'une part, la difficulté d'estimer la partie héritée (pré-exposition) et d'autre part, de quantifier l'érosion. Plusieurs stratégies d'échantillonnage des surfaces géomorphologiques (terrasses et cônes alluviaux, moraines, etc...) sont en général mises en œuvre pour tenter d'estimer ces paramètres. Ces stratégies sont en premier lieu dépendantes des dynamiques

variées des systèmes fluviaux et glaciaires. On peut en effet supposer qu'il n'y aura pas la même homogénéisation du matériel transporté par une rivière drainant un bassin versant kilométrique qu'un fleuve au bassin versant de plusieurs centaines de kilomètres de long. Il en va de même pour les systèmes glaciaires, un petit glacier suspendu ne mobilise peut-être pas le même matériel qu'un glacier de plusieurs kilomètres à dizaines de kilomètres de long.

La manière d'estimer à la fois l'érosion et l'héritage consiste à utiliser la propriété de décroissance exponentielle du profil du taux de production avec la profondeur (Brown et al., 1992 ; Anderson et al., 1996 ; Granger et al., 2000 ; Ritz et al., 2003 ; Siame et al., 2004 ; Vassallo et al., 2005). Pour cela il faut échantillonner en profondeur la formation que l'on veut dater et il est donc nécessaire d'avoir un accès au sédiment en profondeur ce qui n'est pas toujours simple et possible.

Faute d'accès à la sub-surface, seuls des échantillons en surface seront collectés. La collecte et l'analyse d'un grand nombre d'échantillons (8-10) est alors le seul moyen d'avoir une représentativité statistique de la surface analysée. Dans de nombreux cas il est alors possible d'écartier dans une population d'échantillon donnée les échantillons qui ont soit une histoire d'exposition complexe (concentration plus grande impliquant une pré-exposition par exemple) soit une histoire post-dépôt anormale (concentration plus petite dû à de l'érosion/altération locale ou à un remaniement d'ordre bio- ou cryo-génique par exemple) (e.g., Biermann et al., 1995 ; van der Woerd et al., 1998, 2002, 2006 ; Mériaux et al., 2004, 2009).

Le choix de la taille des blocs et de la lithologie échantillonnée est sans doute à prendre en compte dans certaines situations (Ritz et al., 2006 ; Behr et al., 2010) mais dans certains exemples bien documentés, les gros blocs comme les galets montrent la même distribution d'âge (Briner et al., 2009 ; Chevalier et al., 2005), et des lithologies variées (blocs granitiques/veine de quartz) montrent des distributions semblables (Chevalier, 2006).

3.1.2.4. Les erreurs sur l'âge des surfaces

Une fois l'âge de chaque échantillon obtenu, reste à déterminer l'âge de la surface. Seul des échantillons de surface ont été analysés et bien qu'en général 8 à 10 échantillons ait été prélevés sur chaque surface, seuls quelques échantillons par surface ont pu être analysés et datés dans le cadre de cette thèse. Dans certains cas, la cohérence des âges obtenus permet de calculer une moyenne, dans d'autres cas, l'étendue des âges pour donner des bornes minimales et maximales des âges est utilisée.

3.1.2.5. La quantification des décalages

Plusieurs types d'images satellitaires ont été utilisés dans cette thèse. Des images Landsat à 28.5 m de résolution, des images SPOT à 10 m et à 2.5 m et des images Ikonos à 1 m de résolution disponibles sur Google Earth pour certaines zones. Nous disposons aussi de modèles numériques de terrain, MNT SRTM (90 m) et MNT SPOTdem (20 m de résolution horizontale et 10-20 m en vertical) pour les deux massifs étudiés. Les images SPOT à 2.5 m ont été orthorectifiées et géoréférencées par SPOT-Image. Les images Ikonos ont été extraits de Google Earth par capture d'écran et ont été géoréférencées avec le logiciel Arcview. Les profils topographiques ont été extraits des SPOTdem avec le logiciel Global Mapper et le traitement pour extraire des informations sur l'hydrographie a été effectué avec Spatial Analyst (un module complémentaire d'ArcView).

Les décalages ont été mesurés sur le terrain avec un GPS portable (style Garmin) et un théodolite distancemètre laser (Leica ou Wild). Les profils topographiques obtenus ont été systématiquement complétés par des profils topographiques extraits du MNT afin de caler si nécessaire l'altitude absolue.

La mesure du décalage d'une surface datée peut présenter une incertitude. Elle est généralement due à la méthode utilisée pour la mesurer. Une incertitude de 25 % peut parfois être attribuée au décalage.

Dans cette thèse, nous prenons généralement l'étendue maximum de la distribution d'âge et des décalages pour fournir une estimation de la vitesse de glissement avec son incertitude. Cette incertitude est parfois élevée, mais fournit dans tous les cas des bornes minimales ou maximales de la vitesse.

3.2. Late Pleistocene-Holocene slip-rates on the normal faults of the Ama Drime horst (South Tibet) from in situ ^{10}Be and ^{26}Al cosmogenic isotopes dating

Manuscript in preparation.

Authors:

E. Kali, J. Van der Woerd, P.H. Leloup, J. Liu-Zeng, R. Thuizat, M.L. Chevalier

Abstract

Late-Pleistocene vertical slip-rates are determined for the normal faults of the Ama Drime horst and Mabja massif based on cosmogenic isotopes ^{10}Be and ^{26}Al dating of faulted alluvial and glacial surfaces. Topographic profiles across normal fault scarps indicate offsets of 10-15 m for the Holocene (10-13 ka), 20-40 m for the Last Glacial (20-70 ka) moraines and 120-150 m for the penultimate interglacial (120 ka) terraces. These measurements constrain the rates of vertical displacement along the normal faults to range between 0.7 and 1.4 mm/yr since 10-15 ka. The 20-70 ka rate is less well constrained but is of the same order, between 0.4 and 1.7 mm/yr. These rates are comparable with the long-term exhumation rates (\sim 1 mm/yr) for the last 6 Ma deduced from petrographic and thermochronologic data from the ductile fault zones of the Ama Drime massif (Kali et al., 2010). Together with evidence of a change from N-S to E-W extension between 13 and 12 Ma along the Ama Drime horst, the late Pleistocene active fault slip-rates and the Pleistocene exhumation rates, it imply that the E-W extensional tectonic regime started in the middle Miocene, probably in response to southward propagation of the Himalayan frontal thrust together with outward spreading of south Tibet. Considering similar rates along the other rifts of southern Tibet implies a total E-W extension rate of about 5 to 10 mm/yr for the last 150 ka, comparable to the short-term geodetic derived rates and corroborates kinematic models that link extension (5-10 mm/yr) to south Tibet spreading over underthrusting India at a rate of 2 cm/yr (e.g. Armijo et al., 1986).

3.2.1. Introduction

Normal faulting has long been recognized as the main present tectonic regime in the south of the Tibetan plateau (Tappognier and Molnar, 1977; Molnar and Tappognier, 1978; Ni and York, 1978; Tappognier et al., 1981; Rothery and Drury, 1984; Figure III.4). This extension is in contrast with the present day thrusting just south of it in the Himalayas and around most of the northern and eastern margins of the plateau. Mostly localized in the southern part of the Tibetan plateau, south of the Bangong suture, the timing, the rate and the emplacement of this extensive tectonic regime are keys to a better understanding of high continental plateau evolution.

Previous attempts to determine rates of active faulting along normal faults in Tibet were mostly concentrated in central Tibet (Yin et al., 1999; Blisniuk et al., 2001; Blisniuk and Sharp, 2003), where extension is more localized and related to connected strike-slip faulting (Armijo et al., 1986; Yin, 2000; Taylor et al., 2003) (Figure III.5). Very contrasted rates are proposed, but quantitative measurements based on U-series dating of pedogenic carbonates (Blisniuk and Sharp, 2003) suggest rates below 0.5 mm/yr for the last several 100 ka along the Shuang Hu graben, the most prominent extensional feature north of the Bangong suture. In contrast, a rate of more than 5 mm/yr has been determined in southeastern Tibet along the Daju normal fault at the foot of the Yulong Shan based on in-situ cosmogenic isotope dating of offset terraces of the Yangtse (Kong et al., 2009, 2010; Perrineau, 2010). There, the high rate is best explained by localized extension in a right step along the Zhongdian-Red River right-lateral strike-slip fault system (Armijo et al., 1989; Wu et al., 2009; Perrineau, 2010).

In this paper, we determine, for the first time since the seminal studies by Armijo et al. (1986; 1989), the late Pleistocene slip-rate of some of the normal active faults of south Tibet, by precise measurements of vertical offset moraines and terraces dated using in-situ cosmogenic isotopes. We present results along the southern Xainza-Dinggye rift system (88°E longitude) (Figures III.5 and III.6). We combine geomorphic mapping based on field-work, analysis of satellite images at various resolution (1 m Ikonos, 5 m SPOT-5 and 28 m Landsat), topographic data (SPOT-5 digital

elevation model and 1:50000 scale topographic maps) and surface exposure dating of abandoned glacial moraines and alluvial terraces. We then discuss the implications of our results for the recent kinematics of Tibet.

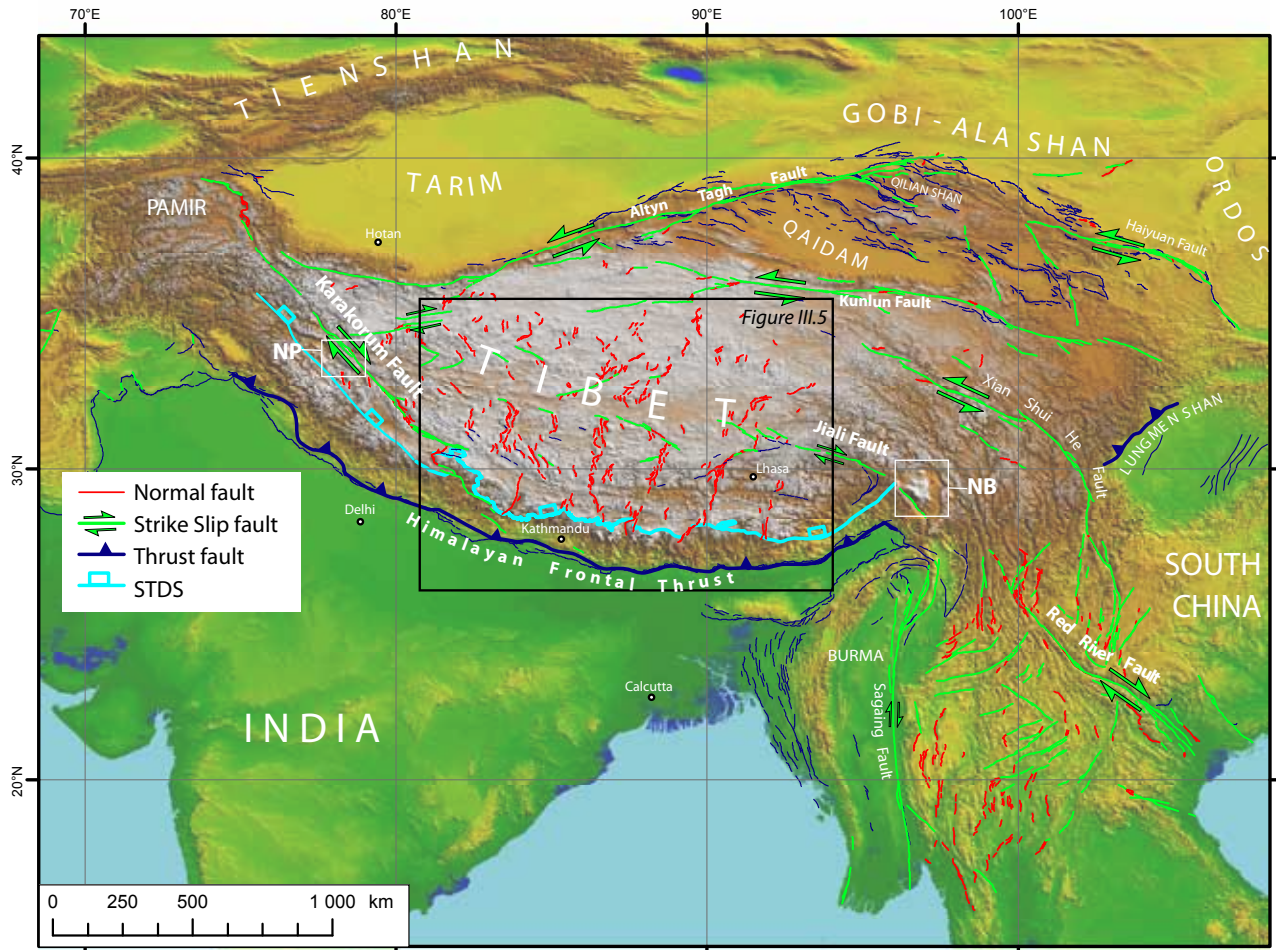


Figure III.4: Map of the active faults of Tibet. Faults traces are from Armijo et al. (1986), and a compilation of IPG Paris (pers. comm. R. Lacassin) derived from satellite image interpretations (Landsat, SPOT, ASTER, Quickbird and Ikonos), air photos, and field work. STDS (South Tibetan Detachment System) is from Leloup et al., 2010 (see Annexe A), NP = Nanga Parbat, NB = Namche Barwa

3.2.2. Geological and geomorphological context

Seven main rifts characterize the tectonics of the southern Tibetan plateau south of the Bangong suture (Armijo et al., 1986) (Figure III.5). This zone of extension is limited to the west by the southern Karakorum fault and to the east by the eastern Himalayan syntaxis (Nanga Parbat). To the north they connect with the Karakorum-Jiali shear zone defined as left-stepping en-échelon 200-300 km-long right-lateral faults along and mostly south of the Bangong suture. To the south, the grabens although discontinuous across the Yarlung suture reach into the high Himalayan range, on average about 150 km north of the Main Frontal Thrust, although some of the normal faults reach further south (Thakkola, Kartha, Yadong). On average, the 300-400 km-long by 5-10 km-large grabens are evenly distributed and separated by about 150-200 km (Armijo et al., 1986; Yin et al., 1999). The Xainza-Dinggye rift is situated in the central part of the south Tibetan plateau. The well-developed Xainza graben to the north connects with the right-lateral Gyaring fault (Armijo et al., 1986, 1989; Taylor et al., 2003) (Figure III.5). It extends to the south for a length of 160 km. It is clearly bordered to the west by an active normal faults outlined by steep triangular facets and straight spurs that cross-cut recent and older alluvial fans and terraces and moraines. To the east, the range front is also clearly outlined, but faulting seems more subdued although it becomes more active towards south. At the latitude of the Yarlung Tsangpo (N29.35°E), a 30 km-long and 6 km-large basin bordered to the east and west by normal faults allows for the exceptional widening (6 km) of the river bed. Normal faulting resumes 50 km farther south along the Mabja range as a 15 km-long west-dipping fault along the massif and along the Lagoï Kangri Massif as a 30 km-long west-dipping fault (Kali et al., 2010) (Figures III.6 and III.7).

South of Mabja, the eastern flank of the Ama Drime range is clearly outlined by a 60 km-long east-dipping active normal fault, the Dinggye fault, at the foot of steep triangular facets separated by glacial valleys. South of the Lagoï Kangri, a 30 km-long west-dipping normal fault (Cuomaï fault) bounds the Dingmu Co basin (Figures III.6 and III.7). Further southeast, the western flank of the Ama Drime massif is outlined by normal faulting (Pumqu fault of Armijo et al., 1986 or Sangkar and Kharta faults of Kali et al., 2010). These faults and the Dinggye fault delimit the Ama Drime horst. Both Dinggye and Kharta faults extend southward into the Himalayas. The Dinggye and Kharta faults can be followed southward to 27.9°N (Figure III.7).

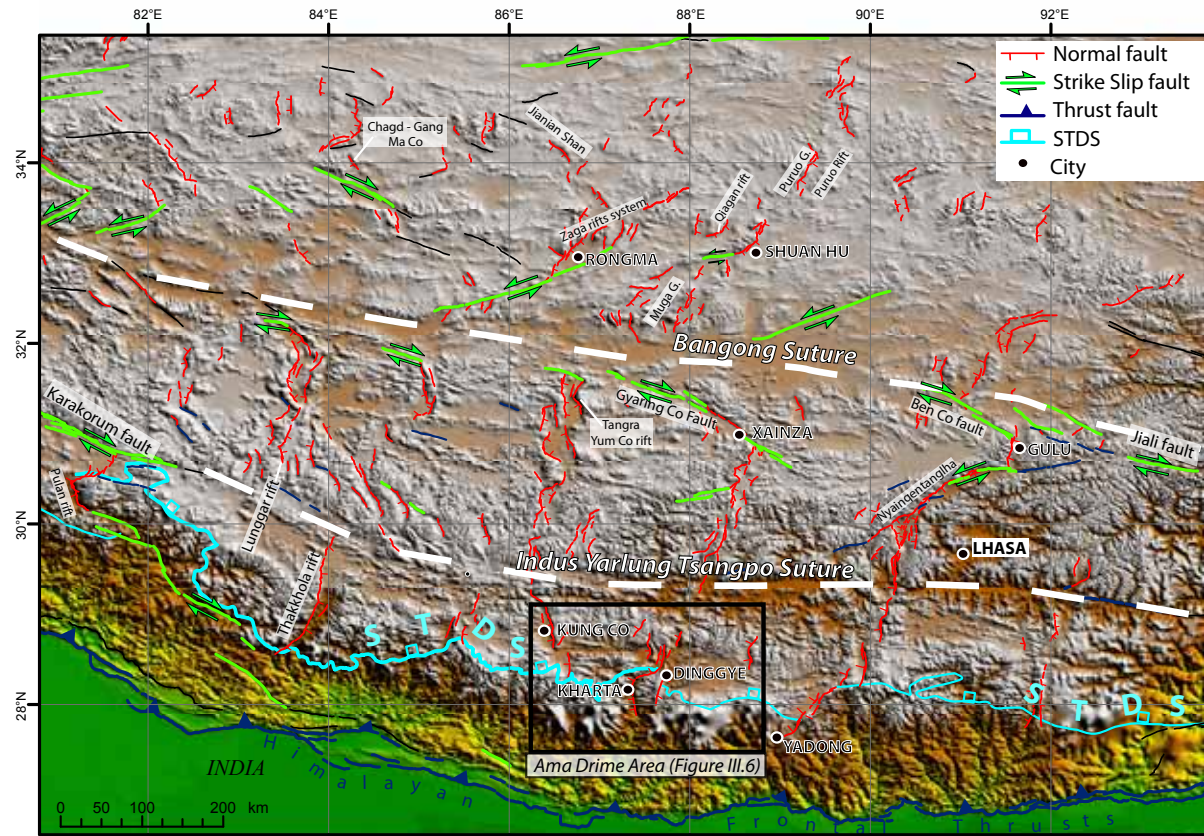


Figure III.5: Map of the active faults of central and south Tibet. Named areas refer to normal faults systems and basins that were targeted in recent studies. STDS (South Tibetan Detachment System) is from Leloup et al., 2010 (see Annexe A), Puruo G = Puruo Gangri, Muga G = Muga Gangri.

It is along the western Kharta fault, just east of mount Everest, that the Pumqu – Arun river succeeds to cross-cut the high Himalayan crystalline massifs towards India (Figure III.6). At a more detailed level, at two places the river leaves the graben to enter the footwall of the main normal fault, in the north near the Yo Ri (Wager, 1937; Armijo et al., 1986) and to the south, southeast of Kharta (See Figures III.8 and III.9). While different interpretations have been proposed for the northern loop of the river into the footwall of the Kharta normal fault, antecedance (Wager, 1937) or capture (Armijo et al., 1986), there is ample evidence that the river has been dammed several times in the Yo Ri gorge separating the upper Pum Qu catchment and basins from the Himalayan Arun outlet. Lake deposits and several levels of shorelines up to 300 m, i.e. at 4400 m a.s.l., above the present basin level attest to alternate lacustrine and drained phases.

The two main active faults that limit the Ama Drime massif to the east and west thus define a horst (Figure III.7). These faults cross-cut the E-W trending South Tibetan Detachment System (STDS) and N-S ductile normal shear zones (see chapter 2). The reconstitutions of the Pressure-Temperature-Time-Deformation paths of the ductile shear zones that allowed exhumation of the eclogite-rich orthogneiss of the Ama Drime massif (Kali et al., 2010; Leloup et al., 2010; Lombardo & Rolfo, 2000; Groppo et al., 2007) imply a change of extension direction from N-S along the STDS until 13 Ma to E-W along the N-S normal faults initiating prior to 11 Ma. The N-S normal faults have accounted for a total exhumation of about ≤ 0.5 GPa (18 km) that probably occurred in two phases: the first one until ~ 9 Ma and the second one since 6 to 4 Ma at a rate of ~ 1 mm/yr. Now the active normal faults crosscut moraines and terraces that fill small basins on each side of the horst (chapter 2). Similarly, the Mabja range is a leucogranite-orthogneissic dome (Lee et al., 2004) bordered on the western side by the active Mabja normal fault (Figure III.7).

In the following section we describe in more details sites targeted along these faults that allow to constrain the slip-rate of the active faults.

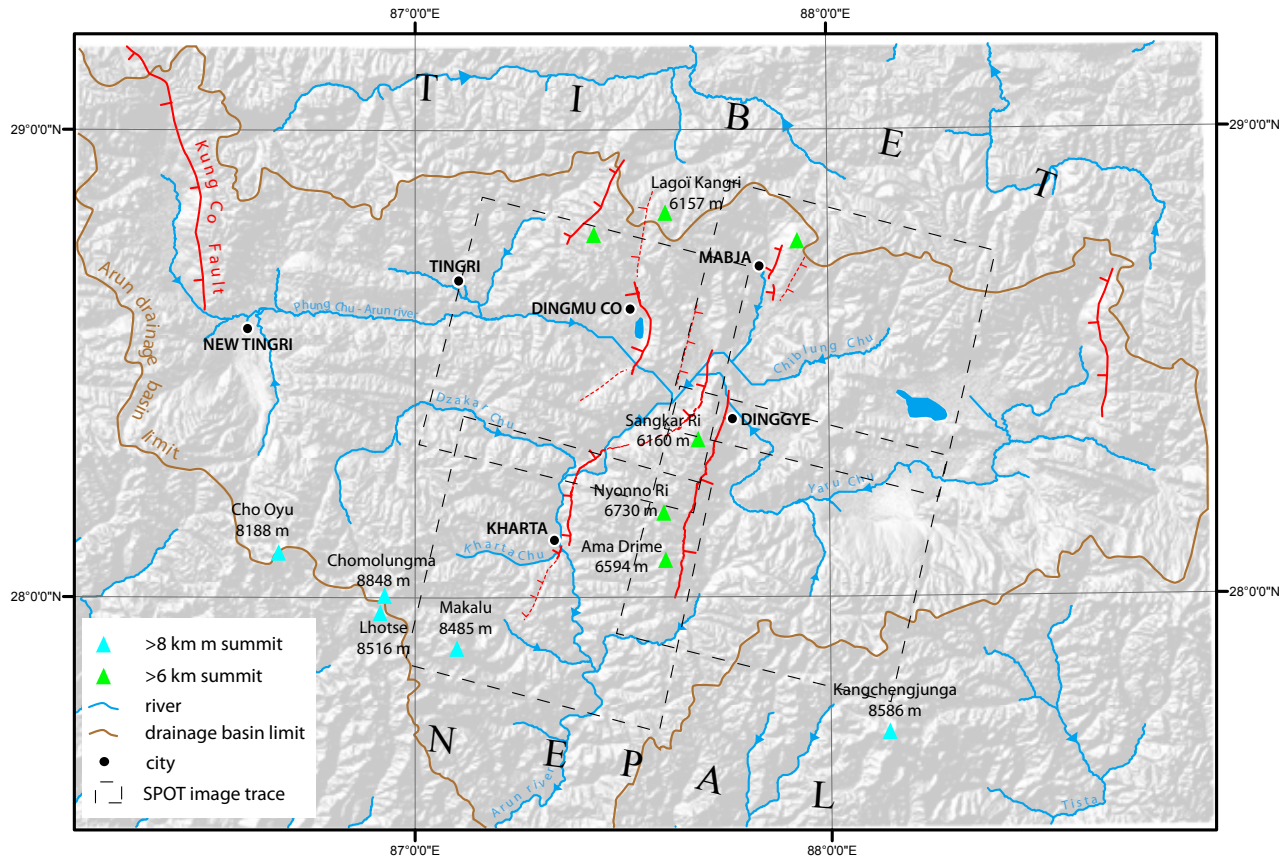


Figure III.6: Map of the Ama Drime area extended to the drainage basin of the Arun river. Projection is UTM45. Hydrologic network and basin are drawn from 90 m resolution SRTM with the ArcGis software, and from Wager (1937). Faults are mapped from fieldwork, interpretation/analysis of 2.5 m resolution SPOT satellite and Landsat images and from Armino et al. (1986). See Figure III.7 to visualize the SPOT satellite images.

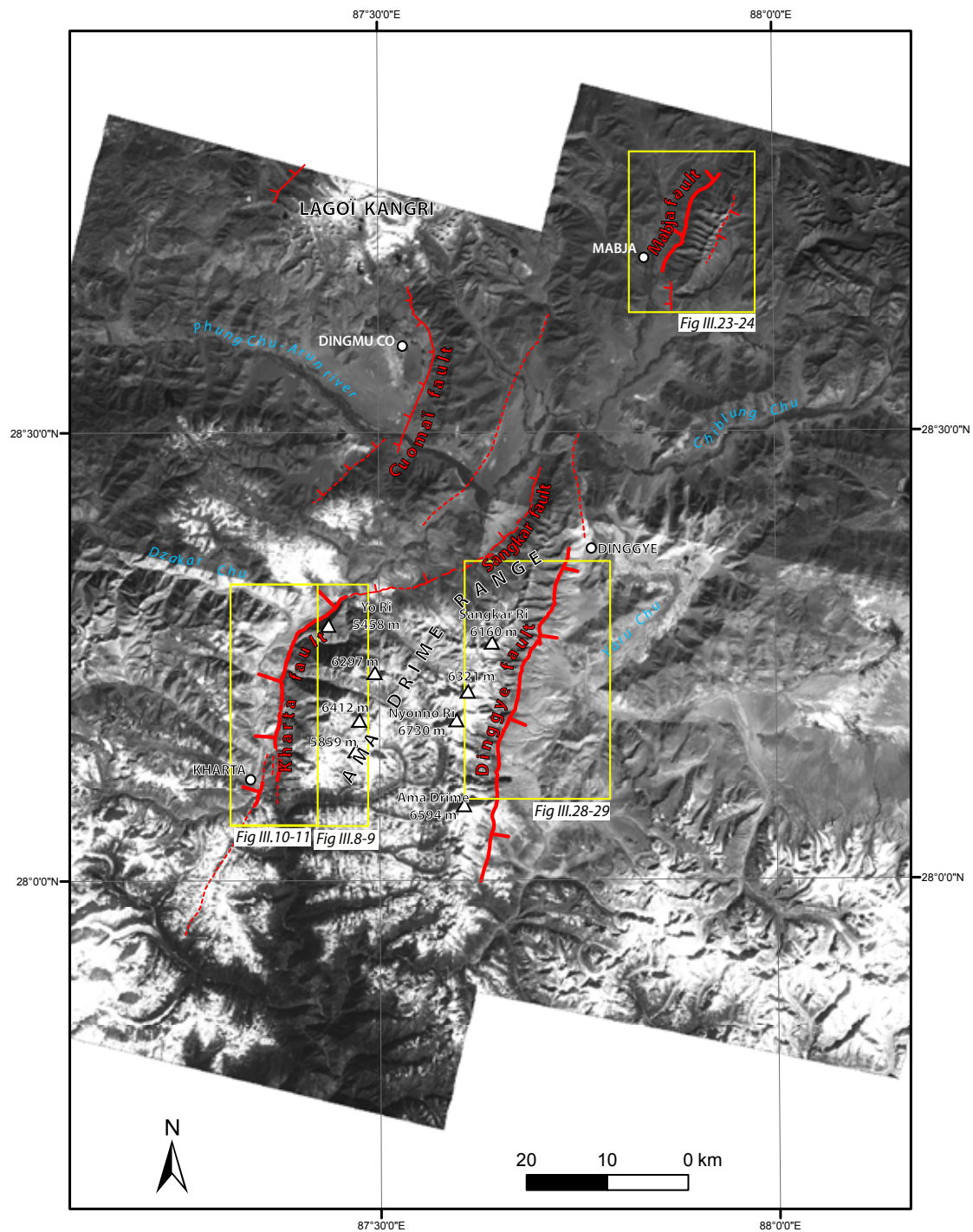


Figure III.7: Map of the Ama Drime - Mabja Area. Four SPOT5 satellite images (resolution, 2.5 m) are used in the mapping of the quaternary formations. See Figures III.8 to 11, III.23 and III.28-29 representing close up map of the studied sites

3.2.3. Description of faulted structures

3.2.3.1. The Kharta Fault

The Kharta normal fault is clearly outlined along the western side of the Ama Drime at the base of typical triangular facets (Armijo et al., 1986) (Figures III.8 to 11). It can be followed from 27.9°N to 28.35°N, for a length of about 40 km. The clearest section is located in the Kharta basin, where the fault strikes N-S for 20 km as a single trace outlined by a scarp cutting through most of the river terraces and moraines (Figures III.10 and 11). It is also here that the highest triangular facets can be seen, reaching a height of about 1500 m for an average slope of 37° (Yo Ri facet, Figure III.8). To the south of Kharta, the faults splay into two fault strands, the western one turning slightly to the SSW (strike N20°; Figures III.7, III.10.11). The western main fault strand, leaves the Kharta basin and Arun valley and reaches higher ground where it offsets moraines before entering the high Himalayan summits area. Its trace can be followed until 27.9°N on high-resolution satellite images. To the north of the Kharta basin, the fault makes a turn to NE-SW (N70°E) for 20 km. The triangular facets are smaller (500 m) and this section may accommodate a left-lateral component of movement (Armijo et al., 1986). Farther north, the fault resumes a N15°E strike and its trace is less clear due to either less tectonic activity or a subdued trace affected by paleolake level changes.

The basin bordering the Kharta fault is slightly narrower than the basin along the Dinggye fault. It is filled by sediments of the Arun and Kharta rivers (a minimum thickness of ~50 m is estimated from the cross-section view in the terrace risers of the Arun) (Figure III.14). These sediments, principally pebbles to boulders of gneiss and granite, are now reincised by the Arun river abandoning a set of 5 main terraces (Figures III.10 and 11). The upper terraces deposits are covered by fans of the Arun tributaries, post-glacial fans and relict moraines of hanging U-shaped glacial valley of the Ama Drime. Although the Arun River flows for ~280 km (and the Yaru Chu for ~190 km) north of the STDS before entering the Kharta Basin, no tethyan metasediments have been found in the Kharta basin deposits. In contrast, quaternary deposits north of the STDS along the Yaru Chu are composed of granitic and metasedimentary pebbles to boulders implying that the Kharta Basin is essentially filled by material from the proximal slopes of the Ama Drime Massif.

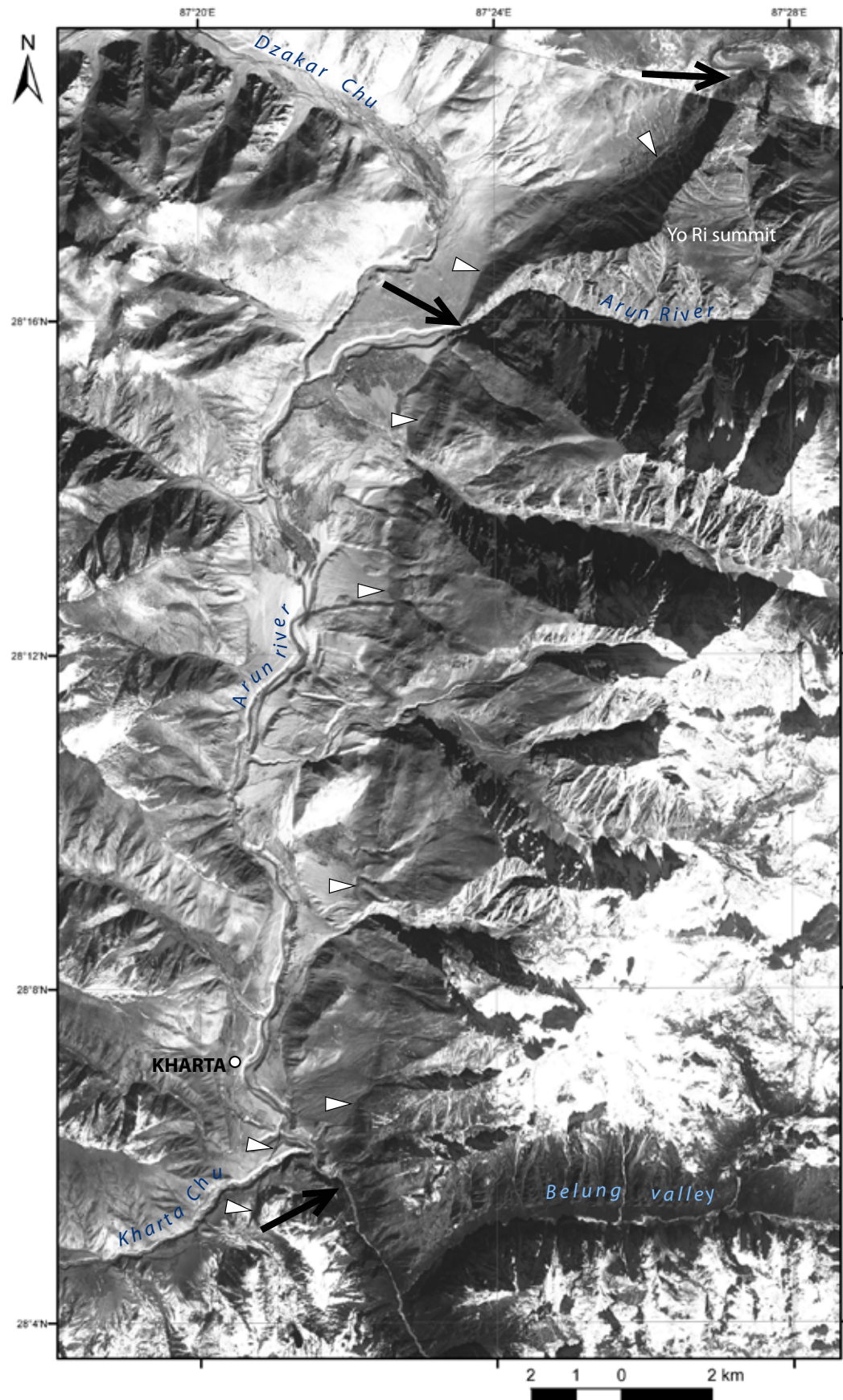


Figure III.8: : Zoom of the SPOT5 satellite image of the Kharta Basin drained by the Arun river. Note clear triangular facets outlining the trace of the Kharta normal fault. White triangles show the fault trace and three black arrows point the place where the Arun River crosses the fault scarp.

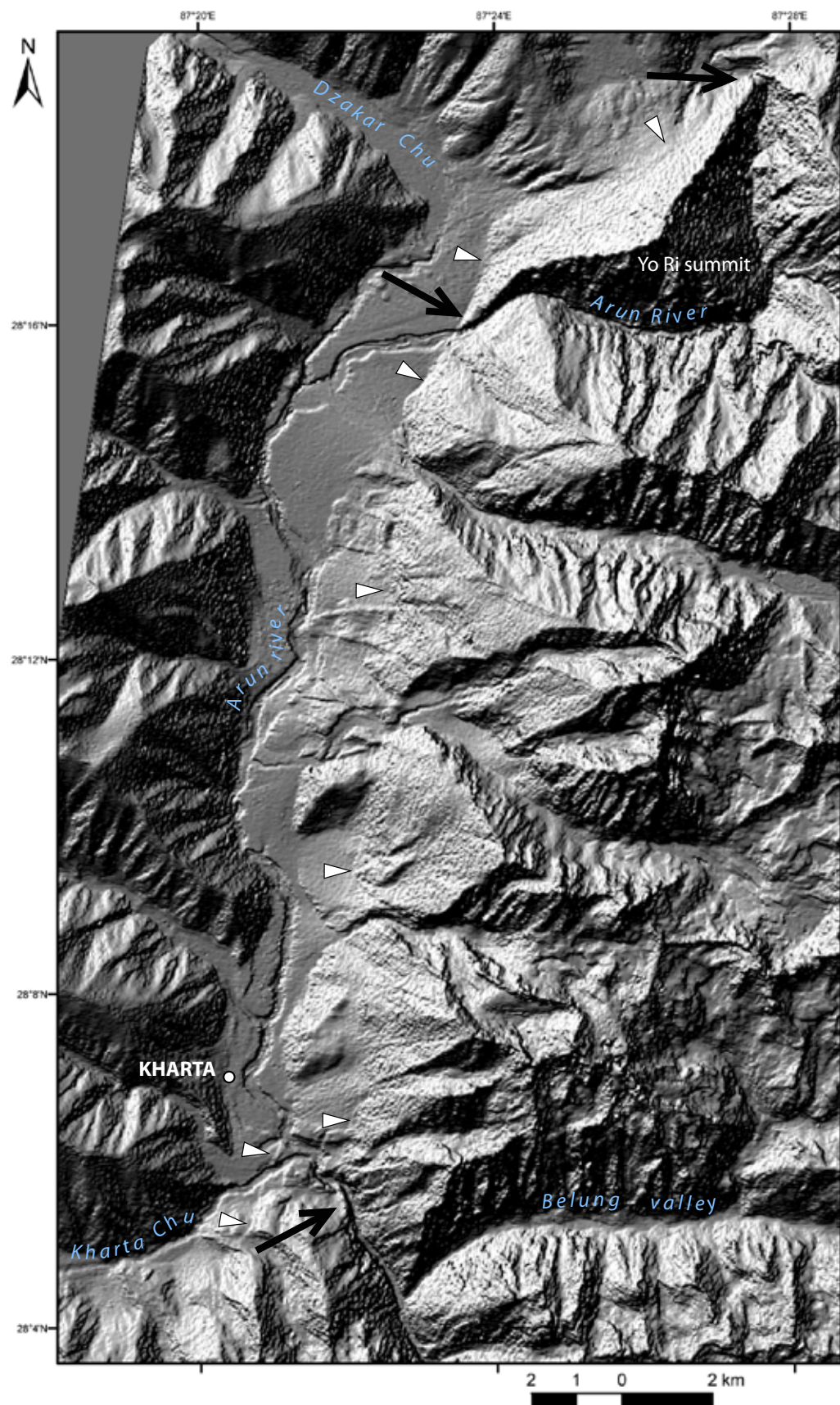


Figure III.9: SPOT5 DEM of the Kharta Basin. White triangles show the fault trace and three black arrows point the place where the Arun River crosses the fault scarp.

Interpretation from analysis of SPOT satellite images, topographic profiles constructed from the SPOT-DEM and field-work lead to a geomorphic interpretation of the relative stratigraphy of moraines, fans and alluvial terraces and allowed the reconstitution of a first order chronology (Figures III.10 and 11).

The oldest structures in the basin are moraines (M) and hanging remnant terraces (T4-T5). A remnant terrace of T4 is situated at the southern extremity of the “Yo Ri facet”. Another is located just south of the Kharta– Arun rivers confluence (see the title picture, p. 155-156, for illustration). Other old structures are mounds buried by younger fan deposits between the Arun and Dzaakar Chu rivers in the north. After or during deposition of these formations, the sedimentation of the T4-F4 structures occur (see relations between moraines and T4-F4 on the map Figure III.10 and on the profiles projection Figure III.11).

Subsequent to these old deposits, a post-Last Glacial Maximum complex of fluvio-glacial fans and alluvial terraces developed. Several generations of fluvio-glacial fans (F4 to F2), which contribute to the removal of moraines, are imbricated with a succession of inset alluvial terraces (T4 to T2). The T3 terrace level can be followed all along the N-S profiles across the Kharta Basin (Figure III.10), implying a link with a major phase of deposition in the basin probably related to the last glacial-interglacial transition (LGM to Holocene). T2 and T4 terraces levels are found essentially in the south of the basin. Relics of T4 probably exist under the large fans of the eastern 3 glacial valleys. The geometry and particularly the slopes of the deposits along the basin from north to south (Figure III-10) show that subsequent to a phase of aggradation, marked by a high depositional level sloping regularly 0.5° to the south (terrace level T3), a phase of incision followed propagating from south to north as marked by the convex shape of the lower terrace profiles (T2-T1) and their, in general, steeper slopes south of the basin than north (e.g., Harkins et al., 2007). The Arun incision is thus much deeper in the south (~ 100 m) than in the north (~ 50 m) (Figure III.11).

On top of the post-LGM complex, two landslides of debris can be seen at the base of the triangular facets (Figures III.8, 9 and 11). These landsliding events have occurred after deposition of terrace T2-T3 and the scars of the two landslides are still visible in the triangular facet above the seismic fault scarp. The landslides are likely linked with shaking during large seismic events along the fault and

may testify of the recent activity of the Kharta fault. Another landslide deposit is clearly identified on the western side of the Arun River, at the Arun-Dzaakar Chu confluence.

The fault cross-cuts all these fluvio-glacial deposits, offsetting them vertically. In order to quantify vertical throw rates along the fault, the more accessible sites were targeted for morphochronology. First, the northernmost fans and hanging remnant terraces have been sampled, just at the exit of the first gorges of the Arun River (the Yo Ri site, Figure III.12 to 15). Second, south of Kharta village, the fans and moraines offset by a splay of the main fault have been dated at the confluence with the Kharta River (the South-Kharta site, Figures III.16 to 21).

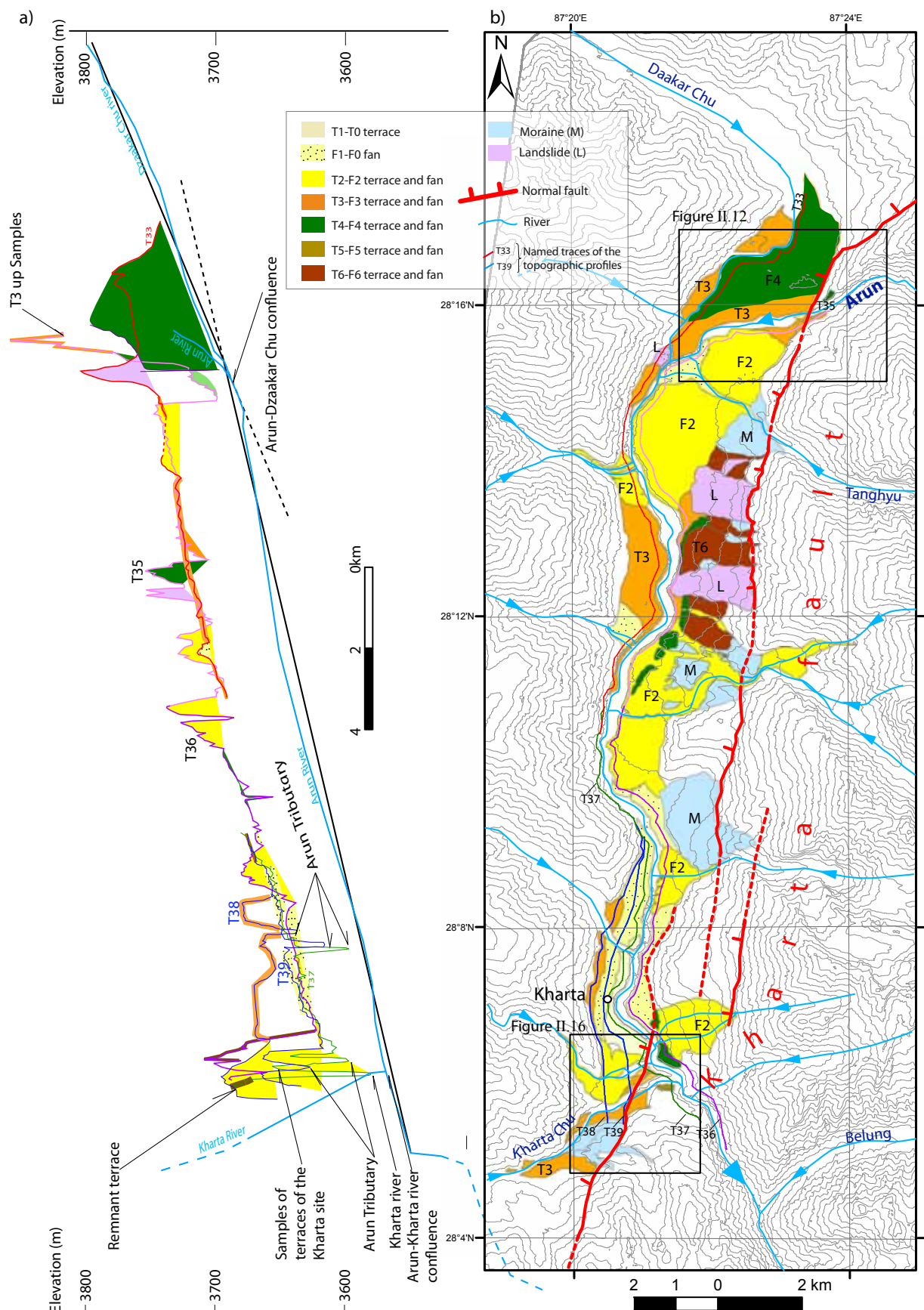


Figure III.10: (a) Topographic profiles of the terraces along the Arun-Phung Chu river projected in the N-S direction. They have been extracted from the SPOT5 DEM with Global Mapper software. Profiles traces are represented in (b). Profiles names are, on the western bank of the Arun River : T33 (red line), T37 (green line), T38 and T39 (two blue lines), on the eastern bank :T35 (pink line) and T36 (purple line). The profiles are highlighted by the geomorphological interpretation. (b) Map of the quaternary deposits and the Kharta active normal fault. Traces of the profiles are represented. See details of the sampling sites in the Figures III.12 (South-Kharta site) and III.16 (Yo Ri site).

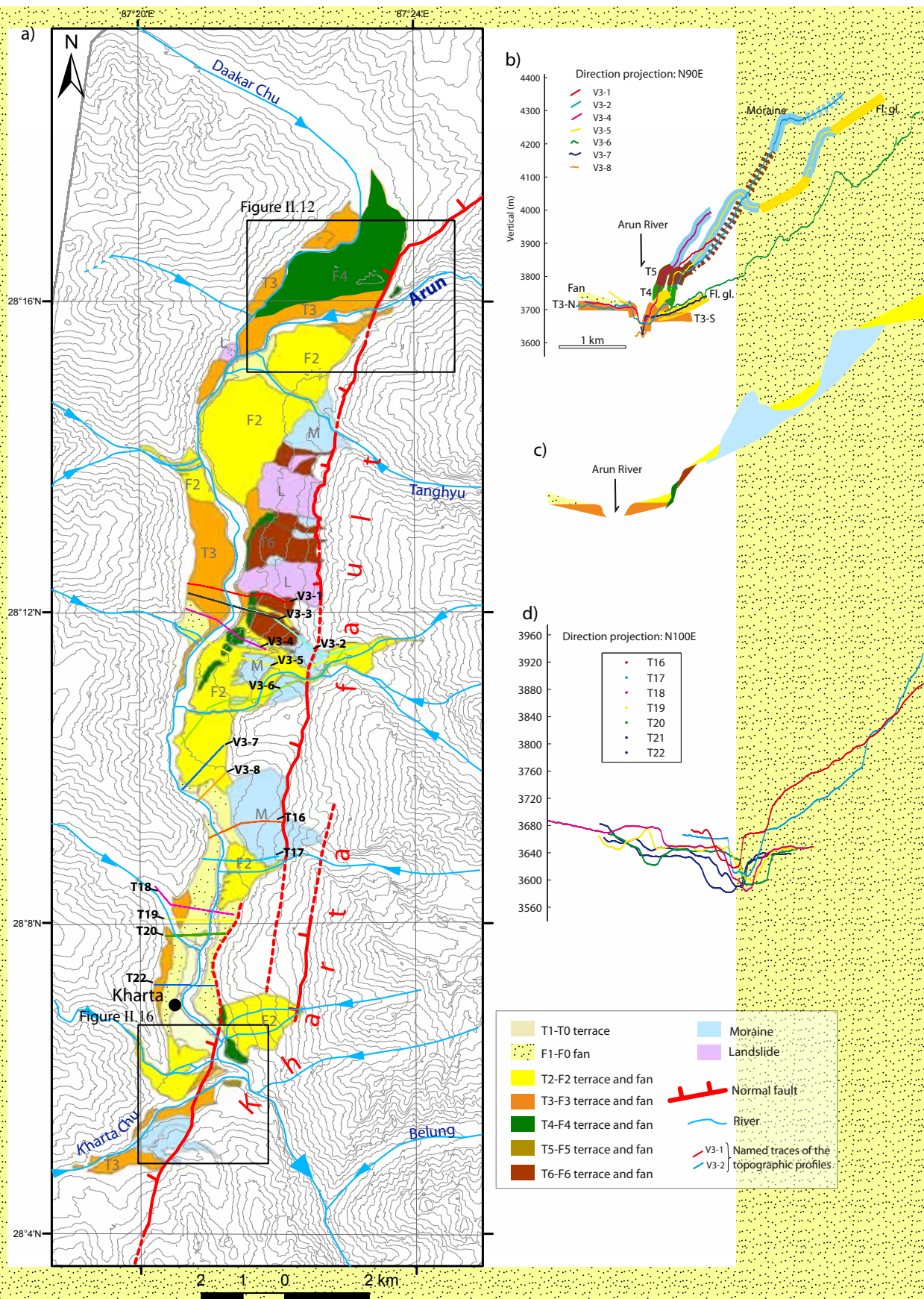


Figure III.11: (a) Map of the quaternary deposits and the Kharta active normal fault. (b) Projection of seven E-W profiles (numbered V3-1 to V3-8) in the N90°E direction. Profiles traces are represented in (a). They are highlighted by the geomorphological interpretation. (c) Interpretation of the E-W profiles. (d) Projection of seven E-W profiles (numbered T16 to T22) in the N100°E direction. Profiles traces are represented in (a). See details of the sampling sites in the Figures III.12 (South-Kharta site) and III.16 (Yo Ri site).

Yo Ri Site

North of the Arun River, at the southern edge of the Yo Ri triangular facet, relics of a large fan (F4) and older terrace (T4) are hanging on the fault footwall (Figures III.12, 13 and 14). In more details, three sub-levels of T4 are recognized, T4a, b and c (Figure III.12 and Appendix III-3). F3 fan is clearly recognized on the hanging wall near the Arun river, while remnants of the T4-F4 level may be visible away from the Arun towards north. The F3 fan is covered by large blocks (F4) on the sides of an old channel. These blocks (up to 10 m in diameter) are attributed to a debris avalanche from the Arun gorge (5 blocks have been sampled; Appendix III-5). The F4 fan deposits mantle old mounds, on each side of the Dzaakar Chu, that may be attributed to moraine remnants of a glacier coming down from the Nyonno Ri range (Wager, 1937) (Figure III.12). South of the Arun river, terrace T3 is clearly offset by the Kharta normal fault separating a 500 m long remnant of T3 upstream from its counterpart downstream of the fault (Figures III.14 and 15; Appendix III-1).

Handheld GPS profiles, checked against topographic maps (1:100000) and SPOT 5 DEM (20 m resolution), allow to constrain the minimum offset of the T4 sub-levels to range between 100 to 120 m (Figure III.15a). The T3 level is offset about 12 to 17 m (Figure III.15b).

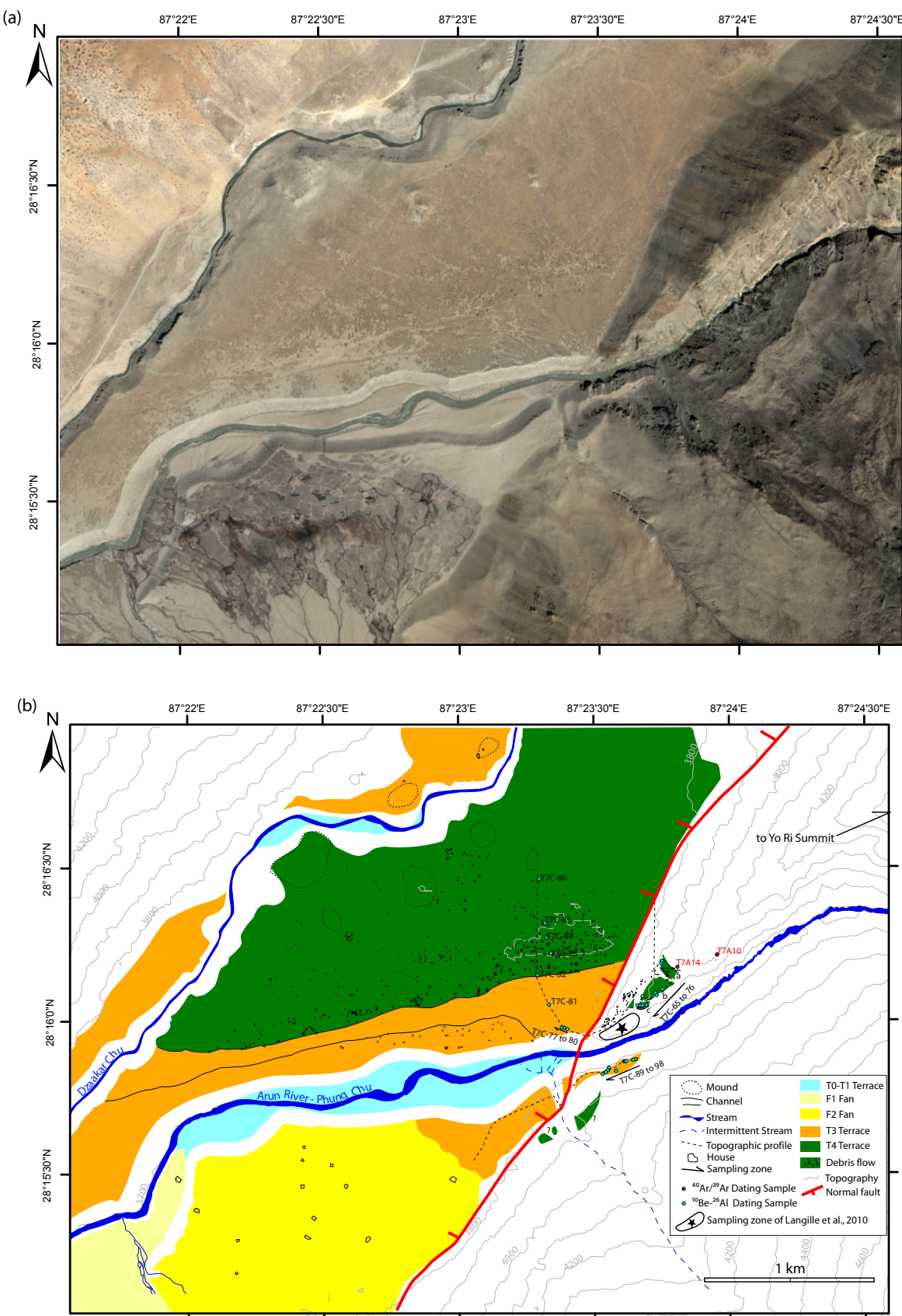


Figure III.12: (a) Ikonos satellite image from Google Earth and (b) Geomorphic interpretation of image of the Yo Ri sampling site. Traces of the topographic profiles of the Figure III.15 are indicated (heavy dashed line). Samples used for the study of the long-term deformation are represented here (in red and with the star), see section 2.2.2.4 (p. 99) for an explanation.

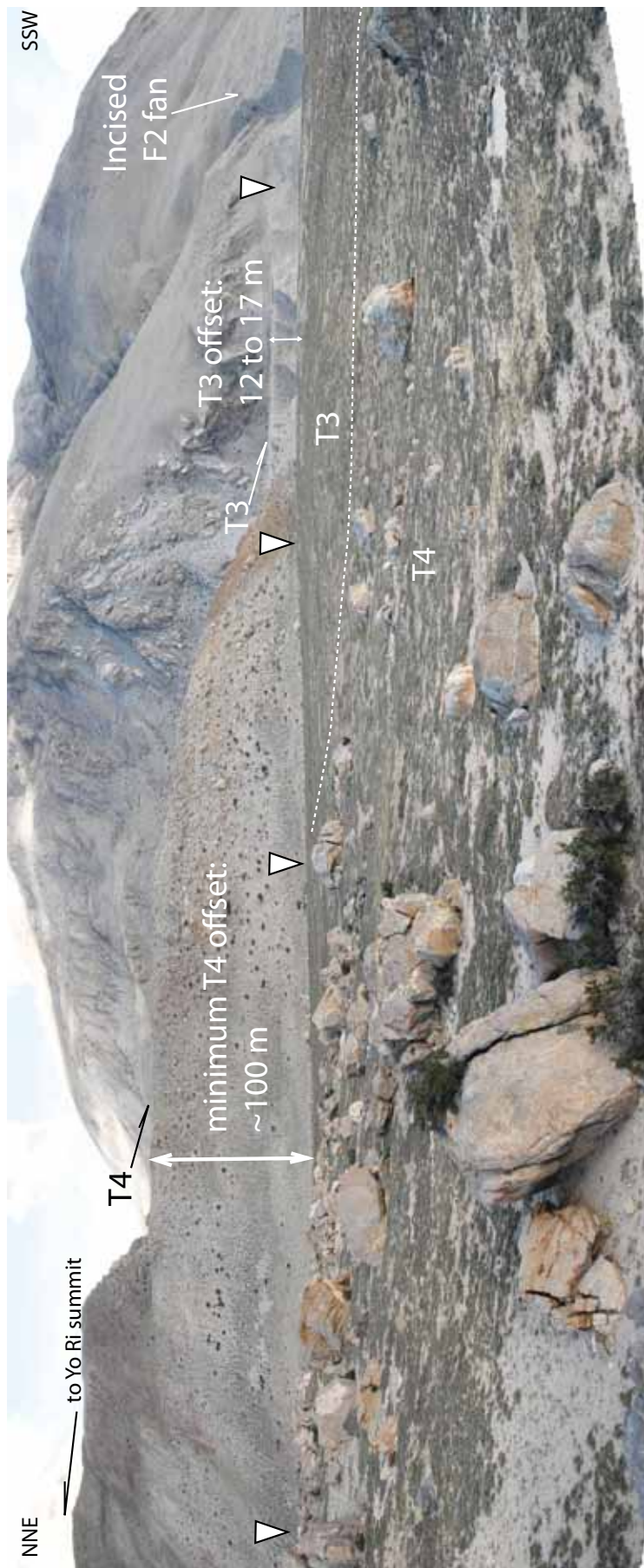


Figure III.13: Eastwards view of southern part of the Yo Ri triangular facet. The trace of the Kharta fault is marked by the white triangles. The hanging T4 terrace is situated ~ 100 m above the hanging wall block of the fault. The T3 terrace shows an offset between 12 and 17 m. Big blocks belong to the debris flow relicts embedded in the T4 surface.

(a)



(b)

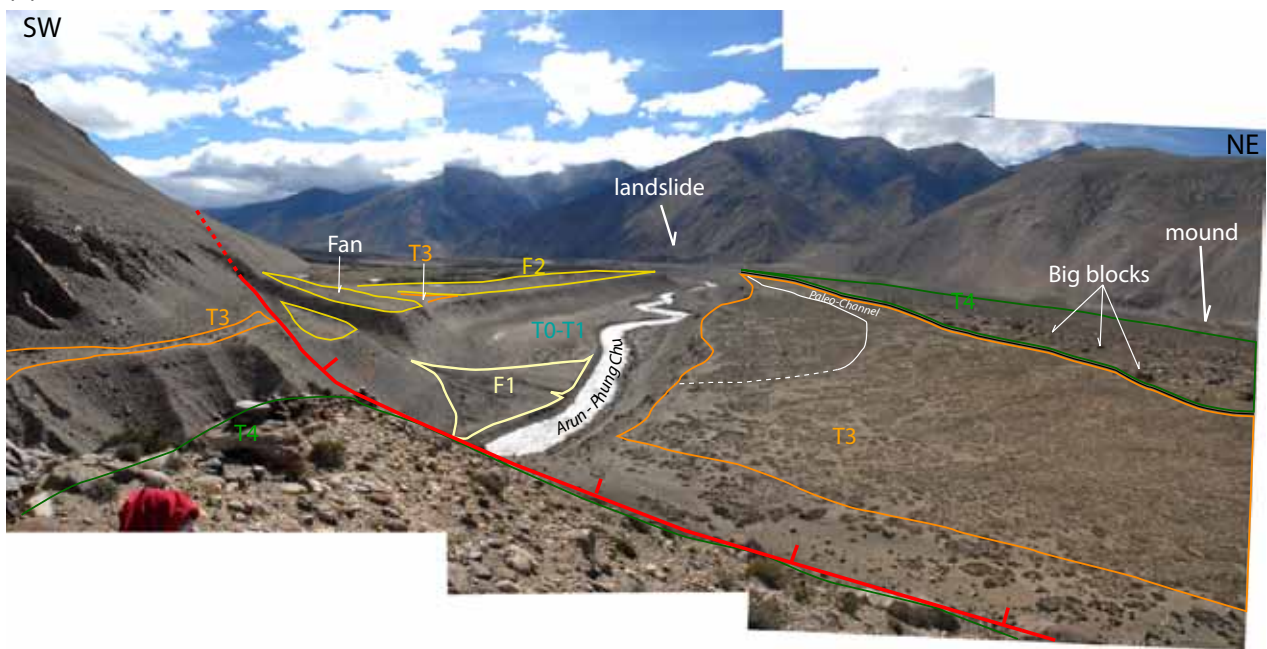


Figure III.14: (a) Bird view of the Yo Ri site. Arun river has incised and abandoned a regional T3-T4 level now offset by the normal fault. (b) Interpreted view.

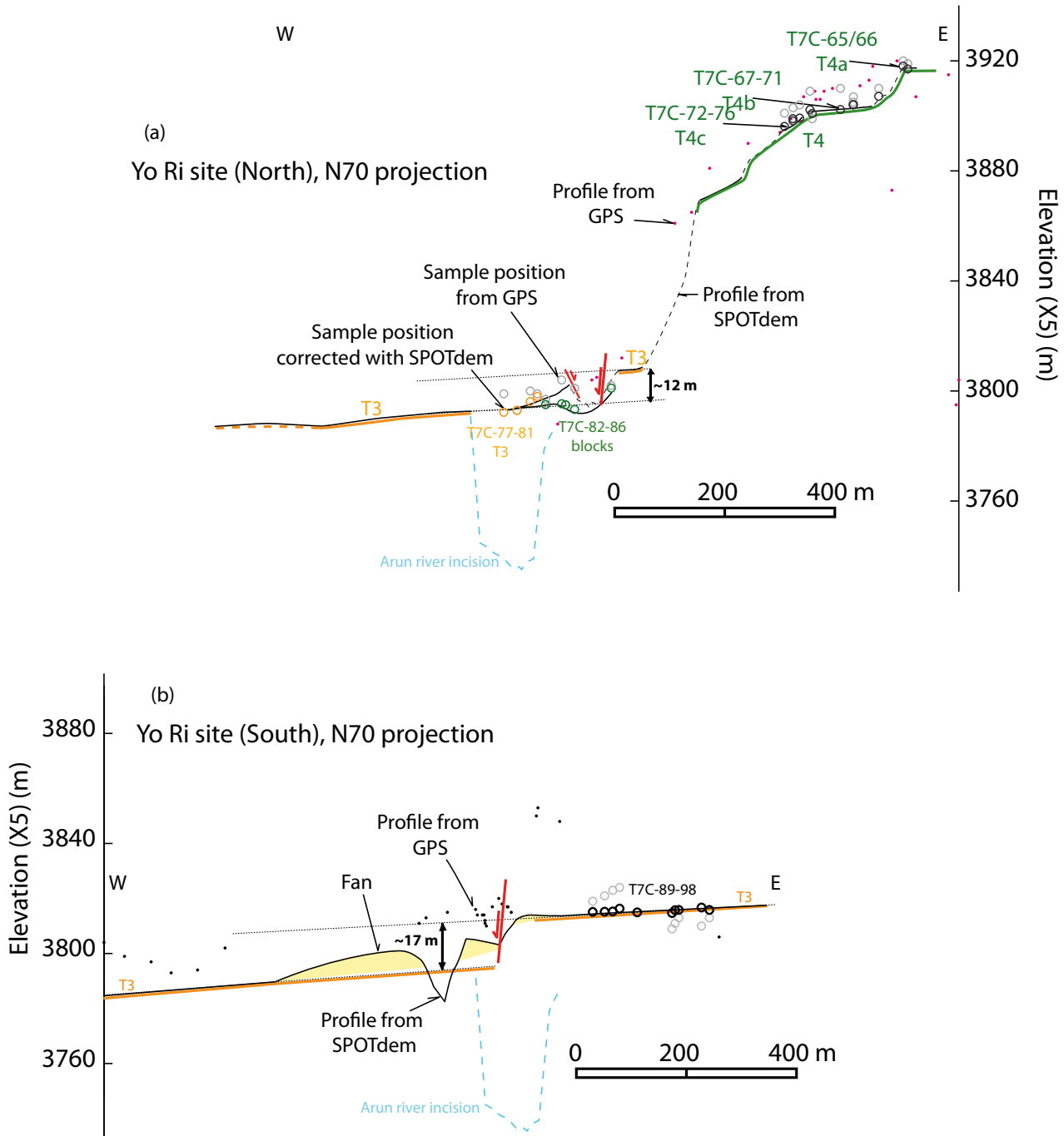


Figure III.15: Topographic cross sections of the Arun river terraces (projection is sub-parallel to Arun river bed). at the Yo Ri sampling site, (a) north of the Arun river, (b) south of the river. Traces of the profiles are drawn in Figure III.12.

South-Kharta Site

In the southern Kharta basin, the main Kharta normal fault splays into two sub-parallel branches. The eastern branch follows the foot of the largest triangular facet. The western branch, steps to the west at about 1 to 2 km, striking NS for about 8 km, and then turns westward to strike N20 (Figure III.10). South of the village of Kharta, the main western branch of the Kharta fault crosses the southeast flowing Arun river and cuts across a set of terraces abandoned at the confluence between the Arun and Kharta river (Figures III.16 and 17). The highest terrace level, in the same stratigraphic position as the T3 level north of the Kharta basin is assigned to T3 (Figure III.20). Fast incision of the Kharta river due to the fast Arun river base level drop has lead to the abandonment of lower terrace levels (T2) inset into the T3 conglomerate (Figures III.17, 18 and 19). Farther southwest, the fault crosses the Kharta river and cuts through a moraine complex of a north-south tributary valley of the Kharta river (Figures III.18 and III.22). The northeastern lateral moraine ridge is cleanly cut and vertically offset by the normal fault, although it is clearly visible in the field and on high resolution images, that the northwestern hanging wall has been later reoccupied by a glacier pecten (Figure III.16a).

Offsets were constrained in a similar way as those in the north. The T3 and T2 terraces have similar vertical offset across the Kharta fault scarp of about 15 ad 14 m, respectively (Figure III.21). The nice scarp at the end of the lateral moraine amounts about 20 to 40 m and may represent a minimum offset for the reasons discussed above. (Figure III.22).

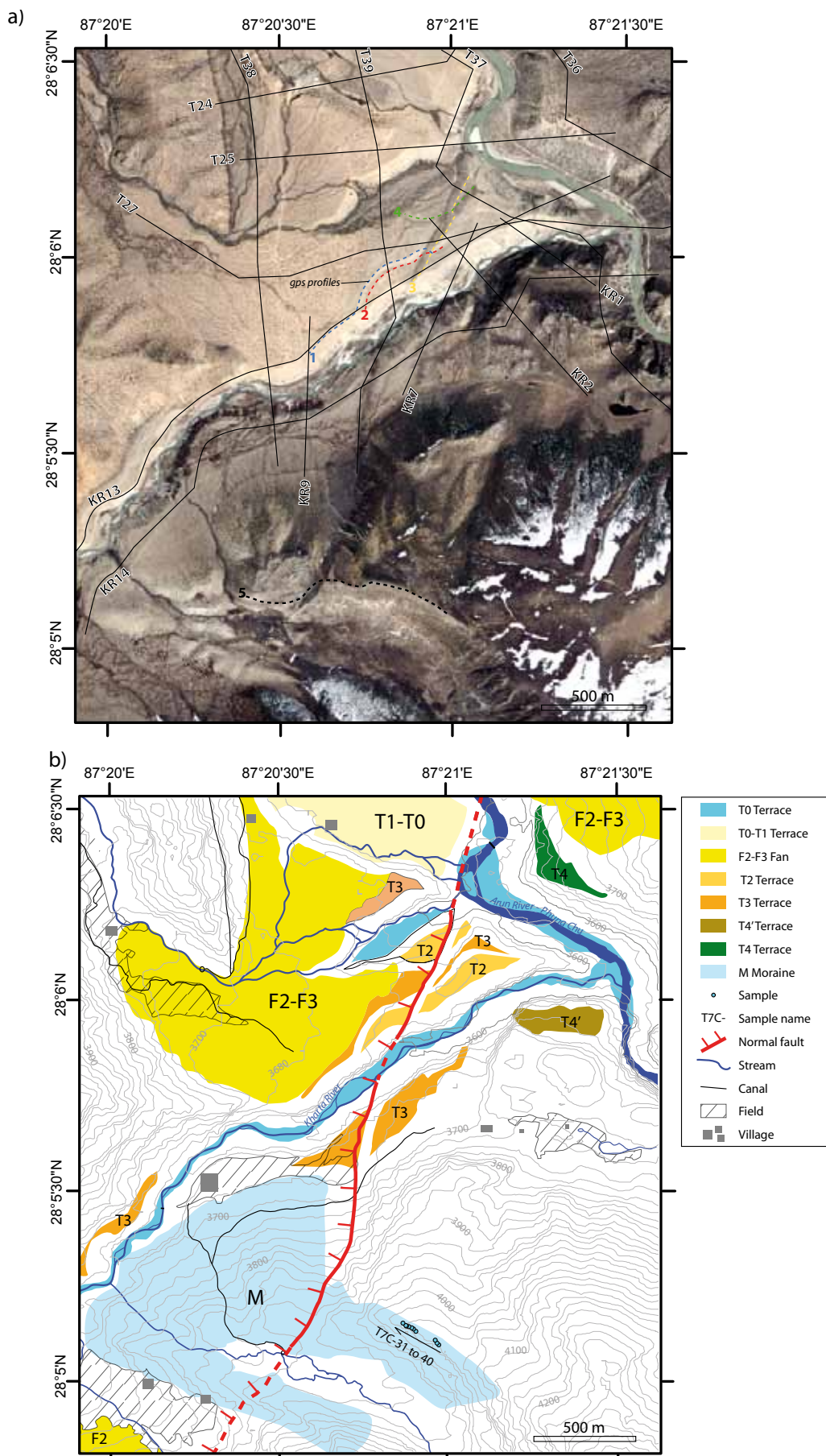


Figure III.16: (a) Ikonos satellite image of south Kharta site (from Google Earth). The traces of the topographic profiles of the Figure III.20 are indicated. (b) Geomorphic interpretation of south Kharta site. (See the title picture, p. 155-156, for illustration).

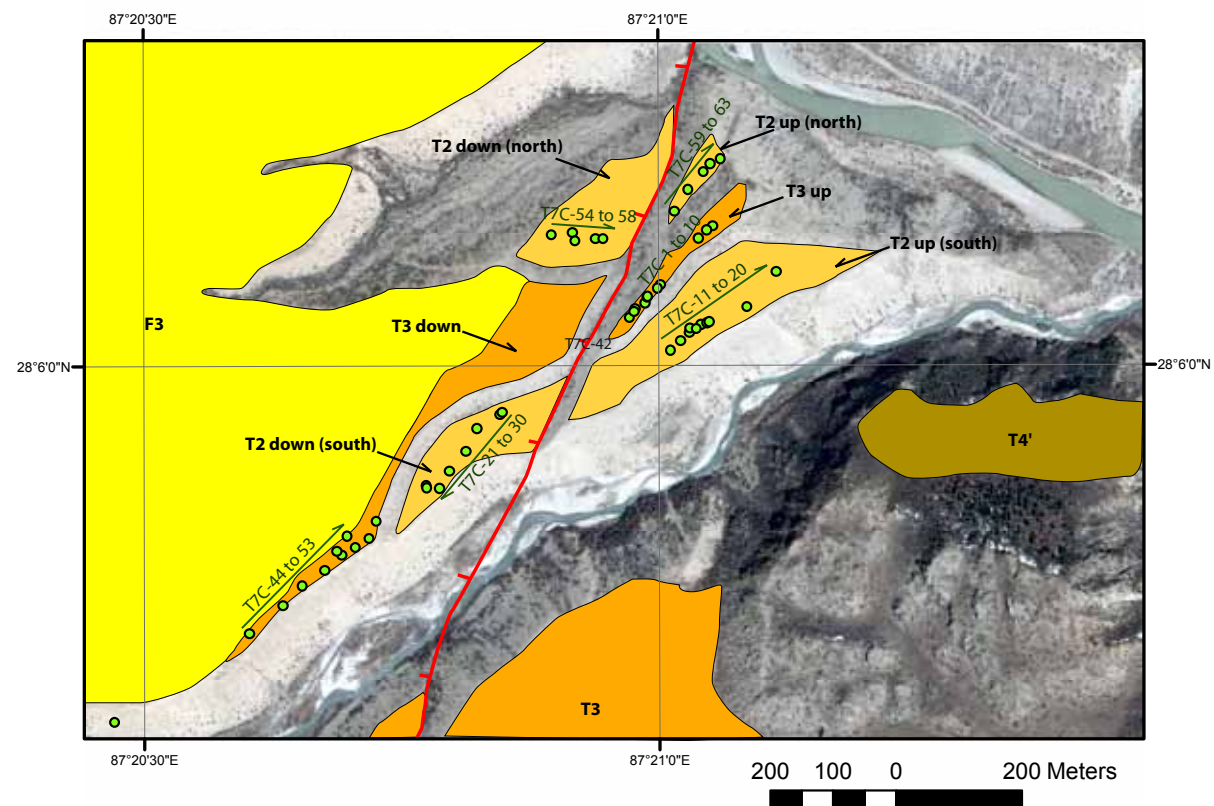
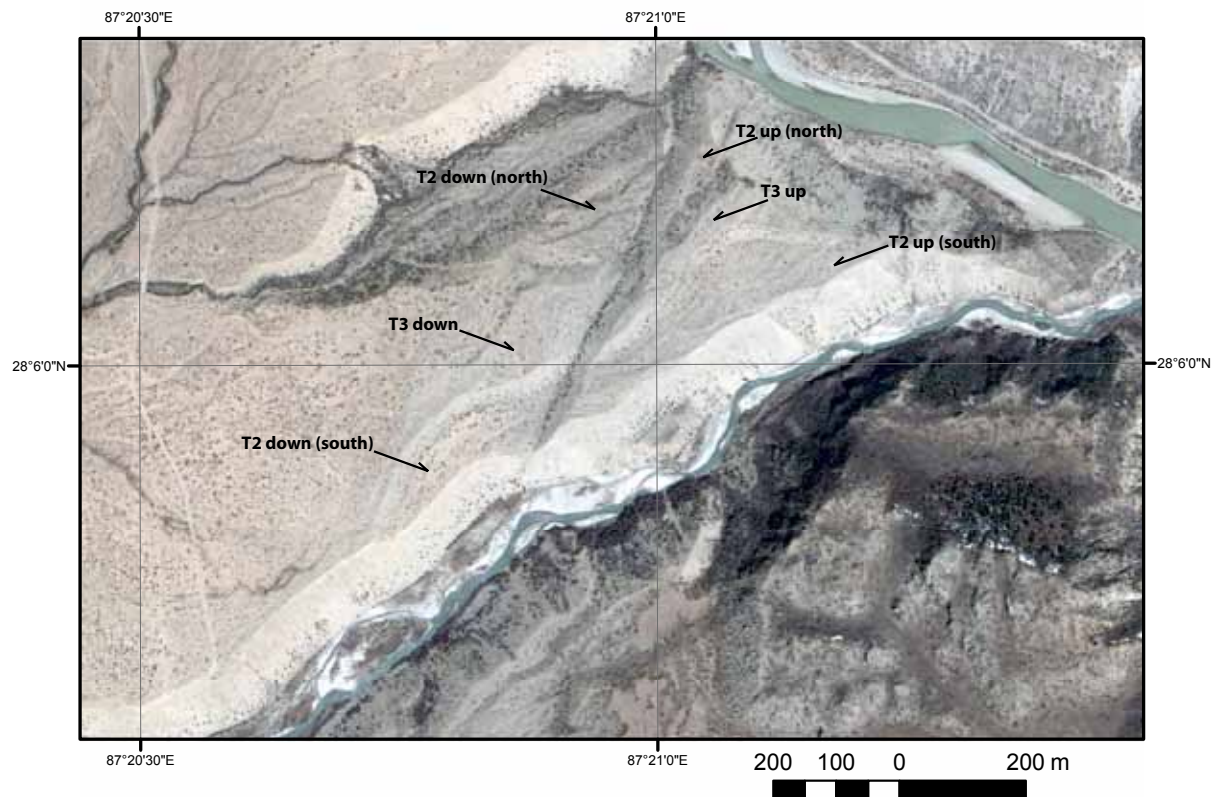


Figure III.17: (a) Close-up view of the south Kharta site, Ikonos image. (b) Geomorphic interpretation of image and samples positions.

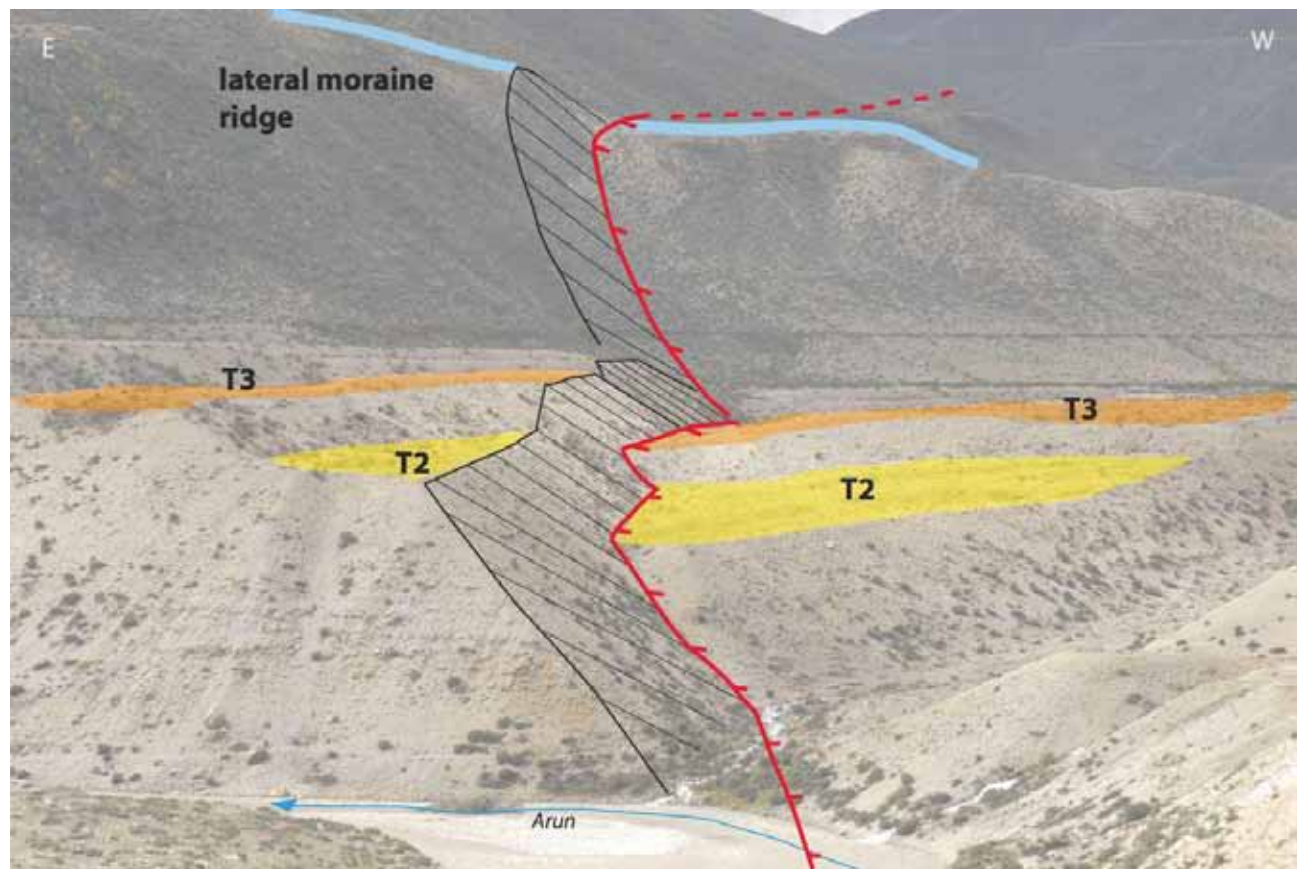


Figure III.18: The Kharta site from eastern bank of the Arun river. a) View of the fault scarp across the sampled terraces moraine, above the Arun River, and the b) interpretation.

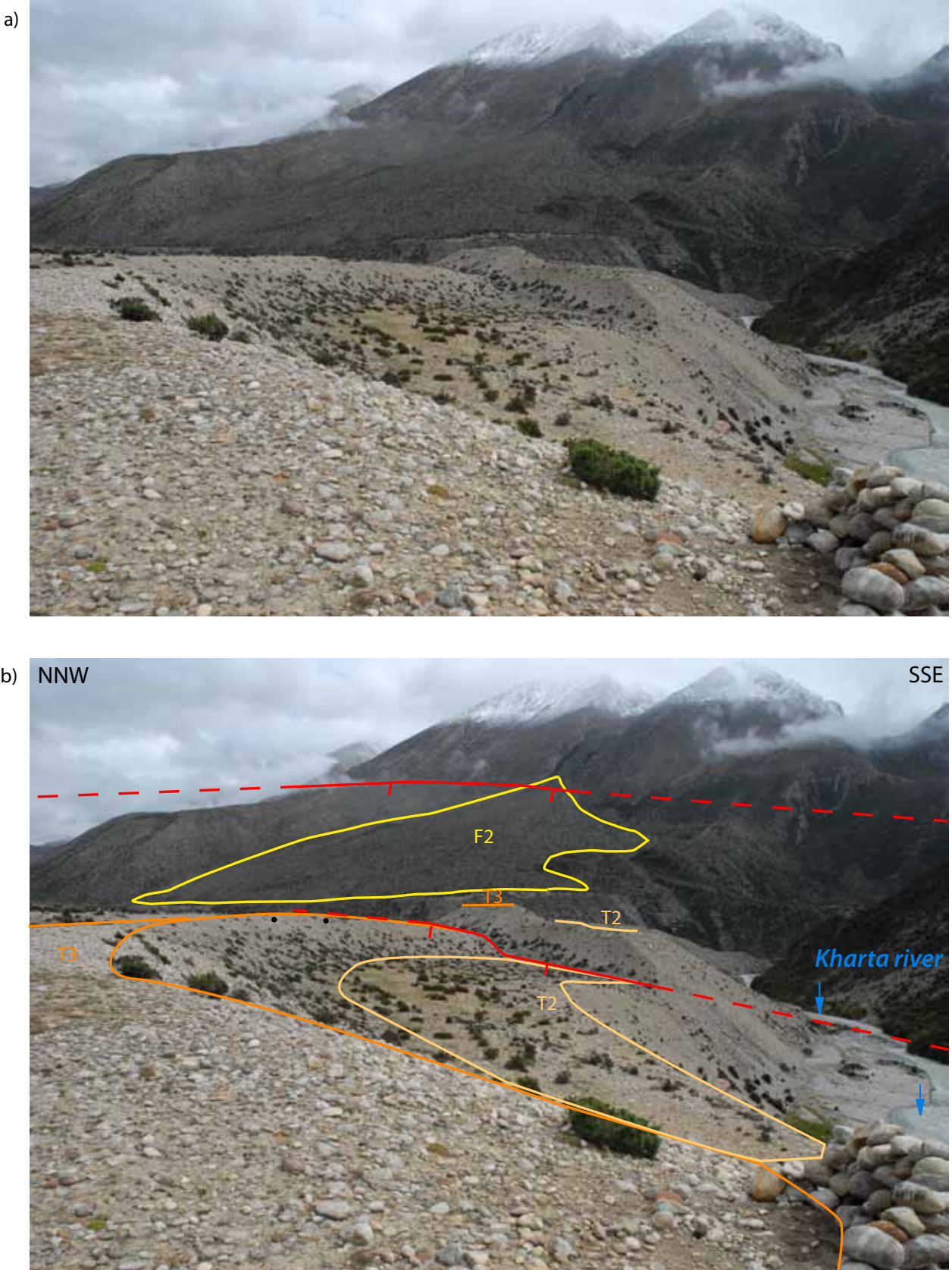
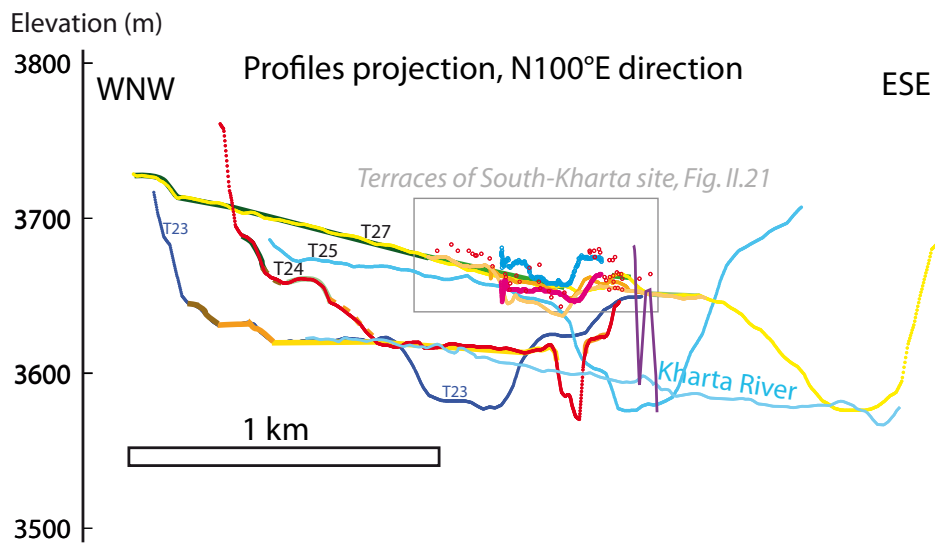


Figure III.19: a) View to the East, terraces of the Kharta sampling site. b) Interpretation

(a)



(b)

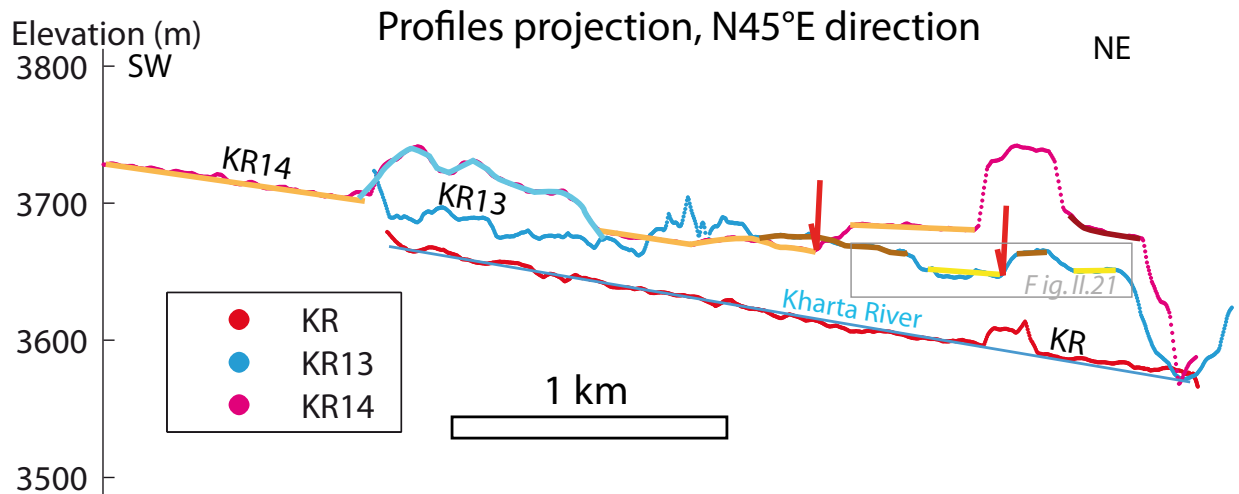


Figure III.20: a) Projection of the profiles T24 to T27 in the N100°E direction; b) Projection of the profiles KR, KR13 and KR14 in the N45°E direction. Profiles are highlighted by the color of the corresponding quaternary formation. Their traces are indicated in the Figure II.16a.

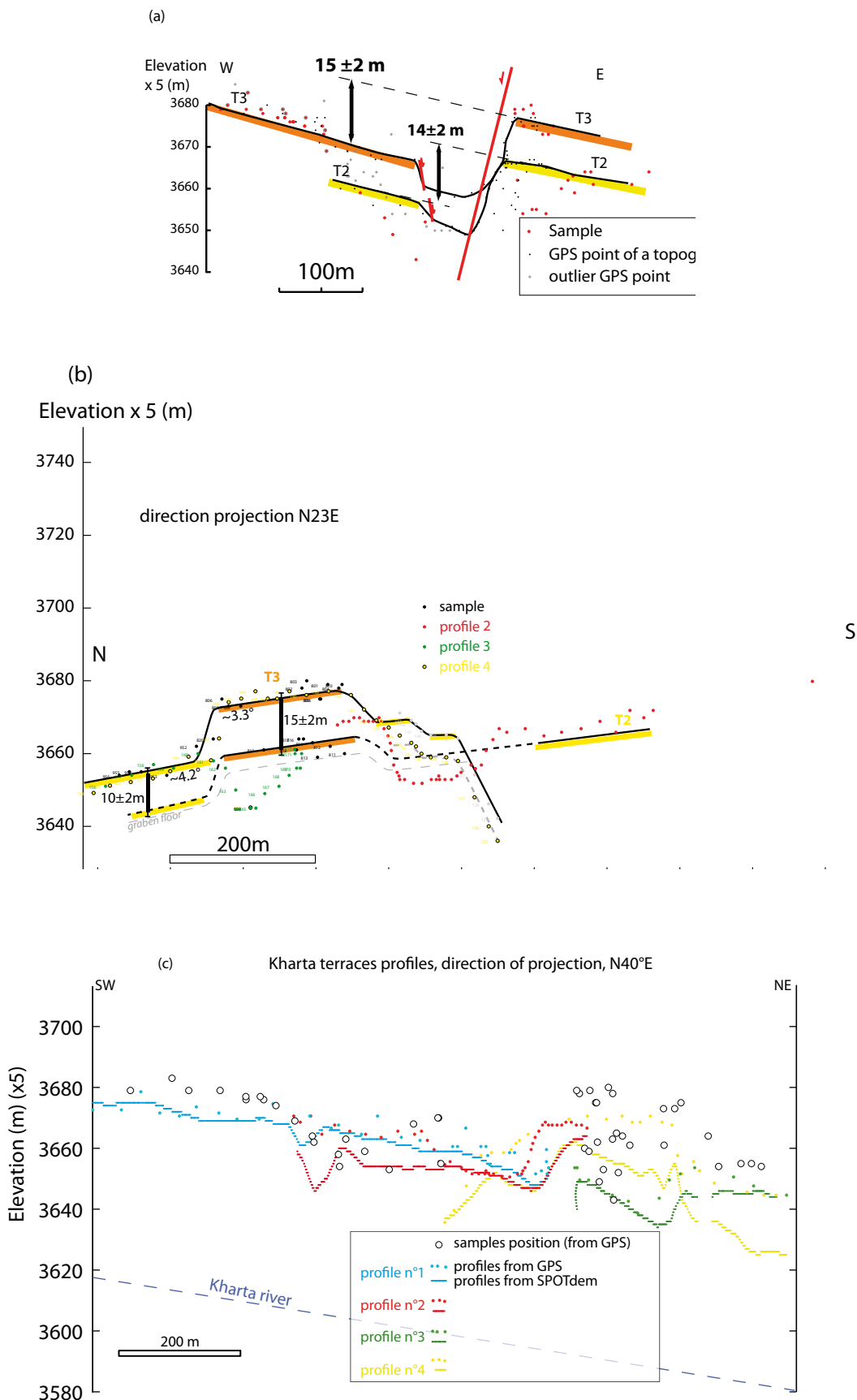


Figure III.21: a) profiles 1 to 4 projected perpendicularly to the fault, b) profiles 1 to 4 projected parallel to the fault, c) profiles 1 to 4 projected parallel to the dip of the terraces (GPS data and DEM profiles). Traces and names of the topographic profiles are indicated Figure II.16a)

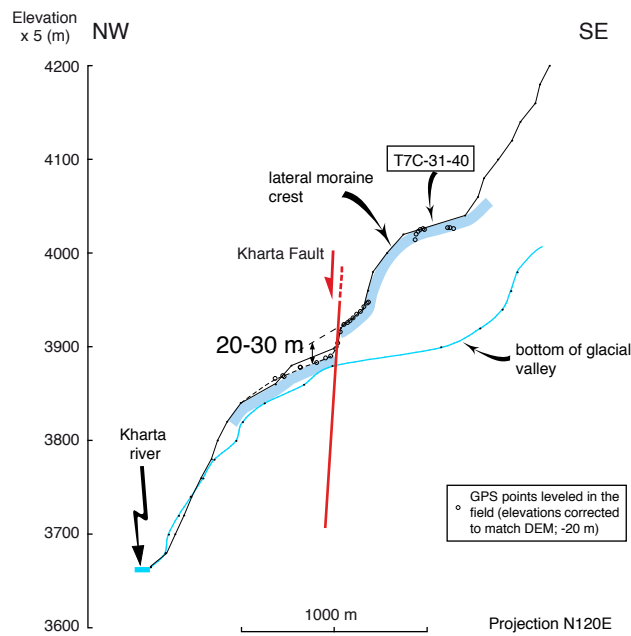


Figure III.22: a) Topographic profile (N°5) across the crest of the sampled moraine Trace of the topographic profile is indicated Figure II.16a.

3.2.3.2. The Mabja Fault

North of the Ama Drime massif, the western flank of the Mabja range presents a clear succession of triangular facets separated by glacial hanging valley outlining the trace of a 10 km long west dipping normal fault (Armijo et al., 1986; Figures III.23 and 24). The scarp is particularly well marked by a free-face at the base of a triangular facet (Figure III.25) and across the glacial deposits and para-glacial fans at the outlet of the glacial valleys (Figure III.25). Several generations of moraines can be distinguished and we mapped the clearest latest advance (Figure III.24) attributed to the LGM from interpretation of satellite images (SPOT5 images, 5 m pixel; high resolution images from GoogleEarth, 1 m pixel). The trace of the fault in the south of the massif is less clear, probably because it is below 4400 m a.s.l., i.e., under the highest paleo-lake shore line (Figure III.24) and cuts trough soft lake deposits. Nevertheless, its trace remains clear particularly across the deposits at the outlet of the main river crossing the southern Mabja range.

To constrain the slip-rate of the Mabja normal fault, we targeted a site located in the southern part of the range. The sampling site is situated below a hanging glacial valley, where a morainic surface is cut by several normal fault scarps. (Figures III.25 and 26; Appendix III-10, -11). We determine a loosely constrained offset of about 20 to 40 m based on handheld GPS measurements and large-scale topographic map (1:100000) and SPOT 5 DEM (20 m pixel resolution) (Figure III.27).



Figure III.23: Landsat satellite image of the Mabja Massif. White arrows show the localisation of the main fault scarp. See general location on the Figure III.7.

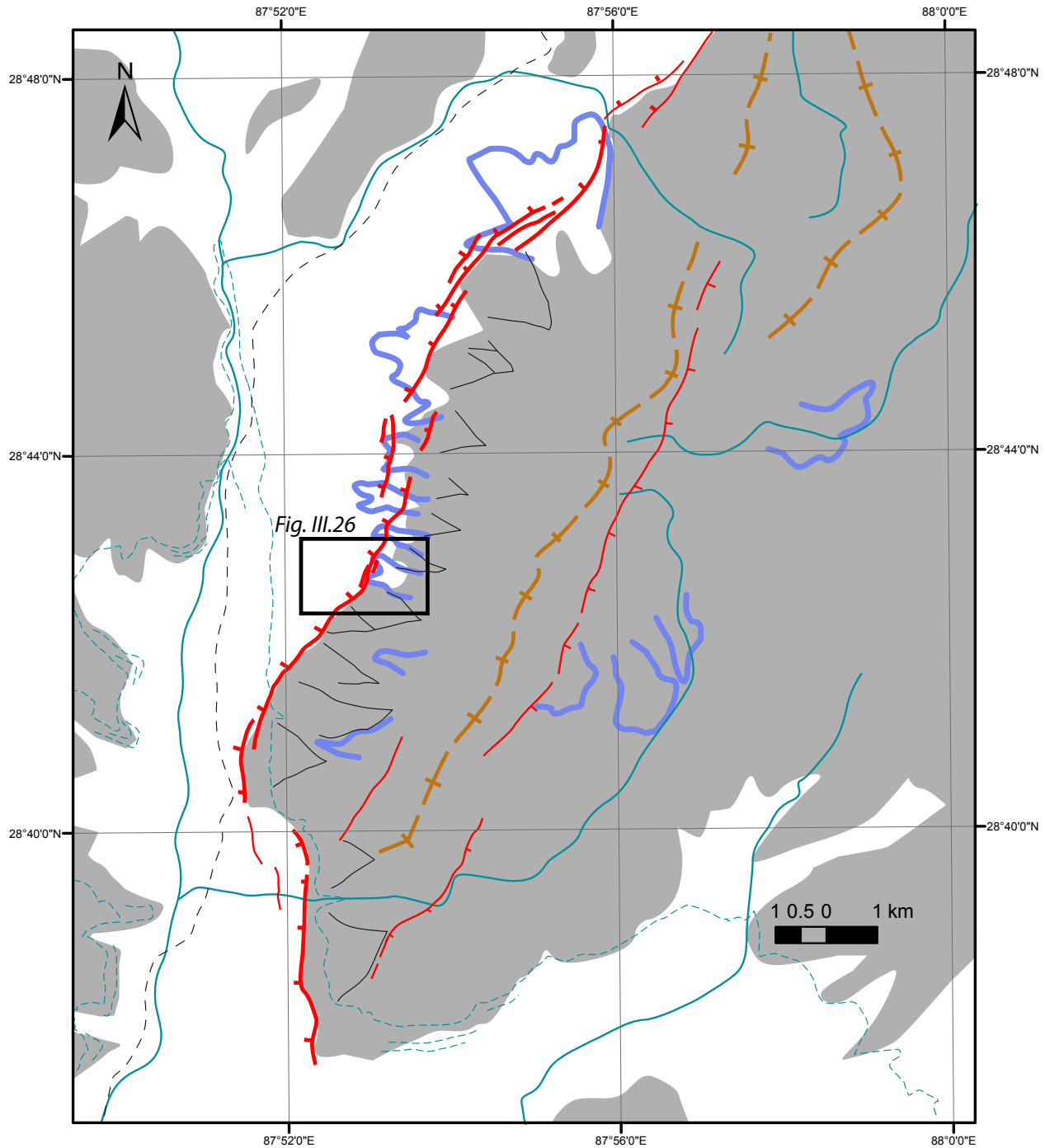


Figure III.24: Simplified geomorphological map of Mabja massif. Red lines indicate normal faults. Brown line corresponds to the massif crest. Thick blue line indicate maximal LGM glacial advance interpreted from high resolution satellite images (Google Earth). The dashed blue line are abandonned shore line of the Arun paleo-lake. Note that southern Mabja fault enters the paleolake area. The shaded area represents the bed rock and the white one corresponds to quaternary deposits See general location on the Figure III.7.

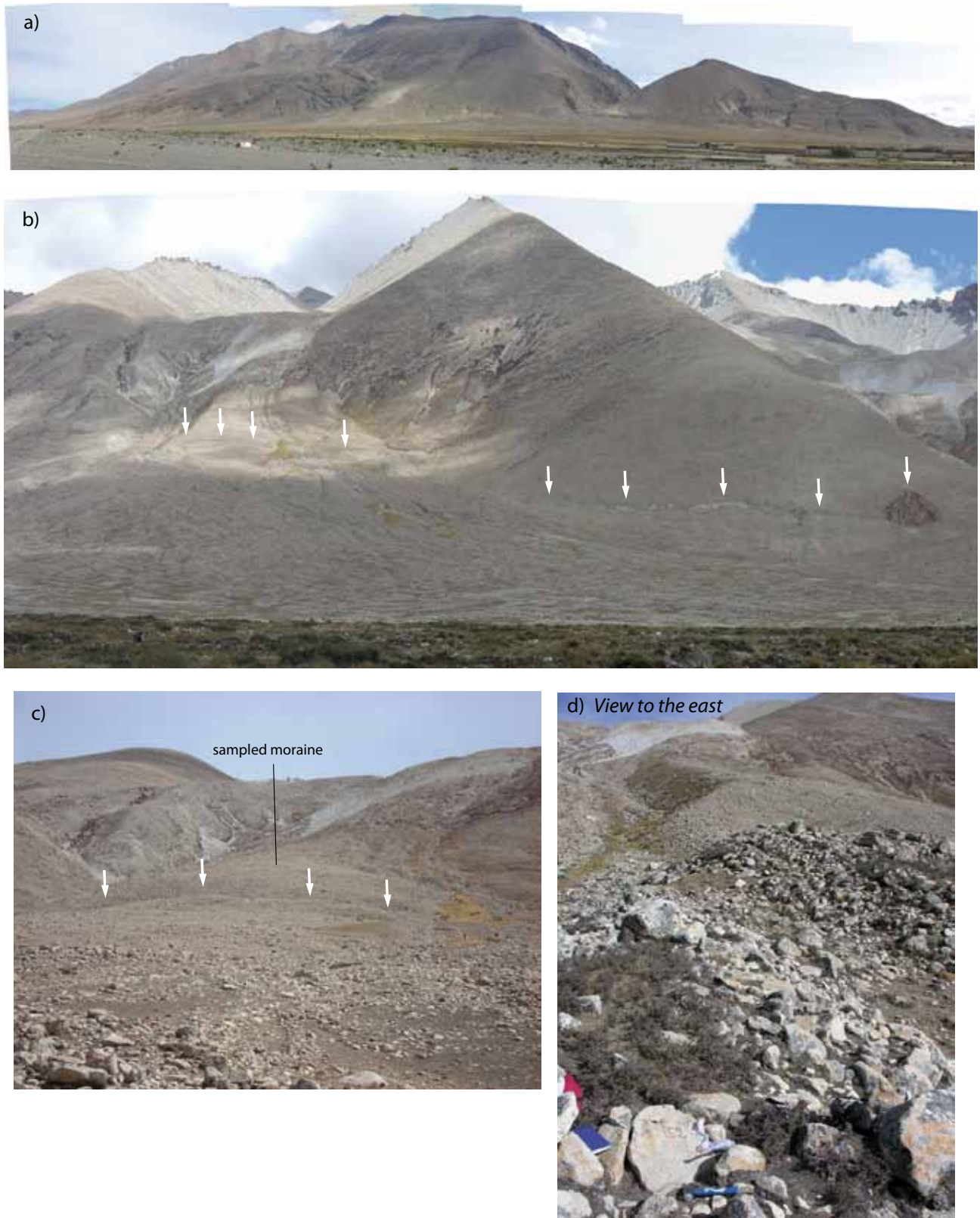


Figure III.25: The Mabja massif and moraine targeted for surface exposure dating. (a) Panoramic view of southern part of Mabja active range front. White arrows represent the fault scarp. (b) Hanging glacial valley above abandoned moraine and paraglacial fan offset by active normal fault. Note steep bedrock free face scarp at base of triangular facet on the right of photo. (c) Close-up view of offset moraine surface with clear 20-40 m-high cumulative scarp. (d) close-up of block sampled for ^{10}Be dating. In background, moraine ridge.

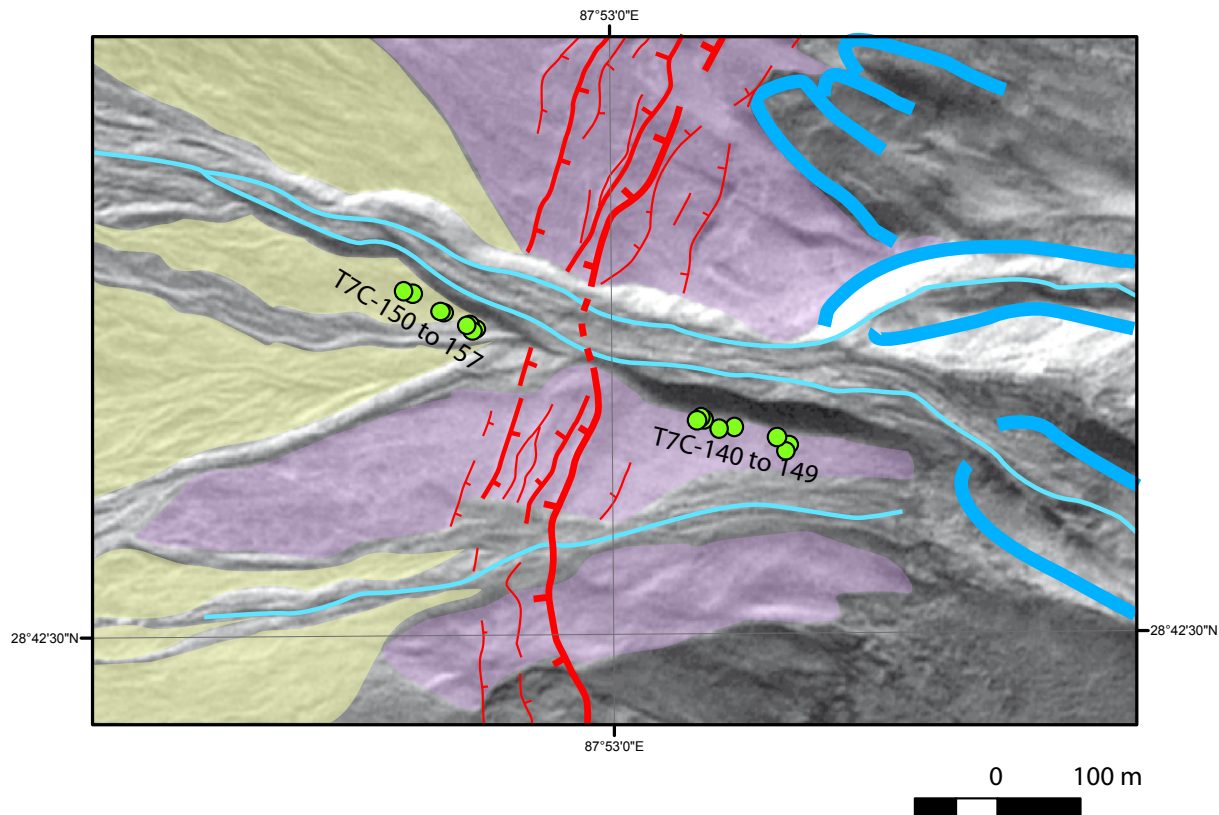


Figure III.26: Close-up view of SPOT5 satellite image of the sampling site along Mabja fault. With simplified interpretation, and active normal fault traces (in red). Purple zone correspond to moraines, yellow areas are paraglacial deposits and thick blue line correspond to maximal LGM. Green circles are samples positions.

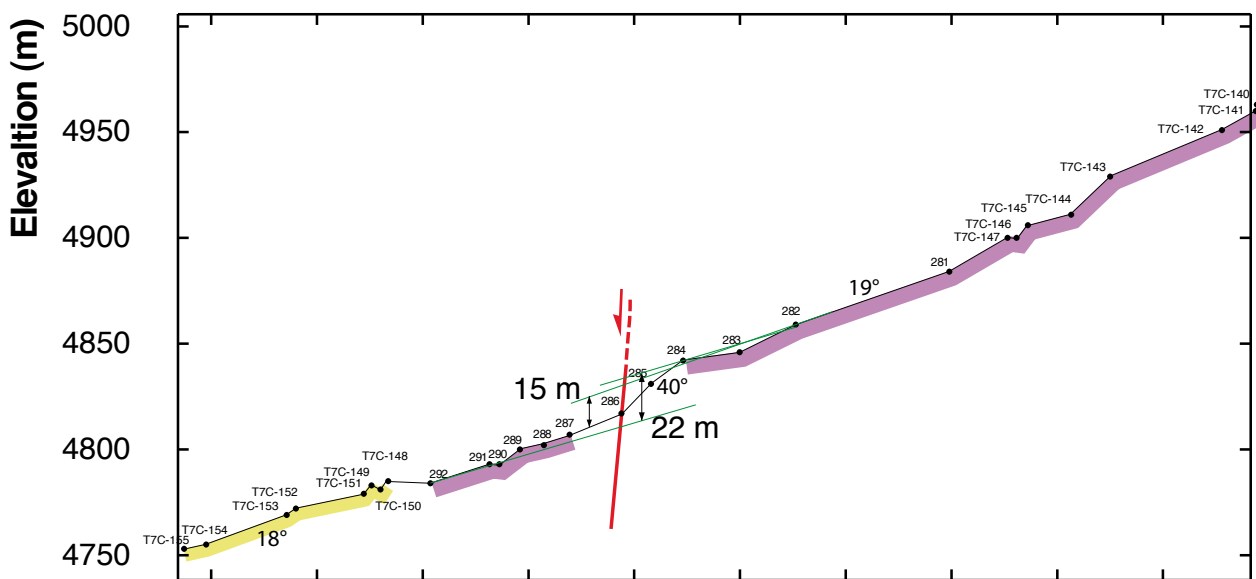


Figure III.27: Topographic profiles at sampling site along Mabja fault from GPS points measured in the field. Purple line highlights the moraine and the yellow line represent the paraglacial fan. 281 to 292 are GPS points and T7C-140 to T7C-155 are samples.

3.2.3.3. The Dinggye Fault

The eastern side of the Ama Drime range is bounded by the N10°E striking Dinggye normal fault for a length of about 70 km (Figures III.28 and 29). The fault trace is particularly clear to the south at the foot of spectacular triangular facets and where the Dinggye fault cuts and offsets moraines of glaciers originating from the highest summits of the range (Figure III.30). To the north of the city of Dinggye, the fault becomes less clear, probably owing to less tectonic activity in connection with the width diminution of the range (from 25 km in the south to 5 km in the north; Figure III.7). The fault trace may be also less clear due to its lower elevation (below 4400 m a.s.l.) and similarly to the southern Mabja fault, it may be subdued.

Several generations of moraines can be distinguished in the hangingwall of the normal fault. The recent moraines mixed with fluvio-glacial deposits in the glacial valleys (glaciers are still present in the southern part of the massif), and two generations of moraines that extend away from the range front, a smoother, hence older one, and an inset, more rugged, hence younger one (Figure III.28 and 29). This latter one being related to the last glacial advances (LGM or later), while the older one is related to the previous glacial advances around MIS 4 and MIS3b (Chevalier et al., in press to Quaternary Science Review; Table III.4).

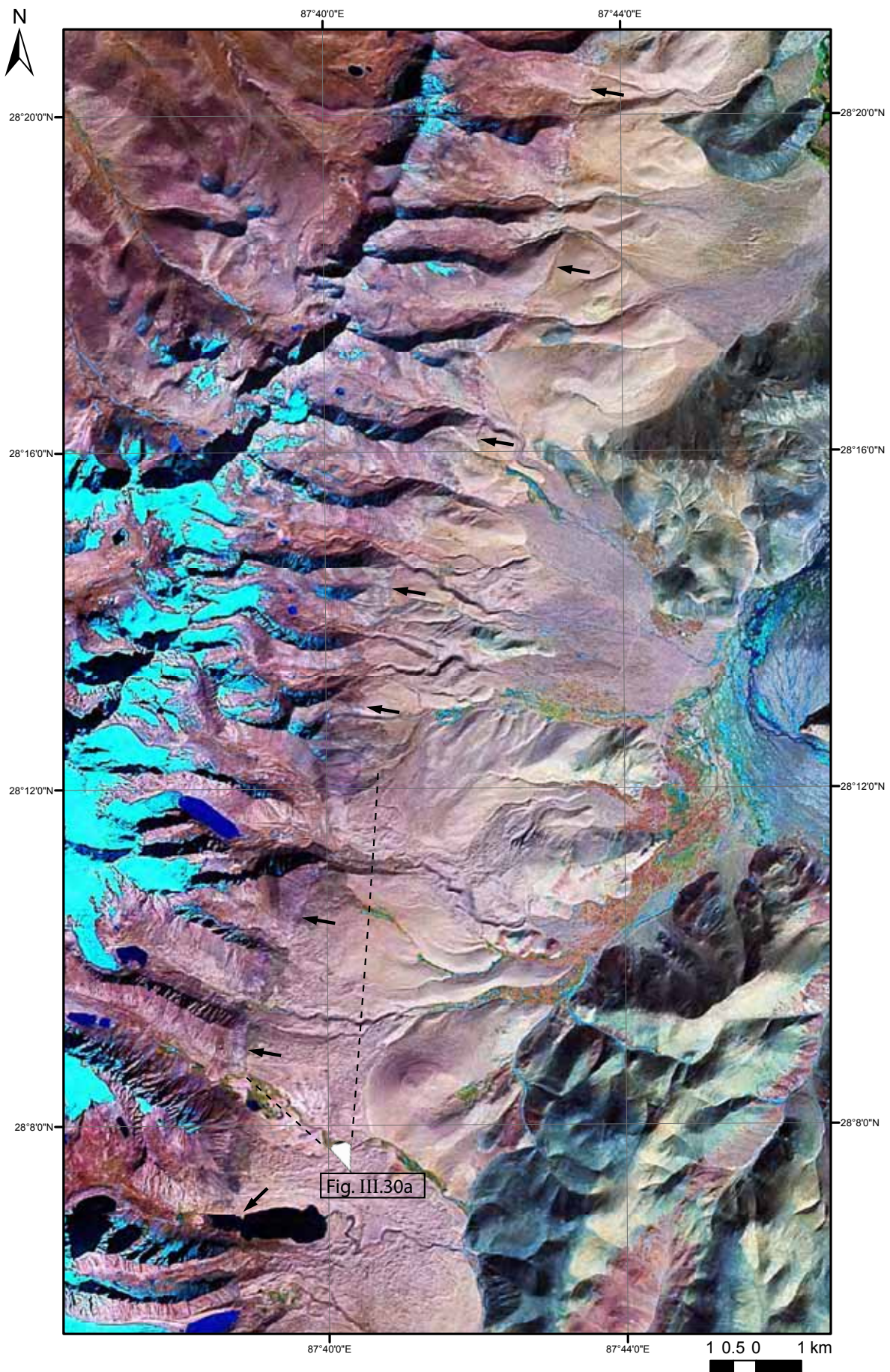


Figure III.28: Landsat image of Dinggye normal fault (eastern Ama Drime massif). See general location on the Figure III.7. Black arrows show the fault scarp. The white eye localizes the point of view of the picture of the Figure III.30a.

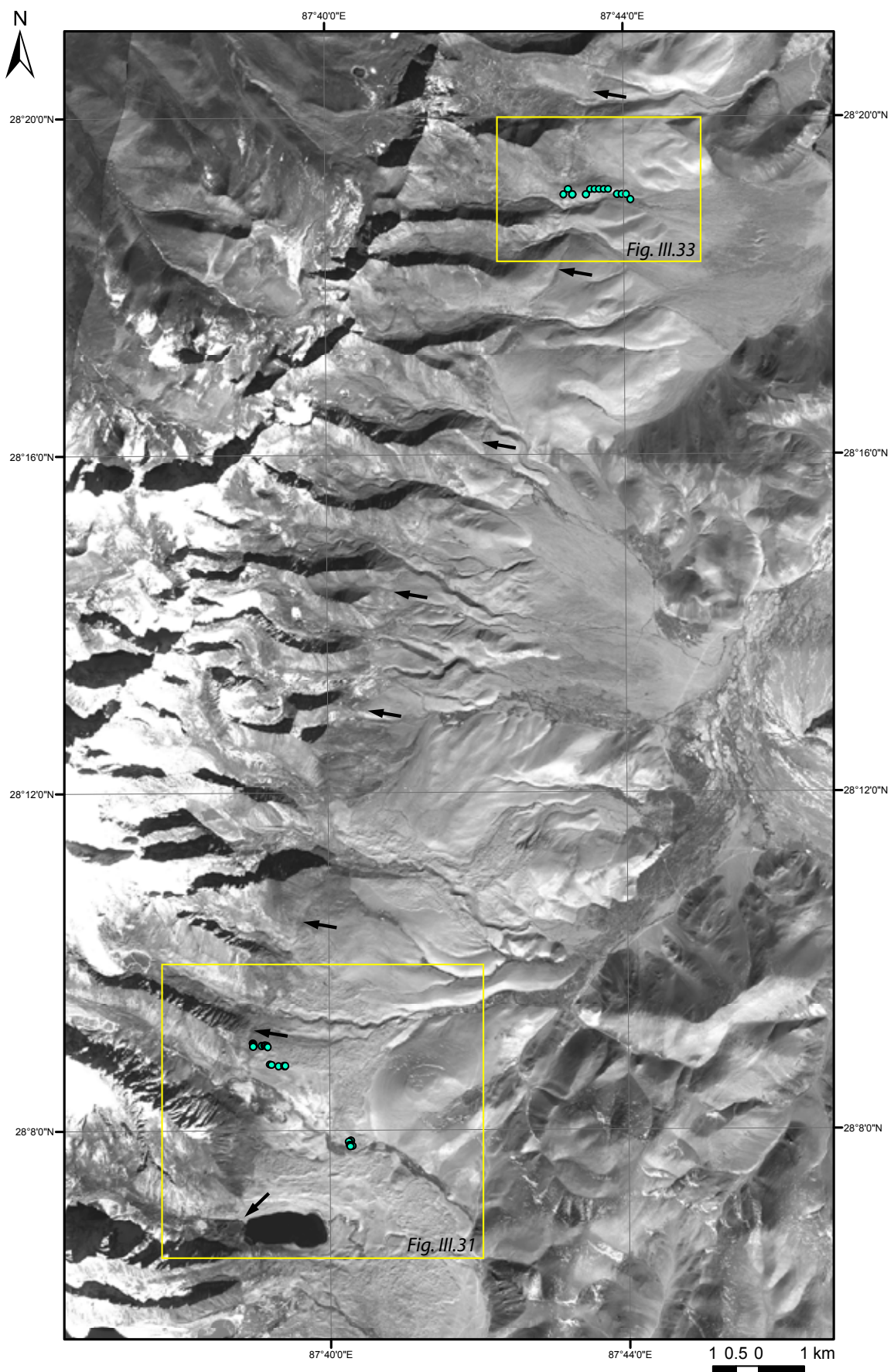


Figure III.29: SPOT5 satellite image of Dinggye normal fault (eastern Ama Drime massif). See general location on the Figure III.7. Black arrows show the fault scarp. Circles are the samples positions. See details of the dated surface in Figures 31 and 33

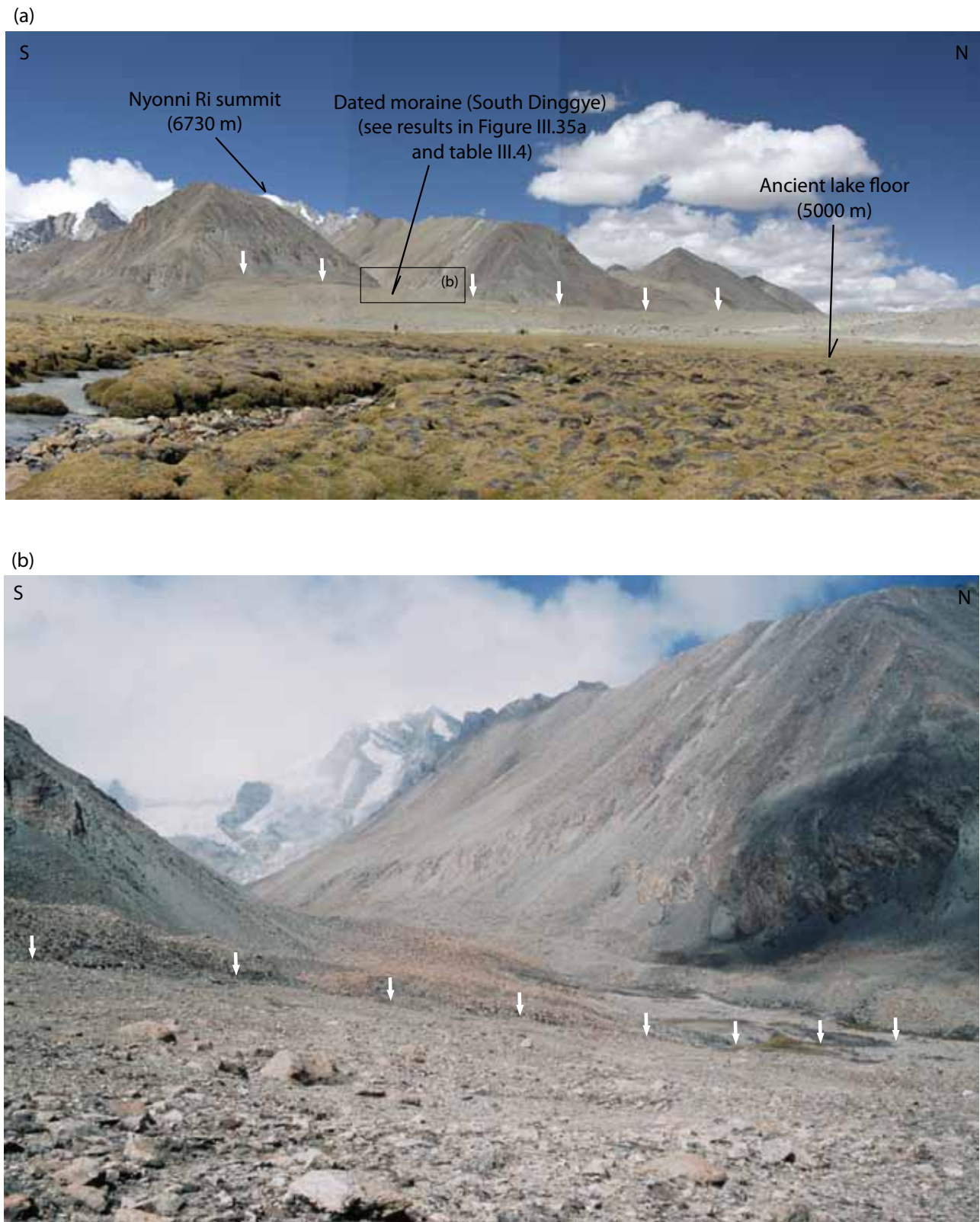


Figure III.30: (a) Southern Dinggye active normal fault marked by steep triangular facets. Point of view is indicated on the Figure III.28. White arrows show the fault scarp. (b) Close-up view of cumulative scarp across abandoned lateral moraines and bottom of glacial valley. Cumulative scarp across moraines about 10-20 m, scarp across bottom glacial valley reaches about 5 m. Point of view is indicated on the Figure III.31b. See the dating results in the Figure III.35a and in the table III.4.

We will use the moraine ages determined by Chevalier et al. (in press) to constrain the slip-rate of the Dinggye normal fault. To the south, a set of moraine crests is dated to the LGM advance with 22 ^{10}Be ages ranging from 11 to 40 ka (Figure III.35). One of the frontal moraine 2 km away from the range front fault is well dated with 6 samples with an average age of 19 ± 2 ka (Figure III.31 and III.35; Table III.4). To the north (southwest of Dinggye City), a moraine crest with a smoother topography at the outlet of a small (2 km-long) presently deglaciated catchment (Figure III.32-33) has been dated with 14 samples, which ages distribution range from 17 to 280 ka (Figure III.35). The youngest samples (20 to 40 ka) are found near the fault scarp, while the older ones (40 -130 ka) are found away downward along the moraine crest. It is thus likely that this smooth moraine crest results from several advances, the latest one being related to the isotope stage MIS-3b and that the LGM advance remained upstream from the normal fault scarp.

While no precise measurements of offsets were performed in the field, combination of handheld GPS measurements with SPOT5 DEM analysis, lead to loosely constrained cumulative offsets at both sites. In the south, a minimum of 10-20 m offset may have accumulated after the LGM glacial advance, while in the north an offset of 20-40 m is assigned to the MIS-3b moraine ridge.

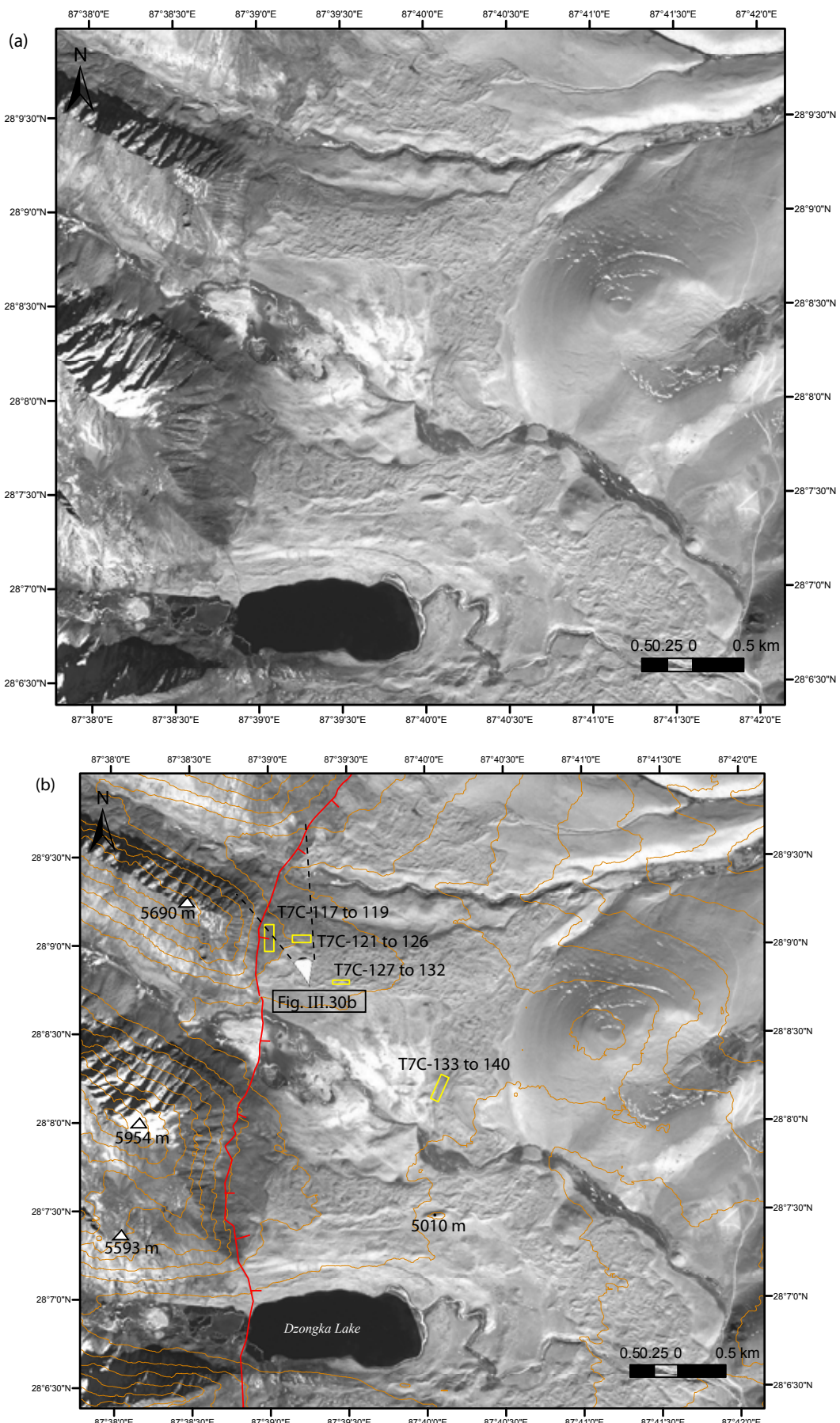


Figure III.31: Southern Dinggye fault moraine site. (a) SPOT5 image enhancement of moraine site. (b) The fault trace (in red) and the samples positions are indicated (yellow boxes), orange topographic contours are from the SPOT DEM, equidistance is 10 m. The white eye indicates the point of view of the picture in the Figure III.30b. See the dating results in the Figure III.35a and in the table III.4.



Figure III.32: Northern Dinggye fault. (a) View toward west of offset abandoned moraine ridge sampled for surface exposure dating (Chevalier et al., in press). Note 20-40 m-high scarp across the moraine. (b) view towards north from dated moraine: scarp traces are visible in the steep slope of the triangular facet.

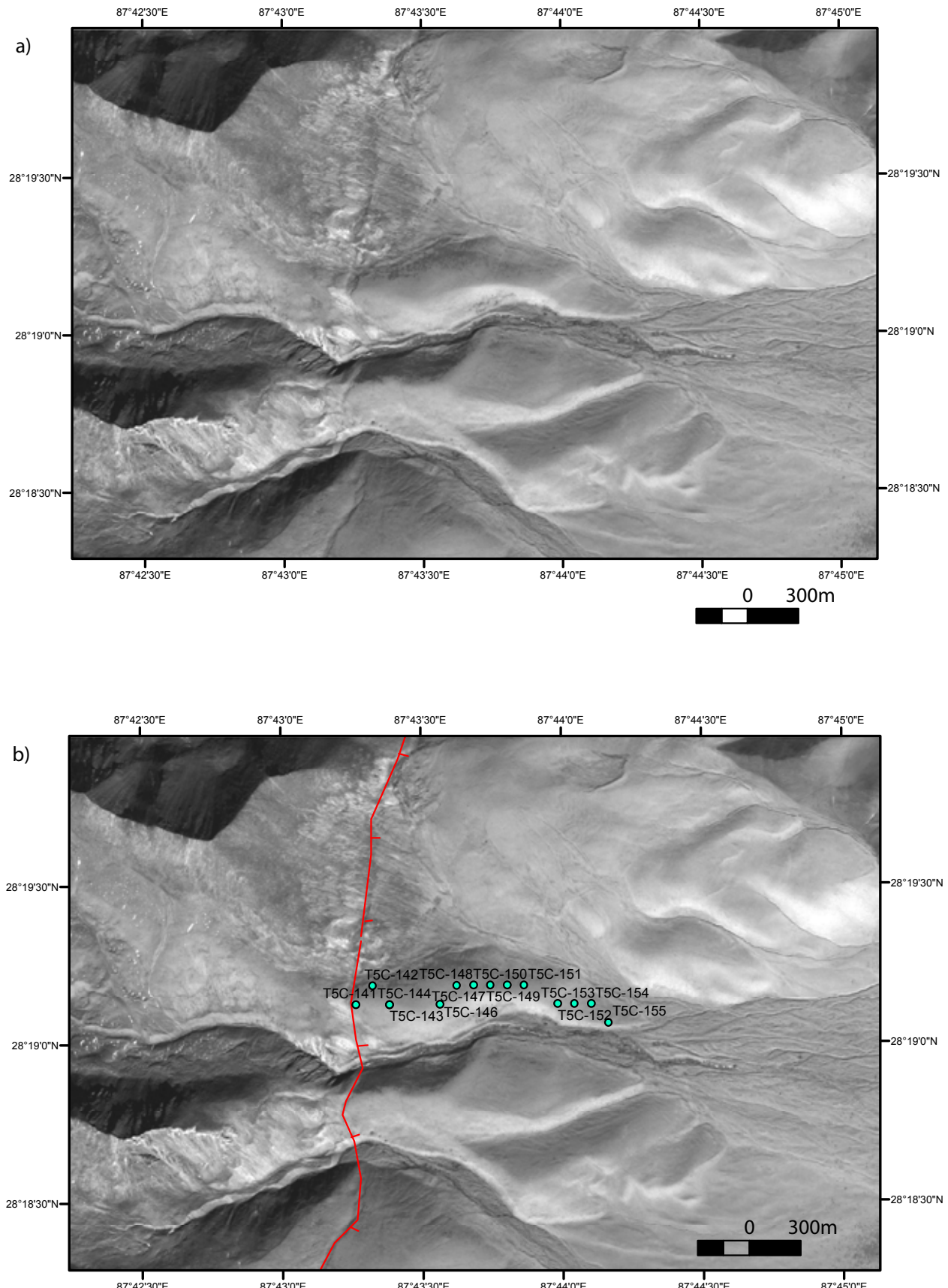


Figure III.33: northern Dinggye fault. (a) SPOT5 image enhancement of moraine site. The moraine surface has a smooth texture indicating it is older than the moraine to the south. (b) The fault trace and the samples positions are indicated.

3.2.4. Surface dating and vertical throw rates

3.2.4.1. Dating Method

Terraces and moraines were sampled by collecting embedded cobbles or fragments of boulders and blocks on the top of the surfaces (see Appendices III-1 to 11; Chevalier et al., in press). The rock types are quartz vein, granite, pegmatite or gneiss (Table III.3). In general, about 10 samples per surface were sampled, however, only 2 to 4 samples per surface were dated. For most of the samples, ^{10}Be and ^{26}Al were extracted. Each rock was crushed, sieved, and cleaned to isolate the quartz-rich fraction. Quartz was isolated by progressive HF/HNO₃ leaches to etch the exterior portion of the quartz crystals that may contain garden-variety ^{10}Be and ^{26}Al that was sorbed on the mineral surfaces (e.g. Brown et al., 1991; Kohl and Nishiizumi, 1992; Gosse and Phillips, 2001). Acid-resistant and mafic minerals were removed from the residue leach by heavy liquid and/or magnetic separation. 0.5 mg of ^9Be carrier of known concentration was added to the purified quartz that was then dissolved in HF. After dissolution, total Be and Al were measured in the sample solutions by ICP-MS at LHyGeS Laboratory (UMR CNRS/UDS 7517, EOST, Strasbourg, France). Thus, Be excess or depletion during chemical analysis, and Al background concentrations were determined. ^{27}Al carrier is added if necessary (i.e., if less than 2 mg is present). When no ICP-MS measurements were made the weighted ^9Be carrier mass was used in calculations. Nuclides were chemically isolated using ion exchange columns. After precipitation, Be(OH)₂ and Al₂(OH)₃ were fired to BeO and Al₂O₃, and the $^{10}\text{Be}/^9\text{Be}$ and $^{26}\text{Al}/^{27}\text{Al}$ ratios were measured at the Accelerator Mass Spectrometer ASTER at CEREGE, Aix-en-Provence, France. This ratio was finally converted to ^{10}Be and ^{26}Al nuclide concentrations using the measured total Be and Al concentrations prior to chemical separation.

We used the CRONUS 2.2 calculator (Balco et al., 2008) to calculate each sample exposure age from its ^{10}Be and ^{26}Al concentrations. Lal and Stone (2001) time-dependent scaling scheme was used and ages are calculated assuming no or negligible erosion (Tables III.3 and III.4).

3.2.4.2. Results

Results of dating and analysis details are presented in Tables III.3 and III.4 and in Figure III.34 and III.35.

Cosmonuclides concentrations

Six samples present values of ${}^9\text{Be}$ higher than the 0.5 mg of ${}^9\text{Be}$ carrier added to the purified quartz before dissolution (Table III.3). These samples are usually pegmatites or granites, and the presence of beryl inclusions in quartz phases may explain the excess. Three samples originate from the Mabja massif, one from the Kharta terrace, and two sampled in the northern Arun terraces most likely originate from the Ama Drime massif.

10 samples (among 43) present high ${}^{27}\text{Al}$ content over 80 mg (Table III.3). We noticed that these samples had large undissolved precipitates leading to a depleted ${}^9\text{Be}$ content when compared to the 0.5 mg of ${}^9\text{Be}$ carrier added. Be concentration measurements are not affected by the depletion because it is quantified and enough Be remains for the AMS analysis. However, ${}^{27}\text{Al}$ is not well determined relative to the dissolved quartz weight, and thus ${}^{26}\text{Al}$ concentrations are usually underestimated, and we disregarded the Al data in these cases.

In the following sections below we thus discuss only the ${}^{10}\text{Be}$ ages available for all the samples

Ages of terraces and moraines

Arun terraces along the Kharta fault (T2, T3, T4, landslide)

At the Kharta site (southern Kharta basin), we sampled terrace levels T3 and T2-south abandoned by the Kharta river and T2-north inset into T3 but incised and abandoned by a tributary of the Arun river. These terraces are offset by the normal fault at the Arun and Kharta river junction. All 3 terraces were sampled both east and west of the fault.

T3 is a smooth cobble paved terrace on both sides of the fault (Appendix III-6). On T3, two cobble samples east of the fault (up side) (T7C-2 and -10) have similar ages of 12.3 ± 1.1 and 12.7 ± 1.1 ka,

two cobble samples west of the fault (down side) (T7C-44 and 51) have ages of 11.3 ± 1.0 and 17.4 ± 1.7 ka (Table III.3). The average of these 4 samples is 12.7 ± 3.4 ka. Considering that sample T7C-51 is significantly different than the other samples (no overlapping error bar), the average becomes 12.1 ± 0.7 ka (Figure III.34).

T2-south is a similarly cobble-paved surface as T3, also its surface is less smooth and retains more fresh stream-bed morphologies (Appendix III-7). West of the fault, T2 is partly covered by windblown loess and sand. Two samples, a block and a cobble, T7C-13 and -20, respectively, east of the fault (up side) have ages of 10.9 ± 1.0 and 10.0 ± 0.9 ka, and two samples, a cobble and a block, T7C-21 and -28, respectively, west of the fault (down side) have ages of 11.2 ± 1.1 and 10.6 ± 1.0 ka (Table III.3). The average of these 4 similar ages is 10.7 ± 0.5 ka (Figure III.34).

T2-north abandoned by a smaller river than the Kharta river has a steeper slope although it is inset into T3 at roughly the same level when it crosses the fault. It is more rugged, particularly west of the fault (Appendix III-7). Two samples, a block (T7C-58 west of the fault) and a cobble (T7C-61 east of the fault) have ages of 11.9 ± 1.2 and 9.3 ± 0.9 ka (Table III.3). The average of these 2 samples is 10.6 ± 1.8 ka. Clearly, T2-south and T2-north were abandoned roughly at the same time and we will take the average of the 6 T2-north and T2-south samples ages as the age of abandonment of T2, i.e. 10.7 ± 0.9 ka (Figure III.34).

At the Yori site (northern Kharta basin), the Arun river has abandoned several terrace levels while incising its deep gorge. Terraces T3 and T4, and blocks from the large debris-flow deposit were sampled (Figure III.14).

The terrace T3 is well preserved downstream from the fault on both side of the Arun gorge (Appendix III-1). Upstream of the fault, it is well preserved only on the southern side of the Arun. There, the terrace is a smooth cobble-paved surface similar to the T3 terrace near Kharta. Avoiding blocks originating from recent rock falls from the steep gorge wall that cover partly the terrace conglomerate, 4 cobble-size samples were collected east of the fault south of the Arun on T3. Samples T7C-90, -92, -95 and 96 have ages that range from 9.2 to 15.5 ka with an average of 12.5 ± 2.6 ka (Table III.3). Two cobble-size samples were collected on T3 west of the fault on the northern side of the Arun gorge. Samples T7C-77 and -81 have ages of 12.5 ± 1.2 and 10.0 ± 1.1 ka that average at $11.3 \pm$

1.8 ka (Table III.3). The terrace threads of T3 on both side of the fault have thus similar ages and the average of all T3 samples at Yo Ri is thus 12.1 ± 2.3 ka. This age is the same as the age of T3 at Kharta (12.1 ± 0.7 ka) (Figure III.34). This corroborates our geomorphological mapping throughout the Kharta basin and shows that a regional alluvial level has been deposited and abandoned by the Arun river throughout the Kharta basin during the last glacial-interglacial transition, i.e., the Pleistocene-Holocene transition.

Clear remnants of terraces (T4) are hanging in the Yori facet about 150 m above the present Arun river bed (Figure III.15a; Appendix III-3). The surface of the terrace is relatively flat and well preserved, although large granitic blocks protruding 1 to 2 m above the average surface show clear evidence of alteration and erosion. Note also that parts of the terrace are occupied by presently destroyed buildings, which may imply some surface modifications. However, sublevels of the main T4 level are still clearly identified towards south above the gorge wall separated by ~1m-high risers. We sampled three distinct levels that we called T4a, b and c.

On terrace T4a, the top of a large gneissic block (1.5 m high; T7C-66) yields an age of 166 ± 15 ka and a well-rounded granitic cobble (T7C-68) yields a younger age of 51.2 ± 4.7 ka. On terrace T4b, an angular quartz-vein cobble (T7C-70) has an age of 104 ± 10 ka. On terrace T4c, a rounded granitic cobble (T7C-74) and a quartz-vein block (T7C-76) have ages of 30 ± 3 and 70 ± 6 ka, respectively (Table III.3). The large dispersion of ages (30 to 166 ka) on the T4 levels confirms significant surface modification since it was abandoned and precludes calculation of an average age, the oldest ages, 104 and 166 ka, of a cobble and a block, respectively, may be indicative of the true age of the terrace (Figure III.34).

Downstream side of the fault, we also sampled some of the large blocks associated to the huge debris flow (Appendix III-5). These blocks are embedded in a terrace level only a few meters above the T3 terrace, but clearly were deposited before T3. It is thus possible that these blocks are related to the T4 terrace level but no such block sizes were found on the T4 remnant east of the fault. Three sampled blocks up to 8 m in diameter, T7C-82, -83 and -84 have ages of 24, 138 and 99 ka, respectively (Table III-3). The large spread in ages is here again best explained by alteration and

erosion of the top of the blocks. The oldest age, 138 ka, may be close to the true age of the debris flow, thus in relation with the abandonment of terrace T4 (Figure III-34).

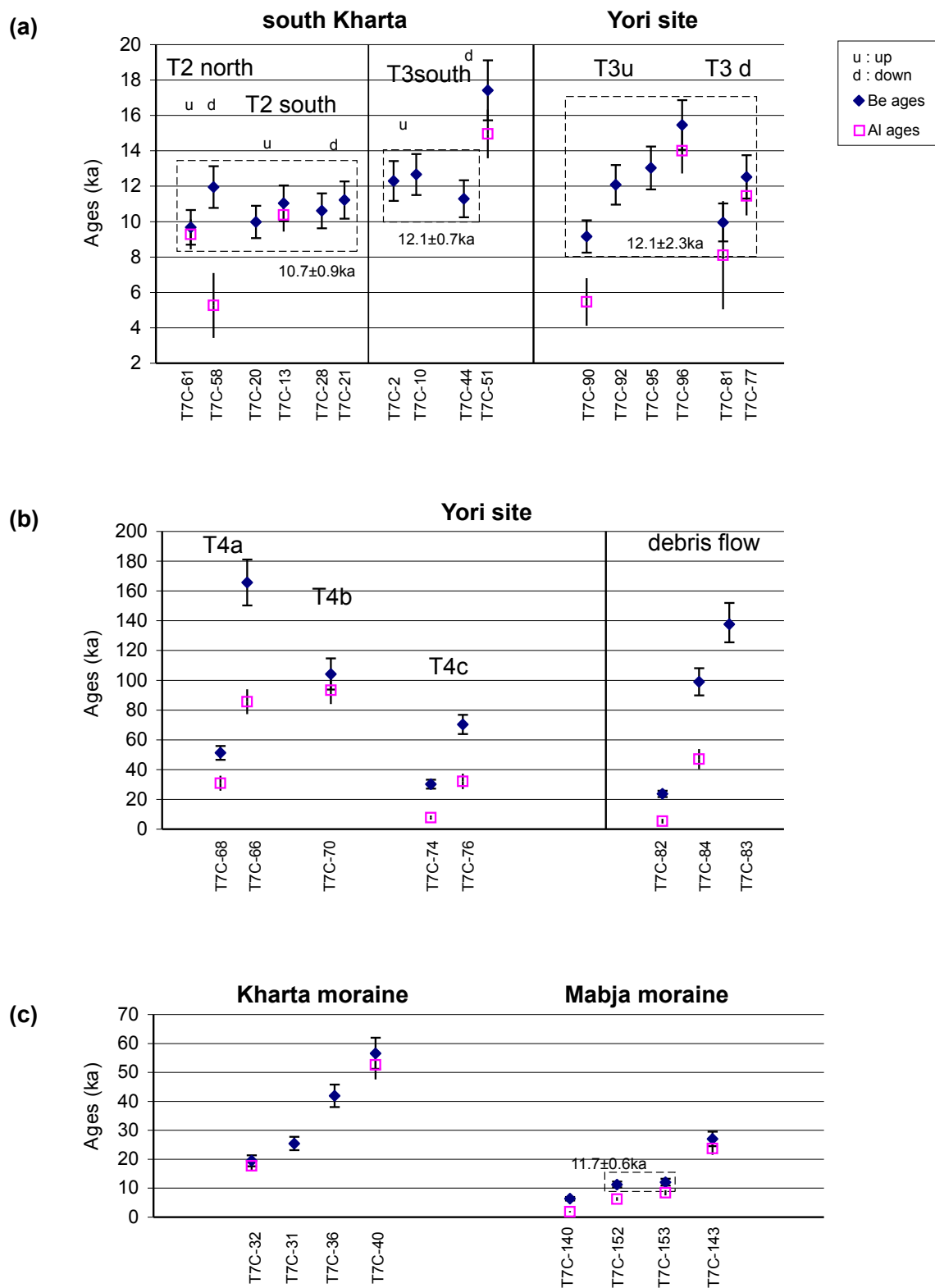


Figure III.34: 10Be and 26Al ages plot for terraces and moraines dated in the Ama Drime – Mabja area (Table III.3). (a) Ages of the T2-T3 Arun terraces, south Kharta and Yori sites. (b) Terrace T4 and debris flow ages at Yori site. (c) Ages of moraines at south Kharta and Mabja.

Kharta and Mabja moraines

South of Kharta, we sampled the abandoned eastern lateral moraine of a few kilometer-long north-vergent glacial catchment. Four samples from the top of the crest, from cobble-size (T7C-32, -36), 50 cm-size block (T7C-40), to meter-large block (T7C-31) have ages of 20, 42, 57 and 25 ka, respectively (Table III-3). These few ages do not allow to calculate an average age, but may indicate formation of the moraine ridge at the beginning of the last glacial period (60-40 ka) with partial modification and deposition during the last glacial maximum (25-20 ka) (Figure III.34).

At Mabja, a smooth moraine ridge clearly cut and offset by the normal fault has been targeted for surface exposure dating (Appendices III-10 and 11). Two samples were dated. T7C-40 is one of the large blocks (diameter about 1.5 m) found near the top of the steep cumulative scarp. Pieces from the top of the block yield an age of 4.5 ka. T7C-143 is a smaller block (about 50 cm large) well embedded in the moraine surface and yields an age of 27 ka (Table III.3). It is thus possible that the age of sample T7C-40 does not represent the age of the moraine but more likely reflects recent slope modification in the vicinity of the block. Downside of the fault, the apex of a para-glacial fan has been sampled. Two 40-50 cm-large blocks were sampled on top of a ridge. Samples T7C-152 and -153 yield similar ages of 11.3 ± 1.0 and 12.1 ± 1.2 ka, with an average of 11.7 ± 0.6 ka (Table III.3). Although preliminary, these ages likely indicate formation of the moraine during the last maximum glacial advances (20-40 ka) followed by glacial retreat and incision of the moraine with deposition of debris fans at the glacial-interglacial transition during the early Holocene (Figure III.34).

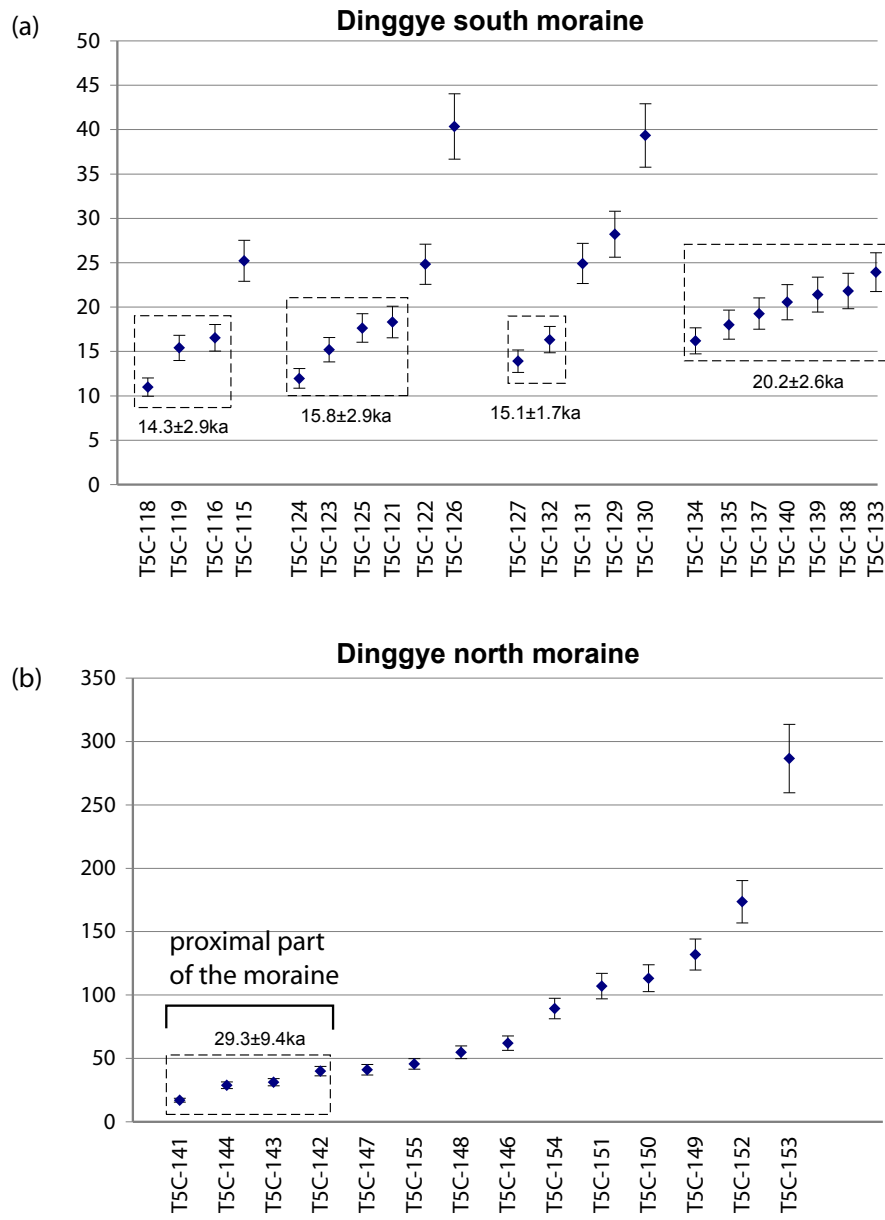


Figure III.35: ^{10}Be ages of the moraines along the Dinggye normal fault (eastern Ama Drime) (Table III.4 ; Chevalier et al., subm.).

3.2.4.3. Vertical throw rates in the Ama Drime – Mabja area

To determine the slip-rates of the normal faults bounding the Ama Drime horst and the Mabja massif, we calculate vertical throw rates from the cumulative offsets of the terraces or moraines and their respective abandonment ages (Figures II.34 and 35). At Kharta, terraces T3 and T2 have ages of 12.1 ± 0.7 and 10.7 ± 0.9 ka and vertical cumulative offsets of 15 and 14 m, respectively (Figure III.21). These offsets measurements and age determinations constrain a vertical throw rate of the western branch of the Kharta normal fault at $1.2\text{--}1.3 \pm 0.3$ mm/yr. A more loosely constrained rate of 0.2–1.3 mm/yr is determined from the offset moraine ridge along the same fault. Assuming the offset is a minimum (see discussion above) then this rate is in fair agreement with the rate obtained with the alluvial terraces.

In the northern Kharta basin, at the Yori site, the terrace T3 offset of about 14.5 m postdates 12.1 ± 2.3 ka constraining the vertical throw rate to 1.2 ± 0.4 mm/yr for the main Kharta normal fault. Both offset and age of T4 are less well constrained. The T4 terrace downstream of the fault in the hangingwall may be correlated with the large debris flow level but it may as well be lower than the present surface of T3, its offset is thus in the range of 100 to 160 m (Figure III.15). Similarly, its age is loosely constrained around 104 to 166 ka, although it may likely be correlated to the penultimate interglacial period of MIS-5 stage at 125 ka. In any case, the vertical throw rate would thus be on order of 1 ± 0.5 mm/yr for the last 125 ka, in rough agreement with the rate determined for the Holocene.

While the age of the moraine at Mabja is preliminary (27 ka) it is consistent with emplacement of the moraine during the maximum glacial advances around 40 and 20 ka and with deglaciation during the early Holocene as corroborated by the age of the highest and closest to the moraine para-glacial fan at 11.7 ± 0.6 ka. Considering a cumulative vertical offset of 20 to 40 m, a vertical throw rate on order of 1 ± 0.5 mm/yr is determined.

Along the Dinggye normal fault, the young LGM moraine and the older MIS-3b moraine have respective offsets of 10–20 m and 20–40 m that are consistent with vertical throw rates of about 1 mm/yr.

To summarize, the vertical throw rate of the Kharta normal fault on the western side of the Ama Drime massif is well constrained at 1.3 ± 0.3 mm/yr for the Holocene at sites distant about 20 km. Although less constrained, this rate may be constant for the last 125 ka. Along the western flank of the Mabja massif and along the eastern flank of the Ama Drime massif, both Mabja and Dinggye faults may have vertical throw rates on the order of 1 mm/yr.

3.2.5. Discussion and conclusion

3.2.5.1. Terrace age and formation modulated by climate

In general, the ages we obtain both on terraces and moraines along the normal faults of the Ama Drime massif corroborate results obtained elsewhere in Tibet. For instance paleoclimate data in the Himalayas or in the nearby Ronbuk valley (Owen, 2009; Owen et al., 2009), as well as data from ice cores at Gulyia (Thompson et al., 1997) indicate maximum glacial conditions during the LGM at about 18-24 ka followed by rapid warming. Moraine dating along the Karakorum fault in western Tibet constrain the ages of glacial advances at 40 and 20 ka (MIS-3b and MIS-2), as well as during the previous glacial period around 150 ka (MIS-6)(Chevalier et al., 2005a; Chevalier et al., in press). Similar MIS-3b and MIS-2 glacial advances are well dated along the Gulu-Yangbajain graben (Chevalier et al., in press.; chapter III.2). Similar LGM glacial advances followed rapid warming around 12 ka are also described along the northern margin of Tibet in the Altyn Shan (Mériaux et al., 2004) or in the Qilian Shan (Lasserre et al., 2002; Owen et al., 2003).

All these data concur to show that the glacial advances in and around Tibet followed closely the global climate variations, and in particular the glacial-interglacial transitions. While we only processed only a few ages from the moraines at Kharta and Mabja, the ages obtained (Figure III.34c) correlate well with the glacial advances described in Tibet during MIS-3b and MIS-2. We are thus confident that the moraine ridge at Kharta was most likely formed and shaped during the last 40 to 20 ka, while the younger advances probably remained inset into this moraine ridge at Mabja, although glacial tongues managed to reach the valley outlet across the normal fault trace.

Along the southern Dinggye normal fault, the most distal frontal moraine is well dated at 20 ka (Figure III.35a). Younger inset moraine ridges are dated about 15 ka (Figure III.35) indicating rapid retreat and the return of warmer climate conditions after 15 ka. The older moraine to the north shows clearly reworking during the maximum glacial advances of MIS-3b and MIS-2, while it may have been shaped starting around the previous glacial maximum of MIS-6 (150 ka).

The regional terrace T3 level across the Kharta basin is thus likely correlated to the major warming phase at the onset of the Holocene. The age of 12 ka we obtain for this terrace is reminiscent of other post-glacial terraces dated elsewhere in and around Tibet with cosmogenic nuclides and radiocarbon (Van der Woerd et al., 2001, 2002; Lasserre et al., 1998; Brown et al., 2002; Mériaux et al., 2004, 2005; Blisniuk and Sharp, 2003).

While the ages we obtain for terrace T4 do not allow to tightly constrain its age, they may indicate that the terrace formed during the previous glacial to interglacial period around 125 ka as documented in several global climate change records.

3.2.5.2. Consistent slip rates on the normal faults of south Tibet

Our study directly constrain the vertical throw rate of the Kharta normal fault to be 1.3 ± 0.3 mm/yr, and puts constraints on the less well determined throw rates of the Mabja and Dinggye normal faults at about 1 ± 0.5 mm/yr. The total cumulative rate of normal faults across the Ama Drime horst is thus about 2 mm/yr. Although very few rate determinations exist, these rates are similar to other normal fault rates determined in southern Tibet with similar methods. Along the Pulan graben, the western bounding normal fault of the Gurla Mandatha massif has a vertical throw rate $>1.5 \pm 0.3$ mm/yr (Chevalier et al., 2010) determined by offset terraces of 35 ka and 10 ka. They are also on the same order of rates determined along the Yadong-Gulu rift at Gulu, Damxung and Yangbajain, of about 1-2 mm/yr (part 3.3).

It thus seems that the average rate of vertical throw along each of the grabens of southern Tibet is about 1.5-2 mm/yr, in good agreement with estimates made by Armijo et al. (1986), and confirms that rates of normal faulting are much larger in south Tibet than north of the Bangong suture (Armijo et

al., 1986; Blisniuk and Sharp, 2003). For instance, along the Shuang Hu graben, the most prominent graben of central Tibet north of the Bangong suture (Figure III-5), the normal throw rate is found to be about 0.07 mm/yr for the last 233 kyrs with a maximum of about 0.3 mm/yr (Blisniuk and Sharp, 2003), i.e, at least one order of magnitude lower than in south Tibet.

3.2.5.3. Implication for the geodynamic of Tibet

For a maximum throw rate of 2 mm/yr and a assuming a dip of normal fault plane between 45 and 60°, a horizontal extension rate along the Ama Drime system reaches 1.5 ± 0.8 mm/yr. The similar rates found at Pulan (Chevalier et al., in prep.) and along the Nyainqntanglha (part 3.3) lead to assume that this rate is similar in the 7 major rifts of southern Tibet (Figure III-5). In this case, the total spreading rate would reach about 1 ± 0.5 cm/yr across southern Tibet.

This rate is in fair agreement with geodetic estimates from GPS velocity fields that indicate slightly higher extension rates across south Tibet of about 20 mm/yr (Zhang et al., 2004; Wang et al., 2001). Similarly, Chen et al. (2004) report an extension rate of about 5.9 ± 0.7 mm/yr for the Yadong-Gulu rift, although given the position of the GPS station west of the rift, at least two other rifts are involved in this estimate. Distributing the ~6 mm/yr rate over 3 rift systems may indicate rates of about 2 mm/yr from GPS data modeling, in better agreement with the late Pleistocene-Holocene rates we obtain.

Initiation of rifting in southern Tibet has been suggested to be Plio-Quaternary (Armijo et al., 1986), although there is evidence of N-S or NE-SW upper Miocene normal shear along at least some of the rifts (Harrison et al., 1995; Kali et al., 2010; part 2.3). Whether extension has been continuous since the upper Miocene throughout south Tibet and at the same rate, remains a question for further studies. Despite increasing information of fault slip-rates (Chevalier et al., in press; this study; part 3.3), of initiation of ductile normal shear (Murphy et al., 2002; Kali et al., 2010; Leloup et al., 2010; Harrison et al., 1995; Kapp et al., 2005), the evolution in time and space of the distribution of normal faulting remains uncertain. In particular, while some models have tempted to explain extension as a response of the subducting plate and predict arc-parallel extension, these models fail to explain the

present northward fanning of the graben directions away from the Himalayan front (grabens to the east are right-stepping, grabens to the west are left-stepping) (Armijo et al., 1986; Murphy et al., 2010; Ratschbacher et al. 1994) and they fail to explain the relatively uniform NS strike of each of the linear graben sections across south Tibet indicating almost pure E-W extension (Armijo et al., 1986, 1989; Hinterbersger et al., 2010).

In any case, our study provides the first throw rate determination of normal faulting along the southern part of one of the south Tibetan grabens for the late Pleistocene-Holocene but is a step towards quantitatively documenting the extension in south Tibet. The rates we found concur to estimate the total E-W extension rate in south Tibet at about 15 mm/yr for the last 150 ka, a rate comparable to the short-term geodetic derived rates across the rift of southern Tibet (Wang et al., 2001; Zhang et al., 2004; Chen et al., 2002) and corroborates kinematic models that link extension (10-15 mm/yr) to south Tibet spreading over underthrusting India at a rate of 2 cm/yr and right-lateral shear along the Jiali fault zone (e.g. Armijo et al., 1986; McCaffrey et al., 1998; Lee et al.,).

Acknowledgements

Marie-Luce Chevalier for sharing moraine ages data along the Dinggye normal fault. CEREGE ASTER facility for AMS measurements. Liu Xiaohan and ITPR for field logistics and access. INSU-CNRS for fieldwork support and funding. SPOT 5 images and SPOT5 DEM were acquired thanks to ISIS programme #XX, co-funded by CNES and CNRS. Project PRA #XX granted to JVDW and Liu-Zeng Jing to work on extension in south Tibet. Ministère de la recherche for PhD funding to the first author. We also thank LHyGeS (UMR CNRS/UDS 7517) and particularly the Laboratoire de Chimie Isotopique in Strasbourg for various facility access and R. Boutin for ICP-MS measurements.

Table III-3: Analytical results of terrestrial cosmogenic nuclide ^{10}Be and ^{26}Al geochronology, Ama Drine Massif, Kharta-Mabja Are

site	Sample	Latitude ^a	Longitude ^a	Elevation ^b	Rock type ^c	Thickness (m.s.l.)	(cm)	Production rate ^d			AI ^e	Shielding factor	Be ^f	Be age ^g	\pm^{in}	\pm^{ik}	\pm^{i}	$[^{10}\text{Be}]$	\pm^{i}	$[^{26}\text{Al}]$	\pm^{i}	$[^{26}\text{Al}]/[^{10}\text{Be}]$	\pm^{i}	Age ^h	\pm^{in}	\pm^{ik}	\pm^{i}				
								spall	muons	spall																					
T7C-13	28.10496	87.35049	3655	q.v.	5	0.0597	0.9872	37.41	0.533	252.38	4.512	20.67/07	0.5003	2.742E-13	2.9	418349	15881	10.9	1.0	1.273E-12	3.1	2596339	89650	10.3	0.9	6.2	0.2				
T7C-20	28.10134	87.35190	3645	q.v.	7	0.0442	0.9872	36.90	0.530	--	--	20.6535	0.5125	2.397E-13	2.6	375954	10623	10.0	0.9	--	--	--	--	--	--	--	--	--			
T2 (South-Kharta site)	28.09919	87.34776	3647	q.v.	8	0.9366	0.9820	36.53	0.529	--	--	20.6936	0.5149	2.646E-13	3.2	415622	16855	11.2	1.1	--	--	--	--	--	--	--	--	--			
T7C-28	28.09815	87.34657	3650	g	6	0.0510	0.9820	36.86	0.531	--	--	20.7121	0.5149	2.556E-13	2.9	399568	15160	10.6	1.0	--	--	--	--	--	--	--	--	--			
T7C-58	28.10168	87.34910	3640	g	6	0.0510	0.9882	36.97	0.530	249.43	4.484	20.7218	0.487/0	3.011E-13	3.3	450038	22836	11.9	1.2	119.0	9.990E-15	33.3	1272869	426933	5.3	1.8	2.8	1.0			
T7C-61	28.10266	87.35098	3640	q.v.	8	0.9366	0.9800	36.17	0.527	244.00	4.456	20.0923	1.1/1.96	9.793E-14	3.0	341142	16843	9.3	0.9	2.2	8.363E-13	3.4	2053963	69607	8.4	0.8	6.0	0.4			
T3 (South-Kharta site)	28.10082	87.35011	3665	q.v.	8	0.9366	0.9867	38.10	0.530	--	--	20.9648	0.5043	3.025E-13	2.5	461506	12484	12.3	1.1	--	--	--	--	--	--	--	--	--	--		
T7C-2	28.10082	87.35048	3665	q.v.	4	0.9676	0.9867	38.10	0.539	--	--	20.7015	0.5092	3.139E-13	2.6	490850	12386	12.7	1.1	--	--	--	--	--	--	--	--	--	--		
T7C-44	28.09618	87.34382	3670	q.v.	5	0.0597	0.9871	37.82	0.536	--	--	20.1309	0.5161	2.695E-13	2.9	435855	16503	11.3	1.0	--	--	--	--	--	--	--	--	--	--		
T7C-51	28.09740	87.34543	3670	q.v.	6	0.0519	0.9871	37.41	0.534	252.42	4.513	19.95/12	0.519/0	4.128E-13	3.0	680078	32505	17.4	1.7	2.3	1.459E-12	3.1	3800572	116831	15.0	1.4	5.6	0.3			
T7C-77	28.26611	87.39028	3797	q.v.	6	0.0519	0.9831	39.73	0.530	268.03	4.651	19.9851	0.514/3	3.104E-13	3.1	510036	24887	12.5	1.2	2.4	1.157E-12	4.4	3086764	130586	11.5	1.1	6.1	0.4			
T7C-81	28.26752	87.39290	3793	g	8	0.9354	0.9831	38.96	0.530	262.85	4.609	20.6532	0.478/2	2.473E-14	6.7	397618	26623	10.0	1.1	186.4	1.040E-14	36.5	217421	791201	8.1	3.1	5.4	2.0			
T7C-90	28.26460	87.39310	3815	g	5	0.9621	0.9840	39.40	0.536	266.72	4.690	20.6532	0.481/82	2.778E-13	5.0	377935	19916	9.2	0.9	147.4	8.97E-15	22.95	1428887	329295	5.5	1.3	3.84	0.9			
T7C-94	28.26452	87.39343	3810	q.v.	8	0.9366	0.9621	38.53	0.548	--	--	20.7259	0.5185	3.003/1E-13	2.9	476987	17886	12.1	1.1	--	--	--	--	--	--	--	--	--			
T7C-95	28.26452	87.39343	3810	g	5	0.0590	0.9621	39.72	0.536	--	--	20.8594	0.5167	3.334E-13	3.0	526928	20161	13.0	1.2	--	--	--	--	--	--	--	--	--			
T7C-96	28.26405	87.39240	3810	q.v.	8	0.9366	0.9621	38.77	0.532	261.57	4.631	20.5572	0.500/8	3.942E-13	2.9	616059	19458	15.5	1.4	3.4	1.004E-12	3.3	3600947	121384	14.0	1.3	5.9	0.3			
T7C-66	28.26968	87.39592	3915	q.v.	5	0.0597	0.9812	42.59	0.574	286.58	4.82	20.0640	0.73/24	3.344E-12	2.1	8264/65	239843	1657	15.4	50.7	--	--	--	--	--	--	--	--	--	--	
T7C-68	28.26813	87.39557	3900	g	9	0.9815	0.9815	41.36	0.562	275.720	4.719	19.9403	0.344/6	2.174E-12	2.9	484055	77550	51.2	4.7	13.9	9216980	1282595	30.8	5.1	3.7	0.5					
T7C-70	28.26788	87.39542	3900	q.v.	8	0.9366	0.9815	41.36	0.562	279.06	4.75	20.05/07	0.503/7	3.029/1E-12	3.5	506379	2531/24	104.2	10.5	59.9	4.1330E-13	4.1	28880543	1190365	93.3	9.2	5.7	0.4			
T7C-74	28.26745	87.39466	3895	g	6	0.0510	0.9794	41.76	0.565	281.75	4.78	20.20/3	0.69/9	2.542E-12	3.1	1379731	66582	30.2	2.9	86.9	2.30E-14	14.8	220/262	32246	77	1.3	1.6	0.2			
T7C-76	28.26748	87.39503	3900	g	5	0.0590	0.9794	42.02	0.57	283.52	4.794	20.70/06	0.3776	2.786E-12	3.1	3459/93	112455	70.4	6.5	115.8	7.749E-14	13.5	99/21/0	13384/38	32.0	5.2	2.9	0.4			
Debris flow (Yo Ri site)	T7C-82	28.26919	87.38825	3795	g	10	0.9202	0.9831	38.40	0.530	259.370	4.578	20.04/02	0.25/14	1.199E-12	3.4	979322	36180	23.7	2.2	99.6	1.239E-14	27.8	1360758	382431	5.4	1.6	1.4	0.4		
T7C-83	28.27037	87.38899	3800	q.v.	5	0.0597	0.9831	40.01	0.552	--	--	20.67/04	0.5105	4.136/12	2.6	665641	2193/12	138/6	13.0	--	--	--	--	--	--	--	--	--	--		
T7C-84	28.27126	87.38856	3804	g	6	0.0510	0.0831	39.84	0.56	268.76	4.657	17.47/14	0.5574	2.179/12	2.9	4614353	138/27	99.0	9.1	173/0	6.67/0-14	11.1	1472/23/4	1633395	47.1	6.7	3.2	0.4			
South-Kharta moraine	T7C-31	28.08478	87.35050	4020	g	5	0.0590	1	46.22	0.589	--	--	20.3954	0.5143	4.444/9	2.3	444/49	2.5/5	3.1	4.73/0-14	3.0	14330/4	92349	11.1	3.7	5.7	0.3				
T7C-32	28.08488	87.34990	4020	q.v.	6	0.0519	1	45.83	0.587	309/23	4.97	20.32/95	0.497/3	5.832E-13	2.9	930034	433/29	19.5	1.9	3.5	1.439E-12	3.0	5536874	165889	17.7	1.6	6.0	0.3			
T7C-36	28.08555	87.34866	4030	g	7	0.9432	1	45.28	0.583	--	--	20.3521	0.4937	1.402/12	2.8	2274/14	78427	41.9	3.9	--	--	--	--	--	--	--	--	--			
T7C-40	28.08575	87.34822	4030	q.v.	5	0.0597	1	45.91	0.587	309/74	4.970	20.02/64	0.506/6	1.810/12	2.1	30361/68	124874	56.6	5.4	7.5	2.228E-12	3.3	18683/6	615245	52.6	4.9	6.2	0.3			
T7C-40	28.71028	87.38653	4926	g	6	0.0510	1	0.73	0.73	49.40/4	6.12	471/84	0.52/5	2.179/12	2.9	461521	21526	64	5.3	17.9	0.00	11.20	81103/34	92349	1.88	1.27	1.79	0.2			
paleo shore line of lake	T7C-43	28.71046	87.38865	4926	g	6	0.0510	1	0.65	0.5450	0.608	465.91	15.89/07	1.829/7	0.515/4	8.29/5/12	0.5	13446/62	2785/08	205.9	18.8	--	--	--	--	--	--	--	--	--	--
T7C-44	28.71046	87.38856	4898	g	6	0.0510	1	0.73	0.69/06	0.608	--	--	20.1981	0.5093	7.218/12	0.7	1213/30/6	259/028	186/7	17.0	--	--	--	--	--	--	--	--	--		
T7C-44	28.71166	87.38819	4751	g	6	0.0510	1	0.70	0.64/40	0.587	49.79/2	12.70/4	7.218/12	0.515/2	1.646/13	1.3	1223/4/95	457/6/8	187.9	18.2	2.2	2.942E-11	1.7	697/10/3	1679/024	168.6	16.1	5.7	0.3		
T7C-153	28.71168	87.38815	4751	g	7	0.9432	1	0.70	0.64/40	0.585	432/05	21.53/8	4.064/13	4.7	79/128	207/82	27.88	0.00	6.26	3.673/84/2	8.43	9.0	4.64	0.4							
T7C-102	28.61373	87.21760	4380	q.v.	4	0.9676	1	0.64	0.54/170	0.537	365/05	21.53/8	4.064/13	4.7	132/0/38/3	487/78	20.1	2.10	2.10	0.00	1.46	75/35/55/7	169/75/55/7	188/44	18.05	5.74	0.2				
T7C-103	28.61																														

Table III.4 : Analytical results of terrestrial cosmogenic nuclide ^{10}Be geochronology - Moraines of the Ama Drime Massif, Dinggye area. Modified from Chevalier (2006) and Chevalier et al., in press.

Site	Sample	Latitude ^a	Longitude ^a	Elevation ^b	Rock type ^c	Thickness (cm)	Scaling factor	Shielding factor	Be muons	Be spall	Quartz	Total $^{9}\text{Be}^g$ (mg)	$[^{10}\text{Be}]$ (at/g)	\pm^i (%)	$\pm_{j,k}$ (at/g)	$\pm_{l,m}$ (ka)	Production rate ^{d,e,f}	
main moraine	T5C-115	28.1305	87.64966	5254	g	4	0.967	0.958	0.799	78.28	19.4795	0.3594	1.778E-12	2.6	2142301	71892	25.22	2.30
	T5C-116	28.15034	87.64979	5247	q	4	0.968	0.958	0.799	78.09	10.8335	0.3440	6.567E-13	2.5	1342932	45157	16.54	1.51
	T5C-118	28.15008	87.64974	5250	q	4	0.968	0.958	0.799	78.19	20.6337	0.3582	8.005E-13	3.1	878070	34091	10.98	1.02
	T5C-119	28.14993	87.64971	5254	q	4	0.968	0.958	0.800	78.33	18.0891	0.3603	9.734E-13	2.8	1245100	44850	15.41	1.42
	T5C-121	28.15001	87.65166	5223	q	4	0.968	0.987	0.794	79.63	20.1193	0.3576	1.331E-12	4.1	1529952	72687	18.31	1.78
	T5C-122	28.15002	87.65165	5225	q	4	0.968	0.987	0.795	79.69	16.4233	0.3578	1.507E-12	2.5	2143677	70784	24.83	2.26
	T5C-123	28.1501	87.65224	5220	q	4	0.968	0.987	0.794	79.52	16.6245	0.3580	9.003E-13	2.5	1245239	41334	15.20	1.38
	T5C-124	28.15013	87.65248	5216	q	4	0.968	0.987	0.793	79.39	9.5029	0.3583	4.051E-13	3.0	970266	36801	11.97	1.11
	T5C-125	28.15001	87.65258	5215	q	4	0.968	0.987	0.793	79.35	9.7375	0.3614	6.106E-13	2.5	1463957	48803	17.64	1.61
	T5C-126	28.14983	87.65303	5220	q	4	0.968	0.987	0.794	79.52	15.6353	0.3619	2.484E-12	2.4	3791472	121129	40.36	3.68
inner moraine	T5C-127	28.14632	87.65344	5151	q	4	0.968	0.992	0.781	77.56	21.8615	0.3629	1.042E-12	2.5	1104924	36930	13.92	1.27
	T5C-129	28.1446	87.65534	5146	q	4	0.968	0.992	0.780	77.39	25.8700	0.3637	2.612E-12	2.7	82223	2822	2.59	
	T5C-130	28.14604	87.65662	5140	g	4	0.967	0.992	0.779	77.14	20.0204	0.3706	2.921E-12	2.4	3561987	112014	39.35	3.58
	T5C-131	28.14602	87.65682	5142	q	4	0.968	0.992	0.780	77.26	20.2256	0.3712	1.742E-12	2.6	2086179	69876	24.92	2.27
	T5C-132	28.14608	87.65692	5143	g	4	0.967	0.992	0.779	77.24	20.2834	0.3572	1.155E-12	2.5	1308768	43625	16.33	1.49
	T5C-133	28.13124	87.67135	5006	g	4	0.967	0.998	0.755	73.15	20.1419	0.3578	1.634E-12	2.5	1888902	62157	23.94	2.18
	T5C-134	28.13121	87.67136	5012	q	4	0.968	0.998	0.756	73.39	20.0017	0.3581	1.073E-12	2.5	1233384	41214	16.21	1.48
	T5C-135	28.13098	87.671	5011	q	4	0.968	0.998	0.756	73.36	20.4238	0.3584	1.224E-12	2.4	1384715	45341	18.01	1.64
	T5C-137	28.13039	87.67115	5009	q	4	0.968	0.998	0.756	73.3	15.2926	0.3584	9.827E-13	2.5	1488399	49612	19.27	1.76
	T5C-138	28.1303	87.67135	5007	q	4	0.968	0.998	0.755	73.23	15.3710	0.3577	1.128E-12	2.6	1703076	57842	21.83	1.99
frontal moraine	T5C-139	28.13014	87.67179	5012	q	4	0.968	0.998	0.756	73.39	20.7436	0.3579	1.493E-12	3.0	1233384	41214	16.21	1.48
	T5C-140	28.13004	87.67129	5004	g	4	0.967	0.998	0.755	73.09	15.1402	0.3579	1.040E-12	3.9	1591689	72495	20.56	1.98
	T5C-141	28.318	87.72	5071	q	5	0.960	0.987	0.761	74.03	20.5684	0.3585	1.171E-12	2.5	1313370	43462	17.02	1.55
	T5C-142	28.319	87.721	5061	q	3	0.976	0.987	0.769	74.92	20.3264	0.3714	2.921E-12	3.2	3516184	135560	39.90	3.74
	T5C-143	28.318	87.722	5043	q	2	0.984	0.987	0.771	74.94	23.5217	0.3700	2.535E-12	2.5	2613944	85750	31.25	2.85
	T5C-144	28.318	87.722	5018	q	2	0.984	0.987	0.767	74.12	19.4552	0.3447	2.045E-12	2.4	2369812	76417	28.94	2.63
	T5C-146	28.318	87.725	4960	g	3	0.975	0.987	0.750	71.6	22.0228	0.3573	4.820E-12	2.6	5174849	169969	62.07	5.70
	T5C-147	28.319	88.726	4937	q	5	0.960	0.987	0.739	69.87	23.4344	0.3572	3.392E-12	4.7	3403912	176910	41.10	4.11
	T5C-148	28.319	88.727	4907	q	6	0.952	0.987	0.730	68.38	22.3771	0.3576	4.184E-12	2.5	4418096	143810	54.89	5.03
	T5C-149	28.319	88.728	4864	q	4	0.968	0.987	0.730	68.17	18.1590	0.3579	8.255E-12	2.5	10821447	344104	131.93	12.29
Dinggye Nord (moraine)	T5C-150	28.319	88.729	4835	q	3	0.976	0.987	0.729	67.83	20.6431	0.3577	7.966E-12	2.9	9173178	324703	113.27	10.65
	T5C-151	28.319	87.73	4812	q	4	0.968	0.987	0.720	66.45	22.5022	0.3583	7.979E-12	2.7	8439260	283533	107.04	9.98
	T5C-152	28.318	87.732	4773	q	3	0.976	0.987	0.718	65.82	20.6918	0.3553	1.171E-11	3.1	13389312	501281	173.65	16.73
	T5C-153	28.318	87.733	4741	q	4	0.968	0.987	0.708	64.33	20.6183	0.3571	1.835E-11	1.4	21190533	517772	286.56	27.04
	T5C-154	28.318	87.734	4727	q	3	0.976	0.987	0.710	64.44	19.4464	0.3446	5.688E-12	1.8	6686115	179413	89.31	8.08
	T5C-155	28.317	87.735	4696	q	5	0.960	0.987	0.697	62.49	19.3416	0.3582	2.808E-12	2.6	3425182	112807	45.60	4.17

See Table III.3 for the caption.

Yo Ri Sampling Site

T3 surface, down:



T3 surface, up:



Appendix III-1

Yo Ri Sampling site
T3 surface
Dated Samples

T3 down:



T3 up:



Yo Ri sampling site
Views of the T4 surface

Mounds and big blocs of the T4 surface (down) :



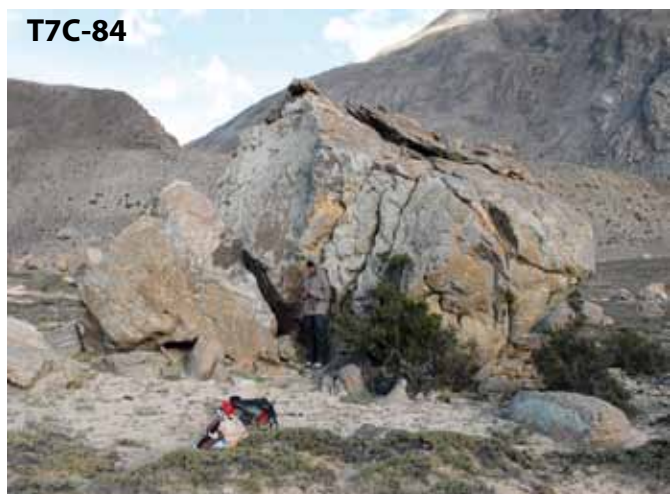
Views of the Hanging T4 surface :



Yo Ri sampling site
T4 surface (T4a, b, c)
Dated Samples



Yo Ri Sampling site
T4 surface, down
Analysed blocks

T7C-82**T7C-82, zoom****T7C-83****T7C-83, zoom****T7C-84****T7C-84, zoom**

Khartा Sampling site
T3 surface and
Dated Samples

T3, uplifted



T3, down



T7C-2 (T3up)



T7C-44(T3down)



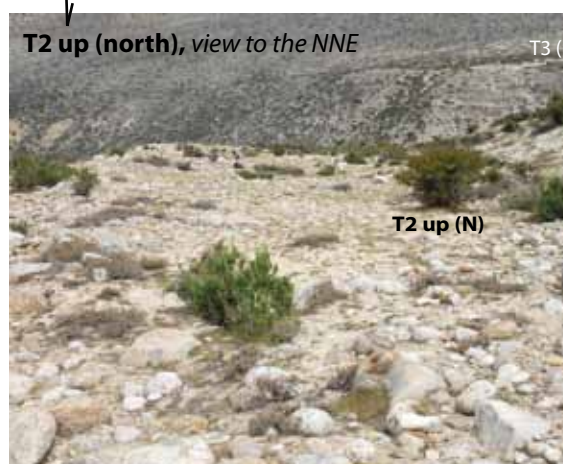
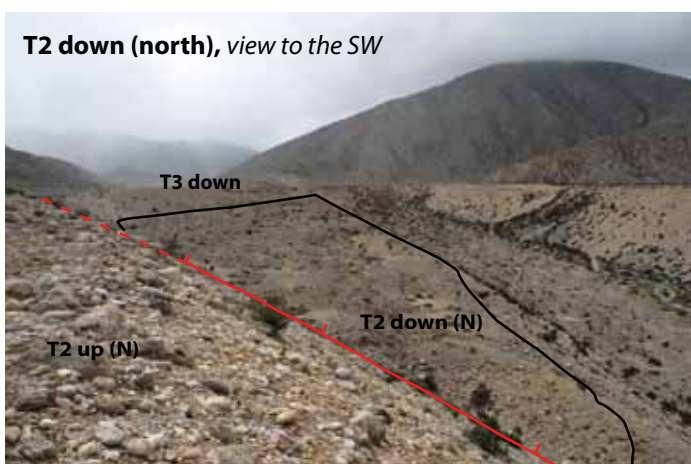
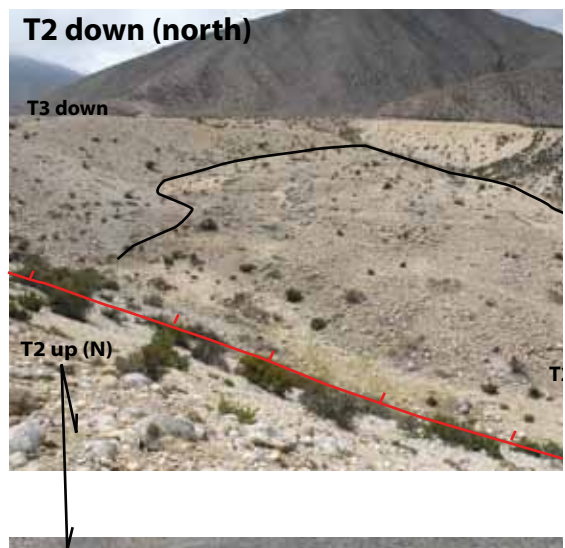
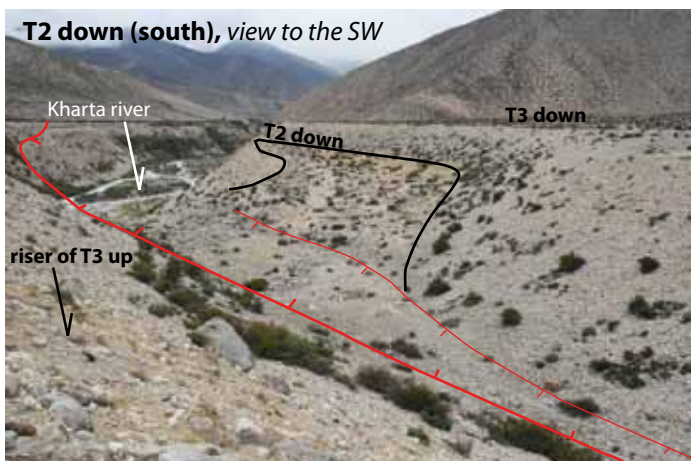
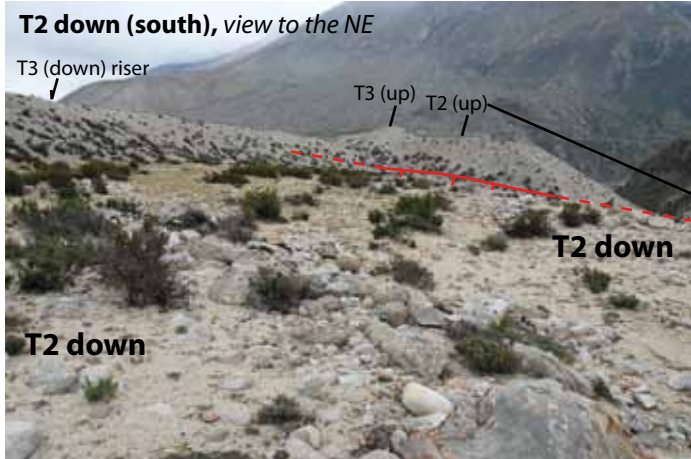
T7C-10 (T3up)



T7C-51(T3down)



Khartा sampling site
T2 surfaces



Khatta Sampling site
T2 surface
Dated Samples



South Kharta, sampled moraine and dated samples





Mabja area
Sampled moraine
Dated Samples



3.3. Late Pleistocene kinematic constraints on the active faults of the Gulu-Yangbajain rift from cosmogenic nuclide dating

Manuscript in preparation.

Abstract

We determine the first late Pleistocene vertical throw rates from ^{10}Be dating of offset moraines and alluvial terraces at 5 sites along the northern part of the Yadong-Gulu rift of south Tibet. At Gulu, a late Pleistocene lateral moraine offset 40 ± 10 m is well dated at 16 ± 1 ka ($n=13$) yielding a rate of 2.2 ± 0.8 mm/yr. 15 km to the south, an alluvial terrace is nicely offset 28 m but its age remains uncertain. At Damxung, the fault system strikes obliquely to the average E-W extension direction, and we determine both normal and sinistral slip-rates. A terrace offset vertically a total of 20 m by two branches of the fault system is well dated at 17.0 ± 1.3 ka ($n=6$) yielding a normal rate of 1.2 ± 0.2 mm/yr. The horizontal offset of this terrace may range between 20 to 45 m thus yielding a sinistral slip-rate of 1.8 mm/yr. The 145 m vertical offset of a high terrace level is less well dated at about 260 ka ($n=2$), which yields a rate of 0.5 ± 0.2 mm/yr. Further southwest, in the Yangbajain basin, a lateral moraine ridge west of Chepa abandoned between 20 and 40 ka ($n=17$), is offset 33 ± 7 m yielding a vertical throw rate of 1.1 ± 0.6 mm/yr. In the eastern Yangbajain basin, two sub-parallel N-S west dipping normal faults offset alluvial fans 20 and 90 m. The not well constrained ages of two fans (110 ± 50 ka; $n=2$; 240 ± 40 ka; $n=3$) may indicate that they correlate with the last interglacial stages of MIS-5e and MIS-7. The rates of the two faults is thus of 0.2 ± 0.1 mm/yr and 0.4 ± 0.1 mm/yr, or a total of 0.6 ± 0.2 mm/yr. Total vertical throw rate in the south may thus reach 1.7 mm/yr. In summary, the vertical throw rate along the Yangbajain-Gulu rift range between 1.6 to 2.2 mm/yr from north to south, and reaches 1.2 mm/yr near Damxung where part of the faulting is accommodated by left-lateral slip at a rate of 1.8 mm/yr. These rates corroborate previous estimates of normal faulting for the Quaternary (Armijo et al., 1986; Wu et al., 2004) and when compared to more long-term exhumation rates (1-1.5 mm/yr for the last 8-10 Ma) may indicate slightly faster rates during the late Pleistocene. A simple explanation is thus that one phase of extension began in the upper Miocene and continued until present (Harrison et al., 1995; Kapp et al., 2005), although several phases of extension cannot be excluded (Armijo et al., 1986), as well as other processes for the late Miocene exhumation in the Nyainqntanglha (Wu et al., 2007).

3.3.1. Introduction

The Yadong-Gulu graben is one of the major and most studied rifts system of southern Tibet (Allègre et al., 1984 ; Chang et al., 1986 ; Armijo et al., 1986, 1989 ; Harrison et al., 1995 ; Kapp et al., 2005; Edwards and Ratschbacher, 2005 ; Wu et al., 2004, 2007) (Figures III.36a and III.36b). It extends from Yadong in the south to Gulu in the north, for about 500 km across the Lhasa block and the Yarlung-Tsango suture. To the north, the Gulu half-graben connects with the Beng Co right lateral strike-slip fault (Armijo et al., 1989; Figure III.36b). The rift can be separated into two parts. South of the Yarlung-Tsango suture, the rift system is formed by en-échelon half-grabens with west-dipping normal faults that propagate into the high Himalayan summits (Armijo et al., 1986 ; Ratschbacher et al., 1994). North of the suture, the normal faults outline two north-south striking rifts, Yangbajain in the south and Gulu in the north, connected by a left-lateral extensional fault zone along the southeastern flank of the Nyainqntanglha massif (Figure III.36b to 41). This rift is thus specific and is characterized by an oblique NE-SW 120 km-long section, a unique setting among the grabens of south Tibet. In addition, the southwestern flank of the Nyainqntanglha range is bounded by a low dipping ductile shear zone. Although the impact of this ancient deformation zone on the present rift structure is clear, the link between the shear zone and the active normal faults is not well established. In this study we aimed at determining quantitatively the present slip-rates of the normal faults of the northern part of the Yadong-Gulu graben, using vertical offset measurements of geomorphological landforms, which ages are determined using ^{10}Be surface exposure dating. While several rate estimates have been made in the past, we present here the first normal slip-rate determination for the late-Pleistocene.

3.3.2. The study area

We have selected five sites along the Yangbajain-Gulu graben where geomorphic offsets could be measured and dated (Figure III.41). Two sites are located in the southern Yangbajain graben, the West-Chepa and Gyekar sites (Figure III.46). At West-Chepa, a lateral moraine ridge is offset by the western normal fault. At Gyekar, alluvial fans are offset by several strands of west-dipping normal faults in the eastern part of the graben. One site is located near the city of Damxung, where,

both normal and left-lateral faults offset alluvial terraces (Figure III.42). Two other sites are located along the Gulu half-graben, one site to the south (south Gulu) and the other to the north (north Gulu) (Figure III.54). At south Gulu, an alluvial terrace is nicely offset by the main unique strand of the normal fault. At north Gulu, an abandoned lateral moraine is cut and offset by the normal fault.

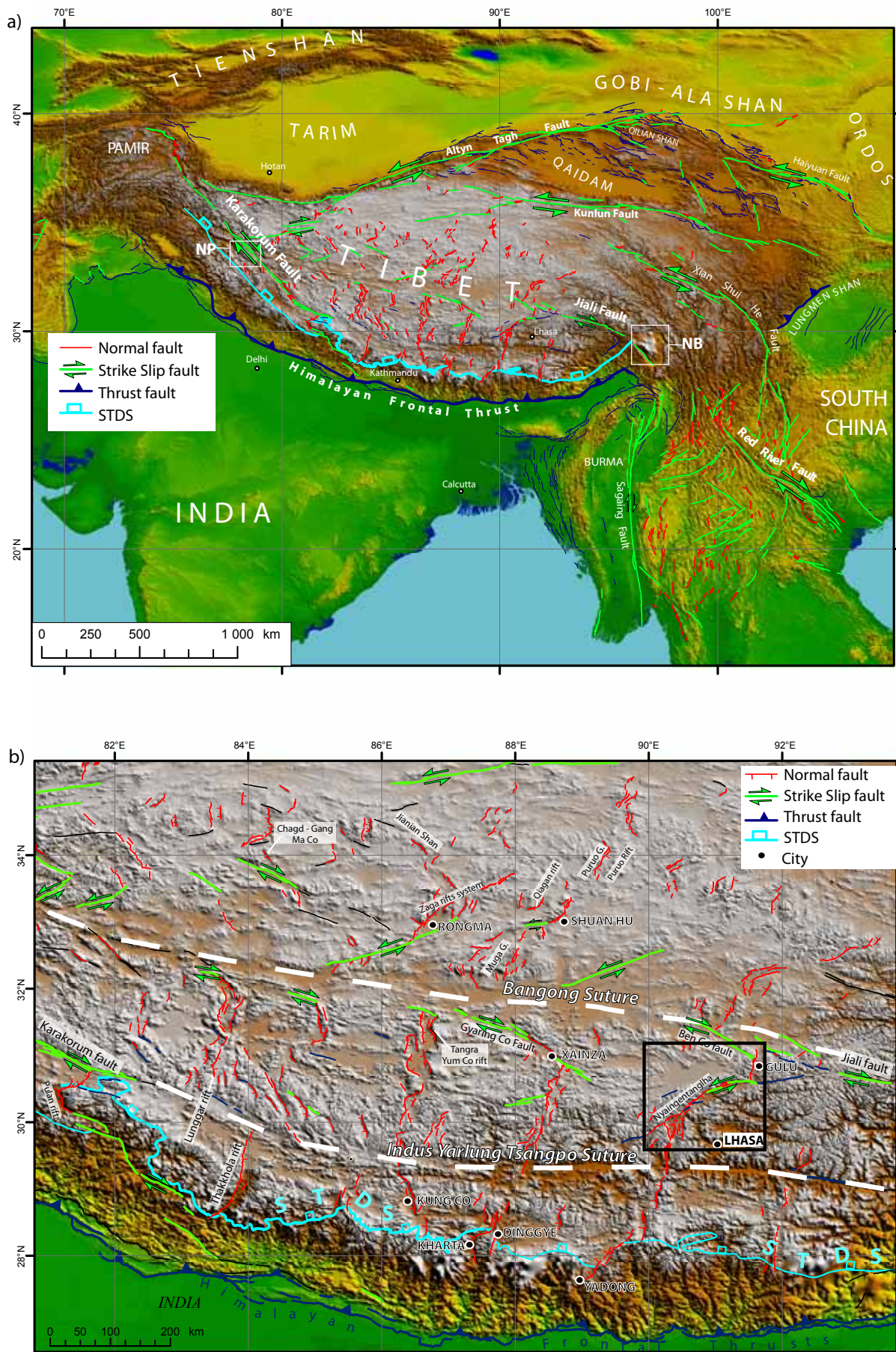


Figure III.36: (a) Active faults map of the Indo-Asia collision zone. STDS (South Tibetan Detachment System) is from Leloup et al., 2010 (see Annexe A), NP = Nanga Parbat, NB = Namche Barwa (b) Active fault map of south Tibet. Rectangle outlines figures III.37-41 of northern Yadong-Gulu graben area. Puruo G = Puruo Gangri, Muga G = Muga Gangri

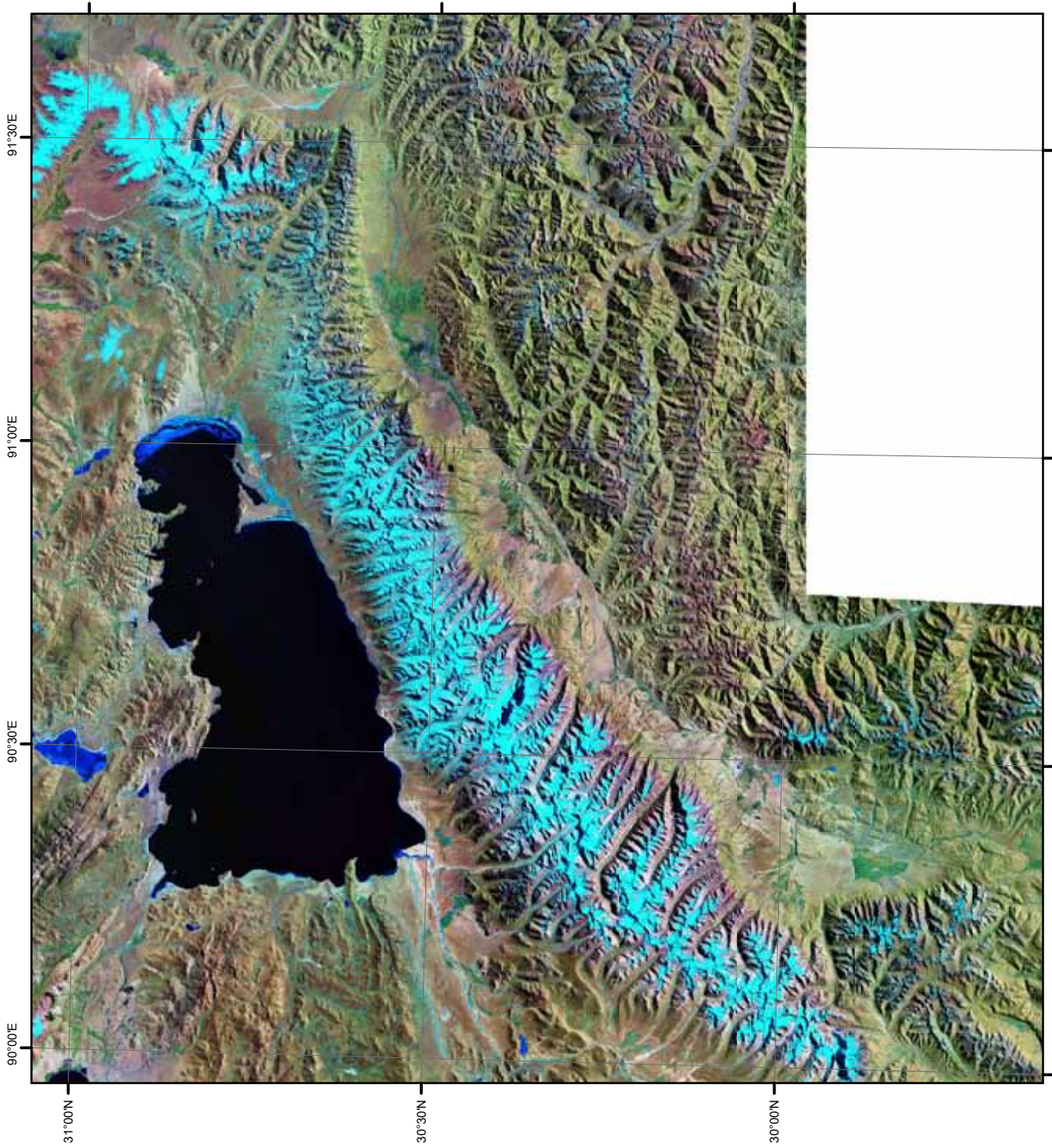


Figure III.37: Landsat satellite image of the Nyainqntanglha massif

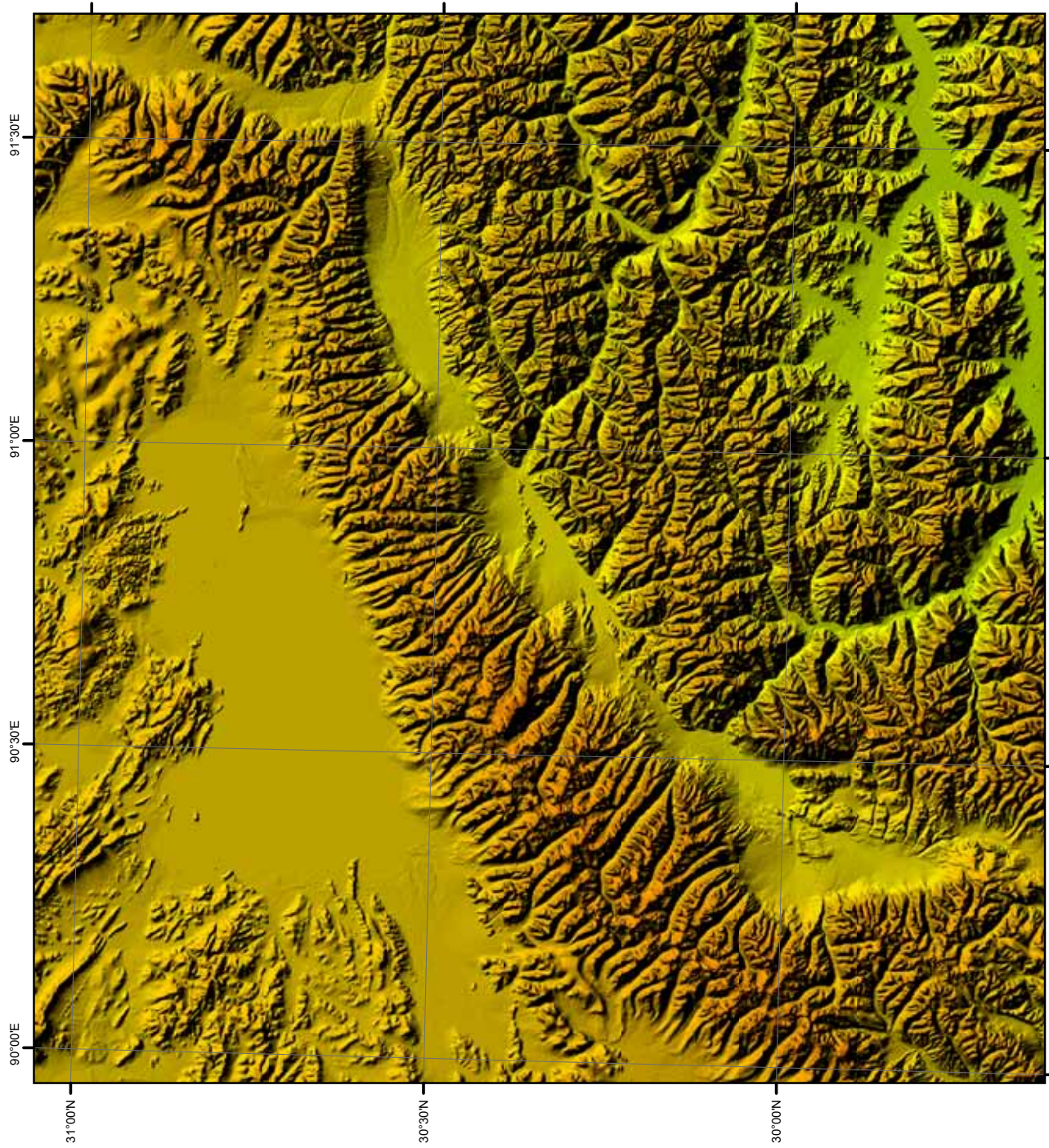


Figure III.38: SRTM DEM (resolution 90 m) of the Nyainqntanglha massif

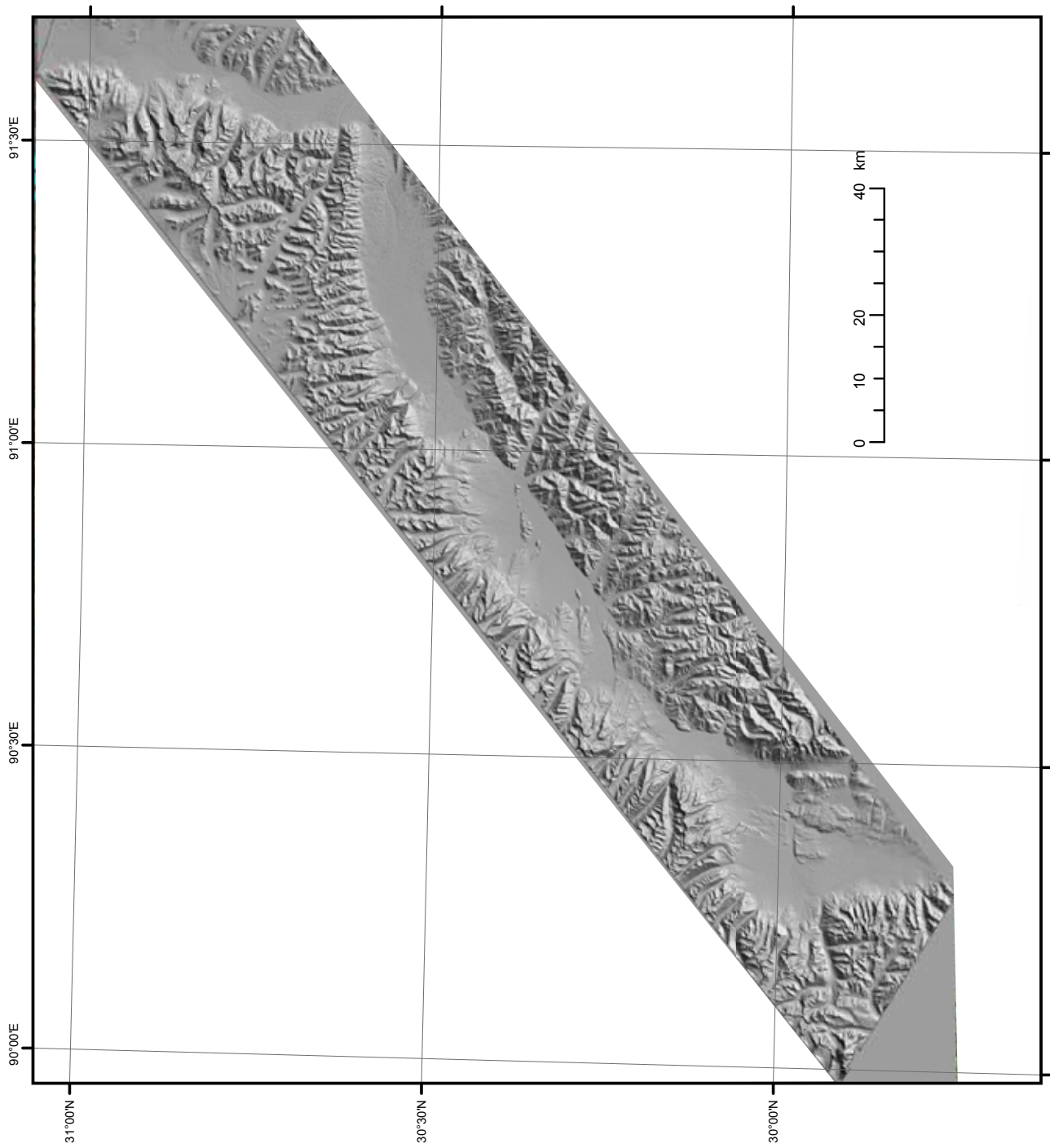


Figure III.39: SPOTdem (resolution 20 m) of the Gulu-Yangbjain rift

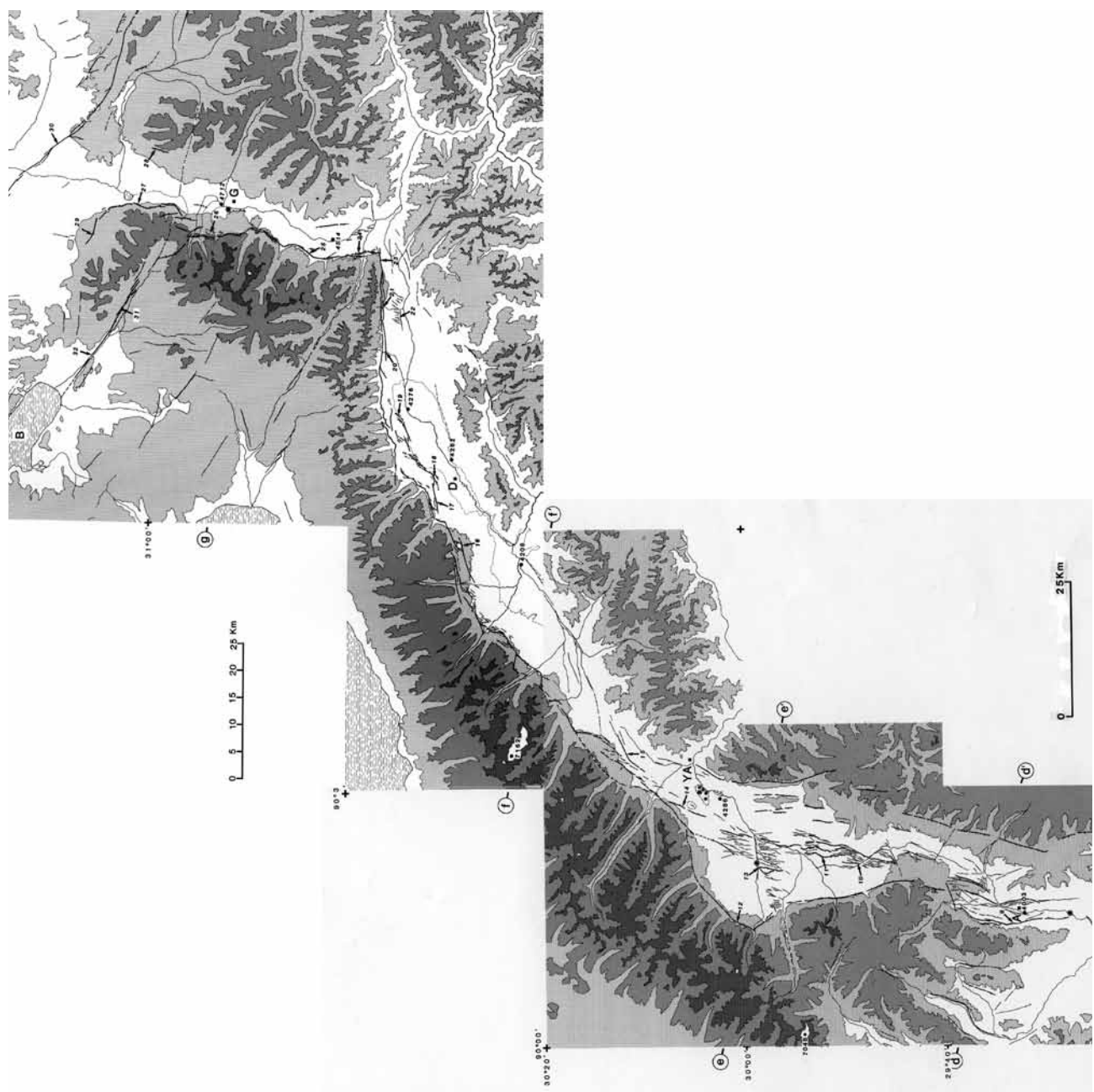


Figure III.40: Active faults map of the Yadong-Gulu rift, from Armijo et al, 1986

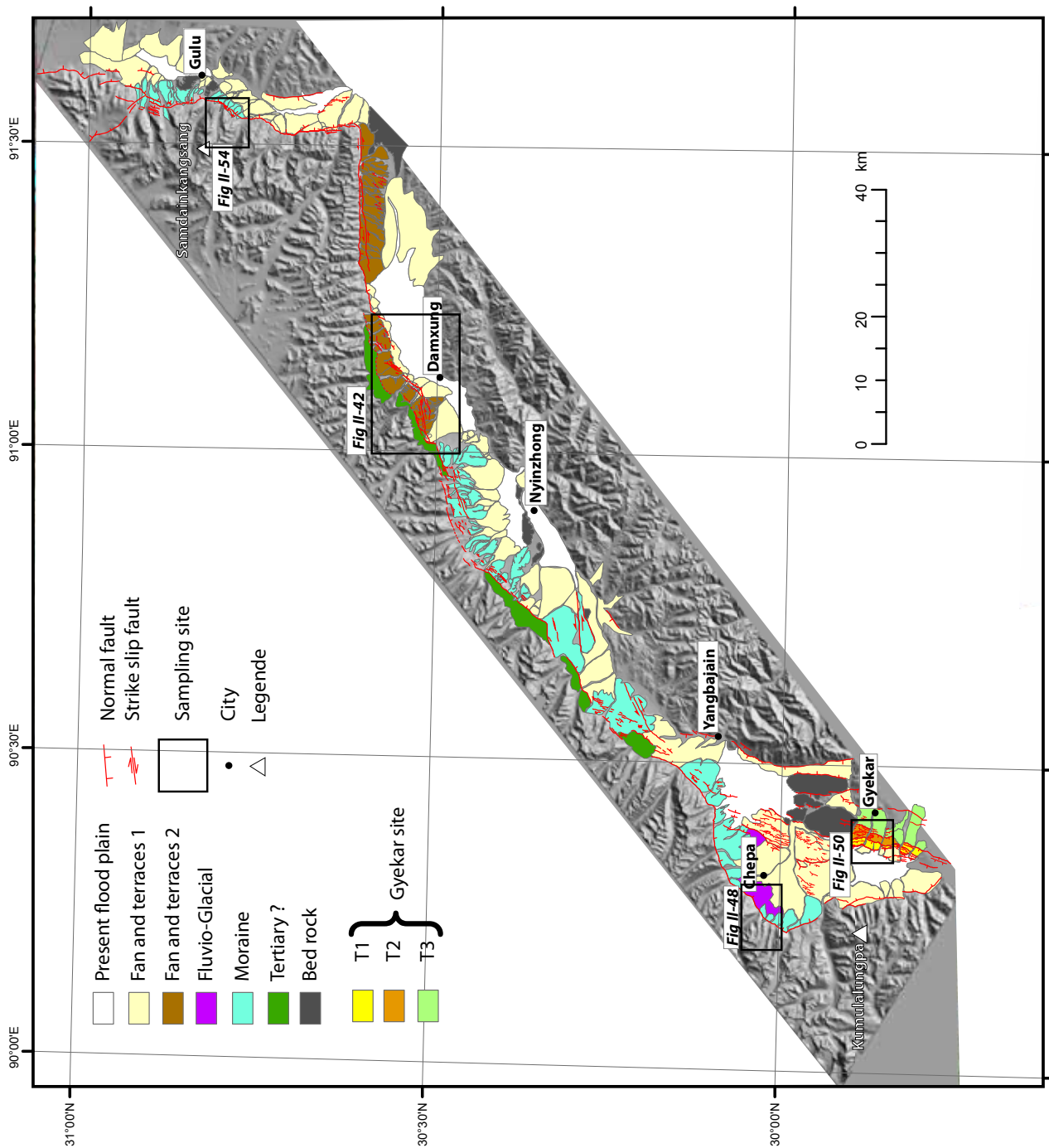


Figure III.41: Map of the quaternary active faults and deposits of the Gulu-Yangbajain rift. Projection is UTM45. The digital elevation model is from SPOT. Active faults are traced from Armijo et al., 1986 and interpretation of Landsat, Ikonos, SPOT (10 m) satellite images, and SPOTdem. Boxes correspond to the studied sites.

3.3.3. The Damxung site

The Damxung corridor is the section of the Yangbajain-Gulu rift that presents both normal and left-lateral strike-slip faults. In this corridor, two large rhomb-shaped basins are separated by a bottleneck structure. The western basin is centered on Nyinzhong city while the second one includes Damxung city (Figure III.41). North of Damxung, the active fault system involves two main faults. Along the range front recent normal fault scarp are clear at the base of the triangular facet (structural surface of the ductile shear zone) (Figure III.42). 1 to 2 km away from the range front, the main fault strand is left-stepping, forming a succession of N80E striking left-lateral strands and N30-50E normal strands (see description of sites 15 to 21 in Armijo et al., 1986). We studied in more details a site located north of the city of Damxung (Figures III.42, 43 and 44), at site 18 of Armijo et al., (1986) (Figure 16 in Armijo et al., 1986). At this site, the main fault splits in two major branches that cut fan shaped terraces located 20 (T1) and 140 m (T2) above the present stream bed (Figures III.43, 44 and 45). The N50E northwestern fault is purely normal while the N75E southwestern fault is both normal and strike-slip. Handheld GPS profiles leveled across the fault strands constrain the maximum vertical offset to be 9 and 11 m on each of the fault strands, thus a total of 20 m accumulated since abandonment of T1. Terrace T2 about 125 m above T1 is thus offset a minimum of 145 m vertically. The southwestern limit of terrace T1 is offset horizontally by the main fault (Figure III.44). The base of the riser is offset about 23 m, while the upper part of the riser is offset 45 m. These offset values thus constitutes maximum horizontal offset for T1.

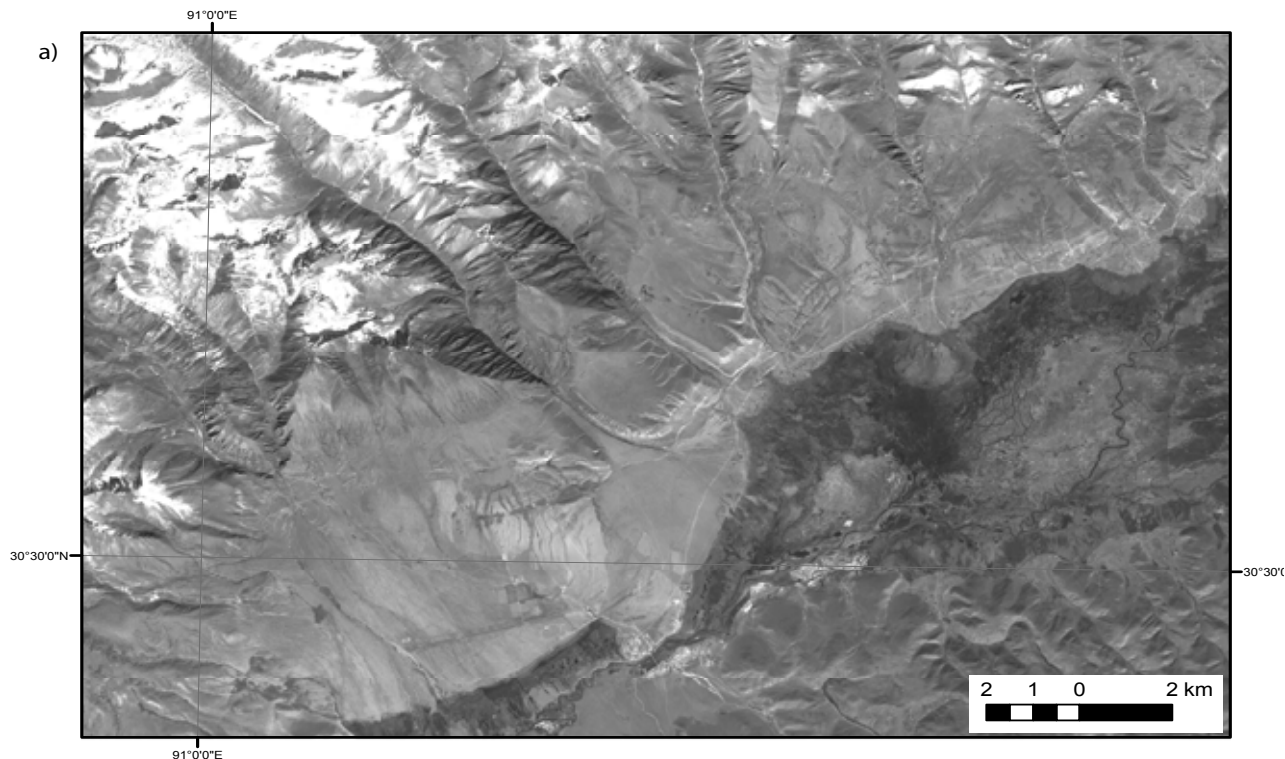
Six cobble-size samples collected at the surface of T1 yield very similar ^{10}Be exposure ages that range from 15 to 19 ka, with an average of 17.0 ± 1.3 ka (Table III.5; Figure III.61). We interpret this age to represent the time of abandonment of T1.

Four samples collected at the surface of T2 have been analyzed. Two large block samples were sampled from the top of the surface. The blocks (35 to 50 cm in diameter) were sitting on top of the conglomerate but embedded in the soil and turf cover. T5C-92 and T5C-93 yield very young ages of 4 and 12 ka (a replicate of T5C-93 yields a similar age of 15.2 ka) (Table III.5; Figure III.61). These ages are younger than the lower terrace T1 dated at 17 ka. We interpret these young ages to be due to recent displacements of the blocks from a position below the surface in the riser conglomerate outcrop to the surface (most likely of anthropic origin). Two cobble samples were collected from the top conglomerate outcropping on the rim of the terrace. These samples, T5C-97 and 101, yield much

older ages of 223 and 291 ka (Table III.5; Figure III.61). Without additional constraints on erosion or inheritance, we will take the range of these ages to best represent the time of abandonment of T2 (260 ± 60 ka).

Considering that the 20 m total offset of T1 accumulated since abandonment of terrace T1 at 17.0 ± 1.3 ka, we determine a vertical throw rate of about 1.2 ± 0.2 mm/yr. Assuming the minimum offset of T2 of 145 m accumulated after the abandonment of T2 at about 260 ± 60 ka, constrains the vertical throw rate at about 0.6 ± 0.2 mm/yr.

A maximum left-lateral slip-rate is determined when combining the maximum offset of T1 of 23-45 m with the age of T1 (17 ka), thus a rate of 1.8 ± 1.0 mm/yr.



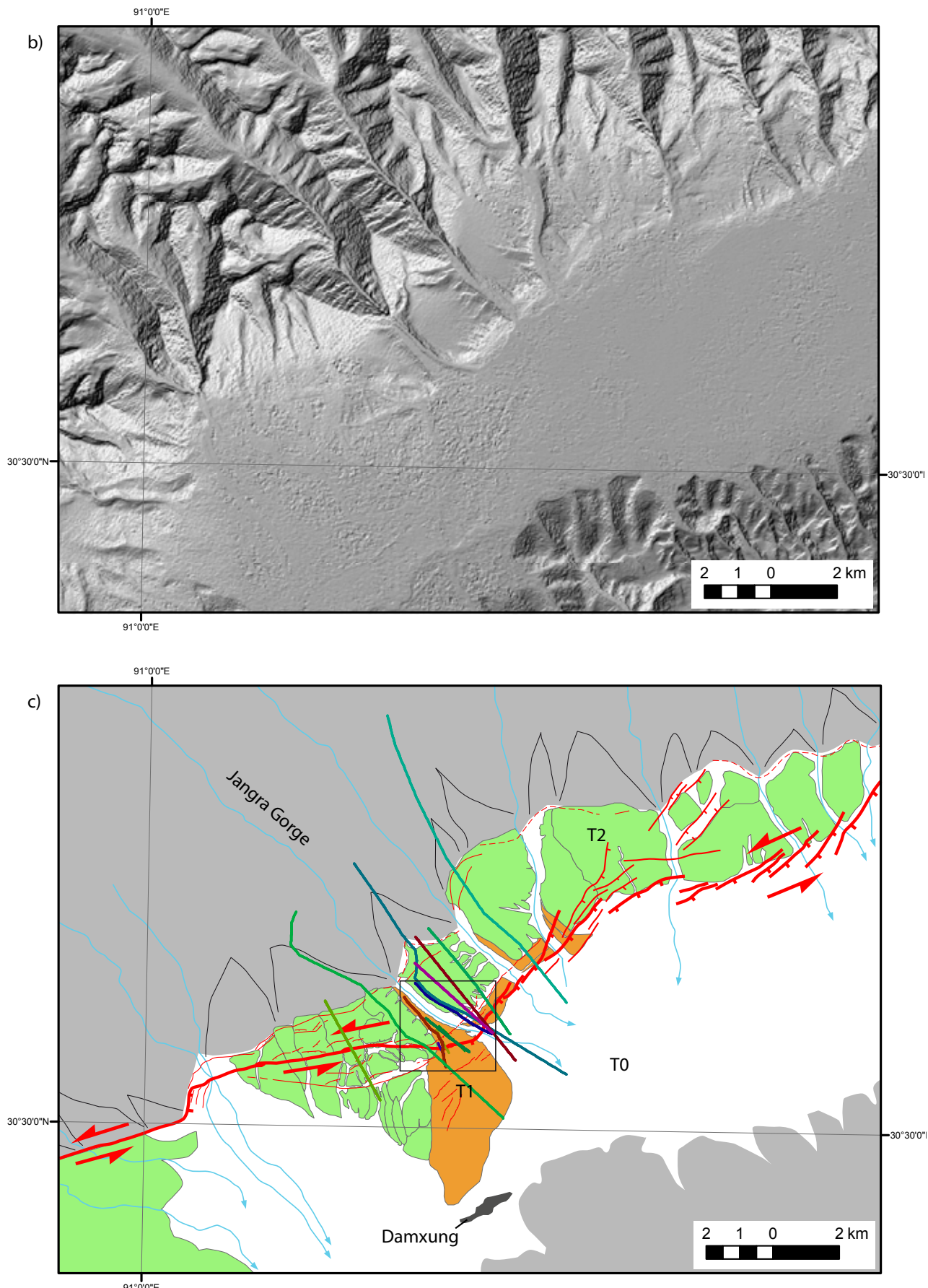


Figure III.42: a) SPOT satellite image (resolution: 10 m) of the Damxung area. b) SPOTdem of the Damxung area (resolution: 20 m). c) Map of the active faults and of the older quaternary deposits of the Damxung area, inset correspond to Figures III.44 and III.45. Traces of the topographic profiles of Figure III.45a are indicated

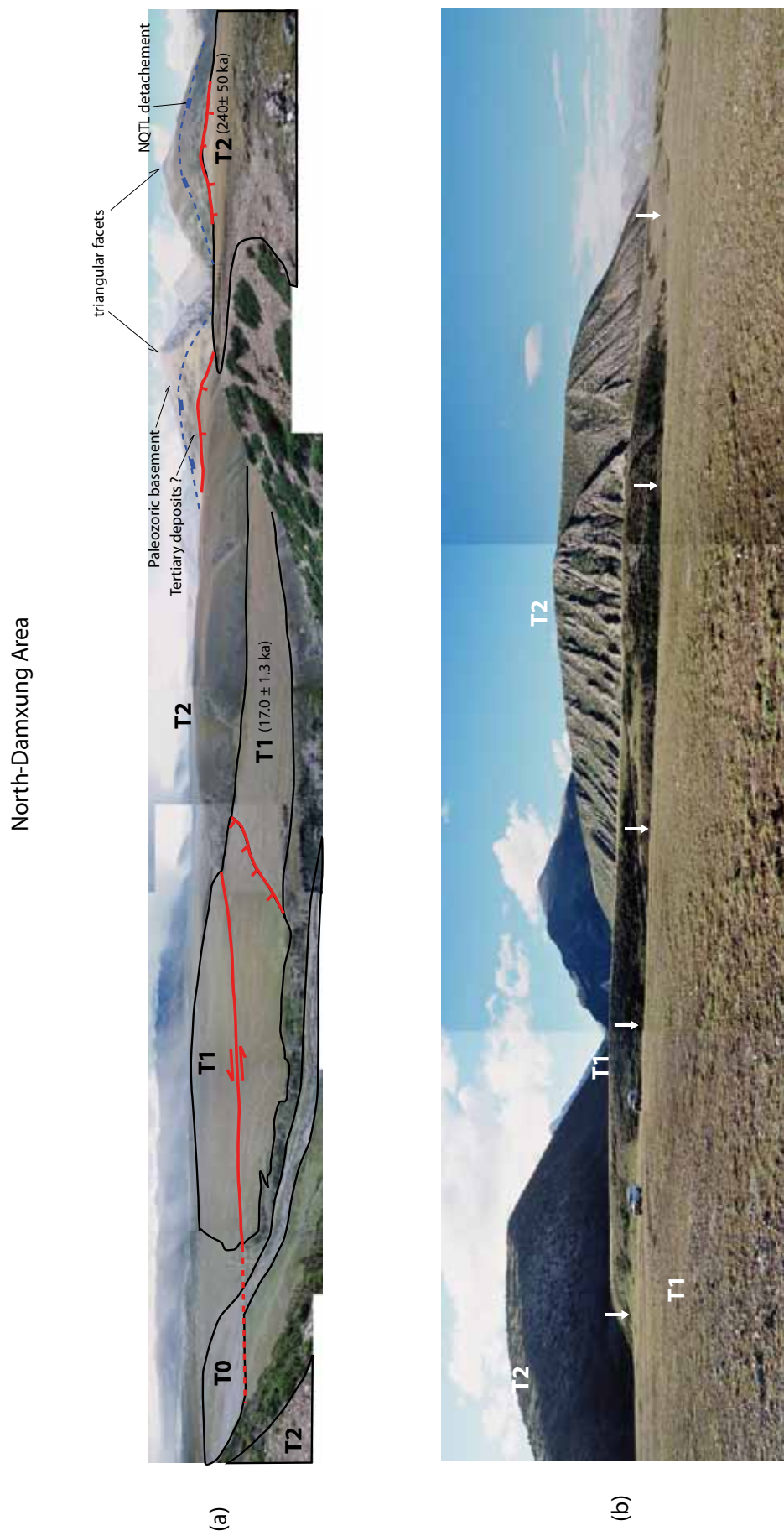


Figure III.43: a) View to the S-W of the Damxung sampling site. b) View to the North of the sampled surfaces. White arrows show the fault scarp.

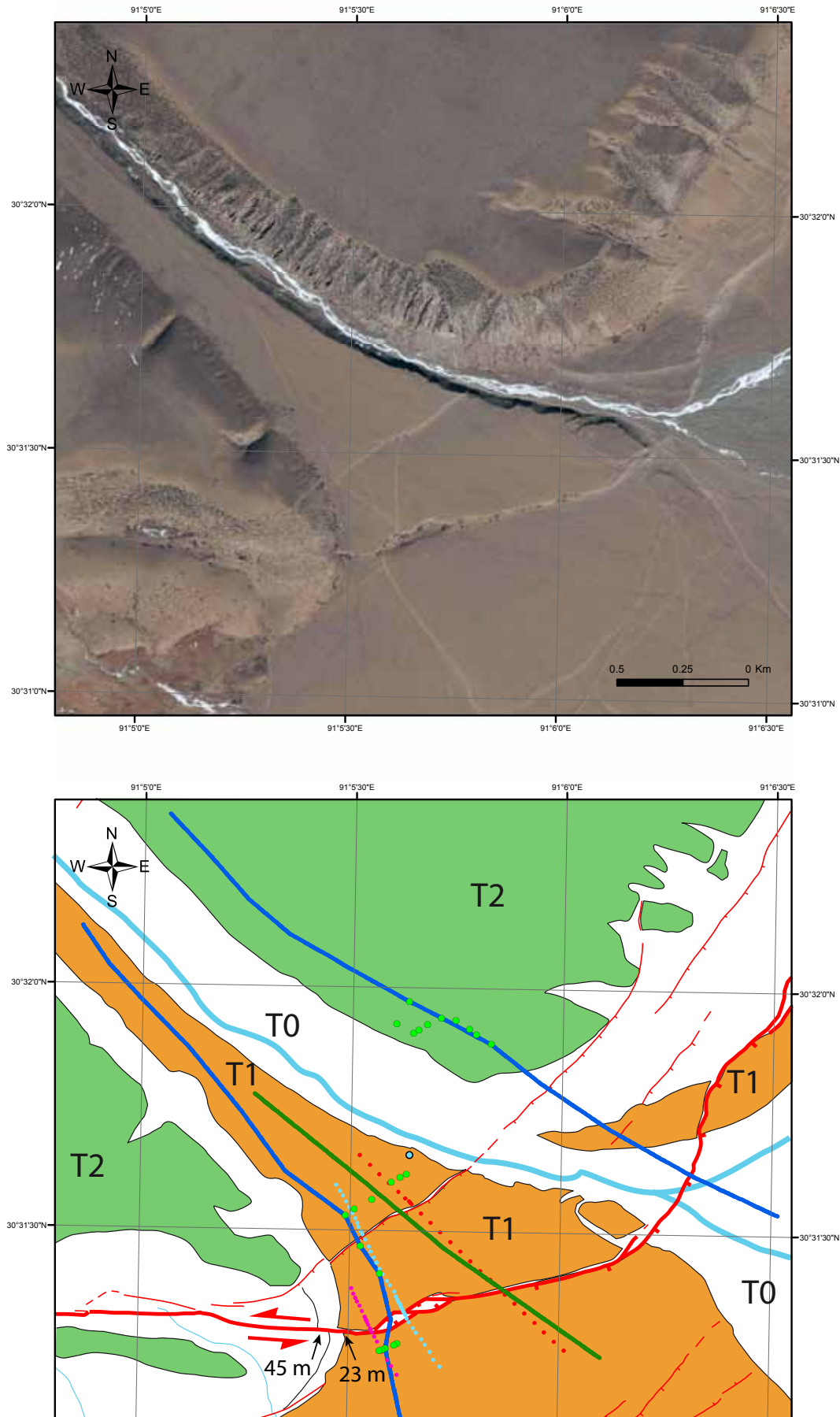


Figure III.44: (a) Ikonos satellite image of the Damxung site (from Google Earth). (b) Geomorphic interpretation of Damxung site. Traces of the topographic profiles of Figure III.45b are indicated.

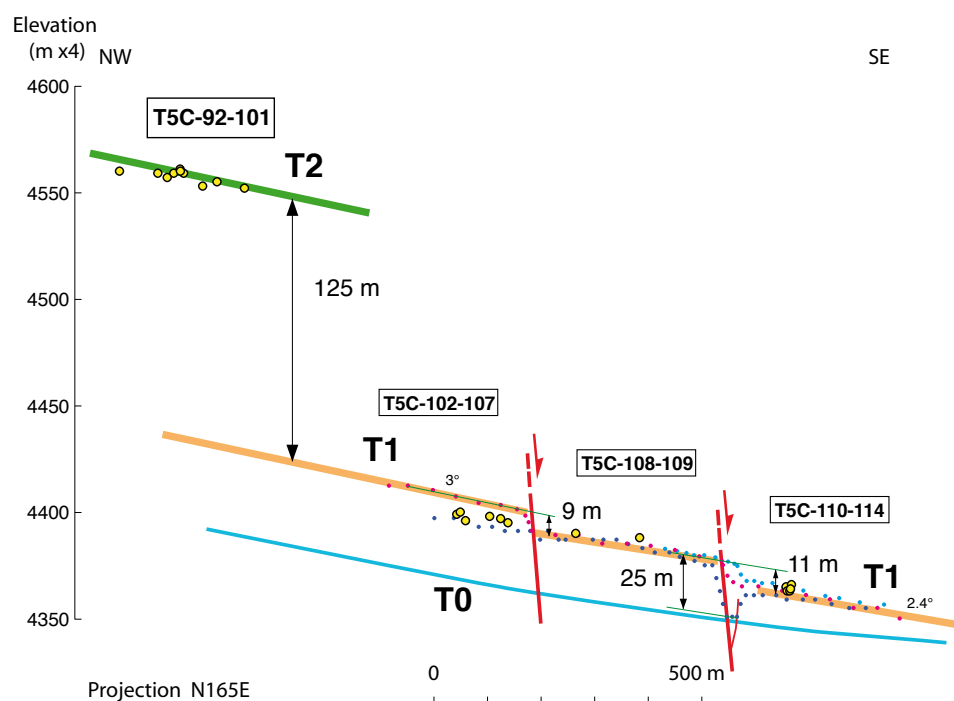
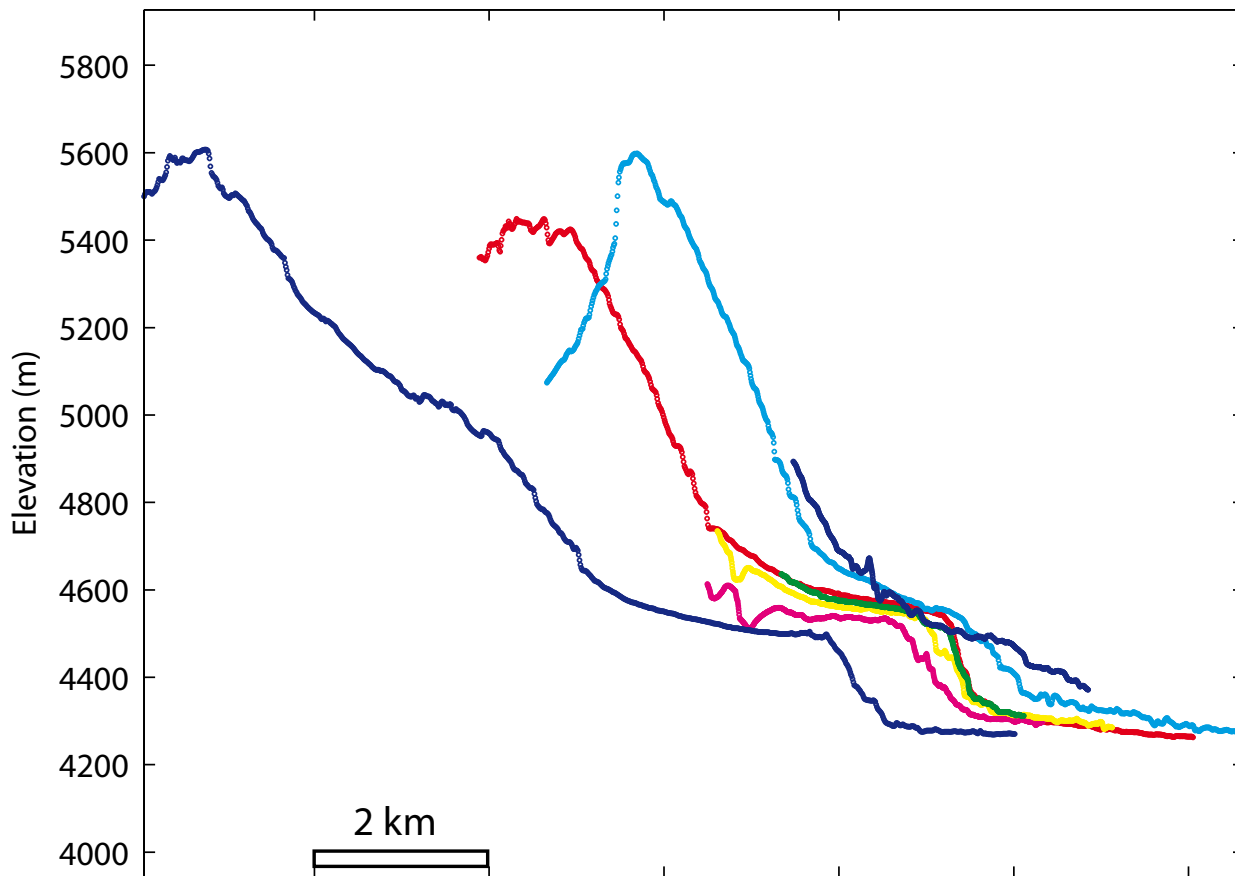


Figure III.45: Topographic profiles at sampling site across Damxung faults (a) Large scale profiles from SPOTdem. See location in Figure III.42a. (b) Topographic profiles from GPS points leveled in the field. Yellow dots are position of ^{10}Be samples. See location in Figure III.44b.

3.3.4. Yangbajain basin

The Yangbajain basin is limited to the east and west by faults of opposite dip. To the west, a main normal fault follows the foot of clear triangular facets at the foot of the range. To the east, the relief is less developed and faulting is distributed among sets of sub-parallel west-dipping normal faults (Armijo et al., 1986) (Figures III.41 and 46).

3.3.4.1. The West-Chepa moraine site

The main fault west of Chepa is characterized by prominent triangular facets (Figure III.47). The site is located at the outlet of a small hanging glacial valleys (site 12 in Armijo et al., 1986; Figures III.47 and 48), where abandoned lateral moraines are cleanly cut and offset by the main normal fault (Figures III.47 and 49). The slope of the moraine ridge is different on each side of the fault, ~22° on the upper part and ~12° for the lower part, allowing for a large uncertainty on the determination of the vertical offset of the lateral moraine, i.e. 33 ± 7 m (Figure III.49).

We sampled both the lateral moraine ridge, upstream and downstream of the fault scarp, and an inner moraine, 500 m upstream from the fault scarp for ^{10}Be exposure dating. The ages confirm the morpho-stratigraphic analysis, the inner moraine is younger (11-18 ka) than the lateral moraine (20-45 ka) (Table III.5; Figure III.61). The lateral moraine thus formed during the last glacial advances of MIS-3b and the LGM at 18-24 ka, while the younger inner moraine may correspond to the younger Dryas cold spell.

Considering that the vertical offset of 33 ± 7 m accumulated after or during the maximum advances of 20-45 ka, constrains the vertical throw rate at 1.1 ± 0.6 mm/yr.

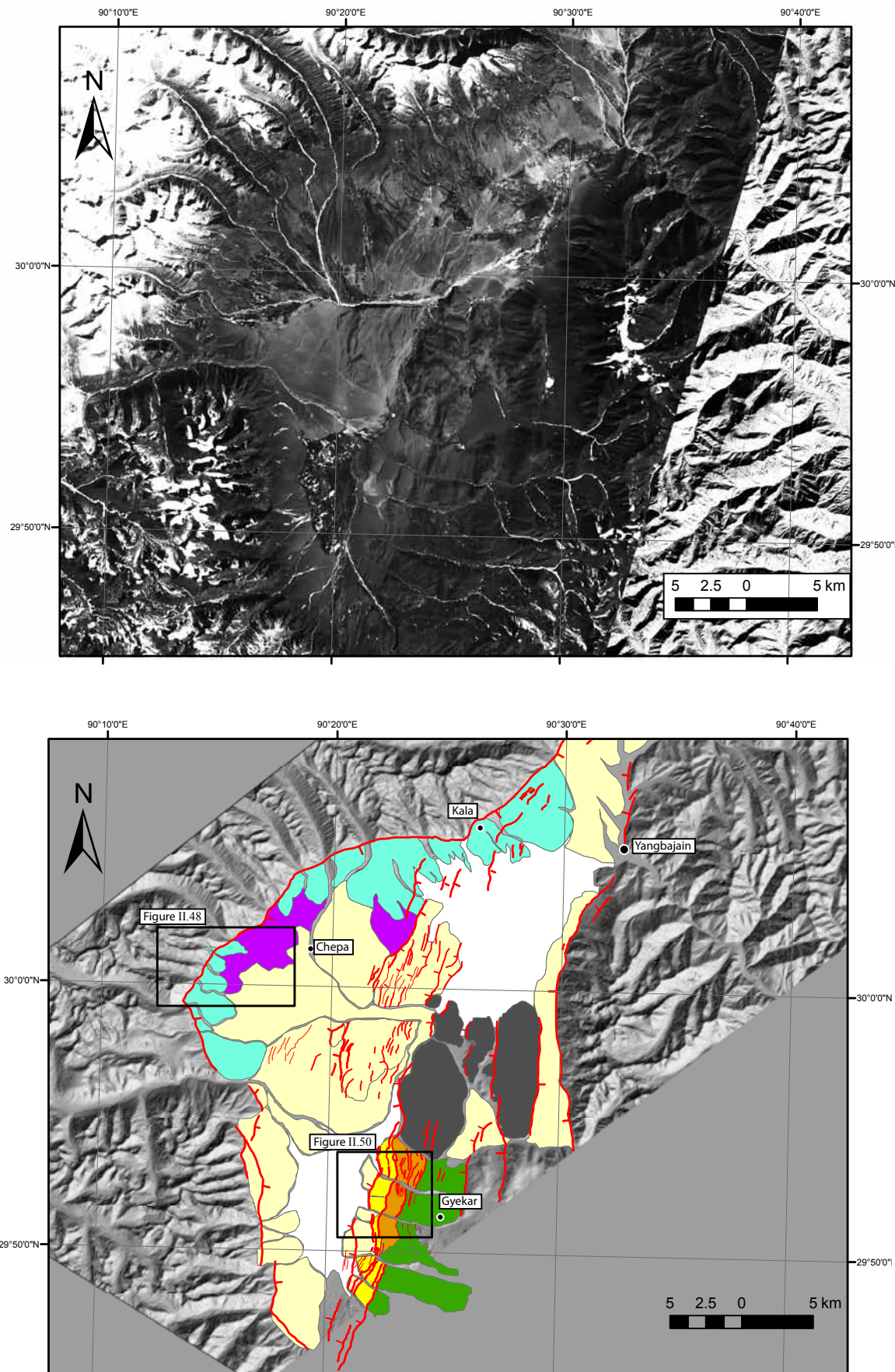


Figure III.46: a) SPOT satellite image (resolution: 10 m) of the Yangbajain basin. b) SPOTdem of the Yangbajain basin (resolution: 20 m) with geomorphic interpretation, inset correspond to Figures III.48 and III.50

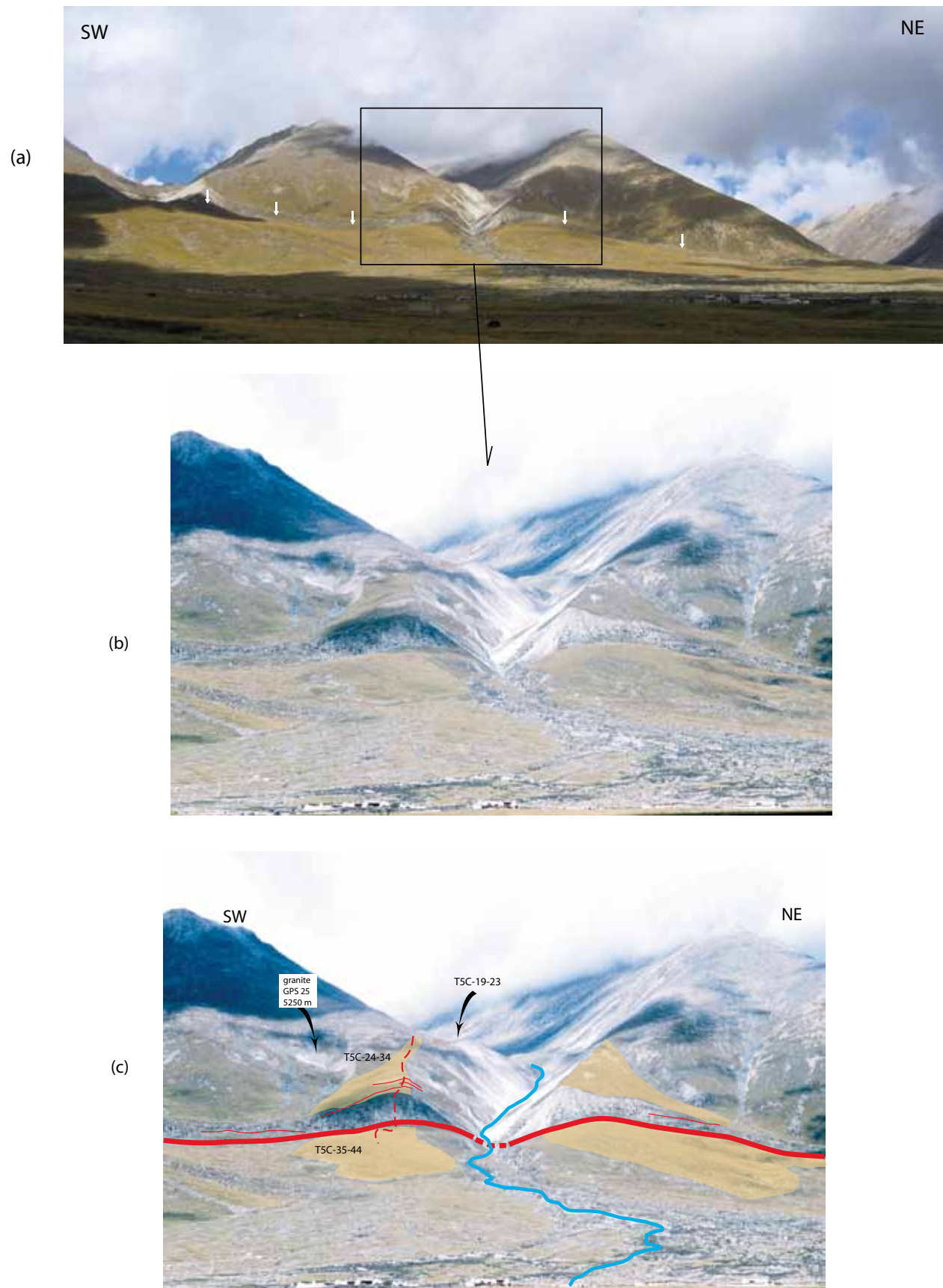


Figure III.47: (a) View of normal fault scarp west of Yangbajain basin and offset moraines, to the west of Chepa. (b) Close-up view on Chepa moraine site. (c) Simplified geomorphic interpretation and samples positions. Yellow patches correspond to lateral moraine ridges offset by normal fault. Lateral moraine ridge to the south and inset moraine have been targeted for ^{10}Be dating.

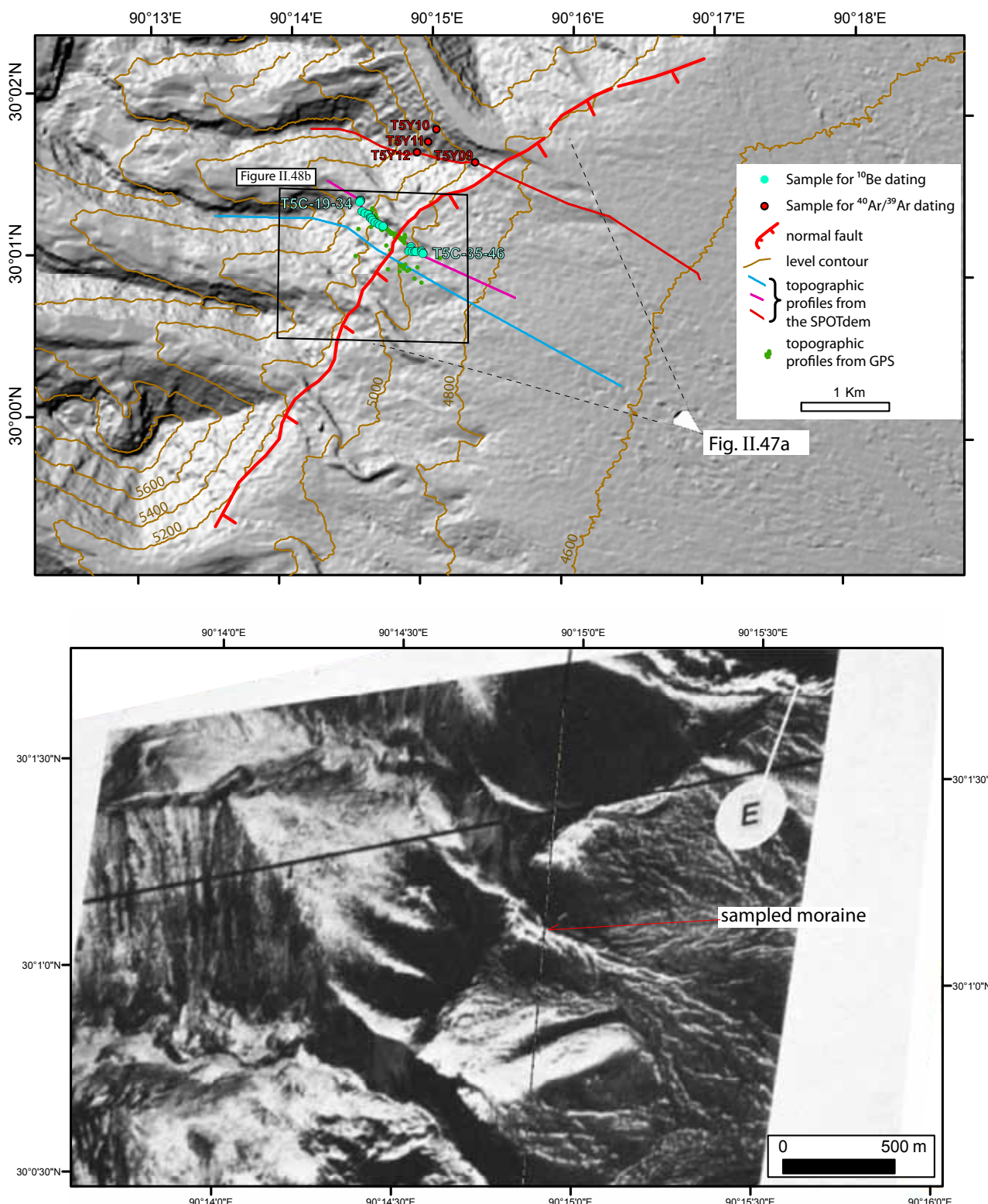


Figure III.48: (a) View of the SPOTdem of the West-Chepa site. ^{10}Be dating samples positions and traces of the topographic profiles of Figure III.49 are indicated. $^{40}\text{Ar}/^{39}\text{Ar}$ samples of the long-term deformation study are also represented for comparison. See Figures II.31 to 33 for a review. (b) Air photo centered on the sampled moraine, from Armijo et al. (1986). Photo is georeferenced without orthorectification.

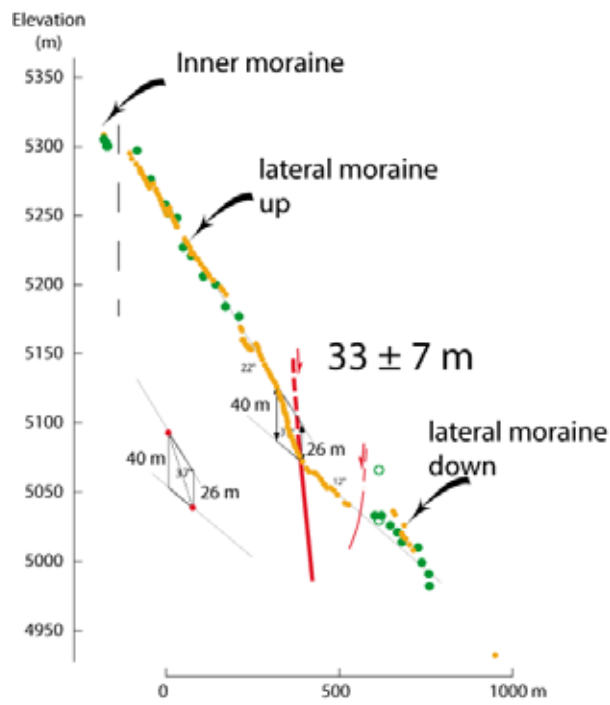
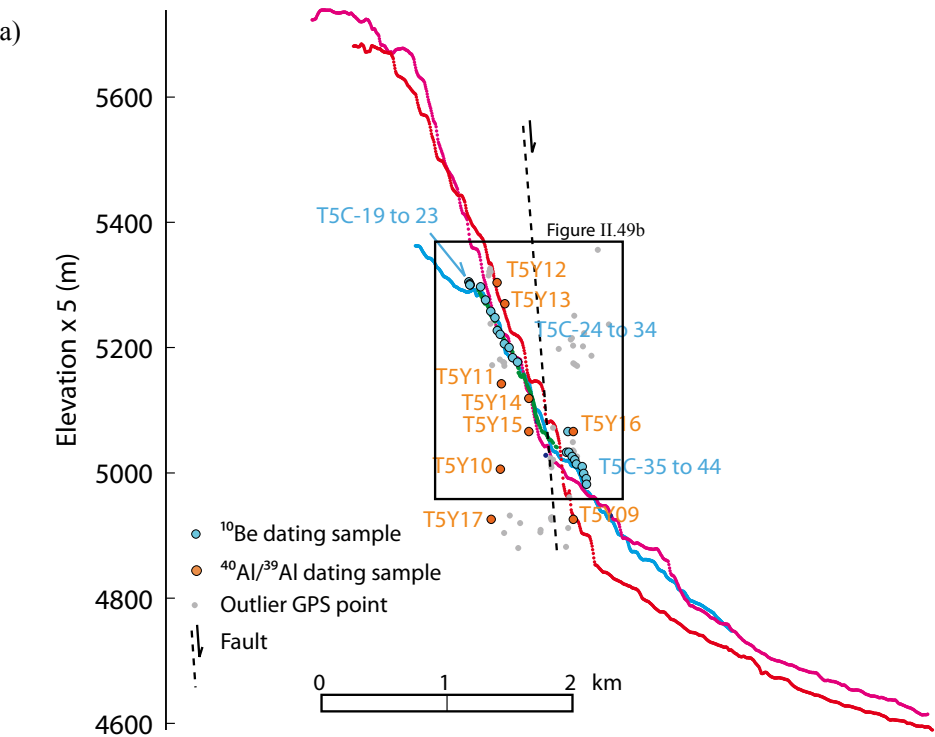


Figure III.49: Topographic profiles at Chepa moraine site (a) Large scale profiles from SPOTdem. $^{40}\text{Ar}/^{39}\text{Ar}$ samples of the long-term deformation study are also represented for comparison. See Figures II.31 to 33 for a review. (b) Profiles from GPS points leveled in the field. See location in Figure III.48a.

3.3.4.2. The Gyekar terraces site

The dense network of subparallel scarps oriented ~N12°E truncate the alluvial fans of the graben floor forming a stairs morphology (Figures III.41, 50, 51 and 52). We selected a site west of the city of Gyekar (near site 11 in Armijo et al., 1986) where a set of different terrace levels (T1, T2 and T3) are vertically offset by several normal faults (Figure III.51). Topographic profiles leveled in the field with a theodolite and large scale topographic profiles from the SPOTdem, allow to constrain the vertical offset of T1 and T2. T1 is offset about 20 m and T2 about 92 m above T1 (Figures III.51 and III.53). Additional smaller normal faults scarps disrupt the surface of T0 with a minimum throw of about 3 to 4 m.

Terraces T1 and T2 were sampled for ^{10}Be exposure dating. Two cobble-size samples on T1 yield ages of 62 and 161 ka (Table III.5; Figure III.61). Four cobble-size samples on T2 yield ages of 90, 210, 227 and 267 ka (Table III.5; Figure III.61). The age of abandonment of T1 may thus be bracketed between 60 and 160 ka (110 ± 50 ka), while the age of abandonment of T2 may be constrained by the ages of the three older samples between 210 and 270 ka (240 ± 40 ka). We note that sample T5C-56 of 90 ka has the most discrepant ^{26}Al versus ^{10}Be age (Table III.5), which further justifies to discard this age. Although the ages thus determined are not strongly constrained, we note that terraces T1 and T2 could have been formed and abandoned closely after the largest penultimate and ante-penultimate interglacial stages of MIS-5e (125 ka) and MIS- 7 (240-220 ka).

Considering the vertical offset of T1 of 20 m to have accumulated after the abandonment of T1 at 110 ± 50 ka, we determine a rate of about 0.2 ± 0.1 mm/yr for the western fault. The offset of T2 of 92 m accumulated after 240 ± 40 ka allows to determine a vertical throw rates of 0.4 ± 0.1 mm/yr for the eastern fault. The total vertical throw rate is thus 0.6 ± 0.2 mm/yr. Because there are other faults to the east and west of these major faults, this rate is a minimum for the eastern part of the Yangbajain basin.

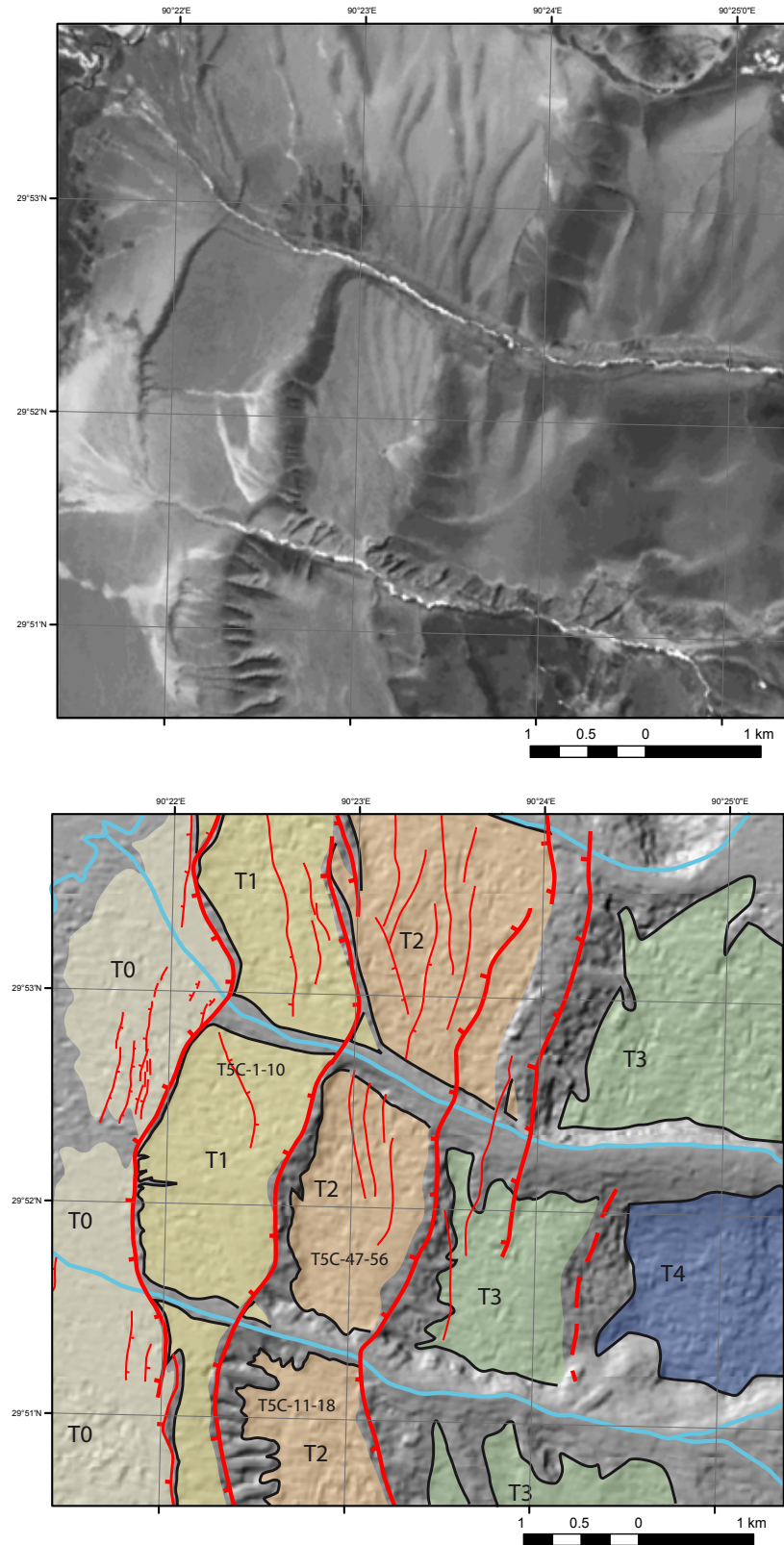
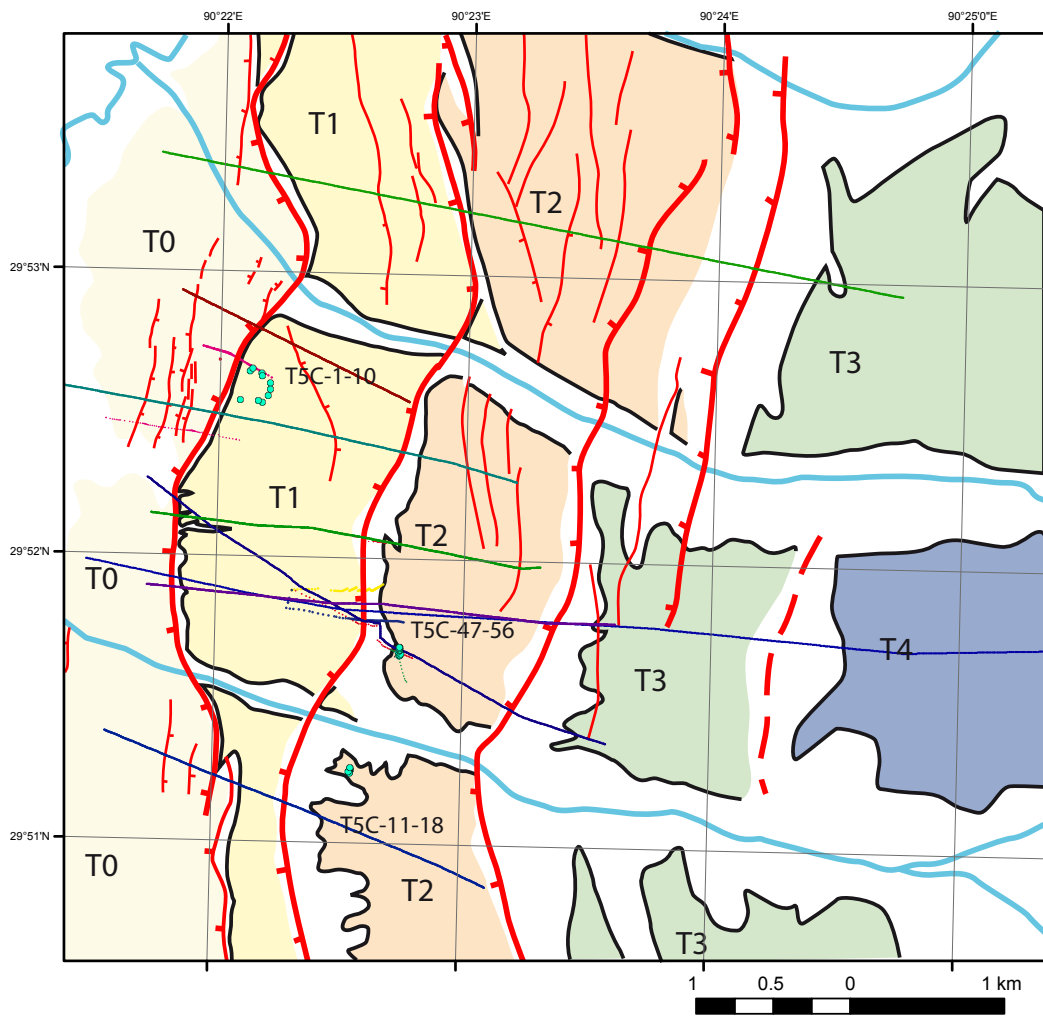


Figure III.50: a) SPOT satellite image (resolution: 10 m) of Gyekar site. b) SPOTdem of Gyekar site (resolution: 20 m) with geomorphic interpretation.



Projection des profils TYsamples p198a255ybj TY1 TY4 TY5 TY8 dans la direction N100E

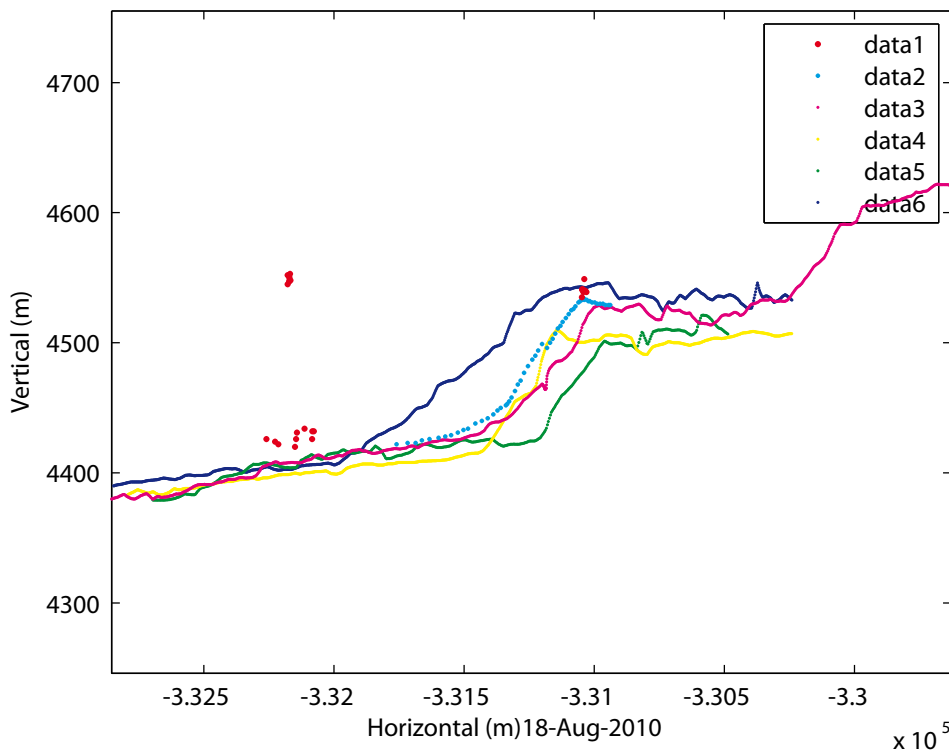


Figure III.51: a) Geomorphic interpretation of the Gyekar site, position of samples and traces of profils of Figure III.51b and III.53 are indicated. b)Topographic profiles at Gyekar sampling site.



(a)



(b)



(c)

Figure III.52: Views of the Gyekar site.

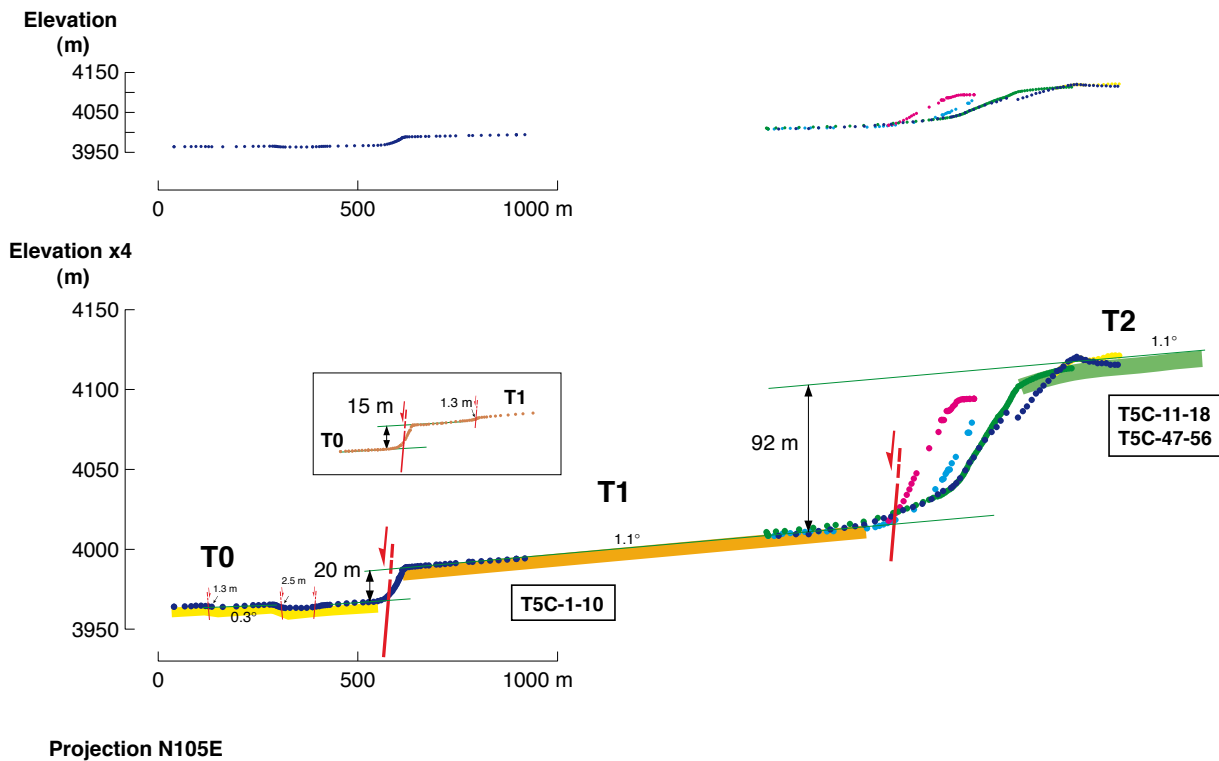


Figure III.53: topographic profiles leveled in the field. See location of profiles in Figure III.51a. Samples names are indicated. Top, 1x1 scale, bottom, vertical exaggeration of 4.

3.3.5. The Gulu half-graben

The Gulu half-graben is the northernmost graben of the Yadong-Gulu rift system. It is characterized by localized normal faulting along the western side of the graben, at the foot of the northeastern end of the Nyaingqentanglha range. The fault is well localized at the base of triangular facets and the cumulative fault scarp is well expressed as it was refreshed during the Beng Co-Damxung 1951, Nov. 18th M 8 earthquake.

3.3.5.1. North Gulu moraine site

In the middle part of the Gulu half-graben we selected a site where lateral moraines are cut and offset by the normal fault at the outlet of a still glaciated valley. (Figures III.54, 55 and 56). The cumulative scarp is sliced into smaller scarps with very fresh morphologies (Figure III.55). Topographic profiles from SPOTdem and GPS measurements in the field are used to constrain the cumulative offset of the southern lateral moraine ridge. Despite the wide fault zone (400 m) and the multiple normal fault scarps, the total cumulative offset reaches 40 ± 10 m (Figure III.57).

To constrain the age of this offset, blocks embedded on top of the ridge on both side of the fault were samples for ^{10}Be exposure dating. From a total of 15 samples (7 in the footwall, 8 in the hangingwall), 13 samples yield very concordant ages of 16 ± 1 ka (Table III.5; Figure III.61). The two older samples yield LGM ages of 19 ka probably indicating continuous glacial occupation of the fault zone from LGM to 16 ± 1 ka. We note that this 16 ka advance has been already documented in the next glacial valley to the south of our site (Owen et al., 2005). If the cumulative offset of 40 ± 10 m accumulated after the glacial advance of 16 ± 1 ka, then we determine a vertical throw rate of 2.5 ± 1 mm/yr. However, if this late advance did not completely reset the shape of the LGM moraine as may be indicated by 2 older samples, the rate may be slightly slower at 2.2 ± 0.8 mm/yr.

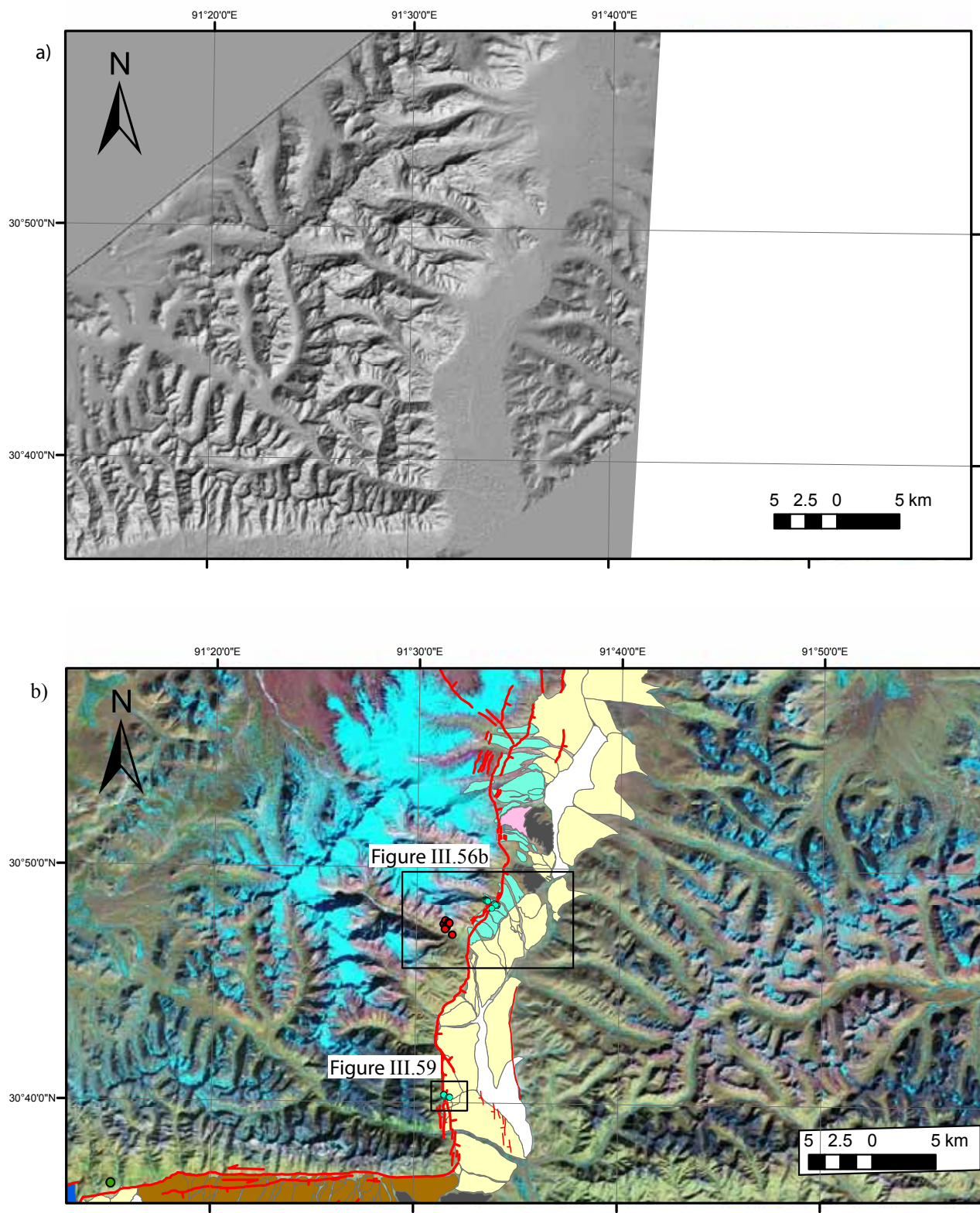


Figure III.54: a) SPOTdem of the Gulu half graben (resolution: 20 m). b) Landsat satellite image of the Gulu half graben (resolution: 90 m) with geomorphic interpretation. Rectangles correspond to north Gulu moraine site and south Gulu terrace site, Figures III.56b and III.59, respectively.

Sampled Moraine

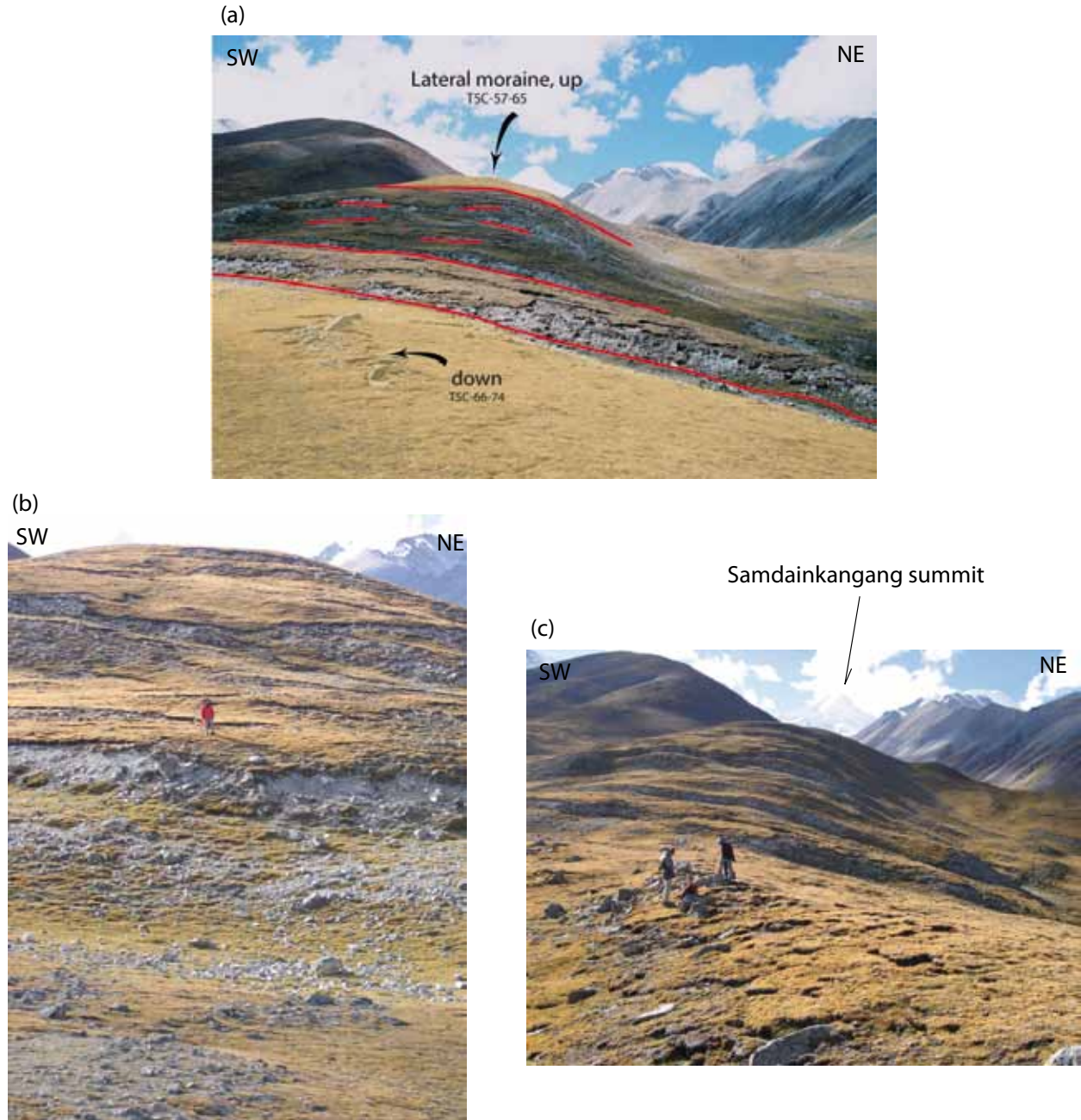


Figure III.55: North Gulu site. (a) view to west of abandoned southern lateral moraine offset vertically by the normal fault. (b) Close-up of 1951 earthquake surface breaks of Nov. 18, 1951 Beng Co – Damxung M 8 earthquake (Armijo et al., 1989). (c) close-up of lateral moraine with large blocks sampled for ^{10}Be dating.

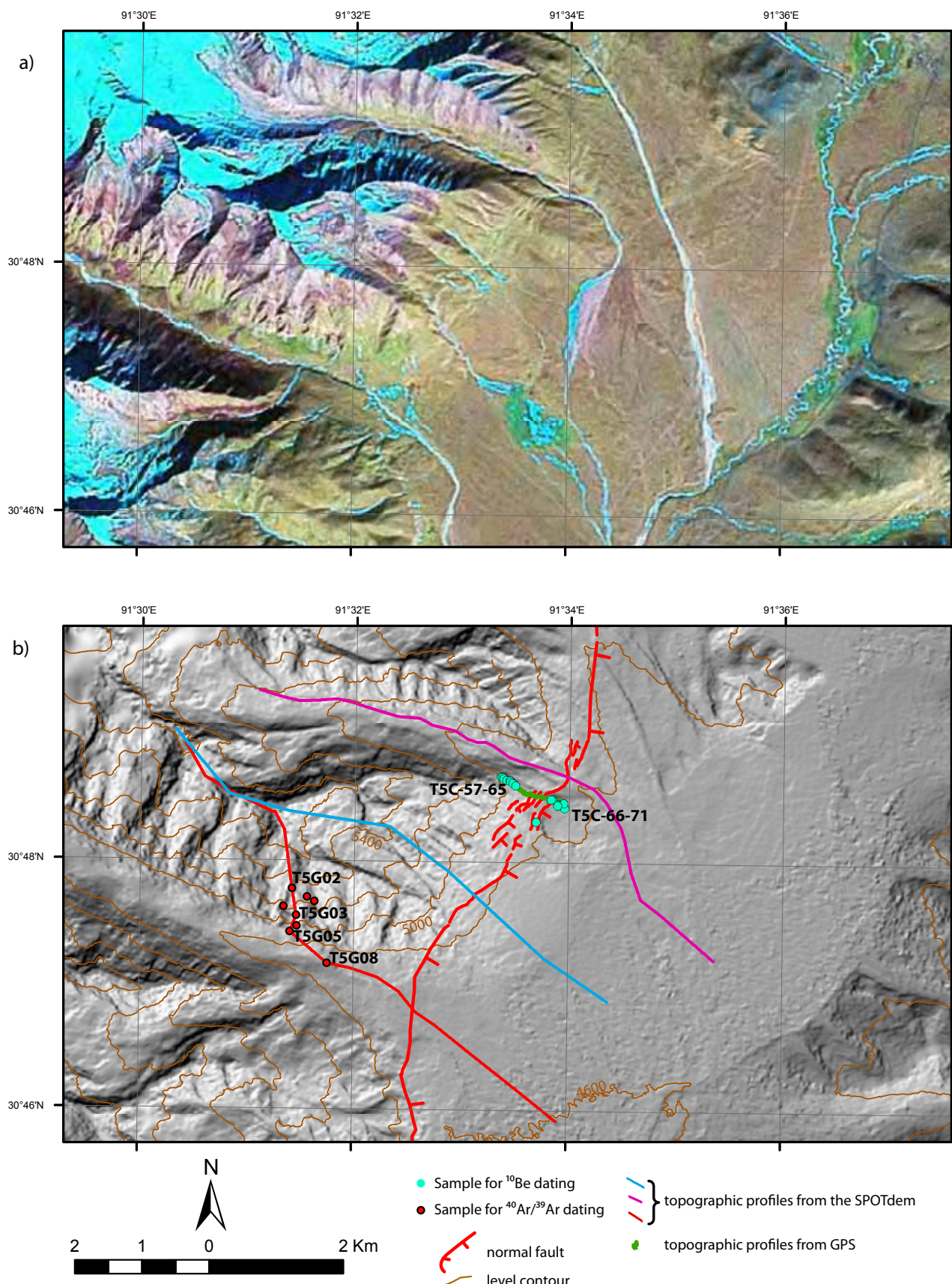


Figure III.56: a) Landsat satellite image of the N-Gulu half graben (resolution: 90 m). b) SPOTdem of the N-Gulu half graben (resolution: 20 m) with geomorphic interpretation, ^{10}Be samples positions and traces of the topographic profiles of Figure III.57 are indicated. $^{40}\text{Ar}/^{39}\text{Ar}$ samples of the long-term deformation study are also represented for comparison. See Figures II.38 to 40 for a review.

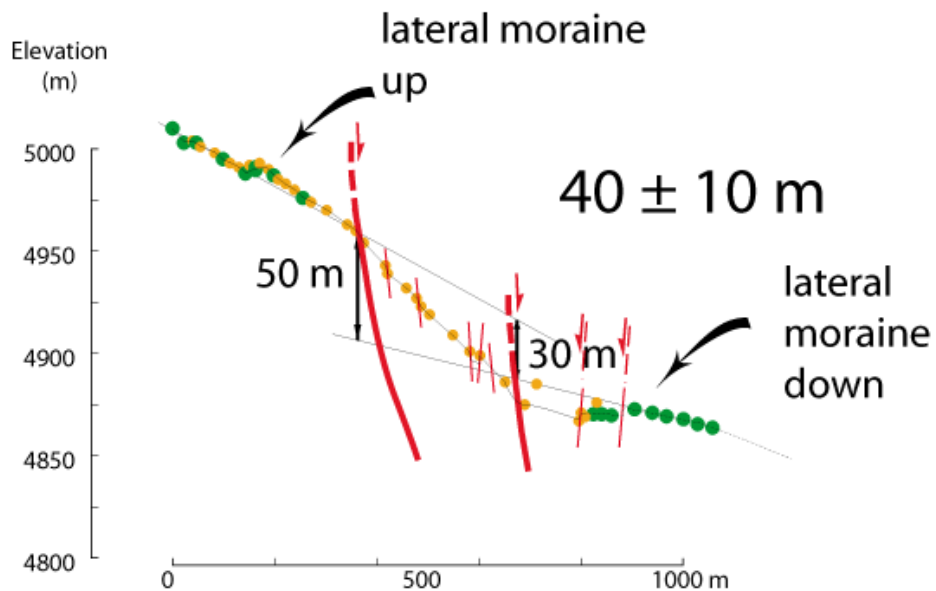
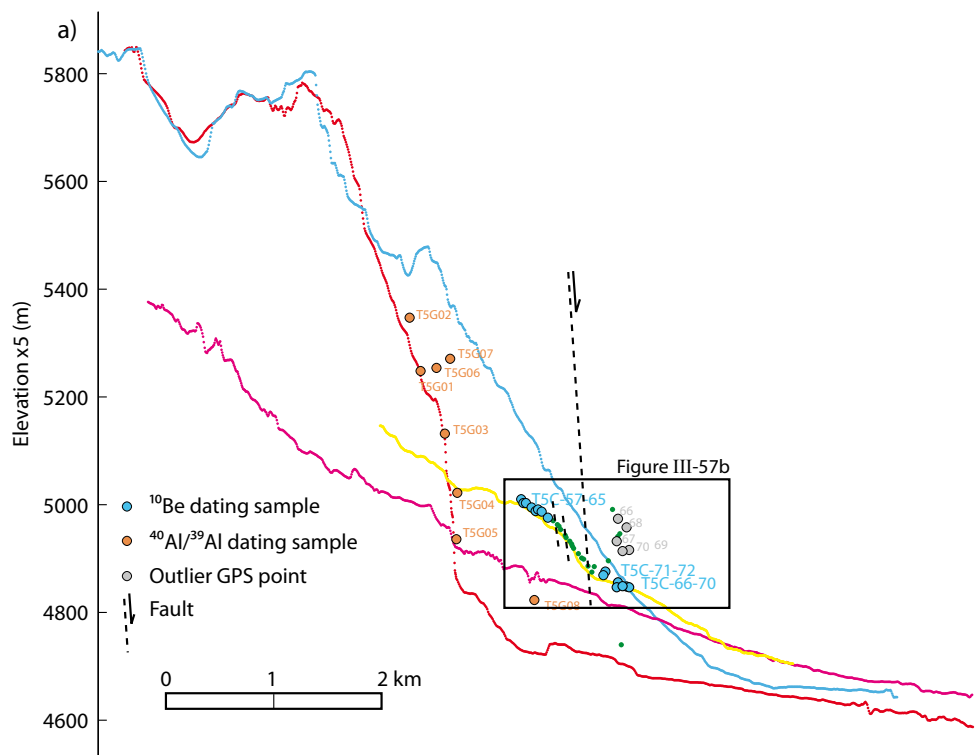


Figure III.57: Topographic profiles at north Gulu site (a) Large scale profiles from SPOTdem. $^{40}\text{Ar}/^{39}\text{Ar}$ samples of the long-term deformation study are represented for comparison. See Figures II.38 to 40 for a review. (b) Profiles from GPS points leveled in the field. See positions of profiles in Figure III.56b.

3.3.5.2. The south Gulu terrace site

About 15 km south of the north Gulu moraine site, a small 2 km long catchment was only partially glaciated. As a consequence, the fault zone has not been crossed by glaciers, and the normal fault sharply cuts alluvial deposits of the steep V-shaped fluvial valley (Figure III. 58). The apex of a large alluvial fan is cut by the fault and offset about 28 m vertically (Figures III.59 and 60).

To constrain the age of the fan we sampled cobbles and blocks embedded in the surface from both side of the fault (Table III.5; Figure III.61). Five samples have been analyzed, 3 upstream and 2 downstream of the fault scarp. The ages range from 3 to 14 ka upstream and from 50 to 358 ka downstream. These results may suggest that the lower surface is older, however, the opposite is expected. Indeed, the uplifted surface upstream may more likely be older as the more it is uplifted, the more it is preserved from the possibility of re-deposition. This is not the case for the lower surface that may likely be younger as it may be flooded and covered by younger deposit. We note, nevertheless, that the remnant fan surface upstream may be feeded by colluvial debris from the steep range slope to the north. This may explain the very young ages of 3 and 4 ka on top of this surface.

Without any better constraints on the age of this fan and thus on the normal fault slip-rate, we note that the localized fault trace may allow to use the rate defined in the north to estimate the age of the 28 m cumulative offset. If this offset accumulated after abandonment of the fan surface at an average rate of 2.2 mm/yr, then the fan may be about 12 ± 4 ka old.

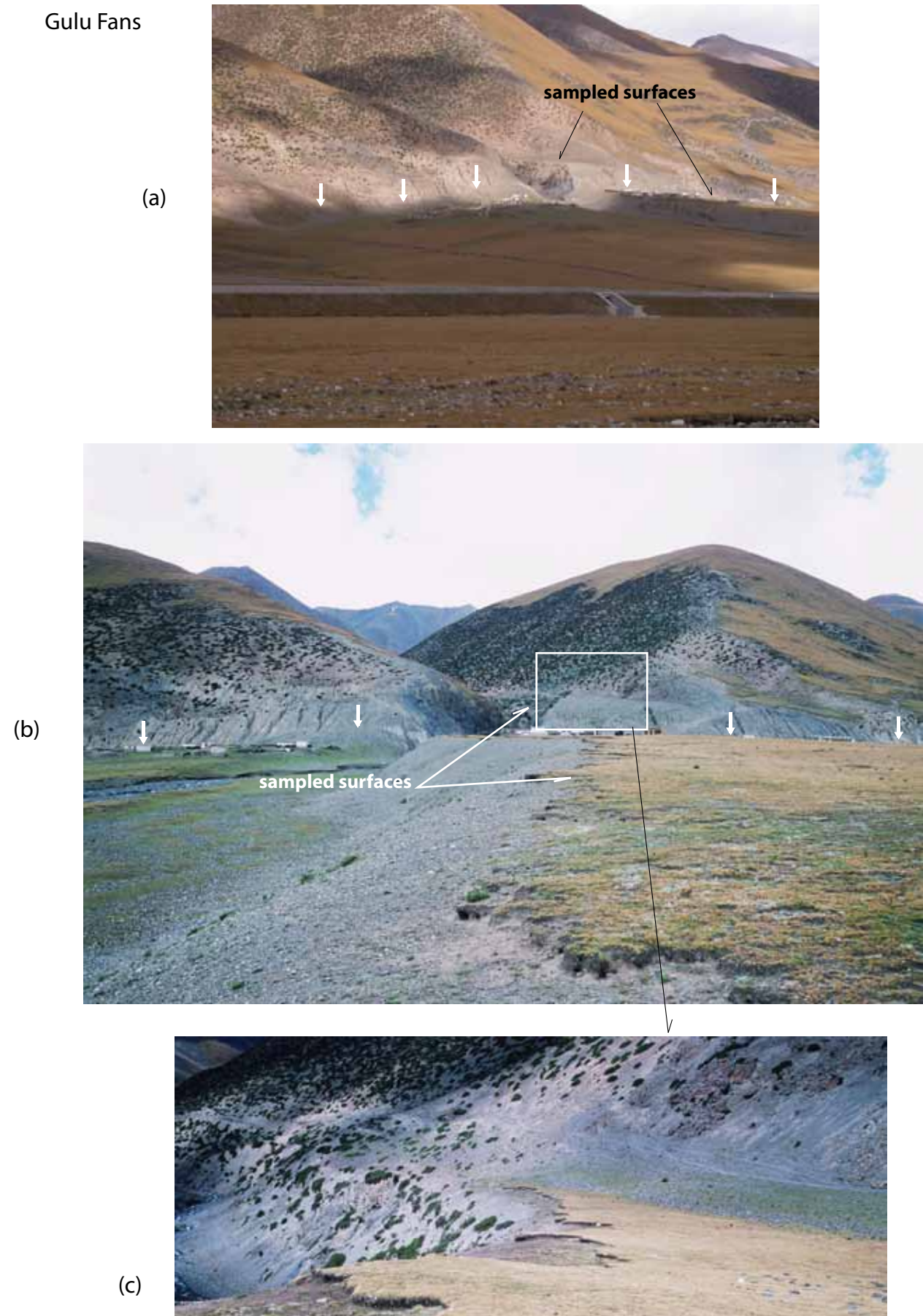


Figure III.58: South Gulu terrace site. (a) View to north of steep 20-30 m high normal fault scarp across alluvial fans (white arrows). (b) View to west of terrace T1 offset. (c) Close-up of top surface of uplifted terrace T1.

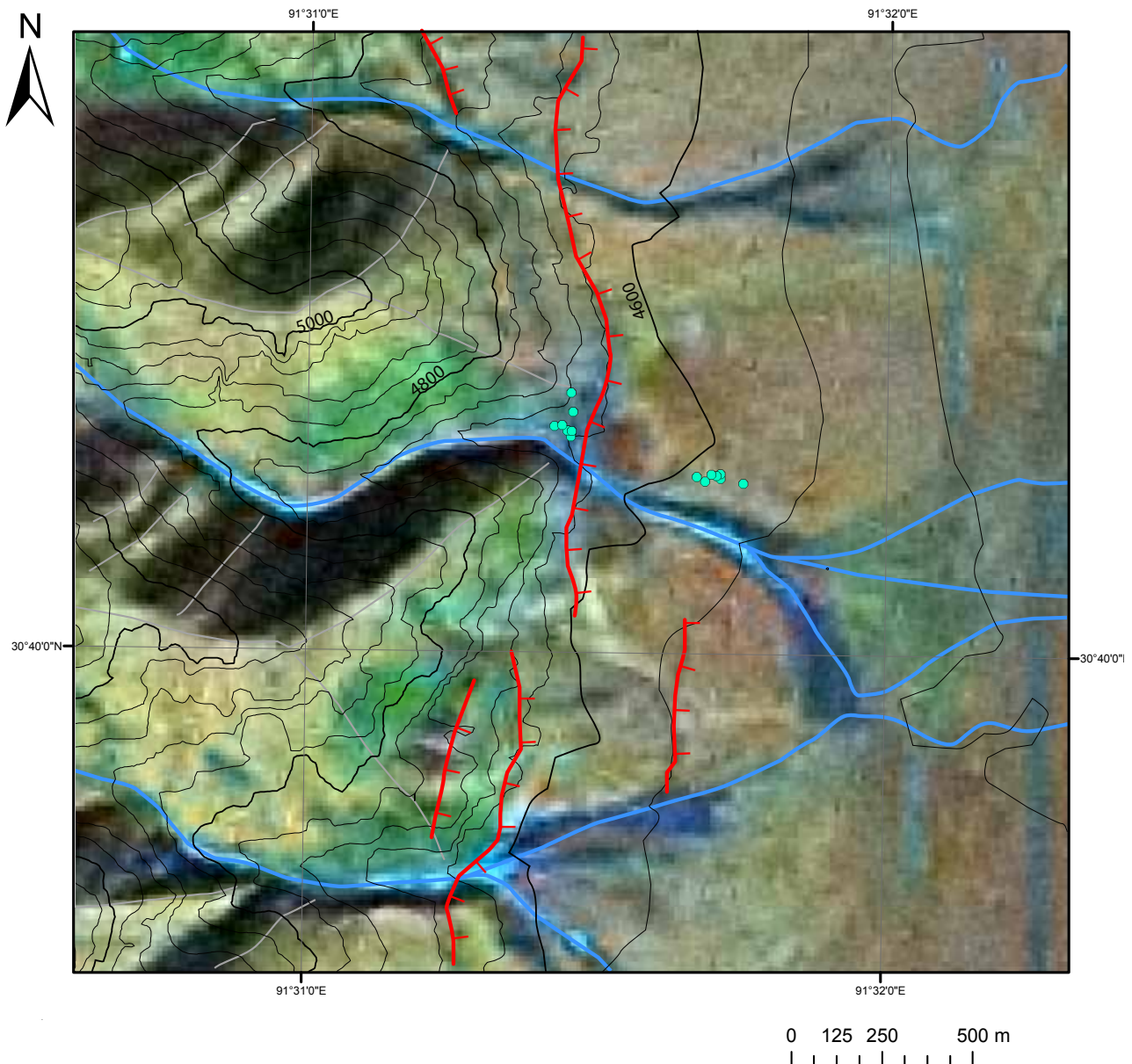


Figure III.59: Landsat satellite image of the S-Gulu half graben (resolution: 28.5m). Topographic contour are from SPOT dem. Positions of samples are indicated.

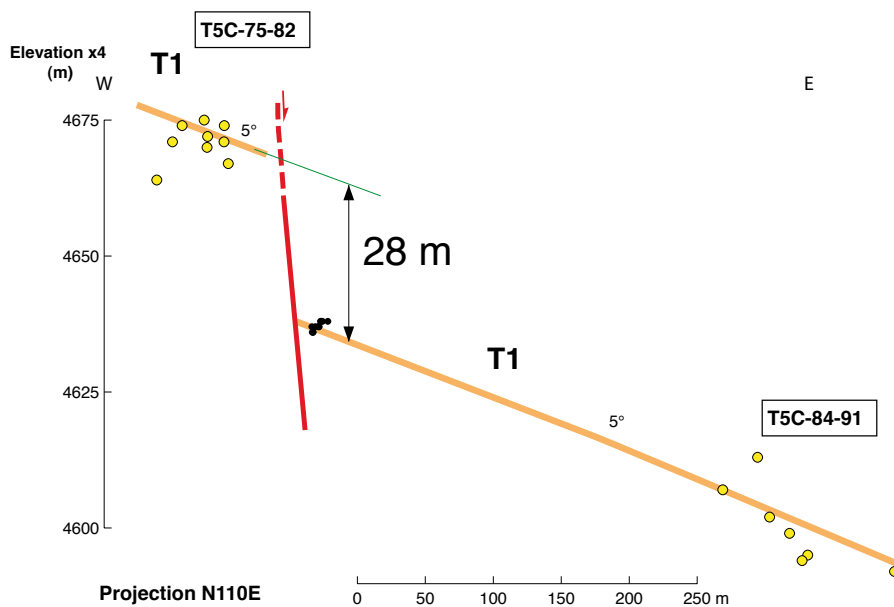
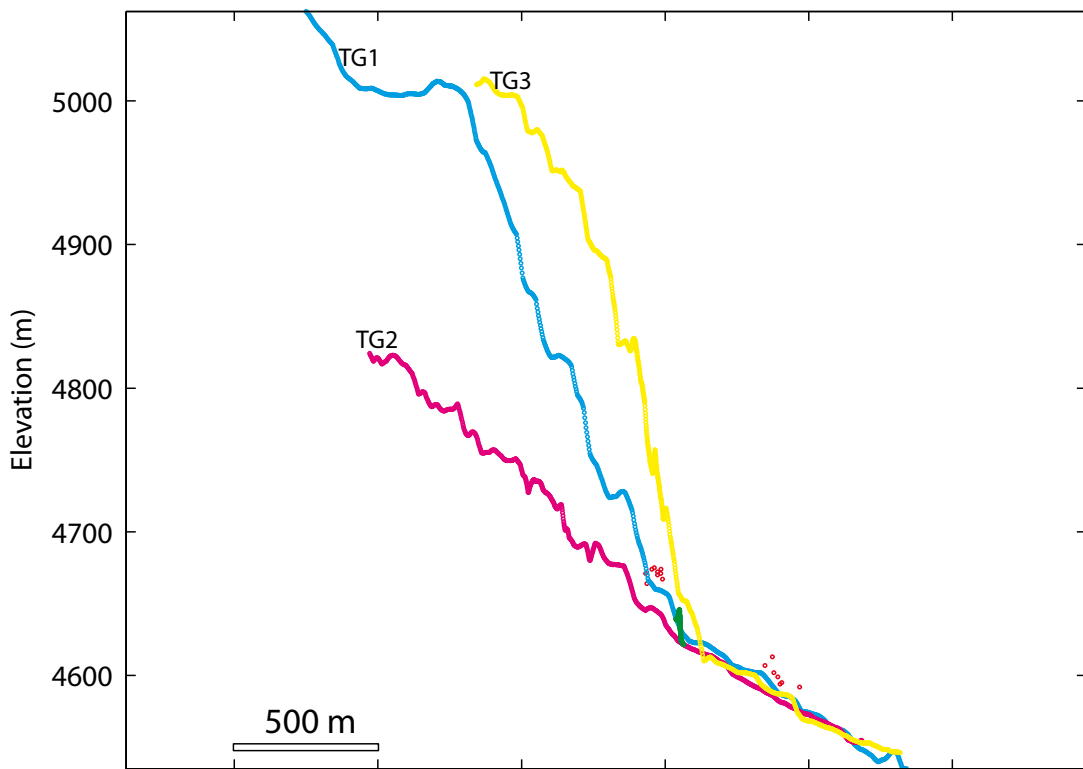


Figure III.60: Topographic profiles at S-Gulu sampling site (a) Large scale profiles from SPOTdem. (b) Profiles from GPS points leveled in the field.

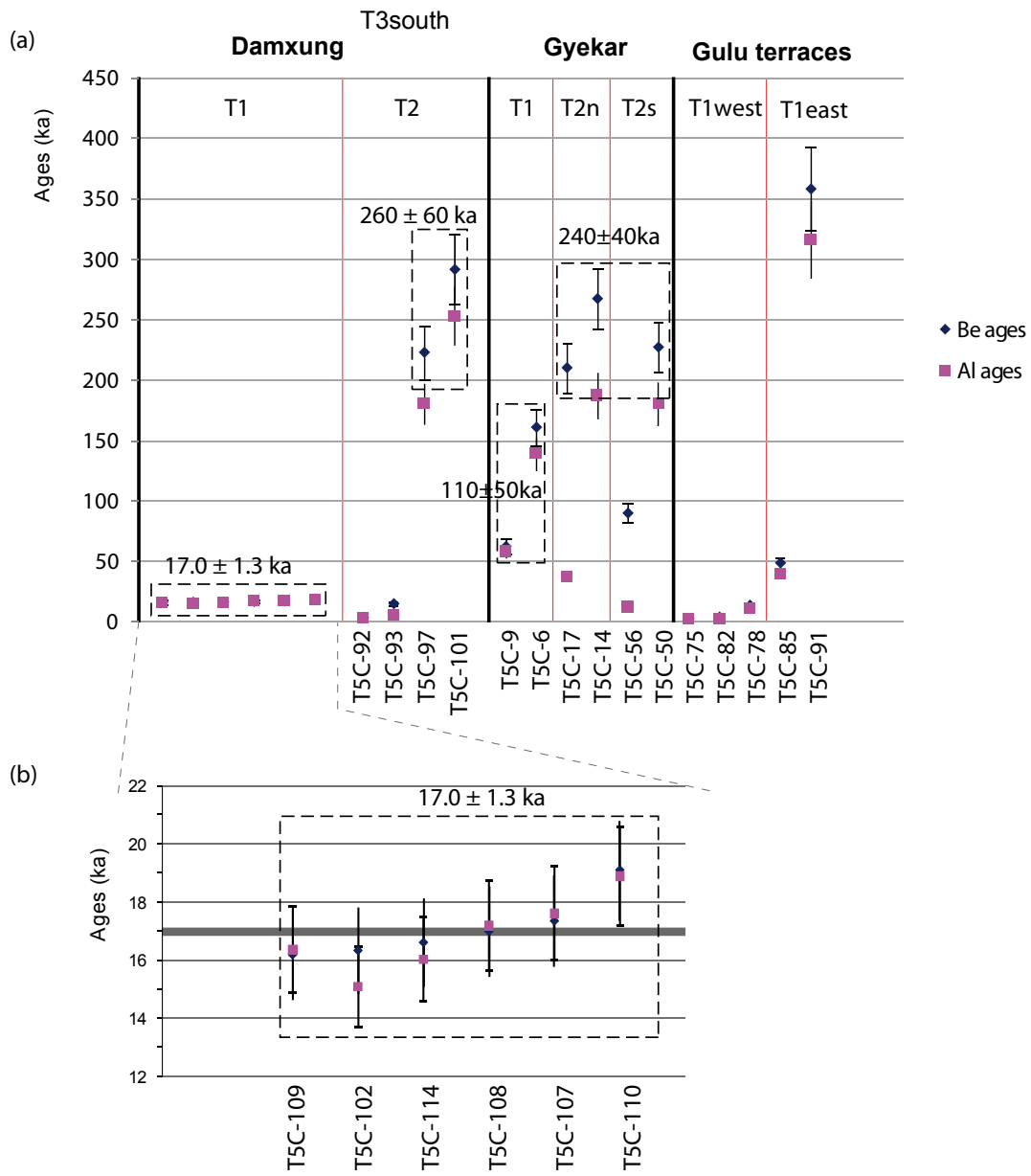


Figure III.61: a) Ages of the sampled terraces in the Gulu-Yangbajain rift. b) Zoom on T1 surface Damxung site

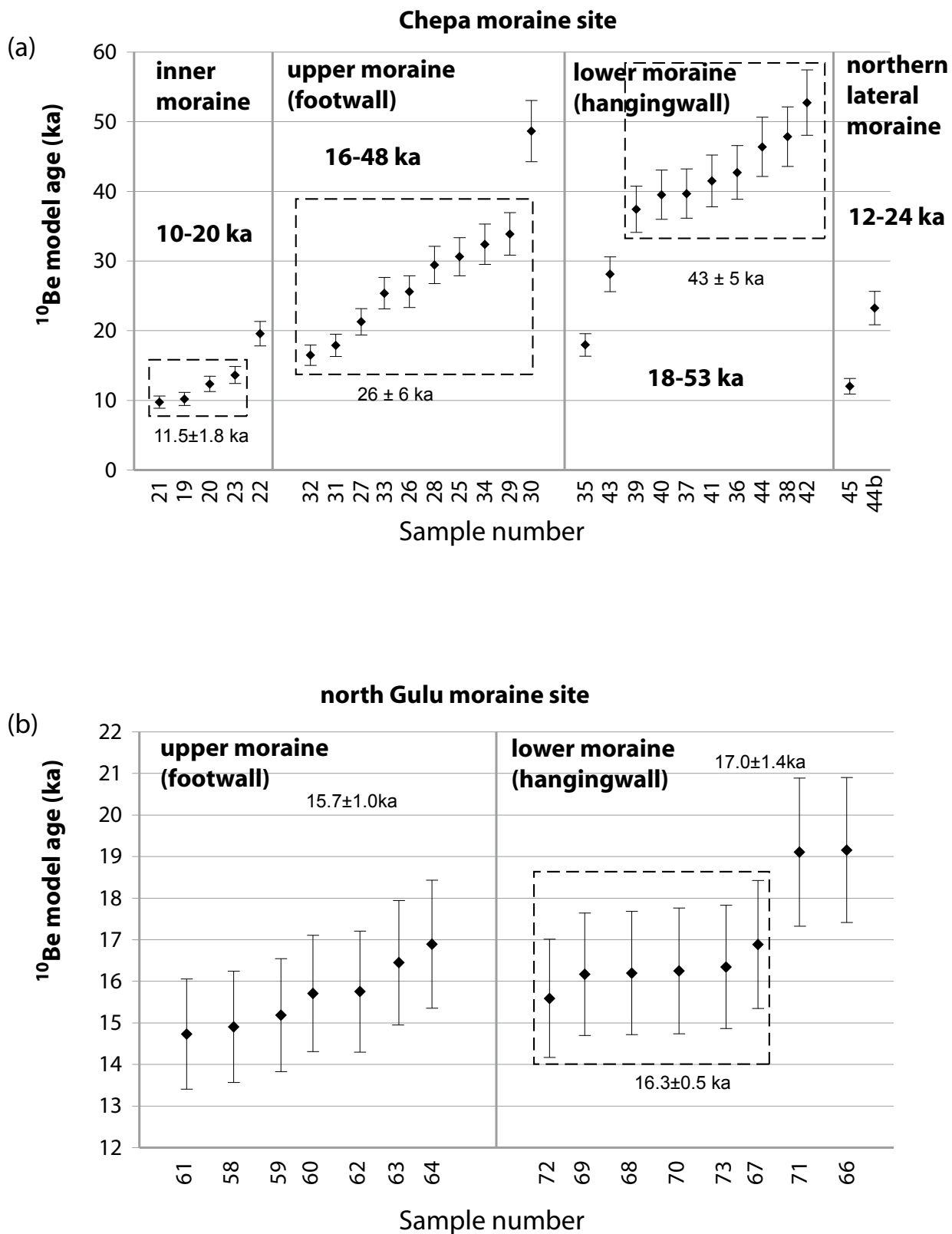


Figure III.62: ^{10}Be ages of the sampled moraines in the Gulu-Yangbajain rift. a) West-Chepa site. b) North Gulu site.

3.3.6. Discussion and conclusion

In the half-graben of Gulu, a main normal fault offsets the recent geomorphology and a vertical throw rate of 2.2 ± 0.8 mm/yr is determined for the last 18 ka (16-20 ka). In Damxung, sinistral slip and normal faulting are combined, and a vertical throw rate of 1.2 ± 0.2 mm/yr is determined for the normal component and a rate of ~ 1.8 mm/yr is determined for the left-lateral component since 17 ka. The age of the upper terrace (260 ka) is less well constrained but could indicate a slower vertical throw rate of about 0.6 ± 0.2 mm/yr. In Yangbajain, at the Chepa site, one main fault characterizes the western boundary of the graben and a vertical throw rate of 1.1 ± 0.7 mm/yr is determined for the last 40 ka (20-45 ka). To the east, at the Gyekar site, several west-dipping normal faults cut the graben bottom. The poorly constrained ages of the terraces (190-290 ka) may however allow to estimate a rate of 0.6 ± 0.2 mm/yr since 240 ka. This rate is comparable to the rate found at Damxung for the same time period. To summarize, at Gulu, the vertical throw rate of 2.2 ± 0.8 mm/yr is faster than at Chepa (1.1 ± 0.7 mm/yr) and at Damxung (1.2 ± 0.5 mm/yr) since 20-40 ka.

At first order, the rates vary from site to site. This may be explained by the distribution of strain among the different faults. In Gulu, a unique normal fault accommodates all the extension across the graben. In Damxung, the fault system is partitioned between normal faults and sinistral faults, these latter ones accommodating partially extension and thus normal faulting is slower. West of Chepa, the rate over 20-40 ka is only determined on the western border fault, and thus part of the extension is not taken into account.

To better compare these sites, we can compare the total extension rate over the whole fault system. Thus, by assuming that the active normal faults dip is 60° , the extension rate in Gulu since 20 ka would be 1.3 ± 0.5 mm/yr. In Chepa, the extension rate of 0.6 mm/yr of the western border fault should be augmented by the extension accommodated in the east of the basin, and the rate may reach about 1 mm/yr, comparable to the rate in Gulu. In Damxung, the sinistral rate of 1.8 mm/yr along N70-80E striking faults is of the same order and in agreement to accommodate east-west extension in Gulu and Yangbajain.

Acknowledgements

Marie-Luce Chevalier for sharing moraine ages data of Gulu and Yanbajain sites. CEREGE ASTER facility for AMS measurements. Liu Xiaohan and ITPR for field logistics and access. INSU-CNRS for fieldwork support and funding. SPOT 5 images and SPOT5 DEM were acquired thanks to ISIS programme #XX, co-funded by CNES and CNRS. Project PRA #XX granted to JVDW and Liu-Zeng Jing to work on extension in south Tibet. Ministère de la recherche for PhD funding to the first author. We also thank LHyGeS (UMR CNRS/UDS 7517) and particularly the Laboratoire de Chimie Isotopique in Strasbourg for various facility access and R. Boutin for ICP-MS measurements.

Table III.5: Analytical results of terrestrial cosmogenic nuclide ^{10}Be and ^{26}Al geochronology, Nyainqntanglha Massif

Site	Sample	Latitude ^a (°N)	Longitude ^a (°W)	Elevation ^b (m a.s.l.)	Rock type ^c	Thickness factor	Shielding factor	Be muons	Al muons	Al spall	Quartz	Total $^{10}\text{Be}^d$ (at/g/yr)	$^{10}\text{Be}^e/\text{Be}^3$ (%)	$^{10}\text{Be}^f/\text{Be}^3$ (%)	Be age ^g (at/g)	Be age ^h (ka)	Total $^{26}\text{Al}^{ij}/\text{Al}^o$ (%)	$^{26}\text{Al}^{ij}/\text{Al}^o$ (%)	$^{26}\text{Al}^{ij}$ (mg)	$^{26}\text{Al}^{ij}$ (at/g)	$^{26}\text{Al}^{ij}$ (ka)	$^{26}\text{Al}^{ij}$ (%)	Al age ⁱ (ka)	$\pm_{j,m}^{k,n}$	$\pm_{j,m}^{k,n}$	$\pm_{j,m}^{k,n}$	$\pm_{j,m}^{k,n}$			
TSC-92	30.33208	91.09345	4556	v	0.2597	0.9987	0.670	61.95	5.623	417.98	20.0124	0.50/0.3	1.575E-13	3.1	241.631	125.48	4.0	0.4	5.8021E-3	4.18	1488708	67609	3.8	0.4	6.16	0.43				
Danxiung	TSC-93	30.53286	91.09393	4562	gres grit	5	0.2597	0.9987	0.671	62.13	5.631	20.1553	0.32/0.0	7.796E-13	3.3	806.147	400.02	12.7	1.2	299.16	8.6851E-15	25.01	2869437	721.170	6.8	1.8	3.56	0.91		
site_Higher	TSC-93b	30.53286	91.09393	4562	gres grit	5	0.2597	0.9987	0.671	62.13	5.631	20.1553	0.3852	7.796E-13	3.3	971983	331.16	15.2	1.4	283.44	8.6851E-15	25.01	2718304	681.725	6.5	1.7	2.80	0.71		
	TSC-97	30.53232	91.09521	4558	peg	5	0.2597	0.9987	0.671	62.01	5.626	418.38	20.1612	9.4051E-12	1.0	15986946	58.3503	223.0	21.7	1.82	4.1510E-11	1.42	8196742	1226356	181.0	17.0	5.13	0.20		
TSC-101	30.53143	91.09720	4544	v	0.2597	0.9987	0.668	61.60	5.606	415.59	20.4556	0.4952	1.257E-11	1.0	203.12794	738851	291.5	28.8	2.16	4.7074E-11	1.28	110748873	1720803	253.5	24.7	5.45	0.22			
TSC-102	30.52906	91.09392	4596	?	0.2597	0.9980	0.671	57.19	5.406	385.83	20.1258	0.4559	6.1801E-13	3.3	969386	33817	16.5	1.5	2.02	2.6292E-12	3.45	3875756	204247	151.1	1.4	6.05	0.30			
Danxiung	TSC-108	30.52447	91.09214	4593	qc	5	0.2597	0.9980	0.644	57.10	5.401	385.23	20.1915	0.4755	6.731E-13	3.0	103.2288	324.25	17.3	1.6	2.02	3.1070E-12	3.32	6930002	230822	17.6	1.6	6.71	0.31	
Danxiung	TSC-109	30.52253	91.09292	4582	v	5	0.2597	0.9960	0.642	56.79	5.387	383.16	20.7428	0.4648	6.934E-13	2.8	866.193	26351	14.8	1.3	2.01	2.8794E-12	2.94	6752400	199795	17.2	1.5	6.68	0.30	
Terrace	TSC-109b	30.52353	91.09292	4582	v	5	0.2597	0.9960	0.642	56.79	5.387	383.16	20.7428	0.5100	5.954E-13	2.8	952869	44289	16.2	1.6	2.06	2.8794E-12	2.94	6361787	190541	16.4	1.5	6.68	0.37	
	TSC-110	30.52114	91.09366	4562	?	0.2597	0.9981	0.639	56.36	5.36	380.24	20.1621	0.4761	7.334E-13	2.9	1131165	341.36	19.1	1.7	1.95	3.4176E-12	2.89	7373984	213983	18.9	1.7	6.52	0.27		
Yangbajain	TSC-114	30.52090	91.09290	4570	qcze	5	0.2597	0.9981	0.640	56.58	5.371	381.71	20.8240	0.4865	6.417E-13	3.2	976630	351.98	16.6	1.5	2.67	2.1750E-12	2.98	6203038	197268	16.0	1.5	6.35	0.31	
Yangbajain	TSC-6	29.87901	90.37154	4416	qcze grit	5	0.2597	0.9987	1	0.646	56.70	5.421	382.52	6.3188	0.2527	4.0021E-12	2.9	10680049	379397	161.1	13.80	1.2809E-12	2.91	60015261	2143509	139.1	13.6	5.62	0.28	
site T1	TSC-9	29.87333	90.37074	4407	v dep ^d	5	0.2597	0.9987	1	0.645	56.45	5.409	380.85	8.7282	0.2408	2.2210E-12	2.6	4085222	136379	62.6	5.8	34.49	2.8609E-13	4.24	25652019	1171782	58.7	5.8	6.13	0.35
	TSC-14	29.85420	90.36619	4405	gres grit	5	0.2597	0.9987	1	0.645	56.38	5.407	380.38	16.1241	0.2402	1.7741E-11	1.2	17211893	393.95	267.4	2.50	40.62	1.3870E-12	2.89	77981065	3037209	187.5	19.1	4.53	0.20
Yangbajain	TSC-17	29.85402	90.36610	4401	rhzo?	5	0.2597	0.9987	1	0.644	56.27	5.401	379.64	20.2256	0.3752	1.116E-11	2.3	13825128	1641.27	210.3	20.1	73.80	1.9955E-13	4.99	16233863	8779633	38.1	3.9	11.7	0.07
	TSC-50	29.86442	90.37923	4516	br Si	5	0.2597	0.9987	1	0.662	59.49	5.557	401.37	11.0286	0.2469	1.0511E-11	1.2	15711102	349727	227.3	21.0	31.60	1.2376E-12	2.93	79143796	2780425	180.9	18.1	5.04	0.21
site T2 N	TSC-56	29.86668	90.37929	4513	?? Conn.	5	0.2597	0.9987	1	0.662	59.41	5.553	400.80	20.1405	0.2850	6.535E-12	2.3	6175938	191963	90.1	8.3	48.57	9.7252E-14	7.95	4982451	407129	12.4	1.5	8.81	0.07
	TSC-73	30.67214	91.53248	4651	qcze	5	0.2597	0.9987	1	0.688	62.25	5.379	402.21	20.2768	0.5474	1.0361E-13	3.1	182971	6962	30.0	6.32	1.4717E-13	6.65	9858330	67901	24.7	0.3	5.39	0.42	
Gulh site	TSC-78	30.67229	91.53239	4645	qcze	5	0.2597	0.9987	1	0.686	65.07	5.751	438.97	20.1095	0.5313	5.280E-13	2.9	928065	328.28	13.9	1.3	1.87	2.4610E-12	2.99	5121162	186501	11.7	1.1	5.52	0.28
Tsop	TSC-82	30.67217	91.53249	4651	qcze	5	0.2597	0.9987	1	0.687	65.25	5.759	440.21	5.1450	0.2370	8.784E-14	4.1	254688	12780	4.0	0.4	14.89	1.7904E-14	16.23	1156740	189866	2.9	0.5	4.54	0.78
Gulh site Tmf	TSC-85	30.67107	91.52791	4593	?	5	0.2597	0.9987	1	0.677	63.48	5.678	428.29	10.0559	0.2384	2.317E-12	3.1	3663368	13.3994	48.9	4.6	2.94	2.9347E-12	3.19	19139157	715710	39.7	3.7	5.22	0.27
Gulh site TSC-91	30.671091	91.52925	4580	gres qc	5	0.2597	0.9987	1	0.675	63.09	5.660	425.65	20.1807	0.4876	1.544E-11	0.9	24911297	588827	358.1	3.33	5.45355E-11	1.06	137802287	30989854	316.7	32.4	5.53	0.18		

^aDetermined with hand GPS.^bElevation of samples was determined from SPOT Digital Elevation Model.^cA density of 2.7 g/cm³ was used for granitic samples (g) and 2.65 was used for quartz vein (q.v.)^dProduction rates were determined with the CRONUS-Earth online calculator [Balco et al., 2008] version 2.1 (<http://hess.washington.edu/math/>)^eTime-dependent local production rate model based on Lal [1991] and Stone [2000]. A sea-level, high-latitude value of 4.8 at 10 Be/g quartz was used.^fTime-dependent local production rate model based on Hesinger et al. [2002a,b]^gTotal ^{10}Be represent carrier and natural ^{10}Be of the sample. For some sample, weighted mass of carrier was used (normal police) and for the other, ICP-MS measurement was used (italic police).^hNIST_2790 standard was used, ratio are uncorrected by blank value.ⁱASTER standard was used, ratio are uncorrected by blank value.^jA mean blank value of 512260 ± 36943 ^{10}Be atoms ($^{26}\text{Al}^{12}\text{Al}$ = 5.0131 $\times 10^{-14}$ ± 44.7%) was used normal police values to correct by the blank.^kPropagated uncertainties include error in the blank, carrier mass, and AMS analysis^l ^{10}Be and ^{26}Al model ages were calculated with the CRONUS-Earth calculator, time dependent Lal [1991] and Stone [2000] scaling scheme was choosed. ^{10}Be half-life of 1.36 $\times 10^6$ years was used.^mPropagated error in the model ages include the uncertainty in the production rate of ^{10}Be and the uncertainty in the ^{10}Be decay constantⁿTotal ^{26}Al represent carrier and natural ^{26}Al of the sample determined by ICP-MS measurement. Aluminum analysis was not proceed for all samples^oASTER standard was used, ratio are uncorrected by blank value.^pA mean blank value of 202394 ± 79951 ^{10}Be atoms ($^{26}\text{Al}^{12}\text{Al}$ = 5.0131 $\times 10^{-15}$ ± 21.1%) was used for other values to correct by the blank.^qPropagated uncertainties include uncertainties of the ^{26}Al and ^{10}Be concentrations.^rFor the T7C-61 sample, the blank correction represent 50% of the ^{10}Be concentration, therefore the calculated age have to be used carefully^sBecause of very low ^{10}Be / ^{9}Be ratio due to ^{9}Be excess, blank correction has not been applied for T7C-81 sample. Therefore the calculated age have to be used carefully

Table III.6 : Analytical results of terrestrial cosmogenic nuclide ^{10}Be geochronology - Moraines of the Nyantingtangha Massif. Modified from Chevalier (2006) and Chevalier et al., in press.

Site	Sample	Latitude ^a	Longitude ^a	Elevation ^b (m a.s.l.)	Rock type ^c	Thickness ss (cm)	Shielding factor	Be muons	Be spall	Quartz	Total ^{10}Be ^e (mg)	$[^{10}\text{Be}]$ ^f (at/g)	\pm^i	$[^{10}\text{Be}]$ ^g (at/g)	\pm^k	Be age ^h (ka)	Production rate ^{d,e,f}	
																	at/g/yr	at/g/yr
YBJ	T5C-19	30.02319	90.24192	5305	q	4	0.968	0.999	0.802	86.08	4.5308	0.3620	1.775E-13	2.8	89/272	32491	10.2	
inner	T5C-20	30.02313	90.24197	5302	g	4	0.967	0.999	0.801	85.91	9.3399	0.3931	4.036E-13	2.1	1084689	32947	12.4	
	T5C-21	30.02313	90.24197	5302	g	4	0.967	0.999	0.801	85.91	17.4125	0.5615	4.200E-13	2.1	854516	26001	9.7	
	T5C-22	30.02308	90.24198	5300	q	4	0.968	0.999	0.801	85.89	19.0603	0.5681	9.146E-13	1.8	1771005	48856	19.6	
	T5C-23	30.02298	90.24185	5300	g	4	0.967	0.999	0.801	85.84	18.1290	0.5396	6.278E-13	2.0	1198183	35766	13.6	
outer up	T5C-25	30.02181	90.24252	5276	g	4	0.967	0.982	0.796	83.49	16.4345	0.5362	1.322E-12	1.8	2831331	78054	30.6	
	T5C-26	30.02171	90.24297	5258	g	4	0.967	0.982	0.793	82.84	15.2732	0.5447	9.839E-13	1.8	2294233	63628	25.6	
	T5C-27	30.02140	90.24315	5248	q	4	0.968	0.982	0.792	82.53	15.5222	0.5443	8.162E-13	1.9	1861896	53358	21.3	
	T5C-28	30.02133	90.24332	5227	g	4	0.967	0.986	0.787	82.05	19.6758	0.5380	1.484E-12	2.6	2661221	88849	29.4	
	T5C-29	30.02113	90.24345	5221	g	4	0.967	0.999	0.786	82.91	20.0043	0.3987	2.402E-12	2.3	3148830	98236	33.9	
	T5C-30	30.02091	90.24372	5206	g	4	0.967	0.999	0.784	82.37	19.3252	0.3843	3.619E-12	2.2	4758912	141348	48.6	
	T5C-31	30.02077	90.24406	5200	g	4	0.967	0.999	0.783	82.15	15.4784	0.3648	1.008E-12	2.0	1536930	44365	17.9	
	T5C-32	30.02077	90.24406	5200	g	4	0.967	0.999	0.783	82.15	20.7194	0.3653	1.236E-12	1.8	1406368	39453	16.5	
	T5C-33	30.02065	90.24432	5184	g	4	0.967	0.999	0.778	81.57	20.1426	0.3649	1.891E-12	1.8	2238713	62114	25.4	
outer down	T5C-34	30.02053	90.24472	5177	g	4	0.967	0.999	0.778	81.32	19.9552	0.3644	2.448E-12	1.8	2936725	79940	32.4	
	T5C-35	30.01850	90.24805	5033	g	4	0.967	0.999	0.753	76.26	19.9478	0.3633	1.220E-12	1.8	1434535	40103	18.0	
	T5C-36	30.01823	90.24807	5033	g	4	0.967	0.999	0.753	76.26	19.9443	0.3670	3.173E-12	2.1	3851722	114543	42.7	
	T5C-37	30.01804	90.24783	5066	g	4	0.967	0.992	0.759	76.85	22.8149	0.3618	3.398E-12	1.8	3549969	96585	39.7	
	T5C-38	30.01801	90.24822	5026	g	4	0.967	0.992	0.751	75.48	19.5830	0.3626	3.515E-12	1.7	4297588	114902	47.9	
	T5C-39	30.01802	90.24849	5021	g	4	0.967	0.992	0.751	75.31	19.6065	0.3703	2.600E-12	1.5	3230645	82794	37.4	
	T5C-40	30.01801	90.24865	5014	g	4	0.968	0.992	0.751	75.12	20.6234	0.3618	2.988E-12	1.9	3453048	96263	39.5	
	T5C-41	30.01810	90.24931	5010	g	4	0.967	0.992	0.749	74.94	20.0251	0.3626	3.066E-12	1.8	3659399	98648	41.5	
	T5C-42	30.01796	90.24933	4999	g	4	0.967	0.992	0.747	74.57	18.2324	0.3444	3.700E-12	1.4	4619488	112723	52.7	
	T5C-43	30.01784	90.24949	4991	g	4	0.967	0.999	0.745	74.83	24.1376	0.3401	2.500E-12	1.6	2303288	60288	28.1	
	T5C-44	30.01782	90.24950	4982	g	4	0.967	0.986	0.744	73.55	19.2521	0.3732	3.175E-12	2.6	4061692	136112	46.4	
across	T5C-44biss	30.02390	90.24490	5239	g	4	0.967	0.986	0.749	82.49	18.1676	0.3582	1.598E-12	5.4	204678	120600	23.3	
	T5C-45	30.02400	90.24400	5261	g	4	0.967	0.986	0.794	83.29	16.9135	0.3562	7.627E-13	3.1	1022742	39166	12.0	
GULU	T5C-58	30.81139	91.55621	5003	g	4	0.967	0.991	0.75	76.96	19.3415	0.3611	9.840E-13	2.0	1177053	34676	14.9	
up	T5C-59	30.81126	91.55642	5003	g	4	0.967	0.991	0.75	76.96	19.7756	0.3626	1.021E-12	2.0	1201171	35263	15.2	
	T5C-60	30.81102	91.55689	4995	g	4	0.967	0.995	0.749	76.99	19.6924	0.3632	1.053E-12	1.8	1246636	35066	15.7	
	T5C-61	30.81096	91.55768	4988	g	4	0.967	0.000	0.748	76.75	19.3363	0.3592	9.746E-13	2.1	1152299	34846	14.7	
	T5C-62	30.81083	91.55754	4991	g	4	0.967	0.000	0.748	76.85	19.7917	0.3521	1.093E-12	2.9	1248243	45809	15.8	
	T5C-63	30.81083	91.55754	4991	g	4	0.967	0.000	0.748	76.85	19.6623	0.3733	1.071E-12	2.5	1308529	43716	16.4	
	T5C-64	30.81062	91.55782	4987	g	4	0.967	0.994	0.748	76.64	19.8097	0.3725	1.109E-12	2.6	1343437	45452	16.9	
down	T5C-66	30.80781	91.56497	4974	g	4	0.967	0.000	0.745	76.41	19.5813	0.3611	1.286E-12	2.5	1534174	51303	19.2	
	T5C-67	30.80783	91.56484	4932	g	4	0.967	0.000	0.738	74.97	16.9452	0.3595	9.625E-13	2.5	1313933	44159	16.9	
	T5C-68	30.80751	91.56579	4958	g	4	0.967	0.997	0.743	75.86	19.7669	0.3732	1.047E-12	2.7	1270419	44534	16.2	
	T5C-69	30.80732	91.56593	4916	g	4	0.967	0.997	0.735	74.43	22.7549	0.3725	1.183E-12	2.5	1244064	41763	16.2	
	T5C-70	30.80798	91.56578	4914	g	4	0.967	0.997	0.735	74.36	20.1576	0.3707	1.058E-12	3.1	1249845	48201	16.3	
	T5C-71	30.80849	91.56405	4876	g	4	0.967	0.000	0.728	73.01	23.0078	0.3423	1.522E-12	3.1	1462216	56344	19.1	
	T5C-72	30.80851	91.56379	4869	g	4	0.967	0.000	0.727	72.77	20.9191	0.3435	1.112E-12	2.5	1169150	39418	15.6	
	T5C-73	30.80770	91.56486	4855	g	4	0.967	0.000	0.725	72.31	20.7804	0.3444	1.150E-12	2.5	1223359	40309	16.3	

See Table III.5 for the caption.

North Damxung Area
T1 surface
Dated Samples



North Damxung Area
T2 surface
Dated Samples



Gyekar Area
Dated Samples



Gulu Fans
Dated Samples



Partie 4

DISCUSSION

-

CONCLUSION

4. DISCUSSION - CONCLUSION

Dans cette thèse, nous apportons des nouvelles contraintes sur les vitesses de déformation long-terme et court-terme au niveau de deux systèmes de failles normales, constituant deux des sept rifts Nord-Sud du Sud-Tibet (Figure IV.1).

Comparaison Ama Drime - Nyainqntanglha

Pour le massif de l'Ama Drime, concernant la déformation long-terme, les trajets P-T-t-D ont permis de déterminer une vitesse d'exhumation verticale apparente de ~ 1.2 mm/an depuis ~ 12 Ma et les âges (U-Th)/He sur apatite montrent une vitesse d'exhumation verticale apparente de ~ 1 mm/an depuis 4 Ma, suggérant une vitesse plus rapide entre 12 et 4 Ma.

Les vitesses de déformation court-terme du Pléistocène supérieur sont du même ordre de grandeur. La faille de Kharta, bordant le flanc Ouest de l'Ama Drime, montre une vitesse de glissement vertical de 1.3 ± 0.3 mm/an depuis 12 ka voire même probablement depuis 125 ka. Les vitesses au niveau des failles de Dinggye et Mabja, à l'Est et au Nord de l'Ama Drime respectivement, sont moins bien contraintes, mais un ordre de grandeur d' ~ 1 mm/an a été déterminés pour ces deux failles. Cette vitesse quaternaire d' ~ 1 mm/an semble n'avoir pas varié depuis 4 Ma, et en considérant une histoire continue, elle n'aurait pas varié non plus depuis 12 Ma.

En terme d'extension, ces vitesses de glissement verticale quaternaires correspondent à des vitesses d'extension de 0.7 ± 0.2 mm/an et ~ 0.6 mm/an sur les failles de Kharta et Dinggye respectivement. Ce qui donne une vitesse d'extension totale de 1.3 ± 0.2 mm/an pour une période depuis ~ 40 ka pour le horst de l'Ama Drime.

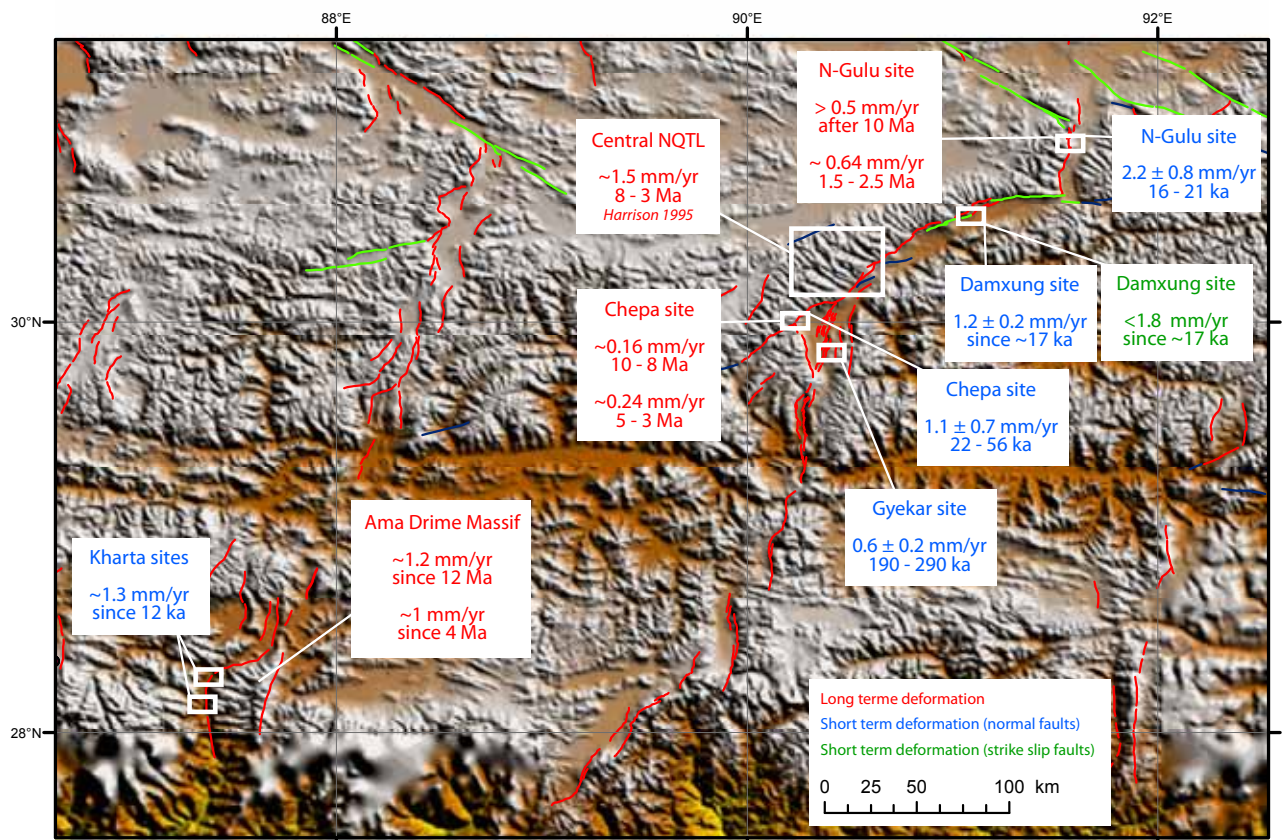


Figure IV.I: Long-term (exhumation rate) and short-term (vertical throw rate) deformation rates along Ama Drime and Nyainqntanglha massifs.

Au niveau du rift de Gulu-Yangbajain, l'initiation de l'exhumation rapide a commencé un peu plus tard, à 10 Ma à Gulu et après 8 Ma au niveau de Chepa-Ouest. Les âges $^{40}\text{Ar}/^{39}\text{Ar}$ sur biotite indiquent que ~10 km ont été exhumés depuis 10 et 8 Ma à Gulu et Chepa-Ouest, respectivement (en considérant une température de fermeture des biotites d'~300°C un géotherme de 30°C/km), impliquant une vitesse d'exhumation verticale d'~1 à 1.2 mm/an, comparable à la vitesse d'exhumation verticale de 1.5 mm/an proposée par Harrison et al. (1995). Or les vitesses déterminées avec les relations âge-altitude sont largement inférieures à 1 mm/an, entre 0.16 et 0.2 mm/an à Chepa-Ouest et ~0.6 mm/an à Gulu (et 1.2 mm/an depuis 8 Ma à Kumulalungpa). Ceci montre que des variations de vitesses d'exhumation ont eu lieu entre l'initiation de l'exhumation et aujourd'hui.

En considérant un pendage de 60° des failles normales actives, les vitesses d'extension au niveau des différents sites d'échantillonnage semblent comparables pour une période de ~15 à 60 ka. A Gulu on obtient 1.3 ± 0.5 mm/an. A Chepa-Ouest, la vitesse d'extension de 0.6 ± 0.4 mm/an est à ajouter à l'extension accommodée par les failles situées à l'Est du bassin de Yangbajain et suggère donc une vitesse d'extension plus rapide au niveau du bassin entier (~1 mm/an). A Damxung la faille normale est oblique et l'extension est plus faible (0.6 mm/an). Ceci permet de déterminer une vitesse d'extension de 1.4 ± 0.6 mm/an pour le rift de Gulu-Yangbajain pour la période 0-60 ka. Cette vitesse est en accord avec la vitesse de 1.4 ± 0.8 mm/an (considérant un pendage entre 45 et 60° pour les failles normales) déterminée par Armijo et al., 1986 (avec des rejets cumulés et des âges supposés des dépôts Quaternaires) au niveau du même rift (jusqu'à Yadong) pour une période du Pliocène au Quaternaire.

Pour résumer, au niveau du rift de Gulu-Yangbajain, les vitesses d'exhumation verticale apparente long-termes sont comprises entre ~1 et ~1.5 mm/an depuis 8-10 Ma et les vitesses de glissement vertical court-termes sont comprises entre ~1.6 et ~2.2 mm/an depuis 40 ka (voire même depuis 300 ka). Donc au premier ordre, les vitesses long-termes et court-termes sont comparables. Nous avons vu que pour l'Ama Drime, les vitesses de déplacement verticales sont de 1 à 2 mm/an depuis 12 Ma. Les vitesses de déformation long-termes et court-termes sont donc du même ordre de grandeur pour les deux massifs.

Comparaison entre le Nord- et le Sud-Tibet

Au Nord-Tibet (au nord de la suture de Bangong), la présence des failles normales paraît plus diffuse, l'espacement des rifts est plus réduit et les failles sont moins continues avec moins de relief (Armijo et al. 1986). La morphologie des systèmes de failles normales au Nord-Tibet semble donc indiquer des vitesses d'extension moins importantes.

La seule étude comparable à celle menée dans cette thèse est celle du graben de Shuang Hu (Blisniuk et Sharp 2003). Elle indique des vitesses de glissement vertical entre 0.06 et 0.3 mm/an. Les autres grabens au Nord-Tibet ayant une morphologie comparable, ont certainement des vitesses d'extension du même ordre de grandeur. Ceci confirmerait que les vitesses d'extension des failles normales au Sud-Tibet sont plus importantes qu'au Nord-Tibet.

Généralisation des vitesses d'extension court terme à tout le Sud-Tibet

Pour la déformation court-terme, la seule étude comparable est le graben de Pulan (à l'ouest du Gurla Mandhata). La faille bordière Est décale des terrasses alluviales et des moraines. Deux terrasses décalées de 15 et 53 m ont été datées par le ^{10}Be à 8.3 et 34 ka définissant une vitesse verticale de 1.7 ± 0.2 mm/an. Une vitesse semblable est déterminée par le décalage de moraines du dernier maximum glaciaire (Chevalier et al. 2010).

Par conséquent trois des sept rifts Nord-Sud du Sud-Tibet montrent des vitesses de déplacement vertical de ~ 1.5 mm/an au Pléistocène supérieur. En supposant que cette vitesse est applicable à tous les rifts, on obtient une vitesse de déplacement vertical totale de ~ 10.5 mm/an pour tout le Sud-Tibet. Cette vitesse est en accord la vitesse de 13 ± 4 mm/an depuis le Pléistocène, déterminée à partir de rejets cumulés et sans datation absolue (Armijo et al., 1986). Aussi, elle est comparable avec les vitesses GPS, qui indiquent une vitesse d'extension de 13 ± 1 mm/an entre Lhasa et la faille du Karakorum (Zhang et al., 2004b, Chen et al., 2004b, Wang et al., 2004).

Les limites

Il faut garder en vue que les histoires d'exhumation restent peu contraintes par les données de thermochronologie et laissent envisager une variété de scénarios d'évolution. Une densification du « signal thermochronologique » est nécessaire pour avoir une meilleure résolution sur l'évolution du plateau. Pour les vitesses quaternaires, le même type d'étude devra être mené sur les autres rifts pour confirmer la tendance à $\sim 1\text{-}2 \text{ mm/an}$ sur chaque système de rift.

Comparaison entre les rifts du Sud-Tibet

Concernant les autres rifts du Sud-Tibet aucune étude de ce type fournissant des vitesses long terme et court terme sur les mêmes massifs n'a été menée. Néanmoins, pour certaines études l'un ou l'autre type de vitesses est disponible ainsi qu'un certain nombre d'indications sur les âges et les morphologies des structures déformées.

Pour la déformation long terme, les données d'âges et/ou de géologie structurale au niveau de quatre autres rifts sont à confronter. D'Ouest en Est (Figure IV.2) :

- Le dôme du Gurla Mandhata et le rift de Pulan : Le dôme métamorphique du Gurla est bordé par un détachement à pendage ouest et par le rift actif de Pulan. Le détachement était actif vers 9 Ma et montre 35 à 65 km de glissement (Murphy et al., 2002). Il a fonctionné à une période recouvrant ou proche de la période de fonctionnement de la faille du Karakorum au nord (Murphy et al., 2002) et du STDS qu'il recoupe (Leloup et al., 2010). Ceci implique des interactions possibles entre ces trois structures.
- Le rift et le détachement de Lunggar : des évidences de déformations ductiles associés à de la déformation cassante ont été documentées (Kapp et al., 2008). Ces auteurs fournissent des âges U/Pb sur zircon de 9 et 15 Ma et (U-Th)/He sur apatite entre 0.4 et 1.8 Ma pour des leucogranites déformés dans le mur de faille. Ils indiquent aussi des mesures de rejet et de soulèvement, mais ne les associent pas aux âges pour fournir des vitesses d'exhumation. Les âges de leucogranites déformés suggèrent une initiation de l'exhumation des roches dans le mur du détachement du Lunggar à 15 Ma au minimum.

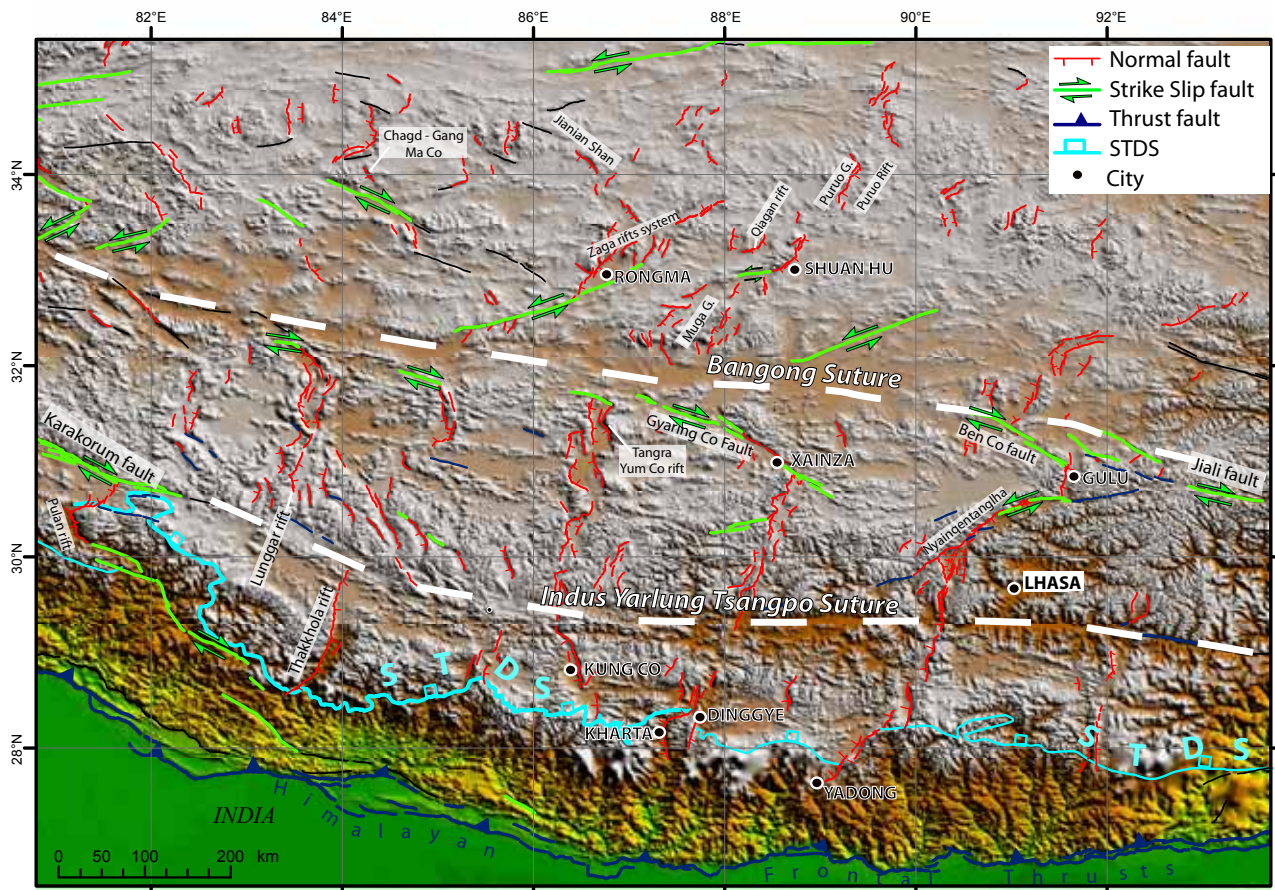


Figure IV.II: Map of active faults of central and south Tibet. Named areas refer to normal faults systems and basins that were targeted in recent studies. Karakorum, Beng Co and Jiali dextral faults and sutures are also indicated. South Tibetan Detachment System (STDS) is from Leloup et al., 2010 (see Annexe A).

- Le demi-graben de Thakkola : les dépôts déformés par la faille normale active sont plus jeunes que 7 Ma (Garzzone et al., 2003) voire même 5 Ma (Colchen 1999), indiquant un âge d'initiation de l'extension à 7 Ma au maximum. Aucune estimation de rejet vertical sur ce graben et ne permet pas d'en déduire une vitesse.
- Le demi-graben de Kung Co : l'étude thermochronologique du granite exhumé au mur de la faille normale active permet de déterminer une initiation de l'extension à 4 Ma avec des vitesses d'exhumation verticales apparentes entre 0.35 et 0.95 mm/an depuis cette initiation (Mahéo et al., 2007).

Au premier ordre, du Miocène supérieur à l'actuel, l'extension au sud-Tibet au niveau des sept grabens semble homogène :

- La plupart des sites montrent à la fois des structures d'extension anciennes ductiles et actives cassantes.
- Les vitesses de déplacement et la direction d'extension quaternaires sont comparables.

Mais les différences entre ces systèmes sont notables, par exemple :

- L'âge de l'initiation de l'exhumation est différente pour chaque site : 15 Ma à Lunggar, 7 Ma à Thakkhola, 4 Ma à Kung Co, 12 Ma au Sud de Xainza Dinggye (Ama Drime) et entre 8 et 10 Ma au nord de Yadong-Gulu (Nyainqntanglha).
- L'association des zones de cisaillement et détachement avec les failles actives ne présentent pas la même configuration pour tous les rifts : l'Ama Drime est un horst, ce qui est peu fréquent parmi les systèmes de failles normales du Sud Tibet (Figure IV.2) ; le dôme du Gurla Mandhata et le bassin de Pulan se situe à la terminaison de la faille du Karakorum et recoupent le STDS (Figure IV.2).
- D'après Kapp et al., 2008, les détachements du Nyainqntanglha et du Lunggar montrent de nombreux points communs dont l'absence de recouplement du détachement par les failles normales actives du rift associé. Ils proposent un modèle de système d'extension commun pour tous les rifts en se basant sur les données du Lunggar et du Nyainqntanglha (modèle de «rolling hinge»). Or nous avons montré dans la deuxième partie de cette thèse que le détachement du Nyainqntanglha est recoupé par les failles normales entre Chepa et Kala (carte Figure II.22). De plus le rift de Yadong-Gulu qui borde le Nyainqntanglha n'est pas seulement constitué de failles normales, mais aussi de failles décrochantes. Un régime tectonique différent est à associer pour le détachement de direction moyenne N45E et pour le rift. Ceci implique que leur association dans un même modèle de déformation continue n'est pas justifiée. D'autre part, le rôle de la *Damxung Jiali Shear Zone (DJSZ)* (cisaillement ductile dextre ou senestre?; Armijo et al., 1989, Wu et al., 2007, Edwards et Ratschbacher 2005) dans le prolongement Est du détachement n'est pas bien compris dans l'histoire d'évolution tectonique du rift de Yadong-Gulu depuis le Miocène. Si la DJSZ a fonctionné en même temps que le détachement, une interaction entre les deux structures peut être envisageable (Lee et al., 2003). De plus le modèle de «rolling hinge» appliqué à Lunggar et au Nyainqntanglha n'est pas adapté pour l'Ama Drime qui est un horst. Enfin plusieurs phases d'extension successives sont envisageables. Par conséquent il nous paraît difficile d'expliquer la structure de tous les rifts par un seul modèle.

- Pour le demi-graben de Kung Co, la vitesse d'exhumation est en dessous de celle déterminée pour les massifs de l'Ama Drime et du Nyainqntanglha. Mahéo et al., 2007 proposent plusieurs phases de déformations pour expliquer les données à Kung Co et les âges d'initiations différents entre les systèmes d'extension. Nos données de thermochronologie au massif de l'Ama Drime ne permettent pas de trancher entre un scénario simple d'exhumation constante depuis l'initiation et une exhumation en deux phases d'extension. Le signal thermochronologique plus complexe pour le bord Ouest du massif (faille de Kharta) laisse supposer une histoire plus complexe. Pour le Nyainqntanglha, le manque d'âge, la contradiction entre les relations âge-altitude et les vitesses nécessaires pour expliquer les âge $^{40}\text{Ar}/^{39}\text{Ar}$ sur biotite (§2.3.4), ainsi que les variations de vitesses nécessaires utilisées par Harrison et al., 1995 pour ajuster son modèle thermomécanique aux données de thermochronologie de la vallée de Balum Chum La (§2.3.4 et Figure II.29), montrent que plusieurs phases de déformations sont possibles et nécessaires pour expliquer les données.

Mahéo et al., 2007, généralisant à l'ensemble des rifts du Sud-Tibet, proposent deux phases d'extension avant et après 4 Ma. Des données supplémentaires sont nécessaires, aussi bien pour les deux massifs étudiés dans cette thèse que pour les autres rifts du Sud-Tibet, pour vérifier cette hypothèse.

Au niveau de l'évolution long-terme, ces grabens montrent des points communs et le contexte géologique local de chacun des rifts (et même à différents endroits d'un même rift) implique des particularités (héritage structural, réactivation d'anciennes structures, interaction avec d'autres structures contemporaines comme le STDS, la zone de Jiali et la faille de Karakorum) pouvant avoir des conséquences significatives sur le fonctionnement des systèmes de failles normales.

On constate finalement que les vitesses et l'évolution court-terme sont plus homogènes entre les différents rifts par rapport à l'évolution long terme qui est plus dépendante des particularités locales. En outre, cette déformation long-terme visible à l'affleurement aujourd'hui correspond à une évolution à des niveaux structuraux de la croûte différents de la déformation courte-terme actuelle se développant en surface. Il faut donc d'abord établir la relation entre ces niveaux de déformations en apparence associés dans les rifts.

5. RÉFÉRENCES BIBLIOGRAPHIQUES

- Allegre, C. J., V. Courtillot, P. Tapponnier, A. Hirn, M. Mattauer, C. Coulon, J. J. Jaeger, J. Achache, U. Scharer, J. Marcoux, J. P. Burg, J. Girardeau, R. Armijo, C. Gariepy, C. Gopel, T. D. Li, X. C. Xiao, C. F. Chang, G. Q. Li, B. Y. Lin, J. W. Teng, N. W. Wang, G. M. Chen, T. L. Han, X. B. Wang, W. M. Den, H. B. Sheng, Y. G. Cao, J. Zhou, H. R. Qiu, P. S. Bao, S. C. Wang, B. X. Wang, Y. X. Zhou, and X. Ronghua (1984), Structure and evolution of the Himalaya-Tibet orogenic belt, *Nature*, 307(5946), 17-22.
- Anderson, R. S., J. L. Repka, and G. S. Dick (1996), Explicit treatment of inheritance in dating depositional surfaces using *in situ* Be-10 and Al-26, *Geology*, 24(1), 47-51.
- Arita, K. (1983), Origin of the Inverted Metamorphism of the Lower Himalayas, Central Nepal, *Tectonophysics*, 95(1-2), 43-60.
- Armijo, R., P. Tapponnier, J. L. Mercier, and T. L. Han (1986), Quaternary Extension in Southern Tibet - Field Observations and Tectonic Implications, *Journal of Geophysical Research-Solid Earth and Planets*, 91(B14), 13803-13872.
- Armijo, R., P. Tapponnier, and H. Tonglin (1989), Late Cenozoic right-lateral strike-slip faulting in southern Tibet, *Journal of Geophysical Research-Solid Earth and Planets*, 94(B3), 2787-2838.
- Arnaud, N., J. C. Aitchison, P. H. Leloup, F. Valli, and S. Wilde (2008), Constraints on the initiation of normal faulting across the Yarlung Tsangpo suture zone, from the Lopu Gangri range, southern Tibet, *Geophys. Res. Abstracts*, 10, EGU2008-A-00000.
- Arnaud, N. O., and S. P. Kelley (1995), Evidence for excess argon during high-pressure metamorphism in the Dora-Maira massif (western Alps, Italy), using an ultra-violet laser-ablation microprobe Ar-40-Ar-39 technique, *Contributions to Mineralogy and Petrology*, 121(1), 1-11.
- Avouac, J. P., and E. B. Burov (1996), Erosion as a driving mechanism of intracontinental mountain growth, *Journal of Geophysical Research-Solid Earth*, 101(B8), 17747-17769.
- Avouac, J. P. (2003), Mountain building, erosion, and the seismic cycle in the Nepal Himalaya, *Adv. Geophys.*, 46, 1-80.
- Axen, G. J., M. Grove, D. Stockli, O. M. Lovera, D. A. Rothstein, J. M. Fletcher, K. Farley, and P. L. Abbott (2000), Thermal evolution of Monte Blanco dome: Low-angle normal faulting during Gulf of California rifting and late Eocene denudation of the eastern Peninsular Ranges, *Tectonics*, 19(2), 197-212.

- Balco, G., J. O. Stone, N. A. Lifton, and T. J. Dunai (2008), A complete and easily accessible means of calculating surface exposure ages or erosion rates from Be-10 and Al-26 measurements, *Quaternary Geochronology*, 3(3), 174-195.
- Banerjee, P., and R. Burgmann (2002), Convergence across the northwest Himalaya from GPS measurements, *Geophysical Research Letters*, 29(13).
- Baur, J. R. (2007), Seismotectonics of the Himalayas and the Tibetan Plateau : moment tensor analysis of regional seismograms, phD thesis, 298 pp, Oregon State University, Corvallis
- Beaumont, C., R. A. Jamieson, M. H. Nguyen, and B. Lee (2001), Himalayan tectonics explained by extrusion of a low-viscosity crustal channel coupled to focused surface denudation, *Nature*, 414(6865), 738-742.
- Beaumont, C., R. A. Jamieson, M. H. Nguyen, and S. Medvedev (2004), Crustal channel flows: 1. Numerical models with applications to the tectonics of the Himalayan-Tibetan orogen, *Journal of Geophysical Research-Solid Earth*, 109(B6), doi:10.1029/2003JB002809.
- Behr, W. M., D. H. Rood, K. E. Fletcher, N. Guzman, R. Finkel, T. C. Hanks, K. W. Hudnut, K. J. Kendrick, J. P. Platt, W. D. Sharp, R. J. Weldon, and J. D. Yule (2010), Uncertainties in slip-rate estimates for the Mission Creek strand of the southern San Andreas fault at Biskra Palms Oasis, southern California, *Geological Society of America Bulletin*, 122(9-10), 1360-1377.
- Bettinelli, P., J. P. Avouac, M. Flouzat, F. Jouanne, L. Bollinger, P. Willis, and G. R. Chitrakar (2006), Plate motion of India and interseismic strain in the Nepal Himalaya from GPS and DORIS measurements, *Journal of Geodesy*, 80(8-11), 567-589.
- Bierman, P. R., A. R. Gillespie, and M. W. Caffee (1995), Cosmogenic ages for earthquake recurrence intervals and debris flow fan deposition, Owens-valley, California, *Science*, 270(5235), 447-450.
- Bilham, R., K. Larson, J. Freymueller, F. Jouanne, P. LeFort, P. Leturmy, J. L. Mugnier, J. F. Gamond, J. P. Glot, J. Martinod, N. L. Chaudury, G. R. Chitrakar, U. P. Gautam, B. P. Koirala, M. R. Pandey, R. Ranabhat, S. N. Sapkota, P. L. Shrestha, M. C. Thakuri, U. R. Timilsina, D. R. Tiwari, G. Vidal, C. Vigny, A. Galy, and B. deVoogd (1997), GPS measurements of present-day convergence across the Nepal Himalaya, *Nature*, 386(6620), 61-64.
- Bird, P. (1991), Lateral extrusion of lower crust from under high topography, in the isostatic limit, *Journal of Geophysical Research-Solid Earth and Planets*, 96(B6), 10275-10286.
- Blisniuk, P. M., B. R. Hacker, J. Glodny, L. Ratschbacher, S. W. Bi, Z. H. Wu, M. O. McWilliams, and A. Calvert (2001), Normal faulting in central Tibet since at least 13.5 Myr ago, *Nature*, 412(6847), 628-632.

- Blisniuk, P. M., and W. D. Sharp (2003), Rates of late Quaternary normal faulting in central Tibet from U-series dating of pedogenic carbonate in displaced fluvial gravel deposits, *Earth and Planetary Science Letters*, 215, 169-186.
- Bollinger, L., J. P. Avouac, O. Beyssac, E. J. Catlos, T. M. Harrison, M. Grove, B. Goffe, and S. Sapkota (2004), Thermal structure and exhumation history of the Lesser Himalaya in central Nepal, *Tectonics*, 23(5), TC5015, doi:10.1029/2003TC001564.
- Bordet, P. (1961), *Recherches géologiques dans l'Himalaya du Népal, région du Makalu*, 275 pp., CNRS, Paris.
- Borghi, A., D. Castelli, B. Lombardo, and D. Visona (2003), Thermal and baric evolution of garnet granulites from the Kharta region of S Tibet, E Himalaya, *European Journal of Mineralogy*, 15(2), 401-418.
- Briner, J. P., T. W. Swanson, and M. Caffee (2001), Late Pleistocene cosmogenic Cl-36 glacial chronology of the southwestern Ahklun Mountains, Alaska, *Quaternary Research*, 56(2), 148-154.
- Briner, J. P., D. S. Kaufman, W. E. Manley, R. C. Finkel, and M. W. Caffee (2005), Cosmogenic exposure dating of late Pleistocene moraine stabilization in Alaska, *Geological Society of America Bulletin*, 117(7-8), 1108-1120.
- Briner, J. P., P. T. Davis, and G. H. Miller (2009), Latest Pleistocene and Holocene glaciation of Baffin Island, Arctic Canada: key patterns and chronologies, *Quaternary Science Reviews*, 28(21-22), 2075-2087.
- Brown, E. T., J. M. Edmond, G. M. Raisbeck, F. Yiou, M. D. Kurz, and E. J. Brook (1991), Examination of surface exposure ages of Antarctic moraines using insitu produced Be-10 and Al-26, *Geochimica Et Cosmochimica Acta*, 55(8), 2269-2283.
- Brown, E. T., E. J. Brook, G. M. Raisbeck, F. Yiou, and M. D. Kurz (1992), Effective attenuation lengths of cosmic-rays producing Be-10 and Al-26 in quartz - implications for exposure age dating, *Geophysical Research Letters*, 19(4), 369-372.
- Brown, E. T., P. Molnar, and D. L. Bourles (2005), Comment on «Slip-rate measurements on the Karakorum Fault may imply secular variations in fault motion», *Science*, 309(5739).
- Brunel, M. (1983), *Etude pétro-structurale des chevauchements ductiles en Himalaya (Népal oriental et Himalaya du Nord-Ouest)*, 395 pp, University of Paris VII, Paris.
- Burchfiel, B. C., and L. H. Royden (1985), North-South Extension within the Convergent Himalayan Region, *Geology*, 13(10), 679-682.

- Burchfiel, B. C., Z. Chen, L. H. Royden, Y. Liu, and C. Deng (1991), Extensional development of Gabo valley, Southern Tibet, *Tectonophysics*, 194(1-2), 187-193.
- Burchfiel, B. C., C. Zhilang, K. V. Hodges, L. Yuping, L. H. Royden, D. Changrong, and X. Jiene (1992), The South Tibetan detachment System, Himalayan Orogen: Extension Contemporaneous with and Parallel to Shortening in a Collisional Mountain Belt., 269 pp., Geological Society of America
- Burg, J. P., F. Proust, P. Tapponnier, and C. G. Ming (1983), Deformation phases and tectonic evolution of the Lhasa block (Southern Tibet, China), *Eclogae Geologicae Helvetiae*, 76(3), 643-665.
- Burg, J. P., and G. M. Chen (1984), Tectonics and Structural Zonation of Southern Tibet, China, *Nature*, 311(5983), 219-223.
- Carosi, R., B. Lombardo, G. Molli, G. Musumeci, and P. C. Pertusati (1998), The south Tibetan detachment system in the Rongbuk valley, Everest region. Deformation features and geological implications, *Journal of Asian Earth Sciences*, 16(2-3), 299-311.
- Catlos, E. J., T. M. Harrison, M. J. Kohn, M. Grove, F. J. Ryerson, C. E. Manning, and B. N. Upreti (2001), Geochronologic and thermobarometric constraints on the evolution of the Main Central Thrust, central Nepal Himalaya, *Journal of Geophysical Research-Solid Earth*, 106(B8), 16177-16204.
- Catlos, E. J., L. D. Gilley, and T. M. Harrison (2002), Interpretation of monazite ages obtained via in situ analysis, *Chemical Geology*, 188(3-4), 193-215.
- Catlos, E. J., T. M. Harrison, C. E. Manning, M. Grove, S. M. Rai, M. S. Hubbard, and B. N. Upreti (2002), Records of the evolution of the Himalayan orogen from in situ Th-Pb ion microprobe dating of monazite: Eastern Nepal and western Garhwal, *Journal of Asian Earth Sciences*, 20(5), 459-479.
- Catlos, E. J., C. S. Dubey, T. M. Harrison, and M. A. Edwards (2004), Late Miocene movement within the Himalayan Main Central Thrust shear zone, Sikkim, north-east India, *Journal of Metamorphic Geology*, 22(3), 207-226.
- Cattin, R., and J. P. Avouac (2000), Modeling mountain building and the seismic cycle in the Himalaya of Nepal, *Journal of Geophysical Research-Solid Earth*, 105(B6), 13389-13407.
- Chen, Q. Z., J. T. Freymueller, Q. Wang, Z. Q. Yang, C. J. Xu, and J. N. Liu (2004), A deforming block model for the present-day tectonics of Tibet, *Journal of Geophysical Research-Solid Earth*, 109(B1).
- Chen, Q. Z., J. T. Freymueller, Z. Q. Yang, C. J. Xu, W. P. Jiang, Q. Wang, and J. N. Liu (2004), Spatially variable extension in southern Tibet based on GPS measurements, *Journal of Geophysical Research-Solid Earth*, 109(B9).

Chevalier, M. L., F. J. Ryerson, P. Tapponnier, R. C. Finkel, J. Van der Woerd, H. B. Li, and Q. Liu (2005), Slip-rate measurements on the Karakorum Fault may imply secular variations in fault motion, *Science*, 307(5708), 411-414.

Chevalier, M. L. (2006), Détermination, par datations cosmogéniques, des variations de la vitesse de glissement sur la faille du Karakorum (Tibet) et reconstruction paléoclimatique depuis 200 ka., Thèse de doctorat. Institut de Physique du Globe de Paris.

Chevalier, M. L., Tapponnier, P., Van der Woerd, J., Ryerson, F. J., Finkel, R. C., Li, H., 2010, Quaternary Slip on the Southern Segment of the Karakorum Fault and Pulan Graben, Western Tibet, American Geophysical Union annual meeting.

Chevalier, M. L., G. Hilley, P. Tapponnier, J. Van der Woerd, J. Liu-Zheng, R. Finkel, F. J. Ryerson, H. B. Li, and X. Liu (in press), Constraints on the Late Quaternary glaciations in Tibet from cosmogenic exposure age dating of moraine surfaces, *Quaternary Science Reviews*.

Clark, M. K., and L. H. Royden (2000), Topographic ooze: Building the eastern margin of Tibet by lower crustal flow, *Geology*, 28(8), 703-706.

Cogan, M. J., K. D. Nelson, W. S. F. Kidd, C. D. Wu, and T. Project Indepth (1998), Shallow structure of the Yadong-Gulu rift, southern Tibet, from refraction analysis of Project INDEPTH common midpoint data, *Tectonics*, 17(1), 46-61.

Colchen, M. (1999), The Thakkhola-Mustang graben in Nepal and the late Cenozoic extension in the Higher Himalayas, *Journal of Asian Earth Sciences*, 17(5-6), 683-702.

Copeland, P., T. M. Harrison, and P. Lefort (1990), age and cooling history of the Manaslu granite - implications for Himalayan tectonics, *Journal of Volcanology and Geothermal Research*, 44(1-2), 33-50.

Copeland, P., T. M. Harrison, P. Yun, W. S. F. Kidd, M. Roden, and Y. Q. Zhang (1995), Thermal evolution of the gangdese batholith, Southern Tibet - a history of episodic unroofing, *Tectonics*, 14(2), 223-236.

Cottle, J. M., M. J. Jessup, D. L. Newell, M. P. Searle, R. D. Law, and M. S. A. Horstwood (2007), Structural insights into the early stages of exhumation along an orogen-scale detachment: The South Tibetan Detachment system, Dzakaa Chu section, eastern Himalaya, *Journal of Structural Geology*, 29(11), 1781-1797.

Cottle, J. M., M. J. Jessup, D. L. Newell, M. S. A. Horstwood, S. R. Noble, R. R. Parrish, D. J. Waters, and M. P. Searle (2009), Geochronology of granulitized eclogite from the Ama Drime Massif: Implications for the tectonic evolution of the South Tibetan Himalaya, *Tectonics*, 28, DOI: 10.1029/2008TC002256.

- Coulon, C. (1986), Mesozoic and Cenozoic volcanic rocks from central and southern Tibet; $^{40}\text{Ar}/^{39}\text{Ar}$ dating, petrological characteristics and geodynamical significance, in Earth and Planetary Science Letters, edited by H. Maluski, et al., pp. 281-302, Elsevier : Amsterdam, Netherlands, Netherlands.
- Coward, M. P., W. S. F. Kidd, P. Yun, R. M. Shackleton, and Z. Hu (1988), The structure of the 1985 Tibet geotraverse, Lhasa to Golmud, Philosophical Transactions of the Royal Society of London Series a-Mathematical Physical and Engineering Sciences, 327(1594), 307-336.
- Daniel, C. G., L. S. Hollister, R. R. Parrish, and D. Grujic (2003), Exhumation of the Main Central Thrust from lower crustal depths, Eastern Bhutan Himalaya, Journal of Metamorphic Geology, 21(4), 317-334.
- Dasgupta, S., J. Ganguly, and S. Neogi (2004), Inverted metamorphic sequence in the Sikkim Himalayas: crystallization history, P-T gradient and implications, Journal of Metamorphic Geology, 22(5), 395-412.
- Debon, F. (1986), The four plutonic belts of the Transhimalaya-Himalaya; a chemical, mineralogical, isotopic, and chronological synthesis along a Tibet-Nepal section, in Journal of Petrology, edited by P. Le Fort, et al., pp. 219-250, Clarendon Press : Oxford, United Kingdom, United Kingdom.
- DeCelles, P. G., D. M. Robinson, J. Quade, T. P. Ojha, C. N. Garzione, P. Copeland, and B. N. Upreti (2001), Stratigraphy, structure, and tectonic evolution of the Himalayan fold-thrust belt in western Nepal, Tectonics, 20(4), 487-509.
- Demets, C., R. G. Gordon, D. F. Argus, and S. Stein (1990), Current plate motions, Geophysical Journal International, 101(2), 425-478.
- Demets, C., R. G. Gordon, D. F. Argus, and S. Stein (1994), Effect of recent revisions to the geomagnetic reversal time-scale on estimates of current plate motions, Geophysical Research Letters, 21(20), 2191-2194.
- Desilets, D., M. Zreda, and T. Prabu (2006), Extended scaling factors for in situ cosmogenic nuclides: New measurements at low latitude, Earth and Planetary Science Letters, 246(3-4), 265-276.
- Dewane, T. J., D. F. Stockli, C. Hager, M. Taylor, L. Ding, J. Lee, and S. Wallis (2006), Timing of Cenozoic E-W Extension in the Tangra Yum Co-Kung Co Rift, south-central Tibet, AGU fall Meeting.
- Dewey, J. F. (1988a), Extensional collapse of orogens, Tectonics, 7(6), 1123-1139.
- Dewey, J. F. (1988b), The tectonic evolution of the Tibetan Plateau, in Philosophical Transactions of the Royal Society of London, Series A: Mathematical and Physical Sciences, edited by R. M. Shackleton, et al., pp. 379-413, Royal Society of London : London, United Kingdom, United Kingdom.
- Dodson, M. H. (1973), Closure temperature in cooling geochronological and petrological systems, Contributions to Mineralogy and Petrology, 40(3), 259-274.

- Dunai, T. J. (2001), Influence of secular variation of the geomagnetic field on production rates of in situ produced cosmogenic nuclides, *Earth and Planetary Science Letters*, 193(1-2), 197-212.
- Durr, S. B. (1996), Provenance of Xigaze fore-arc basin clastic rocks (Cretaceous, south Tibet), *Geological Society of America Bulletin*, 108(6), 669-684.
- Edwards, M. A., W. S. F. Kidd, J. X. Li, Y. J. Yu, and M. Clark (1996), Multi-stage development of the southern Tibet detachment system near Khula Kangri. New data from Gonto La, *Tectonophysics*, 260(1-3), 1-19.
- Edwards, M. A., and L. Ratschbacher (2005), Seismic and aseismic weakening effects in transtension: field and microstructural observations on the mechanics and architecture of a large fault zone in SE Tibet, *High-Strain Zones: Structure and Physical Properties*, 245, 109-141.
- England, P., and G. Houseman (1989), Extension during Continental Convergence, with Application to the Tibetan Plateau, *Journal of Geophysical Research-Solid Earth and Planets*, 94(B12), 17561-17579.
- England, P., and P. Molnar (2005), Late Quaternary to decadal velocity fields in Asia, *Journal of Geophysical Research-Solid Earth*, 110(B12).
- Fechting, H., and Kalbitzer, S. (1966), The diffusion of argon in potassium-bearing solids. In potassium-argon dating (ed. O. A. Shaeffer and J. Zähringer), 68-107. Springer-Verlag, New York.
- Finkel, R. C., L. A. Owen, P. L. Barnard, and M. W. Caffee (2003), Beryllium-10 dating of Mount Everest moraines indicates a strong monsoon influence and glacial synchroneity throughout the Himalaya, *Geology*, 31(6), 561-564.
- Foster, D. A., and B. E. John (1999), Quantifying tectonic exhumation in an extensional orogen with thermochronology: examples from the southern Basin and Range Province, *Geological Society, London, Special Publications*, 154(1), 343-364.
- Foster, G., P. Kinny, D. Vance, C. Prince, and N. Harris (2000), The significance of monazite U-Th-Pb age data in metamorphic assemblages; a combined study of monazite and garnet chronometry, *Earth and Planetary Science Letters*, 181(3), 327-340.
- Fraser, G., D. Ellis, and S. Eggins (1997), Zirconium abundance in granulite-facies minerals, with implications for zircon geochronology in high-grade rocks, *Geology*, 25(7), 607-610.
- Garzione, C. N., P. G. DeCelles, D. G. Hodkinson, T. P. Ojha, and B. N. Upreti (2003), East-west extension and Miocene environmental change in the southern Tibetan plateau: Thakkola graben, central Nepal, *Geological Society of America Bulletin*, 115(1), 3-20.

- Goscombe, B., and M. Hand (2000), Contrasting P-T paths in the Eastern Himalaya, Nepal: Inverted isograds in a paired metamorphic mountain belt, *Journal of Petrology*, 41(12), 1673-1719.
- Gosse, J. C., and F. M. Phillips (2001), Terrestrial in situ cosmogenic nuclides: theory and application, *Quaternary Science Reviews*, 20(14), 1475-1560.
- Granger, D. E. (2006), A review of burial dating methods using ^{26}Al and ^{10}Be , *Geological Society of America Special Papers*, 415, 1-16.
- Groppi, C., B. Lombardo, F. Rolfo, and P. Pertusati (2007), Clockwise exhumation path of granulitized eclogites from the Ama Drime range (Eastern Himalayas), *Journal of Metamorphic Geology*, 25(1), 51-75.
- Grujic, D., M. Casey, C. Davidson, L. S. Hollister, R. Kundig, T. Pavlis, and S. Schmid (1996), Ductile extrusion of the Higher Himalayan Crystalline in Bhutan: Evidence from quartz microfabrics, *Tectonophysics*, 260(1-3), 21-43.
- Grujic, D., L. S. Hollister, and R. R. Parrish (2002), Himalayan metamorphic sequence as an orogenic channel: insight from Bhutan, *Earth and Planetary Science Letters*, 198(1-2), 177-191.
- Guillot, S. (1999), An overview of the metamorphic evolution in Central Nepal, *Journal of Asian Earth Sciences*, 17(5-6), 713-725.
- Guillot, S., and P. Allemand (2002), Two-dimensional thermal modelling of the early tectonometamorphic evolution in central Himalaya, *Journal of Geodynamics*, 34(1), 77-98.
- Hager, C., D. Stockli, T. Dewane, and L. Ding (2006), Episodic Mio-Pliocene rifting in south-central Tibet. Thermochronometric constraints from the Xainza rift, AGU fall Metting.
- Harkins, N., E. Kirby, A. Heimsath, R. Robinson, and U. Reiser (2007), Transient fluvial incision in the headwaters of the Yellow River, northeastern Tibet, China, *Journal of Geophysical Research-Earth Surface*, 112(F3).
- Harris, N. B. W., R. H. Xu, C. L. Lewis, C. J. Hawkesworth, and Y. Q. Zhang (1988), Isotope geochemistry of the 1985 Tibet geotraverse, Lhasa to Golmud, *Philosophical Transactions of the Royal Society of London Series a-Mathematical Physical and Engineering Sciences*, 327(1594), 263-285.
- Harris, N. B. W., M. Caddick, J. Kosler, S. Goswami, D. Vance, and A. G. Tindle (2004), The pressure-temperature-time path of migmatites from the Sikkim Himalaya, *Journal of Metamorphic Geology*, 22(3), 249-264.
- Harrison, T. M., and G. K. C. Clarke (1979), A model of thermal effects of igneous intrusion and uplift as applied to Quattoon Pluton, British Columbia, *Canadian Journal of Earth Sciences*, 16, 411-420.

- Harrison, T. M., M. T. Heizler, O. M. Lovera, W. J. Chen, and M. Grove (1994), A chlorine disinfectant for excess argon released from K-Feldspar during step heating, *Earth and Planetary Science Letters*, 123(1-4), 95-104.
- Harrison, T. M., P. Copeland, W. S. F. Kidd, and O. M. Lovera (1995), Activation of the Nyainqntanghla Shear Zone - Implications for Uplift of the Southern Tibetan Plateau, *Tectonics*, 14(3), 658-676.
- Harrison, T. M., O. M. Lovera, and M. Grove (1997), New insights into the origin of two contrasting Himalayan granite belts, *Geology*, 25(10), 899-902.
- Harrison, T. M., M. Grove, O. M. Lovera, and E. J. Catlos (1998), A model for the origin of Himalayan anatexis and inverted metamorphism, *Journal of Geophysical Research-Solid Earth*, 103(B11), 27017-27032.
- Harrison, T. M. (2005), Continuous thermal histories from inversion of closure profiles, *Low-Temperature Thermochronology: Techniques, Interpretations, and Applications*, 58, 389-409.
- Harrison, T. M. (2006), Did the Himalayan Crystallines extrude partially molten from beneath the Tibetan Plateau?, in *Channel Flow, Ductile Extrusion and Exhumation in Continental Collision Zones*, edited by R. D. Law, et al., pp. 237-254, Geological Society, London.
- Hauck, M. L., K. D. Nelson, L. D. Brown, W. J. Zhao, and A. R. Ross (1998), Crustal structure of the Himalayan orogen at similar to 90 degrees east longitude from Project INDEPTH deep reflection profiles, *Tectonics*, 17(4), 481-500.
- Hintersberger, E., Thiede, R. C., Strecker, M. R., and Hacker B. R. (2010), East-west extension in the NW Indian Himalaya, *Geological Society of America Bulletin*, 122, 1499-1515
- Hodges, K. V., W. E. Hames, W. Olszewski, B. C. Burchfiel, L. H. Royden, and Z. Chen (1994), Thermobarometric and Ar-40 Ar-39 Geochronological Constraints on Eohimalayan Metamorphism in the Dinggye Area, Southern Tibet, *Contributions to Mineralogy and Petrology*, 117(2), 151-163.
- Hodges, K. V., R. R. Parrish, and M. P. Searle (1996), Tectonic evolution of the central Annapurna Range, Nepalese Himalayas, *Tectonics*, 15(6), 1264-1291.
- Hodges, K. V. (2000), Tectonics of the Himalaya and southern Tibet from two perspectives, *Geological Society of America Bulletin*, 112(3), 324-350.
- Holland, T. J. B., and R. Powell (1998), An internally consistent thermodynamic data set for phases of petrological interest, *Journal of Metamorphic Geology*, 16(3), 309-343.

- Holt, W. E., N. Chamot-rooke, X. Le Pichon, A. J. Haines, B. Shen-Tu, and J. Ren (2000), Velocity field in Asia inferred from Quaternary fault slip rates and Global Positioning System observations, *Journal of Geophysical Research-Solid Earth*, 105(B8), 19185-19209.
- House, M. A., K. A. Farley, and D. Stockli (2000), Helium chronometry of apatite and titanite using Nd-YAG laser heating, *Earth and Planetary Science Letters*, 183(3-4), 365-368.
- Jamieson, R. A., C. Beaumont, S. Medvedev, and M. H. Nguyen (2004), Crustal channel flows: 2. Numerical models with implications for metamorphism in the Himalayan-Tibetan orogen, *Journal of Geophysical Research-Solid Earth*, 109(B6), DOI: 10.1029/2003JB002811
- Jessup, M. J., D. L. Newell, J. M. Cottle, A. L. Berger, and J. A. Spotila (2008), Orogen-parallel extension and exhumation enhanced by denudation in the trans-Himalayan Arun River gorge, Ama Drime Massif, Tibet-Nepal, *Geology*, 36(7), 587-590.
- Ji, W. Q., F. Y. Wu, S. L. Chung, J. X. Li, and C. Z. Liu (2009), Zircon U-Pb geochronology and Hf isotopic constraints on petrogenesis of the Gangdese batholith, southern Tibet, *Chemical Geology*, 262(3-4), 229-245.
- Johnson, M. R. W., G. J. H. Oliver, R. R. Parrish, and S. P. Johnson (2001), Synthrusting metamorphism, cooling, and erosion of the Himalayan Kathmandu Complex, Nepal, *Tectonics*, 20(3), 394-415.
- Kali, E., P. H. Leloup, N. Arnaud, G. Maheo, D. Y. Liu, E. Boutonnet, J. Van der Woerd, X. H. Liu, L. Z. Jing, and H. B. Li (2010), Exhumation history of the deepest central Himalayan rocks, Ama Drime range: Key pressure-temperature-deformation-time constraints on orogenic models, *Tectonics*, 29.
- Kapp, J. L. D., T. M. Harrison, P. Kapp, M. Grove, O. M. Lovera, and D. Lin (2005), Nyainqntanglha Shan: A window into the tectonic, thermal, and geochemical evolution of the Lhasa block, southern Tibet, *Journal of Geophysical Research-Solid Earth*, 110(B8).
- Kapp, P., A. Yin, C. E. Manning, T. M. Harrison, M. H. Taylor, and L. Ding (2003), Tectonic evolution of the early Mesozoic blueschist-bearing Qiangtang metamorphic belt, central Tibet, *Tectonics*, 22(4).
- Kapp, P., and J. H. Guynn (2004), Indian punch rifts Tibet, *Geology*, 32(11), 993-996.
- Kapp, P., A. Yin, T. M. Harrison, and L. Ding (2005), Cretaceous-Tertiary shortening, basin development, and volcanism in central Tibet, *Geological Society of America Bulletin*, 117(7-8), 865-878.
- Kapp, P. (2007), The Gangdese retroarc thrust belt revealed, in *GSA Today*, edited by P. G. DeCelles, et al., pp. 4-9, Geological Society of America (GSA) : Boulder, CO, United States, United States.
- Kapp, P., M. Taylor, D. Stockli, and L. Ding (2008), Development of active low-angle normal fault systems during orogenic collapse: Insight from Tibet, *Geology*, 36(1), 7-10.

- Kelsey, D. E., C. Clark, and M. Hand (2008), Thermobarometric modelling of zircon and monazite growth in melt-bearing systems: examples using model metapelitic and metapsammitic granulites, *Journal of Metamorphic Geology*, 26(2), 199-212.
- Kohl, C. P., and K. Nishiizumi (1992), Chemical isolation of quartz for measurement of insitu-produced cosmogenic nuclides, *Geochimica Et Cosmochimica Acta*, 56(9), 3583-3587.
- Kohn, M. J., E. J. Catlos, F. J. Ryerson, and T. M. Harrison (2001), Pressure-temperature-time path discontinuity in the Main Central thrust zone, central Nepal, *Geology*, 29(7), 571-574.
- Kohn, M. J., M. S. Wieland, C. D. Parkinson, and B. N. Upreti (2004), Miocene faulting at plate tectonic velocity in the Himalaya of central Nepal, *Earth and Planetary Science Letters*, 228(3-4), 299-310.
- Kohn, M. J., M. S. Wieland, C. D. Parkinson, and B. N. Upreti (2005), Five generations of monazite in Langtang gneisses: implications for chronology of the Himalayan metamorphic core, *Journal of Metamorphic Geology*, 23(5), 399-406.
- Kong, P., D. E. Granger, F. Y. Wu, M. W. Caffee, Y. J. Wang, X. T. Zhao, and Y. Zheng (2009), Cosmogenic nuclide burial ages and provenance of the Xigeda paleo-lake: Implications for evolution of the Middle Yangtze River, *Earth and Planetary Science Letters*, 278(1-2), 131-141.
- Kong, P., D. Fink, C. Na, and W. Xiao (2010), Dip-slip rate determined by cosmogenic surface dating on a Holocene scarp of the Daju fault, Yunnan, China., *Tectonophysics*.
- Lal, D. (1991), Cosmic-ray labeling of erosion surfaces - insitu nuclide production - rates and erosion models, *Earth and Planetary Science Letters*, 104(2-4), 424-439.
- Langille, J. M., M. J. Jessup, J. M. Cottle, D. Newell, and G. Seward (2010), Kinematic evolution of the Ama Drime detachment: Insights into orogen-parallel extension and exhumation of the Ama Drime Massif, Tibet-Nepal, *Journal of Structural Geology*, 32(7), 900-919.
- Larson, K. M., R. Burgmann, R. Bilham, and J. T. Freymueller (1999), Kinematics of the India-Eurasia collision zone from GPS measurements, *Journal of Geophysical Research-Solid Earth*, 104(B1), 1077-1093.
- Lave, J., and J. P. Avouac (2000), Active folding of fluvial terraces across the Siwaliks Hills, Himalayas of central Nepal, *Journal of Geophysical Research-Solid Earth*, 105(B3), 5735-5770.
- Le Fort, P. (1975), Himalayas - Collided Range - Present Knowledge of Continental Arc, *American Journal of Science*, A275, 1-44.
- Lee, H. Y., S. L. Chung, C. H. Lo, J. Q. Ji, T. Y. Lee, Q. Qian, and Q. Zhang (2009), Eocene Neotethyan slab breakoff in southern Tibet inferred from the Linzizong volcanic record, *Tectonophysics*, 477(1-2), 20-35.

- Lee, J., B. Hacker, and Y. Wang (2004), Evolution of North Himalayan gneiss domes: structural and metamorphic studies in Mabja Dome, southern Tibet, *Journal of Structural Geology*, 26(12), 2297-2316.
- Lee, T. Y., and L. A. Lawver (1995), Cenozoic plate reconstruction of Southeast Asia, *Tectonophysics*, 251(1-4), 85-138.
- Leeder, M. R., A. B. Smith, and J. X. Yin (1988), Sedimentology, paleoecology and palaeoenvironmental evolution of the 1985 Lhasa to Golmud geotraverse, *Philosophical Transactions of the Royal Society of London Series a-Mathematical Physical and Engineering Sciences*, 327(1594), 107-&.
- Leier, A. L., P. G. DeCelles, P. Kapp, and L. Ding (2007), The Takena formation of the Lhasa terrane, southern Tibet: The record of a Late Cretaceous retroarc foreland basin, *Geological Society of America Bulletin*, 119(1-2), 31-48.
- Leloup, P. H., T. M. Harrison, F. J. Ryerson, W. J. Chen, Q. Li, P. Tapponnier, and R. Lacassin (1993), Structural, Petrological and Thermal Evolution of a Tertiary Ductile Strike-Slip Shear Zone, Diancang Shan, Yunnan, *Journal of Geophysical Research-Solid Earth*, 98(B4), 6715-6743.
- Leloup, P. H., G. Maheo, N. Arnaud, E. Kali, E. Boutonnet, D. Y. Liu, X. H. Liu, and H. B. Li (2010), The South Tibet detachment shear zone in the Dinggye area Time constraints on extrusion models of the Himalayas, *Earth and Planetary Science Letters*, 292(1-2), 1-16.
- Li, D., Q. Liao, Y. Yuan, Y. Wan, D. Liu, X. Zhang, S. Yi, S. Cao, and D. Xie (2003), Shrimp U-Pb zircon geochronology of granulites at Rimana (Southern Tibet) in the central segment of Himalayan Orogen, *Chinese Sci. Bull.*, 48(23), 2647-2650.
- Lifton, N. A., J. W. Bieber, J. M. Clem, M. L. Duldig, P. Evenson, J. E. Humble, and R. Pyle (2005), Addressing solar modulation and long-term uncertainties in scaling secondary cosmic rays for in situ cosmogenic nuclide applications, *Earth and Planetary Science Letters*, 239, 140-161.
- Liu, S. W., J. J. Zhang, G. M. Shu, and Q. G. Li (2005), Mineral chemistry, P-T-t paths and exhumation processes of mafic granulites in Dinggye, Southern Tibet, *Science in China Series D-Earth Sciences*, 48(11), 1870-1881.
- Liu, Y., W. Siebel, H. J. Massonne, and X. C. Xiao (2007), Geochronological and petrological constraints for tectonic evolution of the central Greater Himalayan Sequence in the Kharta area, southern Tibet, *Journal of Geology*, 115(2), 215-230.
- Lombardo, B., P. Pertusati, and A. Borghi (1993), Geology and tectono-magmatic evolution of the eastern Himalaya along the Chomolungma-Makalu transect. , in *Himalayan Tectonics*, edited by P. J. Treloar and M. P. Searle, pp. 341-355, Geological Society of London, London.

- Lombardo, B., and F. Rolfo (2000), Two contrasting eclogite types in the Himalayas: implications for the Himalayan orogeny, *Journal of Geodynamics*, 30(1-2), 37-60.
- Lovera, O. M., F. M. Richter, and T. M. Harrison (1989), The $^{40}\text{Ar}/^{39}\text{Ar}$ thermochronometry for slowly cooled samples having a distribution of diffusion domain sizes, *Journal of Geophysical Research-Solid Earth and Planets*, 94(B12), 17917-17935.
- Lovera, O. M., F. M. Richter, and T. M. Harrison (1991), Diffusion domains determined by ^{39}Ar released during step heating, *Journal of Geophysical Research-Solid Earth and Planets*, 96(B2), 2057-2069.
- Lovera, O. M. (1992), Computer-programs to model $^{40}\text{Ar}/^{39}\text{Ar}$ diffusion data from multidomain samples, *Computers & Geosciences*, 18(7), 789-813.
- Lovera, O. M., M. Grove, T. M. Harrison, and K. I. Mahon (1997), Systematic analysis of K-Feldspar $^{40}\text{Ar}/^{39}\text{Ar}$ step heating results .1. Significance of activation energy determinations, *Geochimica Et Cosmochimica Acta*, 61(15), 3171-3192.
- Macfarlane, A. M. (1993), Chronology of Tectonic Events in the Crystalline Core of the Himalaya, Langtang-National-Park, Central Nepal, *Tectonics*, 12(4), 1004-1025.
- Maheo, G., P. H. Leloup, F. Valli, R. Lacassin, N. Arnaud, J. L. Paquette, A. Fernandez, L. Haibing, K. A. Farley, and P. Tapponnier (2007), Post 4 Ma initiation of normal faulting in southern Tibet. Constraints from the Kung Co half graben, *Earth and Planetary Science Letters*, 256(1-2), 233-243.
- Makovsky, Y., S. L. Klempner, L. Y. Huang, and D. Y. Lu (1996), Structural elements of the southern Tethyan Himalaya crust from wide-angle seismic data, *Tectonics*, 15(5), 997-1005.
- Martin, A. J., G. E. Gehrels, and P. G. DeCelles (2007), The tectonic significance of (U,Th)/Pb ages of monazite inclusions in garnet from the Himalaya of central Nepal, *Chemical Geology*, 244(1-2), 1-24.
- Mattauer, M. (1986), Intracontinental subduction, crust–mantle decollement and crustal-stacking wedge in the Himalayas and other collision belts, *Journal of geological Society of London Special Publication*, 19, 37-50.
- Matte, P., P. Tapponnier, N. Arnaud, L. Bourjot, J. P. Avouac, P. Vidal, L. Qing, Y. S. Pan, and W. Yi (1996), Tectonics of Western Tibet, between the Tarim and the Indus, *Earth and Planetary Science Letters*, 142(3-4), 311-&.
- McCaffrey, R., and J. Nabelek (1998), Role of oblique convergence in the active deformation of the Himalayas and southern Tibet Plateau, *Geology*, 26(8), 691-694.
- McDougall, I., and T. M. Harrison (1999), *Geochronology and thermochronology by the $^{40}\text{Ar}/^{39}\text{Ar}$ method*, Oxford University Press : New York, NY, United States, United States.

- Meade, B. J. (2007), Present-day kinematics at the India-Asia collision zone, *Geology*, 35(1), 81-84.
- Meier, K., and E. Hiltner (1993), Deformation and metamorphism within the Main Central Thrust zone, Arun tectonic Window, eastern Nepal, in *Himalayan Tectonics*, edited by P. J. Treloar and M. P. Searle, pp. 511-523, Geological Society of London, London.
- Meigs, A. J., D. W. Burbank, and R. A. Beck (1995), Middle-Late Miocene (Greater-Than-10 Ma) Formation of the Main Boundary Thrust in the Western Himalaya, *Geology*, 23(5), 423-426.
- Meriaux, A. S., F. J. Ryerson, P. Tapponnier, J. Van der Woerd, R. C. Finkel, X. W. Xu, Z. Q. Xu, and M. W. Caffee (2004), Rapid slip along the central Altyn Tagh Fault: Morphochronologic evidence from Cherchen He and Sulamu Tagh, *Journal of Geophysical Research-Solid Earth*, 109(B6).
- Meriaux, A. S., P. Tapponnier, F. J. Ryerson, X. W. Xu, G. King, J. Van der Woerd, R. C. Finkel, H. B. Li, M. W. Caffee, Z. Q. Xu, and W. B. Chen (2005), The Aksay segment of the northern Altyn Tagh fault: Tectonic geomorphology, landscape evolution, and Holocene slip rate, *Journal of Geophysical Research-Solid Earth*, 110(B4).
- Meriaux, A. S., K. Sieh, R. C. Finkel, C. M. Rubin, M. H. Taylor, A. J. Meltzner, and F. J. Ryerson (2009), Kinematic behavior of southern Alaska constrained by westward decreasing postglacial slip rates on the Denali Fault, Alaska, *Journal of Geophysical Research-Solid Earth*, 114.
- Metivier, F., Y. Gaudemer, P. Tapponnier, and B. Meyer (1998), Northeastward growth of the Tibet plateau deduced from balanced reconstruction of two depositional areas: The Qaidam and Hexi Corridor basins, China, *Tectonics*, 17(6), 823-842.
- Meyer, B., P. Tapponnier, Y. Gaudemer, G. Peltzer, S. M. Guo, and Z. T. Chen (1996), Rate of left-lateral movement along the easternmost segment of the Altyn Tagh fault, east of 96 degrees E (China), *Geophysical Journal International*, 124(1), 29-44.
- Molnar, P., and P. Tapponnier (1975), Cenozoic tectonics of Asia - effects of a continental collision, *Science*, 189(4201), 419-426.
- Molnar, P., and P. Tapponnier (1978a), Active Tectonics of Tibet, *Journal of Geophysical Research*, 83(Nb11), 5361-5373.
- Molnar, P., and P. Tapponnier (1978b), Active tectonics of Tibet, *Journal of Geophysical Research*, 83(NB11), 5361-&.
- Molnar, P., and J. Stock (2009), Slowing of India's convergence with Eurasia since 20 Ma and its implications for Tibetan mantle dynamics, *Tectonics*, 28, 10.1029/2008TC002271.

Monsalve, G., A. Sheehan, V. Schulte-Pelkum, S. Rajaure, M. R. Pandey, and F. Wu (2006), Seismicity and one-dimensional velocity structure of the Himalayan collision zone: Earthquakes in the crust and upper mantle, *Journal of Geophysical Research-Solid Earth*, 111(B10), DOI: 10.1029/2005JB004062

Murphy, M. A., A. Yin, T. M. Harrison, S. B. Durr, Z. Chen, F. J. Ryerson, W. S. F. Kidd, X. Wang, and X. Zhou (1997), Did the Indo-Asian collision alone create the Tibetan plateau?, *Geology*, 25(8), 719-722.

Murphy, M. A., and T. M. Harrison (1999), Relationship between leucogranites and the Qomolangma detachment in the Rongbuk Valley, south Tibet, *Geology*, 27(9), 831-834.

Murphy, M. A., A. Yin, P. Kapp, T. M. Harrison, C. E. Manning, F. J. Ryerson, L. Ding, and J. H. Guo (2002), Structural evolution of the Gurla Mandhata detachment system, southwest Tibet: Implications for the eastward extent of the Karakoram fault system, *Geological Society of America Bulletin*, 114(4), 428-447.

Nelson, K. D., W. J. Zhao, L. D. Brown, J. Kuo, J. K. Che, X. W. Liu, S. L. Klemperer, Y. Makovsky, R. Meissner, J. Mechle, R. Kind, F. Wenzel, J. Ni, J. Nabelek, L. S. Chen, H. D. Tan, W. B. Wei, A. G. Jones, J. Booker, M. Unsworth, W. S. F. Kidd, M. Hauck, D. Alsdorf, A. Ross, M. Cogan, C. D. Wu, E. Sandvol, and M. Edwards (1996), Partially molten middle crust beneath southern Tibet: Synthesis of project INDEPTH results, *Science*, 274(5293), 1684-1688.

Ni, J., and J. E. York (1978), Late Cenozoic tectonics of Tibetan plateau, *Journal of Geophysical Research*, 83(NB11), 5377-5384.

Owen, L. A., R. C. Finkel, M. W. Caffee, and L. Gualtieri (2002), Timing of multiple late Quaternary glaciations in the Hunza Valley, Karakoram Mountains, northern Pakistan: Defined by cosmogenic radionuclide dating of moraines, *Geological Society of America Bulletin*, 114(5), 593-604.

Owen, L. A., J. Q. Spencer, H. Z. Ma, P. L. Barnard, E. Derbyshire, R. C. Finkel, M. W. Caffee, and Z. Y. Nian (2003), Timing of Late Quaternary glaciation along the southwestern slopes of the Qilian Shan, Tibet, *Boreas*, 32(2), 281-291.

Owen, L. A., R. C. Finkel, P. L. Barnard, H. Z. Ma, K. Asahi, M. W. Caffee, and E. Derbyshire (2005), Climatic and topographic controls on the style and timing of Late Quaternary glaciation throughout Tibet and the Himalaya defined by Be-10 cosmogenic radionuclide surface exposure dating, *Quaternary Science Reviews*, 24(12-13), 1391-1411.

Owen, L. A., R. C. Finkel, M. Haizhou, and P. L. Barnard (2006), Late Quaternary landscape evolution in the Kunlun Mountains and Qaidam Basin, Northern Tibet: A framework for examining the links between glaciation, lake level changes and alluvial fan formation, *Quaternary International*, 154, 73-86.

- Owen, L. A., R. Robinson, D. I. Benn, R. C. Finkel, N. K. Davis, C. L. Yi, J. Putkonen, D. W. Li, and A. S. Murray (2009), Quaternary glaciation of Mount Everest, *Quaternary Science Reviews*, 28(15-16), 1412-1433.
- Pan, Y., and W. S. F. Kidd (1992), Nyainqntanglha Shear Zone - a Late Miocene Extensional Detachment in the Southern Tibetan Plateau, *Geology*, 20(9), 775-778.
- Pan, Y., P. Copeland, M. K. Roden, W. S. F. Kidd, and T. M. Harrison (1993), Thermal and unroofing history of the Lhasa area, Southern Tibet - evidence from apatite fission-track thermochronology, *Nuclear Tracks and Radiation Measurements*, 21(4), 543-554.
- Pandey, M. R., R. P. Tandukar, J. P. Avouac, J. Lave, and J. P. Massot (1995), Interseismic Strain Accumulation on the Himalayan Crustal Ramp (Nepal), *Geophysical Research Letters*, 22(7), 751-754.
- Pandey, M. R., R. P. Tandukar, J. P. Avouac, J. Vergne, and T. Heritier (1999), Seismotectonics of the Nepal Himalaya from a local seismic network, *Journal of Asian Earth Sciences*, 17(5-6), 703-712.
- Parrish, R. R., and K. V. Hedges (1996), Isotopic constraints on the age and provenance of the Lesser and Greater Himalayan sequences, Nepalese Himalaya, *Geological Society of America Bulletin*, 108(7), 904-911.
- Paul, J., R. Burgmann, V. K. Gaur, R. Bilham, K. M. Larson, M. B. Ananda, S. Jade, M. Mukal, T. S. Anupama, G. Satyal, and D. Kumar (2001), The motion and active deformation of India, *Geophysical Research Letters*, 28(4), 647-650.
- Peltzer, G., and P. Tapponnier (1988), Formation and evolution of strike-slip faults, rifts, and basins during the India-Asia collision - an experimental approach, *Journal of Geophysical Research-Solid Earth and Planets*, 93(B12), 15085-&.
- Perrineau, A. (2010), Evolution morphologique et tectonique récente des marges NE et SE du plateau tibétain: lien avec la dynamique des grands fleuves, Thèse de Doctorat, Institut de Physique du Globe de Paris - Ecole et Observatoire des Sciences de la Terre - Université de Strasbourg.
- Powell, R., and J. A. Evans (1983), A New Geobarometer for the Assemblage Biotite-Muscovite-Chlorite-Quartz, *Journal of Metamorphic Geology*, 1(4), 331-336.
- Pullen, A., P. Kapp, G. E. Gehrels, P. G. DeCelles, E. H. Brown, J. M. Fabijanic, and L. Ding (2008), Gangdese retroarc thrust belt and foreland basin deposits in the Damxung area, southern Tibet, *Journal of Asian Earth Sciences*, 33(5-6), 323-336.
- Quidelleur, X., M. Grove, O. M. Lovera, T. M. Harrison, A. Yin, and F. J. Ryerson (1997), Thermal evolution and slip history of the Renbu Zedong Thrust, southeastern Tibet, *Journal of Geophysical Research-Solid Earth*, 102(B2), 2659-2679.

- Replumaz, A., and P. Tapponnier (2003), Reconstruction of the deformed collision zone between India and Asia by backward motion of lithospheric blocks, *Journal of Geophysical Research-Solid Earth*, 108(B6).
- Richards, A., T. Argles, N. Harris, R. Parrish, T. Ahmad, F. Darbyshire, and E. Draganits (2005), Himalayan architecture constrained by isotopic tracers from clastic sediments, *Earth and Planetary Science Letters*, 236(3-4), 773-796.
- Richter, F. M., O. M. Lovera, T. M. Harrison, and P. Copeland (1991), Tibetan tectonics from Ar-40/Ar-39 analysis of a single K-Feldspar sample, *Earth and Planetary Science Letters*, 105(1-3), 266-278.
- Ritz, J.-F., R. Vassallo, R. Braucher, E. T. Brown, S. Carretier, and D. L. Bourles (2006), Using in situ produced ^{10}Be to quantify active tectonics in the Gurvan Bogd mountain range (Gobi-Altay, Mongolia), *Geological Society of America Special Papers*, 415, 87-110.
- Ritz, J. F., D. Bourles, E. T. Brown, S. Carretier, J. Chery, B. Enhtuvshin, P. Galsan, R. C. Finkel, T. C. Hanks, K. J. Kendrick, H. Philip, G. Raisbeck, A. Schlupp, D. P. Schwartz, and F. Yiou (2003), Late Pleistocene to Holocene slip rates for the Gurvan Bulag thrust fault (Gobi-Altay, Mongolia) estimated with Be-10 dates, *Journal of Geophysical Research-Solid Earth*, 108(B3).
- Roberts, M. P., and F. Finger (1997), Do U-Pb zircon ages from granulites reflect peak metamorphic conditions?, *Geology*, 25(4), 319-322.
- Rolfo, F., W. McClelland, and B. Lombardo (2005), Geochronological constraints on the age of the eclogite-facies metamorphism in the eastern Himalaya, *Geologie Alpine, memoire h.s. 20th Himalaya-Karakorum-Tibet workshop*, 44, 170.
- Rothery, D. A., and S. A. Drury (1984), The neotectonics of the Tibetan plateau, *Tectonics*, 3(1), 19-26.
- Royden, L. H., B. C. Burchfiel, R. W. King, E. Wang, Z. L. Chen, F. Shen, and Y. P. Liu (1997), Surface deformation and lower crustal flow in eastern Tibet, *Science*, 276(5313), 788-790.
- Rubatto, D., I. S. Williams, and I. S. Buick (2001), Zircon and monazite response to prograde metamorphism in the Reynolds Range, central Australia, *Contributions to Mineralogy and Petrology*, 140(4), 458-468.
- Schaerer, U. (1984), U-Pb geochronology of Gangdese (Transhimalaya) plutonism in the Lhasa-Xigaze region, Tibet, in *Earth and Planetary Science Letters*, edited by X. Rong-Hua and C. J. Allegre, pp. 311-320, Elsevier : Amsterdam, Netherlands, Netherlands.
- Schaltegger, U., C. M. Fanning, D. Gunther, J. C. Maurin, K. Schulmann, and D. Gebauer (1999), Growth, annealing and recrystallization of zircon and preservation of monazite in high-grade metamorphism:

conventional and in-situ U-Pb isotope, cathodoluminescence and microchemical evidence, Contributions to Mineralogy and Petrology, 134(2-3), 186-201.

Schelling, D., and K. Arita (1991), Thrust Tectonics, Crustal Shortening, and the Structure of the Far-Eastern Nepal Himalaya, *Tectonics*, 10(5), 851-862.

Schelling, D. (1992), The Tectonostratigraphy and Structure of the Eastern Nepal Himalaya, *Tectonics*, 11(5), 925-943.

Schiotte, L., W. Compston, and D. Bridgwater (1989), Ion Probe U-Th-Pb Zircon Dating of Polymetamorphic Orthogneisses from Northern Labrador, Canada, *Canadian Journal of Earth Sciences*, 26(8), 1533-1556.

Schulte-Pelkum, V., G. Monsalve, A. Sheehan, M. R. Pandey, S. Sapkota, R. Bilham, and F. Wu (2005), Imaging the Indian subcontinent beneath the Himalaya, *Nature*, 435(7046), 1222-1225.

Searle, M. P., S. R. Noble, A. J. Hurford, and D. C. Rex (1999), Age of crustal melting, emplacement and exhumation history of the Shivling leucogranite, Garhwal Himalaya, *Geological Magazine*, 136(5), 513-525.

Searle, M. P. (2007), Geological map of the Mount Everest – Makalu region Nepal – South Tibet Himalaya scale 1:100 000., Oxford University, Dept. of Earth Sciences.

Seong, Y. B., L. A. Owen, M. P. Bishop, A. Bush, P. Clendon, L. Copland, R. Finkel, U. Kamp, and J. F. Shroder (2007), Quaternary glacial history of the central karakoram, *Quaternary Science Reviews*, 26(25-28), 3384-3405.

Seong, Y. B., L. A. Owen, C. L. Yi, and R. C. Finkel (2009), Quaternary glaciation of Muztag Ata and Kongur Shan: Evidence for glacier response to rapid climate changes throughout the Late Glacial and Holocene in westernmost Tibet, *Geological Society of America Bulletin*, 121(3-4), 348-365.

Shen, F., L. H. Royden, and B. C. Burchfiel (2001), Large-scale crustal deformation of the Tibetan Plateau, *Journal of Geophysical Research-Solid Earth*, 106(B4), 6793-6816.

Shen, Z. K., C. K. Zhao, A. Yin, Y. X. Li, D. D. Jackson, P. Fang, and D. N. Dong (2000), Contemporary crustal deformation in east Asia constrained by Global Positioning System measurements, *Journal of Geophysical Research-Solid Earth*, 105(B3), 5721-5734.

Siame, L., O. Bellier, R. Braucher, M. Sebrier, M. Cushing, D. Bourles, B. Hamelin, E. Baroux, B. de Voogd, G. Raisbeck, and F. Yiou (2004), Local erosion rates versus active tectonics: cosmic ray exposure modelling in Provence (south-east France), *Earth and Planetary Science Letters*, 220(3-4), 345-364.

Siame, L. L., R. Braucher, D. L. Bourles, O. Bellier, and M. Sebrier (2001), Cosmic ray exposure dating of geomorphic surface features using in situ-production Be-10: tectonic and climatic implications, *Bulletin De La Societe Geologique De France*, 172(2), 223-236.

Simpson, R. L., R. R. Parrish, M. P. Searle, and D. J. Waters (2000), Two episodes of monazite crystallization during metamorphism and crustal melting in the Everest region of the Nepalese Himalaya, *Geology*, 28(5), 403-406.

Spear, F. S. (1993), *Metamorphic Phase Equilibria and Pressure Temperature Time Paths*. 2nd Eds., Mineralogical Society of America, Washington, DC.

Stockli, D. F., M. H. Taylor, A. Yin, T. M. Harrison, J. D'andrea, P. Kapp, and L. Ding (2002), Late Miocene-Pliocene inception of the E-W, extension in Tibet as evidenced by apatite (U-Th)/He data, *Geological Society of America*, 2002 annual meeting.

Stone, J. O. (2000), Air pressure and cosmogenic isotope production, *Journal of Geophysical Research-Solid Earth*, 105(B10), 23753-23759.

Szulc, A. G., Y. Najman, H. D. Sinclair, M. Pringle, M. Bickle, H. Chapman, E. Garzanti, S. Ando, P. Huyghe, J. L. Mugnier, T. Ojha, and P. DeCelles (2006), Tectonic evolution of the Himalaya constrained by detrital Ar-40-Ar-39, Sm-Nd and petrographic data from the Siwalik foreland basin succession, SW Nepal, *Basin Research*, 18(4), 375-391.

Tapponnier, P., and P. Molnar (1977), Active faulting and tectonics in China, *Journal of Geophysical Research*, 82(20), 2905-&.

Tapponnier, P., J. L. Mercier, R. Armijo, T. L. Han, and J. Zhou (1981), Field Evidence for Active Normal Faulting in Tibet, *Nature*, 294(5840), 410-414.

Tapponnier, P., J. L. Mercier, F. Proust, J. Andrieux, R. Armijo, J. P. Bassoulet, M. Brunel, J. P. Burg, M. Colchen, B. Dupre, J. Girardeau, J. Marcoux, G. Mascle, P. Matte, A. Nicolas, T. D. Li, X. C. Xiao, C. F. Chang, P. Y. Lin, G. C. Li, N. W. Wang, G. M. Chen, T. L. Han, X. B. Wang, W. M. Den, H. X. Zhen, H. B. Sheng, Y. G. Cao, J. Zhou, and H. S. Qiu (1981), The Tibetan side of the India-Eurasia collision, *Nature*, 294(5840), 405-410.

Tapponnier, P., Z. Q. Xu, F. Roger, B. Meyer, N. Arnaud, G. Wittlinger, and J. S. Yang (2001), Geology - Oblique stepwise rise and growth of the Tibet plateau, *Science*, 294(5547), 1671-1677.

Taylor, M., A. Yin, F. J. Ryerson, P. Kapp, and L. Ding (2003), Conjugate strike-slip faulting along the Bangong-Nujiang suture zone accommodates coeval east-west extension and north-south shortening in the interior of the Tibetan Plateau, *Tectonics*, 22(4).

- Thatcher, W. (2007), Microplate model for the present-day deformation of Tibet, *Journal of Geophysical Research-Solid Earth*, 112(B1).
- Thiede, R. C., B. Bookhagen, J. R. Arrowsmith, E. R. Sobel, and M. R. Strecker (2004), Climatic control on rapid exhumation along the Southern Himalayan Front, *Earth and Planetary Science Letters*, 222(3-4), 791-806.
- Thompson, A. B., and J. A. D. Connolly (1995), Melting of the Continental-Crust - Some Thermal and Petrological Constraints on Anatexis in Continental Collision Zones and Other Tectonic Settings, *Journal of Geophysical Research-Solid Earth*, 100(B8), 15565-15579.
- Thompson, L. G., T. Yao, M. E. Davis, K. A. Henderson, E. Mosley-Thompson, P. N. Lin, J. Beer, H. A. Synal, J. ColeDai, and J. F. Bolzan (1997), Tropical climate instability: The last glacial cycle from a Qinghai-Tibetan ice core, *Science*, 276(5320), 1821-1825.
- Van der Woerd, J., F. J. Ryerson, P. Tapponnier, Y. Gaudemer, R. Finkel, A. S. Meriaux, M. Caffee, Z. Guoguang, and H. Qunlu (1998), Holocene left-slip rate determined by cosmogenic surface dating on the Xidatan segment of the Kunlun fault (Qinghai, China), *Geology*, 26(8), 695-698.
- Van der Woerd, J., X. W. Xu, H. B. Li, P. Tapponnier, B. Meyer, F. J. Ryerson, A. S. Meriaux, and Z. Q. Xu (2001), Rapid active thrusting along the northwestern range front of the Tanghe Nan Shan (western Gansu, China), *Journal of Geophysical Research-Solid Earth*, 106(B12), 30475-30504.
- Van Der Woerd, J., P. Tapponnier, F. J. Ryerson, A. S. Meriaux, B. Meyer, Y. Gaudemer, R. C. Finkel, M. W. Caffee, G. G. Zhao, and Z. Q. Xu (2002), Uniform postglacial slip-rate along the central 600 km of the Kunlun Fault (Tibet), from Al-26, Be-10, and C-14 dating of riser offsets, and climatic origin of the regional morphology, *Geophysical Journal International*, 148(3), 356-388.
- Van der Woerd, J., Y. Klinger, K. Sieh, P. Tapponnier, F. J. Ryerson, and A. S. Meriaux (2006), Long-term slip rate of the southern San Andreas Fault from Be-10-Al-26 surface exposure dating of an offset alluvial fan, *Journal of Geophysical Research-Solid Earth*, 111(B4).
- Vance, D., and E. Mahar (1998), Pressure-temperature paths from P-T pseudosections and zoned garnets: Potential, limitations and examples from the Zanskar Himalaya, NW India, *Contributions to Mineralogy and Petrology*, 132(3), 225-245.
- Vance, D., and N. Harris (1999), Timing of prograde metamorphism in the Zanskar Himalaya, *Geology*, 27(5), 395-398.
- Vannay, J. C., Z. D. Sharp, and B. Grasemann (1999), Himalayan inverted metamorphism constrained by oxygen isotope thermometry, *Contributions to Mineralogy and Petrology*, 137(1-2), 90-101.

- Vannay, J. C., B. Grasemann, M. Rahn, W. Frank, A. Carter, V. Baudraz, and M. Cosca (2004), Miocene to Holocene exhumation of metamorphic crustal wedges in the NW Himalaya: Evidence for tectonic extrusion coupled to fluvial erosion, *Tectonics*, 23(1), DOI: 10.1029/2002TC001429
- Vassallo, R., J. F. Ritz, R. Braucher, and S. Carretier (2005), Dating faulted alluvial fans with cosmogenic Be-10 in the Gurvan Bogd mountain range (Gobi-Altay, Mongolia): climatic and tectonic implications, *Terra Nova*, 17(3), 278-285.
- Vavra, G., R. Schmid, and D. Gebauer (1999), Internal morphology, habit and U-Th-Pb microanalysis of amphibolite-to-granulite facies zircons: geochronology of the Ivrea Zone (Southern Alps), *Contributions to Mineralogy and Petrology*, 134(4), 380-404.
- Villa, I. M. (1994), Multipath ar transport in K-Feldspar deduced from isothermal heating experiments, *Earth and Planetary Science Letters*, 122(3-4), 393-401.
- Villa, I. M., and M. Puxeddu (1994), Geochronology of the Larderello geothermal field: new data and the “closure temperature” issue, *Contributions to Mineralogy and Petrology*, 115(4), 415-426.
- Villa, I. M. (1996), Age and cooling history of the Manaslu granite: Implications for Himalayan tectonics - Comment, *Journal of Volcanology and Geothermal Research*, 70(3-4), 255-261.
- Viskupic, K., and K. V. Hodges (2001), Monazite-xenotime thermochronometry: methodology and an example from the Nepalese Himalaya, *Contributions to Mineralogy and Petrology*, 141(2), 233-247.
- Visona, D., and B. Lombardo (2002), Two-mica and tourmaline leucogranites from the Everest-Makalu region (Nepal-Tibet). Himalayan leucogranite genesis by isobaric heating?, *Lithos*, 62(3-4), 125-150.
- Wager, L. R. (1937), The Arun River Drainage Pattern and the Rise of the Himalaya. , *The Geographical Journal*, 89(3), 239-250.
- Walker, J. D., M. W. Martin, S. A. Bowring, M. P. Searle, D. J. Waters, and K. V. Hodges (1999), Metamorphism, melting, and extension: Age constraints from the High Himalayan Slab of southeast Zanskar and northwest Lahaul, *Journal of Geology*, 107(4), 473-495.
- Wang, Q., P. Z. Zhang, J. T. Freymueller, R. Bilham, K. M. Larson, X. Lai, X. Z. You, Z. J. Niu, J. C. Wu, Y. X. Li, J. N. Liu, Z. Q. Yang, and Q. Z. Chen (2001), Present-day crustal deformation in China constrained by global positioning system measurements, *Science*, 294(5542), 574-577.
- Wu, Z., X. Zhao, Z. Wu, W. Jiang, D. Hu, and C. Zhou (2004), Quaternary geology anf faulting in the Damxung-Yangbajain Basin, *Acta Geologica Sinica*, 78(1), 273-282.

- Wu, Z., P. J. Barosh, X. Zhao, Z. Wu, D. Hu, and Q. Liu (2007), Miocene tectonic evolution from dextral-slip thrusting to extension in the Nyainqntanglha region of the Tibetan Plateau, *Acta Geologica Sinica*, 81(3), 365-384.
- Wu, Z. H., Y. S. Zhang, D. G. Hu, X. T. Zhao, and P. S. Ye (2009), Late Quaternary normal faulting and its kinematic mechanism of eastern Piedmont fault of the Haba-Yulong Snow Mountains in northwestern Yunnan, China, *Science in China Series D-Earth Sciences*, 52(10), 1470-1484.
- Xu, R.-H. (1985), Magmatism and metamorphism in the Lhasa Block (Tibet); a geochronological study, in *Journal of Geology*, edited by U. Schaefer and C. J. Allegre, pp. 41-57, University of Chicago Press : Chicago, IL, United States, United States.
- Yin, A., T. M. Harrison, F. J. Ryerson, W. J. Chen, W. S. F. Kidd, and P. Copeland (1994), Tertiary structural evolution of the Gangdese thrust system, Southeastern Tibet, *Journal of Geophysical Research-Solid Earth*, 99(B9), 18175-18201.
- Yin, A., T. M. Harrison, M. A. Murphy, M. Grove, S. Nie, F. J. Ryerson, W. X. Feng, and C. Z. Le (1999), Tertiary deformation history of southeastern and southwestern Tibet during the Indo-Asian collision, *Geological Society of America Bulletin*, 111(11), 1644-1664.
- Yin, A., P. A. Kapp, M. A. Murphy, C. E. Manning, T. M. Harrison, M. Grove, D. Lin, X. G. Deng, and C. M. Wu (1999), Significant late Neogene east-west extension in northern Tibet, *Geology*, 27(9), 787-790.
- Yin, A. (2000), Mode of Cenozoic east-west extension in Tibet suggesting a common origin of rifts in Asia during the Indo-Asian collision, *Journal of Geophysical Research-Solid Earth*, 105(B9), 21745-21759.
- Yin, J. X., J. T. Xu, C. J. Liu, and H. Li (1988), The Tibetan plateau - regional stratigraphic context and previous work, *Philosophical Transactions of the Royal Society of London Series a-Mathematical Physical and Engineering Sciences*, 327(1594), 5-&.
- Zhang, J. J., and L. Guo (2007), Structure and geochronology of the southern Xainza-Dinggye rift and its relationship to the south Tibetan detachment system, *Journal of Asian Earth Sciences*, 29(5-6), 722-736.
- Zhang, K. J., B. D. Xia, G. M. Wang, Y. T. Li, and H. F. Ye (2004), Early Cretaceous stratigraphy, depositional environments, sandstone provenance, and tectonic setting of central Tibet, western China, *Geological Society of America Bulletin*, 116(9-10), 1202-1222.

6. ANNEXES

ANNEXE A

Leloup, P. H., G. Maheo, N. Arnaud, E. Kali, E. Boutonnet, D. Y. Liu, X. H. Liu, and H. B. Li (2010), The South Tibet detachment shear zone in the Dinggye area Time constraints on extrusion models of the Himalayas, *Earth and Planetary Science Letters*, **292**(1-2), 1-16.



The South Tibet detachment shear zone in the Dinggye area Time constraints on extrusion models of the Himalayas

P.H. Leloup ^{a,*}, G. Mahéo ^a, N. Arnaud ^b, E. Kali ^c, E. Boutonnet ^a, Dunyi Liu ^d, Liu Xiaohan ^e, Li Haibing ^d

^a CNRS UMR 5570 Université Lyon1 – ENS Lyon, Villeurbanne, France

^b Géosciences Montpellier, Université de Montpellier2, Montpellier France

^c Institut de Physique du Globe de Strasbourg (CNRS, UDS/EOST), UMR 7516, Strasbourg, France

^d Laboratory of Continental Dynamics, Institute of Geology, CAGS, Beijing, China

^e Institute of Tibetan Plateau Research, Chinese Academy of Sciences, Beijing, China

ARTICLE INFO

Article history:

Received 26 October 2009

Received in revised form 17 December 2009

Accepted 17 December 2009

Available online 6 February 2010

Editor: T.M. Harrison

Keywords:

Himalaya

South Tibet Detachment System

chronology

extrusion

ABSTRACT

We investigate the timing of end of motion along the South Tibet Detachment System (STDS), a major normal fault system that runs parallel to the Himalayan range for more than 1500 km. Near Dinggye ($\sim 28^{\circ}10'N, 87^{\circ}40'E$), the STDS dips $\sim 10 \pm 5'$ to the North and separates Paleozoic Tethyan series from Upper Himalayan Crystalline Series (UHCS). Immediately below the STDS, the UHCS is highly deformed in the STDS shear zone, lineations trend NNE and the shear senses are top to the NE. In micaschist, the P-T path constrained by pseudosection and garnet chemistry, shows successive metamorphic conditions of ~ 0.6 GPa and ~ 550 °C and 0.5 GPa and 625 °C. U/Pb dating of monazites and zircons in deformed and undeformed leucogranites suggests that ductile deformation lasted until at least ~ 16 Ma but ended prior to ~ 15 Ma in the STDS shear zone ~ 100 m below the detachment. Ar/Ar micas ages in the footwall span between ~ 14.6 and 13.6 Ma, indicating rapid cooling down to ~ 320 °C, and suggesting persistence of normal faulting, at that time. The STDS is cut and offset by the N-S trending Dinggye active normal fault which initiated prior to 11 Ma thus providing a minimum bound for the end of STDS motion. These data are interpreted as reflecting 0.3 GPa (11 km) to 0.6 GPa (22 km) of exhumation along the STDS starting prior to ~ 16 Ma, ending between 13.6 and 11 Ma. The 1000 km long stretch of the STDS east of the Gurla Mandata probably stopped almost synchronously between 13 and 11 Ma ago, coevally with a sudden switch from NNE-SSW to E-W extension at the top of the accretionary prism, with a jump of the major thrust from the lower Main Central Thrust (MCT) to the Main Boundary Thrust (MBT), and with a change in the India and Asia convergence direction. This synchronism is probably better explained in the frame of a thrust wedge or thrust system model than a lower channel flow model. West of the Gurla Mandata the STDS appears to stop 5 to 3 Ma earlier, possibly related to local interactions with the Karakorum fault in a way that needs to be understood.

© 2009 Elsevier B.V. All rights reserved.

1. Introduction

Since its discovery the South Tibet Detachment System (STDS) has drove the attention of many scientists as this major structure that parallel for more than 1500 km the Himalayan range, which is the archetype of a compressive thrust belt, shows normal faulting in a direction almost parallel to the direction of thrusting (Fig. 1a) (Burg, 1983; Burchfiel et al., 1992). This paradox has inspired a series of deformation models. Early models assumed that the STDS was merging at depth with the Main Central Thrust (MCT), isolating a crustal wedge expulsed upwards (e.g., Burg et al., 1984; Burchfiel and Royden, 1985; England and Molnar, 1993; Hodges et al., 1996; Grujic et al., 1996; Grasemann et al., 1999). Following numerical models

analysis, a second class of models considers that the STDS and MCT never merge, but define respectively the top and the bottom of a channel flow of low-viscosity lower crust expulsed from beneath the Tibetan plateau (e.g., Beaumont et al., 2001). This last mechanism is often considered to be enhanced by focussed erosion on the Himalayan southern slopes. A third class of model, considers that the STDS and the MCT accommodate the southward intrusion of high crystalline series (“tectonic-wedging” of Price, 1986). The main difference with that of the crustal wedge models is that the STDS and MCT merge southward, and that the STDS emerges northward as the Greater Counter Thrust (Yin, 2006; Webb et al., 2007).

Central to all these models are the extent, geometry and kinematics (direction, amount, and timing) of the STDS normal faulting, and their relationships with the MCT. Despite numerous studies, the precise timing of initiation and end of the STDS stays controversial as it is often determined indirectly i.e. from the emplacement timing of granites that are interpreted to be genetically

* Corresponding author. Tel.: +33 4 72 44 62 38; fax: +33 4 72 44 85 93.
E-mail address: herve.leloup@univ-lyon1.fr (P.H. Leloup).

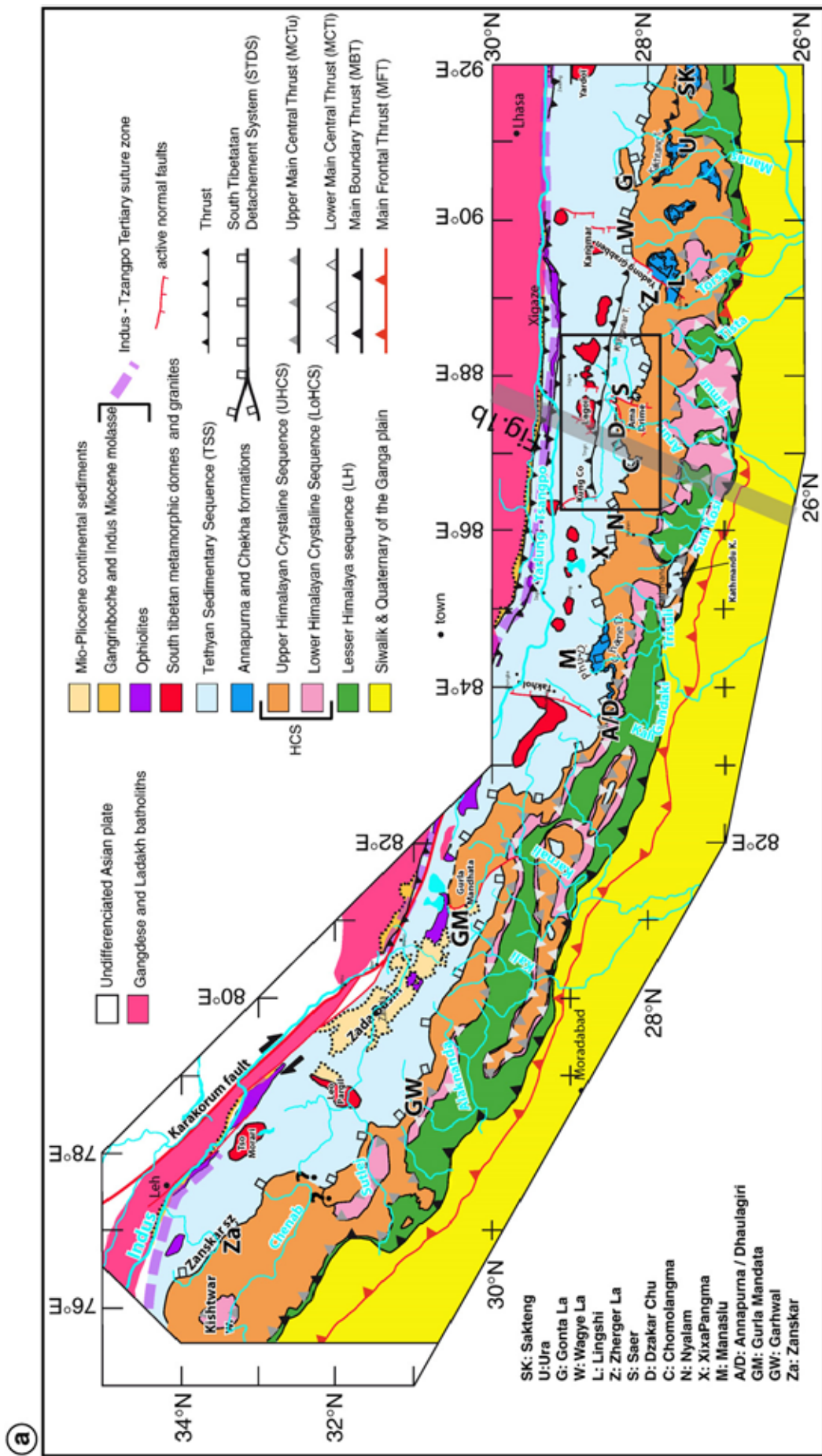


Fig. 1. Himalayas structural map and cross section. a) Simplified structural map of the Himalayan range between 76 and 92°E. Black frame corresponds to Fig. 2a map area and grey trace to Fig. 1b cross section. Bold letters refer to main STDs sites (see Table DR7). An upper and a lower MCT have been distinguished. The trace of the main structures are drawn from local studies (from east to west) by Kellet et al. (2009), Dasgupta et al. (2004), Kali et al. (in press), Searle et al. (1997), Searle and Godin (2003), Decelles et al. (2004), Vannay et al. (2004), and Dèzes et al. (1999, b). Simplified cross section of the Himalayas, NNE-SSW interpretative cross section at ~87°E, a few kilometres west of the Ama Drime range. Main geological units as in Fig. 1a, and main structures geometry from Bollinger et al. (2004). The green line corresponds to the upper relief (i.e., Chomolongma) and the blue line to the lower relief (i.e., Arun valley), no vertical exaggeration. KT, Kangmar thrust; GCT, Great Counter thrust; YT, Yarlung-Tsangpo suture zone.

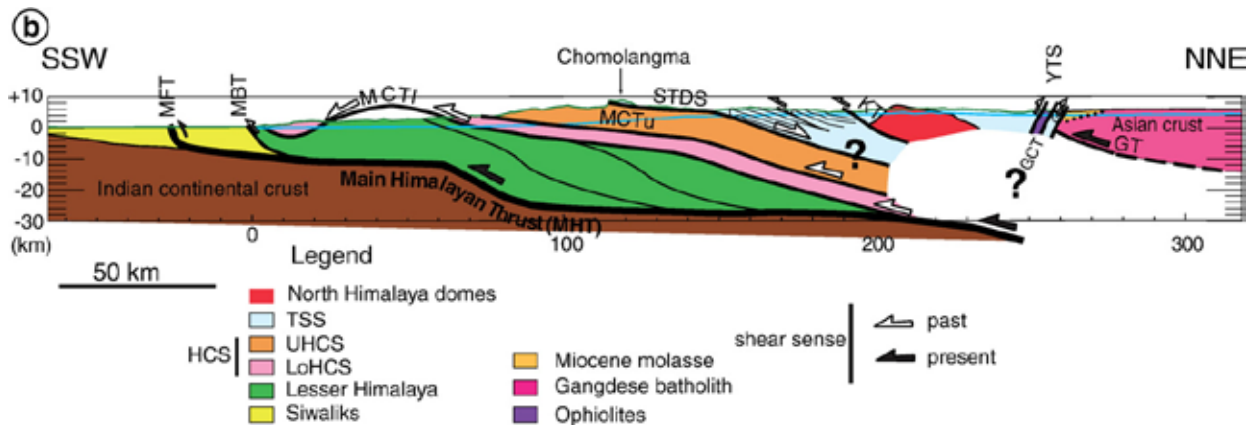


Fig. 1 (continued).

linked with the STDS. Here we present a combination of structural, petrographic and geochronologic data that allow us to constrain precisely the timing of the end of STDS normal faulting in the Dinggye area. We then compare this timing with published age elsewhere along the STDS and discuss implications for the Himalayan orogen evolution.

2. The South Tibet Detachment System (STDS)

The South Tibetan Detachment System corresponds to a series of north dipping structures accommodating top to the North/normal motion of the Tethyan sedimentary series (TSS) of South Tibet with respect to the underlying High Himalayan crystalline series or Himalayan crystalline slab (HCS) (Fig. 1b) (e.g. Burg, 1983; Burg et al., 1984; Burchfiel et al., 1992). Normal motion has occurred on several ~parallel low dipping structures that are from top to bottom: a) few brittle normal faults in the TSS, b) a detachment at the contact between the un-metamorphosed TSS and the underlying metamorphic rocks that will be referred here as the STD and c) a ductile shear zone at the top of the HCS, the STD shear zone, where gneisses are highly deformed, lineation trends NE and numerous shear criteria indicate a normal motion (e.g., Burg et al., 1984; Burchfiel et al., 1992; Edwards et al., 1996; Searle et al., 1997; Carosi et al., 1998). The TSS spans in age from Ordovician to Eocene and are not metamorphosed, unless for a narrow zone of greenschist metamorphism immediately above the STD, and contact aureoles around the North Himalayan (or South Tibetan) Cenozoic plutons outcropping as a discontinuous belt ~70 km north of the STD (Fig. 1a). The HCS shows a much higher degree of metamorphism. The STDS has been studied along several sections, spanning from Zanskar (~76°E) to the Gonto La (~90°E) (Fig. 1a). The upper HCS series are intruded by numerous large leucogranites plutons and sills, which never crosscut the STD. These granites have been interpreted as having triggered STDS motion (e.g., Burchfiel et al., 1992), or as a consequence of decompression induced by the STDS motion (e.g., Harris et al., 2004). In many cases ages of the leucogranites have been taken as reflecting motion along the STDS. The presence of top to the south structures at the base of the TSS close or within the STD shear zone (e.g., Vannay and Hodges, 1996; Coleman and Hodges, 1998; Godin et al., 2001; Vannay et al., 2004) is generally interpreted as the evidence for Top to the South thrusting on the STDS prior to the onset of top to the North normal faulting (*ibid*), or by multiple alternation in shear sense along the STD (Yin, 2006; Webb et al., 2007).

In the Chomolangma area (Fig. 1a and 2a), two low-angle normal faults, which merge to the north into a unique structure, affect the upper part of the HCS (Carosi et al., 1998; Searle, 1999). The upper

fault, the Chomolangma detachment, corresponds to the STD and outcrops just below the summit of the Chomolangma separating the un-metamorphosed Ordovician sedimentary rock above from the North col formation below. The lower Lothse detachment is a ductile shear zone at the top of the HCS. The occurrence of two, possibly diachronous, superpose low-angle normal faults has been reported along other sections of the STDS, for example in the Nar valley east of the Manaslu (Godin et al., 2006a) or in Bhutan (Edwards et al., 1996; Kellett et al., 2009). Some have proposed that the upper STD could still be active east of the Anapurnas in the Takhola graben (Hurtado et al., 2001). Other proposed that there is a major change in the STD kinematics (direction and timing) east of the Yadong graben (Wu et al., 1998; Kellett et al., 2009).

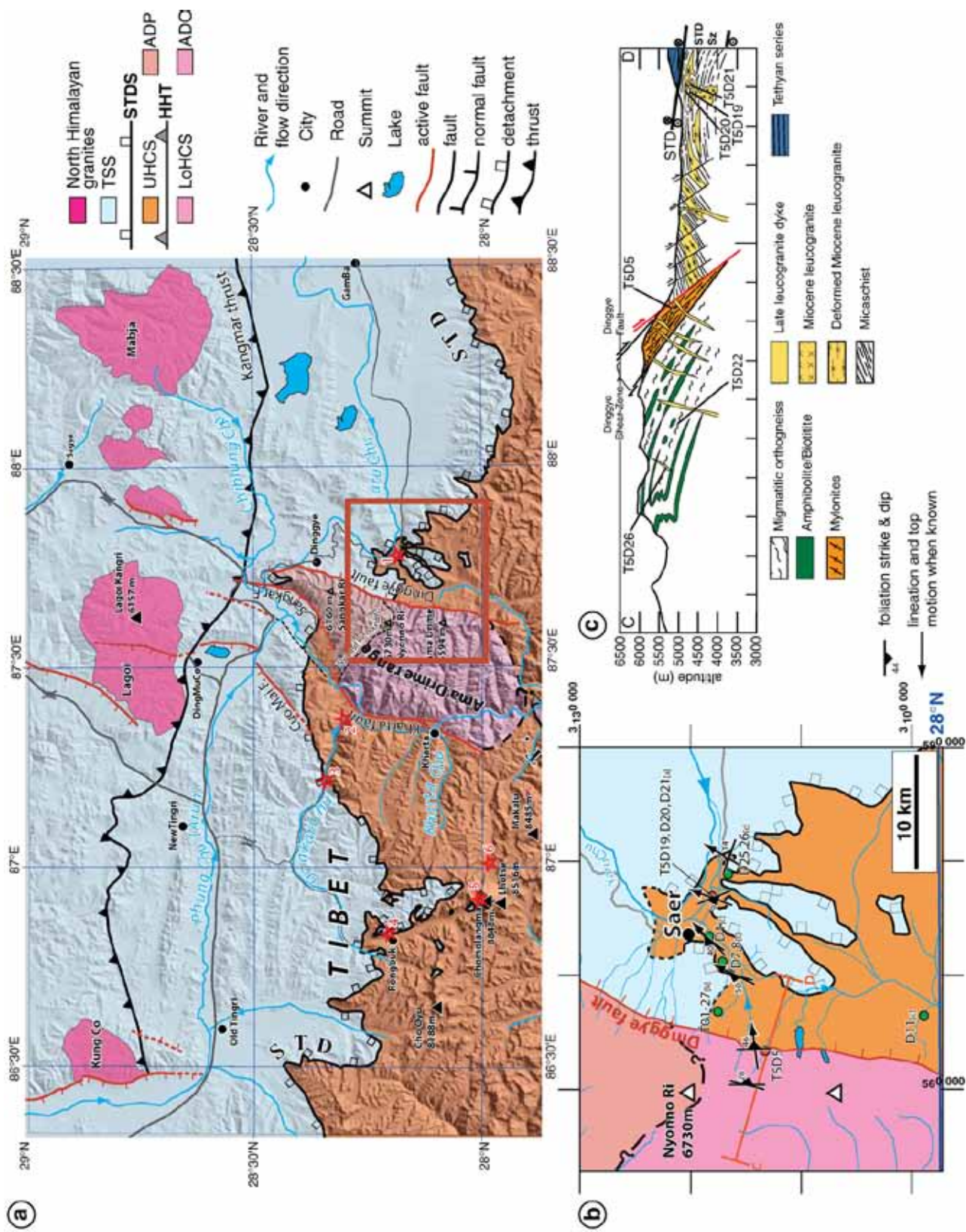
3. Geological setting of the Ama Drime range and surrounding area

3.1. General structure of the central Himalayas

In the central Himalayas, the main litho-tectonic units define strips, more or less parallel to the range, dipping to the north and separated by major tectonic contacts. The central unit, the Himalayan crystalline slab (HCS) is a sliver of gneiss and granites, sandwiched between less metamorphosed rocks (Fig. 1). To the bottom (South) the HCS rests on the phyllites and quartzites of the Lesser Himalaya (LH, Tumlingtar unit). To the top (North) the HCS is separated from the weakly metamorphosed Tethyan sedimentary series (TSS) by the South Tibetan detachment (STD). South of the Ama Drime range, in the Arun area two main litho-tectonic units can be distinguished within the HCS: the Lower and Upper Himalayan crystalline series (LoHCS and UHCS) (Kali et al., *in press*). The LoHCS is mostly composed of strongly deformed rocks with metapelites overlying the Num/Ulleri orthogneiss. These latter are bounded at their base by mylonites (Bordet, 1961; Meier and Hiltner, 1993; Goscombe et al., 2006). The basal contact of the LoHCS will be referred here as the lower Main Central Thrust or MCT (Fig. 1). The UHCS consists mostly of paragneiss, often migmatitic, intruded by Miocene leucogranites (e.g., Borghi et al., 2003). The base of the UHCS also corresponds to a thrust zone: the High Himal Thrust (Goscombe et al., 2006) (MCT of Brunel, 1983; Goscombe and Hand, 2000) that is laterally equivalent to the upper MCT (MCTu, Fig. 1; Kali et al., *in press*).

3.2. The Ama Drime range

The Ama Drime range is a N–S crest culminating at 6730 m a.s.l. (Nyonni Ri), protruding north of the main stretch of the Himalaya



between the Kanchengjunga (8586 m) and the Chomolangma/Everest (8848 m) (Figs. 1a and 2a).

The Ama Drime range is a horst bounded on both sides by N-S active faults at the southern end of the Xainza-Dinggye fault system (e.g., Armijo et al., 1986). Recent activity of the Kharta fault to the west and Dinggye fault to the east are attested by spectacular triangular facets, brittle fault planes, and cataclasites (e.g., Armijo et al., 1986; Holland et al., 1998; Zhang and Guo, 2007; Kali et al., in press). On the eastern side of the range, normal faults parallel to the Dinggye fault slice the foothills to at least 5 km away from the topographic front and have tilted to the west the metamorphic series of the STD shear zone (Burchfiel et al., 1992) (Fig. 2c). Age versus elevation relationship of (U-Th)/He apatite from the Ama Drime suggests an exhumation rate of ~1 mm/yr between ~4 and 1.5 Ma (Jessup et al., 2008b; Kali et al., in press).

Most rocks comprised between the Kharta and Dinggye active faults are migmatitic orthogneiss containing large layers and boudins of metabasites that have recorded eclogite facies metamorphism, (Lombardo and Rolfo, 2000; Groppe et al., 2007; Cottle et al., 2009; Kali et al., in press). These rocks have been designated as the Ama Drime orthogneissic unit (ADO, Fig. 2a) and attributed to the LoHCS (Kali et al., in press) (Fig. 2a). In the northern part of the Ama drime, paragneiss is associated with rare amphibolites and is intruded by numerous leucogranites. These rocks define the Ama Drime paragneissic unit (ADP) that most probably belongs to the UHCS (Kali et al., in press) (Fig. 2).

On both flanks of the Ama Drime, in the immediate footwall of the active normal faults, the HCS rocks are affected by pervasive normal ductile deformation in the Kharta and Dinggye shear zones (Burchfiel et al., 1992; Zhang and Guo, 2007; Jessup et al., 2008b; Kali et al., in press).

3.3. The STDS in the Dinggye–Karta area

Near the Ama Drime range, the STD has been described across the Dzakar river (Burg et al., 1984; Cottle et al., 2007, 2009) (stars 2 and 3, Fig. 2a), and south of Dinggye near Saer (Burchfiel et al., 1992) (star 1, Fig. 2a). The STD separates deformed micaschist of the HCS containing leucogranite pods below, from weakly metamorphosed Tethyan sedimentary series above. Combining published observations, our own field work, and Landsat satellite image interpretation, we propose a map of the STD (Fig. 2a,b). This mapping confirms that the STD is deflected to the north around the Ama Drime range, and is cut and offset by the N-S normal faults and shear zones (Burchfiel et al., 1992; Zhang and Guo, 2007; Jessup et al., 2008b; Kali et al., in press). Kali et al. (in press) estimate that the apparent vertical offsets of the STD are 4.4 to 9.4 km and 1.3 to 4 km along the Dinggye and Sangkar faults respectively.

Below the detachment, in the STD shear zone (STDsz), high-temperature deformation affecting both the micaschists and the leucogranites is characterized by ~E–W foliations dipping to the north, NE trending lineation and top to the north sense of shear (Figs. 3 and 4a).

Near Dinggye, the STD dips $\sim 10 \pm 5^\circ$ to the NNE. Because they have been tilted by late N-S normal faults, foliations locally dip to the NW ($\sim 45^\circ$ on average), but lineation constantly trends NE (Table DR1, Figs. 2c and 3f). Where not affected by late normal faults the micaschist are almost horizontal and the lineation trends NNE (Fig. 3d and f). If foliations tilted in between the late normal faults, are rotated back to nearly horizontal, the corresponding lineation trends N25 in good agreement with the not tilted ones (Fig. 3g).

4. P-T-t-D path in the STD shear zone near Dinggye

South of Dinggye, ~100 m below the STD (outcrop 05-222, N28°11'4.5" E87°46'51.4"), garnet micaschists (sample T5D19) and leucogranites (sample T5D20) are deformed together showing top to the NE shear sense. Few undeformed leucogranites (sample T5D21) crosscut the deformed leucogranites and micaschist (Table DR2, Figs. 2c and 3). Conjoint petrographic, chemical and geochronological analysis of these samples yields constraints on the P-T-D-t path of the STD shear zone.

4.1. Micaschist P-T evolution

T5D19 micaschist contain quartz, plagioclase, biotite, sillimanite, staurolite, garnet, tourmaline and rare white micas. The foliation is defined by preferential orientation of biotites and the lineation by sillimanites. This foliation surrounds aggregates containing garnet with oxides and quartz inclusions, staurolite, plagioclase, biotite and quartz relicts (Fig. 4a). Garnet also occurs outside of the aggregates, as porphyroblasts showing asymmetric biotite-sillimanite tails (Fig. 4a). Biotite and quartz inclusions within these garnets define a relict foliation oblique to the matrix one. C-S relations associated with biotite and sillimanite crystallization show top to the north high-temperature normal movement (Fig. 4a).

Two successive paragenesis are recognised:

- (1) Garnet + staurolite + biotite + quartz + plagioclase in aggregates and in the garnet porphyroblast cores.
- (2) Garnet porphyroblasts + biotite + sillimanite + quartz + plagioclase in the matrix.

Biotites in inclusions within garnet are slightly more Fe-rich than those within the foliation (X_{Fe} 0.72–0.67 and 0.63–0.65 respectively) (Table DR3). Plagioclases from the two paragenesis have similar albitic composition (X_{ab} 0.88–0.89). Staurolite has a high FeO (14.6 wt.%) and low MgO (0.9 wt.%) (Table DR3). Garnet from the aggregates and within the foliation presents the same chemical zoning. Cartographies and profiles show a simple chemical zonation characterized, from core (zone I) to rim (zone II), by almandine and pyrope increase (86 to 89% and 7.5 to 9.5% respectively) and grossular decrease (6.2 to 2.1%) (Table DR3, Fig. 4b,c). Such chemical zoning is typical of garnet growth during prograde metamorphism in greenschist and amphibolite facies rocks (Holland et al., 1998).

Mineral assemblage of the studied metapelites can be described in the NCKFMASH system (Holland et al., 1998). Perple_X'07 has been used for the calculation of pseudosections in the NCKFMASH system using the 2004 revised version of the internally consistent thermodynamic dataset of Holland and Powell (Holland and Powell, 1998). In the calculation H_2O was considered as a saturated phase and quartz as in excess. Whole-rock composition and detailed methodology are given in Appendix A.

According to the pseudosection and garnet isopleths, garnet core composition corresponds to P-T conditions of ~ 0.6 GPa and ~ 550 °C (Zone I Fig. 4d), and the rim to slightly lower P and higher T (0.5 GPa and 625 °C, zone II). Rim temperature was also constrained applying a cationic exchange garnet-biotite thermometer using the Holdaway (Holdaway, 2000) 5AV calibration. Biotite and garnet II pair in close contact give a T of 650 ± 50 °C assuming a pressure of 0.4 to 0.6 GPa. One pair implying a biotite inclusion and a garnet with composition intermediate between I and II give a slightly lower T of 590 ± 10 °C for the same P range. Altogether, pseudosection calculation as well as classical thermometry thus suggest a 100 to 150 °C heating episode and

Fig. 2. Structural frame of the studied area and samples location. a) Structural map of the STD system in the Chomolangma-Dinggye area. Drawn from previous works, satellite image interpretation and fieldwork. Red frame indicates b. Projection is UTM45. Stars locate main outcrops discussed in text – 1: 05-222; 2: Thongmön, 3: Dzakar Chu section, 4: Rongbuk monastery, 5: Chomolangma yellow band, 6: Kangshung. b) Structural map of the Saer area. The same legend as a. Samples from this study [a], Zhang and Guo (2007) [b] and Hodges et al. (1994) [c] are located as well as section C-D (see c). c) Geological cross section of the eastern flank of the Ama Drime range south of Dinggye. See Fig. 2b for location.

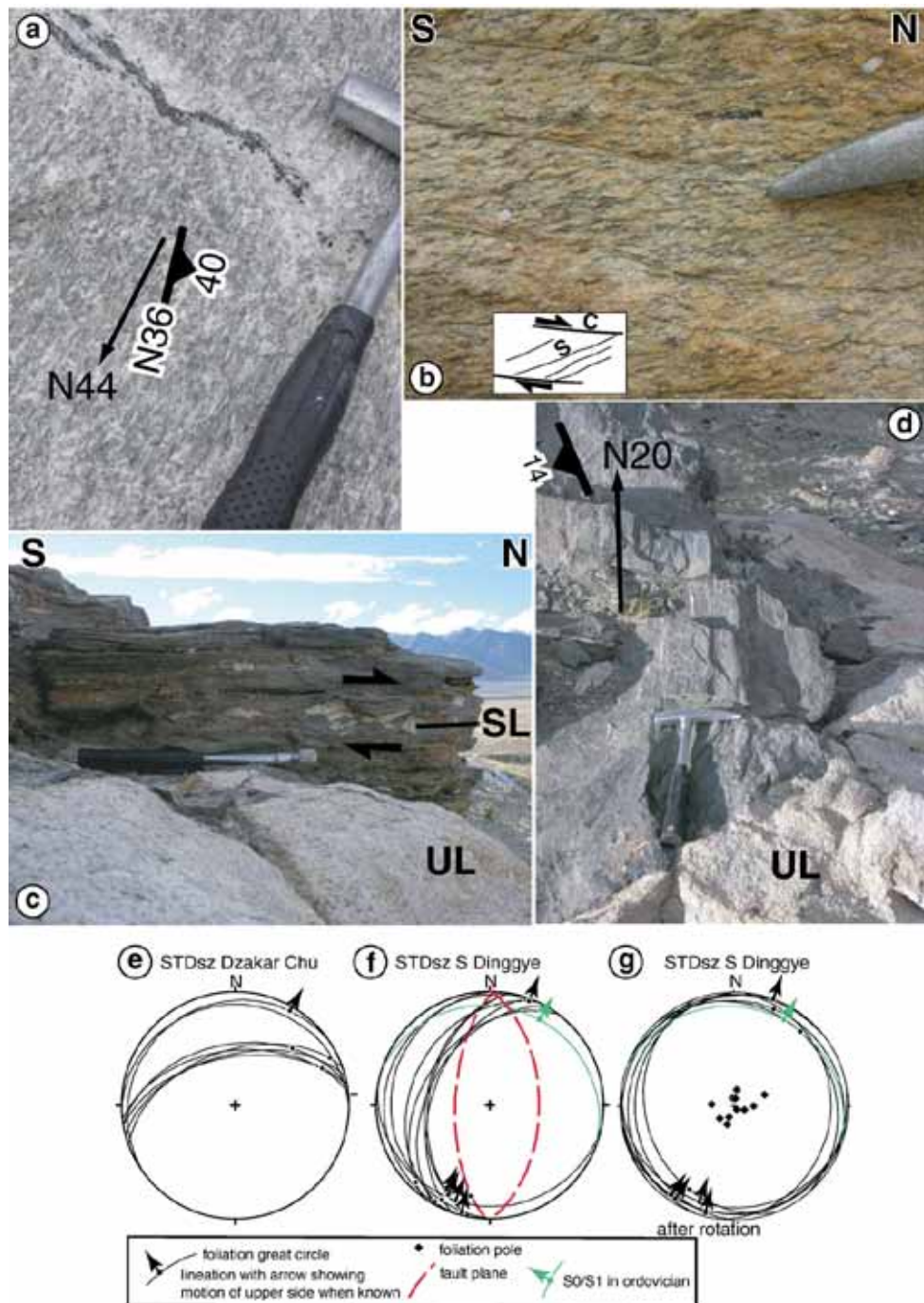


Fig. 3. Deformation characters of micaschist and leucogranites of the STD shear zone. a to d picture of outcrop 05-222, & 182 located south of Dinggye ~100 m below the STD. See Fig. 2b for location. a) Mylonitic leucogranites. Lineation is crosscut by a tourmaline bearing dyke. Oblique view from above. The hammer gives scale. b) C-S criteria indicating top the North shearing in mylonitic leucogranites (see a). The hammer gives scale. c) Flat lying micaschist (sample T5D19) with sheared levels of mylonitic leucogranite (SL, sample T5D21), intruded by undeformed leucogranite pod (UL, sample T5D20). The hammer gives scale. View towards W. d) Undeformed leucogranite pod crosscutting micaschist with N20 trending lineation. View from above. The hammer gives scale. See also c. e to g: Foliation and lineation attitude. Lower hemisphere Schmidt projection. Arrows indicate hanging wall shear direction when known. e) Foliations and lineations in the STD shear zone in the Dzakar Chu valley (stars 2 & 3, Fig. 2a). f) Foliations and lineations in the STD shear zone south of Dinggye. Outcrop 05-222 (star 1, Fig. 2a), and neighbouring outcrops. The green symbols correspond to deformation in the Ordovician sandstones. The red dashed lines are late brittle faults. g) Same as f but with foliations affected by tilting near late ~N-S faults, rotated back to nearly horizontal. Rotation axis: N18° 0°, angle: 45.5°. After rotation average lineation trends N 26°.

a slight decompression (~0.1 GPa) between the garnet core and rim. The PT path during the final exhumation is only constrained by the fact that no vordierite has been observed in thin section (Fig. 4d).

Using cationic exchange garnet–biotite thermobarometry (Hodges et al., 1994) provided P-T estimates for nearby UHCS micaschist (samples D8, D11 and D25 located on Fig. 2b). Sample D11 with

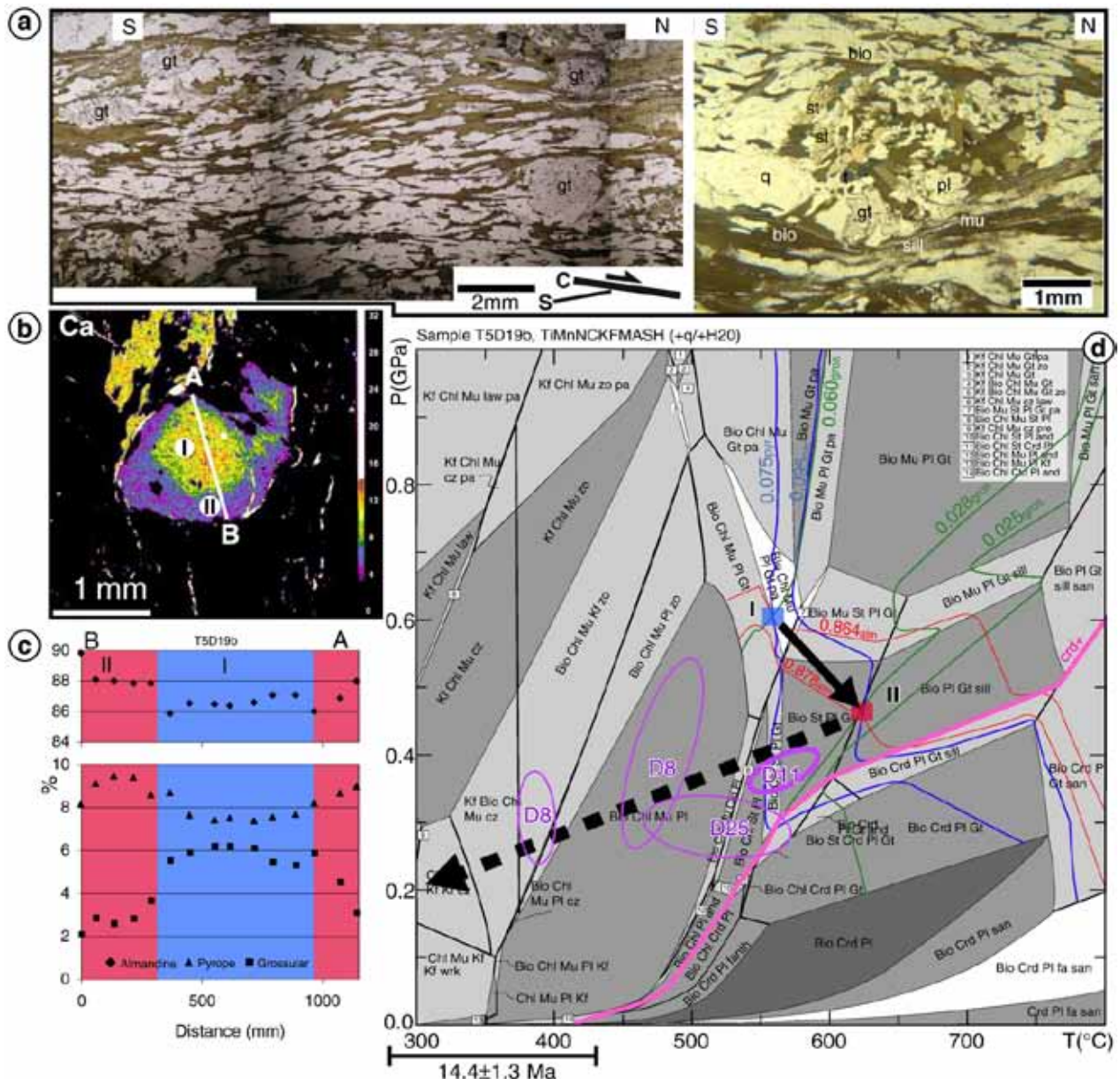


Fig. 4. P-T path in the STD Shear Zone (sample T5D19). a) T5D19 thin section pictures. Section cut parallel to lineation and perpendicular to foliation, natural light. Left: garnets in the foliation (S) and north dipping shear planes (C). Right: garnet, staurolite, plagioclase, biotite and quartz aggregate. Biotite and sillimanite underline the foliation and the shear planes. b) Ca-X-ray map and c) composition profile A-B showing chemical zoning of garnet (Table DR3). d) NCKFMASH pseudosection (Perple_X2007) for the measured whole-rock composition (Appendix A). White, light grey, medium grey and dark grey fields are di-, tri-, quadri- and quinavariant fields respectively. Mineral abbreviations follow Holland and Powell (1998). Green, red and blue lines respectively corresponds to grossular, almandine, and pyrope isopleths. Zone I corresponds to the garnet core and zone II to the garnet rim. The purple ellipses indicate P-T estimates of Hodges et al. (1994) using the garnet-biotite thermometer (Ferry and Spear, 1978). The 14.4 ± 1.3 Ma age corresponds to the average of all Ar/Ar micas ages (this work; Hodges et al., 1994; Zhang and Guo, 2007). The associate temperature (black heavy line) is based on the range of closure temperatures for biotites and muscovites (Harrison et al., 1985; Hames and Bowring, 1994).

similar mineralogy than T5D19b yields slightly lower pressure and temperature (0.4 GPa and 590 °C) than our estimate for garnet rims (Fig. 4d). Sillimanite-absent D8 and D25 samples yield lower temperatures (375–550 °C) (Fig. 4d). Given the large number of leucogranites, the whole Dinggye-Kharta series was heated at the time of intrusion, and it is improbable that the offset in temperature results from a local heating event that would have affected T5D19 but not Hodges's et al. samples. The observed temperature variations observed near Dinggye could result from varying distances to the STD

if, as in the Everest and Zanskar, the peak pressure and temperature increase with structural depth below the STD (Dézes et al., 1999; Jessup et al., 2008a). However, if D8 and D25 appear to have been sampled closer from the STD than T5D19, the structural depth of D11 is unconstrained as the STD has been eroded away in that area (Fig. 2b). Another possibility is that the temperature difference results from methodological uncertainties.

That P-T path documents a phase of slight decompression during heating from 0.6 to 0.5 GPa (from 18 to 22 km depth), followed by a

phase of decompression and cooling (Fig. 4d). A first foliation that is now visible in inclusion within most garnets developed at the time of heating. S-C structures developed during top to the north shearing in high-temperature conditions (garnet rims and sillimanite).

4.2. Geochronology

Single monazites and zircons were analysed with high resolution ion micropores, respectively the SHRIMP II at the Institute of Geology

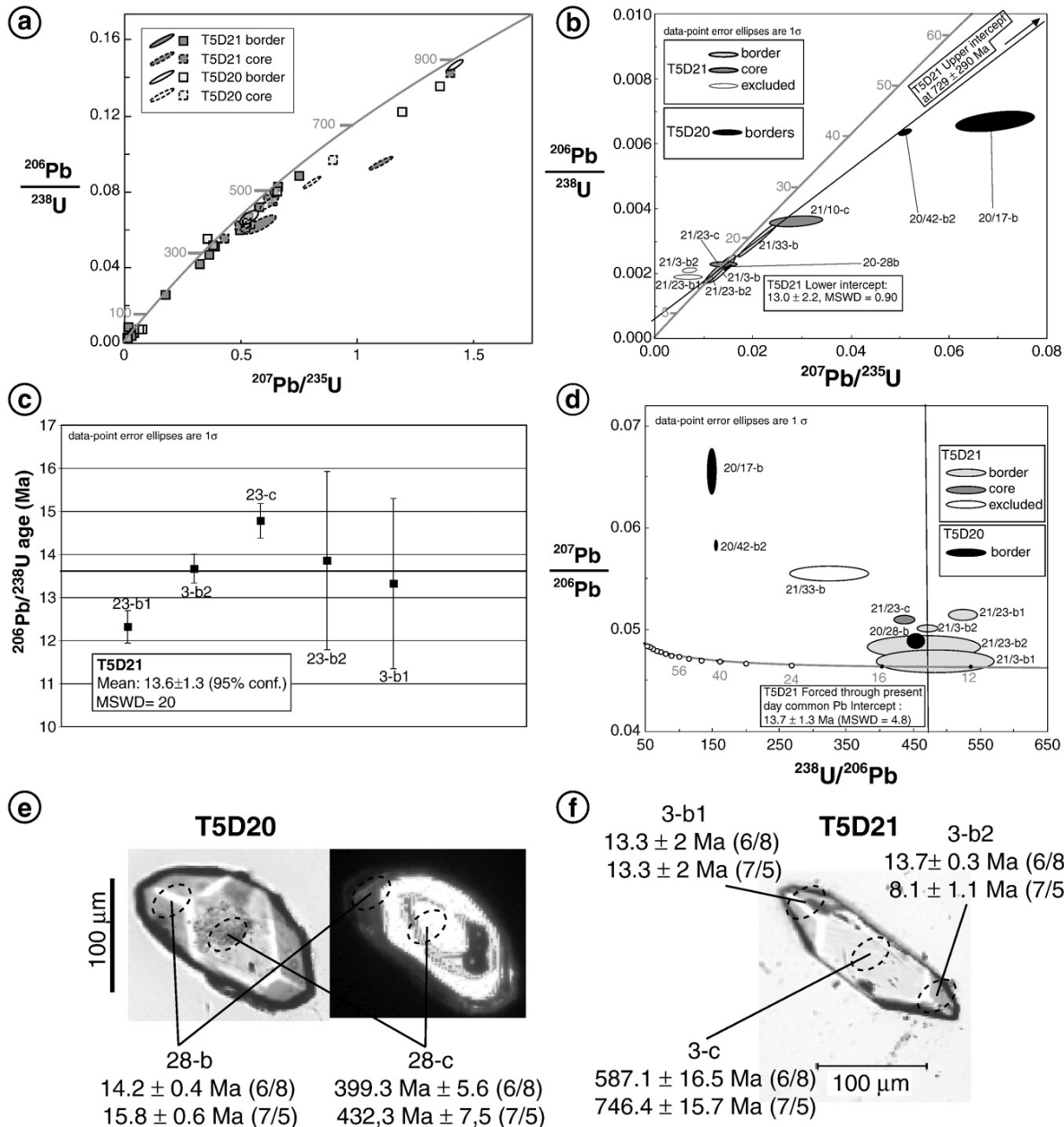


Fig. 5. T5D20 and T5D21 U/Pb results. a to f: Zircons, g to l: monazite. Corresponding data are summarized in Table 1, and listed in Table DR4 for zircons and Table DR5 for monazites. Concordia lines appear in grey. Probe spot names appear as sample/crystal-spot location. 6/8 and 7/5 refer to the $^{206}\text{Pb}/^{238}\text{U}$ and $^{207}\text{Pb}/^{235}\text{U}$ ages respectively. a) $^{206}\text{Pb}/^{238}\text{U}$ versus $^{207}\text{Pb}/^{235}\text{U}$ concordia plot for T5D21 and T5D20 zircons. Error ellipse (2 sigma) plotted only when larger than square symbol. Younger ages detailed in b). b) Cenozoic part of the $^{206}\text{Pb}/^{238}\text{U}$ versus $^{207}\text{Pb}/^{235}\text{U}$ concordia plot for T5D21 and T5D20 zircons. c) Cenozoic $^{206}\text{Pb}/^{238}\text{U}$ ages of T5D21 zircons. An average of 13.6 ± 1.3 Ma is calculated (see text for details). d) T5D20 and T5D21 zircons Tera-Wasserburg diagram, with regression forced through present day common lead for T5D21. e) Natural light (left) and cathodoluminescence (right) images of sample T5D20 zircon crystal #28 with ion probe spots and corresponding ages. f) Natural light picture of sample T5D21 zircon crystal #3 with ion probe spots and corresponding ages. g) T5D21 and T5D20 monazites $^{208}\text{Pb}/^{232}\text{Th}$ ages with proposed average ages. h) T5D20 and T5D21 monazite Tera-Wasserburg diagram, with regressions forced through present day common lead. Two populations are distinguished for T5D21. i) Cumulative probability plot of $^{208}\text{Pb}/^{232}\text{Th}$ T5D21 monazite ages. The asymmetric shape of the plot suggests two populations, see text for details. j) Cumulative probability plot of $^{208}\text{Pb}/^{232}\text{Th}$ T5D21 monazite age for each of the two populations. k) Examples of optical (left) and cathodo-luminescence (right) images of T5D20 monazites with corresponding ages. l) Example of optical (left) and cathodo-luminescence (right) images of T5D21 monazite with corresponding ages.

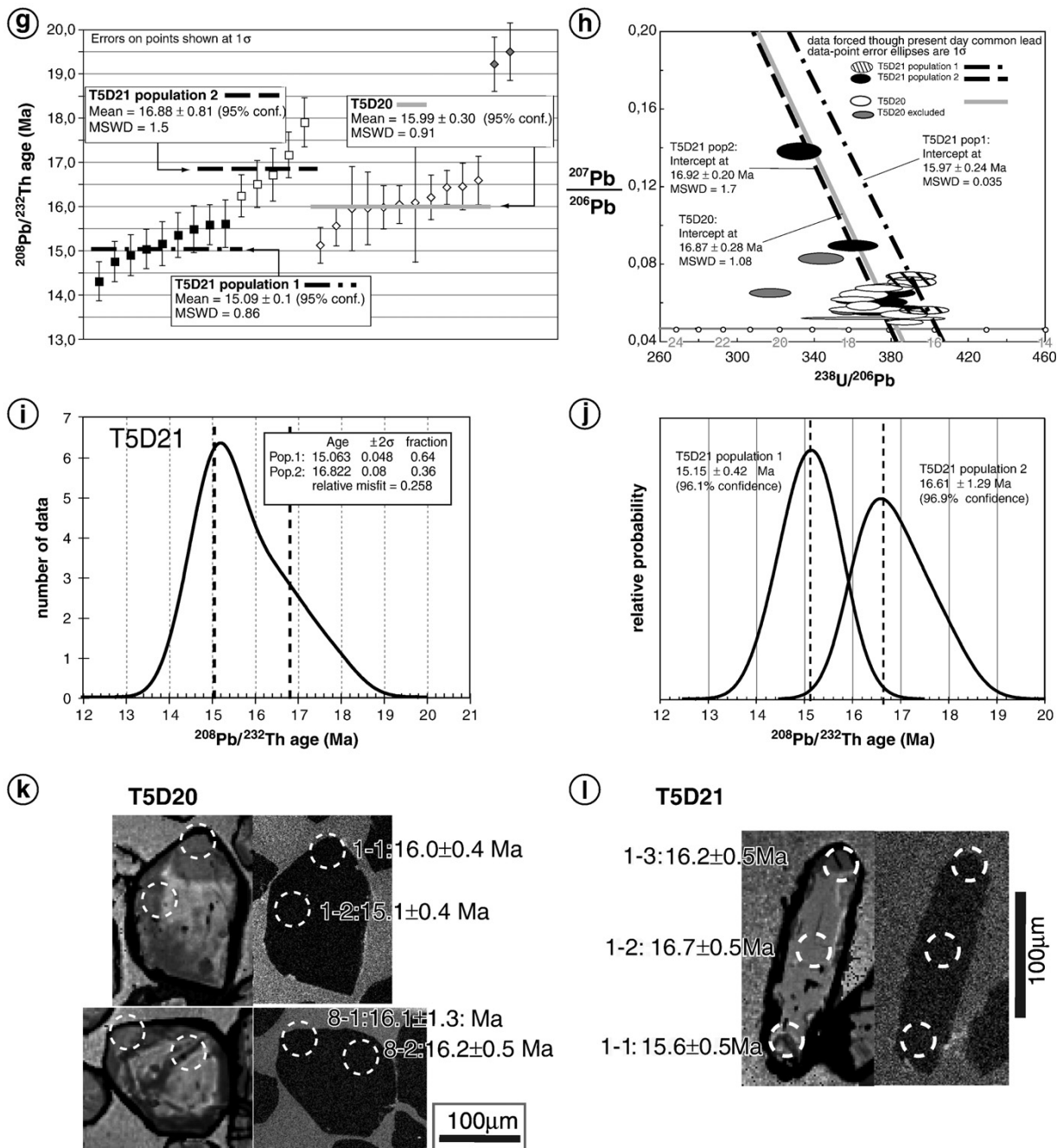


Fig. 5 (continued).

of Beijing, China, and the Cameca IMS 1270 at CRPG in Nancy, France. The Argon spectrometric analysis was conducted during furnace step heating at the University Montpellier2, France. Analytical conditions are given in Appendix A.

4.2.1. U/Pb results

Zircons in both the undeformed (T5D21) and the deformed (T5D20) granites are mostly clear and euhedral in shape, elongated to sometimes acicular (Fig. 5e,f). Rare stocky grains are also found. Blurred cores are found in most zircons whether they are elongated or not. On a concordia

plot, both samples show approximately the same age distribution regardless of the location (cores/rim) of the analysis, with a large Paleozoic to Neoproterozoic (300–900 Ma) inheritance, two even older discordant analyses (>1 Ga), and few Cenozoic ages (Fig. 5a, Table DR4).

In T5D21 (undeformed) seven spots from 4 different crystals including 5 borders and two cores, yield apparent Miocene ages (Fig. 5b, Table DR4-1). All measurements, unless one core (Fig. 5f), from these 4 crystals correspond to young ages and thus suggest zircon neocrystallisation with limited, or undetectable, overgrowth on inherited zircons within the melt.

Two of these data plot slightly above the concordia probably due to excessive common lead correction. The other data correspond to a discordia with a lower intercept at 13.0 ± 2.2 Ma and an upper intercept at 729 ± 290 Ma (MSWD = 0.9) (Fig. 5b). The $^{206}\text{Pb}/^{238}\text{U}$ average age of the five nearly concordant data is 13.6 ± 1.3 Ma (Fig. 5c) in agreement with the lower intercept of the discordia. A regression in the Tera-Wasserburg diagram forced through present day common lead yields, using the same five points, a similar age within errors (13.7 ± 1.3 Ma, MSWD = 4.8) (Fig. 5d).

In sample T5D20 (deformed) only three spots yield apparent Miocene ages with $^{238}\text{U}/^{206}\text{Pb}$ ages between 14.2 ± 0.4 Ma and 43.3 ± 1.7 Ma respectively (Table DR4-2). The youngest of these data corresponds to the tip of a zircon whose core yields a much older age (Fig. 5e). The young age is slightly discordant however (Fig. 5b) and cannot be used to constrain precisely the time of zircon overgrowth.

Monazites from both granites are $100\text{ }\mu\text{m}$ on average, euhedral and have a homogeneous unzoned texture. Grains with obvious zircon or U-rich mineral inclusions were avoided using CL images (Fig. 5k,l). Ages are indistinguishable within errors between cores and rims of each grain (Table DR5). Overall, monazite populations from both the deformed and undeformed granite yield Miocene $^{208}\text{Pb}/^{232}\text{Th}$ ages corrected for common lead via ^{204}Pb analysis.

T5D20 shows fairly homogeneous $^{208}\text{Pb}/^{232}\text{Th}$ ages (15.1–16.5 Ma) if one excludes two outliers at ca. 19.5 Ma (Fig. 5g). The average of the 11 younger data is 15.99 ± 0.30 Ma (MSWD = 0.9), (Table DR5-1, Fig. 5g). Using a Tera-Wasserburg diagram, regression forced though present day common lead gives an age of 16.87 ± 0.28 Ma (9 points, MSWD = 1.08) excluding 4 points, two of which being the outliers at ca. 19.5 Ma (Fig. 5h).

T5D21 shows a larger $^{208}\text{Pb}/^{232}\text{Th}$ age range (14.3–17.9 Ma, Table DR5-2) and a significant asymmetry of the age probability plot suggests that two populations are present, with one dominant population around 15 Ma hiding an older one (Fig. 5i). Age histogram deconvolution using isoplot software (Ludwig, 2003) leads two central ages at 15.06 ± 0.05 Ma and 16.82 ± 0.08 Ma (Fig. 5i), each population having a Gaussian age distribution (Fig. 5j). These ages are almost identical to the weighted averages obtained on two splits of the population below and above 16 Ma: 15.09 ± 0.31 Ma (MSWD = 0.86) for population 1, and 16.88 ± 0.81 Ma (MSWD = 1.5) population 2 (Fig. 5g). Ages and populations do not correlate in any way with spot analysis locations nor other features from the monazites analysed. In the Tera-Wasserburg plot, data corresponding to the 3 youngest ^{204}Pb corrected ages are aligned and yield an age of 15.97 ± 0.24 Ma (MSWD = 0.035), while all other data point to 16.92 ± 0.20 Ma (MSWD = 1.7) (Fig. 5h).

All monazite and zircon U/Pb ages described above span between ~ 12 and ~ 20 Ma confirming a Miocene age for the leucogranites within the STD shear zone (Table 1). In each given sample monazites tend to be older than the youngest zircons which is rather unusual. The fact that monazites show a relatively large $^{208}\text{Pb}/^{232}\text{Th}$ age range and that sub-populations are distinguished whatever the way to analyse the data, suggests that favourable conditions for crystallization monazites have been maintained for some Myrs in both samples while granites were still partly above solidus and thus probably mobile. The age of the youngest monazite population should correspond to the final crystallization of the granite. If one considers the $^{208}\text{Pb}/^{232}\text{Th}$ monazite age this would be 15.99 ± 0.30 Ma for T5D20 (deformed) and 15.09 ± 0.11 Ma for T5D21 (undeformed). The Tera-Wasserburg approach yields ~ 1 Myr older ages: 16.87 ± 0.28 Ma (T5D20) and 15.97 ± 0.24 (T5D21). In both case, the deformed granite is ~ 1 Myr older than the crosscutting one.

The youngest zircons are 13.6 ± 1.3 Ma old in T5D21. This age is identical within 1σ errors with that of the $^{208}\text{Pb}/^{232}\text{Th}$ age of Monazites population 1 (15.09 ± 0.11), confirming that this latter age is probably the best estimate for the granite crystallization. The

Section/ site	Sample	Average						Inverse isochron (Tera Wasserburg)						Concordia					
		206/238 age for zircon and 208/232 age for monazite						207/206 vs 238/206						206/238 vs 207/2356					
		Number	Rock type	Mineral type	Age (Ma)	MSWD	Number of spots	Spots	Age (Ma)	Upper intercept	MSWD	Number of spots	Spots	Age (Ma)	Upper intercept	MSWD	Number of spots		
STD shear zone	T5D21	Undeformed leucogranite	Zircon	Monazite	13.6 ± 2.0	5	40,2,312b 2312b,39	13.7 ± 1.3	Common lead	4.8	5	40,2,312b 2312b,39	13.3 ± 2.0	729 ± 290	0.9	5	3b2b,23b2b3 39,33b1b1,13		
					1.3 ± 0.9	9	7,1,6,1,8,1,12,1,9,1 10,1,7,2,4,1,1,1	$16.0 \pm$ 0.2	Common lead	0.04	3	7,1,6,1,8,1							
					0.1 ± 1.5	5	1,3,11,1,12,3,1,5,1	$16.9 \pm$ 0.2	Common lead	1.7	11			$12,1,9,1,10,1,7,2,4,1,1,1$					
					0.8 ± 16	14	All spots							$13,11,11,12,3,1,5,1$					
					0.6 ± 1	1	15												
STD shear zone	T5D20	Deformed leucogranite	Zircon	Monazite	16.0 ± 0.9	11	1,2,9,1,15,1,9,2,10,1,1,1 8,2,8,1,4,1,14,1,13,1	$16.9 \pm$ 0.3	Common lead	1.1	9			$12,9,1,15,1,9,2$					
					0.3 ± 0.3									$10,1,1,1,8,2,8,1,4,1$					

Table 1
U/Pb data summary.

For samples location see Table DR2 and Fig. 2b. Data plotted on Fig. 6. Detailed data are given in Table DR4 and Table DR5.

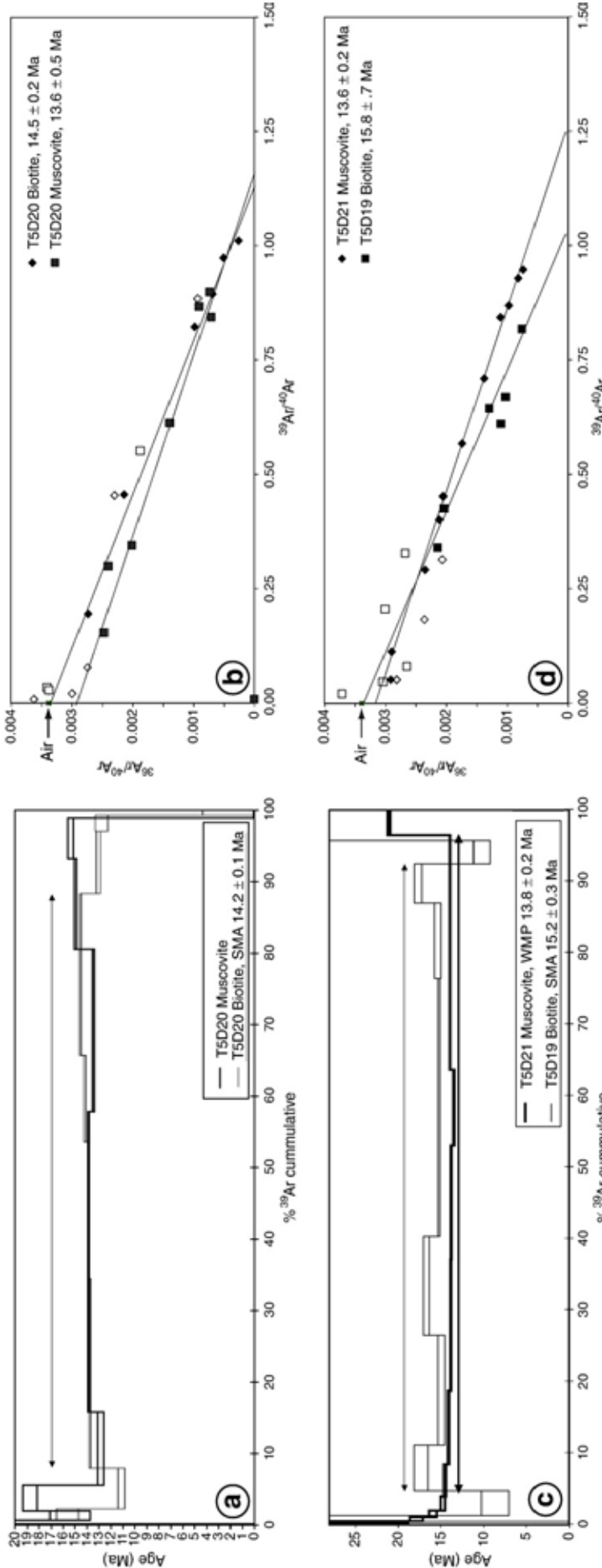


Fig. 6. Argon data. Corresponding data are summarized in Table 2 and listed in Table D6. For age spectrum the double arrows indicate the steps used in age calculation. For inverse isochrone plots empty symbols not used in age calculation.
 a) T5D20 muscovite and biotite age spectra. b) T5D20 muscovite and biotite inverse isochrone plot. c) T5D21 muscovite and biotite inverse isochrone plot. d) T5D19 biotite age spectra.

deformed granite (T5D20) most probably emplaced at ~ 16 Ma within the deforming STD series, while T5D21 emplaced at ~ 15 Ma, sealing deformation in the STD shear zone at this location.

4.2.2. Ar/Ar results

Biotites from T5D19 micaschist yield an irregular age spectra, and a weighted average age of 15.2 ± 0.3 Ma for 6 out of the 11 steps corresponding to 88% of the ^{39}Ar released (Fig. 6c, Table 2, Table DR6-1). This age is similar within errors to the age of the 1000°C and 1050°C steps which account for 47% of the ^{39}Ar released (Fig. 6c, Table DR6-1), and to the inverse isochrone age (Fig. 6b, Table 2). Although this cannot be considered as meaningful as a true plateau age, the 15.2 ± 0.3 Ma appears robust.

Muscovites from the deformed granitic lenses (T5D20) within the micaschist show a saddle-shape age spectra suggesting a maximum age of 13.9 ± 0.2 Ma. The corresponding inverse isochron gives an age of 13.6 ± 0.5 Ma (Fig. 6a,b; Table 2; Table DR6-2). Biotites from the same sample are slightly older with a weighted mean average age of 14.2 ± 0.1 Ma similar within errors to the isochron age (14.5 ± 0.2 Ma) (Fig. 6a,b; Table 2, Table DR6-1).

Muscovite from the undeformed granite sample T5D21 displays a plateau, slightly saddle-shaped, with a weighted average age of 13.8 ± 0.2 Ma almost undistinguishable from the isochron age of 13.6 ± 0.2 Ma indicating a slight excess argon (Fig. 6c,d; Table 2, Table DR6-2).

Such results are in agreement with previous argon dating in the same area. Hodges et al. (1994) collected samples from the STD shear zone south of Dinggye (samples D1, 7, 8, 25, and 26 located on Fig. 2a). Argon dating of muscovites yields ages between 12.8 and 14.9 Ma while biotites are from 14.5 to 15.7 Ma. These data are also in agreement with the muscovite age of 14.2 ± 0.5 Ma found by Zhang and Guo (Zhang and Guo, 2007) for a mylonitic leucogranite within the STD shear zone (sample T01- 27 Fig. 2a).

Overall, biotites and muscovites of the STD shear zone have essentially the same weight mean ages: 14.4 ± 1.3 for biotites and 14.0 ± 0.5 for muscovites (Table 2). This suggests very rapid cooling from $405 \pm 35^\circ\text{C}$ (closure temperature for muscovite calculated for cooling rates between 1 and $100^\circ\text{C}/\text{Ma}$ using the diffusion parameters at ~ 5 kb given by Harrison et al., 2009) to $320 \pm 40^\circ\text{C}$ (closure temperature for biotites, e.g. Harrison et al., 1985) in the 14.4 ± 1.3 (weight mean age of all available mica ages with 2σ error) time interval.

5. Discussion: timing of the STD in the Ama Drime area, comparison with other locations

5.1. P-T-t-D and timing of end of motion in STDS near Dinggye

When combining the data presented above for outcrop 05-222, the picture that emerges, is that of an STD shear zone with top to the NE ductile shearing starting at a depth of ~ 22 km after heating to $\sim 650^\circ\text{C}$

and leucogranite emplacement. Locally ductile deformation stopped at ~ 15 Ma. Argon data indicate that the following cooling was fast and lasted until at least ~ 13.6 Ma, suggesting that deformation pursued for at least ~ 1 Ma, within the STDSz, and/or on brittle structures above outcrop 05-222. Such fast cooling could also be related with fast erosion rather than tectonic denudation. However, the occurrence of nearly un-metamorphosed TSS rocks just above the STD, locally observed as klippen (Burchfiel et al., 1992; Hodges et al., 1994; this study) (Fig. 2b) implies that the total amount of erosion in the area was relatively small and favours the interpretation of a rapid cooling linked to normal faulting.

In the absence of granites crosscutting all structures or low temperature geochronologic data it is difficult to pin down the age of the last down to the North motion. However, as mentioned above, the STDS is cut and offset by the Dinggye N-S active fault and shear zone that correspond to an E-W direction of extension, almost perpendicular to that of the STDS (NNE-SSW). The initiation age of the Dinggye fault will thus provide a minimum age for the end of motion on the STDS near Dinggye.

(U-Th)/He apatite ages within the AmaDrime range suggest exhumation at a rate of ~ 1 mm/yr since at least ~ 4 Ma, and thus that the Dinggye active normal fault is active since at least that time (Jessup et al., 2008b; Kali et al., in press). Kali et al. (in press) also report a leucocratic dyke that crosscuts the ductile deformation fabric in the footwall of the Dinggye normal fault. Monazites from that dyke show two $^{208}\text{Pb}/^{232}\text{Th}$ ages populations at 13.09 ± 0.32 Ma and 10.98 ± 0.39 Ma, the youngest one being interpreted at the timing of crystallization. This implies that down to the east ductile normal faulting was, at least locally, over at ~ 11 Ma, but rapid normal faulting pursued, as micas argon ages suggest a rapid cooling in the 13.7 – 10.2 Ma time interval (Kali et al., in press). It follows that any motion on the STDS ended prior to ~ 11 Ma, time at which down to the west motion on the Dinggye N-S shear zone had already occurred. It can thus be concluded that motion on the STDS near Dinggye ended between 13.6 and 11 Ma.

5.2. Amount of exhumation at the time of STDS activity

T5D19 exhumation (~ 0.6 GPa, ~ 22 km) occurred since the onset of the STDS, with motion absorbed both within the STD shear zone structurally above outcrop 05-222, and along the STD. Combining PT path and cooling ages (Fig. 4d) it appears that the exhumation of the STDSz rocks since 14.1 ± 0.5 Ma, time at which they cooled down to $\sim 320^\circ\text{C}$, is less than 0.4 GPa (paragenesis II $\geq 600^\circ\text{C}$, Fig. 4). Taking into account Hodges et al. (1994) P-T estimates reduces this value to less than 0.3 GPa (Fig. 4). The amount of exhumation linked with the STDS is thus comprised between ≥ 0.3 Gpa (~ 11 km) and ≤ 0.6 Gpa (~ 22 km), which would correspond to between ≥ 64 and ≤ 128 km of slip assuming simple shear and a regular dip of 10° for the STD. For a STD dip of 15° or 5° , the slip range would be 42 – 85 km and 128 –

Table 2
Ar/Ar data summary.

Section/ site	Sample				Plateau age		Inverse isochron age				Total fusion age (Ma)
	Number	Rock type	Altitude	Mineral type	Age (Ma)	Steps	Age (Ma)	40Ar/ 36Ar _i	MSWD	Steps	
STDS shear zone	T5D19b	Garnet-sillimanite micaschist	4263	Biotite	SMA	15.2 ± 0.3 50% of gas	15.8 ± 0.8	302 ± 19	10.7	6 steps/11 (4–9) 90% of gas	16.3 ± 0.2
	T5D20	Deformed leucogranite	4263	Biotite	SMA	14.2 ± 0.1 80% of gas	14.5 ± 0.2	295 ± 9	5.4	6 steps/12 (4–11) 50% of gas	13.9 ± 0.1
				Muscovite			13.6 ± 0.5	349 ± 20	7.6	7 steps/12 (4–6, 8–11) 90% of gas	13.9 ± 0.2
T5D21	Undeformed leucogranite		4263	Muscovite	WMP	13.8 ± 0.2 95% of gas	13.6 ± 0.2	321 ± 4	1.4	11 steps/14 (3, 5–14) 90% of gas	14.2 ± 0.1

See Fig. 6. Detailed data are given in Table DR6.

255 km respectively. As a pure shear component of deformation (vertical flattening) appears widespread in the UHCS rocks below the STD (Law et al., 2004), the amount of throw, and thus of slip, corresponding to a given exhumation is probably overestimated.

Previous estimates for STDS slip in other localities range between more than 15 (W on Fig. 1a), (Edwards et al., 1996) to more than 140 km (SK on Fig. 1a), (Grujic et al., 2002). Estimates for the Dzakar Chu (D) section, the closest from our study area, vary between 50 and 120 km depending on the dip assumed for the STDsz (Cottle et al., 2007). From the available data it appears difficult to get a precise amount of motion on the STDS (see also Yin, 2006), and thus to use this parameter in the discussion on the mechanics of the Himalayas collision zone.

5.3. Timing of the STDS: along strike diachronism?

Several authors have proposed that the STDS and MCT slips were coeval (see Yin, 2006 for a review). However few authors have systematically investigated the STDS timing along strike of the Himalayas. From a compilation of previous studies Godin et al. (2006b) define an upper and a lower STD. For each structure Godin et al. (2006b) estimate a “best-fit age” corresponding to the age at which the fault was active everywhere along strike. These “best-fit ages” are of ~21 Ma for the upper STD and ~18 Ma for the lower one (Fig. 7). The authors also infer that the lower STD was mostly active between 24 and 12 Ma with the upper STD apparently starting latter and lasting longer between 19 and perhaps 0 Ma. That study is however lacking any critical analysis of the data set, and of the diachronism of motion between the various localities along strike that these data seems to imply. We discuss below in more detail the issue of the timing of the end of motion along the STDS and its diachronism/synchronism along strike.

The STD has no clear morphological expression, it is crosscut by the active N-S normal faults (Gurla Mandata, Thakhola, Ama Drime,

Yadong) and no crustal earthquake indicative of ~E-W normal faulting has ever been documented in the South Tibetan crust. The STD is thus a fossil structure.

Most published studies that allow inferring an age for the end of motion on the STDS are listed in Appendix A, and are summarized in Table DR7. Probably based on the idea that melting was linked to normal shear on the STDS, several studies rest on the youngest ages of the leucogranites affected by the STDS, to estimate the age of cessation of normal faulting (squares, Fig. 7). Such analysis yields 22–16 Ma ages along most of the belt, with younger (~12 Ma) ages East of the Yadong active rift (Fig. 7). Taking such ages as proxies for end of motion on the STDS (grey dashed thick line 1, Fig. 7) leads some to hypothesize that the Yadong rift would correspond to a major timing discontinuity, with an STDS lasting ~3 Ma longer east of the rift (Wu et al., 1998). In Butan, Kellett et al. (2009) have proposed that the internal part of the STDS, now outcropping in South Tibet (G and W, Figs. 1a and 7, line 1b), stayed active after 11 Ma, while the external part of the STDS now outcropping below the Tethyan and Chekha klippen (SK, U and L, Figs. 1a and 7 line 1a) became inactive prior to that age. However, this hypothesis only rests on U/Pb emplacement ages of deformed leucocratic melts that only define a maximum, not a true, age for the end of deformation. In many locations STDS deformations appear to progressively localize in the upper part of the shear zone and to last several Ma after the time of magmatic rocks emplacement and the end of ductile shear in the deepest parts of the shear zone. It is thus not judicious to only consider this kind of constraints.

Motion on the STDS is responsible for rapid cooling of footwall rocks, and rapid cooling ages provide a maximum age for the end of motion on the STDS that is probably closer to the real age, slowdown in cooling/exhumation rates reflecting the end of rapid motion. Taking such data in consideration suppresses the need for a major step in age across the Yadong rift, whilst a general tendency of younging towards

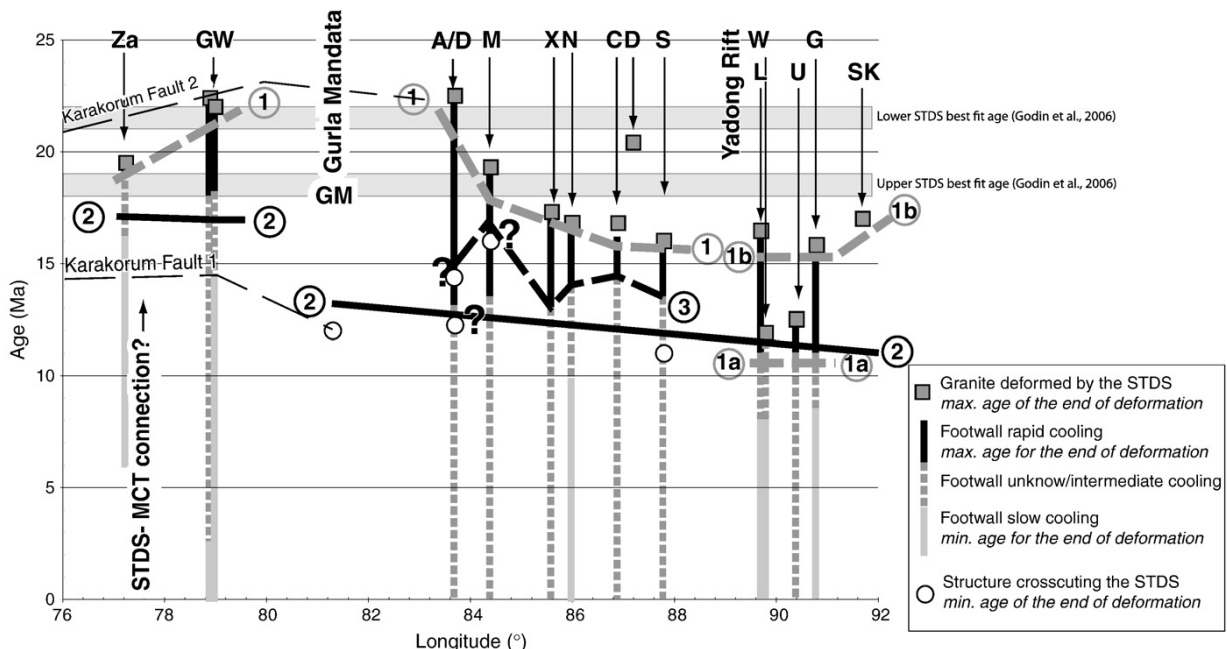


Fig. 7. Timing constraints for the cessation of motion along the STDS. Plot of timing constraints as a function of the longitude. Squares indicate U/Pb emplacement ages of magmatic rocks affected by the STDsz that yield a maximum age for the cessation of shear. Vertical bars represent local cooling histories of footwall rock of the STDS: black, rapid cooling; grey, slow cooling; dashed, unconstrained cooling. Rapid cooling can be interpreted to occur during STDS motion and thus yield a maximum age. Slow cooling can be interpreted as reflecting the end of exhumation and thus yields a minimum age. Open circles correspond to timing of events that occurred after the end of motion along the STDS, providing minimum ages. The best-fit ages of the lower and upper STD proposed from a earliest compilation (Godin et al., 2006b) are reported as well as various hypotheses for the end of motion on the STDS. Line 1 could be proposed considering only the deformed granite ages. Lines 2 and 3 are two extreme ways to take into account most of the data. See text and Table DR7 for details and references, and Fig. 1a for location.

the East is possible with a major step in age of ~5 to ~3 Ma at the level of the Gurla Mandata (GM) (continuous black line 2, Fig. 7).

In few places it is possible to propose minimum ages for the end of motion on the STDS by dating crosscutting structures (S, A/D, M, G, Figs. 1 and 7). Such constraints are fundamental to precisely resolve the timing of the end of deformation. However such data are still rare and often disputable. A critical example is that of the Manaslu area, where the structural cause inferred for the cooling dramatically changes the interpretation. If the cooling is related to the buckling of the STDS, as proposed by Godin (Godin et al., 2006a), the STDS has to have ended any motion by ~16 Ma which would suggest a much more complicated history (dashed black line 3 on Fig. 7). However, between the Annapurnas and Dinggye, the STDS is a continuous structure with no lateral ramps, a fact barely compatible with large variations in rate and/or duration. On the other hand, if the fast cooling is simply related to exhumation in the footwall of the Phu detachment, then a simpler history holds. One could also argue that the white micas dated at ~12 Ma (Godin et al., 2001) and ~14 Ma (Coleman and Hodges, 1995) in the Dhaulagiri area are related to late motion on STDS rather than to the Takhola normal fault, in which case the STDS could have stopped almost synchronously everywhere east of 81°E, between 12 and 11 Ma (continuous black line 2, Fig. 7), whilst a much more complicated history cannot completely be excluded (dark dashed line 3 Fig. 7).

No major step in age is required in the Rothang La area, between the Zanskar shear zone and the Garwhal Himalayas STDS (~79°E, Fig. 1a) where it has been proposed that the STDS merges with the MCT (Yin, 2006; Webb et al., 2007). But a ~5 to 3 Ma step is apparent at the level of the Gurla Mandata (GM, Fig. 7). The fact that this step is located, where the right-lateral Karakorum fault shows a major bend either connecting southward with the GM (e.g., Murphy et al., 2000) or continuing eastward along the Yarlung-Tzangpo suture (e.g., Lacassin et al., 2004), suggests that this fault could play a major role in the STDS history. Indeed some consider that the KF initiated prior to 22 Ma ago (Karakorum Fault 2 on Fig. 7) (Valli et al., 2008), in which case the STDS and the Karakorum fault would have been coeval for at least 4 Ma, and the interaction between the two faults could explain an earlier stop of the STDS west of the GM. However many consider that the Karakorum fault (KF) initiated less than 15.7 Ma ago (Murphy et al., 2000; Phillips et al., 2004) (Line Karakorum 1, Fig. 7), and would thus postdate end of motion on the Zanskar part of the STDS.

5.4. Why did the STDS stop at ~12 Ma?

Combining our results with a compilation of published data leads us to infer that the STDS most likely stopped first in the west, at ~17 Ma in Zanskar but only from ~13 Ma to ~11 Ma east of the GM. If true this suggests a plate-scale mechanism and interaction with the Karakorum fault to control the activity of the STDS. It is important to note that the 15–10 Ma interval corresponds to two major tectonic changes within the Himalayan belt: 1) end of major thrusting phase on the lower Main Central Thrust (MCTI) (Harrison et al., 1997; DeCelles et al., 2001; Catlos et al., 2001, 2002a,b; Daniel et al., 2003; Kohn et al., 2004) and activation of the Main Boundary Thrust (MBT) at ~11 Ma (Meigs et al., 1995); and 2) onset of a first phase of E–W extension in southern Tibet (Garzione et al., 2003; Hager et al., 2006; Dewane et al., 2006; Arnaud et al., 2008; Kali et al., in press). This period also coincides with major changes in the India–Eurasia convergence: a change from ~N29° to ~N14° at 10–12 Ma together with a slight increase in rate from ~46 to 50 mm/yr according to Lee and Lawver (1995); or a ≥40% rate decrease together with a direction change between 20 and ~10 Ma for Molnar and Stock (2009) (Fig. 8).

The timing coincidence suggests that the changes in rate and direction of convergence is linked with the change in locus, direction and rate of thrusting in the orogenic belt, and with the switch from NNE–SSW extension (STDS) to ~E–W extension at the top of the belt. Such synchronous change of the stress directions along ~1000 km of the Himalayan belt more probably results from a sudden change in boundary conditions, not in body forces nor thermal evolution that both occur on longer time scales. It is thus more in accord with thrust wedges or thrust system models rather than mid-crustal channel flow driven by focussed erosion and high elevation of the Tibetan plateau.

In any case, while it appears fundamental to gather more data in order to more tightly constrain the timing of STDS deformations, geodynamic models have to better take into account that timing.

6. Conclusion

Combining structural, petrographical and geochronological data we demonstrated that the STDS ended its motion between 13.6 and 11 Ma ago near Dinggye, East of the Ama Drime range. Combining these data, and published ones all along the Himalayan belt, we

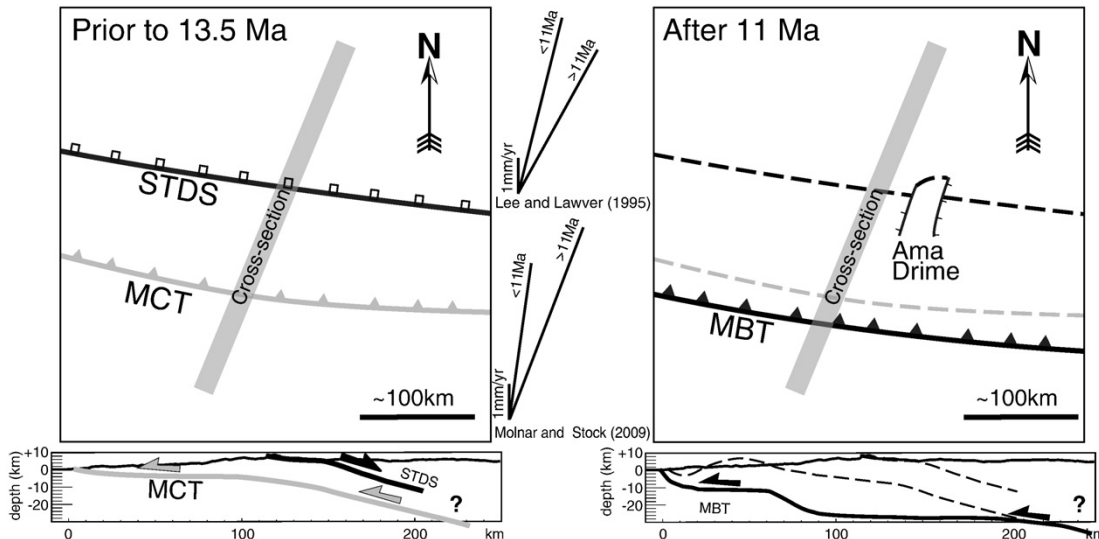


Fig. 8. ~12 Ma tectonic changes in central Himalaya. Schematic maps (top) and cross-sections (bottom) prior (left) and after (right) major tectonic reorganization at ~12 Ma. Structures that become inactive are dashed. Lines between the map depict the direction and amount of India–Eurasia convergence calculated from oceanic kinematics according to Lee and Lawver (1995) (top) and Molnar and Stock (2009) (bottom).

speculate that the STDS stopped first in the west, at ~17 Ma in Zanskar but only from ~12 to ~11 Ma east of the Gurla Mandata. Such timing coincides with the transition of the main thrust motion from the MCT to the MBT, to the switch from NNE-SSW to E-W extension in southern Tibet, and to a change in the direction of the India/Eurasia convergence. This synchronism is probably better explained in the frame of a thrust wedge or thrust system model than a lower channel flow model.

Acknowledgments

We thank E. Deloule and the ion probe team of the CRPG, CNRS UPR 2300, Nancy, France for their help in dating the zircons, Claude Merlet and the electronic microprobe team of Géosciences Montpellier, Université de Montpellier 2, France, and Paul Capiez for the whole-rock X-fluorescence analysis at UMR 5570, Lyon, France. The field trip was financed by an INSU DyETI grant to R. Lacassin and P.H.L. Reviews by An Yin and especially L. Ratschbacher helped to improve the manuscript.

Appendix A. Supplementary data

Supplementary data associated with this article can be found, in the online version, at doi: 10.1016/j.epsl.2009.12.035.

References

- Armijo, R., Tappognier, P., Mercier, J.L., Han, T.L., 1986. Quaternary extension in southern Tibet—field observations and tectonic implications. *J. Geophys. Res.* 91, 13803–13872.
- Arnaud, N., Aitchison, J.C., Leloup, P.H., Valli, F., Wilde, S., 2008. Constraints on the initiation of normal faulting across the Yarlung Tsangpo suture zone, from the Lopu Gangri range, southern Tibet. *Geophys. Res. Abstr.* 10 EGU2008-A-00000.
- Beaumont, C., Jamieson, R.A., Nguyen, M.H., Lee, B., 2001. Himalayan tectonics explained by extrusion of low-viscosity crustal channel coupled to focused surface denudation. *Nature* 414, 738–742.
- Bollinger, L., Avouac, J.P., Beyssac, O., Catlos, E.J., Harrison, T.M., Grove, M., Goffe, B., Sapkota, S., 2004. Thermal structure and exhumation history of the Lesser Himalaya in central Nepal. *Tectonics* 23, TC5015. doi:10.1029/2003TC001564.
- Bordet, P., 1961. Recherches géologiques dans l’Himalaya du Népal, région du Makalu. CNRS, Paris.
- Borghi, A., Castelli, D., Lombardo, B., Visona, D., 2003. Thermal and baric evolution of garnet granulites from the Kharta region of S Tibet, E Himalaya. *Eur. J. Mineral.* 15, 401–418.
- Brunel, M., 1983. Etude pétro-structurale des chevauchements ductiles en Himalaya (Népal oriental et Himalaya du Nord-Ouest). University of Paris VII.
- Burchfiel, B.C., Royden, L.H., 1985. North-south extension within the convergent Himalayan region. *Geology* 13, 679–682.
- Burchfiel, B.C., Zhilang, C., Hodges, K.V., Yiping, L., Royden, L.H., Changrong, D., Jiene, X., 1992. The South Tibetan Detachment System, Himalayan Orogen: extension contemporaneous with and parallel to shortening in a collisional mountain belt. Geological Society of America.
- Burg, J.P., 1983. Carte Géologique du Sud tibet, in: M.o. Geology/CNRS, (Ed), Ministry of Geology/CNRS, Beijing/Paris.
- Burg, J.P., Brunel, M., Gapais, D., Chen, G.M., Liu, G.H., 1984. Deformation of leucogranites of the crystalline Main Central Sheet in southern Tibet (China). *J. Struct. Geol.* 6, 535–542.
- Carosi, R., Lombardo, B., Molli, G., Musumeci, G., Pertusati, P.C., 1998. The south Tibetan detachment system in the Rongbuk valley, Everest region. Deformation features and geological implications. *J. Asian Earth Sci.* 16, 299–311.
- Catlos, E.J., Harrison, T.M., Kohn, M.J., Grove, M., Ryerson, F.J., Manning, C.E., Upreti, B.N., 2001. Geochronologic and thermobarometric constraints on the evolution of the Main Central Thrust, central Nepal Himalaya. *J. Geophys. Res.* 106, 16177–16204.
- Catlos, E.J., Gilley, L.D., Harrison, T.M., 2002a. Interpretation of monazite ages obtained via in situ analysis. *Chem. Geol.* 188, 193–215.
- Catlos, E.J., Harrison, T.M., Manning, C.E., Grove, M., Rai, S.M., Hubbard, M.S., Upreti, B.N., 2002b. Records of the evolution of the Himalayan orogen from in situ Th-Pb ion microprobe dating of monazite: eastern Nepal and western Garhwal. *J. Asian Earth Sci.* 20, 459–479.
- Coleman, M., Hodges, K., 1995. Evidence for Tibetan plateau uplift before 14-Myr Ago from a new minimum age for east-west extension. *Nature* 374, 49–52.
- Coleman, M.E., Hodges, K.V., 1998. Contrasting Oligocene and Miocene thermal histories from the hanging wall and footwall of the South Tibetan detachment in the central Himalaya from Ar-40/Ar-39 thermochronology, Marsyandi Valley, central Nepal. *Tectonics* 17, 726–740.
- Cottle, J.M., Jessup, M.J., Newell, D.L., Searle, M.P., Law, R.D., Horstwood, M.S.A., 2007. Structural insights into the early stages of exhumation along an orogen-scale detachment: the South Tibetan Detachment System, Dzakaa Chu section, eastern Himalaya. *J. Struct. Geol.* 29, 1781–1797.
- Cottle, J.M., Jessup, M.J., Newell, D.L., Horstwood, M.S.A., Noble, S.R., Parrish, R.R., Waters, D.J., Searle, M.P., 2009. Geochronology of granulitized eclogite from the Ama Drime Massif: implications for the tectonic evolution of the South Tibetan Himalaya. *Tectonics* 28. doi:10.1029/2008TC002256.
- Daniel, C.G., Hollister, L.S., Parrish, R.R., Grujic, D., 2003. Exhumation of the Main Central Thrust from lower crustal depths, Eastern Bhutan Himalaya. *J. Metamorph. Geol.* 21, 317–334.
- Dasgupta, S., Ganguly, J., Neogi, S., 2004. Inverted metamorphic sequence in the Sikkim Himalayas: crystallization history, P-T gradient and implications. *J. Metamorph. Geol.* 22, 395–412.
- DeCelles, P.G., Robinson, D.M., Quade, J., Ojha, T.P., Garzione, C.N., Copeland, P., Upreti, B.N., 2001. Stratigraphy, structure, and tectonic evolution of the Himalayan fold-thrust belt in western Nepal. *Tectonics* 20, 487–509.
- DeCelles, P.G., Gehrels, G.E., Najman, Y., Martin, A.J., Carter, A., Garzanti, E., 2004. Detrital geochronology and geochemistry of Cretaceous-Early Miocene strata of Nepal: implications for timing and diachroneity of initial Himalayan orogenesis. *Earth Planet. Sci. Lett.* 227, 313–330.
- Dewane, T.J., Stockli, D.F., Hager, C., Taylor, M., Ding, L., Lee, J., Wallis, S., 2006. Timing of Cenozoic E-W Extension in the Tangra Yum Co-Kung Co Rift, south-central Tibet. American Geophysical Union fall Meeting, abstract with program.
- Dèzes, P.J., Vannay, J.C., Steck, A., Bussy, F., Cosca, M., 1999. Synorogenic extension: quantitative constraints on the age and displacement of the Zanskar shear zone (northwest Himalaya). *Geol. Soc. Am. Bull.* 111, 364–374.
- Edwards, M.A., Kidd, W.S.F., Li, J.X., Yu, Y.J., Clark, M., 1996. Multi-stage development of the southern Tibet detachment system near Khula Kangri. New data from Gonto La. *Tectonophysics* 260, 1–19.
- England, P., Molnar, P., 1993. Cause and effect among thrust and normal faulting, anatetic melting and exhumation in the Himalaya. In: Treloar, P.J., Searle, M.P. (Eds.), Himalayan Tectonics. Geological Society of London Special Publication, Geological Society of London, London, pp. 401–4011.
- Ferry, J.M., Spear, F.S., 1978. Experimental calibration of partitioning of Fe and Mg between biotite and garnet. *Contrib. Mineral. Petrol.* 66, 113–117.
- Garzione, C.N., DeCelles, P.G., Hodkinson, D.G., Ojha, T.P., Upreti, B.N., 2003. East-west extension and Miocene environmental change in the southern Tibetan plateau: Thakkola graben, central Nepal. *Geol. Soc. Am. Bull.* 115, 3–20.
- Godin, L., Parrish, R.R., Brown, R.L., Hodges, K.V., 2001. Crustal thickening leading to exhumation of the Himalayan metamorphic core of central Nepal: insight from U-Pb geochronology and Ar-40/Ar-39 thermochronology. *Tectonics* 20, 729–747.
- Godin, L., Gleeson, T.P., Searle, M.P., Ulrich, T.D., Parrish, R.R., 2006a. Locking of southward extrusion in favour of rapid crustal-scale buckling of the Greater Himalayan sequence, Nar valley, central Nepal. In: Law, R.D., Searle, M.P., Godin, L. (Eds.), Channel Flow, Ductile Extrusion and Exhumation in Continental Collision Zones 268. Geological Society of London Special Publication, London, pp. 269–292.
- Godin, L., Grujic, D., Law, R.D., Searle, M.P., 2006b. Channel flow, ductile extrusion and exhumation in continental collision zones: an introduction. In: Law, R.D., Searle, M.P., Godin, L. (Eds.), Channel Flow, Ductile Extrusion and Exhumation in Continental Collision Zones 268. Geological Society of London Special Publication, London, pp. 1–23.
- Goscombe, B., Hand, M., 2000. Contrasting P-T paths in the Eastern Himalaya, Nepal: inverted isograds in a paired metamorphic mountain belt. *J. Petrol.* 41, 1673–1719.
- Goscombe, B., Gray, D., Hand, M., 2006. Crustal architecture of the Himalayan metamorphic front in eastern Nepal. *Gondwana Res.* 10, 232–255.
- Grasemann, B., Fritz, H., Vannay, J.C., 1999. Quantitative kinematic flow analysis from the Main Central Thrust Zone (NW-Himalaya, India): implications for a decelerating strain path and the extrusion of orogenic wedges. *J. Struct. Geol.* 21, 837–853.
- Groppi, C., Lombardo, B., Rolfo, F., Pertusati, P., 2007. Clockwise exhumation path of granulitized eclogites from the Ama Drime range (Eastern Himalayas). *J. Metamorph. Geol.* 25, 51–75.
- Grujic, D., Casey, M., Davidson, C., Hollister, L.S., Kundig, R., Pavlis, T., Schmid, S., 1996. Ductile extrusion of the Higher Himalayan Crystalline in Bhutan: evidence from quartz microfabrics. *Tectonophysics* 260, 21–43.
- Grujic, D., Hollister, L.S., Parrish, R.R., 2002. Himalayan metamorphic sequence as an orogenic channel: insight from Bhutan. *Earth Planet. Sci. Lett.* 198, 177–191.
- Hager, C., Stockli, D., Dewane, T., Ding, L., 2006. Episodic Mio-Pliocene rifting in south-central Tibet. Thermochronometric Constraints from the Xainza Rift: American Geophysical Union fall Meeting, abstract with program.
- Hames, W.E., Bowring, S.A., 1994. An empirical evaluation of the argon diffusion geometry in muscovite. *Earth Planet. Sci. Lett.* 124, 161–169.
- Harris, N.B.W., Caddick, M., Kosler, J., Goswami, S., Vance, D., Tindle, A.G., 2004. The pressure-temperature-time path of migmatites from the Sikkim Himalaya. *J. Metamorph. Geol.* 22, 249–264.
- Harrison, T.M., Duncan, I., McDougall, I., 1985. Diffusion of 40Zr in biotite: temperature, pressure and compositional effect. *Geochim. Cosmochim. Acta* 49, 2461–2468.
- Harrison, T.M., Ryerson, F.J., LeFort, P., Yin, A., Lovera, O.M., Catlos, E.J., 1997. A Late Miocene-Pliocene origin for the Central Himalayan inverted metamorphism. *Earth Planet. Sci. Lett.* 146, E1–E7.
- Harrison, T.M., Célérrier, J., Aikman, A.B., Hermann, J., Heitzler, M.T., 2009. Diffusion of 40Ar in muscovite. *Geochim. Cosmochim. Acta* 73, 1039–1051.
- Hodges, K.V., Hames, W.E., Olszewski, W., Burchfiel, B.C., Royden, L.H., Chen, Z., 1994. Thermobarometric and Ar-40/Ar-39 geochronological constraints on Eohimalayan metamorphism in the Dinggye area, southern Tibet. *Contrib. Mineral. Petrol.* 117, 151–163.
- Hodges, K.V., Parrish, R.R., Searle, M.P., 1996. Tectonic evolution of the central Annapurna Range, Nepalese Himalayas. *Tectonics* 15, 1264–1291.

- Holdaway, M.J., 2000. Application of new experimental and garnet Margules data to the garnet-biotite geothermometer. *Am. Mineral.* 85, 881–892.
- Holland, T.J.B., Powell, R., 1998. An internally consistent thermodynamic data set for phases of petrological interest. *J. Metamorph. Geol.* 16, 309–343.
- Holland, T., Baker, J., Powell, R., 1998. Mixing properties and activity-composition relationships of chlorites in the system MgO-FeO-Al₂O₃-SiO₂-H₂O. *Eur. J. Mineral.* 10, 395–406.
- Hurtado, J.M., Hodges, K.V., Whipple, K.X., 2001. Neotectonics of the Thakkhola graben and implications for recent activity on the South Tibetan fault system in the central Nepal Himalaya. *Geol. Soc. Am. Bull.* 113, 222–240.
- Jessup, M.J., Cottle, J.M., Searle, M.P., Law, R.D., Newell, D.L., Tracy, R.J., Waters, D.J., 2008a. P-T-t-D paths of Everest Series schist. *Nepal. J. Metamorph. Geol.* 26, 717–739.
- Jessup, M.J., Newell, D.L., Cottle, J.M., Berger, A.L., Spotila, J.A., 2008b. Orogen-parallel extension and exhumation enhanced by denudation in the trans-Himalayan Arun River gorge, Ama Dablam Massif, Tibet–Nepal. *Geology* 36, 587–590.
- Kali, E., Leloup, P.H., Arnaud, N., Mahéo, G., Liu, D., Boutonnet, E., VanderWoerd, J., Xiaohan, L., Liu-Zeng, J., Haibing, L., in press. Exhumation history of the deepest central Himalayan rocks (Ama Dablam range): key P-T-D-t constraints on orogenic models. *Tectonics*. doi:10.1029/2009TC002551.
- Kellett, D.A., Grujic, D., Erdmann, S., 2009. Miocene structural reorganization of the south Tibetan detachment, eastern Himalaya: implications for continental collision. *Lithosphere* 1, 259–281.
- Kohn, M.J., Wieland, M.S., Parkinson, C.D., Upreti, B.N., 2004. Miocene faulting at plate tectonic velocity in the Himalaya of central Nepal. *Earth Planet. Sci. Lett.* 228, 299–310.
- Lacassin, R., Valli, F., Arnaud, N., Leloup, P.H., Paquette, J.L., Haibing, L., Tapponnier, P., Chevalier, M.L., Guillot, S., Maheo, G., Xu, Z.Q., 2004. Large-scale geometry, offset and kinematic evolution of the Karakorum fault, Tibet. *Earth Planet. Sci. Lett.* 219, 255–269.
- Law, R.D., Searle, M.P., Simpson, R.L., 2004. Strain, deformation temperatures and vorticity of flow at the top of the Greater Himalayan Slab, Everest Massif, Tibet. *J. Geol. Soc.* 161, 305–320.
- Lee, T.Y., Lawver, L.A., 1995. Cenozoic plate reconstruction of Southeast Asia. *Tectonophysics* 251, 85–138.
- Lombardo, B., Rolfo, F., 2000. Two contrasting eclogite types in the Himalayas: implications for the Himalayan orogeny. *J. Geodyn.* 30, 37–60.
- Ludwig, K.R., 2003. Isoplots 3.00 a geochronological toolkit for Microsoft Excel, Berkley Geoch. Cent. Spec. Pub. 4.
- Meier, K., Hiltner, E., 1993. Deformation and metamorphism within the Main Central Thrust zone, Arun Tectonic Window, eastern Nepal. In: Treloar, P.J., Searle, M.P. (Eds.), *Himalayan Tectonics*, Geological Society of London Special Publication 74. Geological Society of London, London, pp. 511–523.
- Meigs, A.J., Burbank, D.W., Beck, R.A., 1995. Middle-Late Miocene (greater-than-10 Ma) formation of the Main Boundary Thrust in the Western Himalaya. *Geology* 23, 423–426.
- Molnar, P., Stock, J., 2009. Slowing of India's convergence with Eurasia since 20 Ma and its implications for Tibetan mantle dynamics. *Tectonics* 28. doi:10.1029/2008TC002271.
- Murphy, M.A., Yin, A., Kapp, P., Harrison, T.M., Lin, D., Guo, J.H., 2000. Southward propagation of the Karakoram fault system, southwest Tibet: timing and magnitude of slip. *Geology* 28, 451–454.
- Phillips, R.J., Parrish, R.R., Searle, M.P., 2004. Age constraints on ductile deformation and long-term slip rates along the Karakoram fault zone, Ladakh. *Earth Planet. Sci. Lett.* 226, 305–319.
- Price, R.A., 1986. The southeastern Canadian Cordillera: thrust faulting, tectonic wedging, and delamination of the lithosphere. *J. Struct. Geol.* 8, 239–254.
- Searle, M.P., 1999. Extensional and compressional faults in the Everest–Lhotse massif, Khumbu Himalaya, Nepal. *J. Geol. Soc.* 156, 227–240.
- Searle, M.P., Godin, L., 2003. The South Tibetan Detachment and the Manaslu leucogranite: a structural reinterpretation and restoration of the Annapurna-Manaslu Himalaya, Nepal. *J. Geol.* 111, 505–523.
- Searle, M.P., Parrish, R.R., Hodges, K.V., Hurford, A., Ayres, M.W., Whitehouse, M.J., 1997. Shisha Pangma leucogranite, south Tibetan Himalaya: field relations, geochemistry, age, origin, and emplacement. *J. Geol.* 105, 295–317.
- Valli, F., Leloup, P.H., Paquette, J.L., Arnaud, N., Li, H.B., Tapponnier, P., Lacassin, R., Guillot, S., Liu, D.X., Deloule, E., Xu, Z.Q., Maheo, G., 2008. New U-Th/Pb constraints on timing of shearing and long-term slip-rate on the Karakorum fault. *Tectonics* 27, TC5007. doi:10.1029/2007TC002184.
- Vannay, J.C., Hodges, K.V., 1996. Tectonometamorphic evolution of the Himalayan metamorphic core between the Annapurna and Dhaulagiri, central Nepal. *J. Metamorph. Geol.* 14, 635–656.
- Vannay, J.C., Grasemann, B., Rahn, M., Frank, W., Carter, A., Baudraz, V., Cosca, M., 2004. Miocene to Holocene exhumation of metamorphic crustal wedges in the NW Himalaya: evidence for tectonic extrusion coupled to fluvial erosion. *Tectonics* 23. doi:10.1029/2002TC001429.
- Webb, A.A.G., Yin, A., Harrison, T.M., Celarier, J., Burgess, W.P., 2007. The leading edge of the Greater Himalayan Crystalline complex revealed in the NW Indian Himalaya: implications for the evolution of the Himalayan orogen. *Geology* 35, 955–958.
- Wu, C.D., Nelson, K.D., Wortman, G., Samson, S.D., Yue, Y.J., Li, J.X., Kidd, W.S.F., Edwards, M.A., 1998. Yadong cross structure and South Tibetan Detachment in the east central Himalaya (89 degrees–90 degrees E). *Tectonics* 17, 28–45.
- Yin, A., 2006. Cenozoic tectonic evolution of the Himalayan orogen as constrained by along-strike variation of structural geometry, exhumation history, and foreland sedimentation. *Earth Sci. Rev.* 76, 1–131.
- Zhang, J.J., Guo, L., 2007. Structure and geochronology of the southern Xainza-Dinggye rift and its relationship to the south Tibetan detachment system. *J. Asian Earth Sci.* 29, 722–736.

ANNEXE B

Appendix & Data Repository of

Kali, E., P. H. Leloup, N. Arnaud, G. Maheo, D. Y. Liu, E. Boutonnet, J. Van der Woerd, X. H. Liu, L. Z. Jing, and H. B. Li (2010), Exhumation history of the deepest central Himalayan rocks, Ama Drime range: Key pressure-temperature-deformation-time constraints on orogenic models, *Tectonics*, 29.

Appendix I: Pressure – Temperature path methodology

Whole rock composition of sample T5D39b was obtained from X-fluorescence at the Earth sciences laboratory in Lyon, France (CNRS UMR 5570, University Lyon1 and ENS of Lyon). In weight %, T5D33: SiO₂=73.9; TiO₂=0.8; Al₂O₃=11.7; Fe₂O₃=5.6; MnO=0.05; MgO=1.6; CaO=0.9; Na₂O=0.8; K₂O=3.6, P₂O₅=0.1; LOI (Loss On Ignition)=0.8 / T5D39b: SiO₂=72.3; TiO₂=0.6; Al₂O₃=14.3; Fe₂O₃=4.5; MnO=0.1; MgO=1.2; CaO=1.0; Na₂O=1.7; K₂O=3.2, P₂O₅=0.1; LOI =1.2).

Minerals were analysed with the Cameca SX100 microprobe at the department of Geosciences of Montpellier, France (CNRS UMR 5243). Analyses are reported in Table DR2.

The studied metapelites is described in the NCKFMASMnTi system (Spear, 1993). Perple_X'07 has been used for the calculation of pseudosections using the 2004 revised version of the internally consistent thermodynamic dataset of Holland & Powell (1998). The phases considered in the calculation were: Kyanite, Sillimanite, Andalusite, K-feldspar, Plagioclase, Clinopyroxene, Orthopyroxene, Garnet (Alm, Pyr, Spes, Gros), Ti-Biotite, Phengite, Chlorine, Cloritoid, Cordierite, Amphibole, staurolite and Quartz. Phases and end-members used in the solid-solution models involved in these pseudosections are from Newton et al. (1980) for plagioclase, White et al. (2007) for Ti-biotite, White et al. (2000) for garnet and cloritoid, Holland et al. (1998) for chlorine, Holland & Powell (1998) for phengite and staurolite, Holland & Powell (1996) for clinopyroxen and orthopyroxen, Dale et al. (2000) for amphibole and an ideal solution model for cordierite. Because of the high SiO₂ content, pseudosections were computed considering SiO₂ saturation. The calculation was performed with H₂O saturation.

Appendix II: geochronology

II-1 U-Th/Pb in situ SIMS dating

Zircon and monazite grains were separated using heavy liquids, a Frantz magnetic separator and finally by hand picking under a binocular microscope avoiding the most obvious metamict or dirty grains. The selected grains were mounted together with standard in epoxy resin. The mounts were then abraded and polished to expose at the surface the middle part of the crystals. G91500 zircon standard (Wiedenbeck et al., 1995) and WB.T.329 (Williams, 1996). monazite standards were used. Zircon and monazite grains were imaged using optical and cathodoluminescence (CL) microscopy. Monazites were analysed with the sensitive high resolution ion microprobes (SHRIMP II) at the Institute of Geology of Beijing, China, while zircons were measured using the Cameca IMS 1270 at CRPG in Nancy, France. Calibration parameters, data acquisition and age correction are described in Compston et al. (1984) for the SHRIMP II, and in Deloule et al. (2001) for the Cameca IMS 1270. The error on the

calibration curve is taken into account for the age uncertainty calculation. The spot size was between 30 and 60 μm .

Ion probe U-Th-Pb dating of young minerals is an analytical challenge because of the very small amounts of radiogenic daughter isotopes (^{206}Pb , ^{207}Pb , ^{208}Pb). In case of recent minerals, it is now usual for most geochronologists to consider the $^{238}\text{U}/^{206}\text{Pb}$ ages as the most reliable for zircons (e.g., [Stern and Amelin, 2003]), and the $^{232}\text{Th}/^{208}\text{Pb}$ ages for monazites (e.g., [Catlos et al., 2004]). The isotopic systems of zircons and, to a lesser extent, monazites keep the memory of several distinct magmatic, metamorphic and hydrothermal events. This provides the opportunity to reconstruct complex geological histories but requires cautious interpretation of the analytical results to individualize the different populations.

Within a given population of ion probe data, it is important to distinguish meaningful ages from outliers, which can always occur in spite of careful selection of rocks and minerals, and of rigorous analytical conditions. Age disparity around a mean value may result either from (1) an overlap of the probe beam on zones of distinct ages, (2) large SIMS analytical errors related to low radiogenic Pb content in young zircon overgrowths (Stern, 1997), (3) the occurrence of common Pb, (4) ^{230}Th radioactive disequilibrium in monazites (Schärer, 1984), (5) a partial lead loss due to (a) subsequent high temperature event(s), (6) a combination of these points. Consequently, we consider that the best age estimate of a given population of ion probe data is its mathematical mean with a two standard deviation uncertainty, which will lower the influence of outlier(s).

The Tertiary SIMS data are plotted in the Tera-Wasserburg diagram (Tera and Wasserburg, 1972) (1σ error errors for readability) while others data are plotted in concordia diagrams (1σ ellipse errors or larger symbols when ellipses are too small). Errors mentioned in the text are at the 1σ level, the weighted averages, and the associate 95% confidence errors, were calculated with Isoplot 3.23 of Ludwig (2003).

II-2 $^{40}\text{Ar}/^{39}\text{Ar}$ dating

Minerals were separated using heavy liquids, a Frantz magnetic separator and finally by hand picking under a binocular microscope. The samples were irradiated in two batches during April and December 2007 at the McMaster Nuclear Reactor in the 5C position for 26 h with an approximate 10^{18} neutrons $\text{cm}^{-2}\text{s}^{-1}$ flux. Irradiation interference on K, Ca and Cl were corrected by irradiating and analyzing KCl and CaF₂ pure salts. J factors were estimated by the use of duplicates of the Fish Canyon sanidine standard with an age of 28.02 Ma (Renne et al., 1998).

The samples were analyzed in Montpellier using the same apparatus and the same protocol, as described in (Arnaud et al., 2003). Samples were loaded in aluminum packets into a double vacuum Staudacher type furnace and step

calibration curve is taken into account for the age uncertainty calculation. The spot size was between 30 and 60 μm .

Ion probe U-Th-Pb dating of young minerals is an analytical challenge because of the very small amounts of radiogenic daughter isotopes (^{206}Pb , ^{207}Pb , ^{208}Pb). In case of recent minerals, it is now usual for most geochronologists to consider the $^{238}\text{U}/^{206}\text{Pb}$ ages as the most reliable for zircons (e.g., [Stern and Amelin, 2003]), and the $^{232}\text{Th}/^{208}\text{Pb}$ ages for monazites (e.g., [Catlos et al., 2004]). The isotopic systems of zircons and, to a lesser extent, monazites keep the memory of several distinct magmatic, metamorphic and hydrothermal events. This provides the opportunity to reconstruct complex geological histories but requires cautious interpretation of the analytical results to individualize the different populations.

Within a given population of ion probe data, it is important to distinguish meaningful ages from outliers, which can always occur in spite of careful selection of rocks and minerals, and of rigorous analytical conditions. Age disparity around a mean value may result either from (1) an overlap of the probe beam on zones of distinct ages, (2) large SIMS analytical errors related to low radiogenic Pb content in young zircon overgrowths (Stern, 1997), (3) the occurrence of common Pb, (4) ^{230}Th radioactive disequilibrium in monazites (Schärer, 1984), (5) a partial lead loss due to (a) subsequent high temperature event(s), (6) a combination of these points. Consequently, we consider that the best age estimate of a given population of ion probe data is its mathematical mean with a two standard deviation uncertainty, which will lower the influence of outlier(s).

The Tertiary SIMS data are plotted in the Tera-Wasserburg diagram (Tera and Wasserburg, 1972) (1σ error errors for readability) while others data are plotted in concordia diagrams (1σ ellipse errors or larger symbols when ellipses are too small). Errors mentioned in the text are at the 1σ level, the weighted averages, and the associate 95% confidence errors, were calculated with Isoplot 3.23 of Ludwig (2003).

II-2 $^{40}\text{Ar}/^{39}\text{Ar}$ dating

Minerals were separated using heavy liquids, a Frantz magnetic separator and finally by hand picking under a binocular microscope. The samples were irradiated in two batches during April and December 2007 at the McMaster Nuclear Reactor in the 5C position for 26 h with an approximate 10^{18} neutrons $\text{cm}^{-2}\text{s}^{-1}$ flux. Irradiation interference on K, Ca and Cl were corrected by irradiating and analyzing KCl and CaF₂ pure salts. J factors were estimated by the use of duplicates of the Fish Canyon sanidine standard with an age of 28.02 Ma (Renne et al., 1998).

The samples were analyzed in Montpellier using the same apparatus and the same protocol, as described in (Arnaud et al., 2003). Samples were loaded in aluminum packets into a double vacuum Staudacher type furnace and step

heated; temperature is calibrated by means of a thermocouple. The gas was purified using cold traps with liquid air and Al-Zr getters. Once cleaned, the gas was introduced into a VG3600 mass spectrometer and allowed to equilibrate for 2 min prior to analysis was done statically. Signals were measured by the mean of a Faraday cup with a 10^{11} ohm resistor for ^{40}Ar and ^{39}Ar while ^{39}Ar , ^{38}Ar , ^{37}Ar and ^{36}Ar were analyzed with a photomultiplier after interaction on a Daly plate. Gain between both collectors was estimated by duplicate analysis of ^{39}Ar on both collectors during each analysis, and also by statistical analysis over a period of several years. This gain is 50 and is known at better than 1.5%. This error is included in the age calculation, along with analytical errors on each signal and errors on the blank values. Detailed analytical results are available as electronic supplements. Age plateau given are weighted mean plateaus; the error takes the error on the J factor into account. With the historical decrease of analytical errors, strict plateau criteria (Berger and York, 1981; Dalrymple and Lanphere, 1974) are less frequently met. Thus, pseudoplateaus are used when a significant number of steps overlap globally at 2σ even if contiguous steps do not. For K-feldspars, plateau ages cannot be defined, but since we wish to compare and discuss series of steps with similar ages we used simple mean, thus unweighted, ages. Isochron ages are obtained on an inverse isochron diagram of $^{36}\text{Ar} / ^{40}\text{Ar}$ versus $^{39}\text{Ar} / ^{40}\text{Ar}$ (Roddick, 1978; Roddick et al., 1980), which often allows homogeneous excess components to be identified. Errors on age and intercept age include individual errors on each point and linear regression by York's method (1969). The goodness of fit relative to individual errors is measured by Mean Square Weighted Deviation (MSWD).

Classical furnace step heating was conducted and usually yielded an almost perfectly flat age spectra, from which plateau and isochron ages were calculated and are shown side by side to assess potential excess argon problems. If the inverse isochron age is close to the plateau age and $^{40}\text{Ar} / ^{36}\text{Ar}$ is not significantly different from present day $^{40}\text{Ar} / ^{36}\text{Ar}$ atmospheric ratio (295.5), we consider that the plateau age is reliable. When this is not the case, we suspect a non-atmospheric initial $^{40}\text{Ar} / ^{36}\text{Ar}$ ratio and we thus prefer to rely on the inverse isochron age if this one is well determined.

All errors are quoted at 2 sigmas.

References

- Arnaud, N., P. Tapponnier, F. Roger, M. Brunel, U. Scharer, C. Wen, and Z. Q. Xu (2003), Evidence for Mesozoic shear along the western Kunlun and Altyn-Tagh fault, northern Tibet (China), *J. Geophys. Res.*, 108, DOI: 10.1029/2001JB000904.
- Berger, G. W., and D. York (1981), Geothermometry from Ar-40-Ar-39 Dating Experiments, *Geochim. Cosmochim. Acta*, 45, 795-811.
- Borghi, A., D. Castelli, B. Lombardo, and D. Visona (2003), Thermal and baric evolution of garnet granulites from the Kharta region of S Tibet, E Himalaya, *Eur. J. Mineral.*, 15, 401-418.

- Catlos, E. J., C. S. Dubey, T. M. Harrison, and M. A. Edwards (2004), Late Miocene movement within the Himalayan Main Central Thrust shear zone, Sikkim, north-east India, *J. Metamorph. Geol.*, 22, 207-226.
- Compston, W., I. S. Williams, and C. E. Meyer (1984), U-Pb geochronology of zircons from lunar breccia 73217 using a sensitive high mass-resolution ion microprobe., *J. Geophys. Res.*, 89, 525-534.
- Cottle, J. M., M. J. Jessup, D. L. Newell, M. S. A. Horstwood, S. R. Noble, R. R. Parrish, D. J. Waters, and M. P. Searle (2009), Geochronology of granulitized eclogite from the Ama Drime Massif: Implications for the tectonic evolution of the South Tibetan Himalaya, *Tectonics*, 28, DOI: 10.1029/2008TC002256.
- Dale, J., T. Holland, and R. Powell (2000), Hornblende-garnet-plagioclase thermobarometry: a natural assemblage calibration of the thermodynamics of hornblende, *Contrib. Mineral. Petrol.*, 140, 353-362.
- Dalrymple, G. B., and M. A. Lanphere (1974), Ar-40/Ar-39 Age Spectra of Some Undisturbed Terrestrial Samples, *Geochim. Cosmochim. Acta*, 38, 715-738.
- Deloule, E., M. Chaussidon, B. P. Glass, and C. Koeberl (2001), U-Pb isotopic study of relict zircon inclusions recovered from Muong Nong-type tektites, *Geochim. Cosmochim. Acta*, 65, 1833-1838.
- Farley, K. A., R. A. Wolf, and L. T. Silver (1996), The effects of long alpha-stopping distances on (U-Th)/He ages, *Geochim. Cosmochim. Acta*, 60, 4223-4229.
- Groppi, C., B. Lombardo, F. Rolfo, and P. Pertusati (2007), Clockwise exhumation path of granulitized eclogites from the Ama Drime range (Eastern Himalayas), *J. Metamorph. Geol.*, 25, 51-75.
- Hodges, K. V., W. E. Hames, W. Olszewski, B. C. Burchfiel, L. H. Royden, and Z. Chen (1994), Thermobarometric and Ar-40 Ar-39 Geochronological Constraints on Eohimalayan Metamorphism in the Dinggye Area, Southern Tibet, *Contrib. Mineral. Petrol.*, 117, 151-163.
- Holland, T., J. Baker, and R. Powell (1998), Mixing properties and activity-composition relationships of chlorites in the system MgO-FeO-Al₂O₃-SiO₂-H₂O, *Eur. J. Mineral.*, 10, 395-406.
- Holland, T., and R. Powell (1996), Thermodynamics of order-disorder in minerals.2. Symmetric formalism applied to solid solutions, *Am. Mineral.*, 81, 1425-1437.
- Holland, T. J. B., and R. Powell (1998), An internally consistent thermodynamic data set for phases of petrological interest, *J. Metamorph. Geol.*, 16, 309-343.
- Jessup, M. J., D. L. Newell, J. M. Cottle, A. L. Berger, and J. A. Spotila (2008), Orogen-parallel extension and exhumation enhanced by denudation in the trans-Himalayan Arun River gorge, Ama Drime Massif, Tibet-Nepal, *Geology*, 36, 587-590.
- Li, D., Q. Liao, Y. Yuan, Y. Wan, D. Liu, X. Zhang, S. Yi, S. Cao, and D. Xie (2003), SHRIMP U-Pb zircon geochronology of granulites at Rimana (Southern Tibet) in the central segment of Himalayan Orogen, *Chinese Sci. Bull.*, 48, 2647-2650.
- Liu, Y., W. Siebel, H. J. Massonne, and X. C. Xiao (2007), Geochronological and petrological constraints for tectonic evolution of the central Greater Himalayan Sequence in the Kharta area, southern Tibet, *J. Geol.*, 115, 215-230.
- Lombardo, B., and F. Rolfo (2000), Two contrasting eclogite types in the Himalayas: implications for the Himalayan orogeny, *J. Geodyn.*, 30, 37-60.
- Ludwig, K. R. (2003), Isoplot 3.00 a geochronological toolkit for Microsoft Excel, *Berkley Geochronology Center Spec. Pub.*, 4.
- Newton, R. C., T. V. Charlu, and O. J. Kleppa (1980), Thermochemistry of the High Structural State Plagioclases, *Geochim. Cosmochim. Acta*, 44, 933-941.

- Renne, P. R., C. C. Swisher, A. L. Deino, D. B. Karner, T. L. Owens, and D. J. DePaolo (1998), Intercalibration of standards, absolute ages and uncertainties in Ar-40/Ar-39 dating, *Chem. Geol.*, 145, 117-152.
- Roddick, J. C. (1978), Application of Isochron Diagrams in Ar-40-Dating Ar-39-Dating - Discussion, *Earth Planet. Sci. Lett.*, 41, 233-244.
- Roddick, J. C., R. A. Cliff, and D. C. Rex (1980), The Evolution of Excess Argon in Alpine Biotites - a Ar-40-Ar-39 Analysis, *Earth Planet. Sci. Lett.*, 48, 185-208.
- Scharer, U. (1984), The Effect of Initial Th-230 Disequilibrium on Young U-Pb Ages - the Makalu Case, Himalaya, *Earth Planet. Sci. Lett.*, 67, 191-204.
- Spear, F. S. (1993), *Metamorphic Phase Equilibria and Pressure Temperature Time Paths. 2nd Eds.*, Mineralogical Society of America, Washington, DC.
- Stern, R. A. (1997), The GSC Sensitive High Resolution Ion Microprobe (SHRIMP); analytical techniques of zircon U-Th-Pb age determinations and performance evaluation., *Current Research - Geol. Surv. Can.*
- Stern, R. A., and Y. Amelin (2003), Assessment of errors in SIMS zircon U-Pb geochronology using a natural zircon standard and NIST SRM 610 glass, *Chem. Geol.*, 197, 111-142.
- Tera, F., and G. J. Wasserburg (1972), U-Th-Pb Systematics in 3 Apollo 14 Basalts and Problem of Initial Pb in Lunar Rocks, *Earth Planet. Sci. Lett.*, 14, 281-&.
- White, R. W., R. Powell, and T. J. B. Holland (2007), Progress relating to calculation of partial melting equilibria for metapelites, *J. Metamorph. Geol.*, 25, 511-527.
- White, R. W., R. Powell, T. J. B. Holland, and B. A. Worley (2000), The effect of TiO₂ and Fe₂O₃ on metapelitic assemblages at greenschist and amphibolite facies conditions: mineral equilibria calculations in the system K₂O-FeO-MgO-Al₂O₃-SiO₂-H₂O-TiO₂-Fe₂O₃, *J. Metamorph. Geol.*, 18, 497-511.
- Wiedenbeck, M., P. Alle, F. Corfu, W. L. Griffin, M. Meier, F. Oberli, A. Vonquadt, J. C. Roddick, and W. Speigel (1995), 3 Natural Zircon Standards for U-Th-Pb, Lu-Hf, Trace-Element and Ree Analyses, *Geostand. Newslett.*, 19, 1-23.
- Williams, C. T. (1996), Analysis of rare earth minerals, in *Rare earth minerals. Chemistry, origin and ore deposits*, 7, edited by A. P. Jones, et al., pp. 327-348, Chapman and Hall, London.
- York, D. (1969), Least Squares Fitting of a Straight Line with Correlated Errors, *Earth Planet. Sci. Lett.*, 5, 320-&.
- Zhang, J. J., and L. Guo (2007), Structure and geochronology of the southern Xainza-Dinggye rift and its relationship to the south Tibetan detachment system, *J. Asian Earth Sci.*, 29, 722-736.

Table DR1 : micro-structural data

general location (Fig. 3a)	zone	GPS outcrop	GPS handset UTM coordinates easting nording	altitude (m)	facies	structure	plane strike & dip	direction Azimuth or pitch	sense
STDsz Dzakar Chu	a	7-74	536333 3127952	3755	micaschists and gneiss	foliation	N090 12N	/	
		7-22	527382 3134169	3883	micaschists and deformed leucogranites	foliation / lineation	N080 45N	P 45E	
					deformed leucogranite	foliation / lineation	N070 50N	P 10E	
					deformed leucogranite	foliation / lineation	N080 45N	P 22E	
					micaschists	foliation	N083 50N	/	
					micaschists	foliation	N075 53N	/	
North-Kharta basin	b	7-75	525128 3134736	3910	micaschists and defomed leucogranites	foliation / lineation	N055 10N	Az 30	top to the N
					deformed granite	foliation / lineation	N000 45W	P20N	
					deformed granite	foliation / lineation	N000 40W	P20N	
					plan plus tardif	foliation / lineation	N005 63W	/	
					deformed granite	foliation / lineation	N170 30W	P20N	
					deformed granite	foliation / lineation	N155 45W	P0	
North-Kharta	c	7-21	522482 3135439	3976	micaschists and defomed leucogranites	foliation / lineation	N150 30W	/	
					migmatitic gt paragneiss	foliation	N000 25W	/	
					migmatitic gt paragneiss	foliation	N154 40W	Az 30	
		7-30	533268 3112113	3680	migmatitic gt paragneiss	foliation / lineation	N156 45W	/	
					migmatitic gt paragneiss	foliation / lineation	N150 30W	Az 40	
					Chlorite bearing fault	fault plane	N160 54W	/	
					Chlorite bearing fault	fault plane / striation	N022 50E	p82N	
					migmatitic gt paragneiss	foliation / lineation	N135 50W	P50S	top to the S?
					migmatitic gt paragneiss	foliation	N160 50W	/	
		7-69	534388 3112074	3611	migmatitic gt paragneiss	foliation	N145 68W	/	
					migmatitic gt paragneiss	foliation / lineation	N162 53W	P62S	
South-Kharta	d				migmatitic gt paragneiss	foliation / lineation	N150 54W	P54S	
					migmatitic gt paragneiss	foliation / lineation	N155 62W	p35S	
					migmatitic gt paragneiss	foliation / lineation	N142 62W	P40S	
					migmatitic gt paragneiss	foliation / lineation	N155 60W	P52S	
		7-70	533710 3115063	3638	migmatitic paragneiss		N150 45W	/	
		7-71	533358 3116258	3684	migmatitic paragneiss		N150 42W	P70S	
Arun South gorges	e				migmatitic gt paragneiss	foliation	N050 70N	/	
		7-26	530582 3106039	3761	migmatitic gt paragneiss	foliation	N045 80N	/	
					migmatitic gt paragneiss	foliation	N050 80N	/	
		7-27	531028 3106176	3737	migmatitic gt paragneiss	foliation	N050 70N	/	
					migmatitic gt paragneiss	foliation	N045 30N	/	
		7-28	533390 3107737	3650	migmatitic gt paragneiss	foliation	N050 40N	/	
		7-58	535328 3108180	3575	green schist foliation	foliation	N000 55W	/	
		7-64	535382 3107980	3586	mylonitic orthogneiss	foliation / lineation	N170 60W	P60S	top to the W
		7-57	535400 3107973	3595	phlogopite rich level	foliation / lineation	N150 60W	P67S	
		7-63	535429 3107977	3588	Mylonitic orthogneiss	foliation	N015 75W	/	
					Mylonitic orthogneiss	foliation	N005 60W	/	
West Tanghyu valley	f	7-56	535459 3107968	3583	Chlorite cataclasite	foliation	N170 47W	/	
		7-40	535890 3107836	3596	folded quartz cataclasite	foliation	N165 13W	/	
		7-41	535996 3107755	3609	cataclasite	foliation / lineation	N020 37W	Az 100	
		7-62	535994 3107747	3628	cataclastic orthogneiss	foliation / lineation	N000 40W	Az90	
		7-61	536095 3107586	3670	mylonite	foliation / lineation	N000 55W	/	
		7-55	536161 3107508	3665	garnet micaschist	foliation / lineation	N000 25W	Az 25	
		7-54	536207 3107381	3648	mylonite	foliation / lineation	N176 58W	P82N	
		7-53	536408 3106929	3702	mylonitic orthogneiss	foliation	N010 40W	/	
		7-42	536644 3106653	3749	Leucocratic gneiss	foliation / lineation	N130 35S	Az 130	
		7-51	536694 3106562	3761	garnet micaschist	foliation / lineation	N165 34W	P 48N	
		7-50	536731 3106479	3735	gneiss	foliation	N014 44W	/	
					gneiss	foliation / lineation	N173 62W	P82N	
		7-49	536752 3106372	3707	gneiss	foliation / lineation	N000 50W	Az 115	top to the W
					gneiss	foliation	N160 45W	/	
		7-48	536834 3106266	3710	leucocratic gneiss	foliation	N170 28W	/	
		7-47	537011 3106030	3686	gneiss	foliation / lineation	N000 42W	P 42N	top to the W
		7-46	537084 3105891	3665	gneiss	foliation	N020 55W	/	
					gneiss	foliation	N030 20W	/	
		7-45	537157 3105723	3647	orthogneiss	foliation	N025 55 W	/	
		7-65	537487 3123305	4078	Mylonitic quartzite	foliation	N050 35W	/	
					Mylonitic quartzite	foliation	N045 23W	/	
					brittle fault	fault plane	N020 65W	/	
					Mylonitic gneiss	foliation / lineation	N020 40W	Az 110	
		7-66	537600 3123282	4119	Mylonitic gneiss	foliation / lineation	N015 35W	AZ 115	
					Mylonitic gneiss	foliation / lineation	N015 30W	AZ 112	
					Mylonitic gneiss	foliation / lineation	N175 45W	AZ 110	Top to the W
		7-67	537688 3123260	4117	Biotite rich gneiss with deformed leucocratic veins	foliation / lineation	N155 30W	Az 110	Top to the W
					Biotite rich gneiss with deformed leucocratic veins	foliation / lineation	N030 22W	/	
					deformed granitic dyke	foliation / lineation	N020 26W	Az 100	
		7-68	537931 3123217	4099	"a" fold		N025 55W	Az 111	
							N000 20W	/	
							N05 32W	Az 85	Top to the W
							N05 42W	Az 95	

Data plotted on Fig. 4. For zone locations see Fig. 2a.

Table DR2: Mineral data (1) representative composition of biotite

Sample	T5D39b	T5D39b	T5D39b*	T5D39b*	T5D33	T5D33*						
SiO ₂	35.20	35.08	34.74	34.22	35.07	34.99	34.04	34.96	35.63	35.30	35.24	34.38
Al ₂ O ₃	18.26	19.24	18.67	18.50	19.47	19.86	18.25	19.31	18.70	18.95	18.81	19.89
FeO	22.04	20.15	22.59	21.36	20.59	21.27	19.79	21.34	21.45	20.79	21.48	21.01
MnO	0.19	0.14	0.17	0.16	0.17	0.14	0.17	0.22	0.20	0.15	0.17	0.20
MgO	6.97	8.17	6.88	7.46	7.98	7.37	7.47	7.50	6.98	7.44	7.36	7.99
CaO	0.00	0.00	0.05	0.02	0.00	0.00	0.00	0.00	0.00	0.00	0.00	0.06
Na ₂ O	0.14	0.10	0.13	0.13	0.12	0.14	0.13	0.11	0.14	0.10	0.12	0.19
K ₂ O	10.12	10.15	10.10	10.07	10.26	10.11	10.13	10.18	10.18	10.17	10.20	9.77
TiO ₂	3.61	3.22	3.35	3.14	2.21	2.19	3.56	2.58	3.13	3.78	3.43	1.04
Total	96.64	96.25	96.68	95.06	95.91	96.07	93.56	96.22	96.80	96.83	94.55	97.75
Si	5.46	5.39	5.40	5.38	5.43	5.42	5.41	5.42	5.50	5.42	5.43	5.41
Al tet	2.54	2.61	2.60	2.62	2.57	2.58	2.59	2.58	2.50	2.58	2.57	2.59
Al octa	0.80	0.88	0.82	0.81	0.98	1.04	0.83	0.95	0.90	0.85	0.84	1.10
Fe ²⁺	2.54	2.30	2.61	2.50	2.37	2.45	2.34	2.46	2.46	2.37	2.46	2.39
Fe ³⁺	0.03	0.03	0.03	0.03	0.03	0.03	0.03	0.03	0.03	0.03	0.03	0.03
Mg	1.61	1.87	1.59	1.75	1.84	1.70	1.77	1.73	1.61	1.70	1.69	1.87
Ti	0.42	0.37	0.39	0.37	0.26	0.25	0.43	0.30	0.36	0.44	0.40	0.12
Mn	0.02	0.02	0.02	0.02	0.02	0.02	0.02	0.03	0.03	0.02	0.02	0.03
Li	0.00	0.00	0.00	0.00	0.00	0.00	0.00	0.00	0.00	0.00	0.00	0.00
K	2.00	1.99	2.00	2.02	2.02	2.00	2.05	2.01	1.99	2.00	1.96	1.98
Na	0.04	0.03	0.04	0.04	0.04	0.04	0.04	0.03	0.04	0.03	0.03	0.05
X _{Fe}	0.61	0.55	0.62	0.59	0.57	0.59	0.57	0.59	0.61	0.59	0.60	0.57

Weight oxide (%), cations p.f.u. and X_{Fe}[(Fe/Mg+Fe)] as calculated for each electronic microprobe measurement. Fe³⁺ has been calculated by stoichiometry.* data used for classical thermobarometry.

Table DR2: Mineral data (2) representative composition of muscovite

Sample Location	T5D39b Gt incl	T5D39b Gt incl	T5D39b Gt incl	T5D39b Gt incl	T5D39b Fol	T5D39b Fol	T5D39b Fol	T5D33 Fol	T5D33 Fol	T5D33 Fol	T5D33 Fol	T5D33 Fol		
SiO ₂	49.03	49.97	49.56	49.39	46.05	46.13	47.33	45.53	45.89	46.64	46.26	47.14	47.02	47.20
Al ₂ O ₃	32.02	33.22	34.85	33.97	35.45	34.70	34.24	35.96	34.87	35.58	35.67	34.74	36.71	35.64
FeO	1.62	2.09	1.10	1.66	1.04	1.73	1.15	1.19	1.31	1.12	0.49	1.50	0.55	1.15
MnO	0.03	0.00	0.02	0.03	0.01	0.01	0.02	0.00	-0.01	0.00	0.01	-0.01	0.00	0.00
MgO	0.90	0.65	0.44	0.44	0.58	0.87	0.61	0.47	0.65	0.53	0.47	0.76	0.49	0.50
CaO	0.06	0.05	0.06	0.07	0.00	0.00	0.02	0.00	0.00	0.01	0.00	-0.01	0.01	0.00
Na ₂ O	0.03	0.04	0.05	0.08	0.28	0.43	0.33	0.40	0.37	0.37	0.45	0.30	0.33	0.32
K ₂ O	10.74	11.22	10.66	10.72	11.55	11.02	11.07	11.53	11.39	11.21	11.40	11.52	11.15	11.58
TiO ₂	0.00	0.01	0.01	0.03	0.21	0.02	0.20	0.28	0.43	0.38	0.38	0.11	0.03	0.02
Total	94.42	97.25	96.75	96.40	95.18	94.91	94.98	95.35	94.92	95.87	95.16	96.07	96.28	96.40
Si	6.55	6.50	6.43	6.46	6.15	6.18	6.31	6.08	6.15	6.17	6.16	6.24	6.17	6.21
Al tet	1.45	1.50	1.57	1.54	1.85	1.82	1.69	1.92	1.85	1.83	1.84	1.76	1.83	1.79
Al octa	3.59	3.59	3.76	3.69	3.73	3.66	3.69	3.74	3.66	3.72	3.76	3.66	3.84	3.74
Fe ²⁺	0.02	0.03	0.01	0.02	0.01	0.02	0.01	0.01	0.02	0.01	0.01	0.02	0.01	0.01
Fe ³⁺	0.14	0.18	0.09	0.15	0.09	0.15	0.10	0.11	0.12	0.10	0.04	0.13	0.05	0.10
Mg	0.18	0.13	0.09	0.09	0.12	0.17	0.12	0.09	0.13	0.11	0.09	0.15	0.10	0.10
Ti	0.00	0.00	0.00	0.00	0.02	0.00	0.02	0.03	0.04	0.04	0.04	0.01	0.00	0.00
Mn	0.00	0.00	0.00	0.00	0.00	0.00	0.00	0.00	0.00	0.00	0.00	0.00	0.00	0.00
Li	0.00	0.00	0.00	0.00	0.00	0.00	0.00	0.00	0.00	0.00	0.00	0.00	0.00	0.00
K	1.83	1.86	1.77	1.79	1.97	1.88	1.88	1.96	1.95	1.89	1.94	1.95	1.86	1.95
Na	0.01	0.01	0.01	0.02	0.07	0.11	0.09	0.10	0.10	0.09	0.12	0.08	0.08	0.08
Xfe	0.47	0.62	0.53	0.65	0.45	0.50	0.48	0.57	0.52	0.50	0.36	0.50	0.38	0.52
ALVI	3.59	3.59	3.76	3.69	3.73	3.66	3.69	3.74	3.66	3.72	3.76	3.66	3.84	3.74

Weight oxide (%), cations p.f.u. and $X_{\text{Fe}}[\text{Fe}/(\text{Mg}+\text{Fe})]$ as calculated for each electronic microprobe measurement. Fe³⁺ has been calculated by stoichiometry. Inclusion within garnet (Inc) and in foliation (Fol)

Table DR2: Mineral data (3) representative composition of garnet

Weight oxide (%), cations p.f.u. and mineralogic end-members %, as calculated for each electronic microprobe measurement. * data used for classical thermobarometry

Table DR2: Mineral data (4) representative composition of feldspar

Sample Loc	T6D33 Plag Fol	T6D33* Plag Fol	T6D39b Plag Gt incl	T6D39b Plag Gt incl	T6D39b Plag Gt incl - core	T6D39b Plag Gt incl - core	T6D39b Plag Fol - rim	T6D39b Plag Fol - rim	T6D39b Plag Fol	T6D39b Plag Fol	T6D39b Plag Fol	T6D39b* Plag Fol	T6D33 Kfs Fol	T6D33 Kfs Fol	T6D39b Kfs Fol	T6D39b Kfs Fol				
SiO ₂	57.30	58.17	57.75	57.40	59.70	60.30	59.01	60.02	61.37	63.19	62.26	61.96	63.75	61.90	61.58	64.24	63.99	64.33	64.46	
Al ₂ O ₃	27.25	26.75	26.71	27.74	25.33	25.12	25.87	25.28	24.00	23.28	23.69	23.57	24.14	22.82	24.23	24.42	18.62	18.63	18.70	18.70
MgO	0.01	0.00	0.00	0.00	0.00	0.00	0.00	0.01	0.00	0.00	0.00	0.00	0.00	0.00	0.01	0.00	0.01	0.00	0.01	
FeO	0.03	0.02	0.09	0.31	0.07	0.20	0.05	0.02	0.18	0.00	0.02	0.01	0.00	0.13	0.22	0.01	0.00	0.00	0.00	
MnO	0.01	0.01	0.01	0.00	0.00	0.02	0.01	0.00	0.00	0.00	0.01	0.00	0.00	0.00	0.01	0.00	0.00	0.01	0.01	
Cr ₂ O ₃	0.00	0.00	0.00	0.00	0.01	0.01	0.01	0.00	0.00	0.00	0.00	0.00	0.00	0.01	0.00	0.00	0.00	0.00	-0.01	
TiO ₂	0.00	0.00	0.00	0.00	0.02	0.02	0.03	0.00	0.03	0.00	0.00	0.00	0.02	0.02	0.02	0.02	0.01	0.00	0.01	
NiO	0.00	0.00	0.00	0.00	0.00	0.00	0.00	0.01	0.02	0.00	0.00	0.00	0.02	0.00	0.00	0.00	0.00	0.00	0.00	
CaO	9.00	8.40	8.45	9.70	7.00	6.43	7.16	7.02	5.11	4.45	4.94	4.61	5.14	3.98	4.99	5.34	0.06	0.03	0.05	0.05
Na ₂ O	6.37	6.99	6.85	6.19	7.45	8.06	7.26	7.43	8.40	8.71	8.67	8.86	8.75	9.26	8.87	7.89	1.24	1.22	1.40	1.46
K ₂ O	0.22	0.11	0.18	0.08	0.37	0.13	0.37	0.35	0.36	0.44	0.27	0.52	0.25	0.45	0.26	0.17	15.67	15.78	15.41	15.44
Total	100.19	100.44	100.04	101.44	99.95	100.28	99.74	100.15	99.44	100.12	99.88	100.17	100.31	100.32	100.42	99.65	99.89	99.66	99.89	100.13
Site T																				
Si	2.56	2.59	2.59	2.55	2.67	2.68	2.64	2.67	2.74	2.79	2.76	2.77	2.74	2.81	2.74	2.73	2.98	2.98	2.98	2.98
Al	1.44	1.41	1.41	1.45	1.33	1.32	1.36	1.33	1.26	1.21	1.24	1.23	1.26	1.19	1.26	1.27	1.02	1.02	1.02	1.02
Site A																				
Mg	0.00	0.00	0.00	0.00	0.00	0.00	0.00	0.00	0.00	0.00	0.00	0.00	0.00	0.00	0.00	0.00	0.00	0.00	0.00	0.00
Fe	0.00	0.00	0.00	0.01	0.00	0.01	0.00	0.00	0.01	0.00	0.00	0.00	0.00	0.01	0.00	0.00	0.00	0.00	0.00	0.00
Mn	0.00	0.00	0.00	0.00	0.00	0.00	0.00	0.00	0.00	0.00	0.00	0.00	0.00	0.00	0.00	0.00	0.00	0.00	0.00	0.00
Cr	0.00	0.00	0.00	0.00	0.00	0.00	0.00	0.00	0.00	0.00	0.00	0.00	0.00	0.00	0.00	0.00	0.00	0.00	0.00	0.00
Ti	0.00	0.00	0.00	0.00	0.00	0.00	0.00	0.00	0.00	0.00	0.00	0.00	0.00	0.00	0.00	0.00	0.00	0.00	0.00	0.00
Ni	0.00	0.00	0.00	0.00	0.00	0.00	0.00	0.00	0.00	0.00	0.00	0.00	0.00	0.00	0.00	0.00	0.00	0.00	0.00	0.00
Ca	0.43	0.40	0.41	0.46	0.33	0.31	0.34	0.33	0.24	0.21	0.23	0.22	0.24	0.19	0.24	0.25	0.00	0.00	0.00	0.00
Na	0.55	0.60	0.60	0.53	0.65	0.70	0.63	0.64	0.73	0.75	0.75	0.76	0.75	0.79	0.76	0.68	0.11	0.11	0.13	0.13
K	0.01	0.01	0.01	0.00	0.02	0.01	0.02	0.02	0.02	0.02	0.02	0.03	0.01	0.03	0.01	0.01	0.93	0.94	0.91	0.91
Σ	1.00	1.01	1.01	1.01	1.01	1.02	1.00	1.00	0.98	1.00	1.01	1.01	1.01	1.01	1.02	0.95	1.04	1.05	1.04	1.05
% Ab	0.55	0.60	0.59	0.53	0.64	0.69	0.63	0.64	0.73	0.76	0.75	0.75	0.74	0.79	0.75	0.72	0.11	0.11	0.12	0.13
% An	0.43	0.40	0.40	0.46	0.33	0.30	0.36	0.34	0.25	0.21	0.24	0.22	0.24	0.19	0.23	0.27	0.00	0.00	0.00	0.00
% Or	0.01	0.01	0.01	0.00	0.02	0.01	0.02	0.02	0.03	0.02	0.03	0.01	0.03	0.01	0.01	0.89	0.89	0.89	0.88	0.87

Weight oxide (%), cations p.f.u. and mineralogic end-members %, as calculated for each electronic microprobe measurement. * data used for classical thermobarometry.
 Inclusion within garnet (Inc) and in foliation (Fol)

Table DR3: U/Pb zircons detailed data

Sample name	spot name	crystal	spot location b: border c: core	Age (Ma) 206/238	\pm (1 σ)	Age (Ma) 207/235	\pm (1 σ)	Age (Ma) 207/206	\pm (1 σ)	206/238 (%)	207/235 (%)	207/206 (%)	Used in average	U (ppm)	Th (ppm)	Th/U (ppm)	Pb m (%)	com Pb (%)			
T5D26	t5d20ter19	6	b2	7.3	0.2	7.3	1.7	14.3	471.8	0.00113	2.9	0.0072	22.9	0.0584	2.8	X	5953	104	0.02	5.8	0.04
T5D26	t5d20ter4	4	b	9.0	0.3	9.0	2.6	25.3	579.2	0.00139	2.8	0.0089	29.1	0.0497	1.6	X	8708	229	0.03	10.4	0.09
T5D26	4	1	c	9.1	0.4	9.1	1.8	7.5	414.2	0.00141	4.8	0.0090	20.2	0.0460	2.7	X	2889	21	0.01	3.5	0.41
T5D26	t5d20ter20	7	c	10.3	0.2	10.3	0.7	14.0	139.2	0.00159	2.2	0.0102	6.4	0.0495	1.2	X	7930	157	0.02	10.9	1.25
T5D26	t5d20ter7	5	b2	10.3	0.3	10.4	1.0	37.8	203.9	0.00160	3.0	0.0103	9.5	0.0570	2.8	X	8437	206	0.02	11.6	0.82
T5D26	t5d20ter18	6	b1	10.4	0.4	10.4	1.0	15.2	196.7	0.00162	3.5	0.0103	9.4	0.0529	2.9	X	15964	513	0.03	22.2	1.46
T5D26	t5d20ter21	8	c	10.5	0.2	10.5	0.6	15.0	117.2	0.00163	2.4	0.0104	5.6	0.0500	2.0	X	8519	157	0.02	11.9	0.41
T5D26	t5d20ter3	3	b	11.7	0.3	11.8	0.7	35.6	134.3	0.00181	2.5	0.0117	6.4	0.0474	1.1	X	8218	152	0.02	12.8	0.46
T5D26	t5d20ter2	3	c	11.7	0.3	11.7	0.7	6.4	137.2	0.00182	2.5	0.0116	6.4	0.0464	1.4	X	4743	81	0.02	7.4	0.00
T5D26	5	1	b1	21.5	1.0	21.7	6.9	37.9	628.6	0.00334	4.7	0.0216	32.4	0.0467	1.6		11006	113	0.01	31.6	0.00
T5D26	7	2	b	21.9	1.0	21.9	8.9	23.4	769.6	0.00340	4.5	0.0218	41.3	0.0631	3.9		8594	270	0.03	25.1	1.98
T5D26	6	2	c	27.1	1.2	27.1	9.7	24.9	695.2	0.00422	4.6	0.0271	36.5	0.0550	4.7		7847	256	0.03	28.4	1.05

See Fig. 7d and e.

Table DR4: U-Th/Pb monazite detailed data, (1) T5D5

Sample name	crystal	Spot Name	spot location b: border c: core	Age (Ma)	\pm (1 σ)	208/232	\pm (%)	238/206	\pm (%)	207/206	\pm (%)	Used in average	Used in TW	U (ppm)	Th (ppm)	206* (ppm)	comm 206 (%)
T5D5	15	15.1	c	10.44	0.5	.00055	7.3	491.89	2.1	.0618	4.5	Pop1	Pop1	8382	45227	14.6	4.5
T5D5	13	13.1	c	10.51	0.5	.00055	4.1	482.17	2.7	.0968	5.9	Pop1	Pop1	2605	54338	4.6	14.5
T5D5	19	19.1	b c	10.81	0.4	.00058	3.0	512.02	2.2	.0681	4.8	Pop1	Pop1	6510	57747	10.9	11.7
T5D5	3	3.1	c	11.39	0.4	.00058	3.9	473.28	2.4	.0613	6.0	Pop1	Pop1	3811	50193	6.9	6.9
T5D5	3	3.2	b	11.56	0.6	.00059	6.0	453.66	2.7	.0905	6.1	Pop1	Pop1	2684	59805	5.1	9.5
T5D5	9	9.1	b c	11.57	0.5	.00059	4.4	470.30	3.5	.0770	7.8	Pop1	Pop2	2956	56918	5.4	6.4
T5D5	18	18.1	c	12.16	0.5	.00067	3.3	466.95	2.3	.1449	3.7	Pop2	Pop2	8083	37393	14.9	7.9
T5D5	10	10.1	b	12.58	0.4	.00065	3.2	470.71	2.3	.0524	6.0	Pop2	Pop2	5357	52357	9.8	7.7
T5D5	11	11.2	c	12.78	0.3	.00065	2.7	443.80	2.0	.0507	3.9	Pop2	Pop2	10720	57278	20.8	2.4
T5D5	7	7.1	c	12.85	0.5	.00066	3.5	485.23	2.8	.0619	4.7	Pop2	Pop2	8512	53337	15.1	3.3
T5D5	11	11.1	b	12.88	0.4	.00066	2.7	469.37	2.1	.0516	4.6	Pop2	Pop2	7069	45384	12.9	4.4
T5D5	6	6.1	c	13.12	0.4	.00067	2.7	443.66	2.1	.0569	4.5	Pop2	Pop2	6066	60744	11.7	4.3
T5D5	12	12.1	c	13.19	0.4	.00066	2.8	457.23	2.2	.0603	4.6	Pop2	Pop2	5819	56305	10.9	2.7
T5D5	16	16.1	b	13.2	0.4	.00067	2.7	464.95	2.1	.0578	4.6	Pop2	Pop2	6374	60274	11.8	3.6
T5D5	4	4.1	c	13.69	0.5	.00069	3.3	452.95	2.6	.0655	5.0	Pop2	Pop2	5826	55476	11.1	3.1
T5D5	14	14.1	c	13.7	0.4	.00069	3.0	435.87	2.3	.0501	5.7	Pop2	Pop2	5083	53145	10.0	3.7
T5D5	17	17.1	c	13.77	0.6	.00068	4.2	444.79	2.4	.0515	5.8	Pop2	Pop2	11749	84046	22.7	0.0
T5D5	1	1.1	c	13.88	0.4	.00070	2.8	454.36	2.0	.0518	4.3	Pop2	Pop2	11568	91474	21.9	2.5

206*: radiogenic Pb, comm206: common Pb. TW: Tera-Wasserburg. See Fig. 7a, b and c.

Table DR4: U-Th/Pb monazite detailed data, (2) T5D22

Sample name	crystal	Spot Name	spot location b: border c: core	Age (Ma) 208/232	\pm (1 σ)	208/232	\pm (%)	238/206	\pm (%)	207/206	\pm (%)	Used in TW	U (ppm)	Th (ppm)	206* (ppm)	comm 206 (%)
T5D22	5	5.1	c	11.7	0.5	.00059	4.8	469.04	2.1	.0559	3.7	X	10262	106669	18.8	1.9
T5D22	2	2.2	b	12.2	0.4	.00061	3.1	500.76	2.1	.0551	3.9		8964	75560	15.4	2.2
T5D22	8	8.1	c	12.2	0.4	.00063	2.6	476.21	2.0	.0496	4.7	X	9744	56213	17.6	3.8
T5D22	7	7.2	b	12.3	0.4	.00063	2.8	463.68	2.0	.0477	4.5	X	12987	64225	24.1	1.9
T5D22	1	1.3	b	12.4	0.4	.00062	2.8	474.36	2.1	.0499	5.0	X	8075	56189	14.6	0.5
T5D22	3	3.1	c	12.5	0.3	.00062	2.6	482.40	2.1	.0558	3.8	X	11456	101725	20.4	0.0
T5D22	7	7.1	c	12.6	0.3	.00064	2.4	479.82	1.9	.0538	3.2	X	14567	112920	26.1	2.5
T5D22	9	9.1	b	12.9	0.4	.00065	3.0	484.74	2.1	.0629	4.4	X	9483	69708	16.8	2.9
T5D22	1	1.2	b	13.2	0.5	.00067	3.7	464.80	2.4	.0570	4.4	X	7697	56529	14.2	2.3
T5D22	4	4.1	c	13.2	0.4	.00067	3.2	470.39	2.0	.0546	4.0	X	9514	65533	17.4	2.3
T5D22	6	6.1	c	13.3	0.4	.00069	2.8	469.80	2.2	.0537	4.5	X	6826	49713	12.5	5.2
T5D22	1	1.1	c	13.6	0.4	.00068	2.8	467.58	2.2	.0497	5.0	X	7166	50416	13.2	1.8
T5D22	2	2.1	c	13.7	0.4	.00069	2.8	449.58	2.0	.0541	4.2		11338	93410	21.7	1.8
T5D22	4	4.2	b	14.3	0.8	.00073	5.8	446.77	5.1	.0555	3.7		12662	79368	24.3	3.8
T5D22	3	3.2	b	14.4	0.4	.00072	2.7	436.99	2.1	.0488	5.0		8481	61808	16.7	1.2

206*: radiogenic Pb, comm206: common Pb. TW: Tera-Wasserburg. See Fig. 7a, b and c.

Table DR5: Argon detailed data: (1) Dinggye sz biotites

Temperature °C	$^{40}\text{Ar}/^{39}\text{Ar}$	$^{38}\text{Ar}/^{39}\text{Ar}$	$^{37}\text{Ar}/^{39}\text{Ar}$	$^{36}\text{Ar}/^{39}\text{Ar}$ (10^{-3})	^{39}Ar (10^{-14} moles)	$F^{39}\text{Ar}$ released	% $^{40}\text{Ar}^*$	$^{40}\text{Ar}^*/^{39}\text{Ar}$	Age Ma	$\pm 1\sigma$ Ma
T5D6										
		Biotite		J= 0.009545						
700	10.613	0.117	0.071	31.736	0.37	1.08	11.49	1.22	20.87	0.93
750	9.469	0.077	0.033	21.975	0.07	1.30	31.23	2.96	50.22	3.12
800	3.657	0.059	0.029	8.246	0.27	2.09	32.86	1.20	20.57	0.86
833	2.614	0.057	0.028	6.153	0.41	3.30	29.74	0.78	13.34	0.59
866	1.620	0.058	0.016	2.735	0.94	6.07	48.93	0.79	13.60	0.25
900	1.072	0.059	0.011	1.206	2.01	11.99	64.95	0.70	11.95	0.14
933	0.882	0.059	0.009	0.756	5.00	26.73	72.48	0.64	10.98	0.06
966	0.775	0.057	0.010	0.422	6.87	46.98	81.41	0.63	10.83	0.05
1000	0.811	0.053	0.037	0.582	3.98	58.72	76.58	0.62	10.66	0.06
1033	0.862	0.046	0.062	0.768	2.50	66.10	71.77	0.62	10.62	0.09
1066	0.822	0.055	0.026	0.528	3.97	77.80	78.76	0.65	11.11	0.06
1100	0.797	0.058	0.013	0.257	3.96	89.47	88.09	0.70	12.06	0.05
1200	1.146	0.055	0.076	0.841	2.98	98.27	76.98	0.88	15.13	0.08
1400	9.163	0.058	0.151	25.794	0.59	100.00	16.70	1.53	26.17	0.70
T5D10										
		Biotite		J= 0.009075						
700	89.484	0.298	0.062	255.904	0.02	0.28	15.48	13.85	213.58	29.52
750	121.297	0.198	0.177	349.873	0.02	0.51	14.76	17.90	271.58	44.71
800	137.679	0.119	0.102	410.268	0.05	1.20	11.93	16.43	250.77	9.93
850	66.842	0.094	0.048	192.334	0.15	3.27	14.95	9.99	156.57	3.17
900	15.712	0.066	0.025	43.236	0.76	13.57	18.57	2.92	47.15	0.51
950	8.854	0.064	0.021	22.438	1.39	32.40	24.90	2.20	35.74	0.66
1000	11.823	0.062	0.048	30.991	0.81	43.47	22.40	2.65	42.84	0.50
1050	5.060	0.059	0.015	11.535	2.71	80.26	32.25	1.63	26.52	0.14
1100	9.592	0.062	0.030	24.212	1.10	95.25	25.22	2.42	39.18	0.28
1200	91.639	0.104	0.227	258.173	0.18	97.72	16.74	15.34	235.21	7.06
1400	86.586	0.061	0.074	245.933	0.17	100.00	16.05	13.90	214.29	3.56
T5D33										
		Biotite		J= 0.009545						
700	8.658	0.043	0.025	21.518	0.53	1.11	26.34	2.28	38.85	0.72
750	12.419	0.037	0.024	24.095	0.06	1.24	42.52	5.28	88.71	3.00
800	5.884	0.030	0.018	12.654	0.18	1.62	36.13	2.13	36.25	1.14
833	4.283	0.027	0.006	9.042	0.36	2.37	37.16	1.59	27.20	0.68
866	2.738	0.027	0.010	5.691	0.85	4.17	37.88	1.04	17.78	0.32
900	1.571	0.027	0.005	2.533	2.11	8.62	51.10	0.80	13.77	0.19
933	1.117	0.026	0.004	1.388	4.02	17.10	61.50	0.69	11.79	0.07
966	0.954	0.025	0.003	0.924	7.70	33.33	69.30	0.66	11.35	0.05
1000	0.939	0.025	0.007	0.749	5.57	45.08	74.35	0.70	11.98	0.06
1033	1.013	0.023	0.016	0.903	3.40	52.25	71.79	0.73	12.48	0.08
1066	1.054	0.024	0.011	0.816	2.94	58.44	75.29	0.79	13.61	0.07
1100	0.952	0.025	0.006	0.547	4.60	68.14	80.97	0.77	13.23	0.05
1200	0.929	0.025	0.006	0.553	12.98	95.51	80.30	0.75	12.80	0.03
1400	3.631	0.026	0.029	7.735	2.13	100.00	36.55	1.33	22.71	0.21
T539b										
		Biotite		J= 0.009545						
700	24.060	0.226	0.003	51.331	0.02	0.41	36.87	8.87	146.65	12.33
750	36.924	0.111	0.006	71.221	0.01	0.55	42.95	15.86	254.29	30.47
800	15.588	0.042	0.003	42.496	0.03	1.20	19.31	3.01	51.11	7.67
833	5.862	0.032	0.002	14.103	0.09	3.35	28.57	1.68	28.62	2.76
866	2.877	0.027	0.002	6.727	0.21	8.14	30.23	0.87	14.91	1.12
900	1.608	0.025	0.001	2.424	0.44	18.31	54.21	0.87	14.95	0.51
933	1.416	0.024	0.002	2.445	0.80	36.62	47.54	0.67	11.55	0.29
966	1.211	0.022	0.002	1.608	0.53	48.69	59.13	0.72	12.29	0.40
1000	1.614	0.022	0.005	2.146	0.35	56.77	59.49	0.96	16.45	0.60
1033	1.833	0.024	0.003	2.283	0.32	64.15	62.11	1.14	19.50	0.59
1066	1.445	0.023	0.003	1.908	0.43	74.02	59.62	0.86	14.78	0.44
1100	1.205	0.020	0.001	1.209	0.40	83.31	68.70	0.83	14.20	0.35
1200	1.303	0.020	0.019	1.441	0.58	96.58	65.89	0.86	14.73	0.30
1400	18.335	0.030	0.038	55.020	0.15	100.00	11.23	2.06	35.12	2.11

⁴⁰Ar*: radiogenic ⁴⁰Ar. See Fig. 8 and Fig. DR9

Table DR5: Argon detailed data: (2) Kartha sz biotites

Temperature °C	$^{40}\text{Ar}/^{39}\text{Ar}$	$^{38}\text{Ar}/^{39}\text{Ar}$	$^{37}\text{Ar}/^{39}\text{Ar}$	$^{36}\text{Ar}/^{39}\text{Ar}$ (10^{-3})	^{39}Ar (10^{14} moles)	F^{39}Ar released	% $^{40}\text{Ar}^*$	$^{40}\text{Ar}^*/^{39}\text{Ar}$	Age Ma	$\pm 1\sigma$ Ma
T07A10										
		Biotite		J= 0.009545						
700	14.191	0.134	0.043	42.768	0.24	2.15	10.82	1.54	26.26	1.32
750	18.578	0.104	0.105	50.921	0.02	2.37	18.93	3.52	59.58	10.01
800	8.115	0.085	0.025	15.843	0.06	2.90	42.09	3.42	57.88	3.63
833	4.558	0.083	0.019	11.254	0.16	4.30	26.62	1.21	20.78	1.73
866	2.427	0.081	0.029	5.745	0.52	9.03	29.31	0.71	12.21	0.46
900	1.208	0.082	0.023	2.132	1.29	20.73	46.33	0.56	9.61	0.22
933	0.764	0.083	0.008	0.872	3.30	50.60	63.72	0.49	8.37	0.09
966	0.626	0.082	0.005	0.326	2.44	72.66	81.45	0.51	8.76	0.09
1000	1.010	0.078	0.022	1.026	0.60	78.08	68.10	0.69	11.80	0.35
1033	1.076	0.077	0.017	1.224	0.49	82.54	64.64	0.70	11.94	0.38
1066	0.897	0.081	0.008	0.674	0.73	89.16	75.64	0.68	11.65	0.23
1100	0.779	0.083	0.004	0.560	0.75	95.96	76.20	0.59	10.19	0.19
1200	1.223	0.082	0.018	0.956	0.38	99.41	75.36	0.92	15.80	0.32
1400	26.812	0.085	0.029	81.607	0.07	100.00	9.99	2.68	45.56	3.84
T07A14										
		Biotite		J= 0.009545						
700	1.562	0.062	0.027	2.864	2.14	15.58	44.64	0.70	11.97	0.14
750	2.196	0.061	0.017	2.980	0.22	17.16	59.04	1.30	22.19	0.94
800	2.520	0.065	0.017	1.900	0.13	18.08	76.97	1.94	33.10	1.24
833	1.822	0.064	0.012	3.081	0.18	19.40	48.98	0.89	15.31	1.19
866	0.994	0.062	0.006	1.148	0.55	23.41	63.89	0.63	10.90	0.36
900	0.639	0.063	0.006	0.401	2.33	40.36	78.38	0.50	8.60	0.10
933	0.613	0.063	0.006	0.396	3.93	68.89	77.72	0.48	8.19	0.07
966	0.644	0.060	0.018	0.381	1.54	80.10	79.56	0.51	8.80	0.14
1000	0.970	0.050	0.072	0.860	0.59	84.37	72.19	0.70	12.02	0.34
1033	0.938	0.053	0.040	0.740	0.66	89.19	74.80	0.70	12.04	0.28
1066	0.928	0.059	0.020	0.246	0.74	94.55	90.16	0.84	14.36	0.14
1100	1.170	0.061	0.017	0.234	0.45	97.78	92.48	1.08	18.53	0.15
1200	4.141	0.051	0.144	1.097	0.23	99.44	91.90	3.81	64.37	0.39
1400	27.245	0.063	0.183	68.253	0.08	100.00	25.94	7.07	117.78	2.80
T07A19										
		Biotite		J= 0.009545						
700	45.415	0.165	0.079	145.736	0.09	0.49	5.14	2.33	39.76	4.15
750	25.326	0.083	0.099	74.153	0.05	0.74	13.42	3.40	57.62	5.13
800	15.626	0.038	0.089	44.213	0.06	1.05	16.30	2.55	43.34	3.91
833	11.319	0.033	0.105	27.821	0.09	1.53	27.25	3.08	52.35	2.62
866	8.893	0.036	0.147	22.267	0.16	2.41	25.89	2.30	39.22	1.59
900	6.765	0.029	0.048	17.676	0.37	4.43	22.54	1.53	26.07	0.83
933	3.394	0.023	0.013	6.768	1.94	15.05	40.51	1.37	23.52	0.20
966	2.119	0.021	0.007	2.301	3.33	33.27	66.98	1.42	24.27	0.12
1000	2.211	0.021	0.010	2.519	2.09	44.72	65.45	1.45	24.74	0.15
1033	2.762	0.021	0.018	4.476	1.26	51.62	51.44	1.42	24.30	0.19
1066	2.376	0.022	0.018	3.103	1.35	59.03	60.61	1.44	24.63	0.20
1100	1.842	0.020	0.011	1.421	4.89	85.78	76.15	1.40	23.99	0.07
1200	1.854	0.020	0.043	1.032	2.33	98.54	82.61	1.53	26.18	0.11
1400	21.353	0.032	0.129	60.811	0.27	100.00	15.79	3.37	57.13	1.17
T07A33										
		Biotite		J= 0.009545						
700	18.721	0.100	0.079	45.646	0.21	1.32	27.87	5.22	87.68	1.39
750	11.356	0.057	0.057	29.542	0.10	1.97	22.98	2.61	44.39	2.39
800	6.117	0.046	0.054	13.402	0.24	3.44	34.98	2.14	36.48	1.38
833	6.655	0.049	0.044	15.243	0.42	6.02	32.06	2.13	36.37	0.72
866	3.609	0.052	0.032	7.315	0.57	9.57	39.60	1.43	24.44	0.45
900	1.811	0.059	0.020	3.463	1.35	17.93	42.47	0.77	13.20	0.19
933	1.287	0.065	0.017	2.255	2.40	32.86	46.74	0.60	10.33	0.13
966	0.963	0.063	0.021	1.155	2.51	48.48	62.59	0.60	10.35	0.10
1000	1.107	0.047	0.042	1.497	1.91	60.31	58.45	0.65	11.10	0.14
1033	1.113	0.046	0.032	1.492	2.13	73.52	58.77	0.65	11.23	0.12
1066	1.068	0.060	0.022	1.248	1.97	85.76	63.70	0.68	11.67	0.12
1100	1.262	0.066	0.022	1.079	0.99	91.93	73.26	0.92	15.85	0.18
1200	5.480	0.049	0.143	2.566	0.88	97.40	85.96	4.71	79.35	0.25
1400	14.665	0.045	0.131	20.064	0.42	100.00	59.49	8.72	144.31	0.60

 $^{40}\text{Ar}^*$: radiogenic ^{40}Ar . See Fig. 8 and Fig. DR9

Table DR5: Argon detailed data: (3) Kharta sz Muscovites

Temperature °C	$^{40}\text{Ar}/^{39}\text{Ar}$	$^{38}\text{Ar}/^{39}\text{Ar}$	$^{37}\text{Ar}/^{39}\text{Ar}$	$^{36}\text{Ar}/^{39}\text{Ar}$ (10^{-3})	^{39}Ar (10^{14} moles)	$F^{39}\text{Ar}$ released	% $^{40}\text{Ar}^*$	$^{40}\text{Ar}^*/^{39}\text{Ar}$	Age Ma	$\pm 1\sigma$ Ma
T07A20										
	Muscovite			J= 0.009545						
700	12.813	0.075	0.000	30.953	0.23	0.35	28.46	3.65	61.72	1.90
750	8.544	0.041	0.007	19.803	0.10	0.50	31.28	2.67	45.45	2.23
800	2.812	0.015	0.012	5.603	0.26	0.89	40.44	1.14	19.48	0.97
833	1.570	0.014	0.014	3.061	0.43	1.54	41.19	0.65	11.10	0.50
866	1.066	0.013	0.010	1.786	0.70	2.59	48.68	0.52	8.91	0.34
900	0.844	0.014	0.006	1.350	1.42	4.71	50.40	0.43	7.31	0.17
933	0.836	0.014	0.006	1.623	2.11	7.86	40.27	0.34	5.79	0.16
966	0.646	0.013	0.004	0.920	3.29	12.78	54.87	0.35	6.10	0.08
1000	0.686	0.013	0.003	0.818	6.18	22.03	61.88	0.42	7.30	0.05
1033	0.562	0.013	0.002	0.496	9.11	35.66	70.38	0.40	6.80	0.04
1066	0.494	0.013	0.002	0.336	9.83	50.36	75.91	0.38	6.45	0.03
1100	0.494	0.013	0.002	0.318	10.54	66.13	76.94	0.38	6.53	0.03
1200	0.614	0.013	0.003	0.276	20.11	96.22	83.51	0.51	8.81	0.02
1400	3.114	0.014	0.043	5.177	2.53	100.00	50.31	1.57	26.78	0.15
T07A20										
	Muscovite rusty			J= 0.009545						
700	32.504	0.071	0.003	73.580	0.09	0.45	33.05	10.74	176.09	2.35
750	13.168	0.020	0.019	26.957	0.07	0.80	39.36	5.18	87.12	2.19
800	3.934	0.014	0.027	8.204	0.23	1.91	37.90	1.49	25.50	0.57
833	2.277	0.012	0.039	3.377	0.42	3.94	55.41	1.26	21.60	0.29
866	1.968	0.013	0.027	4.017	1.00	8.85	38.76	0.76	13.09	0.26
900	1.190	0.013	0.011	2.143	1.22	14.84	45.14	0.54	9.22	0.15
933	1.047	0.014	0.095	1.893	1.65	22.92	45.25	0.47	8.14	0.10
966	0.890	0.013	0.108	1.182	2.00	32.72	59.25	0.53	9.06	0.07
1000	0.868	0.013	0.112	0.898	3.50	49.87	67.91	0.59	10.12	0.05
1033	1.009	0.013	0.099	0.745	4.25	70.71	76.79	0.77	13.29	0.05
1066	1.832	0.013	0.096	0.927	2.81	84.45	84.27	1.54	26.40	0.06
1100	3.395	0.013	0.159	1.265	1.21	90.40	88.68	3.01	51.12	0.14
1200	6.872	0.014	0.567	1.920	1.64	98.44	91.95	6.32	105.69	0.19
1400	55.813	0.025	4.014	56.509	0.32	100.00	70.48	39.44	576.43	2.01
T7A48b										
	Muscovite			J= 0.009545						
700	39.014	0.116	0.045	42.389	0.15	1.78	67.85	26.47	406.42	2.04
750	10.995	0.045	0.022	12.226	0.07	2.65	66.97	7.36	122.55	2.63
800	4.610	0.017	0.042	6.052	0.16	4.58	60.83	2.80	47.66	1.65
833	3.619	0.015	0.029	3.980	0.18	6.76	67.00	2.42	41.28	1.09
866	5.044	0.015	0.029	4.287	0.28	10.24	74.52	3.76	63.59	1.00
900	1.972	0.014	0.019	2.395	0.32	14.14	63.15	1.25	21.31	0.57
933	2.459	0.016	0.014	4.677	0.37	18.72	43.01	1.06	18.12	0.65
966	1.689	0.013	0.008	1.671	0.45	24.24	69.60	1.18	20.12	0.43
1000	1.213	0.013	0.002	1.142	1.48	42.45	70.56	0.86	14.68	0.18
1033	1.020	0.013	0.001	0.940	1.43	60.03	70.83	0.72	12.41	0.15
1066	1.226	0.013	0.004	0.893	0.79	69.80	76.86	0.94	16.16	0.21
1100	1.441	0.014	0.001	1.000	0.37	74.28	78.12	1.13	19.28	0.33
1200	1.816	0.013	0.002	1.234	1.69	95.12	78.83	1.43	24.48	0.14
1400	29.216	0.022	0.006	31.557	0.40	100.00	68.02	19.87	313.33	0.90
T07A48b										
	Muscovite rusty			J= 0.009545						
700	37.083	0.064	0.113	108.854	0.44	4.28	13.22	4.90	82.53	1.74
800	9.114	0.034	0.100	25.748	0.48	8.93	16.37	1.49	25.51	0.84
850	4.214	0.019	0.092	12.013	0.74	16.10	15.41	0.65	11.15	0.39
900	4.253	0.016	0.064	12.046	1.24	28.10	15.92	0.68	11.62	0.35
950	2.552	0.015	0.054	6.329	1.38	41.37	26.05	0.66	11.41	0.30
1000	2.140	0.015	0.021	4.889	1.61	56.91	31.60	0.68	11.61	0.19
1050	1.394	0.014	0.009	2.337	2.88	84.68	49.09	0.68	11.75	0.12
1100	1.660	0.015	0.013	2.274	0.64	90.84	58.35	0.97	16.60	0.32
1200	1.544	0.016	0.015	1.964	0.75	98.03	61.17	0.94	16.19	0.28
1400	17.267	0.022	0.007	39.414	0.20	100.00	32.44	5.60	93.95	1.49

⁴⁰Ar*: radiogenic ⁴⁰Ar. See Fig. 8 and Fig. DR9

Table DR6: (U-Th)/He data

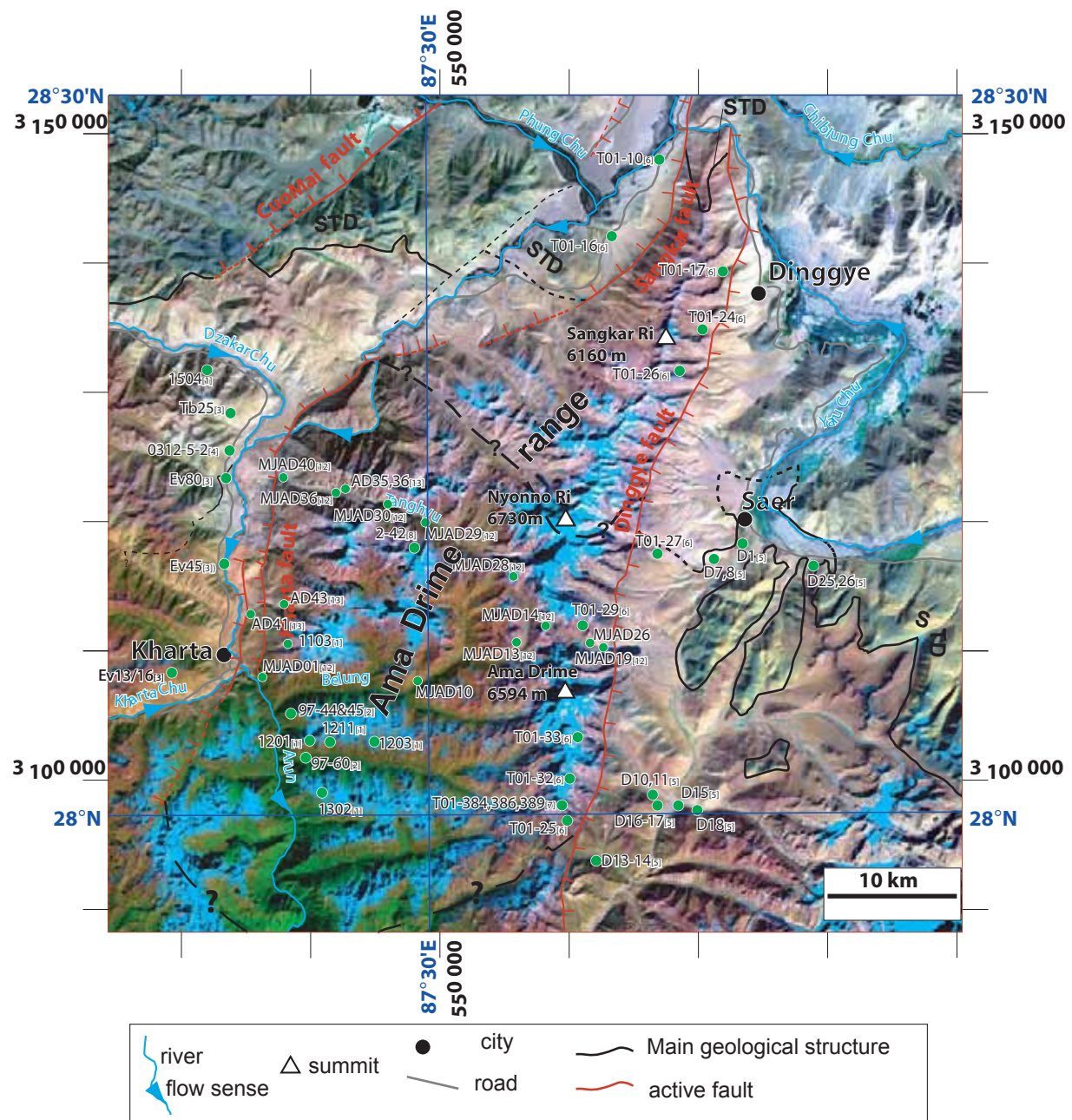
Sample	Elevation (m)	Replicate	nb grains	U (ppm)	Th (ppm)	He (nmol/g)	Radius (µm)	Lengh (µm)	Ft	Raw age (Ma)	Corr Age (Ma)	Mean age (Ma)	1σ error (Ma)
T5D01	5217											3.3	0.3 ⁽²⁾
		T5D01-1	1	134.8	2.9	2.16	126.0	288	0.89	2.9	3.3		
T5D22	5348											3.8	0.2 ⁽¹⁾
		TSD22-1	1	36.0	6.8	0.67	63.0	216	0.78	3.2	4.2		
		TSD22-2	1	40.8	8.4	0.68	54.0	297	0.76	2.9	3.8		
		<i>TSD22-3</i>	1	37.7	4.7	2.85	85.5	378	0.84	13.4	16.0		
		T5D22-4	1	27.2	6.7	0.41	58.5	162	0.77	2.6	3.4		
		T5D22-5	1	54.7	5.6	0.91	58.5	144	0.76	3.0	3.9		
T5D26	5419											3.4	0.2 ⁽¹⁾
		TSD26-1	1	108.9	29.1	1.67	49.5	216	0.73	2.6	3.6		
		TSD26-2	1	88.0	47.8	1.23	45.0	243	0.71	2.3	3.2		
		TSD26-3	1	35.3	4.0	0.59	63.0	297	0.79	3.0	3.8		
		TSD26-4	1	77.5	21.4	1.05	72.0	351	0.81	2.3	2.9		
T5D40	4270											3.2	0.1 ⁽¹⁾
		TSD40-1	1	51.5	11.6	0.69	45.0	243	0.71	2.3	3.2		
		TSD40-2	1	45.7	19.6	0.61	45.0	162	0.70	2.2	3.2		

nb grains: number of grains used for each replicate

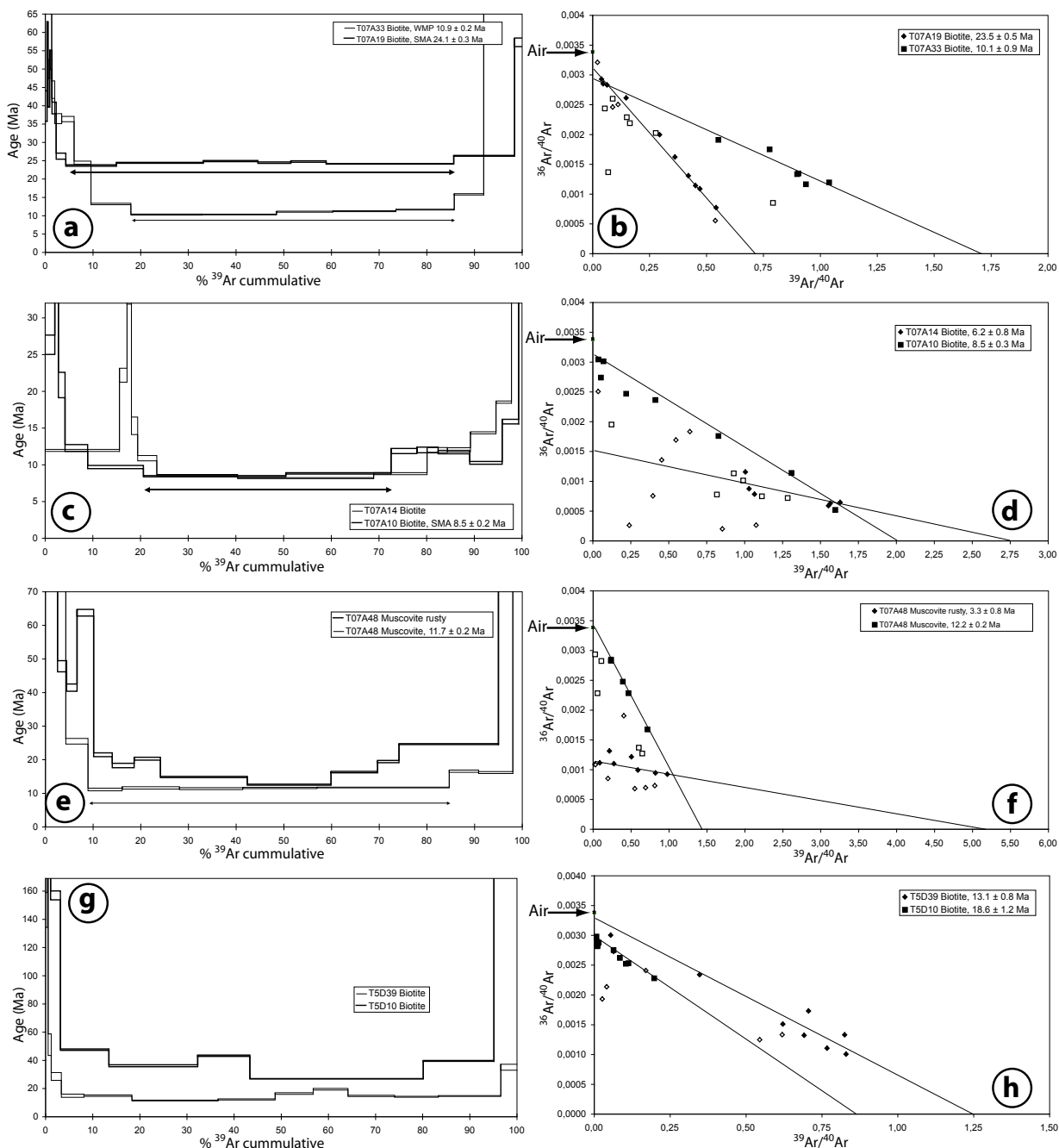
Age in italics is considered as an outlier and was not used for mean age calculation.

Ft: alpha ejection correction after Farley et al. (1996)

The 1σ error is taken either as (1) the standard deviation of the replicate analyses divided by $(n-1)^{1/2}$ where n is the number of replicate analyses performed, or (2) as 10% of the mean age (sample with only one replicate).

**Figure DR7: Landsat image corresponding to Fig. 2a.**

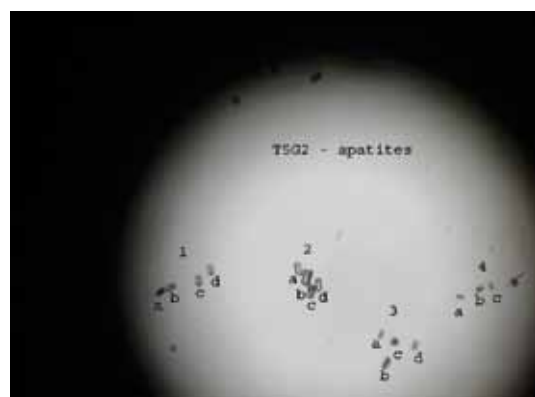
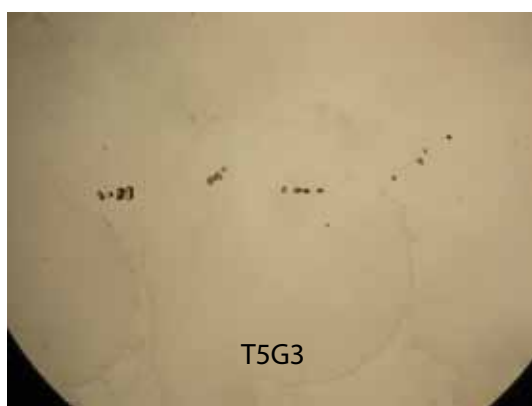
Composite R (Chanel 7), V (Chanel 4), B (Chanel 2) Landsat TM image. Major structures as on Fig. 2a. Samples from the literature discussed in text are located. [1] Liu et al., 2007 (samples 1504, 1211, 1201, 1302); [2] Lombardo and Rolfo, 2000 (samples 97-44 and 97-45); [3] Borghi et al., 2003 (samples Ev 13, 16, 45, 80); [4] Li et al., 2003 (sample 0312-5-2); [5] Hodges et al., 1994 (samples D1, 7, 8, 10, 11, 13, 14, 15, 16, 17, 18, 25, 26); [6] Zhang and Guo, 2007 (samples T01-10, 16, 24, 25, 26, 27, 29, 32, 33); [7] Liu et al., 2005 (samples T01-384, 386, 389); [8] Groppo et al., 2007 (samples EV02-42, 45). [12] Jessup et al., 2008 (samples MJAD1, 10, 13, 14, 19, 26, 30, 36, 40). [13] Cottle et al., 2009 (samples AD35, 36, 41 & 43).

**Figure DR8: Argon Data**

See table DR5 for detailed data. For inverse isochron plots, empty symbols were not used in the regression calculation. a, b) T7A33 and T7A19 biotites age spectra and inverse isochrons. c,d) T7A14 and T7A10 biotites age spectra and inverse isochrones. e,f) T7A48 muscovites (normal and rusty) age spectra and inverse isochrone. g,h) T5D39 and T5D10 biotites age spectra and inverse isochrone.

ANNEXE C

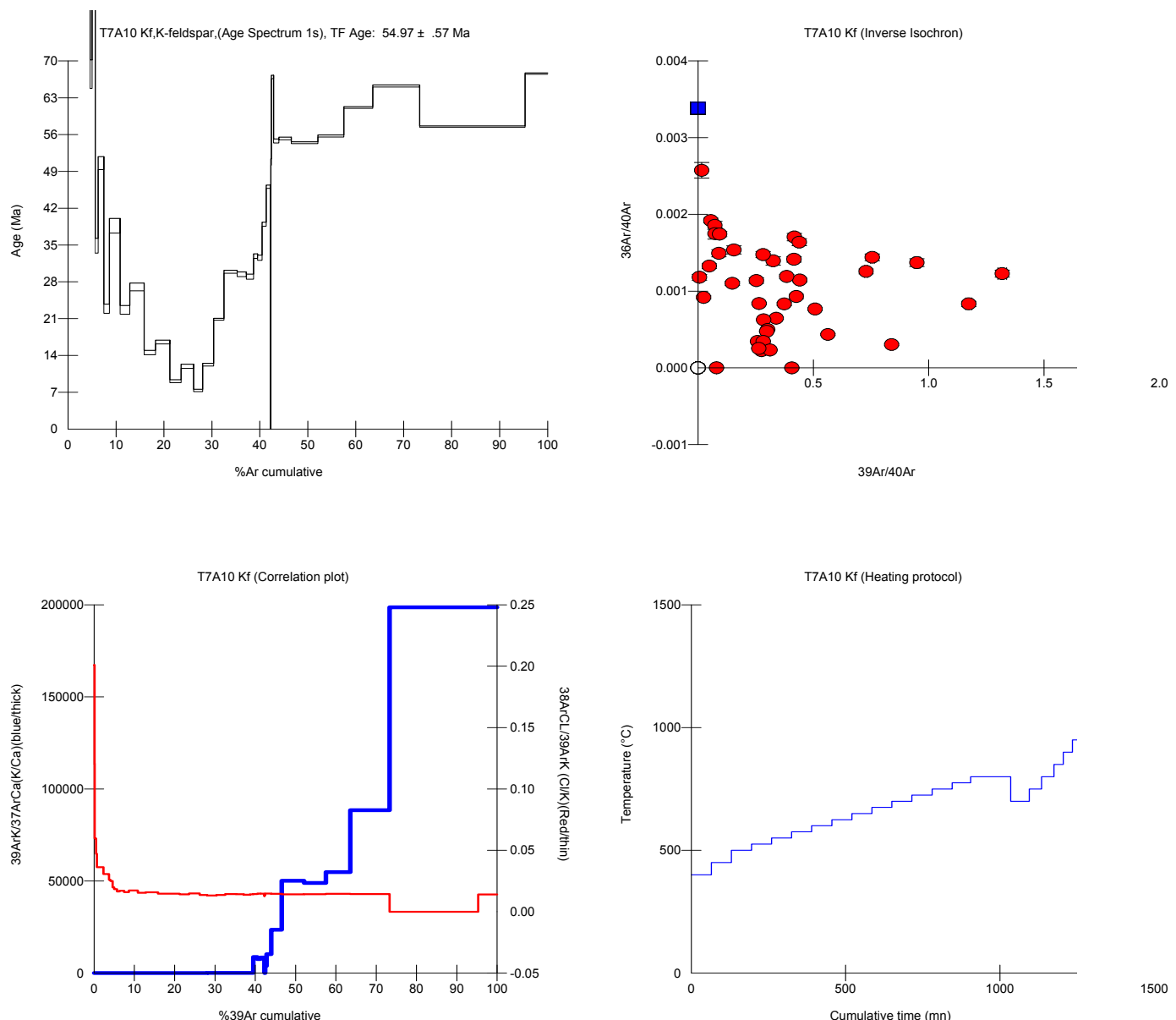
Example of photos of dated apatites (T5G2 & T5G3)



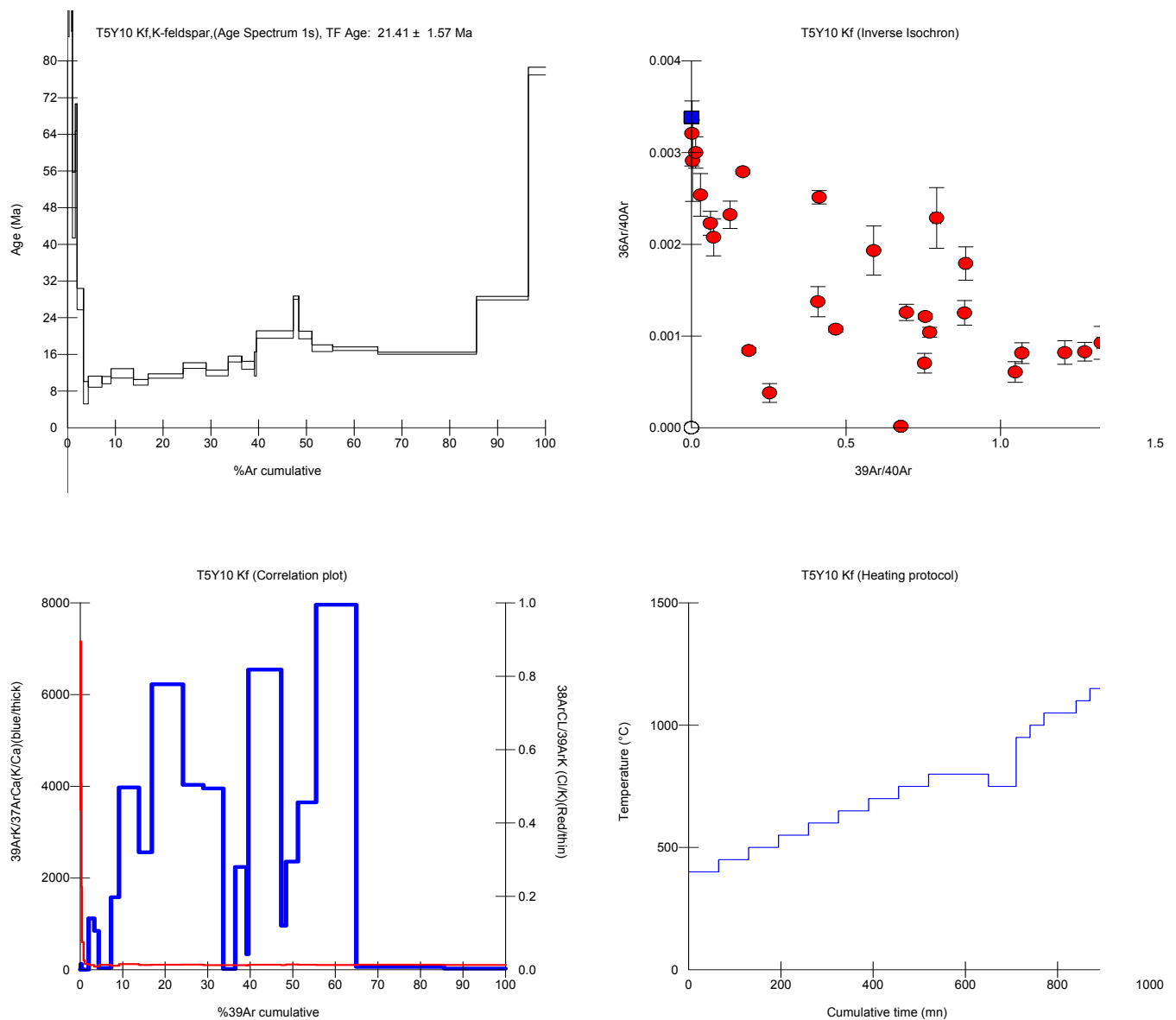
Appendix C

ANNEXE D

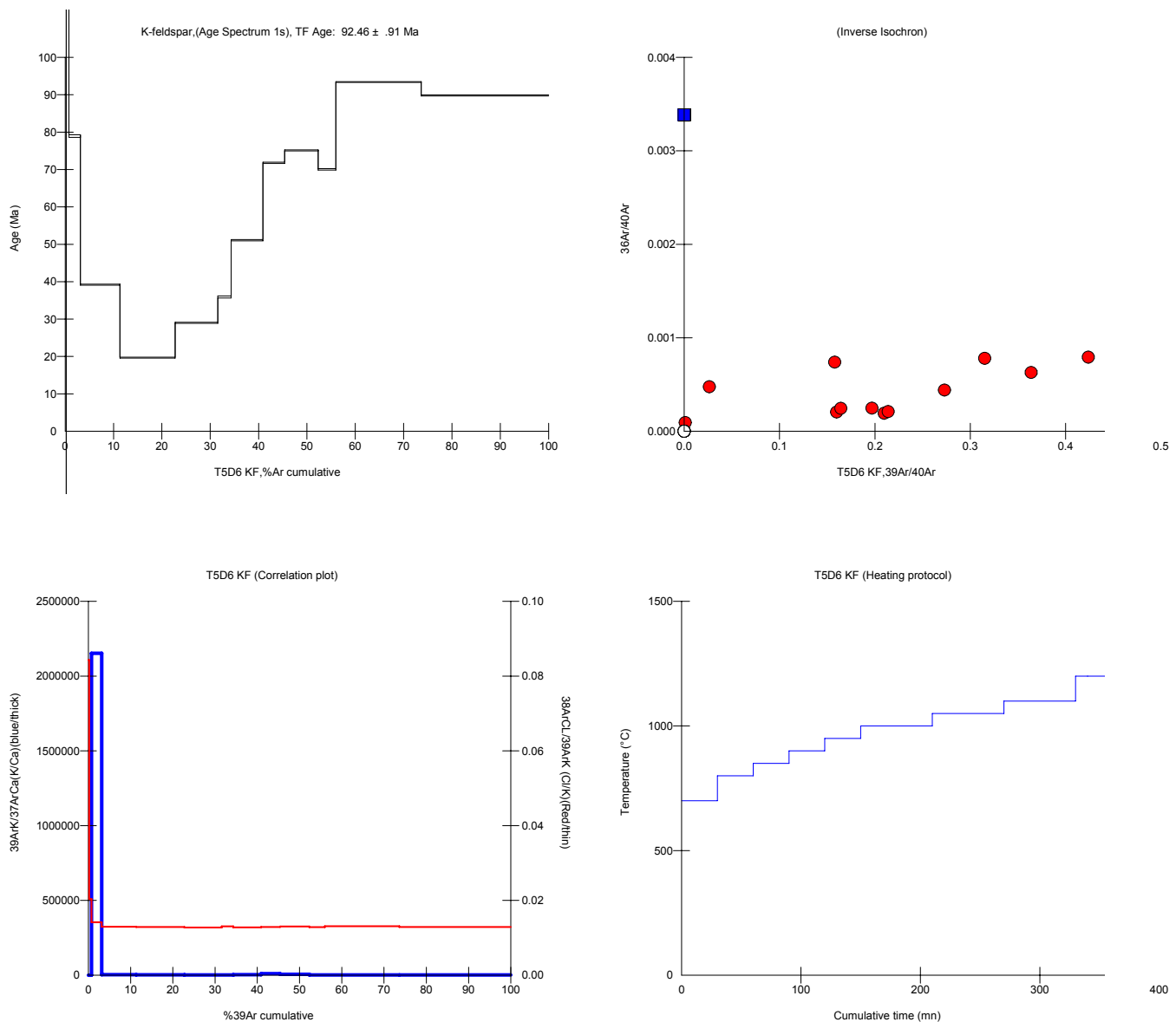
Examples of $^{40}\text{Ar}/^{39}\text{Ar}$ Data



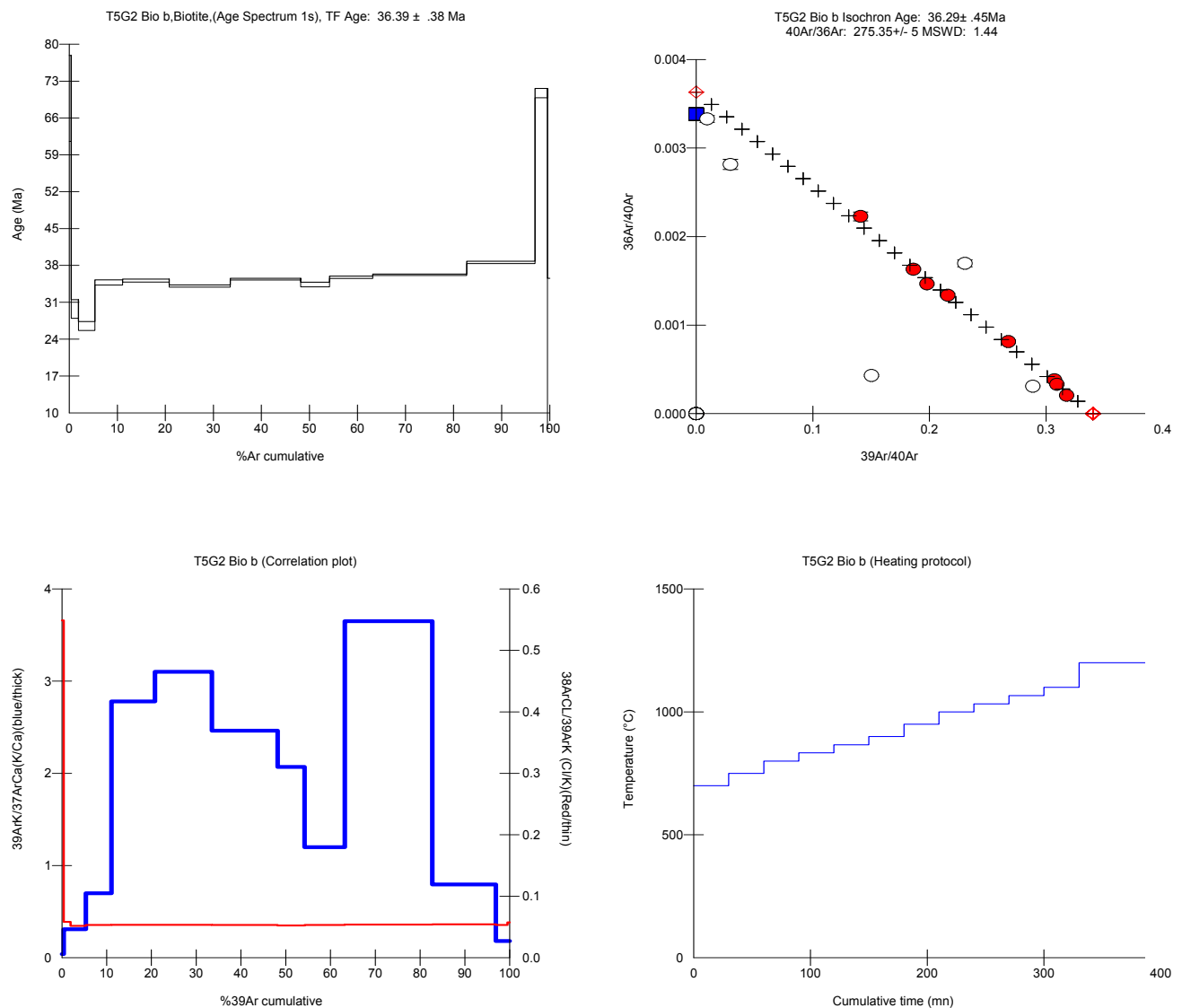
Appendix D: Sample T7A10kf



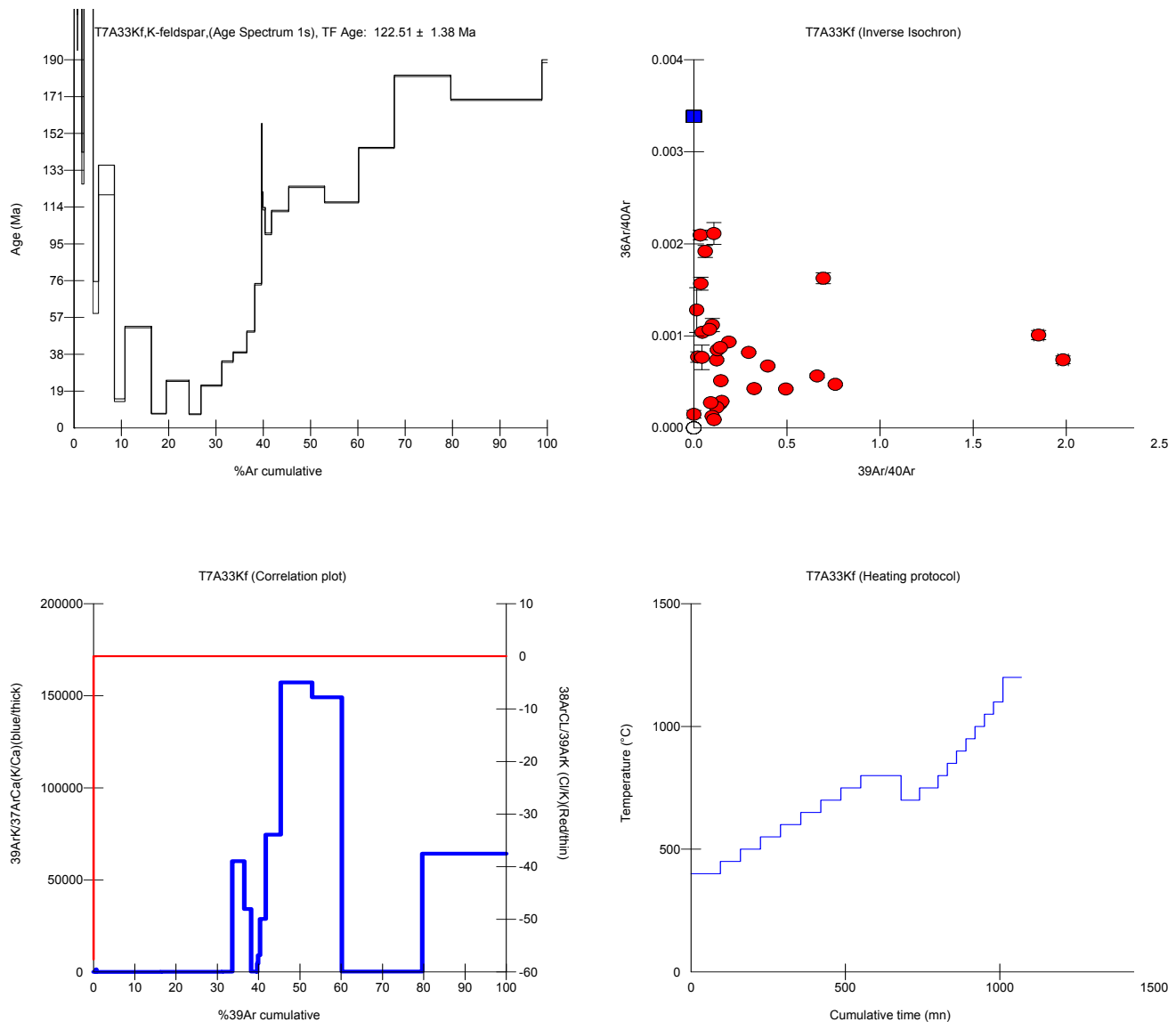
Appendix D : Sampe T5Y10Kf



Appendix D : sample T5D6Kf



Appendix D : sample T5G2bio



Appendix D : sample T7A33 Kf

ANNEXE E

Analysis of the Helium Standard, Durango Fluoroapatite

Table XX: Results of (U-Th)/He dating on the Durango fluoroapatite standard, from helium extraction ligne and ICP-MS of the Geoscience Montpellier Laboratory

Analysis n°	^{238}U (E-3 nmol/g)	^{232}Th (E-3 nmol/g)	^4He (mol)	Age He brut
Std a	1.24452E-12	2.62986E-11	2.70573E-13	28.76
Std b	1.48234E-12	3.26953E-11	3.34901E-13	28.83
Std c	1.31524E-12	2.96099E-11	3.07706E-13	29.3
Std d	1.31787E-12	2.87241E-11	2.98966E-13	29.25
Std e	1.22826E-12	2.62626E-11	2.77613E-13	29.5
Std f	1.53763E-12	3.28353E-11	3.26353E-13	27.8
Std g			2.24657E-13	
Std h	7.24682E-13	1.53685E-11	1.62334E-13	29.47
Std i	7.68577E-13	1.63409E-11	1.7325E-13	29.71
Std j			1.49037E-13	
Std k	1.21071E-12	2.73852E-11	2.78673E-13	28.74
Std L			1.57702E-13	
Moyenne				29.20
Ecart type				0.3737

ANNEXE F

Protocole détaillé d'extraction du Be et de l'Al à partir d'un échantillon quartzeux

Protocole détaillé d'extraction du Be et de l'Al à partir d'un échantillon quartzeux

Ce protocole a été établi à partir des protocoles d'extraction du laboratoire de Lawrence Livermore et du CEREGE (d'après Kohl & Nishiizumi 1992 ; Bierman et al., 2002), et des améliorations apportées au cours de cette thèse.

Les difficultés rencontrées lors de la chimie d'extraction illustrent ce protocole afin d'éviter les mêmes erreurs et d'améliorer la procédure.

Broyage

- Prise de photo avant le broyage (avec une échelle) pour noter l'épaisseur de l'échantillon, et l'estimation de la minéralogie (type de minéraux et part approximative) pour d'optimiser la suite de la procédure.
- Enclume/Masse/Marteau - Attention : garder un morceau représentatif de l'échantillon (1 à 2 cm³) avant de passer au broyeur, afin d'en garder un aperçu
- Broyeur
- Tamisage 4 fractions : Ø < 0,25 mm ; Ø = 0,25 – 0,5 mm ; Ø = 0,5 – 1 mm ; Ø > 1 mm
(Nettoyage entre chaque échantillon)

Chimie

Utiliser la feuille de suivi pour chaque échantillon, y inscrire toutes les pesées et remarques.

1^{ère} pesée :

- utiliser des petits bêchers 150-250 ml
- peser le bêcher et inscrire son poids et y le nom de l'échantillon
- tarer
- pour un échantillon de roche de surface, mettre 100 g d'échantillon de la fraction 0,25 – 0,5 mm et compléter avec la fraction 0,5 – 1 mm si nécessaire.
Pour un sable mettre 150g.

Pour une roche échantillonnée sur un profil vertical, 150 à 250g en fonction de la profondeur.

1 / Bain à l'acide chlorhydrique (HCl) : élimination des oxydes et de la matière organique :

- utiliser les bêchers 2L, les rincer, y inscrire les noms d'échantillons
- rincer les bêchers à l'eau distillée (ED), et les mettre sur la plaque (froide éteinte)
- pour 100g d'échantillon, verser 500 ml d'ED + 500 ml d'HCl à 37% (commencer par verser l'eau)

Solution économique : Pour 100g d'échantillon 250 ml d'ED + 250 ml d'HCl 37%

- verser l'échantillon, doucement au départ en cas de réaction vive
- [test de la présence de titane à l'eau oxygénée, avec 10 gouttes d'H₂O₂ (étape dispensable car actuellement, au CEREGE, le titane ne gène plus lors de l'analyse à l'ASTER)]
- allumer la plaque, chauffer 12h

Rinçage 1^{er} bain HCl : 3 rinçage à l'ED

- rincer le couvercle dans l'évier
- verser l'acide dans le bidon-déchet, en portant le masque de protection
- rincer les parois du bêcher avec la pissette sous la hotte
- rincer l'échantillon, 3 rinçages à l'ED

- remettre l'échantillon dans son bêcher de départ
- mettre à l'étuve à ~70°C
- éteindre la plaque chauffante
- laver les bêchers 2L (ED + scotch-brite)

Pesée après le séchage et avant l'étape de purification du quartz

Pour les échantillons n'étant pas du quartz pur (granite, gneiss, grès altéré...), des séparations mécaniques peuvent être appliquée telle que la séparation magnétique (Frantz) et/ou les liqueurs denses.

2/ Séparations mécaniques

La séparation magnétique (utilisation du Frantz), elle peut être utile pour les granites contenant beaucoup de biotites, et rend les bains HF plus efficaces ensuite. (En fonction du réglage, on peut aussi éliminer les muscovites, les grenats et beaucoup d'autres minéraux)

La séparation par densité (utilisation des liqueurs denses), elle peut être utile pour les échantillons contenant des grenats qui peuvent résister aux bains HF. Cela éliminera aussi les éventuelles muscovites.

3/ Les bains à l'acide fluorhydrique (HF) : purification du quartz

Plusieurs solutions permettent d'arriver à un quartz pur.

En fonction du type de roche, un type de purification sera adopté.

Les bains à ultrasons (3 bains successifs) :

Pour les granites (ou roche contenant moins de 30% de quartz) :
(d'après le protocole de Livermore → Kohl & Nishiizumi 1992)

- Dans les grands bidons en téflon (4L) : sous la hotte, mettre : 1/ l'eau, 2/ l'HF (à 40%), 3/ l'HNO₃, 4/ l'échantillon. La solution utilisée est à 1% d'HF_{40%} et 1% d'HNO₃, avec 7,5g d'échantillon/L.

- Mettre les bidons dans le bac à ultrasons
- Remplir d'eau jusqu'à hauteur de l'évacuation
- Desserrer les couvercles, sinon il y a risque d'explosion
- Allumer les ultrasons pour 12h à 90°C, la nuit
- Le lendemain, sortir les bidons et laisser refroidir
- Vider l'acide dans le bidon poubelle en portant le masque de protection

Sécher puis peser.

Ensuite renouveler l'opération deux fois, avec 15g d'échantillon/L.

Le séchage et la pesée entre chaque bain peuvent être évités en supposant une perte de masse de 10%.

Les bains à l'agitateur :

Pour les quartz purs
(d'après le protocole du CEREGE)

Cette procédure remplaçant le bain « acide hexafluorosilicique + HCl » avant la purification à l'HF pur avec agitateur, par un bain « HCl + ED » diffère du protocole du CEREGE. Pour valider ce remplacement nous avons mesuré les quantités d'aluminium au cours de la purification (Table 1). Aussi pour comparer la purification à l'agitateur aux ultrasons, des pesées ont été faites entre chaque bain (Figure 1 et 2) ainsi que les mesures d'aluminium (Table 1), pour les bains à l'agitateur. La comparaison des pertes de poids semble montrer que les bains à ultra-sons sont plus efficaces pour la purification des granites, pour les veines, les deux méthodes sont équivalentes.

<u>échantillon</u>	<u>Al (mg/ g qz)</u>
T7C-51 initial	0.31
T7C-51 hexa2	0.13
T7C-51 hexa3	0.12
T5C-51 HF2	0.13
T5C-51 HF3	0.10
T7C-51 QD	0.12
T7C-107 initial	3.66
T7C-107 hexa2	0.34
T7C-107 hexa3	0.25
T7C-107 HF2	0.14
T7C-107 HF3	0.14
T7C-107 QD	0.14
T7C-74 initial	1.13
T7C-74 hexa2	0.86
T7C-74 hexa3	0.74
T7C-74 HF2	19.79
T7C-74 HF3	16.40
T7C-74 QD	4.28
AST2.2 HCl	0.93
AST2.2 HF1	0.04
AST2.2 HF2	0.02
AST2.2 HF3	0.02
KN-bulk	79.00
KN-alfter HCl	67.50
KN-after 1st ultra	9.96
KN-after 2nd ultra	0.05
KN-after 3rd ultra	0.05
KN-after 4th ultra	0.06

Tableau 1 : Test de comparaison des purifications aux ultra-sons (suffixe KN- correspond aux tests de Kohl & Nishiizumi 1992) et à l'agitateur en mesurant la quantité d'aluminium des échantillons mesurés à l'ICP-MS, après chaque étape de bain. T7C-51 et AST2.2 sont des galets de quartz pur et T7C-107 est un grès, ces échantillons purifiés par bain à l'agitateur présentent des quantités d'Al raisonnable pour la poursuite du protocole de chimie. T7C-74 est un granite et présente des quantités d'Al élevées difficilement quantifiées à l'ICP-MS. Il a également montré des pertes de Be après la dissolution (voir table III.3 et paragraphe 4-1). Les granites devraient préférentiellement être purifiés aux ultra-sons.

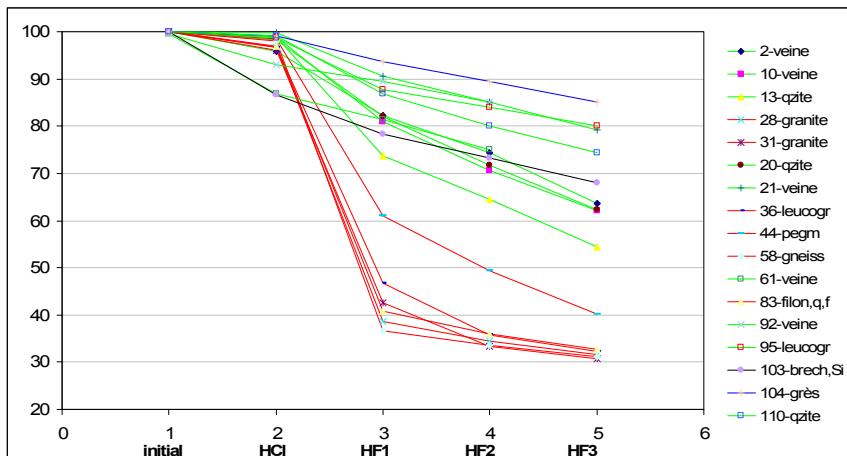


Figure 1 : Pourcentage de perte de masse des échantillons pendant la purification par bain HCl suivi de 3 bains HF à ultrasons. Les courbes rouges désignent les échantillons les moins riches en quartz (de type granite ou gneiss), les courbes vertes correspondant aux veines de quartz, la courbe bleue correspond à un grès et la noire à une brèche siliceuse. Les numéros d'échantillons correspondent à la série T7C- (exemple T7C-2, T7C-10, T7C-13 ect...).

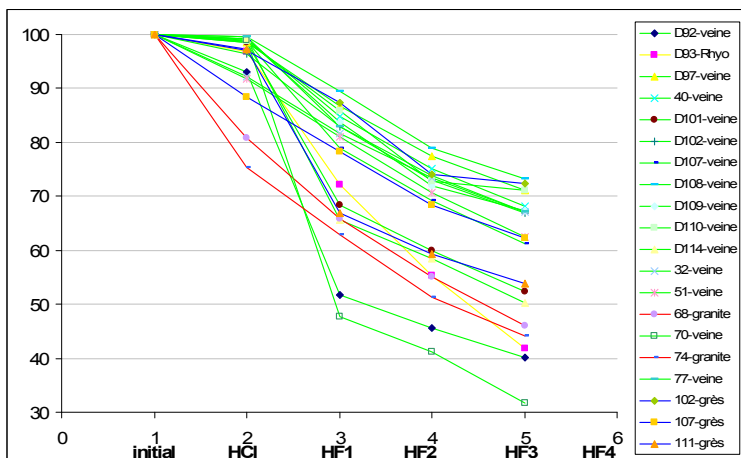


Figure 2 : Pourcentage de perte de masse des échantillons pendant la purification par bain HCl suivi de 3 bains HF à l'agitateur. Les courbes rouges désignent les échantillons les moins riches en quartz (de type granite ou gneiss), les courbes vertes correspondant aux veines de quartz, les courbes bleues aux grès et la courbe jaune est une rhyolite. Les numéros d'échantillons correspondent aux séries T5C- [Damxung] (exemple D92 = T5C-92, D93 = T5C-93) et T7C- (exemple 2=T7C-2 ect...).

Les bains à l'agitateur puis aux ultrasons :

Pour les échantillons de plus de 100g au départ (sables ou échantillons profonds), des bains HF à l'agitateur sont préalablement effectués pour limiter ensuite le nombre de bidons utilisés aux ultrasons). Les deux types de bains successifs sont aussi utilisés pour les échantillons encore impurs après le 4^{ème} bain-HF-agitateur. En fonction de l'opacité de la solution de rinçage et du type des grains restants (reconnu à la loupe binoculaire, dans la mesure du possible), 1 à 3 bains à ultrasons sont effectués après les 3 ou 4 bains-HF-agitateur.

4/ La dissolution de quartz

Entre 5 et 15 échantillons peuvent être dissous avec un blanc.

4-1/ L'ajout de standard

A chaque échantillon est généralement ajouté une quantité de standard de Be et d'Al connue (le porteur).

Pour le Be : 0,5 mg de standard (ou porteur) de ^9Be sont ajoutés avant la dissolution de quartz, car on suppose que la quantité naturelle de Be est insuffisante pour la mesure à l'AMS. Ce n'est pas toujours le cas, nous avons rencontré des exemples d'échantillon naturellement riches en Be : voir table III.3 (échantillon T7C-81/140/143/152/153). La quantité de Be total est systématiquement contrôlée après la dissolution pour vérifier l'excès ou la perte en Be (voir par exemple les échantillons T7C-56/74/76/90, T5C-93, Tables III.3 et III.5). En effet, il existe aussi des problèmes de perte de Be, la quantité de Be mesurée à l'ICP-MS après la dissolution est inférieure à la quantité pesée et ajoutée avant la dissolution. Ceci a lieu généralement pour les échantillons trop riches en aluminium (Table 2, III.3 et III.5).

Pour l'Al : Le standard d' ^{27}Al est ajouté uniquement dans le blanc avant la dissolution. Pour les échantillons, il est éventuellement ajouté après la dissolution, suite à la mesure de l'Al naturel à l'ICP-MS. Si l'échantillon contient plus de 2 mg d'Al, il n'est pas nécessaire d'ajouter du standard. Dans le cas contraire, il faut compléter à 2 mg avec le standard (voir paragraphe 6).

Préparation des solutions de standard dilué :

Pour faciliter les pesées les standards sont dilués 10 fois.

Standard (Be ou autre) dans l' HNO_3 :

- Tarer un flacon de 120 ml
- Prélever 10 ml (donc ~10 mg) de solution standard commerciale avec une micropipette
- Transférer dans le flacon puis peser les 10 ml, noter le poids exact ($\pm 10^{-5}$ près) après stabilisation de la balance.
- Tarer le flacon
- Prélever, transférer et peser 90 ml d' HNO_3 à 0,5 N, noter le poids exact
- Calculer la concentration du standard dilué.

Standard (Be ou autre) dans l' HCl à 2%

→ Voir carnet de laboratoire

4-2/ Les pesées d'échantillons et de standard dilué

Pesée des échantillons :

- Tarer une petite barquette
- Mettre 20 à 100 g d'échantillon dans la barquette (en fonction de l'altitude, la profondeur...)
- Peser la quantité de poudre puis vider le contenu dans un bêcher téflon annoté du numéro de l'échantillon
- Peser et noter le poids des quelques grains restants

Pesée du standard de ^9Be dilué :

Il faut peser un standard dilué par échantillons et un standard pour le blanc.

- Régler la micropipette sur 5 ml (plus ou moins en fonction de l'échantillon)
- Annoter un tube
- Tarer le tube ouvert avec son support
- Prélever 5 ml de standard de Be avec la micropipette et transférer dans le tube
- Peser les 5 ml et noter le poids
- Faire de même pour chaque échantillon et ne pas oublier le blanc

Pesée du standard de ^{27}Al dilué :

Avant la dissolution, pour l'Al, il suffit juste de peser la quantité de standard d'Al à ajouter dans le blanc :

- Annoter et tarer un tube de 50 ml sans le bouchon
- Peser 20 ml de solution standard dilué (donc 2 g d'Al) et noter le poids ($\pm 10^{-5}$ près)

4-3/ La dissolution

Ajout des acides et des standards, sous la hotte :

- Ajouter dans un bêcher téflon -100 ml de HF à 48%
 - ~6 ml de HNO_3
 - le standard dilué contenu dans les tubes préparés,
ATTENTION : bien mettre le standard correspondant à l'échantillon. Rincer 3 fois le tube de standard dans le bêcher téflon pour bien mettre tout le poids pesé.

La dissolution

- Mettre les échantillons sur la plaque chauffante en téflon, régler sur la 2^{ème} graduation, ~150°C (pas plus !)
- Ne pas oublier de couvrir avec les couvercles de téflon pour permettre la dissolution
- Laisser 12h (une nuit)
- Le lendemain vérifier que tout est dissout (en portant le masque), puis découvrir les bêchers en faisant attention de ne pas laisser goutter les couvercles dans les bêchers voisins pour ne pas faire de mélange. Laisser les couvercles sous la hotte sur un papier absorbant et laisser évaporer (du matin au soir)
- Faire couler l'eau sous la hotte pendant toute l'évaporation

5/ HClO_4 fuming

Les rinçage à l' HClO_4 (acide perchlorique) servent à éliminer un maximum de fluor (issu de l'HF) qui est un gros atome, afin de faciliter le passages des échantillons au colonnes ioniques.

ATTENTION : l' HClO_4 est à utiliser en faisant couler l'eau sous la hotte sinon il y a cristallisation de sels et risques d'explosion. ATTENTION, ne pas mettre en contact avec la matière organique, comme le papier absorbant, risques de brûlures.

1^{er} rinçage :

- Rincer les bords du bêcher avec de l'eau distillée (~5 ml)
- Ajouter ~5 ml d'eau distillée
- Ajouter 4 ml d' HClO_4
- Ajouter 10 ml d' HNO_3

-Laisser évaporer complètement, à la fin de l'évaporation vérifier le rinçage en tapotant le bêcher, si de la fumée blanche sort encore, laisser encore évaporer

2^{ème} rinçage : quand tout est évaporé et qu'il n'y a plus de fumée blanche

-Rincer les bords du bêcher avec la pissette (~5 ml)

-Ajouter 2 ml d' HClO₄

-Laisser évaporer

3^{ème} rinçage : idem

A la fin des 3 rinçages quand tout est évaporé, les échantillons se présentent sous forme de petite croûte au fond du bêcher (voir exemple du T7C-142 et du blanc Figures 3 et 4).

Les échantillons plus problématiques, généralement trop riches en aluminium, montrent une croûte qui couvre tout le fond du bêcher, pouvant aller jusqu'à 1 ou 2 cm d'épaisseur et ressemblant parfois à une meringue allant de la couleur blanche à marron foncé (voir exemples Figures 5 et 6). La mise en solution de ces échantillons est plus difficile (il se dissolvent plus facilement dans l'eau que dans l'acide).

Si l'Al et/ou le Be (ou tout autre élément) doivent être mesurés, poursuivre avec la préparation d'aliquotes, sinon passer au paragraphe 6-3.



Figure 3 : T7C-143



Figure 4 : Blanc EK310708



Figure 5 : T7C-41A sable



Figure 6 : T5C-50

6/ Mesures ICP-MS

6-1/ Préparation des aliquotes

-Verser 6 ml d'HCl 6N dans le bêcher, bien mélanger

-Transférer dans un tube 50 ml annoté

-Rincer le bêcher avec 30 ml d'ED

On obtient une solution de 36 ml de solution à 1N

-Centrifuger le tube

Les échantillons montrant un résidu important après l'évaporation présentent un dépôt conséquent après cette étape (Figures 7 et 8). Dans les cas normaux (T7C-96 Figure 7), il y a absence de dépôt.

-Passer en salle de pesée avec tout le matériel nécessaire

-Tarer un tube 50 ml annoté

-Transférer la solution surnageante du tube centrifugé dans le tube taré sans le dépôt (éventuellement finir avec une mauvette)

-Peser la masse de solution transférée

-Prélever 1 ml de cette solution

-Transférer dans un tube taré 15 ml

-Peser et noter le poids

-Diluer 10 fois en ajoutant 9 ml d'HCl 1N

-Peser l'HCl ajouté

L'aliquote est prêt pour la mesure ICP-MS



Figure 7 : Dépôts centrifugés des échantillons après dissolution à l'HF, rinçage à l'acide perchloriques et dissolution avant la mesure ICP-MS. Hormis l'échantillon T7C-96 (à gauche, sans dépôt) ils sont très riches en Al et présentent des pertes en Be par rapport à la quantité de standard introduite (voir la correspondance avec les mesures d'Al et de Be dans le tableau 2 ci-dessous). L'échantillon T7C-81 est un cas spécial puisqu'il montre 10 fois plus de Be que le Be standard introduit avant la dissolution. Cet excès est dû à un enrichissement naturel. Des excès ont aussi été rencontré pour d'autres échantillons (voir Mabja, table III.3)

Echantillon	Type de roche	Al (mg/ g qz)	Al ech (mg)	Be éch (mg) mesure ICP	Incertitude (mg)	Be éch (mg) pesé
T7C-68		8.97	178.90	0.34463	0.00398	0.48803
T7C-76		5.74	115.75	0.37759	0.00310	0.48656
T7C-81		9.35	186.37	4.79742	0.02002	0.48856
T7C-82		4.97	99.56	0.25142	0.00281	0.48555
T7C-84		9.90	173.02	0.55736	0.00462	0.48781
T7C-96		0.16	3.37	0.50079	0.00426	0.48826

Tableau 2 : Quantité d'aluminium et de beryllium dans chaque échantillon après la dissolution (20g de quartz dissoud)

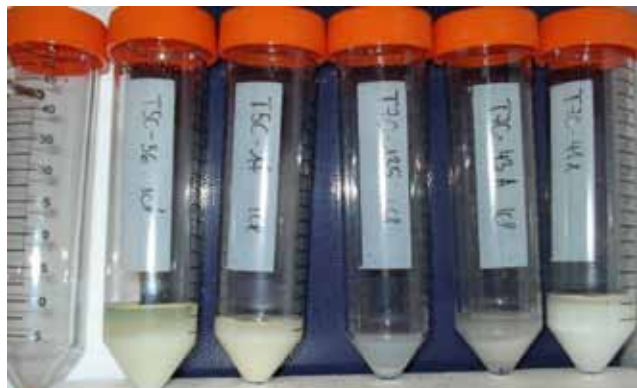


Figure 8 : Dépôts centrifugés des échantillons après dissolution à l'HF, rinçage à l'acide perchloriques et dissolution avant la mesure ICP-MS (autres exemples), (voir Tables III.3 et III.5 pour résultats de mesures Be et Al).

6-2/ Ajout éventuel des standards dilués d' ^{27}Al

Si l'échantillon contient moins de 2 mg d'Al, il faut compléter avec le standard.

Procéder comme dans la partie 3-2 pour peser la quantité de standard nécessaire.

Reprendre les solutions contenues dans les tubes 50 ml, ajouter les standards d'Al si nécessaire puis faire évaporer dans des bêchers téflon sur la plaque chauffante.

6-3/ Quand l'échantillon est complètement évaporé :

- verser 6 ml d'HCl 9N dans le bêcher téflon, bien mélanger pour dissoudre
- transférer dans un tube 15 ml à capuchon avec une mauvette (changée entre chaque échantillon !!)
- l'échantillon est prêt pour la colonne anion
- (-rincer les bêcher à l'ED avant la vaisselle)

7/ Colonne anionique

Références : Bierman et al. 2002 + Terra et al. 1986

Centrifugation

- Centrifuger les tubes pendant 10 minutes (5000 tours/min)
- Inscrire C sur le bouchon du tube centrifugé

Conditionnement (= lavage de la résine)

- Mesurer 60 ml d'HCl avec une éprouvette graduée
- Fermer le robinet de l'ampoule puis verser l'acide
- Placer un contenant-déchet sous la colonne, et vérifier que le robinet de la colonne est fermé
- Remplir l'entonnoir situé au dessus de la colonne pour le rincer
- Ouvrir le robinet sous la colonne
- Renouveler ensuite deux fois le rinçage (3 rinçages en tout)
- Rincer l'éprouvette à l'ED
- Vider le reste de l'ampoule avec la colonne bien bouchée * pour créer un goutte à goutte
- Vider le flacon-déchet dans le bidon-poubelle

*colonne bien bouchée : il faut créer une différence de pression : 1/ Fermer le robinet de la colonne. 2/ Verser jusqu'à la cassure de l'entonnoir. 3/ Mettre le bouchon 4/ Ouvrir le robinet de la colonne. 5/ Ouvrir le robinet de l'ampoule. 6/ Vérifier que le goutte à goutte fonctionne bien.

Fraction ANION 1

- Marquer les flacons 60 ml du mon de l'échantillon et de la fraction
- Fermer le robinet de la colonne
- Avant de transférer l'échantillon dans la colonne, vérifier que le fond du tube ne contient pas une sorte de gélatine, forme sous laquelle certains échantillons à problème peuvent se présenter. Dans ce cas, transférer l'échantillon dans un autre tube avant de transférer dans la colonne avec la mauvette.
- Utiliser la mauvette pour transférer l'échantillon liquide dans l'entonnoir de la colonne, ATTENTION de ne pas aspirer du précipité pour éviter le risque de bouchon dans la colonne et de devoir changer la résine.
- Changer de mauvette entre chaque échantillon ! Et noter la correspondance colonne-échantillon sur le cahier de laboratoire
- Ouvrir le robinet de la colonne
- Quand l'échantillon est passé, verser 35 ml de HCl 9N dans l'ampoule (robinet fermé)
- Remplir 3 fois l'entonnoir comme précédemment
- Vider le reste de l'ampoule avec la colonne bien bouchée
- le Be et l'Al seront contenues dans cette fraction

Fraction ANION 2

- Utiliser les flacons 125 ml, noter le N° d'échantillon
- Fermer tous les robinets
- Verser 80 ml d'HCl 0,1N dans l'ampoule
- Remplir une fois l'entonnoir puis laisser couler en goutte à goutte
- Cette fraction est à conserver jusqu'à l'analyse de l'échantillon, elle sera jetée ensuite si aucun problème n'est décelé.

Quand tout est passé, fermer les ampoules et les colonnes pour ne pas que la résine sèche, y mettre de l'ED si nécessaire. Fermer aussi le flacon contenant l'échantillon.

Evaporation ANION 1

- Prendre les flacons « anion 1 »
- Verser le contenu dans un petit bêcher téflon avec le nom de l'échantillon
- Mettre sur la plaque chauffante (la plaque noire de préférence)
- Quand tout est sec, ajouter 1 ml d'HCl 6N avec une petite éprouvette graduée, mélanger puis transférer dans un tube 15 ml nommé « cation »
- Ajouter 5 ml d'ED dans le bêcher téflon puis transférer dans le même tube avec la mauvette
- L'échantillon est prêt pour la colonne cation

8/ Colonnes cationiques

Centrifuger l'échantillon

Conditionnement

200 ml d'HCl 6N + 60 ml d'ED (2 rinçage d'entonnoir avant le goutte à goutte)

Fraction CATION 1

- Utiliser un flacon 120 ml annoté (N° ech + N° de fraction)
- Transférer l'échantillon dans l'entonnoir avec une mauvette sans aspirer le précipité

-Quand tout est passé, verser 80 ml d'HCl 1N dans l'ampoule (robinet fermé) puis dans la colonne (avec 3 remplissages d'entonnoir pour commencer)
→ Fraction à conserver jusqu'à l'analyse

-Noter la correspondance colonne-échantillon sur le cahier de laboratoire

Fraction CATION 2 → Be

-Changer de flacon, utiliser un flacon 120 ml annoté (N° ech + N° de fraction)
-verser 100 ml d'HCl 1N dans l'ampoule puis dans la colonne
→ Cette fraction contient le Be

Fraction CATION 3

-Changer de flacon, utiliser un flacon 120 ml annoté (N° ech + N° de fraction)
-verser 100 ml d'HCl 1N dans l'ampoule puis dans la colonne
→ Fraction à conserver jusqu'à l'analyse

Fraction CATION 4 → Al

-Changer de flacon, utiliser un flacon 120 ml annoté (N° ech + N° de fraction)
-verser 80 ml d'HCl 2,5N dans l'ampoule puis dans la colonne
→ Cette fraction contient l'Al

Evaporation CATION 2 ou 4

-Verser la solution des flacons dans un grand (de préférence) bêcher téflon
-Mettre sur la plaque chauffante à 150°C maxi
-Attendre l'évaporation totale

Redissolution du précipité

-Verser 2 à 3 ml d'HCl 6N dans le bêcher téflon avec une petite éprouvette graduée.
-Mélanger pour bien dissoudre
-Transférer dans un tube 15 ml
(-Rincer le bêcher téflon pour la vaisselle)
-Vérifier si la solution obtenue est trouble, si oui, il faut centrifuger et transférer la solution dans un autre tube.
-Test du Ti à l'H₂O₂ (2-3 gouttes) si nécessaire (solution rouge = présence de Ti)

9/ Hydroxylation

-Ajout de 2 ou 3 ml d'ammoniaque (NH₄OH) avec une mauvette.
ATTENTION 1 - l'ammoniaque s'évapore très vite
ATTENTION 2 - CHANGER LA MAUVETTE ENTRE CHAQUE PRELEVEMENT MÊME POUR UN MÊME ECHANTILLON pour ne pas contaminer le NH₄OH.
ATTENTION 3 - trop d'ammoniaque provoque une redissolution du Be, il faut rester à pH 8 pour ne pas perdre de Be (voir protocole du CEREGE).
-La solution devient légèrement trouble, laisser reposer quelques heures, voire une nuit pour que le Be précipite complètement.

-Pour les échantillons contenant du Ti, et s'il y a besoin de l'éliminer : faire précipiter le Ti (avant le Be) en ajoutant environ 25 gouttes de NH₄OH en secouant régulièrement le tube pendant la goutte à goutte pour homogénéiser. Ainsi, un précipité vert clair devrait apparaître.

Rinçage du NH₄OH

- Centrifuger les tubes pendant 10 min
- Vider la solution surnageante, le précipité reste au fond du tube
- Verser de l'ED sur le précipité jusqu'à 6 ml
- Secouer (avec le secoueur automatique)
- Centrifuger à nouveau 10 min
- Renouveler 2 fois (3 rinçages au total)
- Inscrire R sur le capuchon

10/ Chauffage

-Transfert du précipité dans un creuset en quartz avec une mauvette, puis rincer le fond du tube avec 3 gouttes d'ED maximum, rincer la mauvette aussi, puis tout mettre dans le creuset
-Couvrir avec un couvercle en quartz

ATTENTION 1 - changer de mauvette entre chaque échantillon

ATTENTION 2 - faire un dessin de la barre en métal dans laquelle sont disposés les creusets pour ne pas inverser les échantillons

-Mettre dans l'étuve à 70-100°C pendant 1 à 2 jours pour que l'eau s'évapore

-Ensuite mettre au four à 750°C pendant 1 heure.

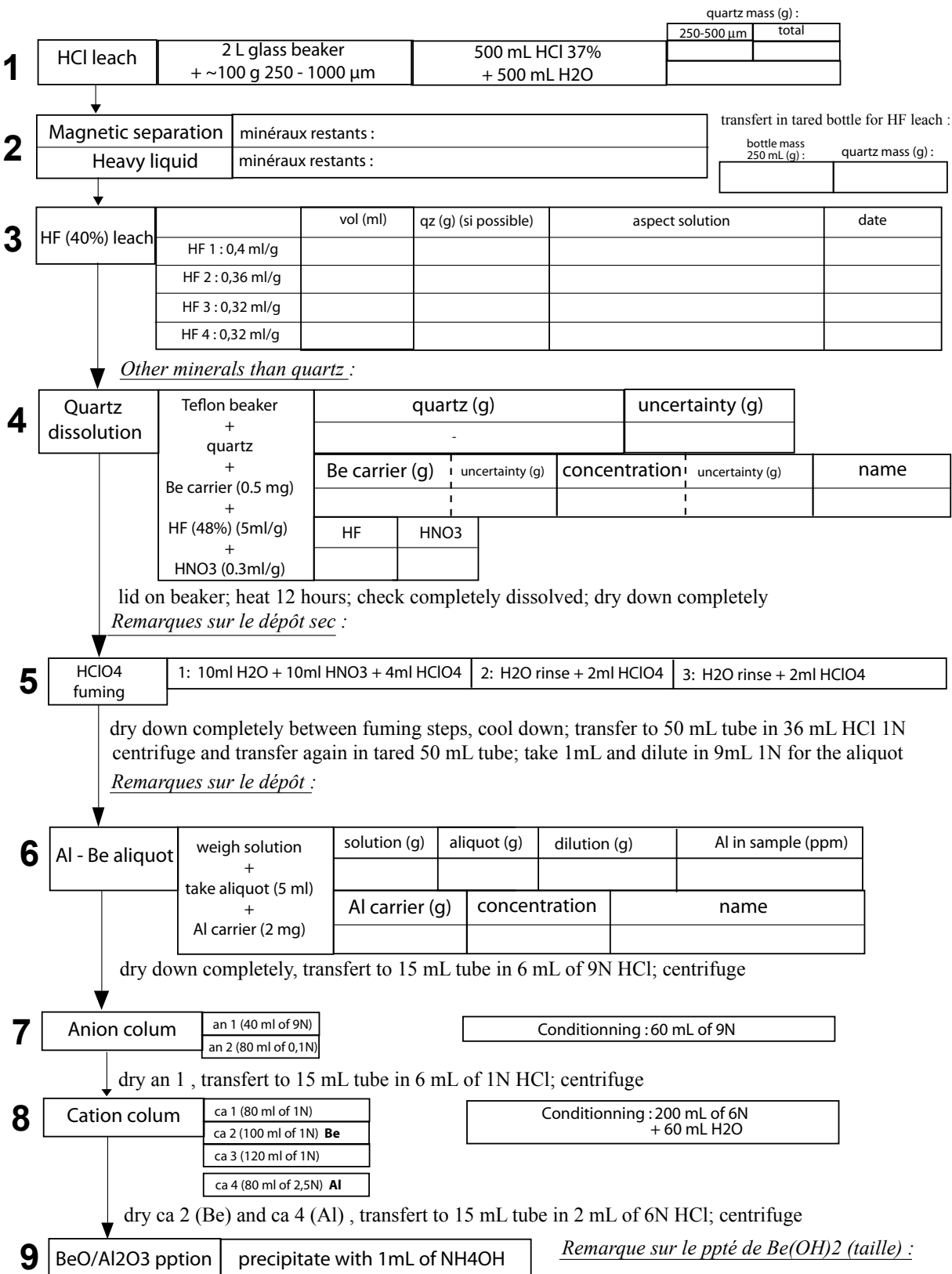
-Arrêter le four et laisser les échantillons refroidir à l'intérieur pour éviter un choc thermique aux creusets en quartz. Sortir du four le soir.

-Conditionner avec parafilm dans un tube rembourré avec du papier absorbant pour l'envoi au CEREGE.

SITE:
type :
mineralogy :

SAMPLE:

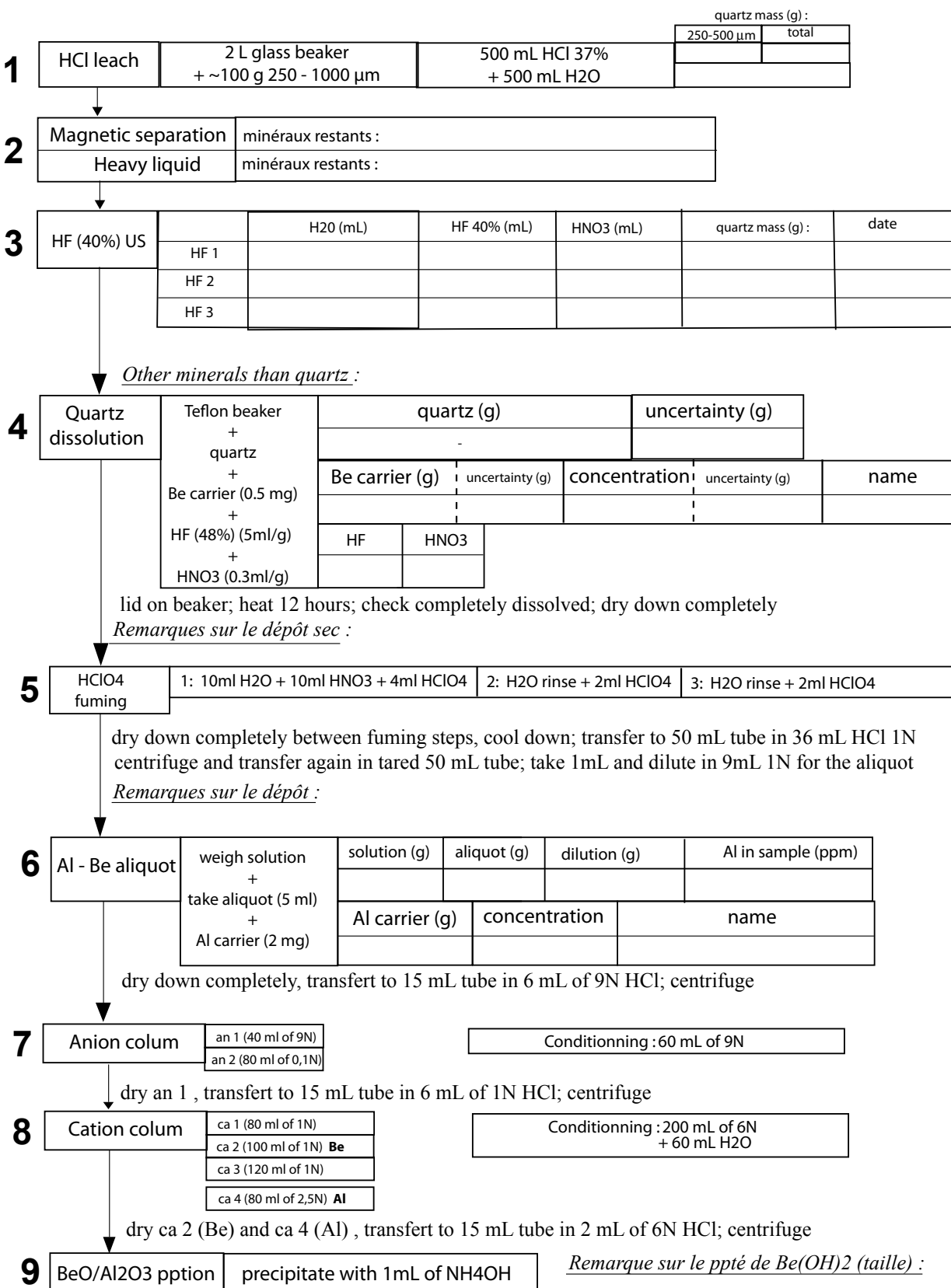
DATE:



SITE:
type :
mineralogy :

SAMPLE:

DATE:



Résumé

Quantifier l'extension long-terme (quaternaire) et court-terme (mio-pliocène) au niveau des massifs de l'Ama Drime et du Nyainqntanglha (Sud-Tibet), par une approche géochronologique multi-méthodes, permet de mieux comprendre le rôle de l'extension dans l'évolution du plateau tibétain, dans le contexte de la convergence Inde-Asie.

Au niveau de l'Ama Drime, l'exhumation tardive a eu lieu entre deux zones de cisaillement N-S en deux épisodes: une 1^{ère} phase entre 12 et 9 Ma, à ~3-4 mm/an (exhumation verticale apparente) dans la zone de cisaillement Est et une 2^{ème} phase, depuis au moins 4 Ma, à ~1 mm/an sur l'ensemble du massif. Au niveau du Nyainqntanglha, l'initiation de l'exhumation a eu lieu entre 10 et 8 Ma. Ceci implique une vitesse moyenne d'exhumation verticale apparente de ~1 à 1,2 mm/an. Cependant, les relations âge-altitude indiquent des vitesses 1,5 à 6 fois plus lentes.

Concernant les déformations court-terme (pléistocènes-holocènes), pour les massifs de l'Ama Drime et du Mabja, les vitesses de glissement vertical le long des failles normales ont été estimées entre 0,7 et 1,7 mm/an. Ces vitesses sont comparables à la vitesse d'exhumation long-terme depuis 4 Ma. Pour le Nyainqntanglha, les vitesses verticales sont comprises entre 1,6 et 2,2 mm/an. Ces vitesses quaternaires semblent plus rapides que les vitesses d'exhumation long-terme depuis 10-8 Ma.

Ces résultats permettent d'estimer des vitesses d'extension de $1,3 \pm 0,2$ mm/an et $1,4 \pm 0,6$ mm/an le long de l'Ama Drime et du Nyainqntanglha, respectivement, depuis ~60 ka. En supposant des vitesses comparables pour les autres rifts N-S, une vitesse d'extension totale de $1 \pm 0,5$ cm/an est déterminée pour le Sud-Tibet.

Mots clés : Sud-Tibet, Extension, Faille normale, Ama Drime, Nyainqntanglha, Thermochronologie, Ages d'exposition, Morpho-tectonique

Abstract

Quantifying the short-terme (quaternary) and long-term (mio-pliocene) extension along the Ama Drime and Nyainqntanglha ranges (South-Tibet), with a multi-method geochronological approach, allows to better understand the role of the extension for the Tibetan plateau evolution, in the frame of the Indo-Asia convergence.

For the Ama Drime, the late exhumation occurs between two N-S shear zones in two phases: the first phase occurs between 12 and 9 Ma, with an apparent vertical exhumation rate of ~3-4 mm/yr in the eastern shear zone, and a second phase, since 4 Ma, at ~1 mm/yr on the whole massif. For the Nyainqntanglha, exhumation initiated between 10 and 8 Ma. This implies an averaged apparent vertical exhumation rate of ~1 to 1.2 mm/yr. However, age-elevation plots indicate much slower rates.

Concerning the pleistocene-holocene deformations, for the Ama Drime and Mabja ranges, the vertical slip rates of the active normal faults range between 0.7 and 1.7 mm/yr. These rates are comparable with the long-term exhumation rate since 4 Ma. For the Nyainqntanglha, vertical rates range between 1.6 and 2.2 mm/yr. These rates are faster than the long-term exhumation rates, since 10-8 Ma.

These results allow to estimate extension rates of 1.3 ± 0.2 mm/an and 1.4 ± 0.6 mm/an for the Ama Drime and the Nyainqntanglha ranges, respectively, since ~60 ka. Assuming similar rates for the other N-S rifts, a total extension rate of 1 ± 0.5 cm/yr is determined for South-Tibet.

Keywords : South-Tibet, Extension, Normal fault, Ama Drime, Nyainqntanglha, Thermochronology, Exposure ages, Morpho-tectonic